PETRA III:
A Low Emittance Synchrotron Radiation Source

Technical Design Report

Editors:
K. Balewski, W. Brefeld, W. Decking, H. Franz, R. Röhlsberger, E. Weckert
DESY, Hamburg, Germany

February 29, 2004

Authors and Contributors

I. Ascone[20], R. Bacher[6], K. Balewski[6], J. Bansmann[52], H.D. Bartunik[21], U. Becker[10], F. Beckmann[14], S. Bessedine[15], Ch. Betzel[46], P. Boesecke[8], R. Böspflug[6], J. Boster[6], G. Bourenkov[21], W. Brefeld[6], T. Brückel[11], Ch. Buhr[6], O. Bunk[27], S. Celik[6], J. Chwiej[63], R. Claessen[38], H. Dau[10], Z. Dauter[4], W. Decking[6], M. Denecke[12], R. Denecke[43], R. Dörner[44], W. Drube[6], P. Duval[6], M. Ebert[6], H.-J. Eckholdt[6], H. Ehrenberg[34], S. Eisebitt[3], M. Faesing[6], G. Falkenberg[6], J. Falta[40], R. Feidenhans'l[27], P. Fischer[23], R. Frahm[54], H. Franz[6], M. Fröba[45], T. Fujisawa[25], R. Gehrke[6], W. Gießke[6], G. Goerigk[11], H. Grabe-Celik[6], W. Graeff[6], J. Grenzer[51], G. Grossmann[32], G. Grübel[6], J.-D. Grunwaldt[9], P. Gürtler[6], L. Hänisch[6], U. Hahn[6], G. Henkel[50], S. Herb[6], Ch. Hermes[7], R. Hilgenfeld[49], K. Hodgson[33], U. Hoppe[52], T. Irving[17], D. Jagnow[6], K. Janssens[57], J.-P. Jensen[6], R.L. Johnson[46], L. Kipp[47], U. Klemradt[28], J. Klute[6], L. Kövér[2], W. Kook[6], J. Kouptsidis[6], T. Kracht[6], B. Krause[6], W. Krechlok[6], M. Krisch[8], G. Kube[6], Ch. Kumpf[55], V. Kuzminykh[5], V. Lamzin[7], M. Lankosz[63], U. Lauströer[6], L. LeFévre[20], A. Leslie[18], A. Leuschner[6], E. Levichev[5], T. Lippmann[14], K.D. Liss[35], D. Lott[14], D. Lützenkirchen-Hecht[54], A. Madsen[8], O. Magnussen[47], J. Maidment[6], E. Mandelkow[21], S. Mangani[64], M. Martins[46], R.V. Martins[14], P. McNally[26], S. McSweeney[8], W. Merz[6], J. Metge[14], W. Meyer-Klaucke[7], A. Meyer[46], M. Minty[6], T. Möller[6], W. Moritz[19], P. Müller-Buschbaum[36], A. Müller[45], K. Müller[6], M. Müller[47], U. Müller[3], B. Murphy[47], M. Nielsen[27], D.V. Novikov[6], F. Obier[6], R. Onken[6], H. Over[45], S. Panjikar[7], O. Paris[22], J. Penner-Hahn[61], J. Perez[31], M.V. Petoukov[7], A. Petrov[6], J. Pflüger[6], U. Pietsch[51], E. Pohl[7], A. Popov[7], J. Prenting[6], A. Pyzalla[37], B. Racky[6], D. Ramert[6], H. Reichert[23], R. Reininger[29], H. Requardt[8], K. Rickers[6,13], I. Robinson[60], J. Röhler[56], R. Röhlsberger[6], G. Rosenbaum[1], J.E. Rubensson[65], R. Rüffer[8], G.K. Sahoo[6], T. Salditt[41], M. Schmidbauer[16], H. Schmidt-Böcking[44], A. Schmidt[7], C. Schmidt[13], Th. Schmidt[40], R. Schmitz[6], J.R. Schneider[6], A. Schreyer[14], C. Schüssler-Langheine[48], W. Schütte[6], U. Schuetz[6], G. Schütz[23], H. Schulte-Schrepping[6], M. Schwartz[6], R. Scott[58], O.H. Seeck[11], M. Seidel[6], B. Sepiol[53], R. Serimaa[59], S.D. Shastri[1], Y.V. Shvyd'ko[46], H. Sinn[1], K. Sinram[6], M. Sladecek[53], S.v. Smaalen[39], J. Strempfer[23], N. Stribeck[46], V.N. Strocov[30], D.I. Svergun[7], M. Szczerbowska-Boruchowska[63], N. Tesch[6], A. Thompson[31], K. Tiedke[6], J. Tiessen[6], M. Tischer[6], L.H. Tjeng[48], M. Tolan[42], D. Trines[6], H. Tsuruta[33], P. Tucker[7], J. Ullrich[44], M.A. Vanoni[62], L. Vincze[57], P. Vobly[5], G. Vogl[53], A. Wanning[6], R. Wanzenberg[6], E. Weckert[6], G. Weichert[6], H. Weise[6], M. Weiss[7], E. Welter[6], M. Wendt[6], M. Wilke[51], S. Wilke[6], R. Willumeit[14], M. Wilmanns[7], K. Wittenburg[6], P. Wochner[23], J.C. Woicik[24], G. Wortmann[50], T. Wroblewski[6], W. Wurth[46], Li Yougjun[6], J. Zegenhagen[8], M.v. Zimmermann[6], K. Zolotarev[5]

[1]APS, Argonne, USA
[2]ATOMKI, Debrecen, Hungary
[3]BESSY, Berlin, Germany
[4]BNL, Upton, USA
[5]Budker Institute of Nuclear Physics, Novosibirsk, Russia
[6]DESY, Hamburg, Germany
[7]EMBL Outstation, Hamburg, Germany

[8]ESRF, Grenoble, France
[9]ETH Zürich, Switzerland
[10]FU Berlin, Berlin, Germany
[11]FZ Jülich GmbH, Jülich, Germany
[12]FZ Karlsruhe, Karlsruhe, Germany
[13]GeoForschungsZentrum, Potsdam, Germany
[14]GKSS Research Center, Geesthacht, Germany
[15]Humboldt-Universität Berlin, Germany
[16]Humbold-Universität, Berlin, Germany
[17]Illinois Institute of Technology, Chicago, USA
[18]LMB Cambridge, UK
[19]LMU München, Germany
[20]LURE, Orsay, France
[21]MPG-ASMB, Hamburg, Germany
[22]MPI Golm, Germany
[23]MPI Stuttgart, Germany
[24]NIST/APS, Argonne, USA
[25]RIKEN, SPring-8, Himeji, Japan
[26]RINCE, Dublin City University, Ireland
[27]RISØ Nat. Lab., Denmark
[28]RWTH Aachen, Germany
[29]Scientific Answers and Solutions, Madison, USA
[30]SLS, Villingen, Switzerland
[31]SOLEIL, Gif-sur-Yvette, France
[32]SRS, Daresbury Laboratory, Daresbury, UK
[33]SSRL, Stanford, USA
[34]TH Darmstadt, Germany
[35]TU Hamburg-Harburg, Germany
[36]TU München, Germany
[37]TU Wien, Austria
[38]Universität Augsburg, Germany
[39]Universität Bayreuth, Germany
[40]Universität Bremen, Germany
[41]Universität Darmstadt, Germany
[42]Universität Dortmund, Germany
[43]Universität Erlangen-Nürnberg, Germany
[44]Universität Frankfurt, Germany
[45]Universität Gießen, Germany
[46]Universität Hamburg, Germany
[47]Universität Kiel, Germany
[48]Universität Köln, Germany
[49]Universität Lübeck, Germany
[50]Universität Paderborn, Germany
[51]Universität Potsdam, Germany

[52]Universität Rostock, Germany
[53]Universität Wien, Austria
[54]Universität Wuppertal, Germany
[55]Universität Würzburg, Germany
[56]Universität zu Köln, Germany
[57]University of Antwerp, Belgium
[58]University of Georgia, Athens, USA
[59]University of Helsinki, Finland
[60]University of Illinois, Urbana, USA
[61]University of Michigan, Ann Arbor, USA
[62]University of Milan, Italy
[63]University of Mining and Metallurgy, Krakow, Poland
[64]University of Siena, Siena, Italy
[65]University of Uppsala, Sweden

Contents

Chapter 1

Introduction

During the past 30 years, research carried out at synchrotron radiation facilities has made significant contributions to basic as well as applied sciences. The development of experimental techniques answering a wide variety of scientific questions is progressing at an unprecedented pace. These improvements have always been strongly correlated to the advances in source brilliance. In the very beginning, scientists, mainly physicists, investigated the basic properties of synchrotron radiation. However, soon its unique properties were recognized: tunability over a large range of the electromagnetic spectrum, extreme collimation, very high intensity, polarization properties and a pulsed time structure. Synchrotron radiation experiments at the synchrotron of the Deutsches Elektronen-Synchrotron (DESY) were among the first and played a key role for the following developments. First experiments in 1967 concentrated on spectroscopic investigations of atoms in the VUV energy range for which no laboratory sources were available. Already in 1970 first small angle scattering experiments using X-rays were carried out on biological samples exploiting the small divergence of the beam. Today, the spectral range used for experiments extends from the infrared to the very hard X-ray range at several 100 keV. Since these early days when only few experts took on the effort to carry out pioneering experiments, the situation has changed dramatically and many synchrotron radiation techniques have reached a considerable state of maturity and a high degree of automation, thus, making these techniques available for a wide user community. The developments in many fields such as surface and interface physics, magnetism, absorption and fluorescence spectroscopy, or diffraction and scattering experiments at high photon energies would be unthinkable without synchrotron radiation. Another very successful field is structural biology, where meanwhile the fraction of protein crystal structures newly deposited in the Protein Data Base (PDB), and measured using synchrotron radiation, is approaching 90%.

Worldwide about 40000 scientists are using synchrotron radiation very often in an interdisciplinary approach. The operational German sources serve about 3000 users per year, 2000 of them using DESY facilities. The applications stretch over such different fields as atomic and cluster physics, condensed matter physics, chemistry, materials science, structural biology, crystallography, geo- and environmental science and medical science. In the beginning, scientists used in a ‘parasitic’ mode the radiation emitted from the bending magnets of synchrotrons and later of storage rings, built for particle physics research. These so-called first generation sources were soon followed by the 2^{nd} generation providing radiation from linear, periodic magnetic arrays of small dipoles, so-called wigglers, in addition to the radiation emitted by bending magnets. Such wigglers provide a 30–100 fold flux of a bending magnet. All these machines have in common relatively large particle beam cross sections of the order of one millimeter. They provide rather large photon beams, which are very well suited for studies of samples of milli- to centimeter sizes such as whole work pieces common in materials science.

For the 3^{rd} generation of synchrotron radiation sources a further, rather dramatic improvement of the photon beam quality has been achieved by exploiting the constructive interference of the radiation emitted from the individual poles of periodic magnetic structures called undulators. For these devices to function efficiently rather small and parallel particle beams are needed. These very demanding requirements and the fast growth of the user community led to the construction of dedicated synchrotron radiation sources specialized for serving undulators with particle energies matching the photon energy range needed for the main applications, e.g. BESSY II in Berlin for the VUV and soft X-ray regime and the European Synchrotron Radiation Facility (ESRF) in Grenoble for hard X-rays.
The main domain of undulator beams is the investigation of small samples or sample regions in the sub-millimeter to sub-micrometer range. The most suitable parameter to compare 3^{rd} generation sources is brilliance, that means the flux per second in a given energy range normalized to the size of the source and to the solid angle under which the radiation is emitted. In Fig. 1.0.1 the brilliance as a function of photon energy is compared for a number of synchrotron radiation sources. The dramatic increase in brilliance from 2^{nd} to 3^{rd} generation facilities has triggered a large number of new techniques and experiments unthinkable before. Meanwhile, focussing of hard X-rays down to a spot size of < 100 nm has been demonstrated at ESRF providing the possibility to analyze samples at very high spatial resolution. A high brilliance beam contains a considerable fraction of coherent photons enabling techniques like phase contrast imaging and X-ray photon correlation spectroscopy (XPCS) to become practical tools for the investigation of the static and dynamic properties of matter. The same holds for a number of other techniques where the basic feasibility was demonstrated at 2^{nd} generation sources but applications to scientifically interesting samples need the high brilliance of 3^{rd} generation sources.

At present, DESY is operating the storage ring DORIS III, a 2^{nd} generation synchrotron radiation source, at a positron energy of 4.45 GeV. The relatively high particle energy provides a considerable flux also at photon energies in the hard X-ray regime beneficial to a number of applications that require penetration into or through larger bulk specimen. The large positron beam at DORIS III provides relatively large photon beams which are ideally suited for the investigation of milli- to centimenter size samples. The corresponding beamlines are robust and easy to operate by users. However, small samples, extremely small foci, experiments at extremely high resolution in reciprocal space or in energy, or coherence experiments are beyond the capability of the radiation provided by this storage ring. For that reason DESY decided to rebuild its 2.304 km long storage ring PETRA II into a 3^{rd} generation synchrotron

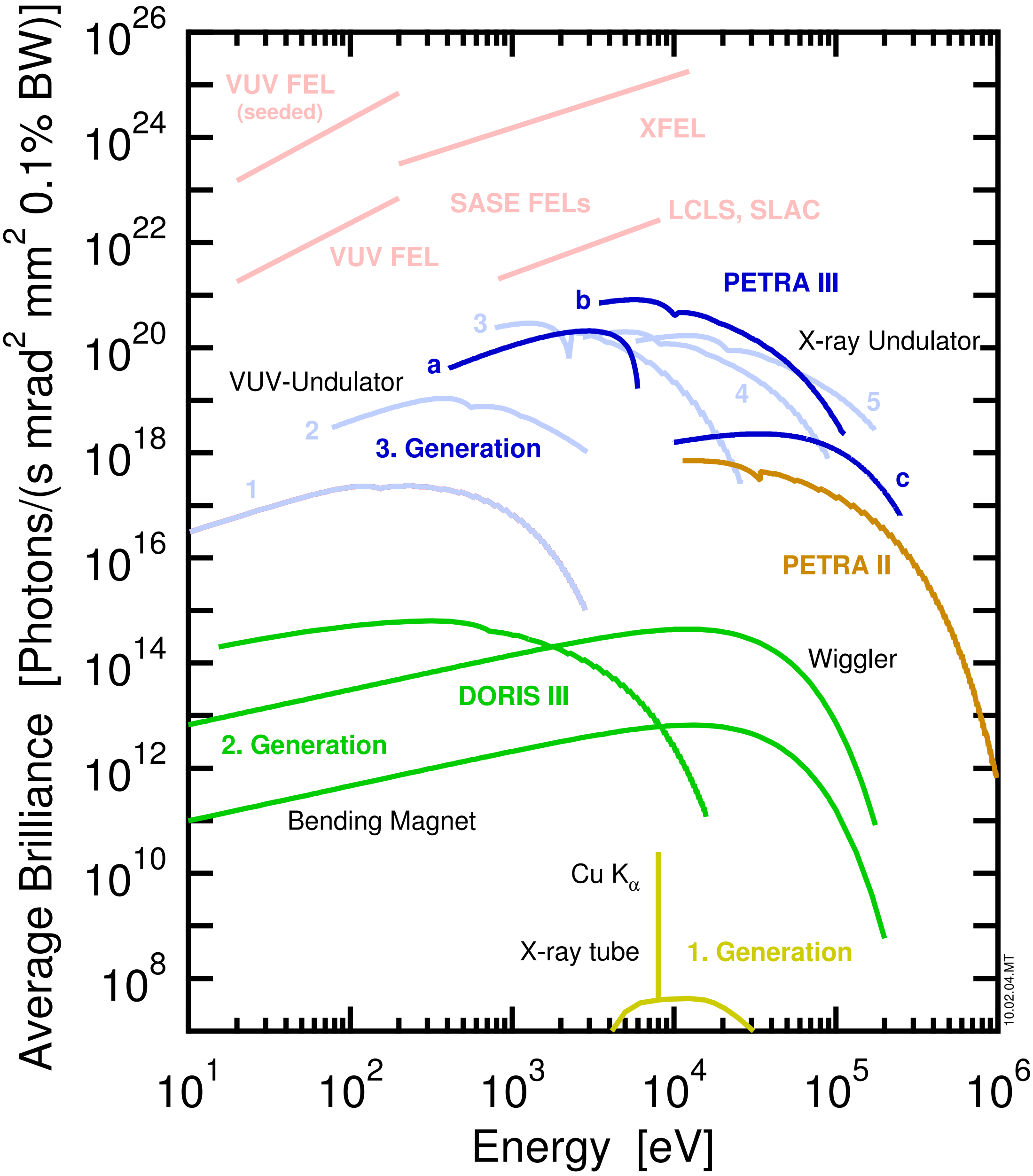

Figure 1.0.1: Average brilliance of synchrotron radiation and free-electron laser (FEL) photon sources available or planned at DESY compared with the actual performance of other 3$^{\mathrm{rd}}$ generation storage rings and the FEL for hard X-rays under construction at SLAC, Stanford. The tuning curves of the DORIS III sources are colored in dark green including the BW2 and BW3 wiggler. The other labels apply as follows: 1. BESSY II U125, 2. ALS U5, 3. DIAMOND U46, 4. ESRF ID16, 5. SPring-8 BL46; PETRA III: a. soft-X-ray undulator (4 m, high-β), b. standard $K_{max} \approx 2.2$ undulator (5 m, high-β), c. hard X-ray wiggler ($K_{max} \approx 7$, 5 m, high-β).

radiation source called PETRA III. The conversion of PETRA will start in 2007. The particle energy of this new source will be 6 GeV at an initial current of 100 mA. Present plans feature 13 independent undulator beamlines for experiments. The emittance of PETRA III will be 1 nmrad which is a so far unrivaled value for storage rings operated at a comparable high particle energy for the production of hard X-rays. PETRA III will provide a maximum brilliance of the order of 10^{21} ph/s/mm^2/mrad^2/0.1% BW with a considerable fraction of coherent photons also in the hard X-ray range. With a coupling ratio of 1% PETRA III will be diffraction limited in the vertical direction up to a photon energy of about 10 keV.
The choice of a particle energy of 6 GeV was motivated by an optimization for a small beam emittance, which scales with the square of the energy, and a sufficiently high particle energy which is needed to provide tunable high-energy photon beams with sufficient flux and brilliance.

After the conversion of PETRA, a number of unique sources will be available for the research with synchrotron radiation at DESY: (i) the high energy storage ring PETRA III for the investigation of matter with sub-millimeter to sub-micrometer spatial resolution, (ii) the storage ring DORIS III for applications that need high flux and that can use beams of millimeter size dimensions, (iii) the VUV-Free Electron Laser (VUV-FEL) for research with extremely intense and coherent photon beams in the VUV and soft X-ray regime down to 6 nm wavelength and pulses of $\approx$ 50 fs duration. In 2012, the planned European X-ray Free Electron Laser Laboratory (XFEL) should provide very short, extremely intense, coherent hard X-ray pulses up to about 12–14 keV photon energy with a peak brilliance about nine orders of magnitude higher than available today. This unique ensemble of X-ray sources will offer most attractive opportunities for photon science.

Today, the ESRF is serving the European synchrotron radiation community with brilliant photons mainly in the hard X-ray regime. However, the ESRF is heavily overbooked and can not fulfil all user requests for beamtime. In the somewhat softer energy range a number of medium particle-energy storage rings like SOLEIL close to Paris, DIAMOND near Oxford and the Spanish light source in the vicinity of Barcelona are planned or under construction in Europe in addition to the existing facilities ELETTRA, MAXLab, BESSY II and the Swiss Light Source (SLS). These facilities attract communities using the photons in the VUV as well as in the soft X-rays regime from undulators and X-ray photons up to about 10–20 keV from wigglers, wavelength shifters, and small gap in-vacuum undulators. With its particle energy of 6 GeV and the future upgrade possibilities for beamlines providing even extremely hard X-ray radiation, PETRA III fits very well into the whole scenario of European sources in order to serve the community with very brilliant X-ray beams at photon energies also well beyond 20 keV photon energy.

Furthermore, with its design parameters (see Sec. 2.2) and future upgrade possibilities the PETRA III storage ring represents a development about half way in between presently operating 3rd generation X-ray sources and what is, according to a theoretical study by the ESRF machine group, considered to be the ultimate storage ring. Especially the very small horizontal emittance is expected to provide significantly better conditions than presently available for the realization of very small focal spot sizes and for experiments exploiting the coherence properties of the beam. Therefore, the PETRA III upgrade represents a unique possibility to strengthen the research infrastructure in the harder X-ray regime and, probably more important, to provide a significant improvement for all techniques that require a low emittance source.

The design study presented in this report has been developed since year 2000 in close collaboration with the synchrotron radiation community and a large number of international experts in the field of beamline instrumentation and synchrotron radiation storage rings. Ten workshops were organized to exchange and discuss ideas.
The technical design concerning the conversion of the storage ring has already been preliminary reviewed by a panel consisting of the DESY machine advisory committee (MAC) and external machine experts from 3^{rd} generation synchrotron radiation sources. According to their first judgement the conversion of PETRA is '...considered to be a cost effective solution ...and ...a very clever design ...'. This panel is expected to accompany the storage ring part of this project.

Experiments requiring the high brilliance of PETRA III were discussed in a series of user workshops which led to a larger number of proposed experiments for PETRA III than the number of available undulator ports. After publication of this report, an external, international advisory board will be established to assist DESY in prioritizing these beamline proposals.

The next chapter in this technical design report will give a comprehensive overview of the PETRA III project including a short description of the proposed experimental stations. The following chapters describe in detail the conversion of the storage ring and the refurbishment of its infrastructure, the proposed insertion devices, the beamline vacuum system, the X-ray optics, and a detailed description of the science case as well as technical issues of the proposed experimental stations. The last chapters of this TDR deal with civil engineering, project costs and personnel requirements, schedule, and future upgrade possibilities.

Chapter 2

Executive Summary

2.1 Science at Low Emittance High-Energy Synchrotron Radiation Sources

Synchrotron radiation science experienced a tremendous boost during the past 10–15 years after the advent of 3^{rd} generation low emittance synchrotron radiation sources like ESRF (Grenoble), APS (Argonne) and SPring-8 (Harima) in the hard X-ray regime and ELETTRA (Trieste), BESSY II (Berlin), SLS (Villingen) and MAXLab (Lund) in the somewhat softer energy range. While the sources of first and 2^{nd} generation operating in parasitic or dedicated mode deliver intense X-ray beams from bending magnets and wigglers, 3^{rd} generation facilities use undulators as their main radiation sources. The total flux of a wiggler at a 2^{nd} generation source like DORIS III at DESY is not significantly smaller than the flux of an undulator beamline at a 3^{rd} generation source but it is distributed over a considerably larger solid angle, thus providing ideal conditions for the investigation of samples of about millimeter to centimeter size. In comparison, the source size of an undulator beam of a 3^{rd} generation source is about two orders of magnitude smaller providing ideal conditions for the investigation of much smaller samples or for micro- to nano-focussed beam. The commonly used quantity to characterize synchrotron radiation sources is the well known brilliance B[1]

$$B = \frac{F}{4\pi^2 \sigma_{Tx}\sigma_{Ty}\sigma_{Tx'}\sigma_{Ty'}} \tag{2.1.1}$$

where F is the spectral photon flux in photons/(s·0.1% BW); σ_{Tx} and σ_{Ty} are the total (index: T) photon source sizes in horizontal and vertical direction, respectively; $\sigma_{Tx'}$ and $\sigma_{Ty'}$ are the total beam divergence in horizontal and vertical direction[2]. Usually, all flux and brilliance values are given for a 0.1% energy bandwidth (BW) which is about seven times larger than the average intrinsic energy bandwidth behind a Si (1 1 1) monochromator. The total photon source size and divergence are given by the convolution of the sizes ($\sigma_{x,y}$) and divergences

[1] Brilliance is often called brightness in American literature. The definition of all quantities in this TDR are according to (Kim, 1995).

[2] All source sizes and divergences will be characterized by their RMS values assuming Gaussian shaped distribution functions.

($\sigma_{x',y'}$) of the electron beam with the intrinsic radiation characteristics ($\sigma_r, \sigma_{r'}$) of a single electron. For that reason the horizontal emittance

$$\epsilon_x = \sigma_x \cdot \sigma_{x'} \tag{2.1.2}$$

of a storage ring is of crucial importance for the photon beam parameters. The vertical emittance is given by $\epsilon_y = \kappa \cdot \epsilon_x$ with the so-called coupling factor κ that depends mainly on the precision of the alignment of the storage ring. Typical values for κ at present synchrotron radiation storage rings are in the range of 1 %. The brilliance is usually given in units of photons/(s mm^2 $mrad^2$ 0.1%BW) and characterizes the number of photons per unit phase space volume. Undulator sources at modern 3^{rd} generation storage rings are very well suited to produce high brilliance due to the small source size and the low divergence of the emitted radiation.
To a certain extent it is also possible to focus the relatively large beam of a wiggler of a 2^{nd} generation source onto a small sample area at the expense of an increased divergence in the focus. However, due to limitations in the achievable demagnification ratio and the small aperture of X-ray optical elements the large source size of 2^{nd} generation storage rings imposes a lower limit for the smallest achievable focal spot size. If an experiment requires both, high flux on a very small sample area and a beam as parallel as possible, then only 3^{rd} generation sources are able to fulfill these demands.

High brilliance is mandatory for a number of experimental techniques:

- Protein crystallography: For many proteins it is extremely difficult to grow large crystals. At the same time interesting structures get more complex, leading to weakly diffracting crystals with large unit cells and a very densely populated reciprocal space which requires a parallel and intense beam to resolve different diffraction orders.
- High resolution diffraction from small sample areas, especially from surfaces and interfaces: These techniques require a very parallel beam conditioned by slits to an appropriate size. Providing a high intensity beam under these conditions is not possible at a 2^{nd} generation source.
- Spectroscopy with sub-μm spatial resolution: These experiments require the smallest possible source size due to the achievable demagnification ratio and the limited aperture of the available X-ray optical elements.
- Small angle scattering with μm spatial resolution or very small samples: This technique requires a micro-focus beam but a divergence small enough to obtain sufficient resolution in the scattering pattern.

A low emittance storage ring operated in the 6–8 GeV range allows to generate well collimated undulator radiation up to quite high X-ray photon energies which have significant advantages in materials science applications where

- very small but intense photon beams can be generated for hard X-rays that are needed to penetrate large samples and components for 3D microscopy with sub-μm spatial resolution.

- Extremely small foci of hard X-rays will also allow for cone beam tomographic techniques for 3D imaging in the 100 nm resolution range.

The spectral flux F of such an undulator is significantly higher than that of a wiggler. Yet, since an undulator emits discrete energy bands the total heat load on the optical elements compared to the flux density available for the experiment is significantly lower than for a wiggler. For this reason an extremely high flux at the sample position can be generated with sufficient stability. This is a prerequisite for experiments that use only a very small wavelength bandpass of the incident radiation such as:

- Inelastic scattering: This technique only became a standard technique due to the availability of 3^{rd} generation synchrotron radiation sources. Experiments on μm-size samples like those used for high pressure studies are still a challenge and need very long data acquisition times.
- Nuclear resonant scattering: Since only a very small part of the energy spectrum of the incident photons can be used, experiments are flux limited at present 3^{rd} generation sources.

Every incoherent source like an undulator at a storage ring provides a certain fraction of coherent photons. The transversely coherent flux F_c is given by

$$F_c = B\left(\frac{\lambda}{2}\right)^2 = \frac{F\lambda^2}{16\pi^2\sigma_{Tx}\sigma_{Ty}\sigma_{Tx'}\sigma_{Ty'}}, \tag{2.1.3}$$

with λ being the photon wavelength. At a PETRA III undulator with a brilliance above 10^{20} ph/(s mm^2 mrad^2 0.1% BW) F_c will be about $4 \cdot 10^{10}$ ph/s in a monochromatic beam[3] at 12 keV photon energy. The transverse coherence length $\xi_{t(x,y)}$ of a beam from an incoherent source of size $\sigma_{T(x,y)}$ at distance L for a particular wavelength is given by

$$\xi_{t(x,y)} = \frac{\lambda \cdot L}{2 \cdot \sqrt{2\ln 2} \cdot \sigma_{T(x,y)}}. \tag{2.1.4}$$

The longitudinal coherence length ξ_l is determined by the monochromaticity of the beam:

$$\xi_l = \frac{\lambda^2}{\Delta\lambda}. \tag{2.1.5}$$

For the intrinsic line of an undulator the relative bandwidth is given by

$$\Delta\lambda/\lambda = 1/nN, \tag{2.1.6}$$

with N being the number of poles and n the harmonic number[4]. Thus the longitudinal coherence length of an undulator line is given by $\xi_l = nN\lambda$. These coherence properties promoted the development of new experimental techniques during the last years:

[3] Behind a Si (1 1 1) monochromator.

[4] In principle $1/nN$ has to be convoluted with the particle energy spread of the storage ring in order to obtain the true $\Delta\lambda/\lambda$. The energy spread contribution, however, is only significant for higher harmonics of very long undulators.

- X-ray photon correlation spectroscopy (XPCS): This technique allows to gain insight into the dynamics of materials on time and length scales that are not accessible with other methods like inelastic neutron scattering or laser correlation spectroscopy using energies in the visible spectral range.
- Phase contrast imaging: In samples where differences in absorption contrast are very small, the interference contrast of neighboring rays that experience slightly different phase shifts due to inhomogeneities of the index of refraction can clearly be detected. This experimental technique provides a totally new, non destructive imaging method mainly for low-Z materials.

The advantages mentioned above hold more or less for all 3^{rd} generation high-energy synchrotron radiation sources such as ESRF, APS and SPring-8. The emittance of PETRA III will be 1 nmrad. This is by a factor of three to four smaller than that of present sources. The smaller emittance translates directly to a smaller source size which results in a higher brilliance and a higher coherent fraction. The experiments that benefit most from the smaller emittance are:

- Micro- or nano-focus experiments; the smaller source size allows the realization of very small focal spots. Since at the same time the divergence of the radiation is also smaller, a significantly larger part of the total beam can be collected by optical elements leading to a higher focal flux density.
- High resolution diffraction experiments for the investigation of fine details in momentum space that derive from long range correlations in real space, because they need extremely high resolution in energy ($\Delta\lambda/\lambda$) and Q-space.
- Coherence applications like XPCS as mentioned before.

In addition to 'standard' size insertion devices that are available at most other synchrotron radiation sources, the geometry of PETRA III allows to install a number of very long (> 20 m) insertion devices. One of them will be implemented already in the first stage. Therefore, very high photon flux can be provided for some of the flux 'hungry' experiments mentioned above.

2.2 PETRA III Conversion Overview

2.2.1 Storage ring

The conversion of the PETRA storage ring will include the total rebuilding of one eighth of the storage ring to provide the electron beam optics for nine straight sections (see Sec. 3.1). Eight of them will provide space for one 5 m or two 2 m long insertion devices (ID). The two 2 m IDs will be inclined towards each other by 5 mrad. This scheme allows to operate two independently tunable undulators in a single straight section with beam paths sufficiently separated for individual beamline optics. The ninth straight section will be suitable for the installation of an insertion device up to a length of 25 m. From the present point of view and

	ϵ_x [nmrad]	E [GeV]	ϵ_x/E^2		ϵ_x [nmrad]	E [GeV]	ϵ_x/E^2
USR	0.3	7	0.006	SLS	4.4	2.4	0.763
PETRA III	1	6	0.027	ELETTRA	7	2.4	1.215
SPring-8	3.4	8	0.053	BESSY II	6	1.9	1.66
APS	3	7	0.061	Spear III	18	3	2
ESRF	3.9	6	0.108	MAX II	9	1.5	4
Diamond	2.5	3	0.2	ANKA	41	2.5	6.56
Soleil	3	2.5	0.48	DORIS III	450	4.5	22.2

Table 2.2.1: Emittance ϵ_x, particle energy E and normalized emittance ϵ_x/E^2 of a number of operating and planned storage rings. 'USR' denotes a study about an ultimate storage ring carried out by the ESRF machine group (Ropert et al., 2000). 'PETRA III' denotes the upgraded PETRA storage ring. Planned sources or feasibility studies are colored in green, sources under construction in blue and operational facilities in black.

taking into a account the available space in the experimental hall, a number of 13 insertion devices (one with 20 m, four with 5 m and eight with 2 m) are planned.
Due to the large radius of PETRA III, the angle between the beams of neighboring straight sections will be 5°. This angle does not allow to have large experimental stations using the radiation from the bending magnets between the undulator beams. However, depending on the exact layout of the undulator beamlines, the option to use radiation from the bending magnets downstream of each undulator will be kept open.
The design values for the new storage ring will be 6 GeV for the particle energy and 100 mA for the current. However, all components handling heat load or dealing with radiation safety will be dimensioned for a current of at least 200 mA in order to leave room for further upgrades. The envisaged particle energy of E = 6 GeV is a compromise between a small horizontal emittance $\epsilon_x \propto E^2$ and a particle energy E sufficiently high to provide also tunable beams of high photon flux in the energy range of 50–150 keV. A complete description of the new parameters of PETRA III is given in Sec. 3.1 and Tab. 3.1.1.
In addition to the straight sections located in the converted eighth of the storage ring, four straight sections with 64.8 m and another four with about 108 m length exist at PETRA. These straight sections will in part be used for damping wigglers (Sec. 3.4) with a total length of 80 m in order to reduce the emittance of the particle beam to its design value of 1 nmrad. Since the emittance of a storage ring scales quadratically with the particle energy, the quantity ϵ_x/E^2 can be used to compare different storage rings. In Tab. 2.2.1 the quantity ϵ_x/E^2 is listed for a number of storage rings that are in operation, under construction or planned. It is obvious that PETRA III compares favorably with present sources at higher particle energies. Only the parameters of a theoretical ESRF study for an ultimate storage ring (USR) would provide a lower emittance beam.
In order to ensure a reliable operation of the storage ring almost all magnet coils of the remaining 7/8 of the storage ring will be replaced (Sec. 3.3) as well as the whole vacuum system (Sec. 3.5). In addition, further upgrades are necessary for the RF system of the storage ring (Sec. 3.6), the magnet power supplies (Sec. 7.2.3) and the cooling system (Sec. 3.13).

	β_x [m]	β_y [m]	σ_{Tx} [μm]	σ_{Ty} [μm]	$\sigma_{Tx'}$ [μrad]	$\sigma_{Ty'}$ [μrad]	ID-length [m]
low-β 5 m	1.3	3	36	6.0	28	3.7	5
high-β 5 m	20	2.4	141	5.5	7.7	3.8	5
low-β 2×2 m	1.4	3	37	5.7	27	5.4	2
high-β 2×2 m	16.2	2.6	127	5.3	9.3	5.5	2
20 m-ID	16	5	126	7.9	8.2	2.7	10
DW-drift	16	16	127	13	8.5	3.3	5
ESRF low-β	0.5	2.73	59	8.3	90	3	5
ESRF high-β	35.2	2.52	402	7.9	10.7	3.2	5
SPring-8	22.6	5.6	277	6.4	13	5	4.5
APS	15.9	5.3	217	12.6	15.3	5.7	4

Table 2.2.2: Overview of typical β functions, photon source sizes $\sigma_{x,y}$ and divergences $\sigma'_{x,y}$ for various ID positions at different storage rings compared to PETRA III. The photon source parameters are given in RMS values for a photon energy of 12 keV. '2×2 m' indicates the inclined undulator insertion device positions at PETRA III. 'DW-drift' denotes possible undulator positions in the straight sections outside the new, converted eighth of the PETRA storage ring. For this position, $\alpha_x = -0.7$ and $\alpha_y = 0.7$. The α values of all other PETRA III insertion device positions are zero which holds also for the dispersion in the straight ID sections. To calculate the values for PETRA III, SPring-8 and APS an emittance (coupling) of 1 nmrad (1%), 3.4 nmrad (0.2%) and 3 nmrad (1%) was assumed, respectively. All values are calculated from published β-functions and emittances using SPECTRA (Tanaka & Kitamura, 2003). ESRF values were taken from *ESRF Highlights 2003*.

The Touschek lifetime is decreasing with the emittance of a storage ring. For this reason the standard bunch filling pattern will consist of a large number (960 bunches corresponding to 8 ns bunch distance) of equally spaced bunches with comparatively low charge. The lifetime for higher charged bunches for timing modes of operation (e.g. 40 bunches with 192 ns bunch distance) at 100 mA will be as low as 2 h compared to about 24 h for the 960 bunch mode. Considering the very good experience of SLS and APS in terms of thermal stability of the storage ring as well as the X-ray optical elements, a topping-up injection mode of operation is foreseen. Since the time between top-up injections can be as small as 70 s for a 40 bunch filling pattern in order to keep the current constant within 1%, a very high availability for the injector (Sec. 3.8) and pre-accelerator systems (Sec. 3.16) is required demanding also significant refurbishments of these systems. The RMS-bunch length at PETRA III will be about 40 ps.

In Tab. 2.2.2 the planned β-functions ($\beta_{(x,y)} = \sigma_{(x,y)}/\sigma_{(x',y')}$, see also Eq. 2.1.2) as well as photon source sizes and divergences in the straight sections of PETRA III are compared to those at other high energy synchrotron radiation sources. Similar to the ESRF there will be the option to have either a low or a high-β value in a straight section of the converted eighth of the storage ring. According to present plans the possibility to switch between these two β-function values during a short shut down period is envisaged. The vertical beam parameters of present high-energy 3rd generation SR sources are very similar since all of them are close

to the diffraction limit in this direction. Therefore, the improvement provided by PETRA III is mainly for the beam parameters in the horizontal direction.
The experiments can only benefit from the small source sizes if the beam stability is very high. For this reason a suitable diagnostics (Sec. 3.9) and beam position control system will be established.

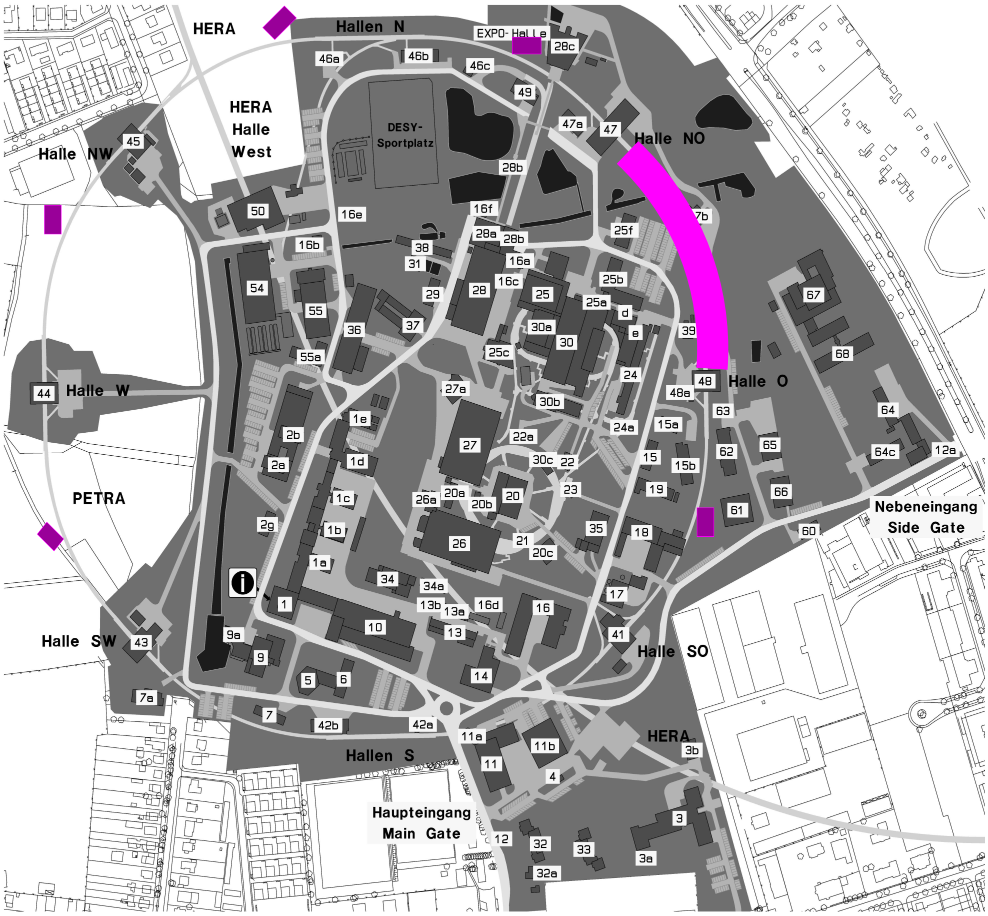

Figure 2.2.1: Schematic position of the new experimental hall (magenta) situated between buildings 47 and 48. Additional buildings for experiments are sketched in dark magenta at positions where further undulator beamlines could be placed in future.

2.2.2 Experimental hall

A new experimental hall (see Chapter 7) will be built at the rebuilt eighth of the storage ring. Its location is schematically indicated in Fig. 2.2.1. Designs for the experimental hall are based on the experience at other synchrotron radiation facilities. The requirements for the floor stability of a synchrotron radiation facility of very low emittance are extreme. Therefore, the whole ring tunnel in the new eighth of the storage ring will be rebuilt and located inside the experimental hall. Both shielding walls will be of 1 m thickness and cast out of heavy concrete. The tunnel roof will consist out of 0.5 m thick removable concrete blocks. The experimental hall will be equipped with a crane able to lift up to 20 tons. The present planning foresees to cast the floor in the experimental hall as one concrete slab about 1 m in thickness which will carry the ring tunnel and the experiments. This slab will be vibrationally decoupled from the experimental hall super structure and the auxiliary buildings. Other possibilities for the design of the experimental hall floor are still under investigation. The dimensions of the hall are such that beamlines can be up to 103 m long inside the experimental hall. For experimental hutches outside the main hall the following options exist:

- The first undulator (20 m ID, counting starts at hall 47) has space for a 210 m long beamline.
- The beamlines of the second and third ID can be extended up to 150 m length.

The air conditioning of the hall will be designed for a temperature stability of ± 1 K. Along the outer perimeter of the experimental hall there will be laboratory and workshop space in the ground floor and office space in the first floor among other necessary infrastructure and facilities. The total space for laboratories and offices amounts to about 1800 m^2. The hall will be accessible from both ends by doors large enough for trucks. In addition there will be four entrances along the outside of the hall large enough for smaller fork lifters.

2.2.3 Expected photon beam performance

The characteristics of the electron beam have already been shortly described above (see Sect. 2.2.1). The vacuum chamber inside the undulators will have an internal aperture of 7 mm. This means that the minimum magnetic gap of the undulators will be limited to a value of about 9.5 mm. In Fig. 2.2.2 the tuning curves of typical PETRA III undulators as well as the flux at higher photon energies through a 1 mm^2 pinhole in 35 m distance from the source are compared with those of existing 3^{rd} generation synchrotron facilities. A more detailed discussion of the PETRA III insertion devices is given in Chapter 4. The majority of the undulators will be designed to be tunable over the whole wavelength regime (K_{max} $\approx$2.2). The highest brilliance available will be above $10^{21}\,\mathrm{ph/(s\,mm^2\,mrad^2\,0.1\%BW)}$. The maximum brilliance of a 2 m insertion device is about 3.2 times less than the one of a 5 m ID while a 20 m ID provides about 2.7 times the brilliance of a 5 m device. This relatively small increase is due to the necessary change in β-function in order to be able to operate such a long device. The increase in flux scales approximately with the length.
The transverse coherence lengths (Eq. 2.1.4) calculated from the values in Tab. 2.2.2 are listed in Tab. 2.2.3. The total coherent flux (Eq. 2.1.3) at about 12 keV is $4 \cdot 10^{10}, 10^{11}$ and $2.5 \cdot 10^{11}$ ph/s/0.01%BW for a 2 m, 5 m and a 20 m insertion device, respectively. With a horizontal and vertical emittance of $\epsilon_x \approx$ 1 nmrad and $\epsilon_y \approx$ 0.01 nmrad, PETRA III will be a diffraction limited source up to photon energies of about 10 keV in vertical direction and up to 100 eV in the horizontal direction, i.e. $\epsilon_x \epsilon_y \leq (\lambda/4\pi)^2$.
Fig. 2.2.2b shows that the photon flux of a high flux wiggler at PETRA III at photon energies

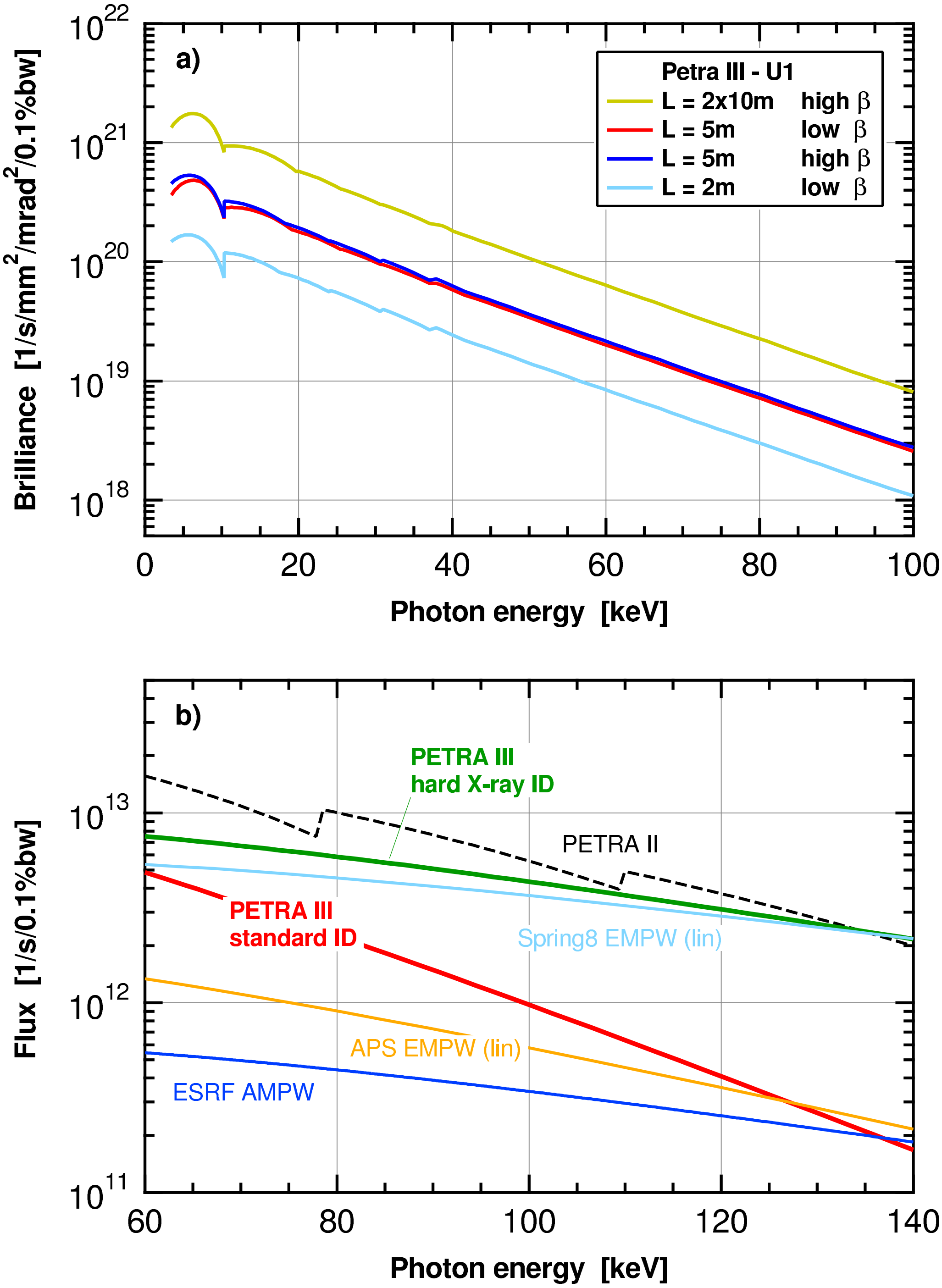

Figure 2.2.2: a. Comparison of the brilliance of typical PETRA III K_{max}=2.2 undulators for different length and β functions (according to Tab. 2.2.2) for the following parameters: 1 nmrad emittance, 1% coupling, 100 mA current, 9.5 mm minimum gap and 29 mm period. b. Flux through a $1 \times 1\,\mathrm{mm}^2$ pinhole at 40 m source distance for a number of high-energy radiation insertion devices. The source distance for the PETRA II undulator is 100 m. Note, this comparison is only relevant for apertures <1 mm.

	$\xi_{t,x}$	$\xi_{t,y}$
high-β	18 μm	500 μm
low-β	72 μm	460 μm

Table 2.2.3: Horizontal and vertical coherence lengths at PETRA III in FWHM calculated for 1 nmrad emittance and 1% coupling at 12 keV photon energy and at 60 m distance from the source.

around 100 keV through a 1 mm^2 pinhole is higher than that of a standard $\mathrm{K}_{\mathrm{max.}} \approx 2.2$ undulator. Very likely both devices will be outperformed by superconducting undulators if the development advances so far that these devices can be manufactured with a phase error small enough for the effective use of the higher harmonics of the spectrum. Another interesting and new development that should be kept in mind are variable period undulators (Shenoy et al., 2003a; Shenoy et al., 2003b).
It should be emphasized that the brilliance calculations above are based on the assumption of a 1% horizontal/vertical coupling. A smaller coupling value would further increase the brilliance especially at higher photon energies due to a smaller vertical source size. However, it will also further reduce the Touschek lifetime. The main difference between PETRA III and current high-energy, 3$^{\text{rd}}$ generation synchrotron radiation sources will therefore be in horizontal emittance which results in a smaller horizontal source size and therefore a larger total fraction of coherent photons or a higher number of photons in a given microfocus.
For photons in the VUV and XUV range, a high-energy storage ring has significant advantages for experiments needing circular polarized photons in the 200–2300 eV range with a high degree of polarization, which can only be obtained in the first undulator harmonic of a helical undulator. The performance of such devices is discussed in Sec. 4.1.1.

2.3 Proposed Experimental Stations

A detailed description of all proposed experimental stations including a description of the scientific applications is given in Chapter 6. In order to define the experimental stations to be proposed for PETRA III a number of user workshops were organized in the years 2002 and 2003 at DESY and the following criteria have been applied for beamline proposals:

1. Exploitation of the unique properties of the X-ray beams provided by PETRA III.
2. Implementation of innovative developments and techniques.
3. Consideration of the requirements of the specific HASYLAB user community.
4. Complementarity to other existing opportunities at large scale synchrotron radiation facilities in Europe and at upcoming X-ray free-electron lasers.

In the following a list of the titles of beamlines or experimental stations proposed for PETRA III is given:

- X-ray diffraction and imaging
  - High energy X-ray diffraction
  - Coherence applications
  - High resolution diffraction
  - Micro- and nano-tomography
- High energy resolution spectroscopy
  - Inelastic scattering
  - Nuclear resonant scattering
- Materials science
  - High energy X-rays for materials science
  - Powder diffraction
  - Small angle scattering
  - Microfocus applications
- X-ray absorption and resonant scattering
  - Absorption spectroscopy
  - High-energy photoelectron spectroscopy
  - Hard X-ray microprobe
  - Resonant scattering
  - Variable polarization XUV beamline
- Structural biology
  - Macromolecular crystallography (EMBL proposal for three stations, MPG proposal for two stations)
  - Biological absorption spectroscopy
  - Biological small angle scattering

In the following sections each proposed station will be described briefly. A full description of each proposal can be found in Sec. 6. For the final layout of the experimental hall it is assumed that in many cases more than one experimental station can be operated in time sharing mode on a single undulator beamline if the requirements for the beamline optics are similar.

2.3.1 X-ray diffraction and imaging

2.3.1.1 High energy X-ray diffraction

With the development of high-energy 3rd generation synchrotron radiation sources, high-energy X-ray diffraction became a powerful tool for the analysis of bulk materials and buried interfaces by the use of extremely collimated and small beams. Since the absorption lengths above 100 keV for most materials lie in the range of 0.1 mm to several cm, studies on thick samples become feasible. For the same reason, thick window materials for sample environments as cryostats or furnaces become less critical or even negligible. Moreover, difficult corrections for absorption, extinction and multiple scattering effects can be avoided in many cases. Another important feature of high-energy X-rays is that reciprocal space can be mapped up to large momentum transfers such as 30–50 Å^{-1}, which is crucial for precise structure determination of liquids and amorphous materials. Up to now most applications of hard X-rays have addressed bulk properties of thick samples. However, the application of high-energy diffraction methods becomes particularly attractive if combined with microfocusing techniques. The high penetration depth allows one to directly access ordering phenomena and phase transitions at buried interfaces that are not accessible with any other technique. It is expected that such studies can be extended into new areas by using high-brilliance X-ray beams delivered at PETRA III.

Using a particle energy of 6 GeV the flux density at 100 keV photon energy delivered by a PETRA III undulator or wiggler is one or two orders of magnitude and the brilliance is more than four orders of magnitude larger than the most powerful hard X-ray insertion device at DORIS III. Upcoming new insertion device techniques, like superconducting in-vacuum undulators, and the very small emittance of PETRA III will provide an even more brilliant beam at higher photon energies. The beam will be further concentrated by refractive lenses and/or bent monochromator crystals. The beamline will be optimized for an energy range of 50–100 keV. A minimum focal spot size in the micrometer range is envisaged for the investigation of buried layers or small volume elements inside larger bulk samples. The beamline will be equipped with a flexible high precision diffractometer. However, there will also be enough space for special setups developed by users.

2.3.1.2 Coherence applications

A recent development at modern synchrotron radiation sources is the use of coherent undulator radiation for both, scattering and imaging applications. If coherent light is scattered from a disordered system it gives rise to a random diffraction or "speckle" pattern. Such a "speckle" pattern is an interference pattern and related to the exact spatial arrangement of the disorder although phase information is lost. Major progress has however been made in recent years (e.g. by the oversampling technique) to retrieve this phase information, thus allowing to reconstruct the pattern and to unravel real space information.
The improved coherence parameters at PETRA III (almost 100 μm spatial coherence length in the low-β configuration, see Tab. 2.2.3) will facilitate the reconstruction of complicated patterns and allow access to shorter (eventually atomic) length scales. One might anticipate

that even disorder in magnetic systems will become accessible. This will only be possible due to the high brilliance B and the correspondingly increased coherent flux $F_c=(\lambda/2)^2 \cdot B$ provided by the PETRA III undulators.
The unprecedented coherence properties of the PETRA III source will also impact imaging techniques in the near field or Fresnel limit. Phase contrast imaging will benefit from an increased degree of coherence and the increased flux will allow not only to improve the resolution but might enable time series of phase contrast images limited only by the detector frame rate.

Of outmost importance is the possibility to study the dynamics of disordered systems with coherent light: If the spatial arrangement of a system changes as a function of time the corresponding speckle pattern will also change and fluctuate. Characterization of temporal intensity fluctuations is usually performed by correlation spectroscopy techniques and X-ray photon correlation spectroscopy (XPCS) gives access to the slow (>ns) dynamics on length scales ($Q>10^{-3}$ Å^{-1}) not accessible to visible coherent light. Many applications lie in the soft condensed matter domain (dynamics of complex fluids, glass forming systems, or capillary wave dynamics) or in the area of critical fluctuations. Here it is in particular the increased coherent flux of the PETRA III facility that will allow to address questions of slow dynamics on even shorter length scales (<100 nm) than presently feasible. Furthermore, the improved beam parameters will permit the operation in heterodyne mixing mode (known from Dynamic Light Scattering) and to finally also address questions of non-equilibrium dynamics. The energy tunability, the polarization properties of the beam and the surface sensitivity of X-rays will allow XPCS to be applied to a multitude of surface/interface phenomena and to the dynamics of magnetic systems being barely possible or unachieved today.

2.3.1.3 High resolution diffraction

High resolution X-ray diffraction (HRXRD) using extremely collimated beams is widely used as a standard technique for structural investigations at a wide variety of length scales, from the atomic level to bulk behavior and to surfaces and interfaces. The technique is used for precise lattice parameter measurements to access very small changes in lattice spacing due to thermal expansion, strain, chemical composition, or due to the exposure to external fields, etc. At solid and liquid surfaces and buried interfaces HRXRD allows to determine parameters, such as layer thickness, chemical composition and interface roughness. By variation of the penetration depth in grazing incidence diffraction also depth-resolved studies are possible. Two-dimensional reciprocal space mapping methods are now standard for these applications. Lattice distortions and crystal quality can be examined by reflection profile analysis. Structural parameters of periodic and non-periodic nano- or mesoscopic structures can be investigated by high resolution reciprocal space maps.

The low emittance and high brilliance of PETRA III provides ideal beam conditions to generate a photon beam of ultra-high collimation and high monochromatization over a wide energy range. The high coherence length of the beam will provide access to length scales ranging up to tens of micrometers. The brilliance available also at higher photon energies (25–45 keV) will enable experiments at internal solid/solid and liquid/solid interfaces. This is of special importance, as interface processes are so far mostly studied in model surface experiments. The high brilliance will also allow in situ studies of process dynamics which determine diffusion, growth and phase transitions. Research on very small sample volumes and highly diluted materials will become feasible. The beamline will be equipped with an UHV chamber connected via a transfer tunnel to a UHV preparation chamber for surface research.

2.3.1.4 Micro- and nano-tomography

In recent years micro-tomography using synchrotron radiation became a valuable tool for the non-destructive three-dimensional investigation of specimens in fields such as medicine, biology and materials science. At DORIS III absorption- and phase-contrast techniques were developed and applied at photon energies in the range of 8 to 150 keV. At the wiggler-beamlines BW2, W2, and BW5, a public user instrument for microtomography makes use of the large, intense, and incoherent X-ray source. Experiments at DORIS III are optimized for performing absorption-contrast microtomography on large samples. Due to the divergence of the source the spatial resolution of a tomogram is limited to about 2 μm.

PETRA III will allow for new absorption- and phase-contrast techniques which make use of the coherence of the X-ray beam. Different features of the specimens can be mapped simultaneously. By using a standard setup the spatial resolution can easily be increased to resolve about 0.7 μm structures. For resolving smaller structures in the 100 nm regime new techniques have to be developed. Recently first results were obtained performing cone-beam tomography by creating a nanometer divergent X-ray source using a KB multilayer arrangement and magnifying the sample onto a two dimensional X-ray detector.
The standard user experiments for microtomography at PETRA III will require a large monochromatic, parallel and intense beam. The photon energies will range from 8 to 150 keV and the required beam size is about 5×1 mm^2. To achieve a smooth beam profile the beamline will have as few optical elements as possible. The experimental hutch will allow for a variable sample detector distance from almost 0 to 10 m. For cone-beam geometry, optical elements will be added to the beamline to achieve a divergent X-ray source in the nm regime. The high brilliance of PETRA III and the development of faster detectors will also enable time resolved tomographic studies.

2.3.2 High-energy resolution spectroscopy

2.3.2.1 Inelastic scattering

Inelastic X-ray scattering (IXS) with meV energy resolution allows one to study elementary excitations in condensed matter, providing detailed insight into the mechanisms of phase transitions and dynamic processes. These properties play a crucial role in nanoscale materials because the modification of the dynamic properties due to the reduced dimensionality very often forms the basis for a new functionality. In this field, inelastic X-ray scattering at PETRA III will open new research areas that are hardly accessible at existing facilities. Particularly exciting are the study of low-energy excitations in disordered metallic alloys and the study of lattice dynamics in high-T_c superconductors and correlated electron systems, for example. A unique feature of IXS at PETRA III will be the combination of inelastic scattering with microfocusing techniques. Experiments on smallest amounts of material like thin films, single crystallites within a polycrystalline material and tiny grains of material in diamond-anvil cells under extreme conditions of pressure and temperature will be possible. Metastable and non-equilibrium phases become accessible that can only be produced in small quantities like tiny crystals or thin films.

The small beam sizes available at PETRA III allow for a very efficient implementation of spectrometers with sub-meV resolution. This will help to clearly identify low-energy collective excitations that are often observed in disordered materials and in the vicinity of phase transformations. KB mirror optics will be used for the generation of sub-μm focal spots for the investigation of extremely small amounts of material. The instrument proposed here consists of a vertical spectrometer for the investigation of excitations in single crystals with 2–3 meV energy resolution and a horizontal spectrometer for the study of dynamical properties of disordered materials with sub-meV energy resolution. In general, the properties of the radiation delivered at PETRA III will stimulate the development of innovative experimental techniques in this field that are hardly possible at existing sources. The utmost performance of these techniques is achieved if the experimental stations are installed at the 20 m long undulator, because many of these experiments are strongly flux-limited. This will put this beamline significantly ahead of those that are currently in operation.

2.3.2.2 Nuclear resonant scattering

Nuclear resonant scattering (NRS) using synchrotron radiation has a long standing history in Hamburg since the first experiments almost 20 years ago at the DORIS storage ring. The advent of high-energy $3^{\rm rd}$ generation synchrotron sources has turned this method into a routine experimental technique. With increasing brilliance of the radiation, this method became sensitive to smallest amounts of material like single monolayers, nanoparticles and samples in high-pressure cells. This trend will continue at PETRA III, so that magnetic ordering and vibrational dynamics in reduced dimensions can be revealed. The narrow energy bandpass makes NRS an ideal tool to study dynamical properties on very short time scales. Examples are diffusive and relaxational processes that can be studied on time scales ranging from ps to μs. The much faster dynamics of phonons becomes accessible in an energy resolved mode with resolutions in the sub-meV range. Moreover, the high brilliance at PETRA III will allow for the application of ultrathin isotopic probe layers to study magnetic and dynamic properties with atomic resolution.

Due to the narrow linewidth of the nuclear resonances involved (typically some neV to μeV) NRS experiments are extremely flux hungry. For this reason such experiments have to be performed at the 20 m insertion device at PETRA III. An experimental station at this insertion device will provide $1.6 \cdot 10^7$ ph/s in an energy bandpass of 0.1 μeV. This is four times higher than on other NRS beamlines at present $3^{\rm rd}$ generation synchrotron radiation sources. Besides the established and widely used techniques where a resonant isotope is needed as part of the sample, the increased spectral flux available at PETRA III could make time-domain interferometry a more widespread technique. This offers the option to study dynamical properties of samples that do not contain resonant isotopes.

2.3.3 Materials science

2.3.3.1 High energy X-rays for materials science

The activities on the new high energy materials science beamline will be concentrating on three intersecting topics: Industrial research, applied research, and fundamental research. The industrial user community will be provided with fast, robust, and standardized experimental techniques and online data analysis routines. Applied research will focus on the in-situ investigation of real manufacturing processes, the optimization of systems of high interest (e.g. fuel cells, battery electrodes), "classic" as well as cutting edge materials (e.g. Mg-base alloys, TiAl, trip-steel, bulk metallic glasses, composites, ceramics, "smart materials"), and materials processing. Fundamental research will yield new insight in the field of metallurgy (e.g. micro structure, grain boundary engineering or the understanding of complex phenomena such as plastic deformation), rapidly emerging fields like biomimetics (e.g. biomineralization) and nanoscience. The length scales at which the different experiments are aiming at will range from the macroscopic over the mesoscopic scale down to the investigation of nano structures, atoms, and their displacements down to the range of 10^{-15} m. All applied techniques will be non-destructive, allowing bulk investigations of several centimeters thick samples.

The beamline will have an insertion device with a main energy of 120 keV, tunable in the range from 50–300 keV and optimized for sub-micron focusing. Positioning units for samples up to 1 t will be available. A 150 m long flight tube will be installed for small angle scattering experiments at high energies. The beamline will stand out by the combination of three unique main features: Firstly, the high flux, ultra fast data acquisition systems, and the beamline infrastructure will be the basis for complex in-situ experiments for the observation of highly dynamic processes. Secondly, an exceptional flexibility in beam shaping and focusing down to spot sizes below 1 μm will be available for the high energy X-rays. Thirdly, the beamline will provide the possibilities to merge different analytical techniques such as diffraction, tomography, small angle scattering, and spectroscopy. By exploiting these techniques simultaneously it will be the first beamline, where the boundaries between the different analytical techniques are gradually disappearing, being one of the prerequisites for a leap in materials science and engineering research.

2.3.3.2 Powder diffraction

Powder diffraction is the method of choice for crystal structure determinations if no single crystals can be obtained or if samples have to be investigated under conditions where single crystals are not stable, for example during a phase transition. New experimental techniques as well as new data evaluation methods developed recently provide means to solve crystal structures from powder diffraction data with increasing complexity.

Other important applications of powder diffraction are in-situ studies such as formation of new phases in chemical reactions. Further examples are reactions of solids with gases or liquids as they are common in catalysis research like the adsorption of molecules into zeolites or ion exchange reactions between solids and liquids.

Undulator photon beams from a low emittance high energy storage ring like PETRA III have several advantages for powder diffraction experiments: (i) the high brilliance provides intrinsically very parallel photon beams that are needed to resolve neighboring diffraction profiles, (ii) even at energies as high as the foreseen 50–60 keV a very high photon flux is available, (iii) very small focal spot sizes can easily be achieved by suitable optics for experiments on small sample volumes as they are needed for example in high pressure investigations. The high photon energy of the proposed station has the advantage of a reduced radiation damage mainly for organic materials that contain mostly light atoms, less absorption and therefore the possibility to collect more accurate data for heavily absorbing samples, and the option to penetrate through sample or reaction containers in case of in-situ studies.

2.3.3.3 Unfocused small angle scattering

Classical Small-Angle X-ray Scattering (SAXS) experiments average over a large sample volume and give structural and quantitative information of high statistical significance on a mesoscopic length scale between 1 and several 100 nm, which can be correlated with macroscopic physical and chemical parameters of the analyzed materials (alloys, semiconductors, glasses, macromolecules in solution, metal nano particles, composites). In addition to the normal SAXS signal, the anomalous signal close to absorption edges of suitable atoms can be exploited for contrast variation. This so-called ASAXS method has gained quite some importance in materials science, catalysis and polyelectrolytes.

Due to the low emittance of PETRA III, the beam parameters at a high-β section are best suited for the design of an unfocused SAXS beamline with high Q-resolution. Additionally the energy spectrum covered by a PETRA III standard undulator will allow to make use of the element-selective ASAXS technique and to extend the classical energy range of this technique (5–35 keV) up to energies of about 90 keV. The extension to higher energies will give access to the K-absorption edges of the heavier elements (Z $>$ 53). The energy range in combination with the high flux of a 3^{rd} generation source offers the opportunity to address numerous challenging scientific objectives in solid state physics, catalyst research, chemistry and biology, which are not accessible by the existing state of the art (A)SAXS-experiments.

2.3.3.4 Microfocus applications

A scattering beamline with micro- or nano-focus capabilities will enable static and time resolved measurements in the WAXS[5] to the USAXS[6] regime for the investigation of phase formations and transformations in a vast variety of isotropic and anisotropic materials like

[5]Wide Angle X-ray Scattering
[6]Ultra Small Angle X-ray Scattering

polymer systems, colloids or nanostructured samples. Using an extremely small focus allows the spatially resolved investigation of hierarchically organized samples in the field of life science like bones or wood and synthetic systems like polymer composites. WAXS, SAXS and USAXS under grazing incidence conditions allow one to study short and long range ordered systems on substrate surfaces like dewetting polymer films on metals, adhesives during detaching from a surface or self organization of quantum dots on semiconductor surfaces. To a certain extent all these techniques can be combined with a micro focus in order to investigate a sample by 2D-scanning techniques.

Due to the extremely low divergence of the undulator located at a high-β section of PETRA III, a focus of 7 μm vertical and 40 μm horizontal width (FWHM) with 13 μrad vertical and 120 μrad horizontal divergence (FWHM) can be achieved. A Kirkpatrick-Baez (KB) mirror arrangement with a first mirror at 57 m behind the source and a second one at 75 m will reach such a focus which is then at 85 m distance from the source and has a total flux of $3 \cdot 10^{13}$ photons/s using a Si(1 1 1) double crystal monochromator at 10 keV. The low divergence still maintained in this focus allows to resolve correlation distances of up to 1000 nm in the vertical direction and about 200 nm horizontally, the latter can be increased by accepting a corresponding flux reduction. This high brilliance beam will surpass all others available for comparable scattering applications at existing 3^{rd} generation synchrotron radiation facilities worldwide.

2.3.4 X-ray absorption and resonant scattering

2.3.4.1 Absorption spectroscopy

In general, X-ray absorption fine structure (XAFS) and X-ray absorption near edge structure (XANES) are no typical high-brilliance applications. However, if very small sample regions have to be investigated as it is the case in high pressure experiments, for example, a highly brilliant source is mandatory. This applies as well for XAFS tomography or for μ-XAFS if a very high spatial resolution is desired. Furthermore, the considerable brilliance of a PETRA III undulator at higher photon energies allows to measure XAFS at the K-edges of heavy elements with reasonable flux. Despite the life time broadening these spectra yield more precise spectral information than measurements at the L_3-edges, because the scan range can be larger and the matrix effects are negligible. Higher energies offer the possibility to study these elements, for example during in situ experiments in catalysts.

The design of the beamline has a monochromatic beam (ΔE/E $\sim 10^{-4}$) tunable over an energy range of up to 2000 eV while covering an energy range between 2.4 and 80 keV using different crystals. It will be followed by an optional pair of mirrors for the suppression of higher harmonics radiation. The final focusing device for spot sizes < 1 μm will be close to the sample. Depending on the photon energy, KB-mirrors and different kinds of lenses will be used. A low-β section will be of advantage to achieve a very small focus. The experimental hutch will be equipped with all necessary installations to perform in-situ experiments with toxic and/or flammable gases and liquids.

2.3.4.2 High-energy photoelectron spectroscopy

Photoelectron spectroscopy is a key method to study electronic properties of matter in solid state physics and materials science, providing unique information on chemical bonding and composition, on electronic correlations and other atomic many-body effects. In conventional applications using UV and soft X-ray excitation, the information is obtained from the topmost atomic layers due to the short electron mean free path. This is a serious limitation since electronic properties near the surface often differ from those of the bulk material. Buried interfaces and structures cannot be reached at all. The high surface sensitivity can be overcome with hard X-rays emitting energetic photoelectrons with a correspondingly larger escape depth up to about 10 nm around 10 keV kinetic energy. At the same time, the short photon wavelength can be utilized to excite X-ray standing waves in crystalline materials thus allowing to correlate structural and electronic information on an atomic scale.

Hard X-ray photoelectron spectroscopy with high-energy resolution down $\approx$ 10 meV is extremely challenging and requires an intense and brilliant source as well as highly sophisticated and efficient electron detection. At present, strong attempts are being made to implement this promising new technique at 3^{rd} generation X-ray sources. The experimental station proposed for PETRA III specifically utilizes the low emittance properties. The low divergence beam from a high-β undulator is ideally suited for high-resolution monochromatization ($\approx$ 10 meV at 10 keV) preserving the high monochromatic flux ($\approx 10^{11}$ photons/s) needed to cope with low photoelectric cross sections and electron analyzer transmission. Furthermore, the achievable resolving power of the analyzer is directly linked to the focus size on the sample which can be easily brought down to 10 μm with suitable optics such as KB-mirrors. If sub-micron focussing of the beam is accomplished, lateral spatial resolution for studies of inhomogeneous materials is achieved in a scanning mode of operation. In combination with the high bulk-sensitivity, this will make the instrument a unique tool for studies of the electronic and chemical properties directly of bulk material and, in particular, buried nano-structures.

2.3.4.3 Hard X-ray microprobe

Hard X-ray microprobe beamlines combine the non-destructive elemental micro-analysis capability of μ-XRF (microscopic X-ray fluorescence analysis) with the ability of performing complementary μ-XAS (X-ray absorption spectroscopy) and/or μ-XRD (X-ray diffraction) measurements. These instruments provide simultaneously correlated information on the local elemental composition, chemical state, the local structural environment of specific elements and/or the local crystallographic structure of the examined materials. Hard X-ray microprobe techniques are mostly applied in materials, geological, biological, biomedical, and environmental sciences, as well as archeology and arts.

The hard X-ray microprobe beamline will enable different complementary X-ray microbeam methods to be performed simultaneously or sequentially during one experiment. Scanning X-ray fluorescence microscopy measurements in combination with broad beam radiography imaging will be the most straightforward technique to characterize heterogeneous

samples in terms of local elemental composition and density. Microscopic X-ray absorption spectroscopy (μ-XANES, also μ-EXAFS) and microscopic X-ray diffraction will provide information on the local speciation and structure. Tomographic methods (fluorescence microtomography, XANES microtomography) and confocal arrangements of X-ray optics for the primary beam and fluorescence photons give access to quantitative three-dimensional measurements.
The beamline will provide beam sizes down to the 100 nm range utilizing the outstanding small source size and high brilliance of PETRA III, but also larger beam sizes of 1–10 μm and an unfocused beam for flat field imaging will be available. The accessible energy range covers the K-edge energies from sulfur to uranium (E = 2.4–116 keV) and the flux is maximized by the use of KB mirrors. For broad band excitations a pink beam option is foreseen.

2.3.4.4 Resonant scattering

Correlated electron materials provide one of the biggest challenges of condensed matter research today. Complex magnetic ordering phenomena occurring in nano structured multicomponent materials are an example of the consequences of electronic correlations. Of particular interest are materials with exceptionally strong electronic correlations. The complex interplay of spin, charge, orbital and lattice degrees of freedom gives rise to a variety of different phases having insulating, metallic or superconducting properties, being anti-ferro, ferro- or paramagnetic and possessing different structures. The most prominent examples are transition metal oxides, which exhibit high-T_c superconductivity or the colossal magnetoresistance effect. The competition between the different phases can result in an electronic or structural phase separation from the Å to the μm scale.
Resonant X-ray scattering is an ideal tool to characterize the ground state of these new materials. It probes correlations of spin, charge, orbital and lattice degrees of freedom. The resonance technique provides element sensitivity and even band selectivity, giving detailed information on the electronic structure.

The resonant scattering experiments will take advantage of the excellent beam properties of the PETRA III source in the following aspects: (i) The high brilliance of more than 10^{21} photons/(s mm^2 mrad^2 0.1% BW) at 12 keV allows the design of X-ray optics that enable a high Q-resolution of about 10^{-5} Å^{-1} with considerable flux. (ii) A highly polarized beam, essential for the resonant scattering technique, can only be obtained on a small emittance source. At PETRA III a very high degree of linear polarization (close to 99.99 %) should be achievable. The high degree of linear polarization combined with small divergence provides the possibility also for a highly circular polarized beam using a phase retarder. (iii) Spatial resolutions ranging from micro- to nanometers can be acquired using a microfocus device which is important when studying nano-devices or phase separated materials. (iv) The high degree of coherence enables speckle experiments to resolve domain shapes and probe dynamic properties utilizing the time correlation function.

2.3.4.5 Variable polarization XUV beamline

Soft X-rays are ideal for spectroscopic investigations ranging from magnetism in nano structures to biological systems. Many absorption edges of practically all important elements lie in the soft X-ray range (100 eV to 3 keV) which opens up the possibility to uniquely determine the element-specific local electronic structure in complex materials by exploiting atomic resonances. Until recently really high brilliance light sources were not available for such investigations. Experiments at the latest 3^{rd} generation synchrotron light sources are now beginning to demonstrate the enormous scientific potential of this spectral region. Currently, investigations are still limited by the light source and improved sources will immediately produce new science. In the future, polarization-dependent studies with soft X-rays will play a key role in enhancing our knowledge of the structure of matter.

Suitable insertion devices at high-energy storage rings can provide very high brilliance of circularly polarized light in the energy range of 500–2000 eV as has been demonstrated at both the ESRF and SPring-8. Helical undulators operating in the first harmonic provide the highest flux and complete polarization, but require machine energies greater than 3 GeV. Insertion devices on lower energy machines like BESSY II, ELETTRA, and ALS only produce circularly polarized light up to about 500 eV in the first harmonic and newer machines like SLS and SOLEIL will extend this limit to 700–900 eV. The variable-polarization soft X-ray beamline at PETRA III will be unique and will open up completely new scientific opportunities by providing the highest brilliance and flux in the important spectral region from 500 eV to 2.5 keV . With current technology it is possible to achieve a spectral resolution of 10000 at 1 keV with an extremely high flux (more than 10^{12} ph/s) focused on the sample. Compared to the best present day sources the PETRA III soft X-ray beamline will provide up to two orders of magnitude higher flux at photon energies above 1 keV. This beamline will promote significant progress in fields ranging from surface science to molecular and cluster physics, magnetic studies, condensed matter physics and nanotechnology.

2.3.5 Structural biology

2.3.5.1 Macromolecular crystallography

Over the last fifty years biological X-ray crystallography has evolved into an advanced field of life sciences and has provided unprecedented three dimensional structural information on the molecular level of a large number of complicated biological processes. Knowledge of spatial structures has allowed to delineate the molecular origins for diseases such as cancer, autoimmune diseases and microbial infections. The performance and contribution of biological X-ray crystallography can be readily assessed by the huge number of new structures being deposited in the Protein Data Base (PDB), which is increasing at a nearly exponential rate. As a result, the growth in demand for synchrotron radiation beamlines for macromolecular crystallographic experiments has risen substantially both in absolute numbers and in overall proportion. New challenges for the future are the understanding of the function of large macromolecular assemblies. At present, the largest structures determined, though bearing internal symmetry, are from viral assemblies. Some of these structures have imposed unprecedented challenges in terms of the size of available crystals, which may be as low as a few microns, and unit cell dimensions, in a few cases even exceeding 1000 Å. Many of these projects have only become feasible with the recent availability of the highest brilliance beamlines at 3^{rd} generation synchrotron sources providing both a small focal spot size and a beam divergence small enough to resolve individual reflections even for the largest unit cells.

A number of beamlines for structural biology at PETRA III are proposed by the EMBL and MPG outstations at DESY (Sects. 6.16, 6.17). Due to the high brilliance of PETRA III about 10^{13} ph/s will be available in the monochromatic beam. Minimal focal spot sizes in the 10 μm range are envisaged. At the same time, the maximal divergence will not exceed 0.5 mrad even for the smallest focus. The different stations will be optimized for different applications such as wide range energy tunability, high-throughput structure determination, microfocus and special applications like investigation of large macromolecular complexes. All of them will be highly automated for optimum use of the beamtime.

2.3.5.2 Biological absorption spectroscopy

X-ray absorption spectroscopy determines the electronic structure of probe atoms and their structural vicinity. In biology typical probe atoms are metals or other elements of limited occurrence. In proteins metals fulfill a variety of essential functions: They stabilize the secondary protein structure, they serve as a binding partner in transport processes, they define the pathway for electron transfer, and they act as the key element in catalytic reactions. In at least 30% of the gene products, metals are believed to play a key role; these are classified as metallo-proteins. Cutting edge applications are (i) Time-resolved BioXAS experiments to facilitate insights in reaction dynamics/kinetics and structural characterization of intermediate states, (ii) spatially resolved XANES (tomography) facilitating spatially resolved speciation with respect to oxidation state and ligand environment and (iii) high-resolution fluorescence for site-specific measurements, these experiments have the added advantage that they provide greatly improved spectral resolution for XANES studies.

A BioXAS station at PETRA III with an energy range from 5 keV to 35 keV will cover K- and L- edges of most important probe elements in biological materials. A 2 m long standard K_{max} = 2.2 undulator will provide sufficient flux for this station. The main advantage of PETRA III for BioXAS will be the small focal spot sizes. For tomography experiments at a low-β section a demagnification below 100 nm is possible with parabolic refractive Be-lenses. With KB mirrors similar spot sizes can be achieved. The high brilliance of PETRA III will also provide sufficient intensity for resonant inelastic X-ray scattering (RIXS) which is looking at the decay of excited states and is a powerful tool in determining site sensitive information on probe atoms as well as in understanding electronic structure of probe atoms and their ligands.

2.3.5.3 Biological small angle scattering

During the last decade, small-angle X-ray scattering (SAXS) has become an increasingly important tool for the study of biological macromolecules. The method enables studies of native particles in solution, from individual proteins to large macromolecular complexes, under nearly physiological conditions. SAXS not only provides low resolution models of particle shapes but in many cases answers important functional questions. In particular, kinetic SAXS experiments allow one to analyze structural changes in response to variations in external conditions. Fundamental biological processes such as cell-cycle control, signalling, DNA duplication, gene expression and regulation, some metabolic pathways, depend on supra-molecular assemblies, and their configurational changes over time can be studies by SAXS techniques. There are well recognized basic problems for studying such complex systems, especially their dynamic changes by other structural techniques like spectroscopy, NMR and macromolecular X-ray crystallography.
The recent resurgence of biological SAXS is due to the synergy of software and hardware development. New powerful data analysis methods have become available, which have tremendously improved resolution and reliability of models deduced from SAXS data leading to an enlargement of the user community.

A SAXS station for biological applications is proposed by the EMBL outstation. As the SAXS pattern is collected in the vicinity of the primary beam, the data quality depends critically on the beam size and divergence. SAXS is therefore among the techniques, which profit most from the low emittance undulator radiation on a 3^{rd} generation sources. Furthermore, the high flux of these sources is extremely important for the analysis of weakly scattering biological samples. Currently, high quality scattering patterns can be collected in less than a second using sub-mm beam sizes on the undulator SAXS beamlines at 3^{rd} generation sources. The biological SAXS beamline at PETRA III will provide a resolution range from about 2000 nm to 0.1 nm and will be tunable in an energy range of 4 to 20 keV in order to enable ASAXS studies using all relevant biological ions from Ca to Mo.

2.4 Future Upgrade Prospects

After the conversion of PETRA described in this report there will still be several future upgrade options for more beamlines. They all have the advantage that they do not need any significant change of the magnetic lattice of the storage ring.

- In the beginning one experimental station per undulator will be built. The efficiency of each beamline can be increased by constructing additional experimental stations with reproducibly positionable roll-in/roll-out equipment.
- In case of sufficient user demands, bending magnet stations can be build where the available space permits.
- The damping wigglers are designed to be cost effective and adapted to their main function to reduce the emittance. They generate a wide fan of extremely hard radiation.

This radiation could be used for materials science experiments where a large beam is needed. However, the possibility to install additional wigglers that are better suited for hard X-ray experiments than the present damping wiggler design also exists.

- A number of positions around the PETRA storage ring exist where additional insertion devices can be placed without major changes of the magnetic lattice. There are two other positions at PETRA (buildings 43 and 45, see map in Fig. 2.2.1) where long undulators could be placed as well as three positions (in or close to buildings 44, 46a/b and 48) for 5 m long IDs. Thus in total about 18 insertion device positions are available at the converted storage ring. The position of the additional insertion device positions are summarized in Tab. 2.4.1.

- On the long term it is envisaged to increase the storage ring current up to 200 mA.

in building	max. ID length [m]	max. BL length [m]
43	20	360
44	5	180
45	20	320
46	5	220
48	5	170

Table 2.4.1: Positions at the PETRA III storage ring where further IDs could be installed. The building number can be looked up in Fig. 2.2.1. The ID position labeled with '46' is actually not in building 46 but in the straight section closest to these buildings.

A detailed description of all upgrade possibilities can be found in Chapter 10. About half of the PETRA storage ring is underground. What seems to be a disadvantage at first sight might be a significant advantage for some of the future upgrade possibilities. Experience with ID's for extremely high photon energies (more than several 100 keV) at ESRF, APS and SPring-8 has shown severe problems with radiation shielding which will be significantly relaxed at underground experimental stations.

2.5 Summary of Project Costs and Timetable

2.5.1 Project costs

The project cost estimates include all costs related to (i) the refurbishment of 7/8, and the reconstruction of 1/8 of the PETRA storage ring, (ii) the refurbishment of the pre-accelerators and accelerator infrastructure, (iii) all construction work necessary for the new experimental hall including radiation protection, offices and laboratories, (iv) the beamlines and experimental stations to be built and operated by DESY, and all costs for manpower.
The PETRA III upgrade project comprises about 13 beamlines at independent undulators. About seven of these beamlines will be built and operated by DESY. All other beamlines will be built or financed by external institutions like EMBL, GKSS and the Max Planck Society (MPG). The cost estimates given in this report do not include the beamlines and experimental stations built by external institutions.
On the basis of year 2003 prices the PETRA III project amounts to about **192 M€** of which 71 M€ are needed for the storage ring, 64 M€ for the new experimental hall including the DESY beamlines, and 57 M€ for personnel. More detailed information on the estimated costs are given in Chapter 8.

2.5.2 Time table

In Fig. 2.5.1 an overall time table of the most important milestones for the PETRA III project is given. A more detailed schedule is compiled in Chapter 9. The preparation and R&D for the PETRA III project has already been started (as of begin of 2004). The construction work will start in **July 2007**. First photons for user experiments are expected in **2009**.

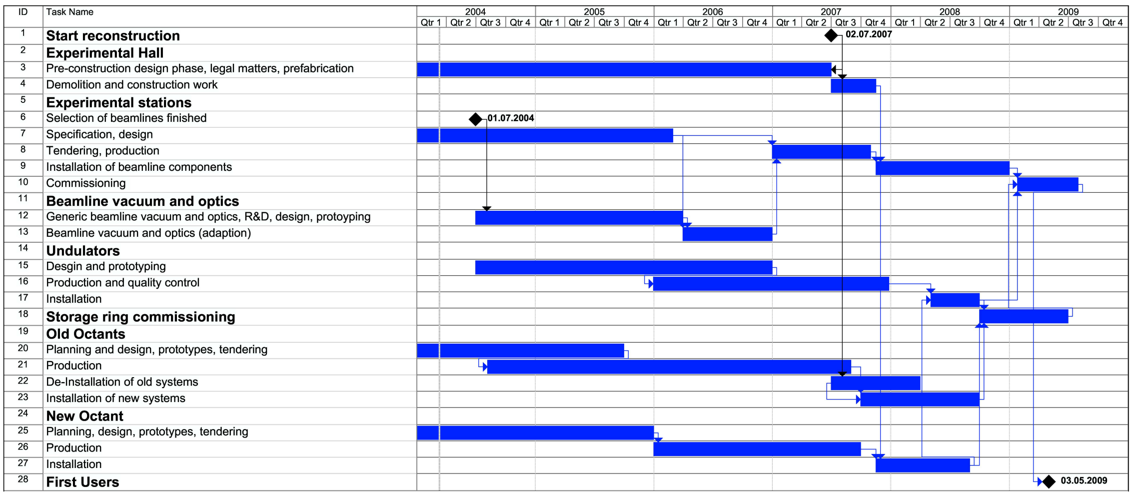

Figure 2.5.1: Summary of the time table and milestones of the PETRA III project. (Please use your readers zoom function for a more detailed view.)

Chapter 3

The Storage Ring

3.1 Introduction

The following part of the design report covers aspects of accelerator physics and technical issues of the PETRA III project. As was already pointed out PETRA III will be designed to be a high brilliant light source in the hard X-ray regime. Although this machine has features of existing light sources it also differs considerably from the design of any present radiation source.
In the introduction we will present the general design philosophy and give reasons why we decide to build PETRA III in this particular form. This part can be viewed as a guide line and a summary for the accelerator and technical part of the project.
The schematic layout of PETRA II is given in Fig. 3.1.1. PETRA II has a large circumference of 2304 m which is considerably larger than any existing light source. The machine consists of arcs and several straight sections. The so-called long straights which have a length of 108 m are located in the North, East, South and West. In between two long straights are short straight sections with a length of 64.8 m. These straights are connected by arcs. The magnetic structure is a simple FODO lattice. The part that extends from the middle of one long straight to the middle of the adjacent short straight is the basic building block of the machine. Since this section is just one eighths of the machine it is called an octant. In principle the magnetic arrangement of one octant is mirror reflected at the middle of the short straight. The machine has therefore a four fold symmetry. Positrons or electrons are injected in the South-East (SE) and travel clockwise around the machine.
The basic design parameters of the new machine PETRA III are given in Tab. 3.1.1. The design is driven by two major criterions. First of all PETRA III should be competitive with the existing high energy synchrotron radiation sources like APS, ESRF and SPring-8 but on the other hand the reconstruction should be cost effective. That last criterion is the reason why the number of insertion devices is relatively small for a machine with a circumference as large as 2304 m. The energy is fixed by a compromise of the different user requirements. The maximum current and the emittances are chosen to achieve a high brilliance. The current is limited by coupled bunch instabilities driven by the parasitic modes of the existing RF cavities. Replacing the exiting cavities would be to costly and does not fit into our present budget. All components of the machine and in particular those which are affected by heat

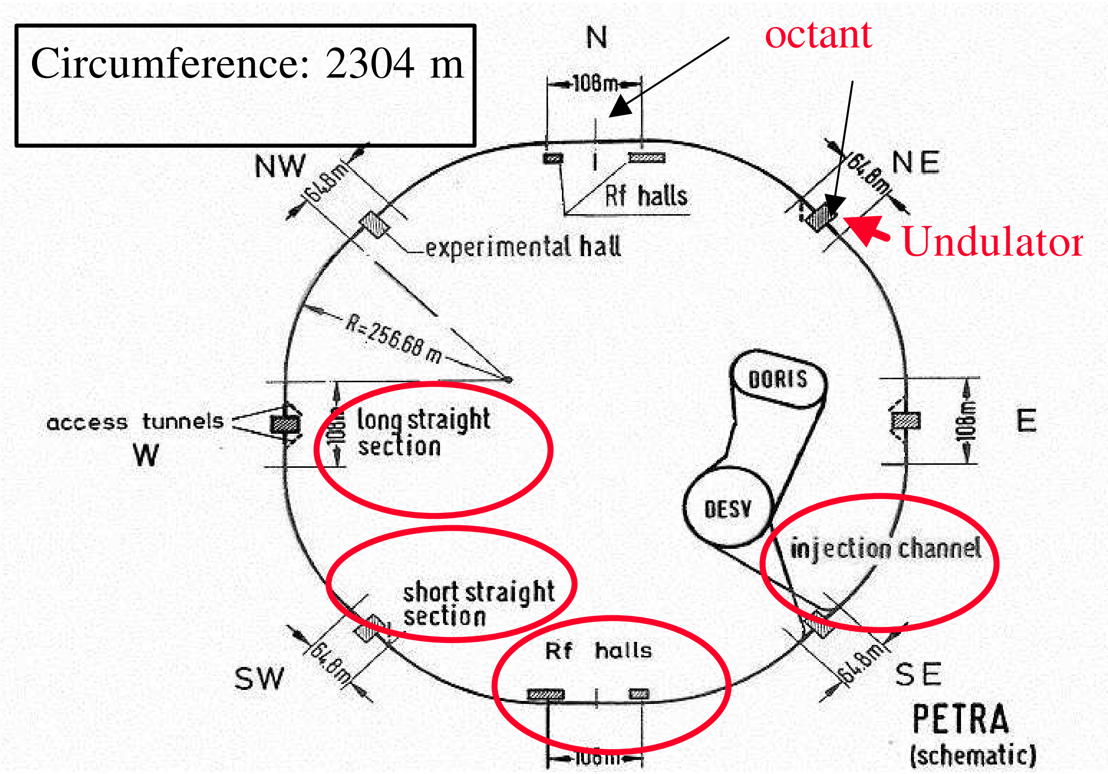

Figure 3.1.1: Overview of PETRA storage ring.

Parameter	
number of insertion devices	13
energy (GeV)	6
current (mA)	100
ϵ_x (nmrad)	1
ϵ_y (nmrad)	0.01

Table 3.1.1: Basic design parameters of PETRA III.

load or radiation should be designed and dimensioned for a current of up to 200 mA in order not to prevent future upgrades. The emittances are rather small compared to achievements of other light sources. To meet the design goal for the emittances is certainly one of the major challenges of this project.

In the following we will show how the design parameters can be accomplished.

We investigated several possibilities to house the insertion devices in the machine. Finally we decided to accommodate the insertion devices in one octant of the machine since this is an effective solution in terms of costs and constructional changes. The octant extending from North-East to East was chosen for reconstruction (see Fig. 2.2.1) because here the machine is above ground and easily accessible which eases the rebuilding. The magnetic lattice of

this new octant consists of nine double bend achromat cells (DBA). Details of the optics and the way how to make room for thirteen insertion devices is described in Sec. 3.2.1.
If the optics of the new octant is combined with an established optics of the remaining seven eighths of the machine, the so-called old octants, the minimum achievable emittance is 4.5 nmrad. So obviously changes to the rest of the machine are necessary to get the emittance down to 1 nmrad. There are basically three different ways to reduce the emittance:

- Using the above mentioned optics for the remaining seven eights of the machine which results in an emittance of 4.5 nmrad and enhancing the radiation damping with damping wigglers to reduce the emittance. These damping wigglers can be installed in two of the four long straights sections where there is plenty of space available. This option is referred to as Optic A.

- A completely new design of the optics of the remaining seven eights of the machine but using the existing hardware. The appropriate candidate for such a lattice would be a so-called theoretical minimum emittance lattice abbreviated TME. This option is referred to as Optic B.

- A completely new design of the optics of the remaining seven eights of the machine with new magnets in particular shorter dipoles so that the bending angle can be significantly reduced which then results in a smaller emittance. The shorter dipoles are integrated into a FODO lattice with a phase advance of $90°$. This option is referred to as Optic C.

Figures 3.1.2 and 3.2.2 show the beta and dispersion functions for the three different choices for an old octant.
We investigated the dynamic aperture of the three different options for an ideal machine i.e. without field and alignment errors. Furthermore all lattices were optimized with respect to first order sextupole effects. Fig. 3.1.3 shows the dynamic aperture for the three different options. This graph clearly indicates that the option with damping wigglers offers the biggest dynamic aperture. The graph indicates that option B and C provide a much too small dynamic aperture especially at injection. This result is not completely unexpected since the sextupole strengths for option B and C are significantly larger than the sextupole strengths for option A. The sextupoles are the main source of non-linear effects in case B and C and the non-linear effects coming from the wigglers for option A mainly affect the vertical plane. This comparison in terms of dynamic aperture and the fact that option B and C tend to be more sensitive to errors because of the higher field strengths of their quadrupole and sextupole magnets clearly favors the option with the damping wigglers. This option is investigated in great detail in Sec. 3.2.2.
The small emittance in combination with the optical function at the source points of synchrotron radiation give beam sizes in particular in the vertical plane in the micron range. That means that orbit stability in the micron or even sub-micron range is required. Our own experience and the experience gained at other laboratories indicate that an active stabilization system will be necessary in order to achieve the specified orbit stability. Our present expectations concerning orbit stability and a schematic layout of an orbit stability system is

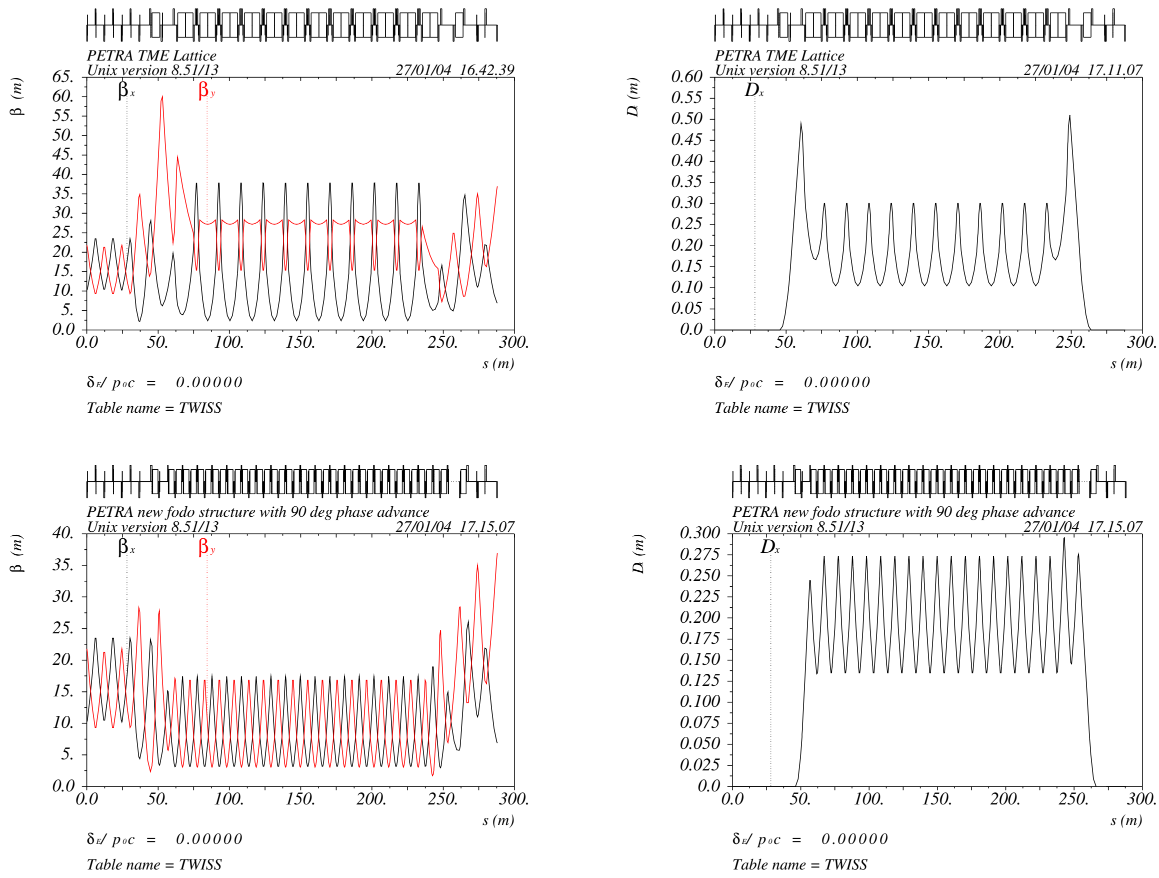

Figure 3.1.2: Top: Beta-functions of a TME based octant (Optic B). Bottom: Beta-functions of a 90° FODO cell based octant (Optic C).

described in Sec. 3.2.4. An essential part of such a system is the orbit measurement. Beam position monitors and electronics are described in Sec. 3.9.

An additional problem with the small emittance is the relatively short Touschek lifetime. For PETRA III two operational concepts are foreseen. In one mode the current is spread over a large number of bunches namely 960. In that case the expected Touschek lifetime is of the order of 50 h so that the total lifetime will be approximately 24 h after including other lifetime limiting effects. A lifetime of 24 h meets the user requirements. In the other mode only a limited number of bunches is allowed namely 40. This small number of bunches is needed to have a sufficiently large distance between bunches so that time resolved measurements are possible. In this case the Touschek lifetime is only 2 hours which is incompatible with the user requirements. The only way out is to inject rather frequently for instance every 5 seconds in order to compensate for the particle losses. This frequent injection is called topping up. This measure has been applied successfully at other synchrotron radiation sources like APS and SLS and most recently also at the ESRF. The radiation safety problem of topping

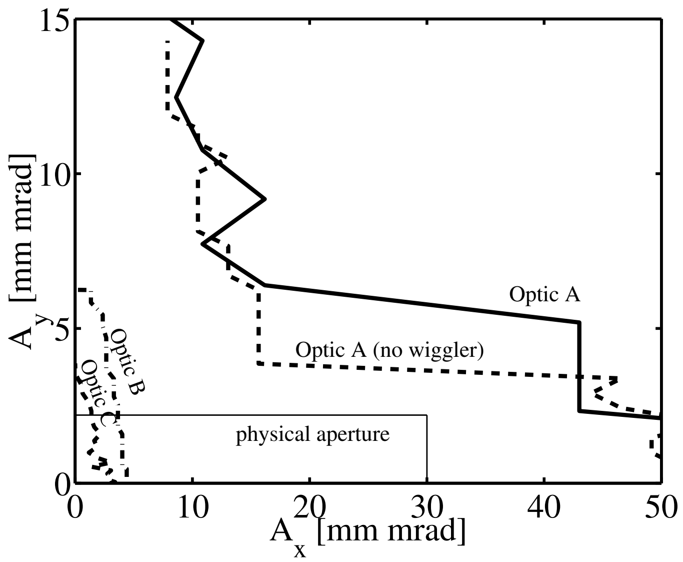

Figure 3.1.3: Dynamic aperture for the various lattice types as described in the text.

up has been looked at and the result and its consequences are presented in Sec. 3.14. This method also imposes strong requirements on the reliability of the pre-accelerators Linac II and the synchrotron DESY II. The feasibility of topping up has been studied at DORIS during machine shifts and the measures to ensure the demanded reliability of the pre-accelerators are presented in Sec. 3.16.

A further advantage of topping up is the constancy of the total current which in turn will lead to thermal equilibrium of components of the machine. Therefore temperature drifts of orbits will be greatly reduced which will certainly relax the burden on the orbit stability system. This fact makes topping up also very attractive for the operation with a large number of bunches and therefore we are aiming at operating the machine entirely in topping up mode. A problem associated with a frequent injection is radiation damage of the insertion devices and damping wigglers due to particle losses. In order to protect the insertion devices and wigglers a collimation system is planned. Such a system will be installed in the short straight section south west where is plenty of room for such a system.

Single bunch and multi bunch current limitations are dealt with in Sec. 3.2.3. A powerful multibunch feedback system (see Sec. 3.10) is necessary in order to reach the design current of 100 mA. Single bunch instabilities will not be an issue as long as the current per bunch stays below 2.5 mA.

There are several technical systems of the machine that have a strong impact on the performance of PETRA III.

The new octant is equipped with completely new hardware. The magnets are described in Sec. 3.3. Another import component is the girders. The principle layout of the girders and their properties are given in Sec. 3.7. Considerations on the vacuum system of the new octant are presented in Sec. 3.5.

The damping wiggler section is certainly a technically challenging part of the machine. The vacuum system and the absorbers have to be designed very carefully. A conceptual design of this section is presented in Sec. 3.4.
Concerning the old octants we want to make use of existing infrastructure and hardware whenever possible in order to be cost effective. Nevertheless there will be also substantial changes to the hardware. For example the present vacuum system will be completely replaced (see Sec. 3.5). In addition we also want to replace the coils of all main magnets because they have been damaged by radiation over the last 25 years. Fig. 3.1.4 shows a radiation damaged coil and magnet with a new coil.

Figure 3.1.4: Damaged and new magnet coil.

The power supplies for both the magnets and the RF system will be replaced (Sec. 3.12). The cooling water system will be renewed in order to fulfill the higher demands on temperature stability. Parts of the RF system will be modernized but the present cavities will be used also for PETRA III (see Sec. 3.6).

3.2 Accelerator Physics Issues

3.2.1 Geometry and optics

Concerning the geometry and optics the basic idea is to keep the lattice structure on seven eighths of the PETRA II machine whereas one eighth will be completely reconstructed.
PETRA II consists of eight arcs (Fig. 3.2.1) connected alternately by four long (108 m) and four short (65 m) straight sections. One octant starts at the center of one straight section and ends at the center of the next one. The optical functions of such a FODO lattice based octant are shown in Fig. 3.2.2. All straight sections are designed for zero dispersion by using the missing magnet principle.
For the octant from North-East to East a new design has been made fitting to the geometrical and optical boundary conditions of the rest of the storage ring. It consists of 9 double-bend achromat (DBA) cells with zero dispersion straight sections for the installation of eight 5 m undulators and one 20 m undulator (Fig. 3.2.3). Following the demand of the users two types

Figure 3.2.1: FODO cell lattice in one of the arcs of PETRA II.

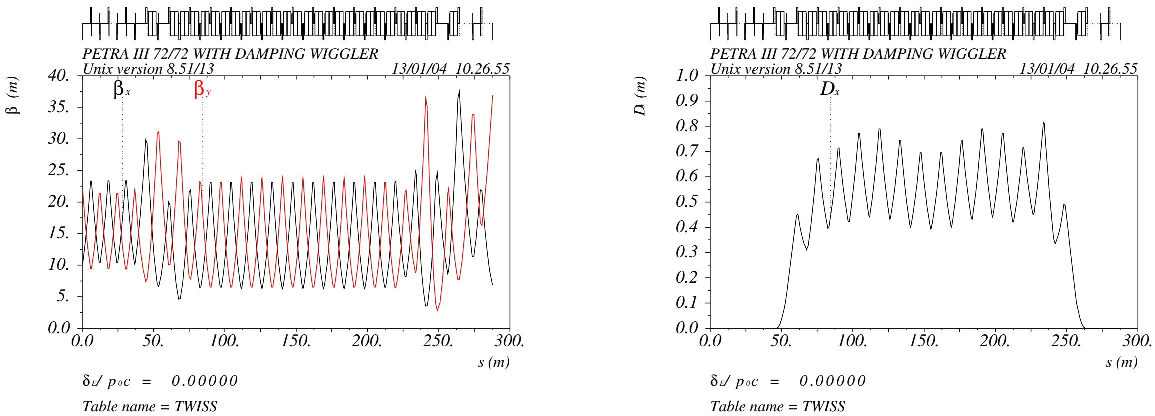

Figure 3.2.2: Beta-functions (left) and dispersion (right) of one octant of PETRA II.

of DBA cells were designed. Having the same geometry the cells differ in the horizontal β-functions (1.3 m and 20 m respectively) at the undulator locations. For the vertical β-functions a middle-sized value was chosen to compromise between the requirements of small beam divergence and small undulator gap. While the 5 m undulators (or alternatively two 2 m undulators (Fig. 3.2.4)) are located in the arc of the octant the 20 m undulator will be installed in the short straight section North-East. The geometry of the DBA cells is shown in Fig. 3.2.5. At the positions where two 2 m undulators are planned a deflection magnet has to be placed between them to separate the synchrotron radiation beams by an angle of about 5 mrad. In this case a small dispersion value is generated (Fig. 3.2.4) which however has no

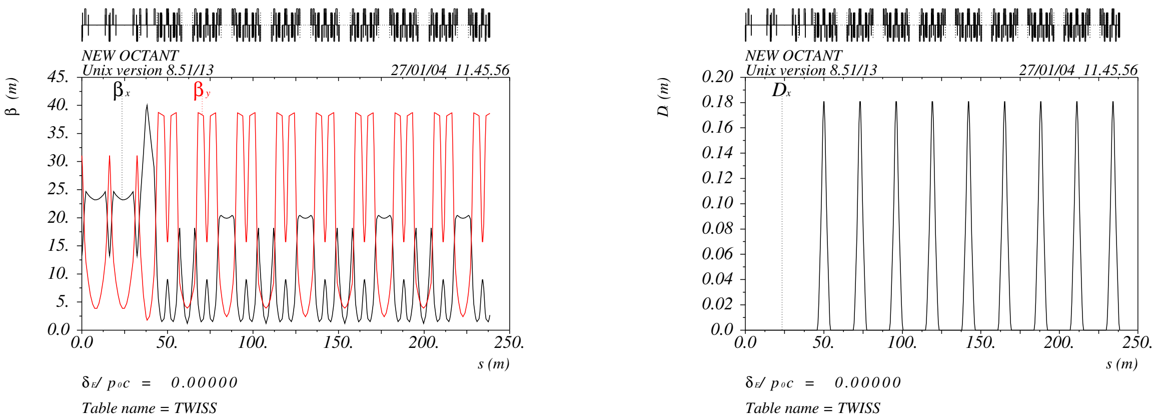

Figure 3.2.3: Beta-functions of the new octant starting with the long undulator followed by nine DBA cells.

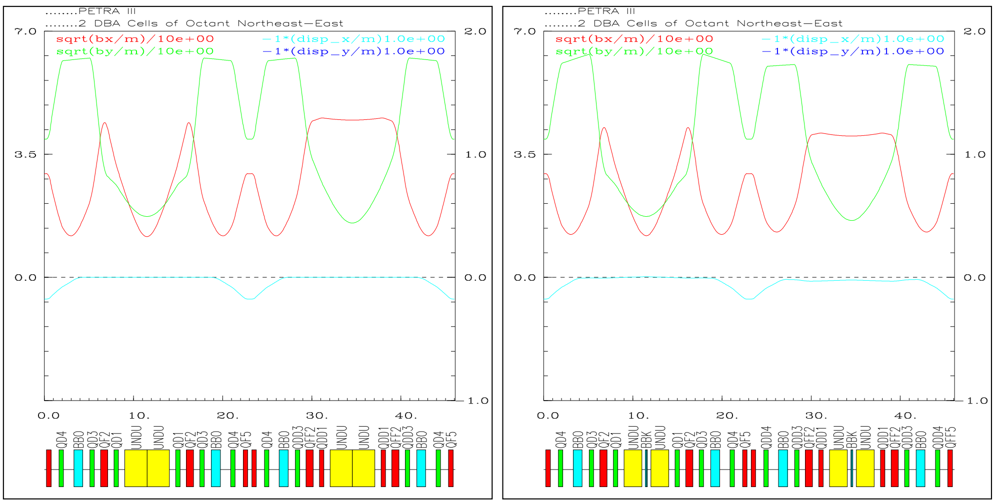

Figure 3.2.4: Optical functions of a low and high β_x DBA cell of PETRA III with one undulator (left) or two undulators per straight section (right).

significant impact on the beam quality. The strength and length of the DBA cell quadrupoles for the different optics scenarios is listed in Tab. 3.2.2. The corresponding β-functions are summarized in Tab. 3.2.1.

Horizontal Emittance and Damping Wiggler Parameters The main contribution to the horizontal storage ring emittance comes from the seven old octants consisting of FODO cells. The phase advance of 72° per FODO cell together with the new octant including undulators leads to a horizontal emittance of 4 nm rad.

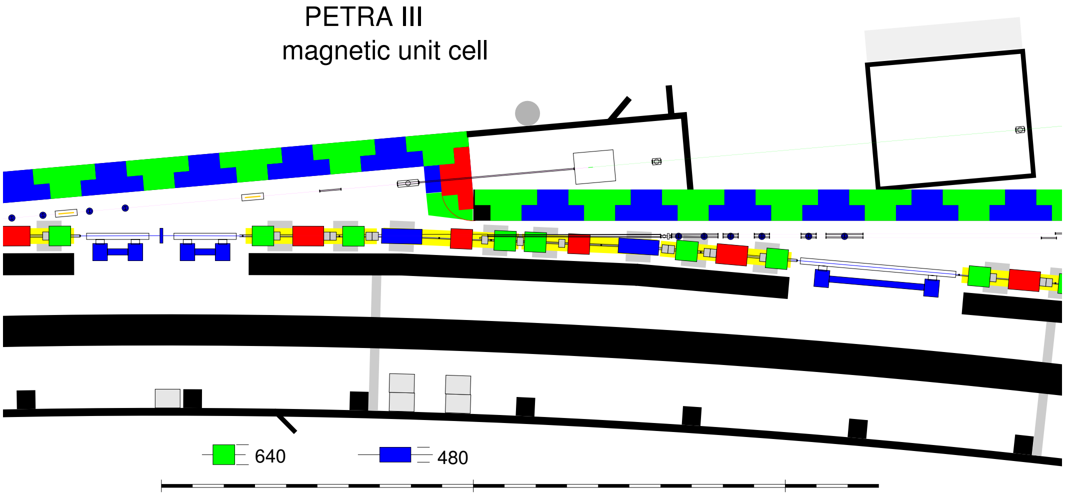

Figure 3.2.5: Structure and geometry of a DBA cell in the new octant of PETRA III.

	5 m undulator		two 2 m undulators	
	low β_x	high β_x	low β_x	high β_x
β_x [m]	1.34	20.00	1.40	16.15
β_y [m]	3.00	2.39	3.00	2.61

Table 3.2.1: Beta-functions in the new octant at the center of the undulator sections.

For a further reduction of the emittance down to 1 nm rad it is planned to install damping wigglers between the quadrupoles of the dispersion free long straight sections West and North (Fig. 3.2.6). A total length of about 80 m is available for damping wiggler magnets to cool the transverse momentum of the stored positrons by synchrotron radiation sufficiently.
The equilibrium emittance in a storage ring is given through the effects of radiation damping, described by the synchrotron integral $I_2 \sim \int B^2 dl$ and betatron oscillation excitation, described by I_5. Damping wigglers increase I_2 while keeping I_5 small. The different emittance contributions of the ring can be combined through the following sum:

$$\epsilon_x = \frac{1}{I_{2;arc} + I_{2;oct} + I_{2;und} + I_{2;wig}} (I_{2;arc}\epsilon_{x;arc} + I_{2;oct}\epsilon_{x;oct} + I_{2;und}\epsilon_{x;und} + I_{2;wig}\epsilon_{x;wig}) \tag{3.2.1}$$

where $\epsilon_x \sim I_5$ is the equilibrium emittance of the various contributions.
The lattice of the FODO arcs and the new octant have been described in Sec. 3.2.1, the values for I_2 and ϵ_x which are necessary to reach a 1 nm emittance are given in Tab. 3.2.4:
The wiggler itself creates an emittance of:

$$\epsilon_{x;wig} = 2\text{–}13 \times 10^{-2} \lambda^2 B_0^3 < \beta_x > \tag{3.2.2}$$

with λ the wiggler period length and B_0 the peak magnetic field. The average beta-function $< \beta_x >$ is around 16 m in the case of PETRA III given by the chosen lattice. This requires

Name	Length [m]	k_1 [m^{-2}]	Gradient [$\mathrm{T/m}$]
Q0K	1.042	-0.09588	-1.92
Q1K	1.042	0.13574	2.72
Q2K	1.042	-0.12723	-2.55
Q4K	1.042	0.13129	2.63
Q5K	0.704	-0.27517	-5.51
Q6N, Q2N, Q4N, Q0N	0.704	-0.17111	-3.42
Q5N,Q3N, Q1N	0.704	0.17130	3.43
Q7N	1.042	0.12848	2.57
Q9N	1.042	-0.13272	-2.66
Q4NW	0.704	-0.16371	-3.28
Q5NW	0.704	0.17430	3.49
QD	0.704	-0.23963	-4.80
QF	0.704	0.23984	4.80
Q0B	1.042	0.17154	3.43
Q1	1.042	-0.15162	-3.03
Q2B	1.042	0.17962	3.59
Q3	0.704	-0.23478	-4.70
Q4B, Q6B	0.704	0.23984	4.80
Q5B, Q5A	0.704	-0.23963	-4.80
Q0A	1.042	0.17400	3.48
QK1	1.042	-0.18792	-3.76
Q2A	0.704	0.26468	5.30
QK3	0.704	-0.21493	-4.30
Q4A	0.704	0.22435	4.49
Q6A	0.704	0.23984	4.80
QDLU	0.704	-0.53766	-10.76
QFLU	0.704	0.22630	4.53
Q4KL	0.704	0.57503	11.51
Q3KL	0.704	-0.53520	-10.71
Q2KL	0.704	-0.18074	-3.62
Q1KL	0.704	0.49910	9.99
Q1KR	0.704	0.09062	1.81
Q2KR	0.704	0.15485	3.10
Q3KR	0.704	0.35133	7.03
Q4KR	0.704	-0.37611	-7.53
QA1	0.5	0.06082	1.22
QA2	0.8	0.43596	8.72
QA3	0.5	-0.65821	-13.17
QA4	0.5	-0.51920	-10.39
QA5	0.5	0.76286	15.27
QB1	0.5	-0.05742	-1.15
QB2	0.8	0.79092	15.83
QB3	0.5	-0.80444	-16.10
QB4	0.5	-0.51920	-10.39
QB5	0.5	0.76286	15.27
QQNL	0.704	-0.24936	-4.99
Q9NL	0.704	0.42164	8.44
Q8NL	0.704	-0.26089	-5.22
Q7NL	0.704	0.24342	4.87
Q6NL	0.704	-0.28193	-5.64
Q5NL	0.704	0.25184	5.04

Table 3.2.2: Strength of quadrupole magnets in PETRA III.

Sextupoles			
Name	Length [m]	k_2 [m^{-3}]	Gradient [$\mathrm{T/m}^2$]
S1	0.286	-4.54902	-91.04
S2	0.286	2.63842	52.80
S3	0.286	-4.54463	-90.95
S4	0.286	2.66295	53.29
Dipoles			
Name	Length [m]	Bending angle [Deg]	Field [T]
BH	5.378	1.60714	0.10
B1	1	2.50000	0.87

Table 3.2.3: Strength of sextupole and dipole magnets in PETRA III.

Figure 3.2.6: A long straight section of PETRA for the installation of damping wigglers.

Section	I_2 [T^2/m]	ϵ_x [nm rad]
FODO Arc	11.5	6.31
New Octant	13.8	3.17
Wigglers	100	0.1
Total	128	1
Undulators	26	0.04
Total	154	0.84

Table 3.2.4: Emittance contributions of different sections of PETRA III

$\lambda^2 B_0^3 < 0.2$ for 0.1 nm wiggler emittance. Figure 3.2.7 shows the maximum allowed period length and the required wiggler length for a given peak magnetic field of a sinusoidal wiggler. The space for wigglers is limited to $\approx 100\,\mathrm{m}$, thus allowing a minimum field of 1.5 T and a period length of $0.2 - 0.25\,\mathrm{m}$.

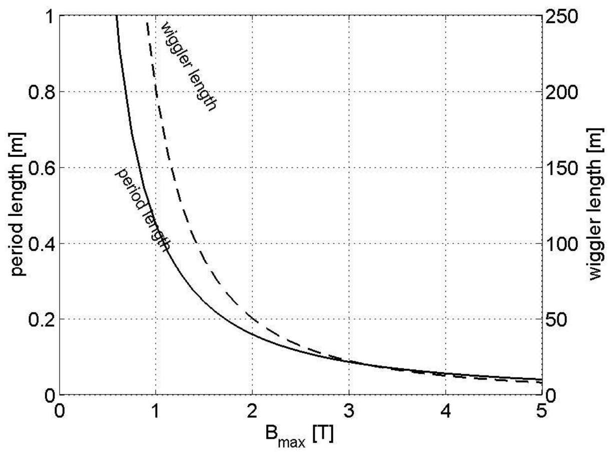

Figure 3.2.7: Maximum period length (solid line) and required wiggler length (dashed line) for a given peak field of a sinusoidal wiggler.

Apertures along the ring Tracking calculations show that for the chosen FODO cell scenario (including the new DBA cell octant) a dynamic horizontal acceptance of 30 mm mrad can be provided. Since this value is also large enough for the injection of the 350 nm rad beam from DESY II with an almost 100 % efficiency it was taken as the basis for the horizontal vacuum chamber aperture. Together with an expected maximum β-function of 50 m it leads to a horizontal inner size of the chamber of 77 mm. From that a design aperture for the new quadrupoles of 70 mm was derived.
Due to experiences of other 3^{rd} generation light sources a vertical aperture of 2.2 mm mrad is foreseen at the undulator locations. As a consequence the inner vacuum chamber height of 7 mm leads to a maximum vertical β-function of about 5.5 m. This is the lower design value for undulator chambers in the DBA cells. It is planned to split the 20 m undulator in the straight section North-East into two parts separated by a quadrupole triplet. The maximal vertical β-function along this undulator will be about 10 m. Therefore a vertical inner size of 9.5 mm is necessary for the corresponding chambers.
Along the damping wigglers a more relaxed acceptance of 3 mm mrad is envisaged which results in 17 mm vertical chamber height for a maximum β-function of about 25 m. For the horizontal plane an inner vacuum chamber size of 60 mm (β-function 30 m) is required.
In order to make the commissioning easier 6 mm mrad was taken for the vertical physical aperture along the rest of the ring. For a vertical β-function of 60 m we need a vertical height of 38 mm. This also takes into account other optics scenarios in the future. Since the dipoles in the old octants have a magnetic gap of 58 mm. This corresponds to 48 mm in the DBA cells.

Injection Section The injection into PETRA III takes place in the short straight section South-East. The position of the septum magnet is unchanged to maintain the present injection line as much as possible. Three kickers are distributed to provide a closed bump with the maximum amplitude at the septum (see Tab. 3.2.5). With a horizontal β-function of 25 m at the position of the septum, a free half-aperture of 30 mm and the width of the septum-bar being 5 mm, approximately $7\,\sigma$ of the beam can be injected into the 30 mm mrad aperture of PETRA III. Fig. 3.2.8 shows the β-function and the amplitude of the kicker injection bump. The required kick strength is of the order of 1.3 mrad, this corresponds to approximately $200\,\sigma$ of the stored beam. Requirements for the bump closure lead to an amplitude accuracy of 5×10^{-3} for a $1\,\sigma$ horizontal beam jitter during injection.

Element	Position (South-East right)	Required kick strength for 25 mm bump amplitude
KICKER 1	12.7 m	1.25 mrad
KICKER 2	31.8 m	1.13 mrad
SEPTUM	37.4 m	
KICKER 3	52.8 m	0.51 mrad

Table 3.2.5: Position and Parameters of PETRA III injection elements.

Although a high injection efficiency is foreseen, the permanent magnets of the wigglers and undulators have to be protected against particles which are injected outside the aperture of PETRA III. For this purpose, a simple collimation section with a pair of movable collimators is foreseen in the South-West straight section of the ring. Particles are either directly intercepted by the collimators or will lose enough energy to get lost in the octant after the collimators, before they reach the first wiggler section.

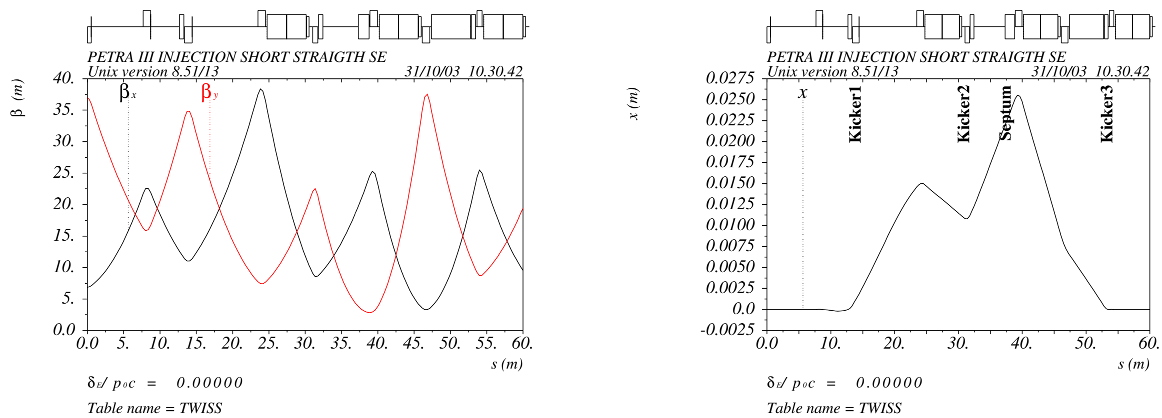

Figure 3.2.8: $\beta-$ functions and injection bump in the injection section.

Linear Optics Error Random errors for the main field components of the magnets arise either from fabrication errors, affecting each single magnet, and from power-supply errors or excitation curve calibration errors, affecting magnets of one family together. Gradient errors of the quadrupoles as well as closed orbit offsets in the sextupoles will perturb the linear optics of the machine and in turn the performance of orbit correction algorithms and the non-linear dynamics. Tab. 3.2.6 summarizes the effects of various errors.

Error	RMS Amplitude	$\Delta\beta_x/\beta_x$	$\Delta\beta_y/\beta_y$
Quadrupole fabrication error	$5 \times 10^{-4}\ \Delta k/k$	0.01	0.01
Power supply jitter	$5 \times 10^{-4}\ \Delta k/k$	0.01	0.01
Closed orbit jitter in sextupole	$20\mu m$	0.014	0.01
Closed orbit offset in sextupole	$200\mu m$	0.1	0.1
Calibration error	$5 \times 10^{-4}\ \Delta k/k$	0.08	0.22

Table 3.2.6: Linear optics errors due to various machine error sources.

The time dependent jitter sources like the quadrupole power supply jitter and the closed orbit variation in the sextupoles will account for a tolerable β-function variation of only 1 %. Larger optic disturbances come from the closed orbit offset in the sextupoles. This contribution can be kept small by beam based alignment and the combined orbit/dispersion correction. Calibration errors will also be corrected through beam based techniques, namely orbit response matrix analysis. With global optics corrections (using only the 5 most effective quadrupole families) the β-beat at HERA could be reduced to within 5 %. At PETRA II the measured β-beat is of the order of 10 %, in accordance with our assumptions above.

3.2.2 Nonlinear dynamics

Chromaticity Correction The chromaticity correction in PETRA is done with sextupoles which are located adjacent to the FODO cell quadrupoles. Compensation of the chromaticity contribution of the 9 DBA cells within these cells would require large sextupole strengths. The reason is a DBA bending magnet deflection of only $2.5°$ together with the dispersion section length of 7.6 m which leads to small dispersion values for all possible sextupole locations. Therefore the chromaticity of the complete ring is corrected only in the seven FODO octants. This requires an over-compensation of roughly 2 per FODO cell, a value which is also reached in colliders with strong focusing in the interaction regions. The dynamic aperture of the lattice without wigglers has been calculated with the tracking code SIXTRACK (Schmidt, 1991), which allows for full 6-dimensional particle tracking without radiation damping.

Fig. 3.2.9 gives an example of the results. On the left graph particles which are stable over 2048 turns ($\approx 1/4$ damping time) are plotted as thick dots versus their initial start amplitudes. Lost particles are plotted as thin dots. In addition, each particle carries a color code according to the difference in tunes between the second and first half of survived turns. This difference gives an indication of chaotic behavior of the corresponding trajectory (Laskar, 1994). On the right graph the same particles are plotted in tune space, with the betatron tune being determined by an interpolated FFT algorithm, leading to accurate determination of the tune. One can easily see the tune dependence on amplitude. Corresponding numbers are summarized in Tab. 3.2.7. Fig. 3.2.9 shows sufficient dynamic aperture for the bare machine.

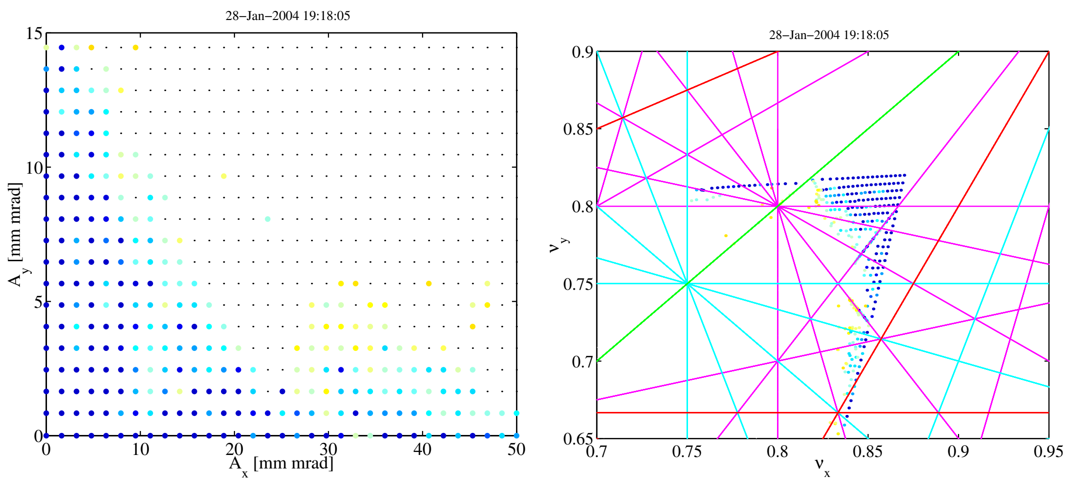

Figure 3.2.9: Dynamic Aperture of bare machine. Left: Initial amplitude of stable particles, Right: Corresponding Tunes

In the following the influence of damping wigglers and undulators as well as multipole errors will be investigated.

Wiggler and Undulator Nonlinearities Wigglers have been used in storage rings for many years. For the same time their influence on the particle beam has been studied. The main problem arises from the fact that the wiggler field is varying strongly in the direction of the beam. Most of the effects will cancel over one wiggler period, while some nonlinear particle motion arises from the effect that the particle trajectory oscillates in phase with the main wiggler field. This leads to linear focusing and additional higher order terms. The vertical focusing is created by the fringe fields and mainly a function of the wiggler field and period length, while the horizontal focusing is influenced by the horizontal field roll-off and thus the pole width.

Analytical descriptions of wiggler fields are usually given in form of the so-called Halbach equations (Halbach, 1981). From there one can derive effective multipole terms to compare basic properties of different wiggler designs. However, especially the horizontal field profile is usually not very well described by the Halbach formulas.

In the design phase the wiggler fields are calculated by magnet field solvers. Tracking through the derived field maps can be done in various ways:

- Direct solution of the equations of motion with a Runge-Kutta type integrator. This method is rather slow and not symplectic, but can be used to verify any of the method given below.

- Fitting the field map to a set of Halbach equations which in turn allow symplectic integration (Litvinenko et al., 2001) or integration by another method.

- Obtain a Taylor map from either form of integration, which in turn can be simplectified with the appropriate generating function (Bahrdt & Wüstefeld, 1990).

The wiggler design has been optimized especially in terms of period length and pole width. As a design criterion a relative field error of $\Delta B_y/B_y|_{10\mathrm{mm}} < 1 \times 10^{-3}$ has been specified. Each wiggler design has been checked with the above mentioned methods. Results of wiggler tracking with a realistic wiggler model are shown in Fig. 3.2.11 in comparison with the machine without wigglers. The wiggler model is based on field calculations.
Additional nonlinearities arise from manufacturing errors and non-complete cancellation of the end-poles of the device. The latter can be largely corrected by choosing an antisymmetric wiggler design, although for a fixed gap device like the damping wigglers this precaution may not be necessary. Contrary to the nonlinear effects arising from the wiggling trajectory, these error fields are well described by usual multipole fields and can be measured along a straight line in the wiggler.

	$\delta\nu_x/\delta J_x$	$\delta\nu_y/\delta J_y$	$\delta\nu_x/\delta J_y$
FODO without wiggler	-5.5×10^{-4}	-8.8×10^{-4}	-3.0×10^{-3}
FODO with wiggler	-1.3×10^{-4}	3.7×10^{-4}	-3.4×10^{-3}
FODO with wiggler and undulator	$+6.5 \times 10^{-5}$	3.4×10^{-3}	-4.1×10^{-3}

Table 3.2.7: Detuning with amplitude

		Wiggler	Undulator
Peak field	T	1.56	0.86
Period length	m	0.25	0.028
Horizontal field parameter	$\mathrm{m}^{-}1$	0.6	0.1

Table 3.2.8: Wiggler and undulator parameters used for tracking

The insertion devices in the new octant are simulated with the parameters given in Tab. 3.2.8. Notable is the smaller field and roll-off parameter k_x, which is achieved due to the smaller possible gap. The main effect of the insertion devices is thus in the vertical plane. In the DBA cells the vertical β-functions at insertion devices are only 4 m, suppressing the influence of the insertion devices on the beam. Only the long undulator has a considerable influence if the vertical β-function is above 10 m.
One of the major effects of the insertion device nonlinearities is the change in the detuning with amplitude as shown in Fig. 3.2.10. This change may require a different optimization of the working point.

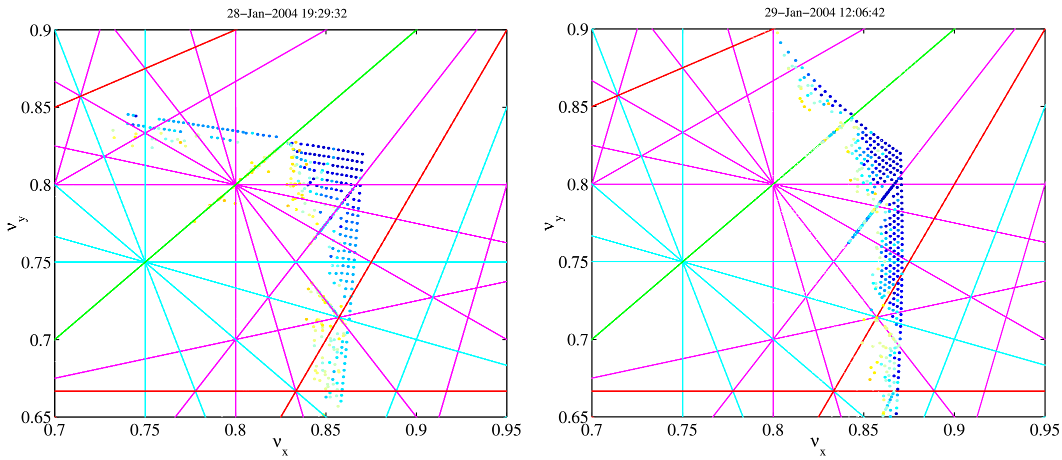

Figure 3.2.10: Stable particles in tune space for PETRA III including damping wigglers (left) and damping wigglers and a full set of insertion devices (right).

Multipole Errors The influence of multipole errors on the dynamic aperture has been calculated. For the existing magnets of the old octants measured field values have been used (Wolff, 1978b; Wolff, 1978a; Rossbach, 1987), while for the magnets of the new octant we have assumed field imperfections based on calculations (Petrov, 2003). The multipole coefficients are summarized in Tab. 3.2.9. A summary of tracking calculations is shown in Fig. 3.2.11. It turns out that the on-momentum dynamic aperture is not affected by multipole

order	dipole	old quadrupoles	new quadrupoles	sextupole
	1×10^{-3}			
1	1.0			
2	0.030	1.0	1.0	
3	0.295	0.565	0.0	1.0
4	0.138	0.174	0.0	1.09
5	0.366	0.217	0.0	2.76
6	0.239	0.435	0.08	0.53
7	0.145	0.107	0.0	0.34
8	0.683	0.415	0.013	0.28
9	0.315	0.217	0.0	3.10
10	0.300	0.674	4.9	0.34
standard deviation of main pole within series	2.5×10^{-4}	5×10^{-4}	1×10^{-4}	2×10^{-3}

Table 3.2.9: Relative multipole coefficients of PETRA III magnets at $r = 50\,\mathrm{mm}$ and standard deviation of main pole amplitude within magnet series.

errors, while the off-momentum aperture requires some re-tuning of the working point to achieve the same performance as without multipole errors.

Injection Efficiency The injected emittance is of the order of 350 nm rad. To reach safely an injection efficiency of close to 100 %, an acceptance of 30 mm mrad is needed. The geometric aperture is limited by the insertion device gaps to 2.2 mm mrad in the vertical plane and to 30 mm mrad in the horizontal plane.
The dynamic aperture for the injection is obtained from tracking calculations for particles with various horizontal and vertical amplitudes. Results for various cases are shown in Fig. 3.2.11. The particles have been tracked for roughly one damping time, corresponding to 8192 turns for the lattice without wigglers and 2048 turns for the lattice with wiggler. The dynamic aperture does thus not reduce the injection efficiency.

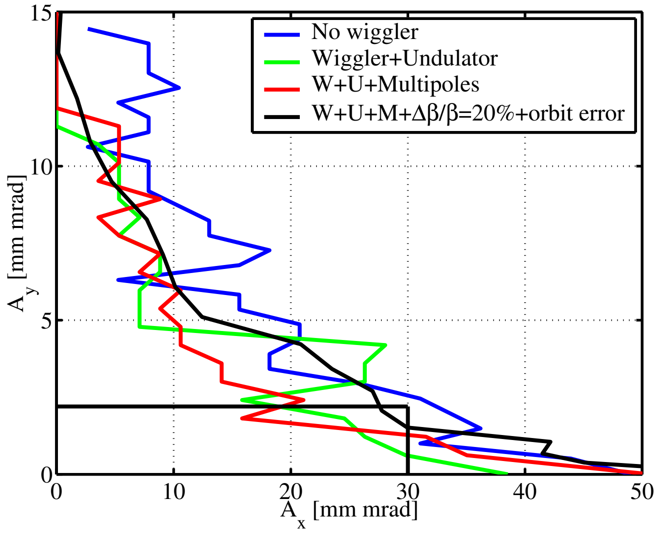

Figure 3.2.11: Dynamic aperture for different initial amplitudes. Damping wigglers, undulators, multipole errors, as well as optics and orbit errors have been included.

Beam Lifetime Beam lifetime is dominated by inelastic scattering of particles within the bunches (Touschek-Effect). The lifetime is proportional to the square of the energy acceptance of the ring, which in turn is given by the installed RF power and the off-energy dynamic aperture. For the Touschek lifetime the off-energy dynamic aperture is important. Tracking calculations for various energy offsets and horizontal amplitudes have been performed, with the vertical amplitude being scaled according to a 1 % emittance coupling. Figure 3.2.12 shows the results, together with lines displaying the betatron oscillation amplitude of a Touschek scattered particle at various positions in the ring. The derived off-momentum aperture varies along the ring between 0.013 and 0.015 %. Further optimization of the working point yields off-momentum apertures above 0.15 %. A cavity voltage of 20 MV ensures that the RF-bucket height is of the same order.

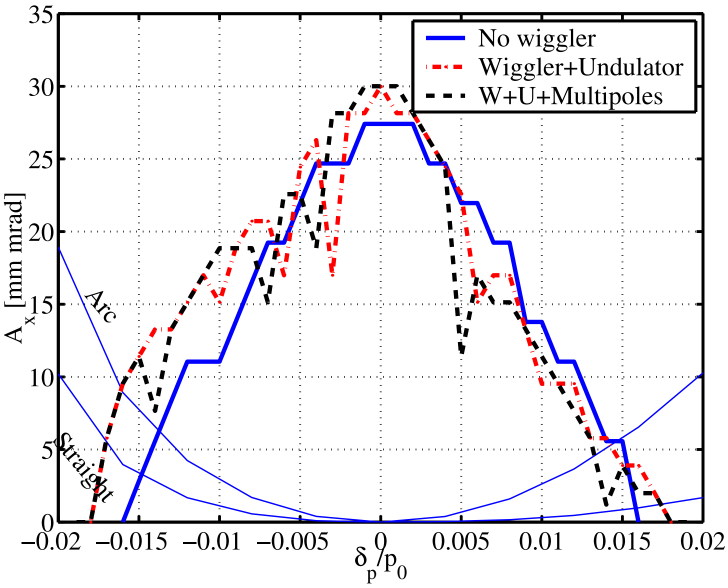

Figure 3.2.12: Momentum aperture of the bare machine and including wigglers, undulators and multipole errors. The thin lines show betatron amplitudes of particles which are Touschek scattered at various locations in the ring.

Based on the above calculated dynamic apertures the beam lifetime can be calculated for the two operation modes. The lifetime for multi-bunch operation is expected to be 35 hours at an average pressure of 2×10^{-9} mbar at 100 mA. The lifetime for single bunch operation is 2 hours at 2.5 mA per bunch.

3.2.3 Current limitations

Introduction A beam circulating in a storage ring interacts with its surroundings via electromagnetic fields induced by image currents in the walls of the vacuum chamber and other objects such as beam position monitors, kickers, RF cavities, bellows etc.. These electromagnetic fields in turn act on the beam and can lead to instabilities. In many synchrotron radiation sources these instabilities limit either the achievable current per bunch or the total current or even both.
In the following we will estimate potential limitations of the single and total current for PETRA III. Also the interaction of the beam with secondary particles like photo electrons in case of positrons or ions in case of electrons may lead to current limitations. At the end of this section a few remarks will be given concerning this problem.

Single bunch instabilities The maximum single bunch current required is 2.5 mA defined by the 40 bunch mode. Since a detailed knowledge of the vacuum chamber is presently not available we will base our estimate on the experience with the existing machine PETRA II. Currently single bunch currents of 10 mA can be stored with no sign of transverse and no evidence of longitudinal instabilities. We can form an impedance model of the machine using old (Weiland, 1981a; Weiland, 1981b; Klatt, Kohaupt & Weiland, 1985) and more recent measurements. We will express the impedance in terms of so-called kick parameters.

$$k_{\|} = \int_{-\infty}^{\infty} ds W_0(s)\lambda(s) \qquad k_{\perp} = \int_{-\infty}^{\infty} ds \quad W_{\perp}(s)\lambda(s)$$

$$k_{\|}(1) = \int_{-\infty}^{\infty} ds W_0(s)\frac{d\lambda(s)}{ds} \qquad \int_{-\infty}^{\infty} ds \quad \lambda(s) = 1$$

Here $W(s)$ denotes the wake potentials and $\lambda(s)$ the line particle density.

In Tab. 3.2.10 the kick parameters of the complete vacuum chamber and the 16 seven cell cavities are given.

In Tab. 3.2.11 the basic machine parameters are listed which are necessary to estimate single bunch limitations.

We will apply the following two formulas to calculate the coherent tune shift of the lowest

Parameter	Vacuum chamber	Cavities	total
$k_{\|}$ (V/pC)	47	81	128
$k_{\|}(1)$ (V/pCm)	-6400	3500	-2900
$k_{\perp}$ (V/pCm)	1000	500	1500

Table 3.2.10: Kick parameters for PETRA III.

Parameter	
I_B (mA)	2.5
$< \beta >$ (m)	20
T_0 (μs)	7.69
R (m)	366.7
E (GeV)	6
Q_s	0.049
h	3840
U_{rf} (MV)	20
α	1.22×10^{-3}
σ_s (cm)	1.1
energy spread σ_E	0.0011

Table 3.2.11: Machine parameters to estimate current limitations.

order modes in the longitudinal and transverse plane.

$$\begin{aligned}\delta\nu_s &= \nu_s \frac{I_B R T_0}{2hU_{rf}} k_0(1) \\ \delta\nu_\beta &= \frac{I_B < \beta > T_0}{4\pi E/e} k_\perp\end{aligned}$$

As long as these tune shifts are considerably smaller than the synchrotron tune no fast head tail instability and no turbulent bunch lengthening will occur. In units of the synchrotron tune the calculated tune shifts are:

$$\begin{aligned}|\delta\nu_s/\nu_s| &= 0.13 \\ |\delta\nu_\beta/\nu_s| &= 0.15\end{aligned}$$

These two relative shifts are small enough that no instabilities should occur which is confirmed by the fact that PETRA II does not suffer from single bunch instabilities up to single bunch currents of 10 mA.
There will be clearly differences between the vacuum chamber of PETRA III and PETRA II. In the old octants the existing vacuum chamber will be replaced by a new one. Although the vacuum chamber has not been designed in detail yet the basic parameters have been fixed (see Sec. 3.5). For example a cross section of the dipole chamber is shown in Fig. 3.2.13.

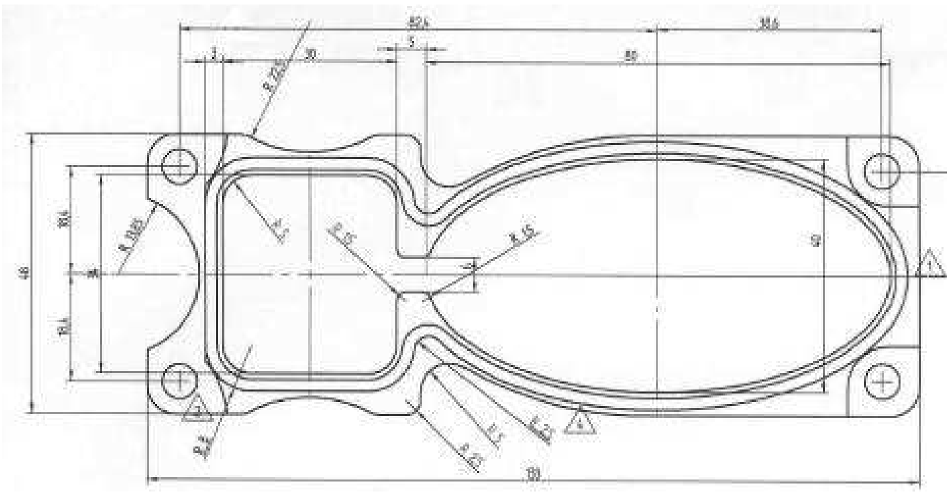

Figure 3.2.13: Cross section of the dipole vacuum chamber in the old octants.

The basic differences of the new chamber compared with the old one are the smaller dimensions and the fact that the chamber has a continuous pumping slit of 6 mm height and 5 mm depth. In order to check that this chamber does not contribute significantly to the impedance of the machine we calculated the kick parameters and higher order modes.
Strictly speaking the higher modes do not limit the single bunch current but may have other negative effects. The frequencies of the higher order modes are within a band extending from

4 up to 10 GHz. These will not trouble for example the monitor electronics which will have a low pass characteristic so that it is not sensitive to signals with a frequency above 2 GHz. Furthermore the higher order modes will not lead to a significant heating of the NEG strip.

The results for the kick parameters of 196 dipole chambers are summarized in Tab. 3.2.12.

Parameter	
$k_{\parallel}$ (V/pC)	-5.5×10^{-3}
$k_{\parallel}(1)$ (V/pCm)	6.3×10^{-3}
$k_{\perp}$ (V/pCm)	-4.7×10^{-2}

Table 3.2.12: Kick parameters of new dipole vacuum chambers.

Compared with the numbers given in Tab. 3.2.10 the new dipole chamber contributes only very little to the impedance of the machine. The necessary vacuum chamber joints and bellows will be carefully designed similar to those existing in the HERA electron ring. In terms of impedance the vacuum chamber of HERA has an even lower impedance than the existing PETRA II vacuum chamber (Klatt & Weiland, 1988). Therefore we assume that concerning the old octants the impedance of the chamber for PETRA III will at least not be larger than the impedance of the PETRA II chamber.

Unfortunately this will not be true for the new octant. The complicated vacuum chamber will significantly contribute to the impedance. To estimate the impedance of the new octant we consider the impedances of the large synchrotron radiation sources APS and ESRF (Harkay, 2002). Based on their experience the new octant will almost double the impedance of the machine. This effect is more pronounced in the transverse plane. However since the relative tune shifts given above are quite small there is some safety margin left that even if the impedance of the machine doubles a single bunch current of 2.5 mA will still be stable. Nevertheless a careful design of the vacuum chamber of the old and new octants will be necessary taking into account the experience gained by the existing synchrotron radiation sources.

Coupled bunch instabilities Presently the total current in PETRA II is limited to rather small values of about 5 mA by coupled bunch instabilities. These instabilities are mainly driven by the parasitic modes of the RF cavities. In order to achieve the required currents for HERA and the parasitic synchrotron radiation operation two powerful transverse feedback systems are necessary. Although the beam is also longitudinally unstable this imposes only a limitation for total beam currents above 55 mA.

For PETRA III the situation will be similar since it is foreseen to keep the existing RF cavities in the machine. In order to find out what kind of countermeasures are necessary to achieve the design current for PETRA III we tried to determine the narrow band impedance of the machine. To this end we measured the threshold currents of coupled instabilities for uniform fillings and the natural damping rate of the beam for all directions. By applying the following two formulas

$$\text{longitudinal}: \frac{1}{\tau} = \omega_s \frac{I_{thres} Z_0^{eff}}{2U_{rf}}$$

$$\text{transverse}: \frac{1}{\tau} = \omega_0 \frac{I_{thres} \beta_{cav.} Z_\perp^{eff}}{4\pi E/e}$$

which express that the growth rates are just balanced by the natural damping at the threshold of the instability we calculate the effective narrow band impedance of the machine.
The results are summarized in Tab. 3.2.13. In case of PETRA III the longitudinal radiation

	longitudinal	horizontal	vertical
I_{thres} (mA)	7	6	6
$1/\tau$ (Hz)	35	50	60
Z_{eff}	3.6 MΩ	45 MΩ/m	54 MΩ/m

Table 3.2.13: Multibunch effects in PETRA III.

damping (125 Hz) is significantly larger than the damping rate quoted in Tab. 3.2.13 but still not sufficient to reach the design current.
The fact that the number of cavities will be reduced from 16 to 12 will not be taken into account in the following but taken as safety margin.
Considering the values in Tab. 3.2.13 it is obvious that additional damping is required which has to be supplied by powerful feedback systems to reach the design current. Including a safety margin of approximately 50 % the required damping of the feedback systems is given in Tab. 3.2.14. Details of the feedback system are described in Chapter 3.10.

Feedback	Required damping (Hz)
longitudinal	800
horizontal	1400
vertical	1400

Table 3.2.14: Basic parameters for multibunch feedback.

Ions and e-cloud instability PETRA III can be run with either positrons or electrons. The limitations by single and multi bunch instabilities are almost identical for both species.
In principle there are two arguments against positrons that is e-cloud instability and the more difficult operation of the pre-accelerators in particular the linac. The e-cloud instability does not seem to be a real issue according to estimates (Wanzenberg, 2003). The ease of operation of the linac is however a good argument against positrons and in favor of electrons. On the other hand the operation with electrons may suffer from ions and dust. In the past we looked for ion and dust effects in PETRA II (Balewski et al., 1996). We have never found any

evidence for ions and never expected any from linear theory. The same should be true for PETRA III. Concerning dust we saw some events in the past.
As there are no other arguments against or in favor for positrons we will make a decision based on the experience gained during the commissioning of PETRA III. We will take up again the investigation of ion and dust effects as basis for a decision against or in favor for electrons.

3.2.4 Closed orbit correction and stability

Closed Orbit Distortion Third-generation light sources need careful alignment, stabilization and corrections. The closed orbit distortion results from field errors and field components arising from magnetic element positioning errors. The most severe effects comes from the misalignment of quadrupole magnets, where the resulting dipole field is proportional to both gradient and alignment error. The closed orbit distortion has been estimated with the alignment tolerances and field errors presented in Tab. 3.2.15. Since the integrated quadrupoles strength in the new octant is two to three times higher than in the old octants the alignment requirements are accordingly tighter. The closed orbit has been simulated for 200 different sets of alignment errors and field errors assuming a Gaussian distribution (truncated at 2 σ) with RMS values given in Tab. 3.2.15.
The closed orbit is obtained using the MAD.X program (Schmidt, 2000) in the presence of damping wigglers and synchrotron radiation. A typical distorted closed orbit at the BPM location is shown in Fig. 3.2.14.
The orbit can have maximum amplitudes of up to 20 mm in both planes. The expected RMS values for the closed orbit in the horizontal and vertical plane are 7 mm and 4 mm respectively as shown in Fig. 3.2.15.

Closed Orbit and Dispersion Correction The closed orbit will be measured by 198 beam position monitors (BPM). In the old octants the BPMs are located next to each horizontal defocusing quadrupole. Extra windings on 130 dipoles and 59 independent magnets are used as horizontal correctors while 187 independent magnets are used as vertical correctors.

	Number of magnets	Δx	Δy	Δs	$\Delta\psi$	Field errors
		[mm]			[mrad]	
Dipole	214	0.25	0.25	0.50	0.2	$\Delta B/B = 0.2 \times 10^{-4}$
Quadrupole old octants	281	0.25	0.25	0.5	0.2	$\Delta k/k = 2 \times 10^{-4}$
Quadrupole new octant	98	0.1	0.1	0.5	0.2	$\Delta k/k = 2 \times 10^{-4}$
Sextupole	140	0.25	0.25	0.50	0.2	
Monitors	198	0.2	0.2			

Table 3.2.15: Magnet and monitor alignment errors and magnet field errors.

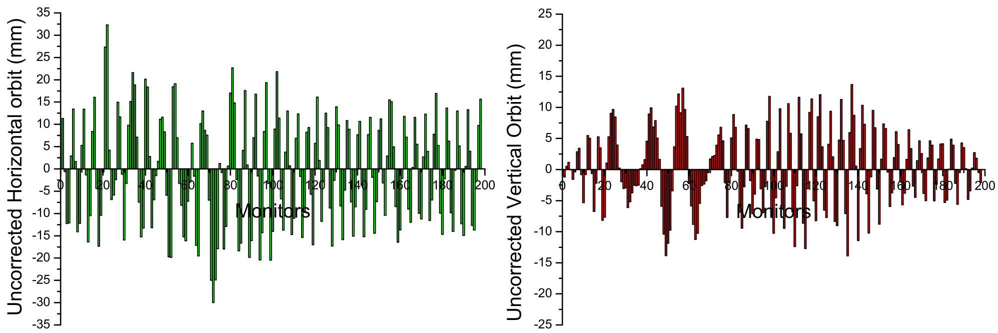

Figure 3.2.14: Horizontal and vertical COD due to random magnet errors (before correction).

Details of BPMs, horizontal and vertical correctors in two adjacent DBA cells in the new octant are shown in Fig. 3.2.16.
Straight forward orbit correction is not sufficient but dispersion correction has to be included. The small vertical emittance imposes tight tolerances on the vertical dispersion. In addition the horizontal dispersion function in the wiggler and undulator sections has to be controlled. Limits for both the horizontal and vertical dispersion are given in Tab. 3.2.16.
An algorithm (Assmann et al., 2000) for the simultaneous optimization of the closed orbit

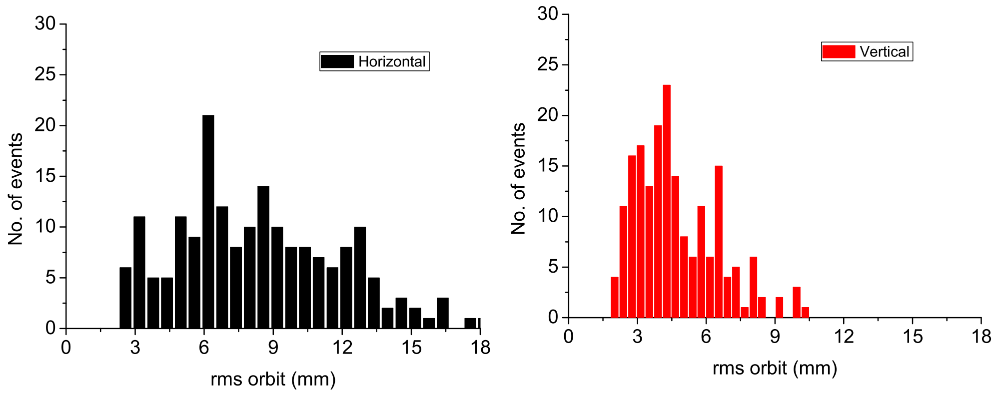

Figure 3.2.15: The horizontal and vertical rms COD produced by 200 sets of random errors before correction.

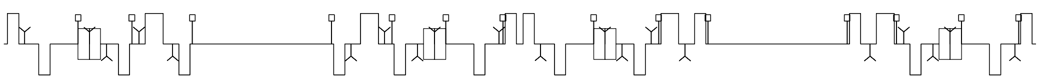

Figure 3.2.16: BPMs and correctors distribution per a double DBA cell, symbolizing beam position monitors, horizontal and vertical correctors.

	D_x [mm]	D_y [mm]
Wiggler section	18	5
Undulator section	33	7
FODO arcs		58
DBA arcs	22	31

Table 3.2.16: Maximum horizontal RMS dispersion distortion yielding 5 % horizontal emittance growth and RMS vertical dispersion yielding $\epsilon_y = 0.01\, nm\, rad$.

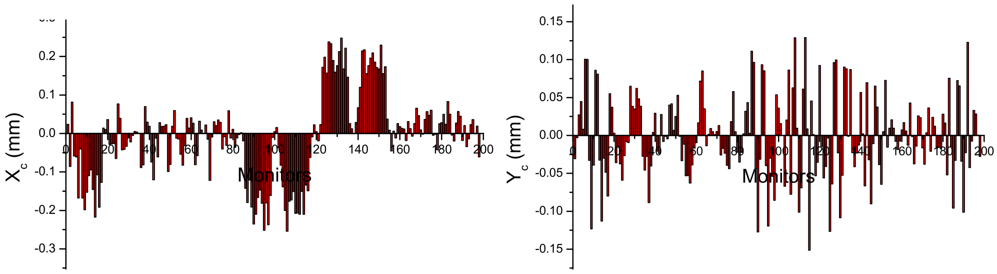

Figure 3.2.17: Horizontal and vertical orbit after orbit correction.

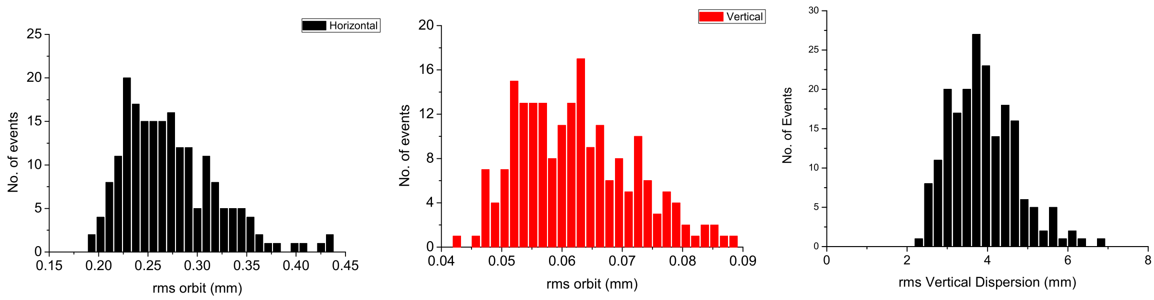

Figure 3.2.18: Calculated rms closed orbit distortion and spurious dispersion produced by 200 sets of random errors (after correction).

and the dispersion in the transverse planes is applied. This algorithm is given by the following system of linear equations:

$$\begin{pmatrix} \alpha\vec{u} \\ (1-\alpha)\vec{D}_u \end{pmatrix} + \begin{pmatrix} \alpha\mathbf{R} \\ (1-\alpha)\mathbf{S} \end{pmatrix} \vec{\theta} = 0 \tag{3.2.3}$$

with $\vec{u}$ being the closed orbit and $\vec{D}_u$ the dispersion measured at the BPMs, $\mathbf{R}$ the orbit response matrix, $\mathbf{S}$ the dispersion response matrix and $\vec{\theta}$ corrector kicks. α is a weight factor used to shift from a pure orbit ($\alpha = 0$) to a pure dispersion correction ($\alpha = 1$). Singular Value Decomposition (SVD) (Press et al., 1987) has proven to be a numerically robust method to solve such equations. In case that more correctors than monitors are available,

SVD minimizes the rms orbit and rms corrector strengths, in the reverse case it leads to a suppression of BPM errors and a smoothing of the orbit.
Closed orbit and dispersion correction has been simulated to verify that the desired vertical and horizontal emittance can be achieved. A typical closed orbit after correction is presented in Fig. 3.2.17. Distributions of the corresponding rms values of the orbit and dispersion after correction are shown in Fig. 3.2.18. The simulations have shown that the RMS vertical dispersion can be kept below 5.0 mm in the whole ring. The maximum corrector strength needed is 0.5 mrad. The required resolution of the corrector power supplies has to be at least 16 bit.
Although the described correction scheme fulfills the dispersion requirements additional skew quadrupoles are foreseen to independently minimize the betatron coupling and locally correct the dispersion coupling generated in the sextupoles. This system is presently under study.

Beam Stability Beam stability is one of the most important requirements in synchrotron light sources. In the previous section it was shown that the design goal for the horizontal emittance and the small value for the emittance coupling can be achieved under realistic conditions. The result of the correction procedure is the so-called golden orbit. Unfortunately this golden orbit is not stable. Changes of the orbit may be the results of complex phenomena for example natural and cultural ground vibrations, tunnel drifts, resonant amplifications due to supports, thermal deformations etc.. These changes can be divided into fast and slow motion. Fast motion ($f >$ a few tenth of a Hz) has to be corrected by a feedback system. Slow motion ($f <$ a few tenth of a Hz) must be corrected by repeated standard orbit correction.
Beam stability requirements are typically 10% of the beam size at the insertion devices. In the case of PETRA III the beam sizes and the divergences in the middle of the insertion sections are as follows:

Device	β_x [m]	β_y [m]	σ_x [μm]	σ'_x [μrad]	σ_y [μm]	σ'_y [μrad]
5m Undulator	1.2	3.95	34.6	28.9	6.3	1.6
5m Undulator	20.01	2.36	142	7.1	4.9	2.1
20m Undulator	16.02	9.89	127	7.9	9.9	1.0

Table 3.2.17: Beam size at insertion device locations.

According to the above mentioned demands an orbit stability of microns in the horizontal and even of half a micron in the vertical plane have to be achieved. The present day's state of the art beam position stability achievements are summarized in Tab. 3.2.18.
According to the table it has been demonstrated at several laboratories that the required stability can be achieved (ELETTRA $< 0.2\mu\mathrm{m}$, SLS $< 0.5\mu\mathrm{m}$ (Schlott, 2002), ESRF $\approx 0.6\mu\mathrm{m}$ (Plouviez, Koch & Uberto, 1998)).
In order to estimate the parameters of the fast feedback for PETRA III, measurements have been performed to identify sources of orbit disturbances like ground motion and vibrations. In addition we measured the orbit distortions in PETRA II in a frequency range from 0.1 Hz to 500 Hz. Since a considerable part of the PETRA III magnetic structure is identically to the

SR facility	FB type	Monitors	max. BW	Stability
ALS*	G	rf-BPMs	< 100 Hz	< 1 µm
APS	G and L	rf & p-BPMs	< 30 Hz < 50 Hz *	< 2 µm < 1 µm *
NSLS	G	rf-BPMs	< 200 Hz	0.5 µm
SPEAR 3*	G	rf-BPMs	< 200 Hz	< 1 µm
BESSY *	L	rf and p-BPMs	< 100 Hz	< 1 µm
DELTA	G	rf-BPMs	< 1 Hz	< 5 µm
ELETTRA *	L	rf-BPMs	< 20 Hz	< 0.2 µm
ESRF	G	rf-BPMs	100 Hz	0.6 µm
MAX-lab	G	rf-BPMs	1 Hz	< 3 µm
SLS *	G	rf & p-BPMs	100 Hz	< 0.5 µm
SRS	L	p-BPMs	0.03 Hz	1 µm
SUPER-ACO	G	Rf-BPMs	< 150 Hz	< 5 µm
DIAMOND *	G	rf-BPMs	100 Hz	< 1 µm
SOLEIL *	G	rf and p-BPMs	100 Hz	0.2 µm
KEK-PF	G	rf-BPMs	3 Hz	< 5 µm
SPRING-8	G	rf-BPMs	< 0.01 Hz 200 Hz *	< 3 µm < 1 µm *

* feedbacks in commissioning, respectively proposed systems
(table comprehends only data, which could be collected until EPAC paper submission deadline and thus might not be complete…)

Table 3.2.18: Achieved orbit stability at selected synchrotron radiation sources. (from Schlott, 2002)

structure of PETRA II these measurements are useful and relevant in order to estimate orbit distortions for PETRA III. Measurements of ground motion have been performed at several locations on the DESY site in the past (Decking, Flottmann & Rossbach, 1990; Brinkmann & Rossbach, 1994; Shiltsev, 1996). Recently some of the measurements have been repeated (Ehrlichmann & Bialowons, 2003) and compared with the situation at other laboratories. The result of the most recent measurements are shown in Fig. 3.2.19. The power spectrum shows the typical form. From 0.1 Hz to a few Hertz the power density is a strongly decreasing function. The ground motion is mainly given by ground waves. The increase around a few Hertz is due to cultural noise. From this figure one can conclude that the situation at DESY and the ESRF are comparable. Fig. 3.2.19 also shows the integrated spectrum which indicates that the most significant contributions to ground displacement come from frequencies below 10 Hz. The rms value of the ground motion is below 140 nm.
This noise spectrum is translated by the magnet supports and the beam optics into orbit distortions. These orbit distortions have been measured at PETRA II and results are shown in Fig. 3.2.20. Comparing the two power spectra (ground motion and orbit) indicates that the orbit is basically determined by the amplification factors of the optics between 0.1 and 10 Hz and that the noise power spectrum is amplified around 20 Hz. This is due to the resonant behavior of the magnet supports in particular the quadrupole stands. The lowest resonance frequency of the quadrupole supports is around 20 Hz.

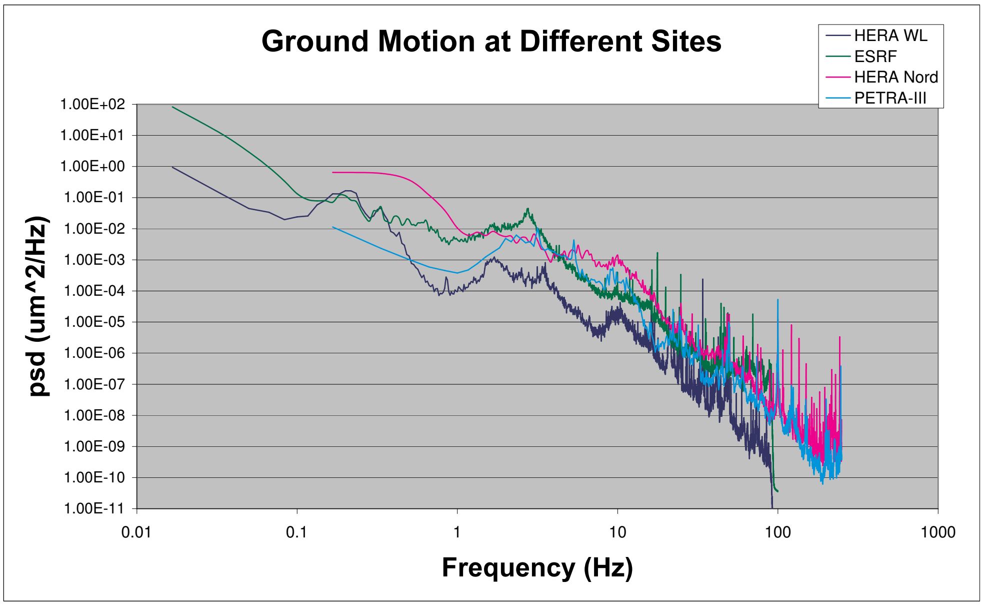

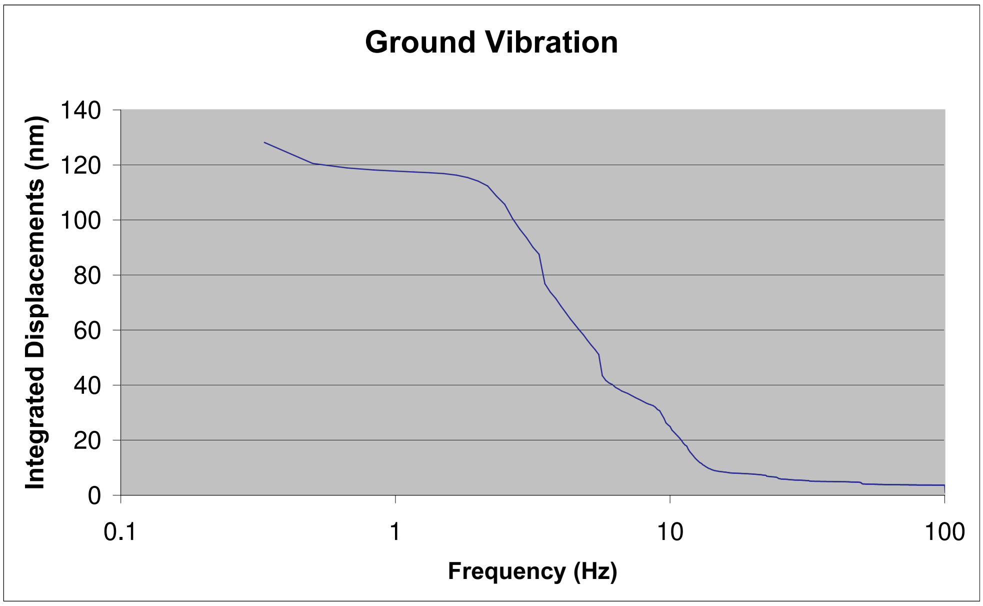

Figure 3.2.19: The power spectral density of the ground motion at different accelerator sites (Ehrlichmann & Bialowons, 2003) (top) and the integrated power spectral density of the ground motion in the PETRA tunnel.

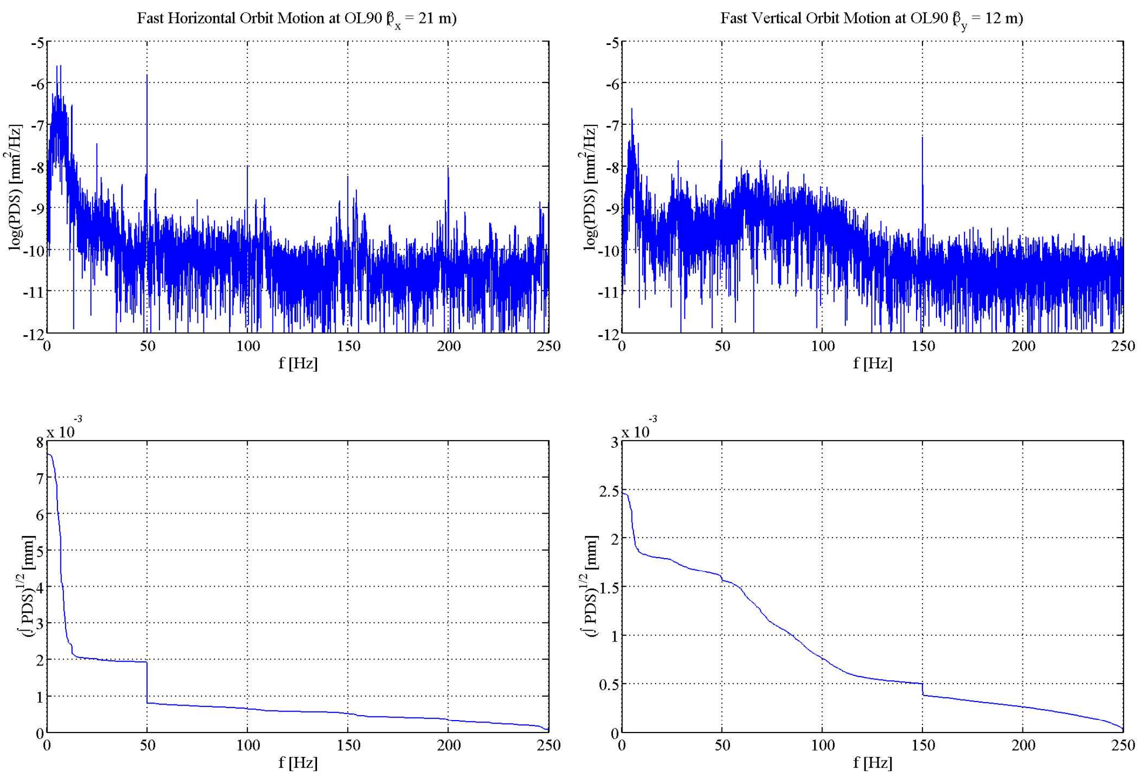

Figure 3.2.20: Power spectral density of horizontal and vertical orbit distortions and integrated power spectral density.

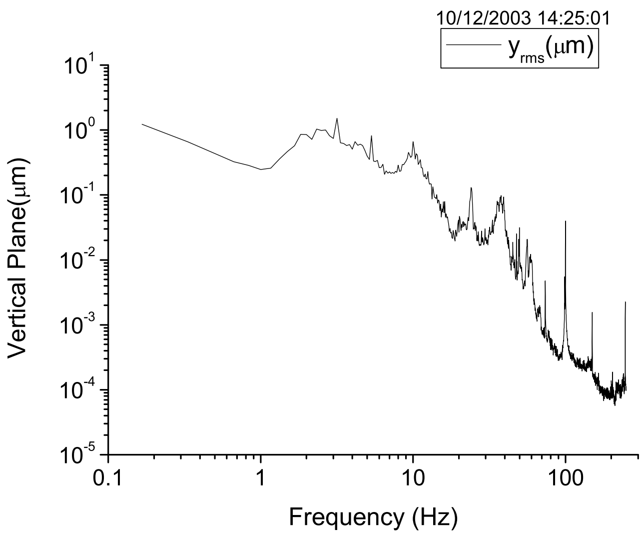

Figure 3.2.21: The power spectral density of orbit motion due to measured ground motion.

Also visible is the line frequency 50 Hz. In the vertical spectrum there are also some components extending from 60 to 100 Hz. The average value of the orbit distortion given by the integrated power spectrum over the whole frequency range is 8 $\mu\mathrm{m}$ in the horizontal and 2.5 $\mu\mathrm{m}$ in the vertical plane. Since the girders in the new octant have also mechanical resonance frequencies above 20 Hz (see Sec. 3.7) and the magnet support structure of the old octants will not be changed the above shown ground motion power spectrum will result in a similar orbit motion for PETRA III.
Assuming that the noise is mainly transferred via the optical amplification factors into orbit distortion the frequency spectrum of the vertical orbit can be estimated and is shown in Fig. 3.2.21.
This estimate is based on the assumption that the orbit distortions are caused by noise. However, part of the excitation will originate from ground waves that can coherently interact with the storage ring i.e. the alignment errors of quadrupoles are correlated. In order to investigate this effect we apply the following model (Rossbach, 1988; Fischer, 1984). The vertical displacement of the n^{th} quadrupole generated by a plane wave is

$$\Delta z_n(t) = \hat{z}\mathrm{Re}\exp\left(\mathrm{i}\left[\omega\mathrm{t} + \frac{\omega\mathrm{R}}{\nu}\cos(\theta_\mathrm{n} - \theta_\omega) + \phi_0\right]\right) \quad (3.2.4)$$

$$\frac{C}{\lambda} = \frac{\omega R}{V} \quad (3.2.5)$$

with C the circumference, λ the wavelength of the disturbance, ω the angular frequency, θ_ω and θ_n the direction of incidence and the position of the quadrupole. The closed orbit distortion due to this displacement is

$$z_c = \frac{\sqrt{\beta_0}}{2\sin\pi Q_z}\sqrt{\beta_{z,n}}\frac{\Delta z_n}{f_n}\cos(\phi_n - \pi Q_z). \quad (3.2.6)$$

Based on equations 3.2.5, 3.2.6 orbit distortion are estimated for the proposed PETRA III lattice. The beam parameters considered for these calculations are betatron tunes of 35.74 and 30.80 and the betatron functions at the center of the insertion devices (1.2 m and 3.95 m). The betatron wave lengths are $\lambda_{\beta x} = 64.5\,\mathrm{m}$, $\lambda_{\beta y} = 74.81\,\mathrm{m}$. The velocity of the incoming ground wave from a far source is taken at 100 m/s. Fig. 3.2.22 shows the amplitude of ground waves as a function of frequency that would cause a change in beam position by 10 % of the beam size.
The actual amplitudes of ground motion in the horizontal plane always stay below the limit. In the vertical plane the limit given in the picture is close to the values shown in the power density plot (Fig. 3.2.19). One has, however, to keep in mind that the ground motion driven above a few Hertz is not determined by coherent ground waves but mainly by cultural noise (Ehrlichmann & Bialowons, 2003).
Summarizing the above findings the orbit distortions for PETRA III will be basically determined by cultural noise. The amplitude of the orbit perturbations will be close to the ones measured for PETRA II. So we expect that the position errors at the insertion devices is around 10 μm in the horizontal and around 3 μm in the vertical plane (see Fig. 3.2.20). Therfore a fast orbit feedback is necessary.

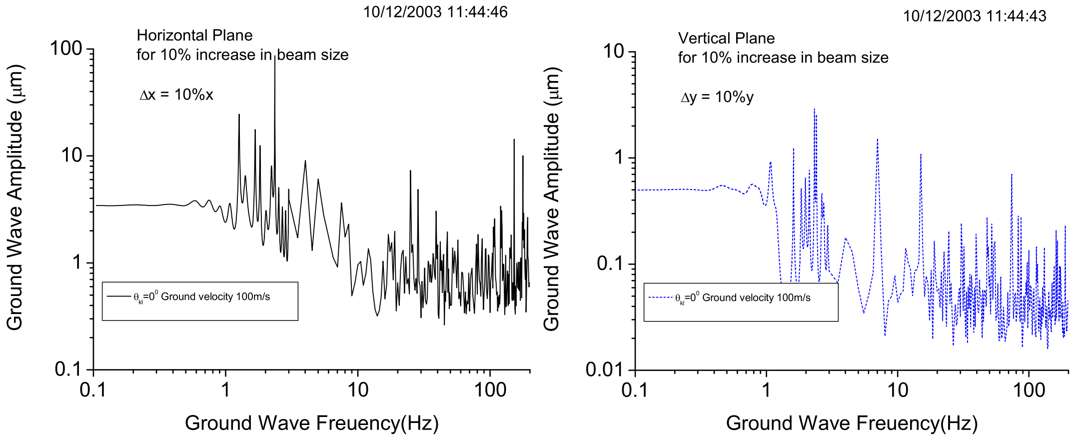

Figure 3.2.22: The amplitudes of a plane ground wave propagating at 100 m/s that will cause a change in beam position of 10 % of the beam size.

According to the integrated power spectrum of the orbit perturbations (Fig. 3.2.20) this system has to fight distortions with frequency components between a few tenth of a Hertz up to approximately 100 Hz. The orbit distortion has to be reduced by a factor less than 10. Such feedback requirements have been proven to be feasible.

At first sight it may be sufficient to stabilize the beam position only at the insertion devices. Unfortunately this is not true. In addition it is necessary to control the orbit in the FODO arcs and in particular in the sextupoles. The orbit position in the sextupoles mainly determines the spurious vertical dispersion and so in turn the vertical emittance of the machine. Therefore the following layout of the feedback has been proposed.

For fast orbit correction all position monitors are taken into account and all fast correctors in the new octant. Furthermore, two fast correctors per plane are installed at both ends of the damping wiggler section and one fast corrector is installed in each of the remaining straights. The efficiency of this arrangement has been studied by simulations. A golden orbit has been determined as described in Sec. 3.2.4. In addition the focusing strength of the quadrupoles has been randomly distorted to get a β-beating of approximately 20 % in both planes. Then a $1\,\mu\mathrm{m}$ misalignment was applied to all the quadrupole magnets of the PETRA III lattice. This orbit was then corrected with respect to the golden orbit. This procedure has been repeated 1000 times and the position at the insertion devices and the emittances in both planes have been recorded. The orbit at the insertion devices stays within the required limits. In Fig. 3.2.23 recorded values of the emittances are presented. The figure shows that the fluctuations in the horizontal emittance are negligible and the fluctuations in the vertical emittance of approximately 8 % stay within the tolerable limit. One should keep in mind that the simulation has been performed assuming rather pessimistic values for the rms amplitude of the ground motion ($1\,\mu\mathrm{m}$) and the β-beating (20 %). This shows that this correction scheme is robust.

The technical realization of the system has not been worked out in detail yet, but some of the key components have been looked at. It is obvious that a precise and low-noise orbit

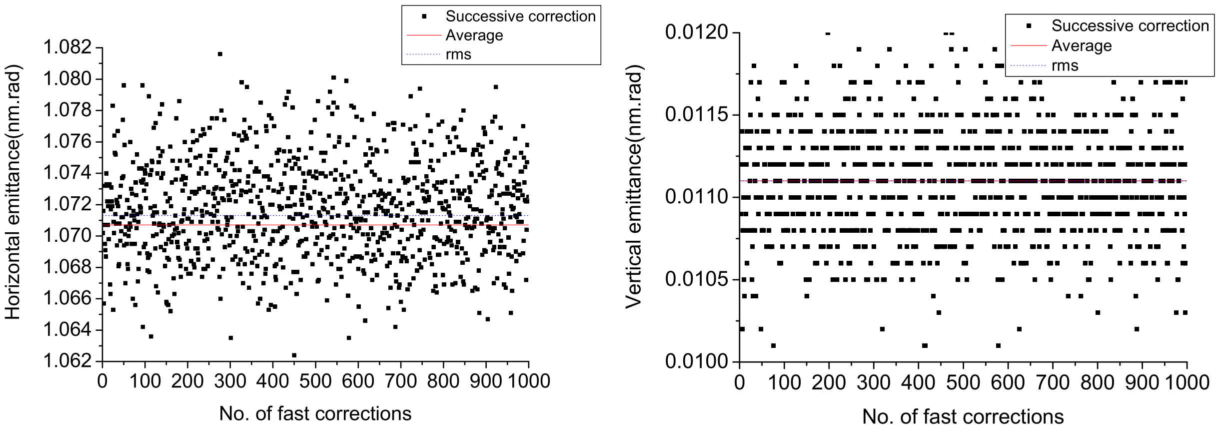

Figure 3.2.23: Horizontal and vertical equilibrium emittance during 1000 successive corrections.

measurement is necessary. Monitors and monitor electronic are presented in section 3.9. Although not easy it is possible to meet the requirements for the orbit measurement accuracy. In order to cover the required frequency range orbit information has to be taken at a rate of 4 kHz which has been demonstrated to be feasible. The amplitudes of the correction kicks are small enough so that they can be supplied by air coil magnets for example similar to those in operation at the ESRF. The data transfer can be accomplished in ways that are used at ESRF and APS (Plouviez, Koch & Uberto, 1998; Carwardine et al., 1997). For the time being we aim for a conventional system gathering all the information in a central unit to determine the kicks with an SVD algorithm and to use a PID controller.
The orbit stabilization system is certainly demanding but it has been shown that such a system is feasible.

3.3 Magnets for the New Octant of PETRA III

In the new octant of the PETRA III machine 68 short and 16 long quadrupole magnets, 18 dipole magnets and correction magnets for beam steering are needed. In this section the design of the quadrupole and dipole magnets will be discussed. The work was done in collaboration with the Efremov Institute. The position of the magnets and their names are shown in Fig. 3.3.1. The synchrotron radiation beamline is located close to the storage ring beam in a separate vacuum chamber with an outer diameter of 20 mm. In the design presented here the distance between the axis of the quadrupole magnets and the synchrotron beam varies between the two dipoles PDA from

76 to 98 mm at the position of the first PQA (closed yoke)
137 to 159 mm at the second PQA position (closed yoke)
172 to 194 mm at the third PQA position (closed yoke)
233 to 255 mm at the PQC position (non-closed yoke).

A major design goal was to minimize the number of different magnet types as well as the manufacturing costs.

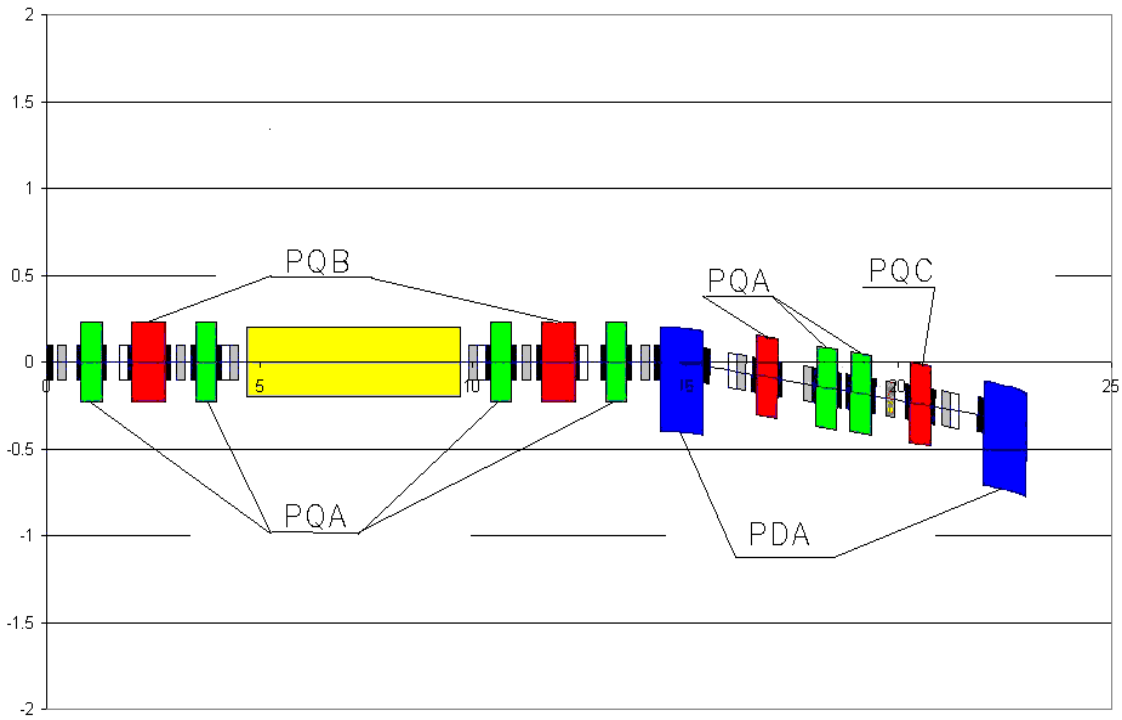

Figure 3.3.1: PETRA III magnetic unit cell.

3.3.1 Quadrupole magnets

According to the layout of the new octant quadrupole magnets with a closed and non-closed iron yoke had to be designed. The main requirements for these quadrupole magnets are listed in Tab. 3.3.1.

The field quality depends on the strength of the different harmonics. For a conventional quadrupole magnet (closed yoke) the lower harmonics values with k = 3, 4, 5 and the so called 'allowed' harmonics values (k = 6, 10, 14, ...) are essential. The lower harmonic values are determined by the quality of the quadrupole assembly whereas the allowed harmonics depend on the quadrupole design. For example a correctly shaped pole profile will generate only a small value for the k = 6 term (dodecapole). If a harmonics value of less than 10^{-4} is required the tolerances of the aperture geometry must be less than 3×10^{-2} mm. In case of a non-closed yoke with non-magnetic inserts or spacers the 'allowed' harmonics are increased due to additional values (k = 4, 8, 12 and so on). The vertical and horizontal displacement of the two halves of such a magnet must be less than 0.03 mm and the rotational misalignment of the two halves must be less than 10^{-4}, otherwise a correction coil is needed.

3.3.2 Specification of the quadrupole magnets

With the main requirements for the quadrupole magnets three types were designed:

Iron length of 500 mm (closed yoke) called PQA,
Iron length of 800 mm (closed yoke) called PQB,
Iron length of 500 mm (non-closed yoke) called PQC.

The quadrupole magnets consist of laminated iron yokes produced from steel sheet metal EBG type 'Stabocor M-1200-100A'. The magnet should be easily separable in the horizontal plane for a subsequent installation of the vacuum chamber. The coils sit symmetrically with

	Closed yoke (PQA)		Non closed yoke (PQC)	
Parameters		Note		Note
Iron length, [m]	0,8/0,5	as short as possible	0,5	as short as possible
Quantity	16		68	
Aperture radius, [mm]	35		35	
Max. field gradient, [T/m]	21		21	
Radius of good field region, GFR, [mm]	25		25	
Field quality in the GFR	$5\cdot10^{-4}$		$5\cdot10^{-4}$	

Table 3.3.1: Main requirements for the quadrupole magnets PQA, PQC

respect to the axis on the quadrant iron and all four coils are electrically connected in series. The main parameters of these magnets are listed in Tab. 3.3.3 (closed yoke) and Tab. 3.3.4 (non-closed yoke) at the end of this section. The nominal current is 190 A. Four water circuits are needed for the coil cooling made from a $9 \times 9\,\text{mm}^2$ copper conductor with a hole of 4.5 mm diameter. The copper conductor is wrapped by three layers of fiber glass band. The thickness of the turn insulation is 0.5 mm per side. The coil has six layers and a total of 57 windings. The correction coil has a copper conductor of $1.25 \times 3.55\,\text{mm}^2$ cross section and consists of two layers of 56 windings. The insulation of the coil is vacuum impregnated. A water temperature rise of 15° C is expected. The gap between the coils for the accommodation of the vacuum chamber is 28 mm. To minimize the tooling costs (stamping tool) the PQB is stacked of the same lamination as the PQA. The length of PQB is increased to 800 mm.

3.3.3 Results of the 2-D calculation for the quadrupole magnets

For the 2-d calculation the OPERA-2D code was used. The material for the yoke is 'Stabocor M-1200-100A' steel with a filling factor of 0.98. In Fig. 3.3.2 the cross section of a quarter of the quadrupole magnet (PQA) with a closed yoke is shown. The horizontal gap of 28 mm height between the coils allows to use this magnet at several positions for the outgoing synchrotron radiation beam. Because of the symmetry one eighth of the cross-section was used for the 2d calculation (red line). The result is shown in Fig. 3.3.3 (a quarter of the yoke is shown). A quarter of the cross-section of the quadrupole magnet with a non-closed yoke (PQC) is shown in Fig. 3.3.4 and the result is shown in Fig. 3.3.5. With the input parameters from Tables 3.3.3 and 3.3.4 at the end of this section, the general results of the calculated field quality, the maximum inductions at the pole (B_p^{max}) and yoke (B_Y^{max}) are listed in Tab. 3.3.2 for the closed and non-closed yokes.

Var.	Ampere turns	Current	Gradient	B_p^{max}	B_Y^{max}
	kA	A	T/m	T	T
Closed yoke	10.7	187.7	21.6	1.45	1.45
Non closed yoke	10.7	187.7	21.6	1.43	1.4

Var.	A_4/a_2	a_6/a_2	a_8/a_2	a_{10}/a_2	a_{14}/a_2	a_{18}/a_2	$\Sigma a_i/a_2$
R_{ref} = 25 mm	10^{-5}						
Closed yoke		0.5		-1.9	-3.2	-3.1	9
Non closed yoke	-0.03	0.5	0.02	-1.9	-3.2	-3.1	9

Table 3.3.2: Results of the calculation for the quadrupole magnets

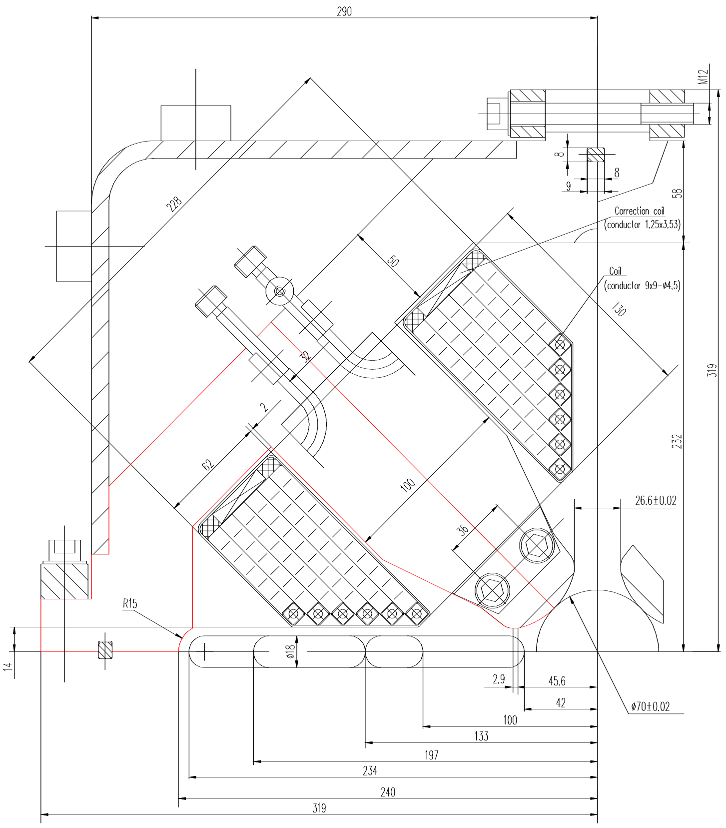

Figure 3.3.2: One quarter cross-section of the quadrupole magnet with a closed yoke.

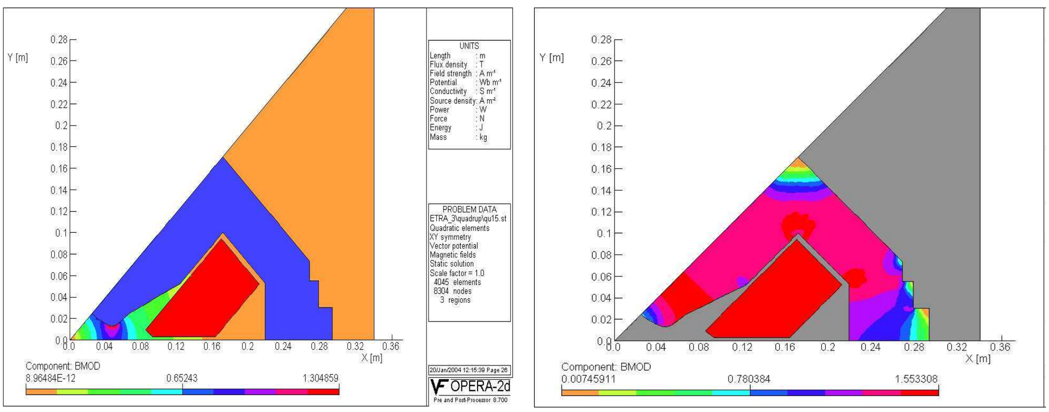

Figure 3.3.3: Results of the calculation for the closed yoke. The induction (BMOD) in Tesla is shown. In the left figure the induction in air and in the right figure the induction in the iron is shown. The coil geometry is shown in red.

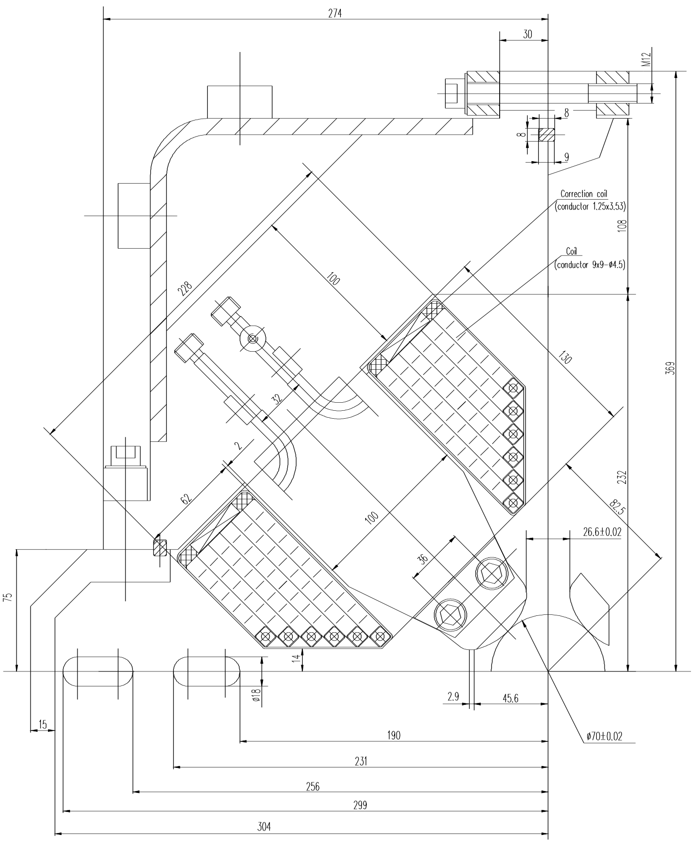

Figure 3.3.4: One quarter cross-section of the quadrupole magnet with a non-closed yoke.

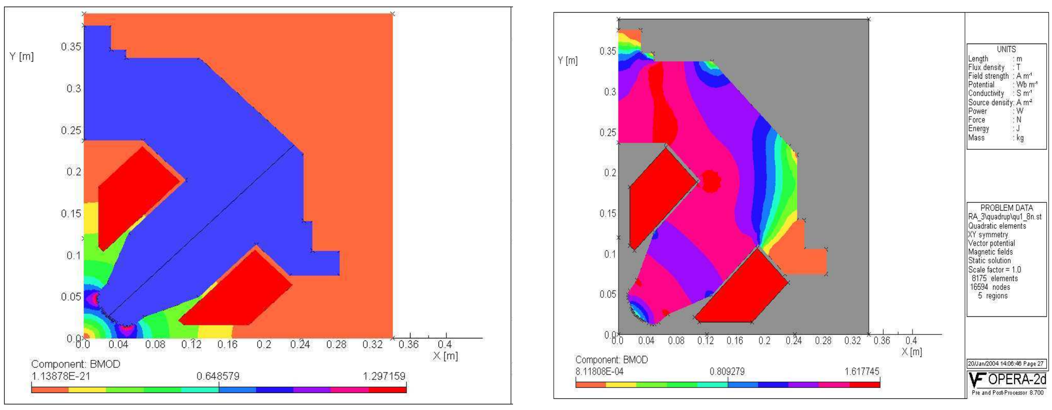

Figure 3.3.5: Results of the calculation for the non-closed yoke. The induction (BMOD) in Tesla is shown. In the left figure the induction in air and in the right figure the induction in the iron is shown. The coil geometry is shown in red.

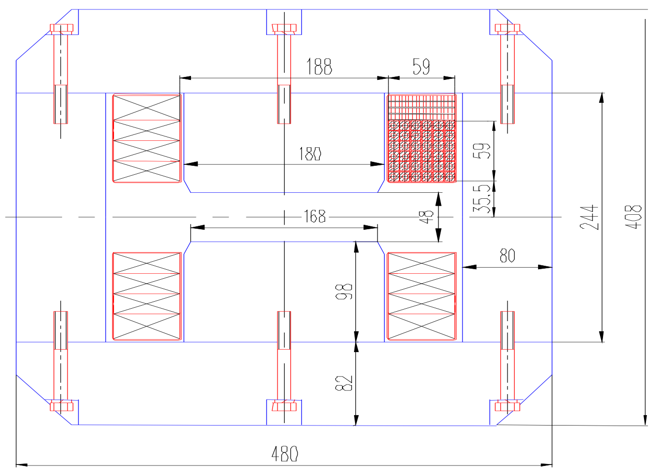

Figure 3.3.6: Cross-section of the PDA dipole magnet

3.3.4 Dipole magnets

The dipole magnet will be a H-type magnet of 1 m length with a maximum induction of 1 Tesla. The vertical gap height is 48 mm. The good field region has to be 60 mm in horizontal and 36 mm in vertical direction. The field quality must be better than 5×10^{-4}. The main parameters are listed in Tab. 3.3.5 at the end of this section. To facilitate the installation and deinstallation of the vacuum chamber into the H-type magnet in the accelerator from the top, a design with separation in the horizontal plane was chosen (Fig. 3.3.6). The iron yoke can be produced either from a solid soft magnetic iron with a coercive force between 75 A/m and 100 A/m with a maximum permeability around 4500 or steel laminations. The gap between the poles is 48 mm. To ensure the field quality the surfaces must be parallel to better than 0.02 mm. The weight of the yoke is 1080 kg. Each coil has three main pancakes and two correction ones. Each main pancake has 12 windings whereas the correction pancake has 38 windings. The main coil is made of a copper conductor with dimensions 9×9 mm^2 and a hole of 5 mm diameter. The turn insulation for the main coil is made of a fiber glass band with a thickness of 0.5 mm. The copper conductor for the correction pancake has a cross section of 2.5×5 mm^2 and the turn insulation is made of fiber glass band with a thickness of 0.3 mm. The coil is vacuum impregnated. Each coil of the dipole has three water cooling circuits.

3.3.5 Results of the 2-D calculation for the PDA dipole

For the 2d calculation the OPERA-2D code was used. The material used is soft magnetic iron with a coercive force of 75 A/m and a maximum permeability of 4500. The results are shown in Figs. 3.3.7, 3.3.8. The maximum field nonlinearity in the good field region (30 mm) is less then $\Delta B/B = \pm 3 \times 10^{-4}$.

For the 3d calculation the MAFIA code was used. Special shims and chamfers provide the

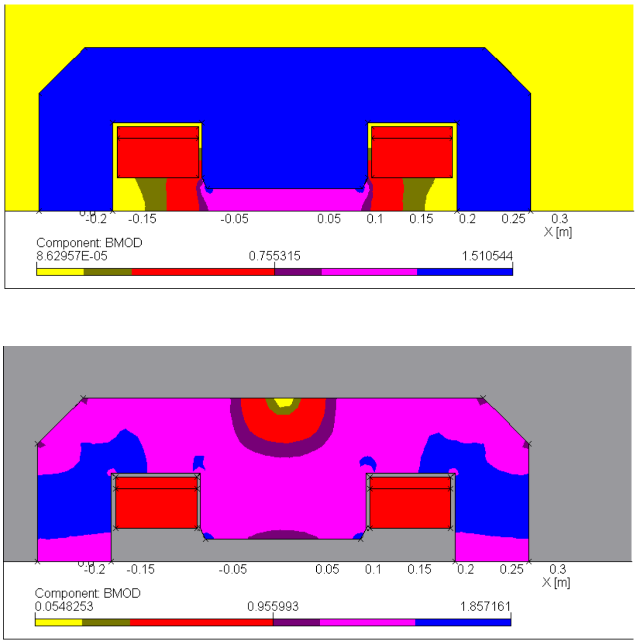

Figure 3.3.7: Results of the B-field calculation for the PDA dipole. The induction (BMOD) in Tesla is shown. In the top figure the induction in air and in the bottom figure the induction in iron is shown. The coil geometry is shown in red.

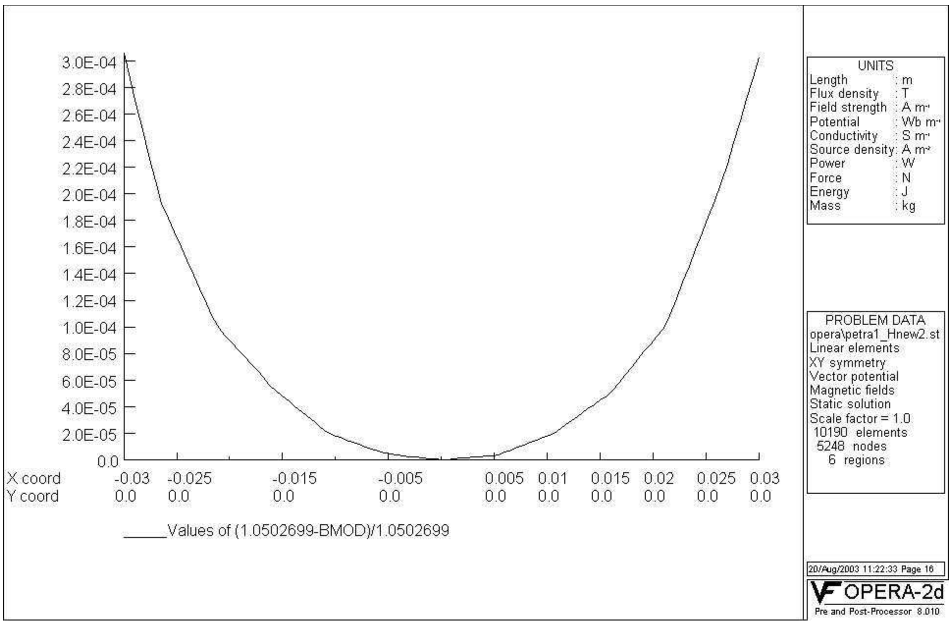

Figure 3.3.8: Field error $\Delta B/B$ of the PDA dipole

required field quality (see Fig. 3.3.9). The result of the optimization of the iron yoke is shown in Fig. 3.3.10. The field errors in the good field region are within the limits of -1×10^{-4} to $+4 \times 10^{-4}$. Shown in Fig. 3.3.10 is the variation of the field integral $(I - I_0)/I_0$ where

$$I = \int_{z=0}^{0.7} B_y(x, y, z)\, dz \tag{3.3.1}$$

$$I_0 = \int_{z=0}^{0.7} B_y(0, 0, z)\, dz \tag{3.3.2}$$

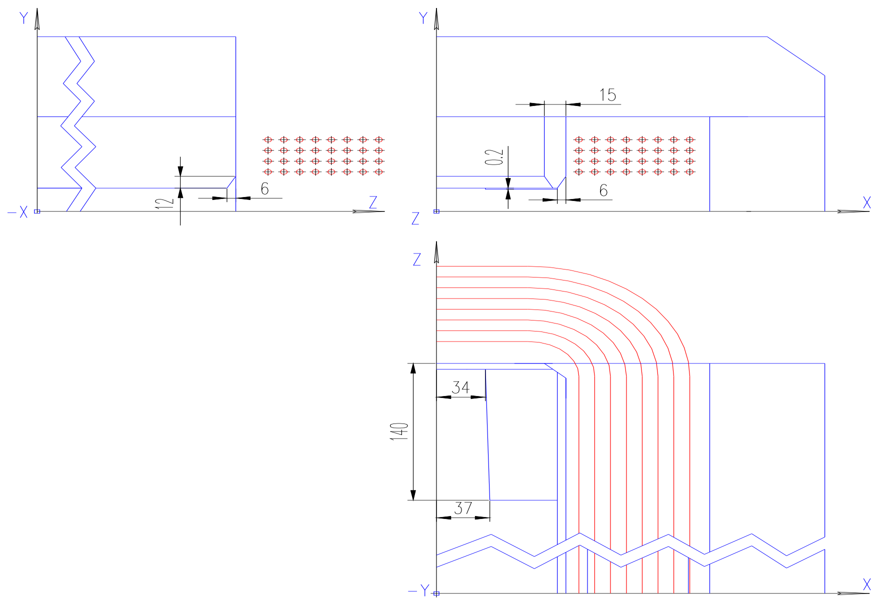

Figure 3.3.9: Dipole magnet chamfers and shims used for the 3D calculation

3.3.6 Corrector magnets

Besides the quadrupole and dipole magnets approximately 40 fast steerer magnets for the fast feedback system and 70 corrector magnets for beam steering are needed in the new octant. The fast steerer magnets will be used for a horizontal and vertical global orbit feedback system. The ESRF fast steerer design will be used and adapted to the specific PETRA III needs. For the 70 corrector magnets a new design is foreseen. These magnets must deflect

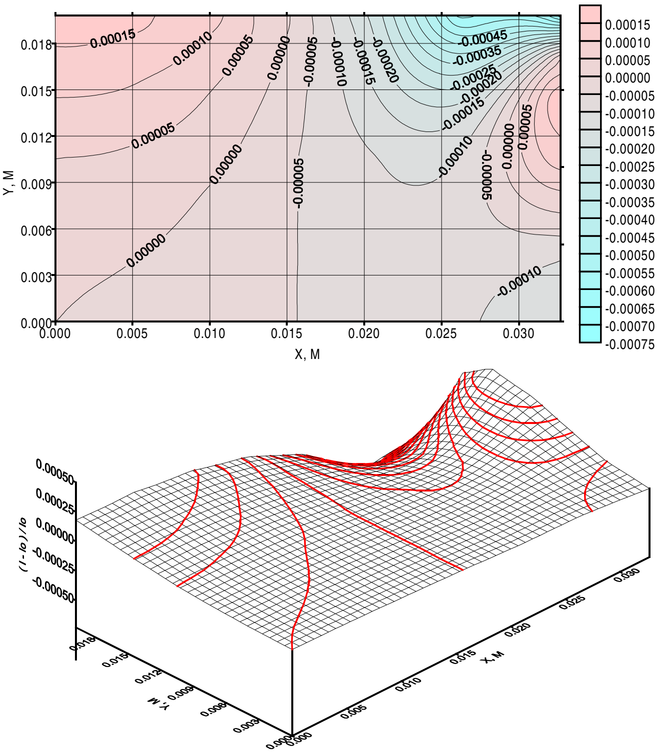

Figure 3.3.10: Variation of the field integral given by Eqs. 3.3.1, 3.3.2 with I = 610 A, B_0 = 1 T for a dipole with shims and chamfer. Shown is the expression $(I - I_0)/I_0$ in the x and y direction for a quarter of the dipole gap.

the beam by 0.5 mrad. The geometrical length has to be shorter than 200 mm in the z-direction. The vertical steerer magnet has to have a 260 mm gap to provide a symmetrical field at the position of the beam. First 2d calculations showed that even for the 260 mm gap the necessary magnetic field of 0.05 T could be achieved using magnets with air cooled coils. For the horizontal beam steering magnets a gap of a least 50 mm is required due to the outer dimensions of the corresponding vacuum chamber.

3.3.7 Magnets for the 7/8 of PETRA III

For the remaining 7/8th of the PETRA III machine the existing magnets will be used with slight modifications in their positioning. Some new corrector magnets for vertical deflection will be installed. The aluminum coils of the magnets showing radiation damage due to the former PETRA high energy physics program have to be replaced. About 630 sextupole coils, 640 quadrupole coils QA, 220 quadrupole coils QA1 and 400 dipole coils must be ordered and exchanged.

Parameters	Value
1. Field gradient, T/m	21.5
2. Aperture radius (r_0), mm	35
3. Field quality ($\triangle B/B$)@ r_{ref} =25 mm better than	$5x10^{-4}$

Parameters	Value	
	Main coils	Correction coils
1.Rated current, A	190	9
2.Voltage drop, V	19.8	14
3. Magnet resistance (T=293 K), Ohm	0.092	1.38
4. Power consumption per magnet, kW	3.7	0.13

Parameters	Value	
	Main coils	Correction coils
1. Number of coils per magnet	4	4
2. Number of turns per coil	57	56
3. Number of turns per magnet	228	224
4. Average turn length, m	1.5	1.5
5. Conductor dimensions, mm	9x9 – Ø4.5	1.25x3.53
6. Conductor Cu-cross-section, mm^2	64.2	4.2

Parameters	Value
1. Operational pressure, bar	6
2. Water pressure drop, bar	4
3.Cooling system is designed for rated pressure, bar	10
4. Water volume in cooling system, l	~ 0.8
5. Water flow speed, m/sec	~1
6. Number of cooling circuits	4
7. Water flow rate, l/min	3.9
8. Water temperature rise, °C	~ 15

Parameters	Value	
	Main coils	Correction coils
1. Yoke steel weight, kg	545	
2. Winding copper weight, kg	196	14

Table 3.3.3: Main parameters of the quadrupole magnet with a closed yoke (PQA). The PQB magnet parameters differ in the higher power consumption (4.9 kW) and a slightly lower water flow rate so that the temperature rise is around 24° C

Parameters	Value
1. Field gradient, T/m	21.5
2. Aperture radius (r_0), mm	35
3. Field quality ($\triangle B/B$) @ r_{ref} =25 mm better than	$5x10^{-4}$

Parameters	Value	
	Main coils	Correction coils
1.Rated current, A	190	9
2.Voltage drop, V	19.8	14
3. Magnet resistance (T=293 K), Ohm	0.092	1.38
4. Power consumption per magnet, kW	3.7	0.13

Parameters	Value	
	Main coils	Correction coils
1. Number of coils per magnet	4	4
2. Number of turns per coil	57	56
3. Number of turns per magnet	228	224
4. Average turn length, m	1.5	1.5
5. Conductor dimensions, mm	9x9 – ø4.5	1.25x3.53
6. Conductor Cu-cross-section, mm^2	64.2	4.2

Parameters	Value
1. Operational pressure, bar	6
2. Water pressure drop, bar	4
3.Cooling system is designed for rated pressure, bar	10
4. Water volume in cooling system, l	~ 0.8
5. Water flow speed, m/sec	~1
6. Number of cooling circuits	4
7. Water flow rate, l/min	3.9
8. Water temperature rise, °C	~ 15

Parameters	Value	
	Main coils	Correction coils
1. Yoke steel weight, kg	750	
2. Winding copper weight, kg	196	14

Table 3.3.4: Main parameters of the quadrupole magnet with a non-closed yoke (PQC).

Parameters	Value
1. Max. field, T	1
2. Magnet gap, mm	48
3. Field quality ($\triangle B/B_0$) better than	$5x10^{-4}$

Excitation parameters

Parameters	Value	
	Main coils	Correction coils
1. Max. current, A	542	13.8
2. Voltage drop, V	31.5	8.6
3. Magnet resistance (T=293 K), Ohm	0.054	0.58
4. Power consumption per magnet, kW	17.1	0.12

Winding parameters

Parameters	Value	
	Main coils	Correct coils
1. Number of coils per magnet	2	2
2. Number of turns per coil	36	76
3. Number of turns per magnet	72	152
4. Average turn length, m	2.6	2.6
5. Conductor dimensions, mm	9x9−ø5	2.5x5
6. Conductor Cu−cross−section, mm^2	60	11.95

Cooling parameters

Parameters	Value
1. Operational pressure, bar	6
2. Water pressure drop, bar	4
3. Cooling system is designed for rated pressure, bar	10
4. Water volume in cooling system, l	~ 2
5. Water flow speed, m/sec	1.65
6. Number of cooling circuits	6
7. Water flow rate, l/min	11.6
8. Water temperature rise, °C	21

Weights

Parameters	Value	
	Main coils	Correct coils
1. Yoke steel weight, kg	1080	
2. Winding copper weight, kg	100	42

Table 3.3.5: Main parameters of the PDA dipole magnet

3.4 Damping Wigglers

3.4.1 Introduction

The upgrade of the PETRA storage ring will provide a horizontal emittance of $\sim$1 nmrad if damping wigglers with a total length of about 80 m are installed in the long straight sections North and West. These dispersion-free sections have a *FODO*-type lattice with twelve $\sim$5.3 m drifts between the focusing and defocusing quadrupoles. Each drift can accommodate a permanent magnet damping wiggler, synchrotron radiation (SR) absorber, horizontal and vertical steering magnet and other necessary equipment (BPMs, pumps, bellows etc.).
At 6 GeV energy and 200 mA maximum current, the total radiation power from the wiggler magnets (about 0.8 MW for two wiggler sections) has to be intercepted by special SR absorbers. About half the radiation power is absorbed by regular copper absorbers placed in the FODO drifts, but the remaining $\sim$200 kW will be intercepted by a long lumped copper absorber accommodated inside and behind the first downstream bending magnet.
This section describes the design of the main elements of the PETRA III damping wiggler system. A concept for a permanent magnet wiggler has been chosen from the viewpoints of minimum contribution to the total beam emittance and effectiveness of the wiggler production, tuning and maintenance.
The wiggler section vacuum chamber is considered including SR absorber system, bellow units, flanges, steering magnets, etc. To finalize the absorber design, the spatial and angular distribution of the wiggler SR power is calculated under realistic circumstances. The most critical element of the absorbing system is the lumped absorber. For this absorber, temperature and stress analysis is performed using the *ANSYS* program. To protect the magnet coil insulation from radiation damage the radiation dose is also estimated.
The power load of the absorbers is rather high and an effective safety system protecting equipment from overheating is obligatory. For reliability this system has to include several monitoring sub-systems: temperature sensors, electron beam position monitors and radiation position monitors. Preliminary considerations on the SR monitor design are given.

3.4.2 Wiggler design

3.4.2.1 Main considerations

The PETRA III damping wigglers have been designed according to the following basic criteria:

- The wigglers have to make a minimum contribution to the total beam emittance.
- The permanent magnets' weight has to be minimized since their price is a significant part of the total cost of the wiggler system.
- The wiggler design has to be reliable and simple in manufacture and adjustment.
- The magnet structure must have low sensitivity to temperature gradients to prevent possible distortion of the closed orbit.

For a periodic planar wiggler, an additional contribution to the total emittance of the ring can be expressed by the so-called I_5 radiation integral (Wiedemann, 1993):

$$I_5 \approx \frac{8}{15} N_w \widehat{\beta}_x \frac{\theta_w^3}{\rho_w^2} \tag{3.4.1}$$

where N_w, θ_w and ρ_w are the wiggler period number, maximum deviation angle and curvature radius respectively, while $\widehat{\beta}_x$ is the horizontal betatron function averaged over the wiggler length. To reduce the I_5 radiation integral for fixed $\widehat{\beta}_x$ and ρ_w, one has to keep the deviation angle as small as possible. A conventional periodic wiggler design with a sin-like magnetic field and half-field poles at both ends complies most with this primarily important condition.
Special attention was paid to the optimization of the wiggler design with respect to cost reduction, which mainly depends on the volume of the magnetic material used for the wiggler production. Another important point is ease of assembly and adjustment of more than 750 wiggler poles: To save the time span required for this procedure as well as to provide reliability of the system, the wiggler tuning process has to be as simple as possible.

3.4.2.2 Detailed layout

At the selected field amplitude of B_w = 1.52 T and vertical gap h = 24 mm the wiggler period length was optimized as λ_w = 20 cm. For a shorter period with the same field amplitude one has to increase the volume of the *NeFeB* permanent magnets significantly. The thickness d_m of the permanent magnets placed between the poles is determined by the following equation

$$B_w \cdot h = B_m \cdot d_m \tag{3.4.2}$$

It can be shown that the optimum operation point of a permanent magnet is B_m = 0.6 T. That yields a magnet thickness of d_m =60 mm. Fig. 3.4.1 shows a schematic design of the wiggler pole magnet structure and the magnetic induction distribution inside.

It is proposed to design wedge-shaped ferromagnetic poles (Fig. 3.4.1). Such a design allows splitting one 60 mm thick magnet into two magnets of half thickness and placing the wedge-like *ARMCO* plate between them. Magnetic symmetry provides that the magnetic potential of this wedge-like plate is zero, therefore the electromagnetic coupling between the poles practically vanishes. This makes it possible to adjust the field amplitude for each pole separately without changing it in the adjacent poles. By that means, the wiggler field tuning procedure becomes simple and is reduced to tuning each individual pole.
The side view of the wiggler and its transverse cross-section are shown in Fig. 3.4.2 and Fig. 3.4.3. Special magnets are placed at the wiggler sides (Fig. 3.4.3) to reduce the leakage flux from the central iron poles. The reduction of the leakage flux minimizes the size of the central iron pole and main magnets. The iron enclosure around the wiggler provides zero magnetic potential of the iron wedge inserted between the magnets.
In order to settle the pole field amplitude within a few percent, special adjustment iron screw-correctors (Fig. 3.4.3) are planned for every pole block. By them moving in and out, the leakage flux changes and the magnetic potential of the pole reduces or increases.

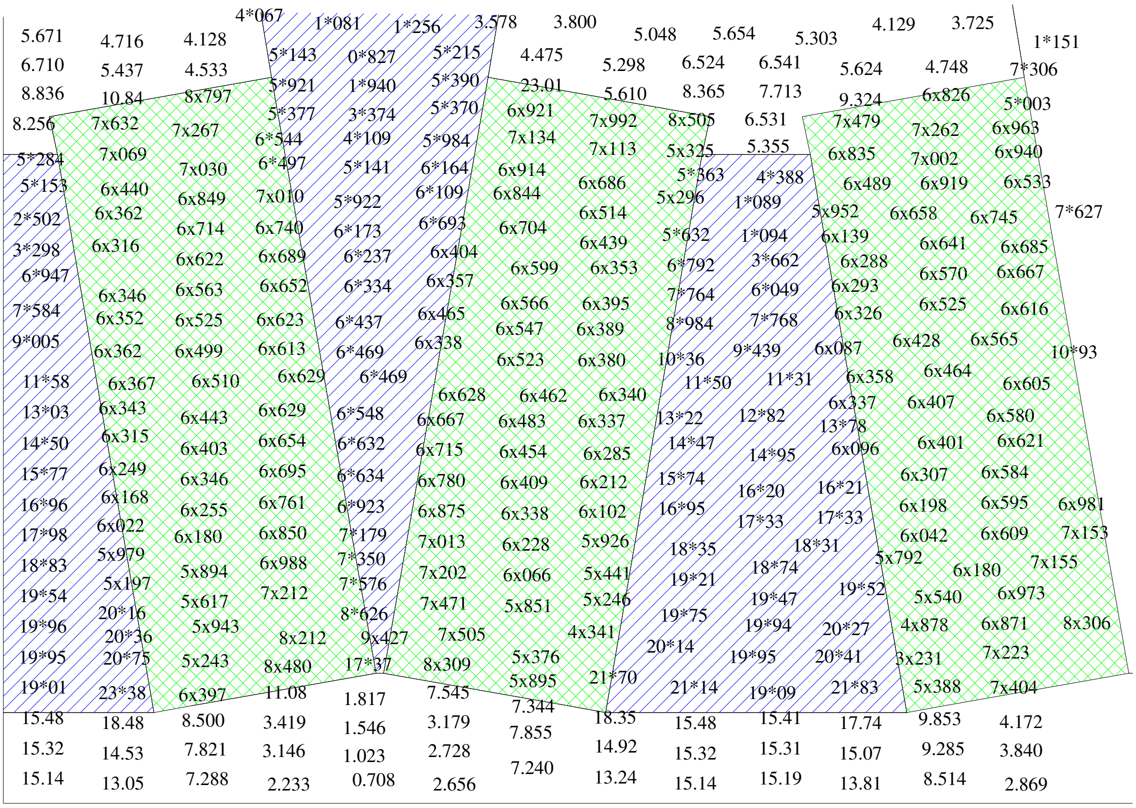

Figure 3.4.1: Magnetic induction distribution (kG) inside the wiggler. '∗', '×', and '.' denote the decimal delimiter of values for the iron poles (blue), permanent magnets (green), and the air gap, respectively.

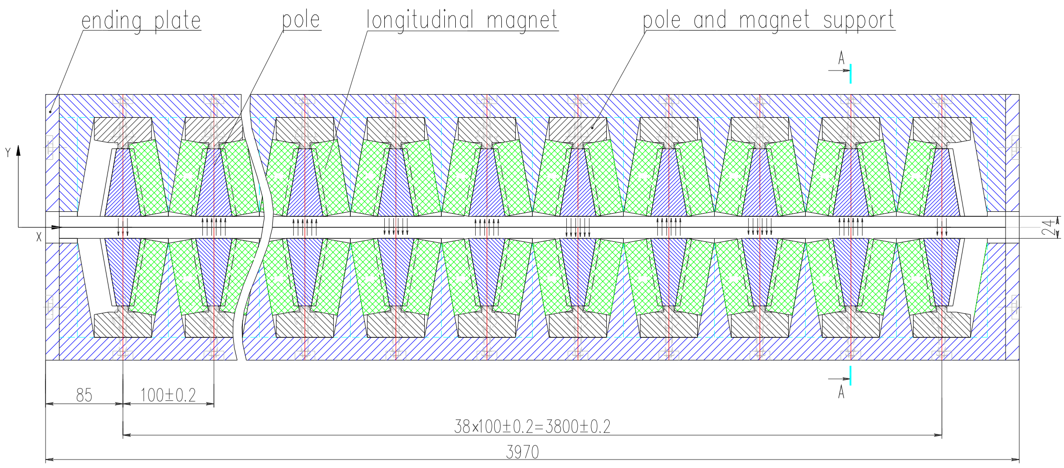

Figure 3.4.2: Side view of the damping wiggler.

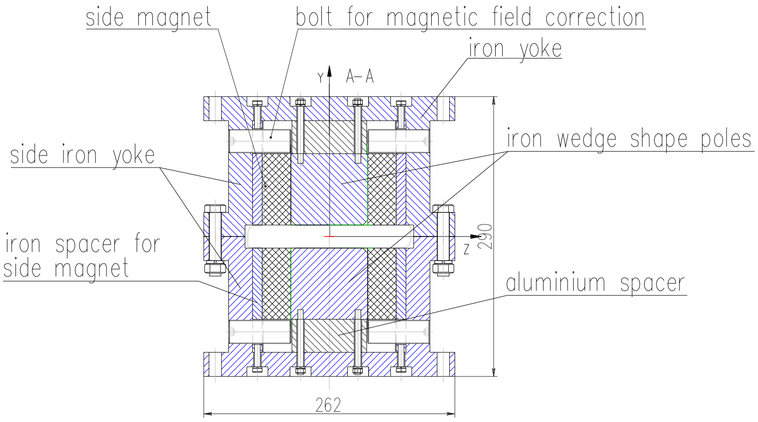

Figure 3.4.3: The transverse wiggler cross-section

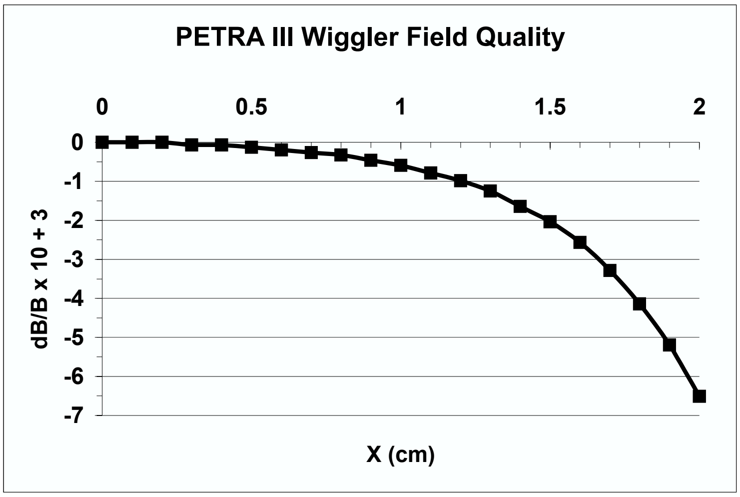

Figure 3.4.4: Transverse distribution of the magnetic field.

Based on tracking calculations, a transverse field quality $\Delta B/B \leq 10^{-3}$ in a good-field region $\Delta x = \pm 1$ cm has been specified in order to inject safely into PETRA III without losses (see Sec. 3.2.2). Therefore, the transverse dimension of magnets and iron poles was chosen to 8 cm. The field distribution at the pole center along the horizontal axis is shown in Fig. 3.4.4 while the longitudinal wiggler field profile is plotted in Fig. 3.4.5. The calculated field amplitude is $B_w = 1.52$ T.

The parameters of the PETRA III damping wiggler are listed in Tab. 3.4.1. The radiation integral I_2, which is a measure for the reduction of the horizontal emittance due to the wigglers

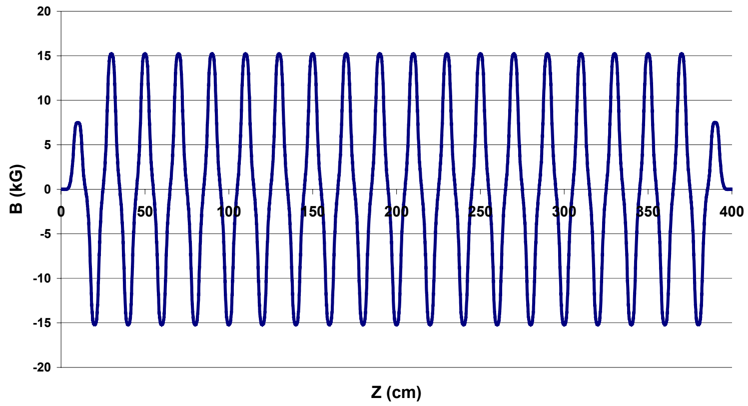

Figure 3.4.5: Longitudinal distribution of the magnetic field.

Peak field B_w	1.52 T
Magnetic gap	24 mm
Period length	0.2 m
Number of periods	20
Number of poles	37 + 2 half poles
Magnet volume per period	2200 cm^3
Field quality at x_0 = 10 mm	$< 10^{-3}$
Damping integral per segment	3.859 T^{2}m
Overall length of wiggler segment	3.97 m
Number of wiggler segments	20

Table 3.4.1: Damping wiggler parameters

is defined as :

$$I_2 = \int\limits_{Wig} \frac{ds}{\rho^2(s)} = \frac{1}{(B\rho)^2} \int\limits_{Wig} B_w^2(s) ds \qquad (3.4.3)$$

The damping integral $\int B_w^2(s)ds = 3.859$ T^{2}m was obtained from the longitudinal wiggler field distribution.

The top and bottom halves of the wiggler are made from a single piece of iron with a milling accuracy of ± 0.1 mm. After the wedge-like poles have been installed, the pole surface facing the gap and the joint plane of top and bottom halves are ground. Our previous experience with this technology shows that the gap accuracy can reach $\pm 30\,\mu$m which is sufficient for our purpose. This manufacturing technique will allow significant simplification and acceleration of the wiggler assembly as well as a reduction of the number of parts in the wiggler design.

The wiggler adjustment includes two stages:

- The magnetic field is measured by a Hall probe array to be inserted in the aperture, and the field amplitude is adjusted by means of the screw-correctors within 1 G over the whole wiggler length.

- A moving wire measures the wiggler field integrals. Measurement accuracy for the first and second field integrals using such a technique is $\pm 5\,\mathrm{G\,cm}$ and $2000\,\mathrm{G\,cm}^2$, respectively. The integrals will be set to zero with the same accuracy.

The use of two wedge-like iron inserts between the magnets and manufacture of each wiggler half from a solid iron lump minimize temperature gradients in the wiggler. In order to exclude temperature effects on the magnetic field due to beam heating it is possible to apply a water cooling to the vacuum chamber of the wiggler. Although the absolute value of the wiggler magnet temperature can vary and lead to a small change of the field amplitude ($\Delta B/B \approx 10^{-3}/K$ for the *NeFeB* magnets), the first and second field integrals, which depend on the temperature gradient, remain constant.

3.4.3 Wiggler radiation power

3.4.3.1 Introduction

The main tasks of the wiggler radiation power calculation are

1. Developing the procedure for calculation of SR power density distribution at different azimuths of the wiggler section.

2. Finding the optimal aperture of the regular absorber to provide uniform absorption along the straight section length.

3. Estimating tolerances for the absorber alignment in the transverse plane as well as for the closed orbit deviation in the wiggler section.

An estimate of the power density is derived for an electron energy of 6 GeV and a maximum beam current of 200 mA. The general characteristics of the damping wiggler radiation are given in Tab. 3.4.2.

SR critical energy	35.84 keV
K - Parameter	28.39
Wiggler length	4 m
Wiggler SR power	42.12 kW
Relativistic factor	1.17×10^4
Vertical SR spread	85.2 μrad
Horizontal SR spread	4.84 mrad

Table 3.4.2: General SR characteristics of the damping wiggler

3.4.3.2 Absorber power load

Fig. 3.4.6 schematically shows the arrangement of the wiggler section. Eight short regular copper absorbers are placed in the drifts 3 to 10 (the first drift corresponds to the first damping wiggler). They will absorb tails of the synchrotron radiation coming from the wigglers. Starting at drift 11 the power accumulated from the wigglers becomes too large and can not be intercepted by the regular copper absorbers. Thus longer absorbers with a different design are placed in drifts 11 and 12.

The SR power density distribution has been calculated in the following way. A reference

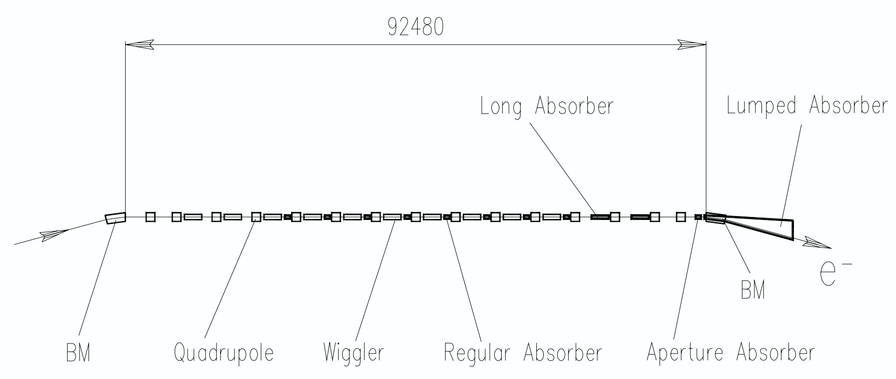

Figure 3.4.6: Scheme of the wiggler straight section

plane perpendicular to the beam axis is defined at the end of each absorber. The longitudinal coordinate of the reference plane is given relative to the center of the first wiggler. The 2D SR power distribution is calculated in the reference plane for each upstream wiggler separately. An example of the calculation is shown in Fig. 3.4.7. The isoline contours show the power density levels, accumulated from all wigglers, 80.3 m downstream of the first wiggler.

The integrated power on one absorber (absorber 4) is plotted in Fig. 3.4.8 as a function of the horizontal absorber aperture. In our model every absorber is represented by a rectangular aperture (slit) placed in the reference plane. The lower aperture limits are given by the physical aperture requirements of the whole ring. The width is $\geq \pm 30$ mm and the minimum full gap is 17 mm at the largest and 12mm at the smallest β-function in the wiggler section. The horizontal absorber aperture was optimized according to the following considerations:

- The absorbers located in the *FODO* drifts have to intercept as much SR power as possible to reduce the power load of the last lumped absorber.
- The linear power density on the absorbers should not exceed 200 W/cm (according to *BINP* experience).
- Every regular absorber will absorb approximately the same power to keep the same design and dimensions.

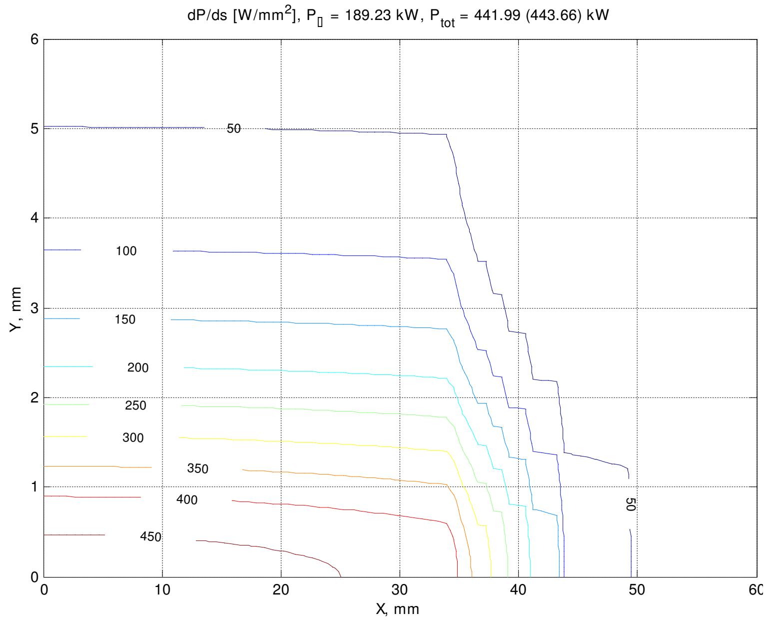

Figure 3.4.7: Power density (W) at 80.3 m from the center of the first wiggler (1/4 of the distribution).

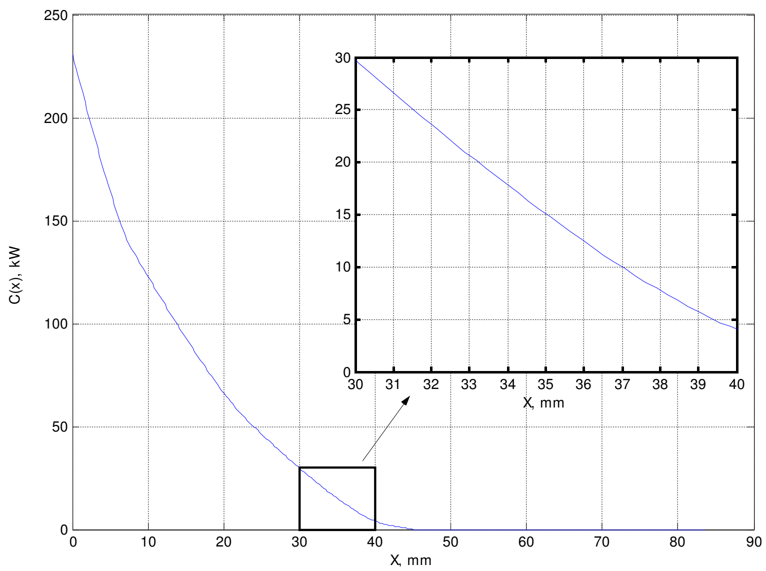

Figure 3.4.8: Accumulated power at the azimuth of the forth regular absorber.

The vertical absorber aperture has to provide reliable shading of the wiggler vacuum chamber. Therefore the aperture will be reduced to 13 mm for all absorbers which are placed close to the horizontal focusing quadrupoles. This yields a maximum allowed incident angle of $\Delta'_R = 163\,\mu\mathrm{rad}$, as shown in Fig. 3.4.9.

The total opening angle of the 1σ RMS radiation fan is equal to

$$\sigma'_R = \sqrt{\sigma'^2_{SR} + \sigma'^2_{ye}}, \tag{3.4.4}$$

where σ'_{SR} = $1/\gamma$ = 85 μrad is the vertical angular spread of the radiation at 6 GeV, $\sigma'_{ye} = \sqrt{\epsilon_y/\widehat{\beta}_y}$ is the natural divergence of the electron beam, being $\approx$ 8 μrad for a mean vertical betatron function in the wiggler of $\widehat{\beta}_y \approx 15\,\mathrm{m}$ and an emittance of $\epsilon_y = 0.5\,\mathrm{nm\,rad}$ (fully coupled beam). With these values the maximum RMS closed orbit is estimated to be:

$$\sigma_{y,cod} = \sqrt{\frac{(\Delta'_R - \sigma'_R)^2}{\langle\gamma\rangle}\langle\beta\rangle} = 0.84\,\mathrm{mm}. \tag{3.4.5}$$

The apertures of all regular absorbers are summarized in Tab. 3.4.3. The power that can be absorbed by each of the absorbers was chosen to be $\approx$ 15 kW for the regular short absorbers (S1-S8) and $\approx$ 70 kW for the long ones (S9 and S10).
The part of the SR power from the 10 damping wigglers which is not intercepted by the regular absorbers amounts to 182.2 kW with a maximal power density of 352.7 W/mm^2. It will be absorbed in the lumped absorber at the end of the straight section.

3.4.3.3 COD and absorbers misalignment tolerance

If the closed orbit has deviations or tilts in the wiggler or the position of the absorbers differs from the projected one, the thermal load on the absorbers can increase. To estimate this effect we have assumed an RMS closed orbit of 1.0 mm in the horizontal plane and 0.5 mm in the vertical plane. This leads to a RMS slope of the closed orbit of 60 $\mu\mathrm{rad}$ horizontally and 33 $\mu\mathrm{rad}$ vertically at the wiggler SR source points. SR power calculations with these closed orbit values yield the maximum increase of SR power on a single absorber as given in Tab. 3.4.4.

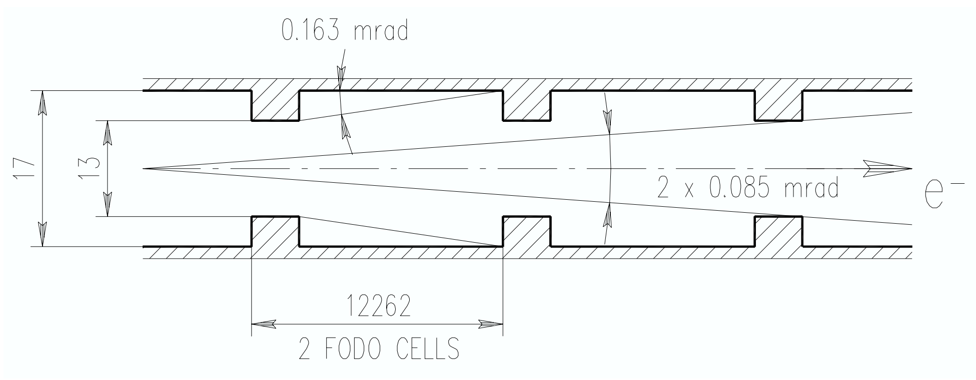

Figure 3.4.9: Scheme of the vertically collimating vacuum chamber of the damping wiggler.

Absorber	Position [m]	Hor. Aperture [mm]	Ver. Aperture [mm]
S1	15.29	± 30.0	± 6.50
S2	21.43	± 30.0	± 8.50
S3	27.56	± 32.2	± 6.50
S4	33.69	± 35.0	± 8.50
S5	39.82	± 38.1	± 6.50
S6	45.95	± 41.7	± 8.50
S7	52.08	± 45.3	± 6.50
S8	58.21	± 48.8	± 8.50
S9	64.34	± 37.8	± 6.50
S10	70.47	± 30.0	± 8.50

Table 3.4.3: Horizontal and vertical aperture of the regular absorbers.

Absorber	P [kW]	ΔP [kW]			
		$\langle\Delta x\rangle =$ 1.0mm	$\langle\Delta y\rangle =$ 0.5mm	$\langle\Delta x'\rangle =$ 60μrad	$\langle\Delta y'\rangle =$ 33μrad
S1	3.97	0.42	0.00	0.04	0.01
S2	12.76	0.84	0.00	0.02	0.00
S3	15.17	1.14	0.00	0.02	0.17
S4	15.16	1.32	0.00	0.04	-0.02
S5	15.27	1.28	0.16	0.09	1.12
S6	15.40	1.40	0.01	-0.11	-0.09
S7	15.93	1.48	0.40	0.03	3.14
S8	16.30	1.57	0.01	0.04	-0.24
S9	69.73	1.94	0.58	-0.01	2.95
S10	59.40	2.66	0.01	-0.02	-2.03

Table 3.4.4: Maximum increase of SR power on a single absorber due to closed orbit errors.

These estimates have yielded the following results :

- The SR power load can increase or decrease for particular absorbers.
- For the vertical plane, the slope in the source points provides higher increase of radiation power than the orbit displacement, while for the horizontal plane it is vice versa.
- For the given values of the closed orbit distortion the power load on certain absorbers can increase by up to 30 %. The absorbers have to be designed with an according safety margin.

3.4.4 Radiation dose

In the absorber, a high-power SR beam enters the absorbing wall surface under a small angle ($\sim 10^{-2}$ rad). SR photons scattered in the thin surface layer over angles $\sim$1 rad pass through the vacuum chamber wall with a noticeable probability and create an intensive radiation field.
Again the most critical device is the lumped absorber inside the bending magnet. Here the $\sim$200 kW SR power is distributed over 10 m length, yielding on average $\sim$260 W/cm line density. For our estimates we assume 20 years of reliable operation of the PETRA III

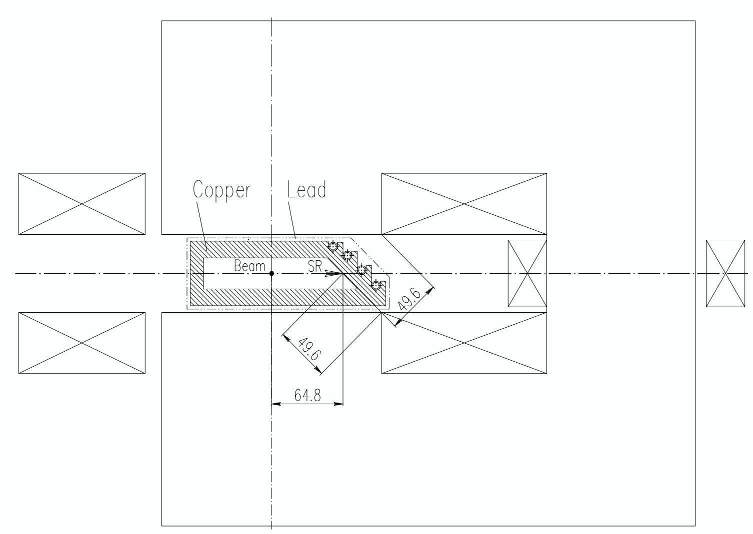

Figure 3.4.10: Geometry of the bending magnet coils.

magnetic system. The allowable dose for the magnet coil insulation (epoxy compound) is taken to be 10^7 Gy. Then the dose rate at the nearest part of the winding (see Fig. 3.4.10) should not exceed 1.6×10^{-2} Gy/s.
The geometry for the analytic estimate of the dose rate for the magnet coil is shown in Fig. 3.4.11. Assuming single scattering events of non-polarized SR photons, a numerical estimate yields for the point *A* a dose rate of

$$I_T = 9.2 \times 10^{-2}\, Gy/s. \tag{3.4.6}$$

Since the multiple scattering dose build-up factor for our geometry is not available, we have checked numerically the corresponding formulas and found that in our case such factors should not be large so we can use the build-up factor $B_{eff} = 3.8$ of the well-known point-like isotropic source in infinite media. To take into account the polarization of the primary SR photons we use an additional factor $P \approx 1.6$, so that the total dose at the point *A* is

$$I = I_T \times B_{eff} \times P = 0.56\, Gy/s. \tag{3.4.7}$$

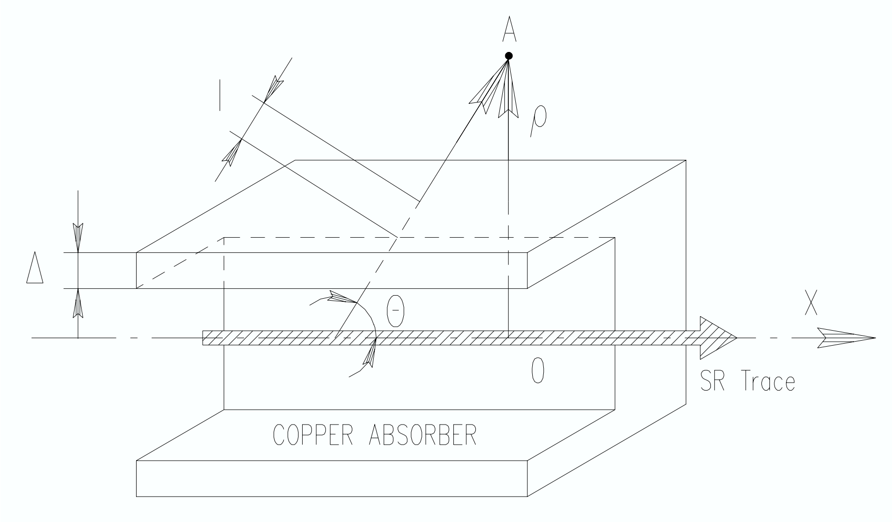

Figure 3.4.11: Geometry for an estimate of the radiation dose rate.

A preliminary Monte-Carlo simulation, carried out with the *EMSH* computer code, has shown that the total energy of photons passed through the copper wall is around 0.01% of the incident SR power. However to convert this data to dose rate is rather difficult without detailed knowledge of the photon spatial-angular distribution. Thus the dose rate estimated by the computer simulation is 2 times less than that obtained by the analytic calculation.
Both calculated values are significantly above the tolerable dose rate. An additional attenuation with the factor K = 35 is necessary to provide a reliable operation of the magnets coils. A $\sim$3 mm thick lead layer will provide this attenuation factor.

3.4.5 Absorbers and vacuum chamber design

The wiggler section vacuum chamber consists of 14 drift vacuum chambers. The typical drift chamber, which is shown in Fig. 3.4.12a, includes the quadrupole magnet vacuum chamber, BPM unit, bellows unit, wiggler vacuum tube and the regular absorber. All the vacuum vessels are made of stainless steel except for the copper beam stop part.

The drift vacuum sections are joined by CF-flanges with RF shields inside. The bellows unit, which is necessary to mount all components of the vacuum system and to compensate thermal expansion, incorporates a BPM and CF-flanges with movable RF shield contacts inside (Fig. 3.4.12c).
Twelve water-cooled copper absorbers intercept the SR power (412.2 kW in total) produced by the 10 damping wigglers installed in the PETRA III long straight section. Ten absorbers are placed in front of the quadrupole magnets and one in front of the bending magnet to protect its vacuum chamber from the radiation fan. One long lumped absorber is accommodated inside and after the dipole magnet.
The thermal design of the absorbers is based on a SR power load of 250 W per 1-cm-length

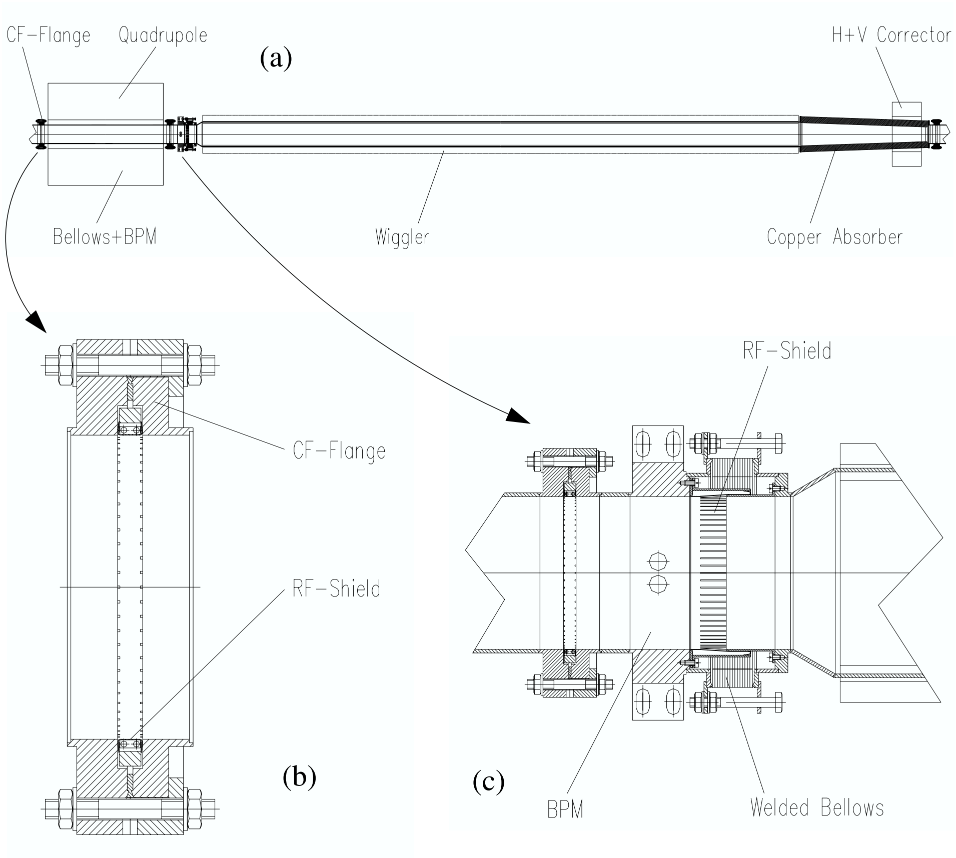

Figure 3.4.12: a) Drift vacuum chamber arrangement, b) CF-flange unit, c) Bellows unit with BPM and CF-flanges

of the absorber, a cooling water pressure drop of 4 bar and a water temperature rise of 30 K. The ten first absorbers trim the tails of the SR power distribution to prevent heating of the

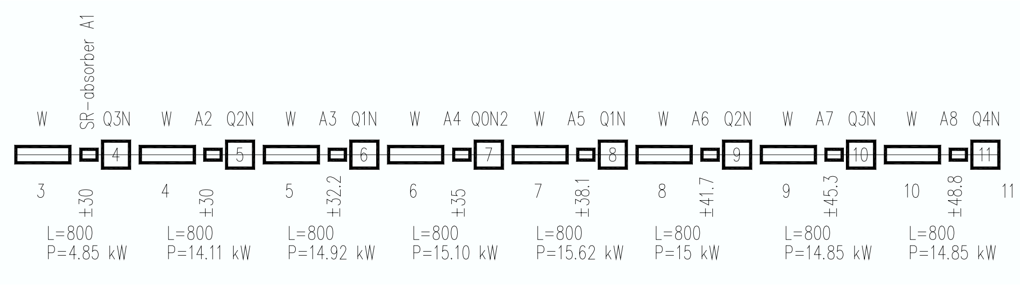

Figure 3.4.13: Short absorbers arrangement (length in mm)

vacuum vessels in quadrupoles and wigglers. The eight short regular absorbers allow the absorption of 16 kW power each (Fig. 3.4.13). The maximum possible power load for the last two long regular absorbers is 80 kW (Fig. 3.4.14). The eleventh absorber is placed just

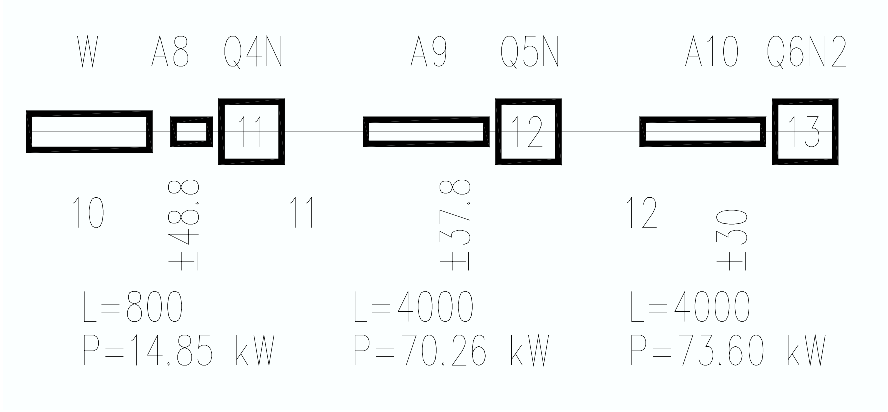

Figure 3.4.14: Long absorbers arrangement (length in mm)

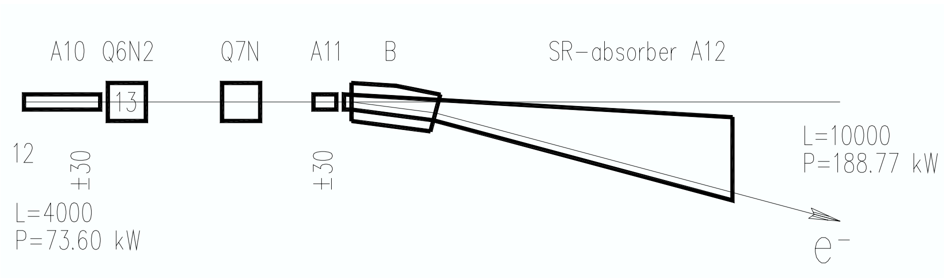

Figure 3.4.15: A schematic view of the lumped beam absorber.

upstream the bending magnet as a safety protection for the bending magnet vacuum chamber. The last lumped beam stop is the largest one and absorbs the rest of the radiation power (around 200 kW). It is shown schematically in Fig. 3.4.15.

This absorber is located partially inside the dipole vacuum chamber and in the 5.5 m long section of the vacuum tube downstream of the bending magnet (Fig. 3.4.16a). To facilitate the production of the long vacuum chamber (10 m) of the lumped absorber, it is planned to split it into several modules each around 1.5 m-long. The cooling water circuits will be arranged according to the following requirements: the water pressure drop $\Delta P \leq 4$ bar and a temperature rise of 30 K. A cross-section of the lumped absorber vacuum chamber is shown in Fig. 3.4.16b (middle module) and Fig. 3.4.16c (last module).
The thermal load analysis was performed using the code *ANSYS* Workbench. The highest linear power density was computed with 200 W/cm for the lumped absorber. The result of the simulation is presented in Fig. 3.4.17. The absorber vacuum chamber has to withstand

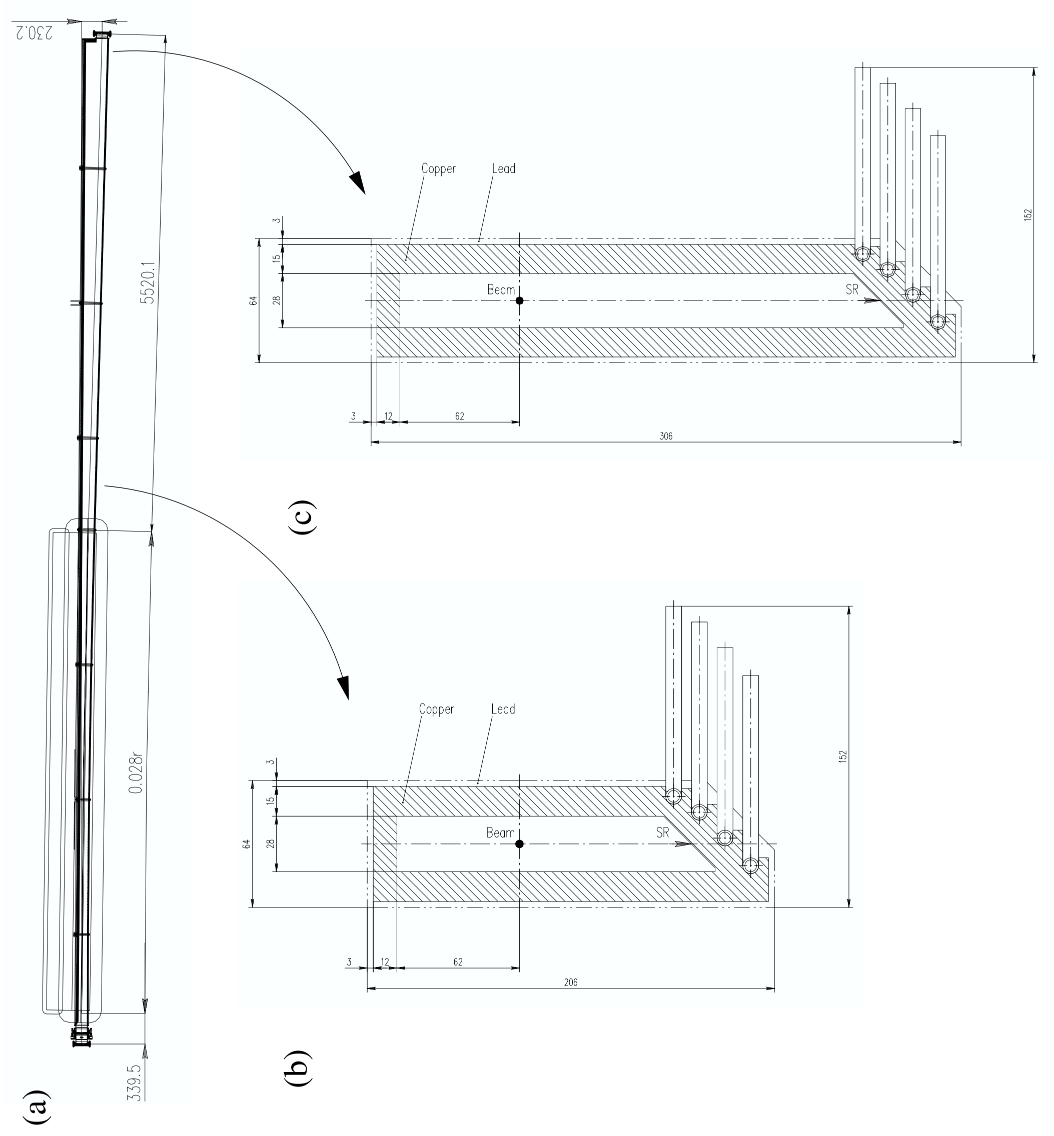

Figure 3.4.16: a) Lumped absorber vacuum chamber, b) Vacuum chamber cross-section (middle module), c) Vacuum chamber cross-section (last module).

the atmospheric pressure. The stress of the lumped absorber vacuum chamber was calculated for a copper chamber width of 300 mm and thickness of the chamber wall as shown in Fig. 3.4.16 and Fig. 3.4.17. The simulation results shown in Fig. 3.4.18 reveals that the maximum deformation is less than 0.015 mm and is below the inelastic deformation threshold of the annealed copper. The maximum stress value in the vacuum chamber material (Fig. 3.4.19) is well under the copper tensile yield of 60 MPa.

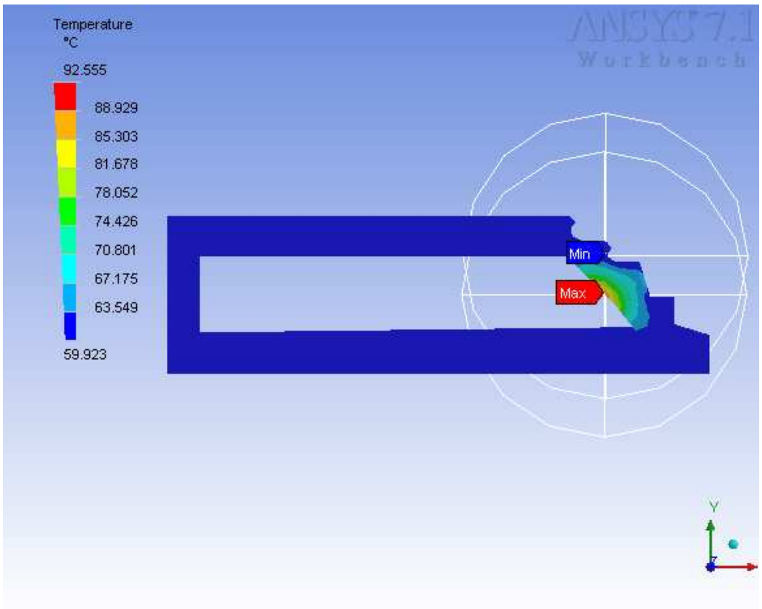

Figure 3.4.17: Thermal analysis of the lumped absorber vacuum chamber.

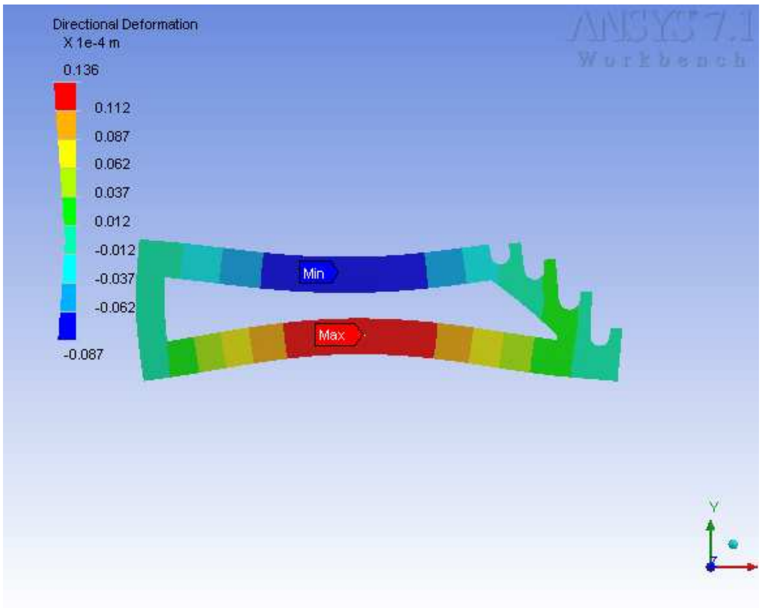

Figure 3.4.18: Stress deformation of the 300-mm-wide module.

It is foreseen to join the units of the lumped absorber vacuum chambers modules by electron-beam welding and high-temperature brazing in a vacuum oven. It is planned to connect the modules with each other with the help of a technology developed at *BINP*. High-temperature silver solder is used to braze two copper-stainless steel flanges to both the ends of the mod-

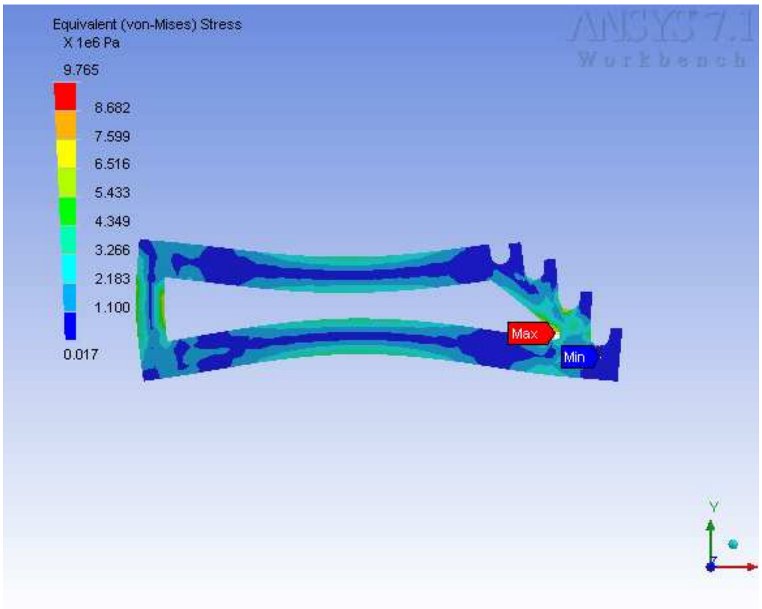

Figure 3.4.19: Stress values for the 300-mm-wide module.

ules. The vacuum chamber is assembled by welding of the stainless steel flanges. The electrical conductivity inside the chamber is provided by gold-coated copper brasses joined by diffusion bonding.

3.4.6 SR monitoring system

The power load to the absorbers is very high, and thus a reliable operation requires different measurements to be incorporated into the interlock safety system, including:

- Absorber temperature measurement with thermo-switches.
- Electron beam position measurement with regular BPMs installed in the wiggler straight section.
- SR beam position detection with special SR monitors. A proposal for these monitors will be described below.

A schematic view of the SR monitor that measures radiation displacement in the vertical plane is shown in Fig. 3.4.20. The monitor is combined with every absorber installed in the focusing quadrupole drift (1). Inside the vertical narrowing of the absorber a special gap is machined and an anode-electrode is placed inside it (3). The gap is closed with a copper foil (2) that screens the electrodes from the primary electron beam and provides electromagnetic smoothness of the vacuum chamber. The electrodes are fixed in the vacuum chamber with a ceramic insulator (4). The gap is connected with the main volume of the vacuum chamber

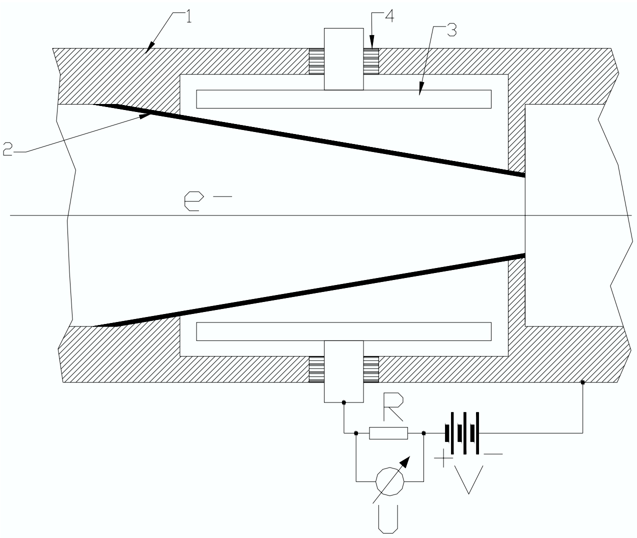

Figure 3.4.20: Scheme of the SR monitor.

by hole(s), which are arranged as to prevent HOM's generated by the electron beam. The foil thickness will be chosen to provide:

- Good RF screening of the electrodes.
- Effective penetration of the SR quanta.
- Effective heat conductivity and low temperature of the foil.
- High photo-current signal.

The operating principle of the system is as follows. Radiation photons absorbed in the foil produce photoelectrons, which are registered by the electrical circuit schematically shown in Fig. 3.4.20 for the lower electrode. A similar circuit is assumed for the upper electrode. A measure for the SR fan deviation is:

$$k = \frac{U_u - U_l}{U_u + U_l} \tag{3.4.8}$$

where U_u and U_l are the upper and lower electrode voltage signal. From our experience, the voltage signal will be sufficient to reliably monitor the SR beam deviation.

3.4.7 Steering magnets

To save space in the damping wiggler drifts a steering magnet that produces both vertical and horizontal magnetic field components is proposed. A schematic cross-section of the magnet is shown in Fig. 3.4.21 together with the magnetic field flux lines. Two different coils are excited to generate either the horizontal field (coil 2) or the vertical one (coil 1).

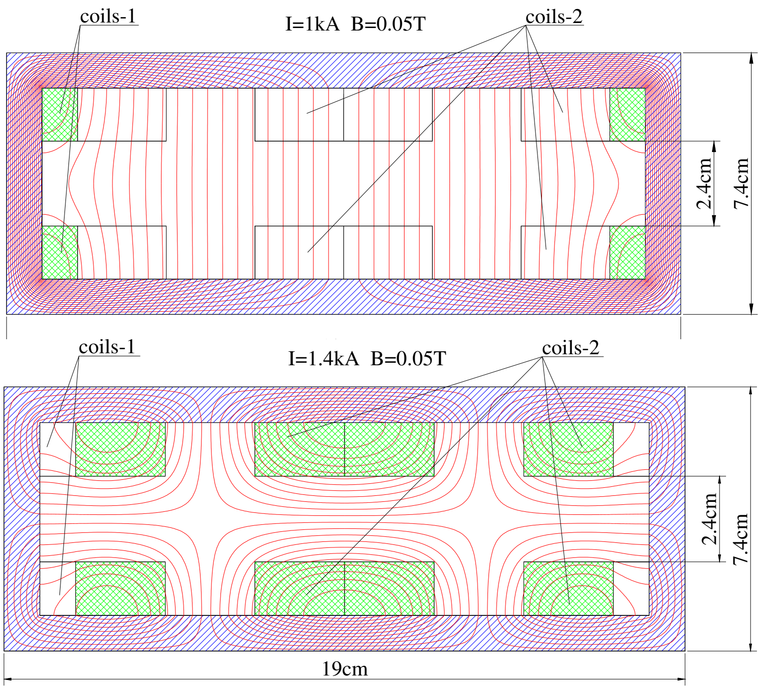

Figure 3.4.21: Top: Vertical field flux lines. Bottom: Horizontal field flux lines.

	Horizontal	Vertical
Max. field	0.05 T	0.05 T
Effective length	0.2 m	0.2 m
Ampere-turns	1.0 kA-t	1.4 kA-t
Max. current	15 A	15 A
Vertical gap	24 mm	24 mm
Cooling	Air	Air

Table 3.4.5: Correctors main parameters.

The main parameters of the magnet are given in Tab. 3.4.5. Such magnets being produced from laminated iron can correct the closed orbit as well as provide beam position stabilization for a frequency range up to several tens of Hertz.

3.5 The Vacuum System of PETRA III

Presently the 25 year old PETRA accelerator is equipped with aluminum chambers and integrated ion getter pumps that use the magnetic field of the dipole magnets. The machine was initially laid out for an electron current of a few mA and an energy of 23 GeV. Today it is used to deliver electrons of 12 GeV and protons of 40 GeV to HERA. The proton RF system as well as injection and ejection elements will be superfluous after the rebuild and will be removed. We distinguish here two sections of the accelerator - the old 7 octants that keep the magnet arrangement but will be equipped with a new vacuum system, and the new octant with short new dipoles and the undulators. It is planned to build major parts of the system, such as the dipole chambers, from aluminum.
There is a third new section with about 100 m active length of damping wiggler magnets. The layout of this section is presently investigated by colleagues from Novosibirsk and is therefore not discussed here (see Sec. 3.4).

3.5.1 Beam parameters and philosophy

3.5.1.1 Vacuum requirements

The goal is to achieve a vacuum lifetime not shorter than the one imposed by the Touschek effect, which is about 50 hours. Of course the overall lifetime issue becomes less critical if the machine is operated in top-up mode but this option should not be used to relax the vacuum requirements. For estimating the maximally acceptable residual gas pressure in PETRA III we consider the two lifetime limiting effects - elastic coulomb scattering and losses from inelastic bremsstrahlung interactions. We assume a gas composition of 25 % CO and 75 % H_2 which is common for electron storage rings. For inelastic scattering the beam lifetime is given by

$$\tau_{\mathrm{inel}}\,[\mathrm{h}] = \frac{-0.695}{\ln(\delta_E)\,\sum_i \frac{P_i\,[\mathrm{pbar}]}{X_{0,i}\,[\mathrm{m}]}} \tag{3.5.1}$$

Here $\delta_E = 1.5\,\%$ is the energy acceptance, $X_{0,i}$ the radiation length of gas i under standard conditions (CO: 321 m, H_2: 7500 m), and P_i the corresponding partial pressure. With a total pressure of $2 \cdot 10^{-9}$ mbar one obtains a lifetime of 94 hours which is larger than the expected Touschek lifetime.
The lifetime-formula for the coulomb scattering reads:

$$\tau_{\mathrm{el}}\,[\mathrm{h}] = 2839\,\frac{E^2\,[\mathrm{GeV}^2]\;A_y^2\,[\mathrm{mm}^2]}{\beta_y^2\,[\mathrm{m}^2]\;\sum_i P_i\,[\mathrm{pbar}]\sum_j k_{ij} Z_j^2} \tag{3.5.2}$$

P_i is the partial pressure of the i-th molecular species and k_{ij} the number of atoms with nuclear charge Z_j contained in the i-th molecule. A_y is the limiting aperture and β_y the vertical β-function. With the above mentioned gas composition and pressure, A_y = 3.5 mm, $\beta_y = 6$ m we obtain a theoretical lifetime of 660 h from elastic scattering. The effective Z of the assumed gas composition amounts to 3.6.

In conclusion we find that an average pressure of $2 \cdot 10^{-9}$ mbar at full beam current with a realistic gas composition will be sufficient for the operation of PETRA III.

3.5.1.2 Synchrotron radiation parameters

The most important properties of the accelerator for the vacuum system are the synchrotron radiation (SR) parameters. The SR causes photo desorption of gases from the chamber walls, which determines the achievable vacuum pressure. In addition the radiation leads to heating of vacuum components which can cause undesirable movements of critical components, as for example the beam position monitors or quadrupole magnets. If the radiation is sufficiently hard it can penetrate the vacuum chamber and may cause damage to the magnet coils or other equipment in the accelerator tunnel. In Tab. 3.5.1 we give some important parameters for PETRA III and compare them with other existing accelerators that use aluminum chambers.

In the old octants of PETRA III the power deposition per length is quite small and thermal effects seem to be no major problem. Also the critical energy of the radiation is small, and even with aluminum as chamber material no additional shielding on the beam-pipe is necessary. This topic is discussed in more detail later. It is interesting to compare the achieved performance of the above mentioned existing machines that use aluminum chambers. APS and PEP-LER employ ante-chambers, whereas LEP used the classical concept to absorb the SR continuously on the outside wall of the chamber without an extra side channel.

The dynamic pressure in a SR dominated vacuum system is roughly given by the following equation:

$$P = \frac{R_0 T}{N_A} \frac{\dot{n}_m}{S'} = \frac{R_0 T}{N_A} \frac{\eta(n_\gamma)\, \dot{n}_\gamma}{S'} \tag{3.5.3}$$

Here P is the pressure, R_0 the gas constant, N_A Avogadro's number, T the temperature, $\dot{n}_m$ the rate of molecules released from the wall, S' the pumping speed per length, $\dot{n}_\gamma$ the

Accelerator	E [GeV]	I_b [A]	ρ [m]	P' [kW/m]	E_{crit} [keV]	$\dot{n}_\gamma$ [m^{-1} s^{-1}]	chamber layout
APS	7.0	0.10	39	2.2	20	$2.3 \cdot 10^{18}$	Alu./Ante
PEP-LER	3.1	2.10	30	3.0	2.2	$2.8 \cdot 10^{19}$	Alu./Ante
LEP	46.0	0.006	3100	0.039	70.0	$1.2 \cdot 10^{16}$	Alu.
PETRA I	18.0	0.006	195	0.23	66.0	$7.2 \cdot 10^{16}$	Alu.
PETRA III (7 octs.)	6.0	0.10	195	0.048	2.5	$4.0 \cdot 10^{17}$	Alu.
PETRA III (1 oct.)	6.0	0.10	22.9	3.5	21.0	$3.4 \cdot 10^{18}$	Steel/Copper

Table 3.5.1: Accelerator parameters of PETRA III in comparison with other accelerators that use aluminum vacuum chambers. The table lists the following parameters: beam energy, beam current, bending radius, radiation power per length in arc, critical energy of the radiation and photon rate per length in arc.

Reference/Date	$\int I_b\,dt$ [Ah]	n_γ [m$^-1$]	$\frac{dP}{dI}$ [pbar/A]	$\frac{dP}{dI}\int I_b\,dt$ [nbar h]
APS[1], 2001	3000	$2.5 \cdot 10^{26}$	4	12
PEP-LER[2], 2001	5000	$2.4 \cdot 10^{26}$	1.3	7
LEP (46 GeV)[3], 1994	33	$3.0 \cdot 10^{22}$	40	1.3
PETRA I (18 GeV)[4], 1980	10	$4.3 \cdot 10^{23}$	250	2.5

Table 3.5.2: Some published performance values achieved in LEP, PEP-LER and APS. Note the wide range of operating currents for the different accelerators in Tab. 3.5.1 (1. Hartog et al., 2001; 2. Wienands, 2001; 3. Billy et al., 2000; 4. Kouptsidis et al., 1980).

photon rate per length. The desorption coefficient η decreases with the number of photons that conditioned the walls of the vacuum chamber. This behavior shall be illustrated here with measurements of the aluminum desorption rate by Mathewson et al. (1990) and a comparison with the observed dynamic pressure in LEP. For larger doses the decrease is roughly proportional to the inverse of the photon dose and is empirically parameterized as follows:

$$\eta(n_\gamma) = \begin{cases} \eta_0 & \text{for} \quad n_\gamma < n_{\gamma 0} \\ \frac{\eta_0 n_{\gamma 0}}{n_\gamma} & \text{for} \quad n_\gamma > n_{\gamma 0} \end{cases} \tag{3.5.4}$$

The parameters $n_{\gamma 0}$ and η_0 can be estimated from those measurements and are used in Sec. 3.5.5.1 to predict the conditioning times for PETRA III. The right plot in Fig. 3.5.1, taken from the same reference, demonstrates that the pressure in the LEP arcs could be predicted quite well using the experimentally obtained desorption rates, and furthermore that the conditioning continues over many orders of magnitude. It is interesting to note that the desorption rate measurement was performed at DCI/Orsay with 3 keV photons, but the LEP radiation is much harder, $E_c = 70\,\text{keV}$. Despite the fact that the prediction ignores the energy and uses only the number of photons, the agreement with the observed conditioning in LEP is good. The measurement at DCI covers photon doses per unit length up to $3 \cdot 10^{21}\,\text{m}^{-1}$ which are reached in the PETRA arcs after only 2 hours operation at full current. For a conditioning time of 1000 hours we should achieve η-values in the sub-10^{-5} range.

If we insert Eq. 3.5.4 in Eq. 3.5.3 we find for larger doses that

$$n_\gamma\,\Delta P/\dot{n}_\gamma = \int I dt\,\Delta P/\Delta I = \text{const.}, \tag{3.5.5}$$

and the constant depends only on chamber geometry, material and pumping speed of the accelerator. The product of integrated current and dynamic pressure is a rough measure of the quality of a vacuum system.

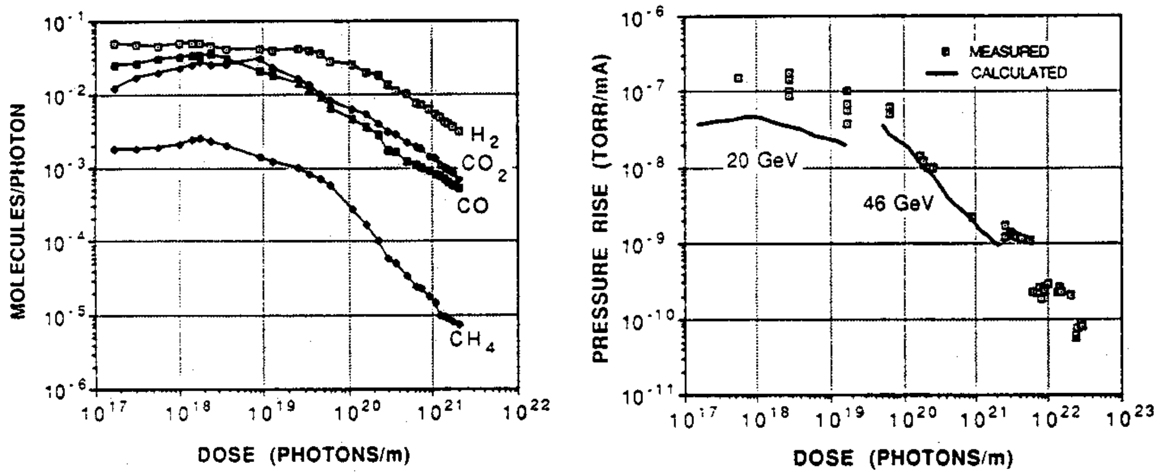

Figure 3.5.1: Left - experimental determination of η during irradiation with 3 keV photons, Right - predicted and observed dynamic pressure in LEP.

3.5.1.3 Choice of material and chamber geometry

One major difference in PETRA III as compared to the present machine is the reduced magnetic field in the dipole magnets at the planned operation energy of 6 GeV, which is not sufficient for the operation of the integrated ion sputter pumps. On the other hand the advantages of a distributed pumping system are obvious. The proposal for the new system is therefore to use NEG strips for distributed pumping instead of the integrated ion pumps.

Another important question is the choice of material. In principle there is a wealth of possibilities out of which three have been discussed in more detail - aluminum profiles with integrated NEG channel, copper profiles with brazed pump channel, and a welded steel construction. The choice of material has to be seen also in connection with the desired geometry of the arc chambers, i.e. ante-chamber like or "classical layout". We give a comparison of a few arguments concerning the choice of material in the following table and discuss the geometry below.

aspect	aluminum	copper	steel
outgassing	high	average	low
heat conductivity	average	best	poor
mechanical stability	average	average	best
production cost	cheap	average	expensive
employment of DESY workshops in production	average	high	average

Concerning the poor outgassing of aluminum one has to note that this statement is definitely true for the early stage of the conditioning process. From measurements (e.g. Mathewson

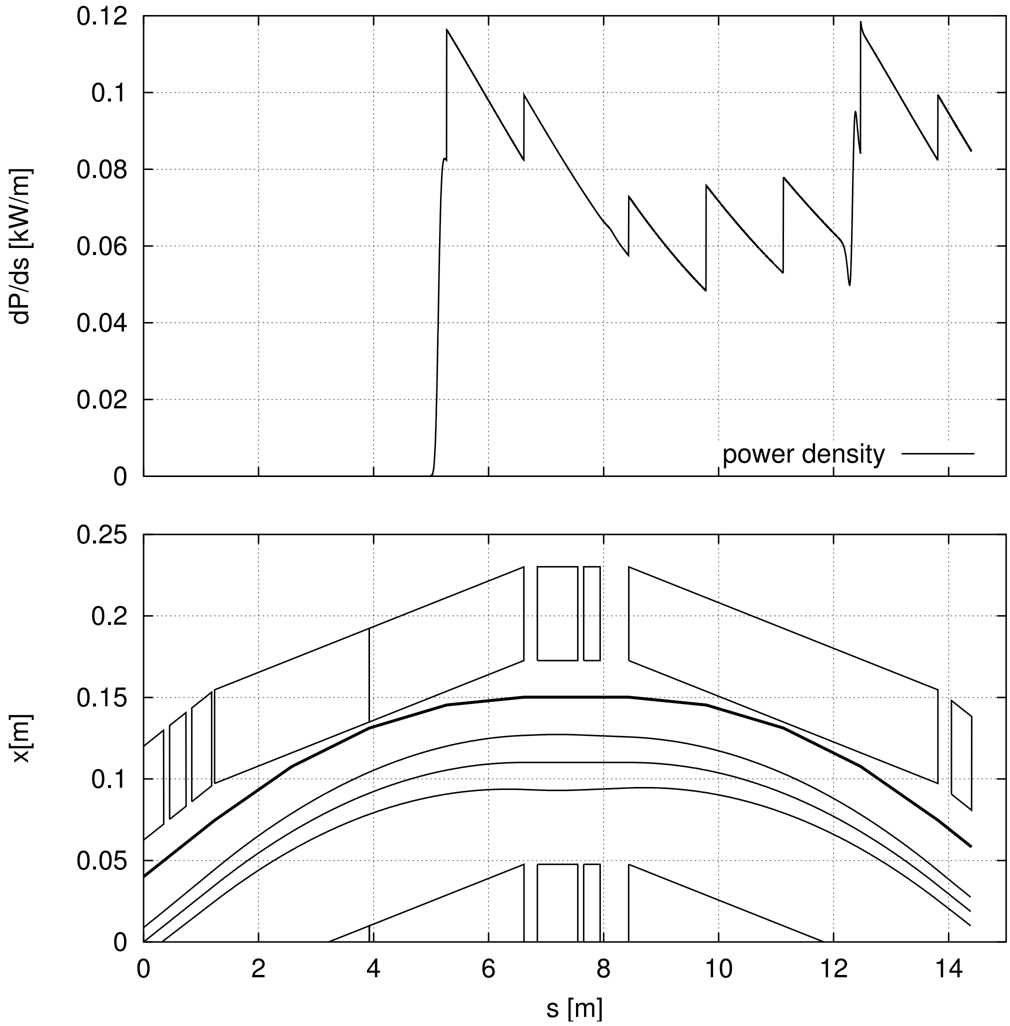

Figure 3.5.2: Power distribution in a FODO cell at the entrance of the standard arc for the maximum anticipated current of 200 mA. In the lower plot the beam is indicated with the three thin lines for orbit and 20 σ envelope. The thick line represents the outside chamber wall.

et al., 1990) it is known that aluminum has an initial outgassing which is an order of magnitude higher than steel, however it conditions faster and reaches the level of the alternative materials at higher doses.

Storage rings with high synchrotron radiation densities mostly rely on copper as chamber material in order to distribute the heat. For the case of PETRA III with a line density of less than 100 W per m, even steel with an outside copper liner and cooling circuit for reasons of thermal stability would be sufficient. Since we are confident that the technical requirements can be achieved also with aluminum, arguments of cost and production issues become more important. We propose to produce the arc chambers from a drawn aluminum profile with integrated water cooling and pumping channel.

Modern Synchrotron radiation sources often use ante-chambers in the arc. There are basically three advantages of ante-chambers:

- providing the possibility for an SR outlet
- thermal decoupling of SR absorber and vacuum chamber
- improvement of particle beam vacuum due to separated pumping of irradiated surfaces.

The first argument is irrelevant for PETRA because in the considered 7/8 section it is not planned to install experimental stations. The second argument is probably also not important since the radiation power is rather low (see Fig. 3.5.2). With a typical water flow of 3 l/min and 250 W radiation power on a 5 m long dipole chamber we obtain a temperature rise of $\Delta T \approx 1.5\,°$C. This leads to relatively small deformations of the chamber. The impact on the BPM is discussed in the next section. The strongest argument for the ante-chamber concept seems to be the separation of SR and particle beam vacuum. Unfortunately there is no free space inbetween the dipole magnets for a separated absorber unit. Fig. 3.5.3 shows the schematic side view of the magnet arrangement inbetween the dipoles. However, there is a possibility for a separated pumping volume as a side channel on the chamber with an extra NEG strip. This version was investigated (Fig. 3.5.4). It turns out to be impossible to extend the radiation channel through quadrupole and sextupole. The side channel has to be discontinued at the end of each dipole using an integrated absorber because of the limited width. Over the length of the downstream round stainless steel chamber the radiation hits the wall, and this section would dominate the pressure along the beam orbit.
An argument against the ante-chamber concept in the 7/8 section is the behavior of the conditioning process. Those surfaces in the chamber that are not hit by direct radiation will still be illuminated by stray light at low rates. However, since these surfaces receive low rates they will be less conditioned as well. In principle these effects could cancel, i.e. integrated dose times instantaneous rate is constant and the specific outgassing is the same everywhere in the chamber. According to the simple parameterization in Eq. 3.5.4 one gains only as long as the dose on the shielded surfaces stays below $n_{\gamma 0}$, which is about $5 \cdot 10^{19}\,\mathrm{m}^{-1}$ (Fig. 3.5.1). For example after 10 Ah the arc chamber has received $1.4 \cdot 10^{23}$ photons per meter, which means the ante-chamber has to shield the inner surfaces by a factor of ≈ 3000 to provide an improvement. Of course, for very low rates there is always an advantage.
The form of the pumping channel of the proposed chamber is still under discussion. The channel runs continuously along each 5 m long dipole chamber, which has significant advantages in terms of production cost. One concern is the deposition of higher order mode power in the channel and on the NEG strip. This issue is discussed in Sec. 3.2.3. The presently assumed height of the channel may be reduced from 6 mm to a minimum of 4 mm, without limiting the pumping speed too much. Numerical simulations on the issue of higher order mode excitation are still going on.
Another issue for the operation with electrons is the release of dust from the NEG strip which could be accelerated and captured by an electron beam. To reduce this risk it is planned to tilt the connecting channel between pump and beam pipe in order to intercept ballistic trajectories of dust particles from the strip to the beam (see 3.5.4). The decision on the height, depth and form of the connecting channel will depend on the outcome of detailed HOM simulations.

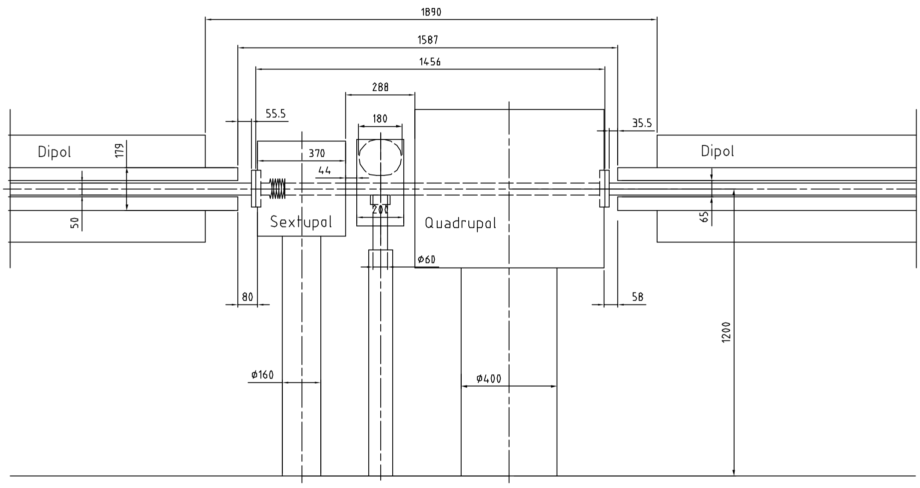

Figure 3.5.3: Side view of the proposed magnet arrangement inbetween dipoles. The element in the center is a vertical correction coil. At this position the beam pipe is supported and contains the beam position monitor.

Also the option to realize pumping with a NEG coating on the walls of the chamber has been discussed. We see two major uncertainties in this concept. There is some experience at DESY with the coating of UHV components using a sputter process. Steel coated ceramics chambers and copper coated steel components were produced for the TESLA Test Facility and had to undergo very stringent tests on the release of dust particles. From these experiences we know that it is very difficult to achieve good adhesion of sputtered layers. Only after electro-polishing before and a high temperature baking cycle after the sputter process it was possible to achieve the TESLA standards. In this context we see potential problems for the PETRA III operation with electrons, if we use the sputtered chambers. In addition there is not much room for thermal isolation of the chambers inside the magnets and the system for thermal activation of the NEG layer will be expensive and difficult to install.

Another potentially important point for the design of vacuum chambers is the shielding of SR. The absorption length of X-rays in material is a strong function of the radiation energy. For high energies the chamber walls become transparent and equipment in the accelerator tunnel like magnet coils or electronics will suffer from radiation damage. It turns out that in the 7/8 section there is no problem as the critical energy (cf Tab. 3.5.1) is low. The attenuation lengths of aluminum and iron are displayed in Fig. 3.5.5. Although the short dipoles in the new octant generate much harder radiation with a critical energy of 21 keV, the steel chambers still provide more than 10 attenuation lengths. Consequently we do not need lead shielding on the surface of the vacuum chambers.

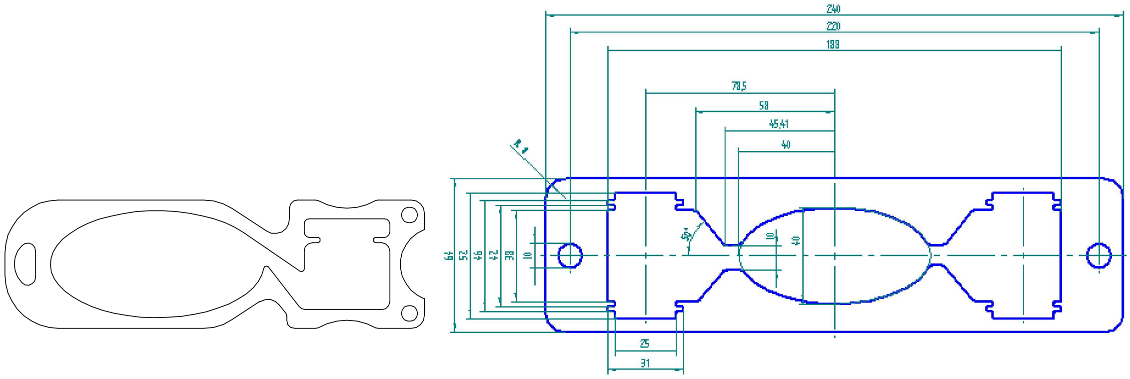

Figure 3.5.4: Left - present proposal (not finalized) of the PETRA III dipole chamber in the old octants. Right - investigated variant with separated pumping channel for SR absorption.

3.5.2 Mechanical considerations

The points of major importance are thermal deformation of the vacuum chambers due to heating by SR and also NEG pump activation, and on the other hand a support concept for the vacuum chambers that guarantees maximum stability for BPM and quadrupole positions. Up to now a few analytical estimates have been carried out. A more detailed finite element simulation of these problems is planned.

A hollow steel support tube with length l, inner and outer diameters d_i, d_o will be bent through the action of a force F at the upper end by an amount:

$$\Delta x = \frac{64 l^3}{3\pi E(d_o^4 - d_i^4)}\, F \tag{3.5.6}$$

$E \approx 2 \cdot 10^7$ N/cm^2 is the elastic modulus of steel. Obviously the length of the support tubes should be as short as possible. A length of 0.5 m will be sufficient if concrete sockets of roughly the same height will be installed underneath. For a tube with 10 cm outer and 8 cm inner diameter the deformation amounts to $\Delta x = 70$ nm/N. The highest force that can occur is the force of the air pressure on a blind flange at the end of the chamber during an installation period. It amounts to about 1000 N, so we expect 70 μm deformation in this case.

The bending of the aluminum chamber due to asymmetric heating by SR can be estimated as follows. The bending is caused by a length difference of the inner and outer side of the chamber. Temperature difference ΔT, length change Δl, bending radius ρ and sector angle θ are related via

$$\Delta l = \Delta T\, \alpha\, \rho\theta = \theta(\rho + h/2) - \theta(\rho - h/2) \tag{3.5.7}$$

Here $\alpha = 2 \cdot 10^{-5}$ °C^{-1} is the expansion coefficient for aluminum and h the width of the chamber. We obtain a bending radius of $\rho = h/(\Delta T\, \alpha)$, and for fixed ends a displacement of the chamber center by $\Delta x \approx \rho\theta^2/8 = \alpha\, l^2\, \Delta T/(8h)$. For a chamber width of 100 mm, a length $l = 5$ m and a temperature difference of 1.5 °C (full current vs. no current) we obtain a displacement of 1 mm.

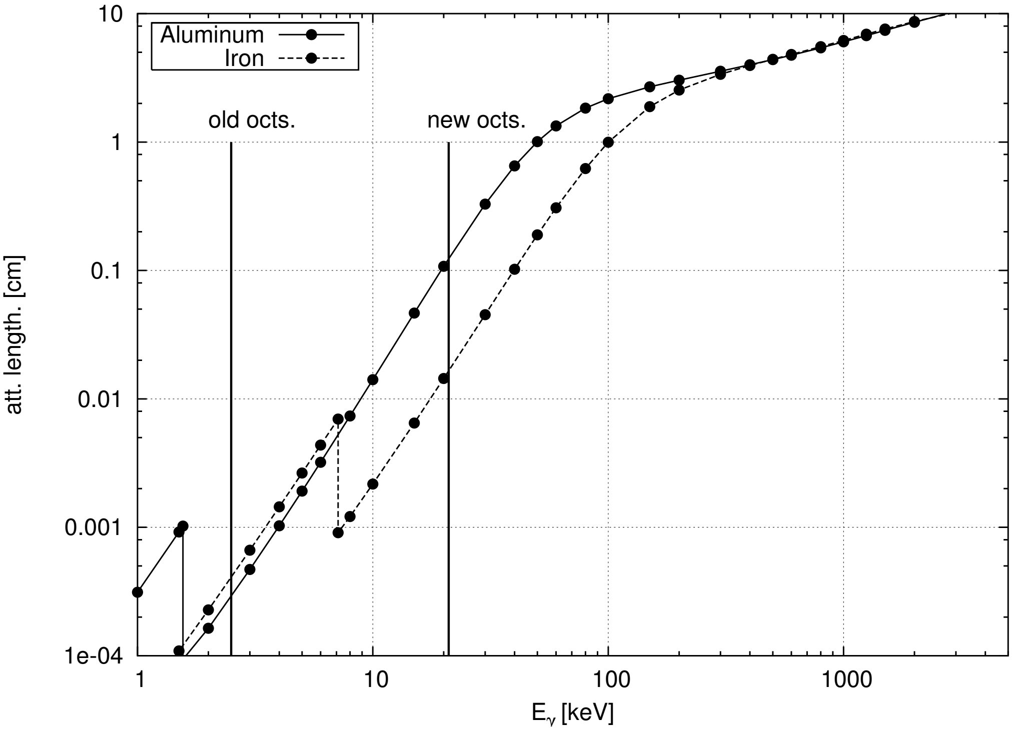

Figure 3.5.5: Attenuation lengths of aluminum and iron as a function of photon energy. The critical energies in the old and new octants are indicated.

The forces due to thermal deformation are difficult to estimate analytically because friction and spring constants of bellows play a role. However, for a force of 100 N the displacement will be less than 10 μm and it can be reduced further by choosing stronger dimensions of the support tube. A specific topic is the reproducibility of the chamber position after NEG regeneration at 200 °C strip temperature. This will be investigated by heating experiments with aluminum chamber samples.

In the present machine the interconnections of the vacuum chambers are done by welding. This has caused problems over the years of operation. For the new machine we are planning to use a flange system. The flanges can be realized using stainless steel with the difficulties lying in the interconnection between steel and aluminum, which can be solved, however, by friction bonding or explosion bonding. Another possibility is the employment of surface hardened aluminum flanges. This principle was tested successfully at local positions in PETRA II.

Regardless of the material choice we are planning to use flat seals, for example a system developed by the company VAT using silver coated copper seals. This system has been successfully used at specific locations of HERA. The advantages over the conflat system is the provision of RF shielding for the flange gap and, according to our experience, better thermal/mechanical robustness.

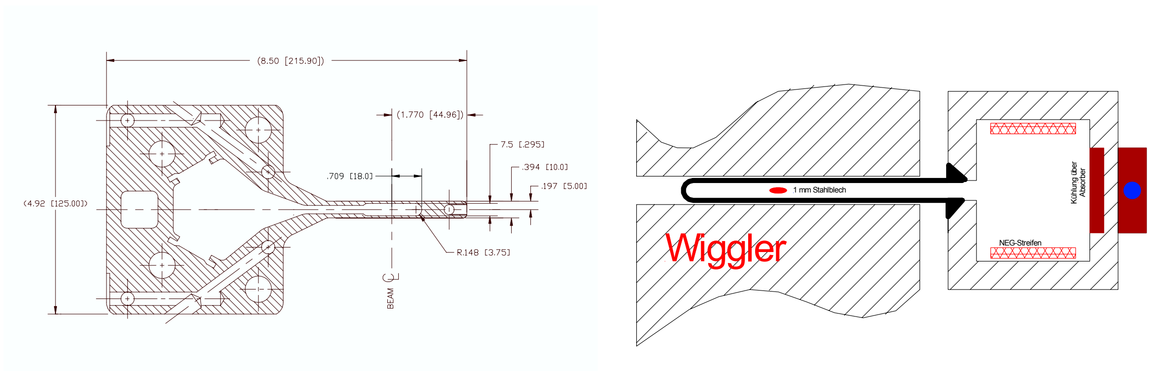

Figure 3.5.6: Left: aluminum wiggler/undulator chamber designed by APS (Trakhtenberg et al., 2003). Right: schematic layout of a possible alternative using steel.

3.5.3 New octant

The new octant will be equipped with undulators for the production of SR. The vacuum pressure on the beam path within those devices is especially critical in view of Bremsstrahlung-background for the experiments. The available space for the undulator chambers is limited since the achievable field strength depends critically on the magnetic gap height.

The dipole magnets in the new octant are much shorter than the ones in the normal arc. Consequently radiation power and critical energy are higher, see Tab. 3.5.1. As mentioned above the shielding of the SR by the chambers becomes much weaker and the consequences for equipment in the tunnel need to be carefully evaluated.

In view of the thin wall our present working model is to use the design from the APS, possibly buying complete profiles from them. The APS profile is drawn from aluminum, has only 1 mm wall thickness and employs NEG pumping in a side channel.

In parallel we investigate a welded steel solution that would possibly allow for smaller wall thickness locally. Also the steel version would be NEG pumped. The choice of steel has the advantage of a lower outgassing at this critical location. The steel version has problems in case of accidental illumination with SR from an upstream dipole. It has to be evaluated if the chamber can be hit by beam mis-steering in the vertical plane, and if so whether one wants to rely on passive (cooled chambers) or active (orbit control) protection systems. Aluminum with its relatively high thermal conductivity provides better passive safety.

Stability is a very important aspect of the new experimental region. The long lever arms of the wiggler radiation fans to the targets imply extremely tight requirements on the beam stability. Quadrupole positions as well as beam position monitor (BPM) positions need to be stable over time. Differential thermal expansion of vacuum chambers can cause movements of BPM's and even quadrupoles. Consequently the new design foresees a strict thermal and mechanical decoupling of heated surfaces and critical components. In the section between two wigglers it is planned to install one crotch absorber that allows for the separation of wiggler photon beam and particle beam, and a second absorber that shields the chamber of the next wiggler. Other surfaces will not be hit by direct radiation. As in the standard arcs the vacuum chambers will not be mounted in the magnets, but on separate rigid supports. The BPM's will be decoupled from neighboring chambers by bellows.

Figure 3.5.7: Top view of magnet arrangement inbetween two undulators in the new octant. The radiation fans of the two dipoles are indicated.

3.5.4 Further modifications of the vacuum system

The PETRA ring contains 8 straight sections. Four of them (N,O,S,W) exhibit a length of roughly 90 m. It is foreseen to install the damping wigglers in two of these sections. The RF system is presently installed in section South. The other four straights (NO,SO,SW,NW) have a length of about 50 m each. It is foreseen to remove all superfluous components from these sections like the proton RF system and positron ejection to HERA. The vacuum chambers in all sections will be replaced by standardized stainless steel components. These components include 98 mm diameter ss-tube (presently often 120 mm) and to this diameter adapted bellows with RF shielding and BPM units. Furthermore it is planned to replace the 25 year old ion getter pumps (400 l/s) by a larger number of new small pumps (60 l/s).

Also the 85 m long transport channel from DESY II to PETRA will be renewed. Again it will be advantageous to reduce the diameter of the beam tubes to 98 mm OD.

3.5.5 Conditioning and expected performance

In view of predictable machine operation it is important to estimate the required conditioning time until the design values of the average pressure can be reached. However, the accelerator can be operated even with an average pressure higher by an order of magnitude, especially in top-up mode. The most important aspect is the pressure in the undulator chambers because scattering of the particle beam with residual gas molecules could cause unacceptable bremsstrahlung background conditions for the experiments. The undulator chambers can be equipped with higher pumping speeds, e.g. two NEG strips if we use the APS chamber. If we decide to use the steel concept it is planned to coat the undulator chambers with NEG material which would lead to very small outgassing and presumably much better conditions than in the standard arc.

For the arc the expected average operating pressure can be estimated either from the laboratory measurements and Eq. 3.5.3, or in a pragmatic way by comparison with the existing accelerators in Tab. 3.5.1. In the next sections this will be done for the old octants.

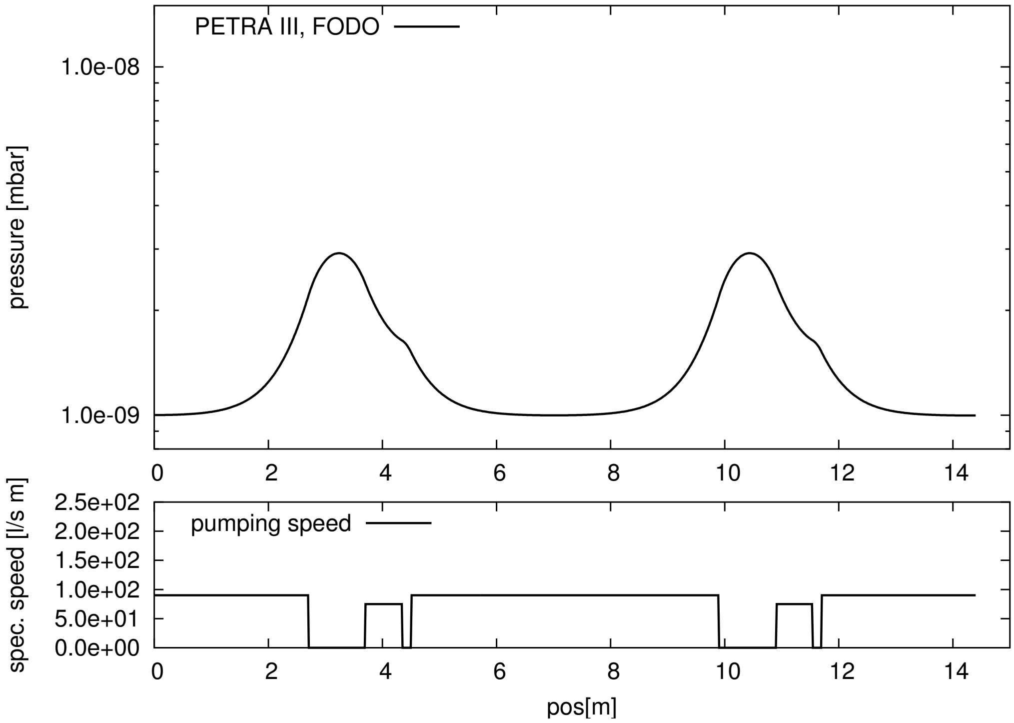

Figure 3.5.8: Pressure profile computed for a constant outgassing rate, $\eta = 5 \cdot 10^{-6}$ and realistic pumping speed distribution.

3.5.5.1 Dynamic pressure prediction from η measurements

An η of $6 \cdot 10^{-6}$ leads to a total outgassing rate of $1.5 \cdot 10^{-7}$ mbar l/s m. Using this value as constant over length and an average pumping speed of 60 l/s m one obtains an acceptable pressure of $1.5 \cdot 10^{-9}$ mbar at 100 mA current in the old octants. The conductance of the vacuum chambers was taken into account by running a simulation code with geometry and pumping speed distribution as input. This is shown in Fig. 3.5.8 for a FODO cell of PETRA. The required conditioning time to reach the $\eta = 6 \cdot 10^{-6}$ can be estimated using the simple parameterization (Eq. 3.5.4) with $n_{\gamma 0} \approx 5 \cdot 10^{19}\,\mathrm{m}^{-1}$, $\eta_0 = 9 \cdot 10^{-2}$ from Fig. 3.5.1. If we further take into account the conversion from Ampere-hours to the number of photons, $n_\gamma / \int I_b\,dt = 1.4 \cdot 10^{22}\,\mathrm{m}^{-1}\,\mathrm{Ah}^{-1}$, the required integrated dose is estimated to be $\int I_b\,dt \approx 54\,\mathrm{Ah}$.

3.5.5.2 Dynamic pressure from comparison with existing accelerators

Another way of estimating the performance of the PETRA vacuum system is to assume that it behaves as the existing accelerators in Tab. 3.5.2. Dynamic pressure rise times integrated current is a figure of merit. This parameter is actually influenced by the chamber geometry, pump distribution and pumping speed per meter. Reducing the complicated behavior to a single number is a strong simplification. Nevertheless it can be used to make a rough prediction of the required conditioning time.

If we assume a value of $dP/dI \cdot \int I\,dt = 2.5$ nbar h as observed in PETRA I, PETRA III will achieve a dynamic pressure of 2 pbar at 100 mA current after 125 Ah. Note, however, that PETRA I had significantly less pumping speed delivered by the integrated ion sputter pumps as compared to the NEG pumps in the new machine.

If we assume 75 mA average current (linear rise from 50 mA to 100 mA) one can conclude that the required conditioning time lies in the range of 700 to 1700 operating hours to reach the design pressure with full operating current of 100 mA. Acceptable machine operation will be already possible after a tenth of this time with a beam lifetime beyond 5 h.

3.6 The RF System

3.6.1 Introduction

3.6.1.1 The existing PETRA II RF system

PETRA II is currently used as proton and lepton pre-accelerator for HERA. In addition it is used as a synchrotron radiation source for HASYLAB. Two 500-MHz RF systems each with 1200 kW nominal output power are installed (see Fig. 3.6.1). One RF system consists of two Philips klystrons supplying eight normal conducting 7-cell cavities. The installed klystron types YK-1301 and YK-1304 are 800 kW tubes. These tubes are also used at HERA and DORIS. The RF output power is limited to 600 kW per tube at PETRA due to the lower nominal voltage of the existing transmitter power supplies (58 kV instead of 75 kV). Each RF system runs at 500 kW in pre-accelerator mode at 12 GeV and 50 mA current. The cavity voltage is 9 MV per RF system. About 50 % of the RF power is needed to compensate the synchrotron radiation losses. The other half generates the cavity voltage. It is possible to supply all 16 cavities by only one transmitter. For this case two 3-dB couplers and a 100 m long waveguide line connecting both transmitters are installed. To switch to the so-called ’one-transmitter-mode’ it is only required to insert two waveguide shorting plates at prepared places at the 3-dB coupler of the passive transmitter station. The ’one transmitter mode’ is the preferred operation mode because of the lower energy consumption.

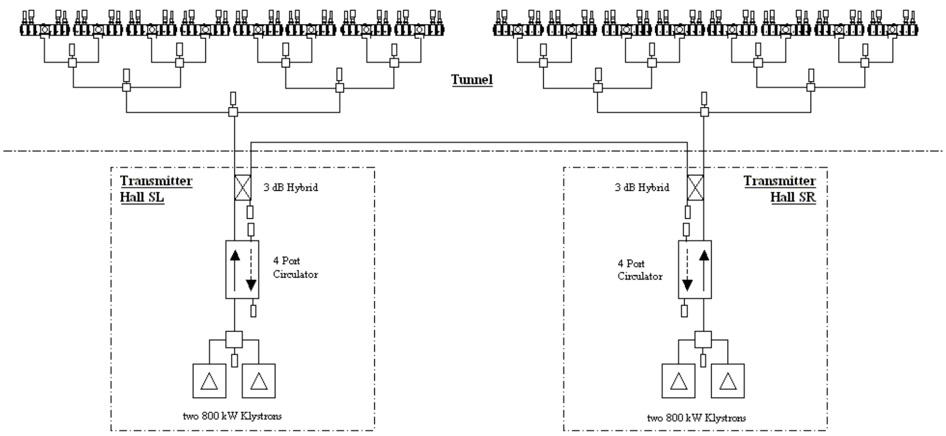

Figure 3.6.1: The RF Systems of PETRA II.

3.6.1.2 Proposal for a new transmitter system for PETRA III

The proposed beam parameters of PETRA III are 100 mA at 6 GeV with the option for a later upgrade to 200 mA beam current.
A total RF power of 1.3 MW is required to compensate the radiation losses in the damping wigglers, undulators, dipole magnets, the cavity copper losses and the (higher order

mode) HOM losses. Furthermore a circumferential voltage of 20 MV is needed for sufficient Touschek lifetime. The output power of the existing RF systems would be sufficient for PETRA III. Although some parts of the system have been modernized some basic components are more than 25 years old. Especially the high-voltage klystron supplies, crowbars, klystron-modulators, interlocks, low level RF, and control systems have to be renewed. Therefore it is intended to build completely new transmitters for PETRA III. The use of IOTs and other klystrons types was considered because of delivery problems of compatible klystron types in the past. The existing cavity system should remain. Due to the available manpower, budget and the tight schedule a new cavity system cannot be realized before 2007.

3.6.1.3 Transmitter concepts

For comparing different transmitter concepts the prices of the essential technical components were determined. No account was taken of possible civil engineering needs. Other conditions taken into account include:

1. Provision of sufficient RF power for a possible later upgrade to 200 mA beam current.
2. Operation of the transmitter tube at a maximum of 80 % of the nominal output power to increase reliability.
3. Powering an equal number of cavities by each RF system.

To study the expected reliability of the different transmitter concepts the RF systems were subdivided into 18 comparable units (transmitter-tube, high voltage power supply, circulator, cavity, RF-loads, fast interlock system, controls, water cooling etc.). For each of these 18 subunits the trip and repair rates were determined. Trips and repairs of the 11 RF systems of HERA, DORIS and DESY were used as a data base. In total 470 events occuring within 4900 transmitter operation-days have been analyzed. The results are summarized in Tab. 3.6.1

Concept No.	1	2	3	4	5	6
Number of RF systems	2	2	4	4	4	16
Number and type of transmitter tubes per RF system	1×1.2 MW Klystrons without M.A.[1]	2×600 kW[2] Klystrons with M.A.	1×600 kW[2] Klystrons with M.A.	2×300 kW Klystrons without M.A.	2×300 kW IOTs	2×75 kW IOTs
Investment[3]	100 %	100 %	145 %	155 %	195 %	185 %
Operation costs[3,4]	125 %	130 %	130 %	140 %	100 %	115 %
Investment & costs for 10 years operation[3]	100 %	105 %	115 %	125 %	115 %	120 %
MTB Trip	6d	5d	4d	3d	2d	1d
MTB Failure	60d	30d	25d	30d	20d	8d

Table 3.6.1: Cost and reliability for different RF-system concepts

[1] M.A. = modulation anode

[2] 800 kW klystrons are not operated at nominal cathode voltage, therefore the power is limited to 600 kW RF power.

[3] Relative to the cheapest concept

[4] Energy and tube costs for 300 Runs p.a.; 4000 operation hours p.a.; 40.000 h avg. tube life time

3.6.1.4 Comparison of costs

Because concepts 1 and 2 have the smallest number of components they are cheaper than the other concepts shown in Tab. 3.6.1. Additionally the two existing 4-MW circulators could be reused.
The concepts using IOTs are the most expensive although IOTs are about 30 % cheaper than comparable klystrons. Since they are only available for less than 90 kW RF power at present they can not compete in costs with klystrons in the MW power range, nevertheless 300-kW IOTs are considered in concept 5. The cost per kW RF power of such tubes would be quite attractive, unfortunately they are not state of the art at present. The additional costs for development, prototype tubes and for generating some kW of drive power makes this concept more expensive than the 300 kW klystron concept which was only considered for comparison.
One significant advantage of IOTs is the 10 % higher efficiency compared to klystrons. Furthermore the efficiency is quite constant over a wide output power range. Due to the operation costs the 300-kW IOT concept would be the most favorable in this respect. However this is offset by the higher initial investment. Regarding investment and operational costs over a period of 10 years concepts 1 and 2 remain the most economic.

3.6.1.5 Comparison of reliability

Reliability of a facility decreases with the number of installed power components. In first approximation one can assume that four 300 kW tubes cause four times more trips than one 1.2-MW tube. This applies also to high power supplies and all essential subsystems. Therefore concept 6 has the lowest expected reliability. On the other hand machine operation would only be affected if more than 3 of the 16 RF systems were off line at the same time. However, beam loss is probably unavoidable when just one RF system trips.
Due to the smaller number of installed power components the highest reliability can be expected for concepts 1 and 2. However, in the case of a serious failure of one of the RF systems operation would only be possible at lower total beam current.

3.6.1.6 Conclusion

Concepts 1 and 2 are the cheapest and the most reliable. Concept 2 has the additional advantage that it is very similar to the existing PETRA II installation and therefore requires the least effort to renew the system.
In the following only concept 2 is considered in more detail.

3.6.2 RF system design for PETRA III

3.6.2.1 Design criteria

The preferred RF system for PETRA III can be very similar to that of PETRA II, as shown in Fig. 3.6.2. To increase the current threshold for beam instabilities it is planned to reduce

the total shunt impedance by reducing the number of cavities. The minimum number of cavities required is a compromise between the maximum transferable power per coupler and the maximum storable beam current with only one of the transmitters in operation.
The maximum reliable power capability of an input-coupler is about 150 kW. In principle the power couplers presently used at PETRA are able to transfer much more power (Gerke et al., 1977), however this limit has been chosen based upon considerable experience in this power range.
The maximum storable beam current is limited by the available RF power. The nominal power of each transmitter could be 1600 kW assuming that the transmitter power supply is laid out to provide the nominal cathode voltage for the type of klystron used. If only one transmitter is available the remaining RF power for operation is 1440 kW (in consideration of 5 % safety margin and 5 % transmission loss). This RF power would be sufficient to run at design current if all 16 cavities were left in the machine. Reducing the number of cavities to 14 would limit the current to 97 mA. The maximum power capability of the input couplers allows the number of cavities to be reduced from 16 to 12. In this scenario the current will be limited to 83 mA in the 'one transmitter mode'.
Coupler power, transmitter power during normal operation and maximum current in 'one transmitter mode' are shown in Tab. 3.6.2 for different cavity numbers.
The basic layout of the existing RF systems can be retained, as mentioned in Sec. 3.6.1.2. However, high-voltage klystron supplies, crowbars, klystron-modulators, interlocks, low level RF, and control systems have to be improved and renewed.
For further information about high-voltage klystron supplies and crowbar systems (see Sec. 3.12.2).

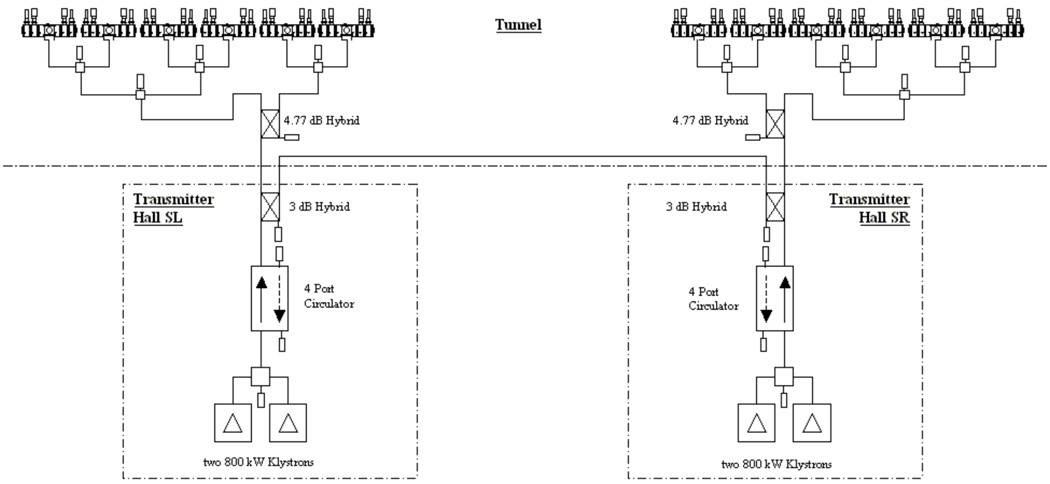

Figure 3.6.2: Modified RF System for PETRA III.

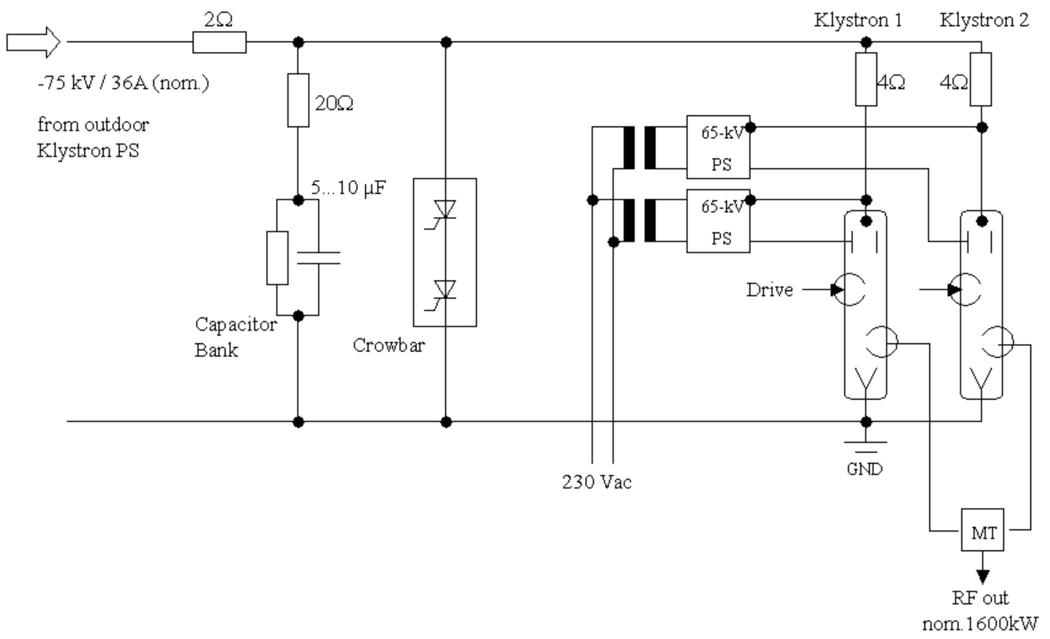

Figure 3.6.3: High Voltage Supply of the Klystrons

3.6.2.2 Klystron high voltage supply

The 500 MHz klystrons of the 13 transmitters at DESY are equipped with modulation anodes. To preserve uniformity with the remaining systems it is prudent to also use this klystron type for PETRA III. However this requires additional modulation anode supplies. To have the possibility to operate klystron types from different suppliers, an independent modulation anode power supply for each klystron is necessary. Fiber link controlled 65 kV power supplies are foreseen to drive the modulation anodes, as shown in Fig. 3.6.3. DESY has extensive positive experience with such units.

3.6.2.3 RF controls

A sketch of the RF controlling system is shown in Fig. 3.6.4

Number of 7-cell cavities installed	Coupling factor for Matching @ 100 mA	Power Transmission per Coupler (kW)	Required Transmitter Power @ 20 MV, 100 mA (kW)	Max. Beam Current with one Transmitter @ 1440 kW (mA)
2 × 8	2.4	81	2 × 690	107
2 × 7	2.2	99	2 × 731	97
2 × 6	2.0	124	2 × 786	83
2 × 5	1.9	163	2 × 863	63
2 × 4	1.7	230	2 × 978	31

Table 3.6.2: Required RF power and maximum beam current versus number of cavities installed

Cavity Voltage Control Loop

The cavity voltage loop is used to control phase and amplitude of summed cavity voltages of each cavity system. The loop acts on the klystron drive. Instead of the commonly used phase and amplitude control loops the higher performance of IQ control loops will be used (Corredoura, 1999). It is foreseen to keep the klystron efficiency at maximum by controlling the cathode voltage and current as a function of klystron output power and drive. A controller algorithm is under development.

Cavity Tuning

Mechanical tuners (plungers) driven by stepper motors are installed in two of the 7 cavity cells. The phase of the pick-up signal from the cavity's center cell is compared with that of the incident input coupler power. The measured difference drives both plungers in parallel to keep the phase difference zero. The cavity then appears as a real load for the incident RF under all operation conditions. Signals of additional pick-up loops in both plunger-cells are used to keep the field distribution symmetric over the 7 cavity cells (Gerke et al., 1977).

Phasing

The phase of each RF system relative to the beam is computer controlled by a phasing-automatic. This calculates the synchronous phase and the phase offset of each RF system and keeps the RF phase difference between the RF systems to zero. The error of this automatic is less than 5°. Experience at HERA shows that this technique is more convenient and precise than the method using the synchrotron frequency (Ebert, 2000).

Transmitter	Units	Nominal Data	Data for nominal beam operation @ 20 MV, 100 mA	Data for 1-Transmitter operation @ 1440 kW
Number of Transmitters	-	2	2	1
Number of Klystrons	-	4	4	2
Klystron Voltage	kV	75	60	73
Klystron Current	A	<18	<13	<17
RF frequency	MHz	499.67	499.67	499.67
Klystron RF - Output Power	kW	800	398	720
Klystron Efficiency	%	>60	>50	>55

Cavities	Units	Nominal Data	Data for nominal beam operation @ 20 MV, 100 mA	Data for 1-Transmitter operation @ 1440 kW
Number of Cavities	-	12	12	12
Cavity - type	-	7-cell, copper	7-cell, copper	7-cell, copper
Shunt impedance per cavity	MΩ	23	23	23
Voltage per cavity	MV	>2.5	1.67	1.67
Overvoltage factor	-	-	2.6	2.6
Beam current	mA	-	100	83
Synchronous phase	deg.	-	22.3	22.3
Cavity detuning	deg.	-	40.4	35.2
Cavity detuning	kHz	-	21.3	17.7
Copper loss per cavity	kW	>150	60.3	60.3
Coupling factor	-	-	2.0	2.0
Power per coupler	kW	200	124	113
Power to beam per cavity	kW	-	63.2	52.5

Table 3.6.3: Summary of data of the planned PETRA III RF system

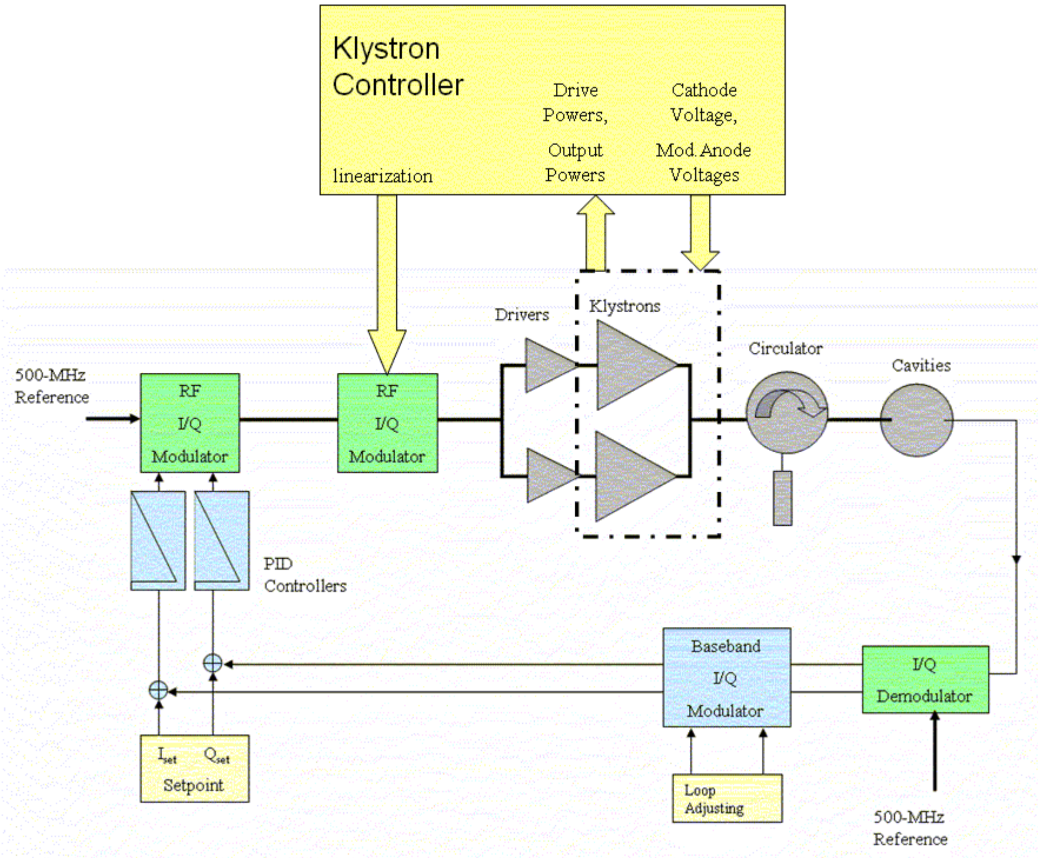

Figure 3.6.4: Schematic diagram of the RF system control

3.6.3 Reliability of RF systems

The success of synchrotron radiation sources depends on high availability. Therefore particular attention must be paid to ensure the reliability of all essential accelerator components.
As has been already mentioned in Sec. 3.6.1.3 system trips and repairs of existing RF-systems at DESY have been investigated. It turns out that the mean time between two trips (MTBTrip) is about 10.5 days which applies to all the e+/e- accelerators at DESY.
An evaluation of the trips of the RF systems at APS (Horan, 2002), ESRF (Mercier, 2002)

and LEP (Frischholz, 2000) shows similar results. The mean time between two trips of these systems is between 8 and 12 days (on average about 10 days). The reliabilities of the different RF systems are shown in Tab. 3.6.4.

Machine	HERA	DORIS-3	DESY-2	APS	ESRF	LEP
Year of Analysis	1999-2000	2001	2002	2001	2001	1999
Number of RF Systems	8	2	1	2	2	20
Type of RF system	2 Klystrons, 10 ... 16 Cavities	1 Kly., 4 Cav.	2 Kly., 8 Cav.	1 Kly., 8 Cav.	1 Kly., 2 ... 4 Cav.	2 Kly., 14 ... 16 Cav.
MTBTrip	1.2d	6.5d	11d	6d	4d	0.45d
MTBTrip per RF system	10d	13d	11d	12d	8d	9d

Table 3.6.4: Reliabilities of RF systems of different facilities

A detailed investigation of the 470 registered trips of the 11 RF systems at HERA, DORIS and DESY showed that only every 6th to 10th trip was necessary for system protection. The majority of the remaining trips was either non-critical or due to false alarms.
The strategy foreseen for PETRA III is to monitor all important signals using two or three independent sensors and/or checking the sensor-signals for plausibility. In this way we hope to decrease the number of non-essential trips. To illustrate this we consider the following example.

Klystron Focus Interlock with sensors for monitoring the

- Current through the solenoid,
- Voltage across the solenoid,
- Magnetic field inside the solenoid

The klystron voltage would only be switched off if at least two of the signals exceed the specified limits. Error trips due to time varying signals may be reduced by including a rate of change threshold.
Klystron Body-Temperature Interlock:

- Slow temperature rise above the limit ⇒ decrease klystron-current until temperature is stable.
- Fast temperature rise above the limit ⇒ switch off klystron high-voltage
- Instantaneous rise above the limit ⇒ ignore (must be sensor or electronic error)

By applying these techniques we hope to halve the number of false trips.

3.6.4 Upgrade to 200 mA beam current

It is foreseen to increase the maximum beam current of PETRA III to 200 mA in an upgrade. The installed 7-cell cavities are not suitable for this current because of their HOM-impedances and must therefore be replaced. Superconducting or normal conducting single-cell cavities with HOM-optimized design and additional HOM-damping are possible solutions. These are considered in the following.

3.6.4.1 Single cell normal-conducting cavities

The maximum allowable power loss on a water cooled copper surface is about 100 W/cm^2. At higher power levels a vapor layer decreases the cooling efficiency. Therefore the maximum power loss in a normal conducting single-cell cavity at 500 MHz is limited to 300 ... 400 kW. Assuming a shunt impedance of 3 MΩ the maximum possible cavity voltage can be 1.3 ... 1.5 MV. Practical values tend to be much lower because of the restricted cooling possibilities due to geometrical constraints near the plunger, beam pipe and coupler flanges. Cavity voltages of 800 kV for a 500-MHz cavity (SPring-8) or 850 kV for a 470-MHz cavity (PEP-2) are state of the art. To generate the required 20 MV at least 25 cavities of such a type would be necessary. The required RF power for 200 mA beam current would then be:

$$P_{CavLoss} + P_{HOM} + P_{beam} = 25 \cdot \frac{800\,\mathrm{kV}^2}{2 \cdot 3\,\mathrm{M\Omega}} + 100\mathrm{kW} + 1318\mathrm{kW} = 4.09\mathrm{MW} \qquad (3.6.1)$$

To calculate the nominal RF power required an additional 5 % transmission loss and 20 % safety margin must be included. The installed RF power has to be at least 5.1 MW.
Retaining the 800 kW klystrons implies a 3rd 1.6-MW transmitter. The available RF power would then be 4.8 MW. Since this somewhat less than required the number of RF cavities must be accordingly increased. Furthermore in order that all RF systems are similar to one another the total number of cavities has to be divisible by 3. In addition operation at 20 MV with $>$ 100 mA beam current must be possible when only 2 of 3 transmitters are available.
The installation of 15 cavities per RF system would meet these requirements. In normal operation (3 RF systems with 45 cavities, 20 MV circumference voltage, 200 mA beam current) the power per cavity-coupler would be quite moderate, namely:

$$P_{CavLoss} + P_{HOM} + P_{beam} = \frac{444\,\mathrm{kV}^2}{2 \cdot 3\,\mathrm{M\Omega}} + \frac{100\,\mathrm{kW}}{45} + \frac{1318\,\mathrm{kW}}{45} = 64\,\mathrm{kW} \qquad (3.6.2)$$

The RF systems would operate at 63 % of their rated maximum power at nominal beam conditions.

3.6.4.2 Single-cell superconducting cavities

Superconducting (s.c.) cavities exhibit several advantages compared to normal conducting (n.c.) cavities. Because of their negligible surface resistivity the dissipated power in the structures is low and higher accelerating voltages can be realized. This offers the possibility to optimism the cavity shape in order to minimize their Higher Order Mode (HOM) impedance. Additionally HOM damping in s.c. cavities is easier compared to n.c. cavities. Both the smaller number of required cavities and their better damped HOMs lead to increased thresholds for beam instabilities. For the DIAMOND project the use of s.c. cavities has been considered (Dykes et al., 2000). For PETRA III the RF systems have to be designed for a beam power of about 1.4 MW at 200mA. Including 5 % transmission losses and 20 % safety margin yields 1.75 MW required RF power. Thus the installed nominal klystron power of 3.2 MW is more than sufficient. Assuming a voltage of 2 MV per cavity (6.7 MV/m) the installation of 10 superconducting cavities would be sufficient. The resulting

	Units	n.c. cavities	s.c. cavities
Number of transmitters	-	3	2
nominal RF power per transmitter	MW	1.6	1.6
RF power per transmitter @ 200 mA	MW	1.02	0.75
total RF power @ 200 mA	MW	3.07	1.49
number of cavities per RF system	-	15	5
total number of cavities	-	45	10
voltage per cavity	MV	0.444	2.0
gradient	MV/m	1.5	6.7
power per coupler @ 200 mA	KW	64	142
power to beam per cavity @ 200 mA	kW	32	142

Table 3.6.5: Superconducting (s.c.) versus normal conducting (n.c.) cavities

coupler power of 142 kW per cavity would be moderate. Use of s.c. cavities for the upgrade of PETRA III would be quite attractive, especially considering the energy consumption. The AC input power for two s.c. RF systems is about 3 MW lower compared to that for three n.c. RF systems. The investment costs are estimated to be at least 10 M€ for either option.
Superconducting cavities require more complex interlock systems compared to n.c. cavities. Therefore one can assume that they trip more frequently. The experience at HERA show a trip rate of about 70 days for a s.c. cavity (compared to 300 days for a n.c. cavity). At LEP the trip rate was about 23 days for a single s.c. cavity. At CESR and KEK-B the experience is similar. The higher trip rate of s.c. cavities is partially compensated by the smaller number required. From the above it is reasonable to expect 1 to 3 trips per week for the PETRA III superconducting RF system. Experience from accelerators which use or intend to use single cell superconducting cavities may help to make a choice between the two alternatives.

3.6.5 Conclusion

Reusing essential parts of the present PETRA II RF system is planned based on cost, schedule and manpower considerations. Renewing the klystron high-voltage supplies, crowbar systems, klystron modulators, interlock electronics and control system is foreseen to ensure reliable operation and efficient diagnostics. To be able to store 100 mA with an 8 ns bunch-spacing, the shunt-impedance of the 500 MHz cavities will be decreased by removing 4 of the 16 installed 7-cell-cavities. Additionally installing a broadband longitudinal multibunch feedback system is foreseen (see Sec. 3.10).

For a future upgrade of PETRA III to 200 mA it is planned to replace the existing 7-cell-cavities by HOM-optimized single-cell cavities. The decision whether superconducting or normal conducting cavities will be more suitable for PETRA III has yet to be made.

3.7 Mechanical Structure of the New PETRA III Octant

The new PETRA III octant is housed in a long hall where the storage ring tunnel is made up of a system of concrete blocks. A crane gains access to the individual devices in this tunnel from the top by removing the concrete roof beams. For the new octant a design of machine elements combined in larger modules ('girder assembly' or 'girder' for short) is planned. The benefit of the girder construction is that all the elements associated with a module can be assembled, surveyed and tested before they are installed in the storage ring tunnel. The general idea is to align the individual components on the girders with accurate jigs and fix-

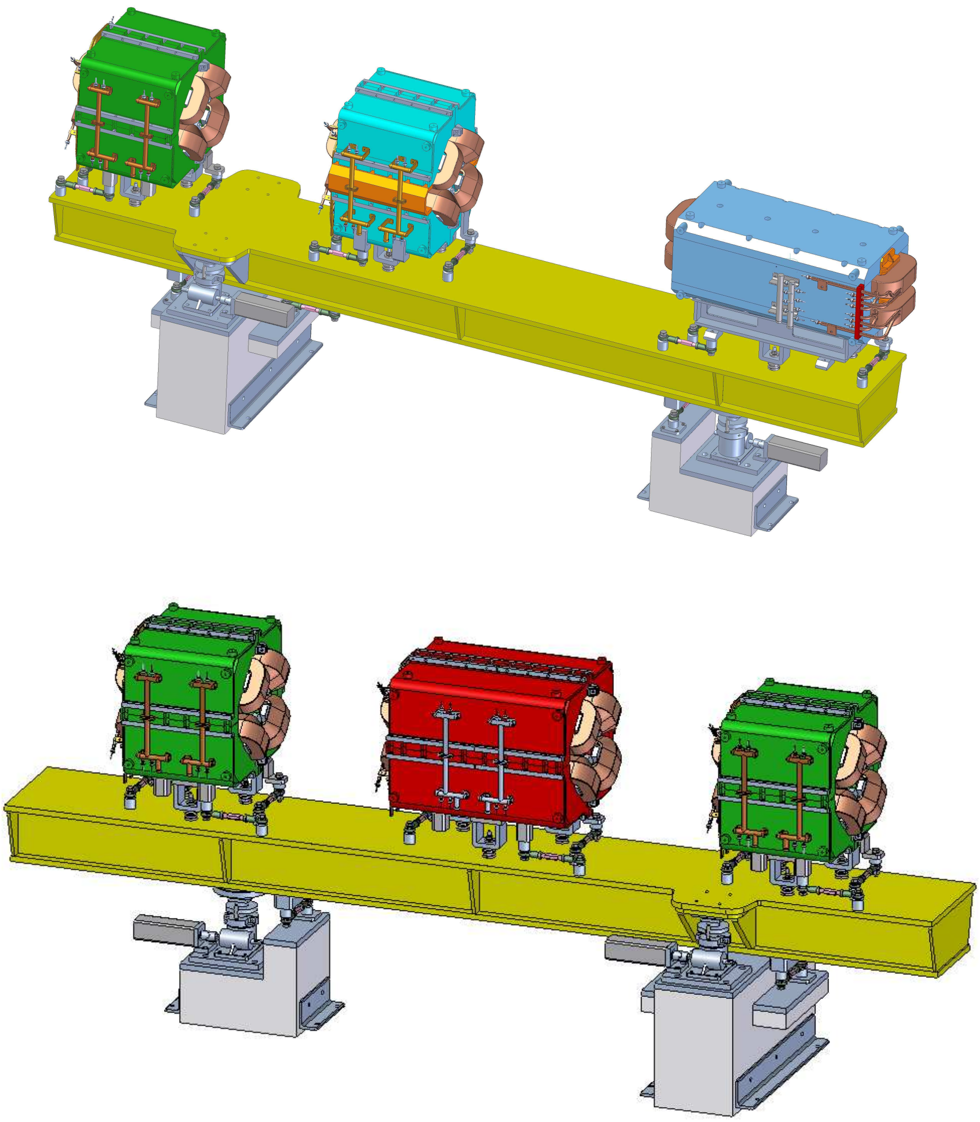

Figure 3.7.1: Layout of the dipole girder (top) and quadrupole girder (bottom).

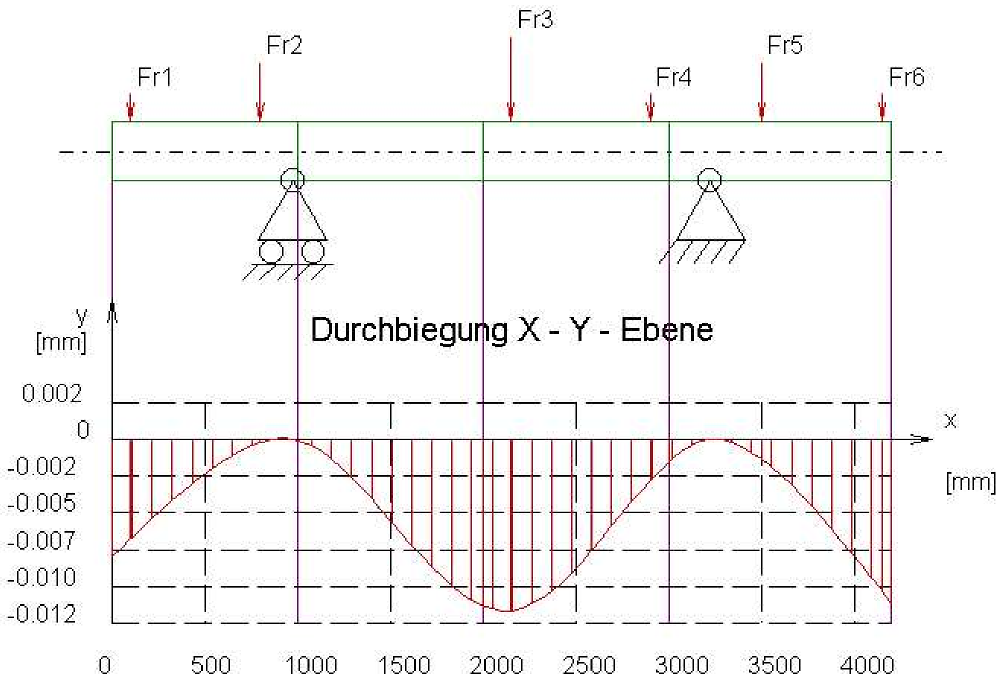

Figure 3.7.2: Result of the bending load calculation of the quadrupole girder

tures outside the machine, and then survey the girder assembly into position in the tunnel rather than the individual elements.

3.7.1 General girder design

The mechanical frame for the new octant of the PETRA machine is build up of eight repetitive units (cell) of four girders each as shown in Fig. 3.7.3. Two of the four girders are called quadrupole girders (QG) carrying three quadrupoles as the main components. The other two are called dipole girders (DG). They support the dipoles plus two quadrupoles, see Fig. 3.7.1. In addition to magnets, other devices like monitors, vacuum pumps, valves and correction magnets will be installed on the girder. The accuracy of the quadrupole magnet axis with respect to the beam on the girder must be within 100 μm ($\pm$ 50 μm on average). The four girders in one cell have to be aligned vertically and horizontally to the beam axis with an accuracy of 0.2 mm (0.1 mm on average) to each other. In the z direction the positioning accuracy must be within 0.5 mm. The girders can be moved vertically by $\pm$ 5 mm remotely controlled with an accuracy of 50 μm during beam operation for beam based alignment.

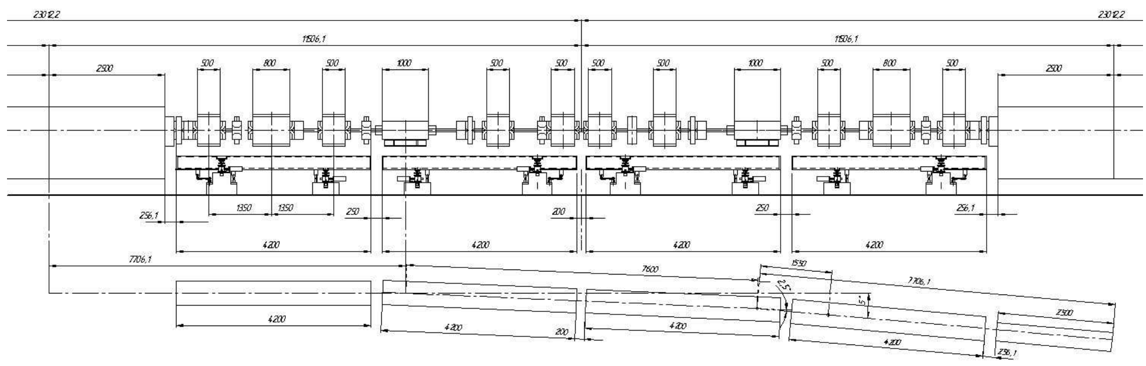

Figure 3.7.3: Layout of one girder cell

3.7.2 Girder

In order to minimize the deflection of the girders the support points for the two types (QG and DG) were chosen individually according to the respective load distribution. The girder is a hollow steel box section with a three point suspension.

It has a cross-section of about 300 mm × 300 mm and a length of 4200 mm. The whole girder is supported by spindle elements resting on concrete sockets which damp vibrations.

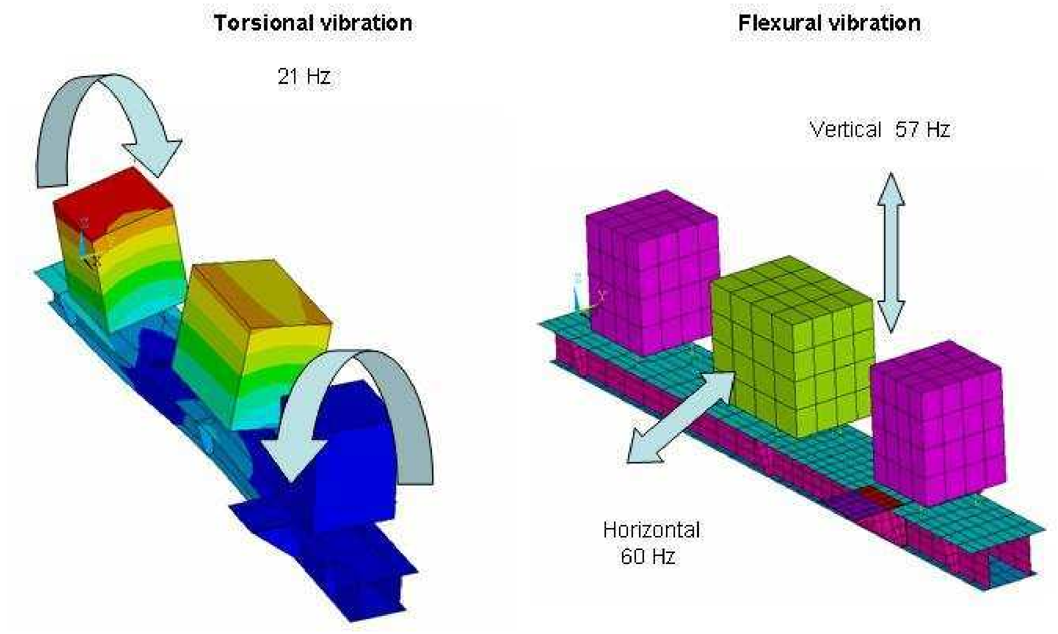

Figure 3.7.4: Illustration of the different flexural and the torsional vibrations

With wall thicknesses between 15 mm (sides) and 25 mm (top, bottom) and the load distribution indicated in Fig. 3.7.1 the quadrupole girder will be deflected by not more than 11 μm, see Fig.3.7.2. In case of the dipole girder the deflection does not exceed 9 μm. The calculated flexural resonance frequency of the girder structure is 57 Hz in vertical and 60 Hz in horizontal direction. The corresponding vibrational modes are sketched in Fig. 3.7.4. The torsional resonance has a calculated value of 21 Hz. Further calculations will be done to check whether torsional vibrations would lead to unacceptable beam oscillations. In this case the girder alignment by three spindle elements will be followed by a fixation of the four corners of the girder. This would increase the torsional resonance frequency by about 50% to more than 30 Hz. The individual magnets are supported by commercial supports with an adjustment accuracy of 40 μm (10 degree rotation) and a setting range of $\pm$ 4.5 mm. After aligning the magnets by means of a laser tracker system they are fixed firmly to their position on the girder. A test setup showed that after transporting of the girder with a crane and on a flat bed trailer the magnets stayed in their correct position with respect to the girder.

3.8 Injection System

3.8.1 Introduction

In order to convert PETRA into a dedicated synchrotron light source, kicker magnets as well as the driving pulsers were studied with respect to their reliability and availability. The PETRA III injection requires high pulse repetition stability for operating the machine in top-up mode.

	PETRA I	PETRA III
Energy	7GeV	6GeV
Number of bunches	4	1920
Beam current	100 mA	200 mA
Deflection	2.88 mrad	2.88 mrad
Kicker length	590 mm	590 mm

Three identical kicker magnets and one septum magnet are included in the PETRA III storage ring magnet system to produce closed bumps during injection of the beam from the DESY II transfer line.
The kickers are designed to run with identical currents and waveforms with an amplitude and pulse length stability of 0.1%.

3.8.2 Concept of the kicker magnet

The kicker magnets can be realized in two different ways. First, one can adopt the present PETRA injection kicker design (Figs. 3.8.1, 3.8.2). A window-frame like ferrite surrounds a sputtered ceramic vacuum chamber. The kicker is outside the beam vacuum system. The metal coated ceramic chamber of the kicker will be renewed. The impedance of the ceramic chambers has to be determined for the new PETRA machine parameters to check that the heat load generated by the beam current is tolerable. The insulation of the conductors must be replaced since it is 20 years old.

An alternative design is a C-yoke ferrite kicker (Fig. 3.8.3) with two conductors around a sputtered ceramic chamber. The advantage of this design is to have sufficient space around the ceramic chamber for air cooling if necessary.
If it turns out that air cooling is necessary then we will realize a C-yoke kicker otherwise we will retain the present kicker design.

Figure 3.8.1: PETRA injection kicker with ceramic chamber.

Figure 3.8.2: The present PETRA kicker ceramic chamber.

Energy	6 GeV
Bxl	57.7 mTm
Pulse current	3.4 kA
Pulse voltage	6 kV
Pulse waveform	11 μs half sine
Inductance	$\approx$5.5 μH
Free aperture	65 mm
Conductor radius	4 mm
Conductor length	439 mm
Kicker length	590 mm
Impedance	1.75 Ω
Deflection	2.88 mrad

Table 3.8.1: Data of present kicker magnets.

Pulse voltage	10 kV
Pulse current	5.6 kA
Pulse waveform	11μs half sine
Frequency	6.250 Hz
Inductance	0.62 μH

Table 3.8.2: Pulser data.

3.8.3 Pulser

At present a thyratron pulser is used for the injection kickers. It generates a half sinusoidal pulse with a pulse length of 15.3 μs. The jitter is about 30–50 ns optimized by thyratron regulation. A new trigger control is needed to reduce this jitter. Aging of the thyratron causes changes in the working point. The thyratron circuit needs a very efficient control. The operation expenses for the thyratron are about 4 times higher than for a semiconductor switch.

For the new pulser (Fig. 3.8.4) of the PETRA III injection we intend to use thyristor technology, i.e. Behlke switches. These switches can be triggered by a 5 V TTL signal. Their jitter is of the order of 1 ns. The switches need a 5 V stabilized supply. The pulser will

be built as a resonant circuit with a positive output pulse. The design should achieve low inductance. Protection against over voltage will be implemented by using an RF-protective element together with a recovery diode. The pulser capacity is about 2 μF.
Similar pulsers with identical switches are in operation at DESY (HERA-e injection and DESY II injection). No failures occured during the last 2 years. The required kicker pulse length can be obtained with a calibration inductance. Amplitude and time stability have to be studied in detail and the target stability of 0.1% is feasible.

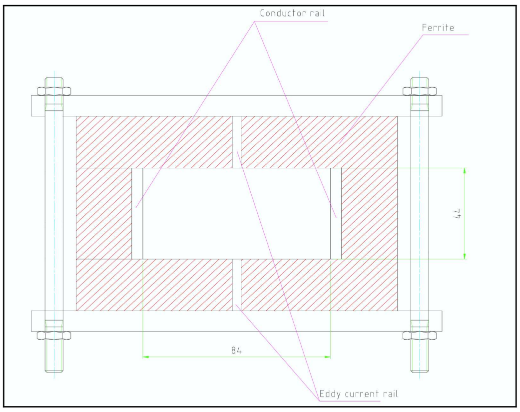

Figure 3.8.3: Cross section of the second kicker.

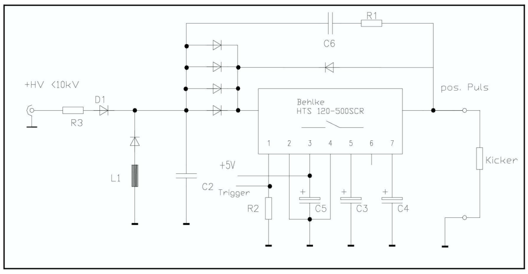

Figure 3.8.4: The kicker magnet power supply principle.

3.8.4 Septum

The existing injection septum is housed in a vacuum vessel with the PETRA vacuum chamber being directly attached. This system, of 6.25 m overall length will be redesigned in order to split it into two smaller devices which are easier to handle.
Thus it will consist of the PETRA beamline vacuum chamber with ports for vacuum pumps (approx. length 4.5 m) and the septum tank with an integrated foil monitor (approx. length 1.8 m). The new design uses a stainless steel pipe as a tank whereas the old one had a more complicated rectangular cross section. The large rectangular flange presently used becomes obsolete. Standard round Conflat (®) flanges can be used. In addition a higher stability with respect to twisting is achieved.
The support structure will be built from two steel pipes and a plate which acts as the basis for the steering gears needed for the final adjustment in all three dimensions. This well proven concept is used at DESY for all dipole and quadrupole magnets.
Whether the septum magnet is designed as an active (current loop inside the gap) or as an eddy current shielded septum still has to be investigated. The eddy current version would result in a much simpler mechanical design but the length of the half-sine current pulse would have to be reduced from 480 μs to approx. 150 μs, i.e a higher charging voltage would be required for the same current amplitude. In principle the conductor could be water cooled. However alternative methods of cooling are under investigation.

3.9 Diagnostics

3.9.1 Electron beam position monitors

The electron beam position monitors (BPM) now installed in PETRA II do not meet the resolution and reproducibility requirements of PETRA III. As a simple upgrade does not seem to be feasible, PETRA III will be equipped with an entirely **new BPM-system**, including new BPM pickup stations, most of the BPM read-out electronics and all the related infrastructure.

quantity	octant	locations	beam pipe aperture	required resolution (v./h.)
16	new	undulators (short)	$\approx$ 40 x 7 mm elliptical	0.2 μm / 0.8 μm
2	new	undulators (long)	$\approx$ 40 x 10 mm elliptical	0.2 μm / 0.8 μm
54	new	quads (arcs)	80 x 40 mm std. pipe	1 μm / 2 μm
35	old	quads (straights)	80 x 40 mm std. pipe	2 μm / 4 μm
98	old	quads (arcs)	80 x 40 mm std. pipe	5 μm / 10 μm

Table 3.9.1: PETRA III BPM's design specifications.

BPM Requirements In PETRA III a total of approximately 200 BPM's (plus reserves) are foreseen (see Tab. 3.9.1). Most BPM's will be housed in the PETRA III standard beam pipe. All BPM's are used for beam orbit observation, but only those with higher resolution ($< 5\ \mu$m) will be used for the orbit stabilization feedback system. The resolution requirements shown in Tab. 3.9.1 include **reproducibility** of the BPM readings under varying beam conditions, including a change of total beam current, bunch charge, bunch pattern or temperature.

The BPM-system has to support two major tasks:

Machine commissioning A sufficient number of monitors will be equipped with *single turn, single pass* capabilities to acquire beam positions measured turn-by-turn, e. g. at injection. In this turn-by-turn operation mode the resolution requirements are relaxed (50...100 μm).

Orbit feedback and observation In synchrotron light operation the orbit of the stored beam has to be held constant (see Sec. 3.2.4.) To achieve the required μm-resolution the system-bandwidth of the BPM-stations has to be reduced, so *averaged position measurements* of many turns are acquired. Temperature stabilization of the electronics racks will help to improve the reproducibility of the BPM-system.

3.9.1.1 BPM principle

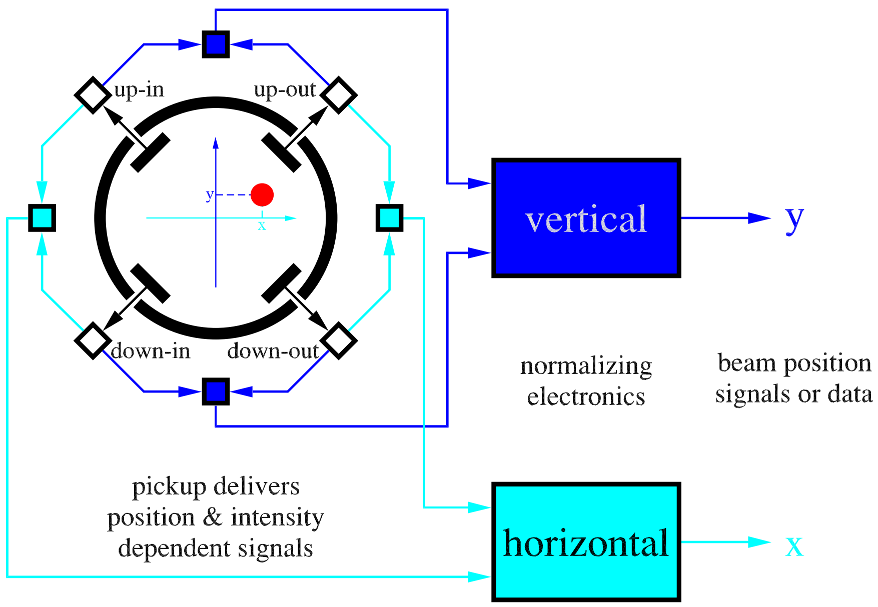

Figure 3.9.1: Schematic of a beam position monitor.

A *beam position monitor* consists of 4 symmetrically arranged *pickup-electrodes*, incorporated into the vacuum chamber and a *read-out electronics* unit to process the pickup signals to derive horizontal and vertical beam position information (Fig. 3.9.1). A single electrode of the BPM pickup delivers a signal voltage

$$V_{\text{electrode}} = s(x,y)Z(\omega)I_{\text{beam}}(\omega) \tag{3.9.1}$$

which is proportional to the current $I_{\text{beam}}(\omega)$ of the passing beam and to the beam-to-electrode distance (x,y) (e.g. transverse beam displacement), which is described by a sensitivity function $s(x,y)$. Because of the rather short electron bunches the frequency spectrum of $I_{\text{beam}}(\omega)$ is of no concern; for the BPM system the bunches behave like *Dirac* pulse excitation signals. The transfer impedance $Z(\omega)$ of the electrode depends on the geometric shape and type (e.g. button, stripline) of the pickup station.

The BPM read-out electronics extracts the beam position (displacement) information from the analog signals of the pickup electrodes. In order to simplify the normalization procedure and to reduce the nonlinearities of $s(x,y)$, symmetrically arranged electrodes are read out. To shield from direct synchrotron light the the electrodes are mounted at an angle, e. g. 45^0. In Fig. 3.9.1 a set of signal-splitters and signal-combiners illustrates one way of forming the (current-dependent) horizontal and vertical beam position signals. In practice a different solution may be realized. The read-out electronics processes the 4 electrode signals for the normalized (beam intensity independent) beam position:

$$\begin{aligned} \text{horizontal beam position} &= C_h \frac{(V_{\text{up-out}} + V_{\text{down-out}}) - (V_{\text{up-in}} + V_{\text{down-in}})}{V_\Sigma} \\ \text{vertical beam position} &= C_v \frac{(V_{\text{up-out}} + V_{\text{up-in}}) - (V_{\text{down-out}} + V_{\text{down-in}})}{V_\Sigma} \end{aligned} \tag{3.9.2}$$

V_Σ is the sum of all 4 electrode signals and C_h, C_v are the horizontal and vertical calibration constants of the electronics.

3.9.1.2 BPM pickup stations

All 3rd generation synchrotron light sources – today in operation, as well as those under construction – use *electrostatic button* pickup stations in their BPM-system. Although other pickup types, like stripline- or resonant cavity BPM's have a potential for higher sensitivity and resolution, their practical implementation in a large scale BPM-system with more than 100 units is too complicated and cost-intensive. For these reasons, and because of a long-term practical experience with button pickup's at DESY, also PETRA III will be equipped with button pickup stations for beam orbit observation and feedback systems.

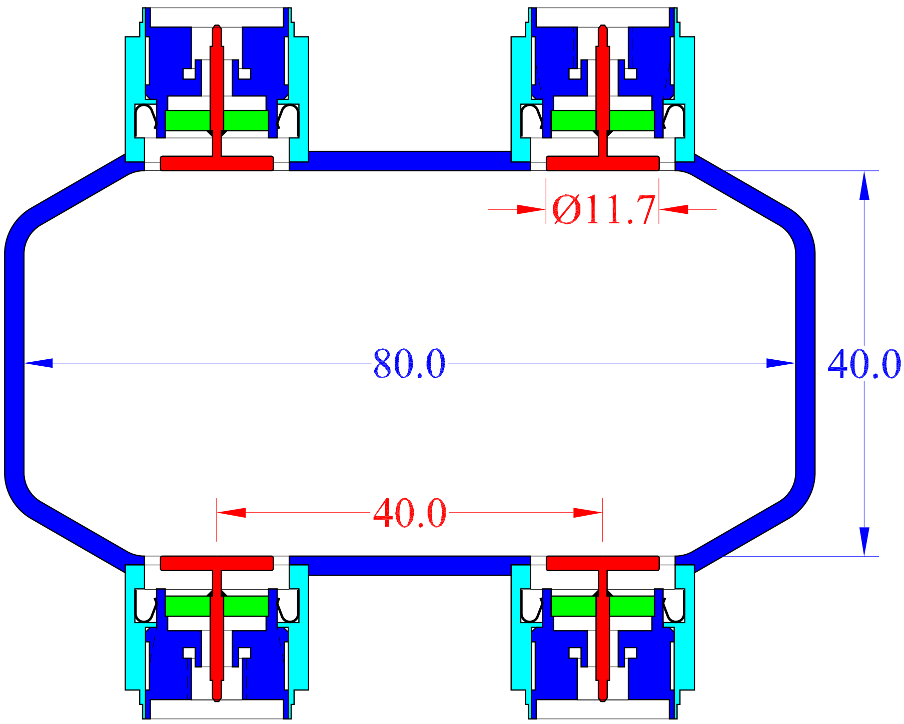

Figure 3.9.2: Cross-section of the PETRA III standard BPM button pickup (draft, measures are in mm).

Fig. 3.9.2 shows a draft of 4 button electrodes integrated into the PETRA III standard vacuum chamber by welding. RF button feedthroughs are commercially available with SMA or N-type connectors from several companies in standard or custom versions. In PETRA III the BPM pickup stations will be located very close to the quadrupoles. *Encoders* are foreseen, to track all movements between pickup and nearby quadrupole due to thermal expansion processes, as done successfully at the *SLS*, Villingen, Switzerland (Dehler et al., 1999). Only the 18 pickup stations with ultimate resolution requirements, located at the undulators, will be realized as separate, rigid BPM blocks between bellows, fixed with *Invar*-supports on resonance-free girders.

The *transfer impedance* of a button electrode can be well estimated for vacuum chambers with a circular cross-section (Marcellini et al., 1996):

$$Z(\omega) \equiv \frac{V_{\text{button}}(\omega)}{I_{\text{beam}}(\omega)} = \varphi Z_0 \left(\frac{\omega_1}{\omega_2}\right) \frac{j\omega/\omega_1}{1 + j\omega/\omega_1} \tag{3.9.3}$$

with

$$\omega_1 = \frac{1}{Z_0 C_{\text{button}}} \qquad \omega_2 = \frac{c_0}{2r_{\text{button}}} \qquad \varphi = F\frac{S_{\text{button}}}{S_{\text{total}}} = \frac{r_{\text{button}}}{4r_{\text{pipe}}}$$

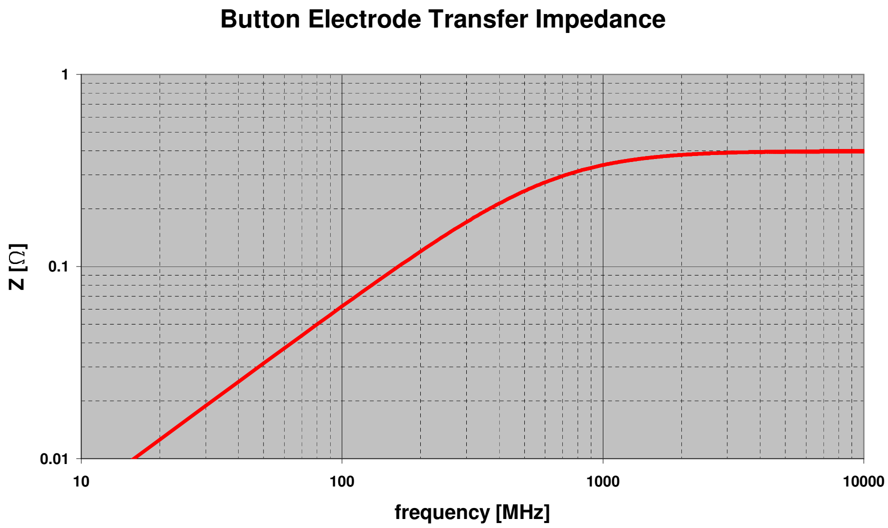

Figure 3.9.3: Transfer impedance of the button pickup of Fig. 3.9.2.

Fig. 3.9.3 shows the magnitude response $|Z(\omega)|$ of (3.9.3), using the following properties of the PETRA III standard BPM pickup (Fig. 3.9.2), assuming a "circular" cross-section:

"circular" vacuum chamber	r_{pipe} = 30 mm
button electrode radius	r_{button} = 6 mm
button-to-ground capacitance	C_{button} = 5 pF
load impedance	Z_0 = 50 Ω

The transfer impedance shows a high-pass transfer characteristic, having a cutoff frequency of $\omega_1 = 4 \times 10^9$ s^{-1} (f = 636.62 MHz) and a maximum transfer impedance of $Z(\omega \gg \omega_1) = 0.4\ \Omega$. Assuming a operating frequency of f = 500 MHz of the read-out electronics and a moderate beam current of 50 mA a level of -28.2 dBm ($\equiv$ 8.73 mV) can be expected, assuming a centered beam in the pickup. A more precise numerical analysis of the transfer characteristics has to be done for the final geometries of all different button pickup stations of PETRA III.

As a total of 800 button electrodes will be installed in PETRA III, they will give a noticeable contribution to the machine impedance. For a single button electrode the *longitudinal coupling impedance* scales with the transfer impedance $Z(\omega)$ and can be roughly estimated:

$$Z_{\|}(\omega) \approx \varphi \frac{\omega_1}{\omega_2} Z(\omega) \tag{3.9.4}$$

It is known that (Eq. 3.9.4) underestimates the coupling impedance, as electromagnetic effects in the annular gap w_{gap} between button and beam pipe wall, e.g. resonant modes, are not taken into account. However, the first resonant mode is of TE_{11} type and has a frequency of

$$f_{\text{gap}}^{TE_{11}} = \frac{c_0}{\pi(2r_{\text{button}} + w_{\text{gap}})}$$

which, with dimensions of Fig. 3.9.2 (r_{button} = 6 mm, w_{gap} = 1.65 mm), results in a frequency $f_{\text{gap}}^{TE_{11}}$ = 12.5 GHz, well above the 5 GHz of the bunch spectrum with a 30 mm FWHM bunch length. At lower frequencies the contribution of the annular gap can be estimated analytically:

$$Z_{\|\text{gap}}(\omega) = j \frac{337\Omega\, \omega (r_{\text{button}} + w_{\text{gap}})^3}{8 c_0 r_{\text{pipe}}^2 \{\ln[32(r_{\text{button}} + w_{\text{gap}})/w_{\text{gap}}] - 2\}} \tag{3.9.5}$$

which gives a total normalized coupling impedance of $800 \times (Z_{\|\text{gap}}/n_{\text{rev}})$ = j 1.5$\times$10^{-2} Ω. The actual vacuum chamber is not circular and an accurate estimate of the coupling impedance requires a numerical analysis using electromagnetic solvers.

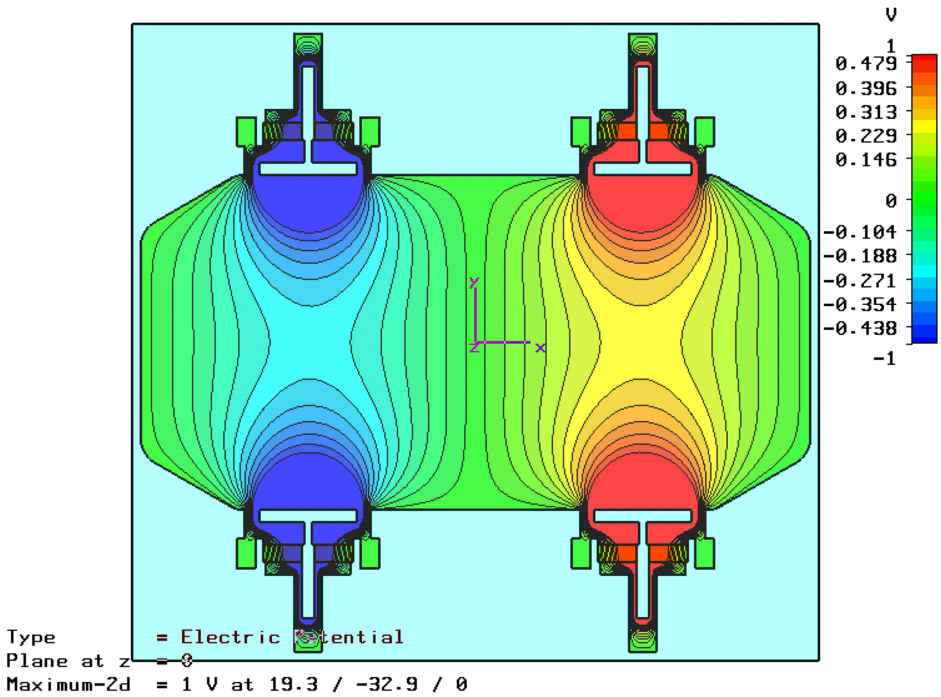

Figure 3.9.4: Normalized horizontal position characteristic of the button pickup of Fig. 3.9.2.

The *position sensitivity* of the pickup station can be computed by solving the *Laplace* equation for the two-dimensional cross-sectional geometry. In the example of a horizontal analysis (Fig. 3.9.4) the slope of

$$\phi_{\text{hor}} = \frac{(\phi_{\text{up-out}} + \phi_{\text{down-out}}) - (\phi_{\text{up-in}} + \phi_{\text{down-in}})}{\Sigma\phi_{\text{buttons}}} = \frac{\Delta_{\text{hor}}}{\Sigma}$$

in the y = 0 plane (see also Fig. 3.9.5) gives the position sensitivity as *monitor constant*.

$$K_{\text{hor}} = \left(\left. \frac{\partial\, \phi_{\text{hor}}}{\partial\, x} \right|_{x=0} \right)^{-1}$$

For our example a monitor constant $K_{\text{hor}} = 56.5$ mm is computed. This signifies a signal change of 1.77×10^{-5} for a 1 μm horizontal beam displacement, which corresponds to a change of only 155 nV or 0.00015 dB (!) at $I_{\text{beam}} = 50$ mA, that has to be detected.

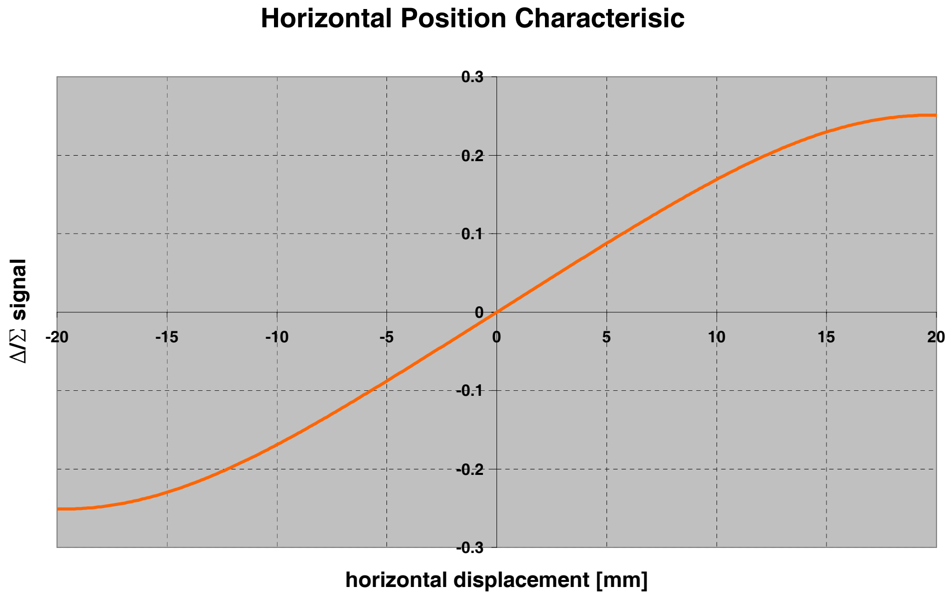

Figure 3.9.5: Normalized horizontal position characteristic of the button pickup at y = 0 mm.

3.9.1.3 BPM read-out electronics

In order to achieve the required resolution, the *noise* of the read-out electronics has to be substantially lower than the difference voltage to be detected, here < 155 nV or < -123 dBm for a 1 μm position resolution. The theoretical noise voltage in an electronics system is given by:

$$v_{\text{noise}} = \sqrt{4kTBR} \tag{3.9.6}$$

which sets the threshold in a $R = 50\,\Omega$ RF-system at room temperature to $v_{\text{noise}} = 0.9$ nV $\sqrt{B}$. (Eq. 3.9.6) shows, the smaller the system bandwidth B is made, the lower will be the noise voltage. For the PETRA III BPM example $v_{\text{noise}} < 155$ nV requires $B < 29$ kHz, to theoretically achieve the 1 μm resolution. As in practice there are several other factors which

further increase this noise voltage, the system bandwidth has to be considerable smaller. The requirements of the orbit feedback system sets a lower limit of the BPM system bandwidth. A brief estimate shows, that a system bandwidth in the range 1 kHz $< B <$ 10 kHz can meet the required resolutions, shown in Tab. 3.9.1.
In contrast, a minimum bandwidth of $B > f_{\text{rev}}$ is required to realize a turn-by-turn measurement capability. In PETRA III: $f_{rev} = 130$ kHz.
From the experience of other 3rd generation synchrotron light sources, two solutions for the PETRA III BPM read-out electronics are considered. Both systems are well established and available as commercial manufactured electronic units. The industry also offers custom modifications, as well as related auxiliary systems (digitizers, racks, power-supplies, etc.) and maintenance contracts.

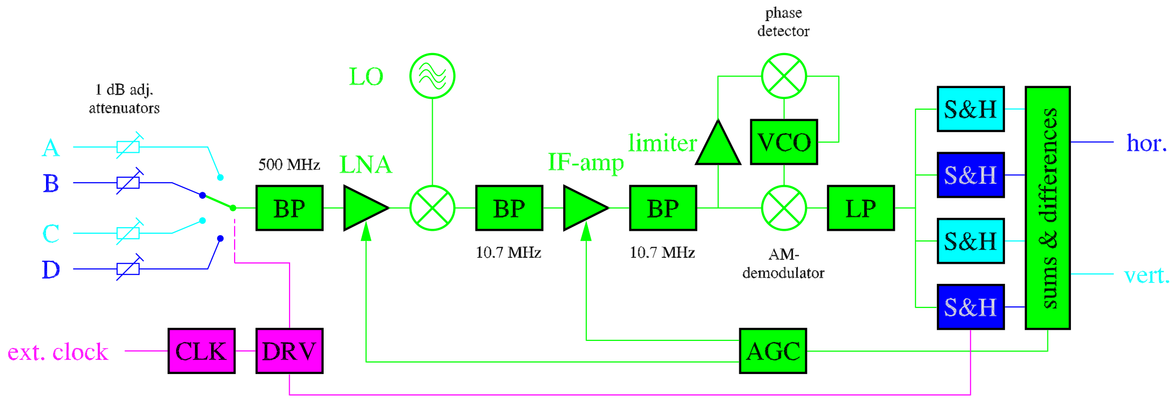

Figure 3.9.6: Analogue, single channel superhetorodyne BPM receiver.

Analogue read-out electronics This BPM RF-receiver is based on the classic *superhetorodyne* principle, which insures an optimum noise figure. In front of the receiver a GaAs multiplexer switches successively between the 4 button signals. This single channel concept is patented by *Bitter et. al., NSLS*, Brookhaven, U.S.A. and eliminates gain drift effects, when compared with separate channel techniques. The commercial available BPM unit of *BERGOZ* is based on the *J. Hinkson* design for the *ALS*, Berkeley, U.S.A. It incorporates an automatic gain control (AGC) feedback and a PLL driven AM synchron demodulator, as well as some other extra features, not shown in Fig. 3.9.6. The local oscillator is programmable for maximum input frequencies of up to 800 MHz. The bandwidth is fixed at about 1 kHz, the analog output signal ranges $\pm$ 10 V and has to be further digitized. *BERGOZ* specifies the low frequency noise (0...1 Hz) of the output signal to $<$ 5 mV_{rms} @ -35 dBm input level. Assuming a gain of 1 V/mm (*BERGOZ* recommendation) a resolution of 5 μm seems to be feasible. Higher input signal levels will further reduce the noise level and improve the resolution to 2 μm for a PETRA III standard BPM pickup.

Digital read-out electronics The digital BPM receiver is based on principles and technologies of digital telecommunication systems. An impressive proof of principle of an entire system was done at the *SLS*, Villingen, Switzerland. Fig. 3.9.7 shows some details of the

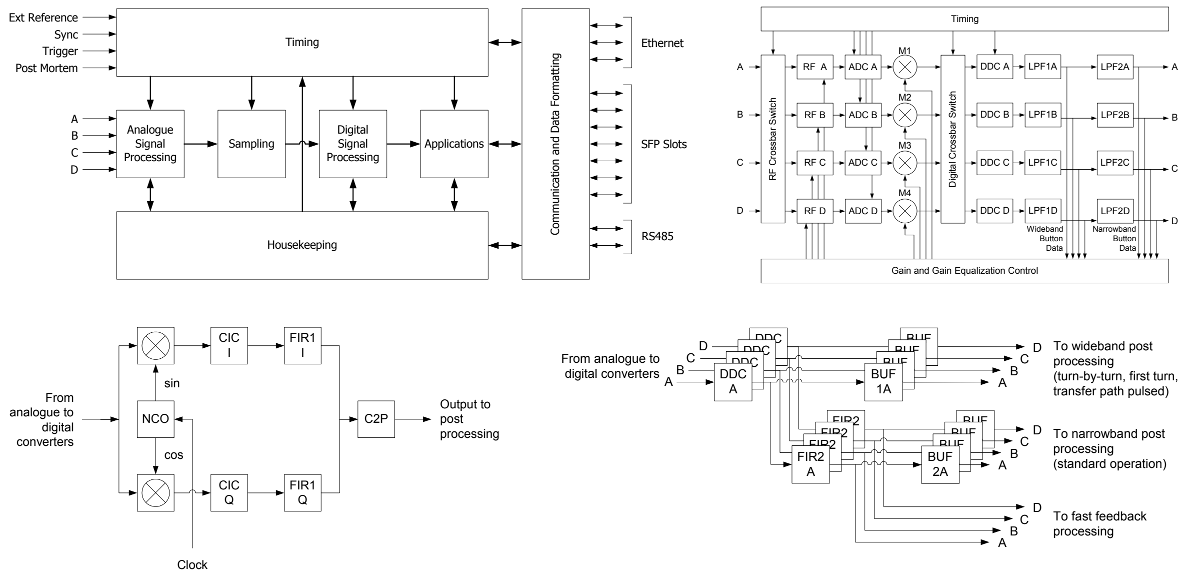

Figure 3.9.7: Details of the digital read-out electronics (courtesy of *R. Ursic, i-Tech*)

.

now commercial available digital BPM read-out electronics manufactured at *i-Tech*. Here the if- and demodulator sections of the superhetorodyne receiver are realized digitally, in a FPGA circuit. To eliminate the gain drifts of the analog part of the 4 channels, a set of 2 crossover switches successively exchanges the read-out channels. This complex system supports turn-by-turn acquisition with a bandwidth of 1 MHz and high resolution beam position measurements with 1 kHz bandwidth simultaneously. The FPGA can be re-programmed, which makes the read-out system even more flexible and offers sufficient resources to store SVD algorithm and data of the orbit feedback. *i-Tech* specifies the resolution limit to 1 μm assuming the PETRA III standard button pickup.
Both read-out electronics, analog or digital, have strong and weak points. The analog system is rather simple, cost-effective and well understood, as most 3rd generation light sources are equipped with this electronics. In order to measure the beam position on a turn-by-turn basis for machine commissioning and maintenance a sufficient number of BPM's (16...32) have to be equipped with additional wideband read-out electronics.
Experience at the *SLS* has shown, that a digital read-out system works well in routine operation. To reach the required performance and to offer high flexibility, a quite complex system of hard- and software has been developed. The differences between digital and analog signal processing cannot be worked out here, but obviously digital systems have advantages in the numerics, which allow a better performance/resolution optimization.
Both read-out electronics are potential candidates for the PETRA III BPM instrumentation, a detailed comparison in a test series on the PETRA II beam has to be done.

3.9.1.4 Environment and infrastructure

Achieving the required BPM resolution and stability must take into account the BPM related environment and infrastructure. Important points to be considered are

- cables and connectors
- pickup support structures
- low noise power supplies
- temperature control of tunnel and electronic racks

High performance semi-rigid cables will be used for all the BPM-signal cabling. SMA-type microwave connectors of highest quality will be used for **all** BPM-signal connections in the front-end signal path.
The broadband (DC...300 MHz) noise of the power supplies of the read-out electronics must be < 5 mV$_{pp}$, the industry standard of high-end VME- and VXI-crates.
The racks of the BPM-electronics have to be temperature stabilized to $< \pm 1^0$. The temperature variation in the temperature stabilized tunnel leads to a vertical BPM movement of $< 0.1\ \mu$m due to the thermal expansion of the *Invar* pickup supports.

3.9.1.5 Conclusion

Resolution and reproducibility requirements for the beam position monitor system of PETRA III are tight (Tab. 3.9.1). However, a BPM system of button-type electrostatic pickup stations and commercially available read-out electronics of latest state-of-the-art technology satisfy these requirements.

3.9.2 Position monitors for the transverse multibunch feedback system

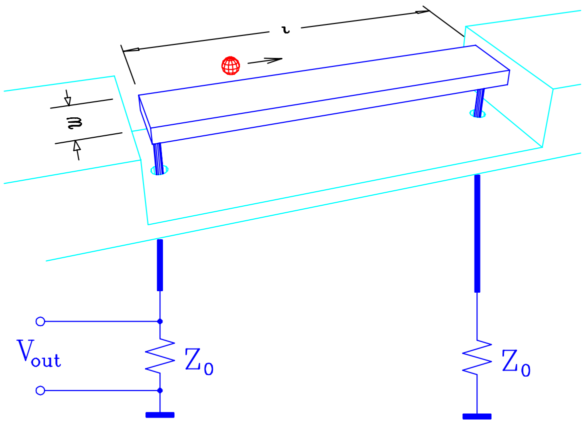

Figure 3.9.8: Stripline electrode.

Two position monitors, a horizontal and a vertical, are required for the transverse multibunch feedback system. A bandwidth of $>$ 250 MHz is required in order acquire single bunch measurements within 2...8 ns (minimum bunch-to-bunch distance in PETRA III). Among the different types of broadband pickups, position monitors based on *stripline* electrodes seem to be best suited.

Fig. 3.9.8 shows a stripline electrode of length l and width w, passed by a charge q of velocity $v \approx c_0$. At both ends the stripline is terminated in it's characteristic impedance Z_0. The impulse response of a stripline electrode is:

$$z(t) = \frac{Z_0}{2}\left[\delta(t) \; - \; \delta(t - \frac{2l}{c_0})\right] \tag{3.9.7}$$

The *Fourier* transform of (3.9.7) gives the transfer impedance:

$$Z(\omega) = j\, Z_0\, e^{-j\frac{\omega l}{c_0}} \sin\left(\frac{\omega\, l}{c_0}\right) \tag{3.9.8}$$

The magnitude of (3.9.8) has a maximum at frequencies where the length is an odd multiple of the quarter-wavelength:

$$f_{\text{center}} = \frac{c_0}{4\,l}(2\,n - 1) \tag{3.9.9}$$

Usually the stripline pickup operates at the first "lobe" (n=1). Its 3dB-bandwidth exceeds an octave:

$$f_{\text{lo}} = \frac{1}{2}\, f_{\text{center}} \qquad\qquad f_{\text{hi}} = 3\, f_{\text{lo}}$$

The electrode arrangement and transverse characteristic is the same as for button type pickup stations. Advantages of the stripline BPM are to operate at maximum transfer impedance (f_{center}) and a defined, resistive source impedance Z_0. The second argument is important when operating in broadband systems, as it helps to minimize reflection effects.
In order to operate at $f_{\text{center}} = 500$ MHz, a physical length $l = 150$ mm of the PETRA III stripline electrodes is foreseen. For the minimum possible bunch-to-bunch spacing of 2 ns this frequency is equal to the lowest bunch harmonic, but also gives highest flexibility for any other bunch spacing. Stripline BPM's of various dimensions have been designed, build and successfully operated in several accelerators on the DESY site. Fig. 3.9.9 shows an example of a "warm" HERA stripline pickup with longitudinal slotted, semi-coaxial stripline electrodes.
The stripline BPM has two major advantages over an equivalent electrostatic "button" BPM:

- The characteristic impedance of the stripline-electrode can be designed for Z_0 = 50 Ω, which results in a resistive 50 Ω source impedance. The button-electrode has a pure capacitive source reactance.

- By adapting the length l of the stripline-electrode the frequency of maximum beam-to-electrode coupling f_{center} can be optimized to the feedback system requirements. The magnitude response of the button pickup has a high-pass characteristic, which requires a rather high operating frequency.

Minimizing signal reflections in broadband multi-bunch feedback systems is essential. The resistive source impedance of the stripline-electrode – it is the signal source – reduces these effects and simplifies the design of the detector electronics.
Furthermore the stripline-electrode gives higher signal power at moderate frequencies, compared to the button-electrode. The signal-to-noise ratio at f = 500 MHz of a stripline-electrode is typically 3..4 times higher compared to an equivalent button-electrode.

3.9.3 Intensity monitors (DCCT, FCT)

Two types of current monitors are foreseen for PETRA III:

1. Fast current transformer (FCT): This type will measure the individual bunch current of each bunch stored in PETRA III. A wide band version of a FCT (bandwidth 1.75 GHz) is commercially available from e.g. BERGOZ which fulfills all requirements in resolution, stability and dynamic rage for PETRA III. A resolution of the bunch current of $< 1\,\mu$A with an analog bandwidth of 500 MHz is foreseen. Experience from HERA shows already a resolution σ <1 ‰ (absolute: 0.3 μA) at 485 μA/Bunch (see Fig. 3.9.10) with an analog bandwidth of 30 MHz.

2. DC current transformers (DCCT): The very high resolution measurement of the DC current will be performed by a parametric current transformer (PCT) from BERGOZ. Experiences from HERA with this type of monitor show a resolution of σ <<1 ‰ (absolute: 3 μA) at 61.7 mA (see Fig. 3.9.11), which is sufficient even for the top-up operation of PETRA III.

3.9.4 Emittance monitoring by synchrotron radiation

Imaging of the electron beam using visible synchrotron radiation has been applied for emittance monitoring (Hofmann & Meot, 1982) in many accelerators. Due to the diffraction limited resolution, this method yields only an unclear information for beam sizes less than 100 μm. In order to overcome the limit given by Fraunhofer diffraction one has to apply interference methods utilizing the spatial coherence of synchrotron radiation in first order to obtain the beam size (Mitsuhashi, 1998). However, according to this reference the limit for beam size measurements is about 5 μm for visible light. For PETRA III this is in the order

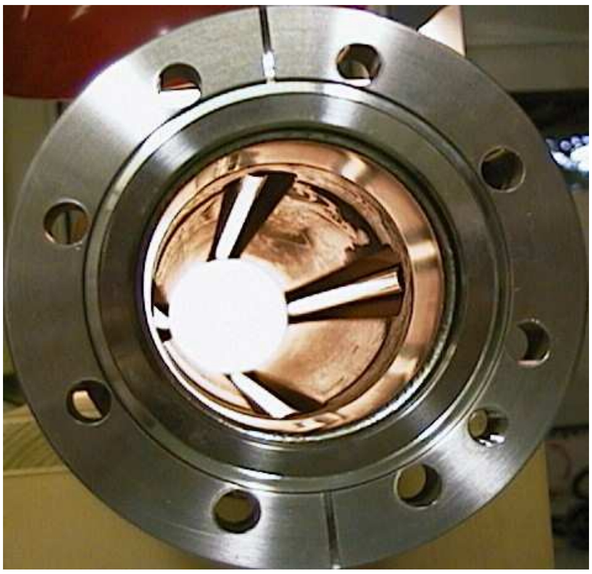

Figure 3.9.9: View inside a stripline BPM.

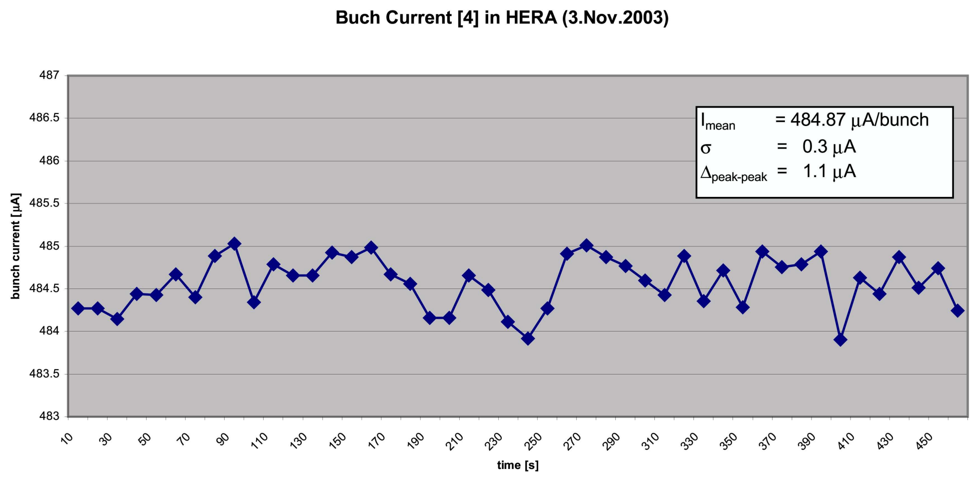

Figure 3.9.10: Plot of the current of the 4th bunch in HERA. The resolution is limited by statistical fluctuations to about $\sigma = 0.3\,\mu$A of the bunch current of 484.87 μA. Each data point is averaged over 70 turns in HERA.

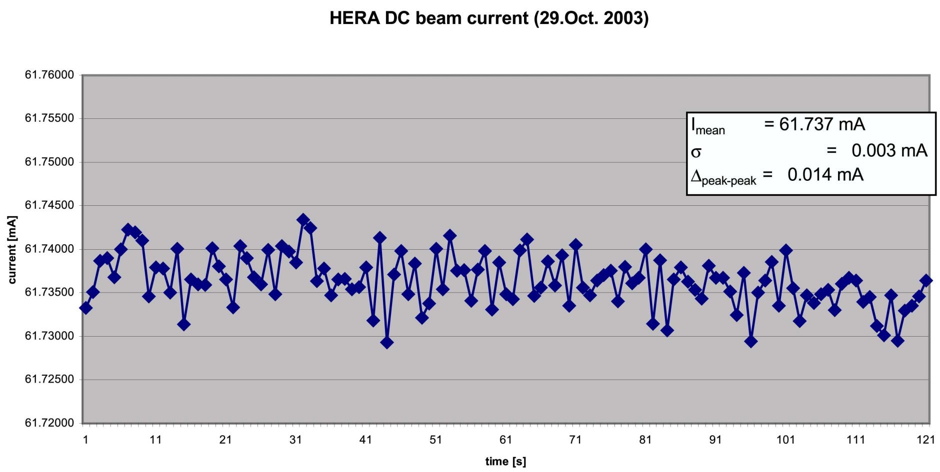

Figure 3.9.11: Plot of the measured DC beam current of HERA over 2 minutes. The resolution is limited by statistical fluctuations to about $\sigma = 0.046$‰ (first 80 seconds) of the beam current of 61.736 mA. The integration time of each data point is 160 ms. The small slope is due to the decaying beam current in HERA.

of the vertical beam size and therefore not applicable.
A straightforward way to improve the monitor resolution significantly is to use shorter wavelengths, i.e. VUV light or X-rays. Analogous to the visible spectral region there are two experimental approaches which differ by principle. The first one is electron beam imaging in the short wavelength region in order to reduce the diffraction limit contribution to the measured beam size. The second one is an indirect method which is based on the determination of the X-ray transverse coherence from which the beam size can be deduced.

For PETRA III the most promising scheme is electron beam imaging in the X-ray region with synchrotron radiation from an undulator or bending magnet. This method gives fast and direct information about the beam sizes with high accuracy. For this purpose the quality of the X-ray optics as well as their heat load stability has to be high to preserve the diffraction limited resolution which can be of the order of 1 μm depending on the wavelength and the type of optics employed (Holldack, J.Feikes & Peatman, 2001). Several kinds of optics have been used already at various synchrotron radiation facilities or are considered to be used for this purpose. Examples are grazing incidence optics in a Kirkpatrick-Baez mirror scheme at the ALS diagnostic beamline (Renner, Padmore & Keller, 1996), crystal based X-ray Bragg-Fresnel lenses at the ESRF (Tarazona et al., 1994; Hartman et al., 1995), X-ray zone plates at APS (Yun et al., 1999) and SPring-8 (Masaki et al., 2001), multilayer Bragg-Fresnel lenses at BESSY (Holldack et al., 1995), or crystal monochromators at PETRA II and ESRF (Hahn & Schulte-Schrepping, 2003; Tarazona & Elleaume, 1995). For the final decision about the type of the optics, their properties will be studied in more detail.
However, for X-ray optics based on a pinhole camera the diffraction limited resolution is in the order of 10 μm which is not applicable for PETRA III (Masaki et al., 2001).
The intensity of synchrotron radiation is no limiting factor for all types of optics mentioned above. For the standard PETRA III dipole with bending radius of 191.7 m and a beam current of 100 mA the number of X-ray quanta per second with energy $\hbar\omega \geq 1\,\mathrm{keV}$ subtending a solid angle of $6.25 \cdot 10^{-6}$ sr is $4 \cdot 10^{16}$ /s. This solid angle corresponds to a projected area of 25 x 25 mm^2 at a distance of 10 m from the source point. The number of photons could be increased to 10^{17} quanta/s using a dipole with bending radius 22.9 m.
There exist different schemes for the determination of the transverse coherence. A method related to the interferometry of visible synchrotron light is intensity interferometry which exploits the second-order degree of coherence in the emission of quanta from the same bunch, see e.g. (Yabashi, Tamasaku & Ishikawa, 2001). However, the measuring time in the X-ray region is in the order of several hours and therefore not practicable for beam diagnostics.
Apart from a further approach to derive beam sizes from nuclear forward scattering (Baron et al., 1996) there is an interesting technique under investigation at the ESRF, which is closely related to in-line holography (Kohn, Snigireva & Snigirev, 2000; Chubar et al., 2001). The method is based on analyzing the visibility of Fresnel interference fringes produced by a well calibrated object like a fiber or a slit which is illuminated by undulator radiation. From the experimental point of view this technique has the advantage that no optical elements are required which can deteriorate the image quality respective transverse coherence and, thus, introduce additional errors in the emittance determination. Although this method of direct measurement of the transverse coherence length from interference fringes requires more experimental studies it is proposed together with electron beam imaging with an appropriate X-ray optic as future method for emittance monitoring at PETRA III.

3.9.5 Emittance monitoring by conventional wire scanners

Modified LEP type wire scanners (Werner & Wittenburg, 2001; Camas et al., 1993) are used in most accelerators at DESY for beam width measurements to determine the beam emittance. The scanner used a very thin (7 μm) Carbon wire which crosses with 1 m/s the

circulating beam. Its spatial resolution is about 1 μm. King (1988) has shown, that the resolution does not suffer much (<3%) as long as the beam diameter is larger or equal the beam size. The vertical beam size of PETRA III at a high β_z will be around 6 μm (ϵ_x = 1 nmrad, 1% coupling), therefore a 5 μm fiber will be used for PETRA III.
The main problem of wire scanners is the heating of the wire due to the wire-beam interaction. Assuming a beam size of 100 μm $\times$ 5 μm, the use of a 1 m/s scanner will be limited to a beam current of only 1 mA (horizontal) and 16 mA (vertical) (for calculation see (Wittenburg, 2000)). The wire heating is directly proportional to the scanning speed. Up to now, scanners with a speed of up to 20 m/s exist and are used at CERN (Burger et al., 2003). With such a speed the limits on the total beam current can be increased by a factor of 20, but the required precise position encoders may not follow this high speed. However, at least three (horizontal, vertical, and 45°) of the existing 4 wire scanners at PETRA-e and PETRA-p will be installed for low beam intensity. This will provide a precise emittance diagnostics. It is planned to increase their speed by using stronger power supplies and another driving unit to about 1.6 m/s for their use in the DESY electron accelerators.

3.9.6 Emittance monitoring by laser wire scanners

A laser wire scanner provides a non-destructive measurement of small beam sizes and, in contrast to solid wire scanners, also at high beam currents. A prototype laser wire scanner is already installed in PETRA II (see Fig. 3.9.12). Care has been taken to achieve a rugged and vibration free mechanical design. The scanner has shown first successful results in 2003. The laser spot of the present prototype reaches already about 5 μm (Kamps et al., 2002). The signal and background conditions were proven to be sufficient for PETRA II and PETRA III (Blair et al., 2001b; Blair et al., 2001a). With recent advances in laser and optical technology laser beam spot sizes of < 1 μm were achieved and very accurate measurements were done on small beams (Ross, 2003). Further improvements of the PETRA laser wire systems will be studied and tested in the next few years. One station utilizing scans in the horizontal and vertical plane is foreseen for PETRA III.

3.9.7 Parasitic bunch measurements

The distance between bunches in PETRA will be defined by the user requirements and might be as short as 4 ns. The adjacent buckets of the 500 MHz RF System should contain as few as possible stored particles. This is of particularly important for time-triggered photon measuring experiments. The parasitic bunch measurement should be able to measure the charge down to a fraction of 10^{-6} of the main bunch within 20 seconds. For this purpose parasitic bunch measurement devices are already installed in DORIS and in PETRA II based on a fast avalanche-photo diode (APD) detecting scattered X-rays from a 1 mm thick graphite foil (Fig. 3.9.13). The APD signal is analyzed using a time-to-digital-converter (TDC) and a multichannel-analyzer (MCA). The timing-resolution of the system is about 0.8 ns and is limited by the APD amplifier. More details can be found in (Franz et al., 2003). This system fulfills already all requirements for PETRA III and can be installed without significant changes.

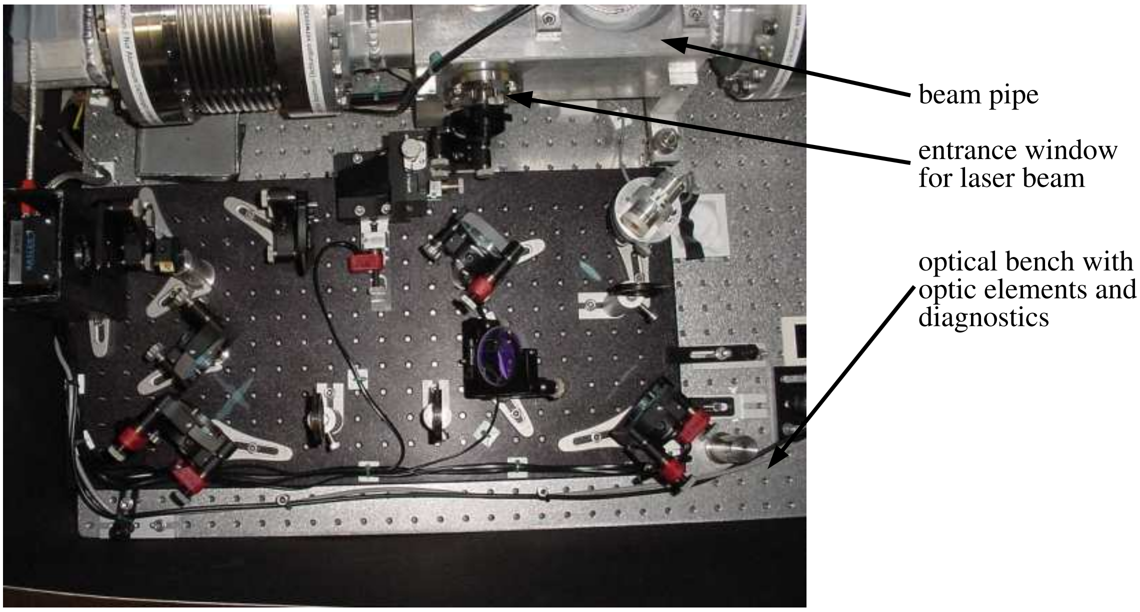

Figure 3.9.12: Part of the laser optics on the optical bench in the PETRA tunnel. The interaction chamber is mechanically decoupled from the beam pipe by bellows (top) and mounted on the same optical table.

3.9.8 Screens

The injected beam position in the PETRA III ring will be measured using the BPMs with single bunch, first turn capabilities. Therefore a threading of the first beam will not need any

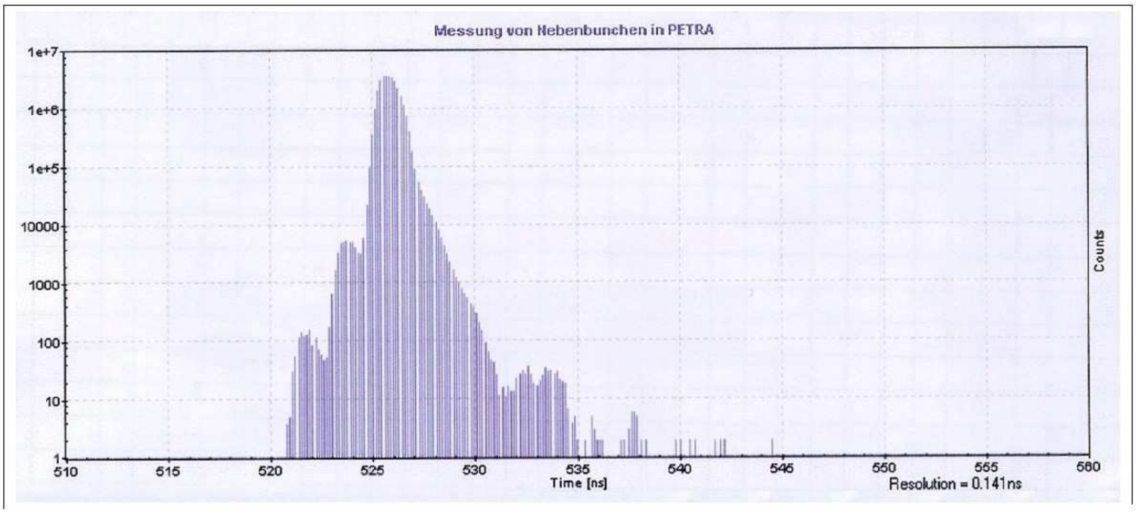

Figure 3.9.13: Main bunch and parasitic bunches from 4 ns ‘before’ to some 10 ns ‘after’ the main bunch in PETRA II (from Franz et al., 2003).

optical screen monitors. However, a few phosphor screen monitors will be used for injection optimization. They will be located around the injection elements (e.g. kickers, septum) and along the injection transfer line. Because the screens will be used only for rough steering of the beam, no sophisticated readout system is required. A simple CCD camera together with a triggerable frame grabber system will be suitable. These screens already exist in the PETRA II injection scheme and will be adapted for PETRA III.

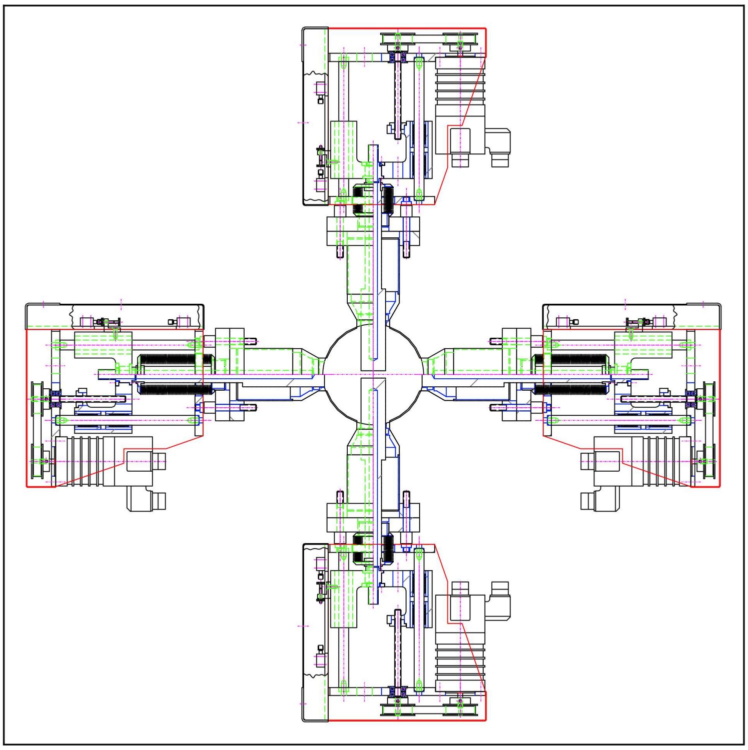

Figure 3.9.14: The scraper of PETRA II with four jaws.

3.9.9 Scrapers

Scrapers are used for beam halo and aperture measurements. The PETRA II scraper system (see Fig. 3.9.14) has four jaws, two for horizontal and vertical directions, respectively. This device and its adjacent control-electronics will be used in PETRA III without major modifications.

3.9.10 Beam stoppers

The personnel interlock system has to ensure personnel safety with the required redundancy during all operating phases. One part of the redundant safety system is to avoid any circulating particles in PETRA III using beam stopper in case of a terminated beam permit. The stoppers are redundant to the beam dump. The stopper consists of a 6 mm thick stainless steel plate, which is pneumatically driven into the beam pipe in case of any security condition. Any circulating particles will scatter on the plate and will be lost within a few turns. For safety reasons, the stopper falls into the beam pipe in the event of any power or pneumatic failure. Two redundant stoppers are foreseen in PETRA III. The two existing stoppers of PETRA II (Figs. 3.9.15) will be used in PETRA III.

3.9.11 Photon beam position monitors

Precise and reliable beam position monitors are mandatory for a safe and stable photon beam line operation. Two different types of monitoring devices are foreseen:
1. Screen: Simple moveable fluorescence screens read out by CCD cameras to set up the photon beam visually at low power operation.
2. Blades: X-ray photon beam position monitors (PBPMs) using photoemission current for fine steering, fast and continuous monitoring of the beam. Both types of monitors are already used in DORIS and PETRA II (Hahn et al., 1998; Hesse & Seebach, 1997).
PBPMs are the most common device in photon beam lines. Fig. 3.9.17 shows the PETRA II

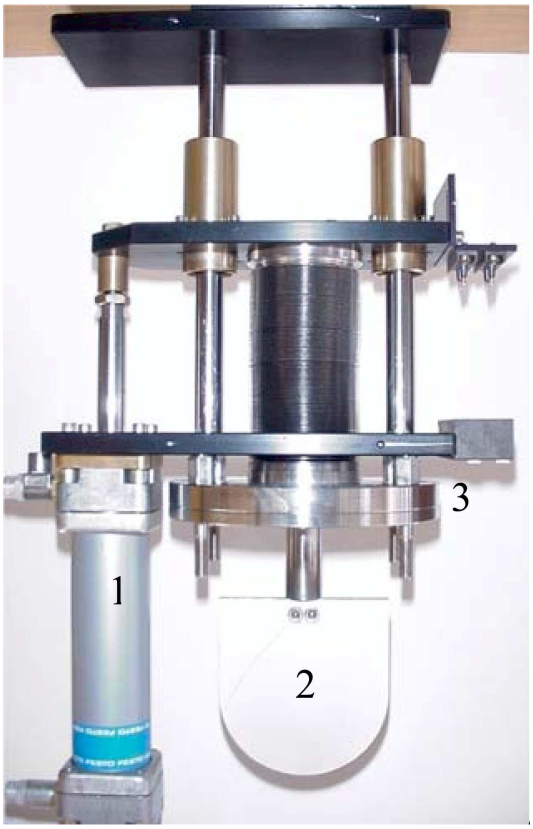

Figure 3.9.15: Beam stopper in PETRA II. 1: Pneumatic driver, 2: Stainless steel plate, 3: Vacuum flange.

Figure 3.9.16: A beam stopper (right) next to a moveable screen monitor in DORIS II.

PBPM. It has an additional tungsten dump electrode (2), mounted in front of the blades (1). These electrodes protect the copper block against melting by a misaligned photon beam. The normalized difference of the photoemission current on the electrodes will indicate the beam position. The PETRA II PBPMs and the adjacent readout electronics provide an internal resolution of about 1 μm (see Fig. 3.9.18). In the figure beam position changes of a few μm are clearly detectable. The steps in the traces are related to the last significant bit (LSB) of the readout electronics, which corresponds to 1 μm. The resolution of such a PBPM can be improved down to few tenth of a micron by more sophisticated designs and a proper installation (avoiding vibrations (Johnson & Oversluizen, 1989)), and by a more sensitive readout electronics. For the high brilliant photon beams of PETRA III additional cooling of the blades has to taken into account. CVD diamond blades have excellent thermal properties and a low absorption coefficient and might be preferred. However, it is well known that the varying characteristics of the undulator radiation with the K-value, the presence of dipole and quadrupole background radiation and the spectral efficiency of the blade material will prevent a universal calibration of the PBPM (Holldack, Ponwitz & Peatman, 2001). Each setting of the undulator will have a unique set of calibration parameters of the PBPM. Only with such a proper calibration, the PBPMs are sufficient for a precise position feedback loop to provide very stable beam conditions at PETRA III.

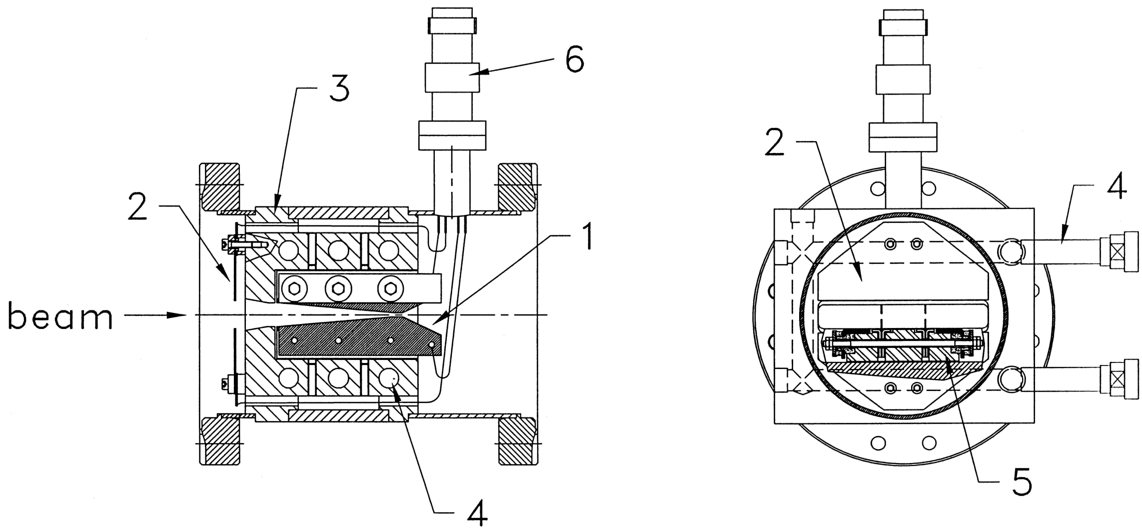

Figure 3.9.17: The PETRA PBPM with (1) tungsten electrode, (2) dump electrode, (3) copper block, (4) cooling channel, (5) monitor module, (6) electrical feed-through (from Hahn et al., 1998).

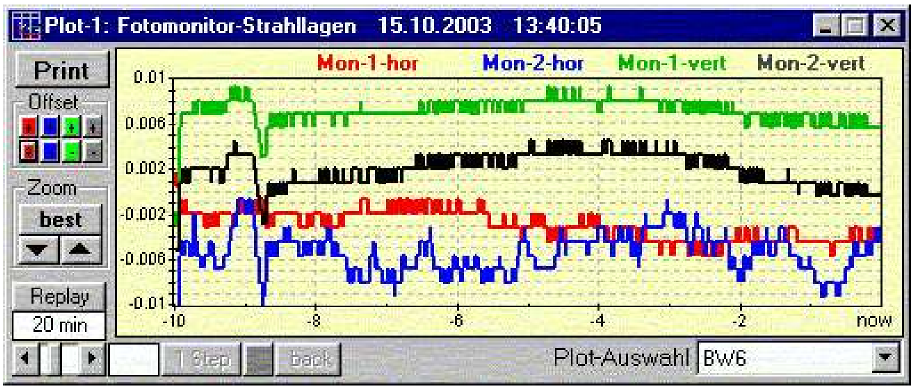

Figure 3.9.18: Signal from two PBPMs in the DORIS photon beam line (horizontal and vertical). Scale: vert. = mm, hor. = minutes.

3.10 Multi Bunch Feedback Systems

3.10.1 Introduction

As has been pointed out in Sec. 3.2.3 the design current in PETRA III can only be achieved with the help of powerful feedback systems. We have already some ten years of experience with feedback systems at DESY (Ebert et al., 1991) since the operation of almost all of DESY's lepton accelerators relies on the successful operation of multi-bunch feedback systems. Unfortunately we cannot use the existing systems because their bandwidth is 5 MHz whereas for PETRA III a bandwidth of at least 60 MHz is required. Feedback systems with even higher bandwidth are now in routine operation in B-factories (Kikutani et al., 2002; Seemann, 1999) to stabilize beam currents that are considerably higher compared to the design current of PETRA III. Therefore a feedback system for PETRA III will be feasible. In the following we will specify the basic parameters of the systems for PETRA III and present a schematic layout.

3.10.2 System design

The feedback will be a bunch by bunch system. The minimum bandwidth is 62.5 MHz determined by the shortest distance between bunches being 8 ns. The required gain of the feedbacks can be calculated with the following formulae:

$$\frac{1}{\tau} = \Omega_s \frac{\partial U/\partial \phi}{2U_c} \tag{3.10.1}$$

$$\frac{1}{\tau} = \omega_0 \frac{\partial U/\partial x \sqrt{\beta_{Kick}\beta_{PU}}}{4\pi E/e} \tag{3.10.2}$$

with $E, U_c, \omega_0, \Omega_0, \beta_{Kick}$, and β_{PU} being the energy, the circumferential voltage, the revolution frequency, the synchrotron frequency, the β-function at the kicker and at the pickup, respectively. In the following table the required damping rates ($1/\tau$), gains ($\partial U/\partial \phi$, $\partial U/\partial x$) and voltages for maximum mode amplitudes are given:

Feedback	Re. damping [Hz]	Gain	Max. mode ampl.	Max. voltages
Longitudinal	800	13.8 kV/°	1°	13.8 kV
Horizontal	1400	9 kV/mm	1 mm	9 kV
Vertical	1400	9 kV/mm	1 mm	9 kV

The phase angle is measured with respect to the fundamental RF frequency (500 MHz). We assume that the beta-function at the kicker and the pick-up is 15 m which is a conservative assumption.

The tolerable residual coherent amplitude of the transverse feedbacks must not exceed a few micrometers which is approximately a tenth of the rms beam dimension in order not to degrade the emittance.

Fig. 3.10.1 shows the schematic layout of a feedback system. The basic building blocks are the monitor with the detector, the digital processing unit and eventually the power amplifiers

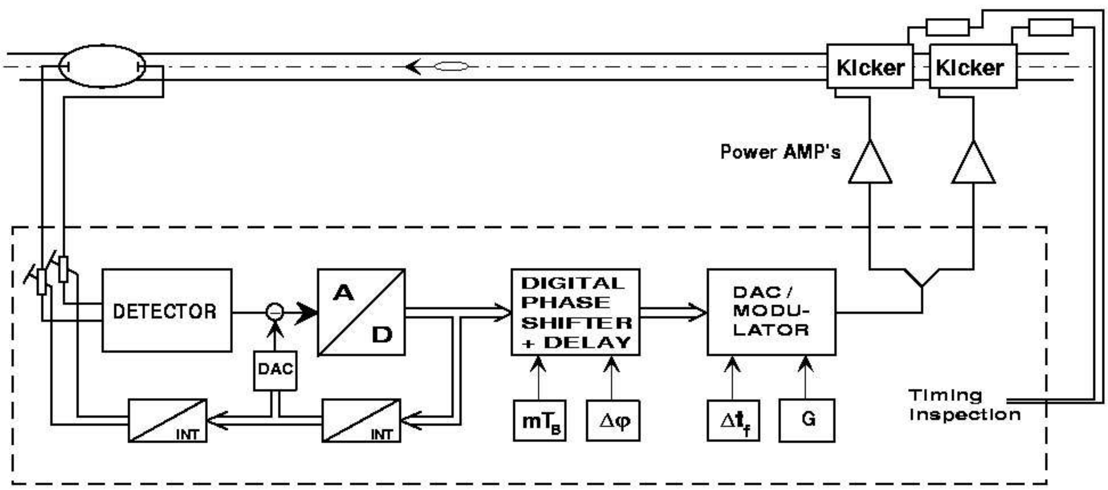

Figure 3.10.1: Schematic layout of the PETRA III feedback system.

with the kickers. In the following we will briefly describe the building blocks for the longitudinal and transverse feedback.

Monitor and detector

For the longitudinal feedback the signal of buttons of a conventional beam position monitor can be combined to give an intensity signal insensitive to transverse beam position. This signal can be processed by analog circuitry to extract the phase signal of each bunch. Such RF front ends are in use at ELETTRA (Bulfone et al., 2002) and SLS and are commercially available.

For the transverse system, button signals of a beam position monitor are combined via a hybrid network to extract the dipole moment of the beam in the horizontal and vertical plane. These signals are transferred into base band with an analog circuit. Similar to the longitudinal plane such RF front ends are in use at ELETTRA (Bulfone et al., 2002) and SLS and are commercially available.

There are also plans to use stripline monitors to measure beam position because they offer a better signal to noise ratio. Since the residual coherent amplitude has to be quite small such a good signal to noise behavior may be necessary. For both the longitudinal and transverse system it will be advantageous not to limit the bandwidth of this part of the feedback to 62.5 MHz but allow for higher bandwidth even 250 MHz so that in case of future upgrades this part does not need modification. In this case a detector that fits our needs would be commercially available.

Digital processing unit

In this unit the analog signal of the detector is digitized and shifted in phase, so that the over all phase advance of the feedback loop is 90°, and appropriately delayed. Finally the signals are converted into analog values for further processing.

This unit will be designed for all systems exploiting modern digital electronics . In this way not only the above mentioned tasks can be fulfilled but the systems can also be used efficiently as diagnostic tools. Regarding the bandwidth of this part the same consideration as for the monitor and detector can be applied.

Power amplifiers and kickers

For the transverse feedback, strip-line kickers will be used which are fed by commercially available solid state amplifiers operating in base band (10 kHz– 250 MHz). Since these amplifiers are expensive economic use of their power is essential. Therefore the kickers must have an adequate shunt impedance which in turn means that the bandwidth must be as small as possible i.e. 62.5 MHz. If in case of an upgrade the bandwidth of the system has to be increased only the kickers have to be replaced.
For one meter long kickers the shunt impedance can be at least 30 kΩ. There will be two kickers for each of the horizontal and vertical directions and the total power per direction will be 1 kW. The new transverse system will be installed in the short straight section south east. The following table summarizes the values for the transverse feedbacks.

Transverse feedback	
Power (kW)	1
# of kickers	2
Kicker shunt impedance (kΩ)	30
Voltage (kV)	11

For the longitudinal feedback we want to use kickers similar to those installed at Daphne (Ghigo et al., 1996), Elettra and SLS (Dehler, 2002). These kickers are strongly loaded pill box like cavities. The operating frequency will be around 1.3 GHz. Since we do not require a bandwidth of 250 MHz as in case of Daphne etc. we can reduce the loading of the cavity in order to get a higher shunt impedance. This is necessary since the power amplifiers are even more expensive than those for the transverse system. We assume that a shunt impedance of 3 kΩ per cavity is achievable. This seems to be realistic if one compares with the values obtained for higher bandwidth (Dehler, 2002). Installing eight cavities and a power of 4 kW yields the required voltage for the longitudinal system. The feedback cavities can be installed close to the 500 MHz RF system in the long straight section south. The following table summarizes the values for the longitudinal feedback.

longitudinal feedback	
Power (kW)	4
# of cavities	8
Kicker shunt impedance (kΩ)	3
Voltage (kV)	14

3.11 General Control System

3.11.1 Introduction

For over two decades, PETRA has been remotely operated by a modular, distributed and multi-layered control system. At PETRA I, the control system consisted of a network of industrial mini-computers running programs written in an interpreted language. The control system was connected through the DESY proprietary long-distance fieldbus system SEDAC (Serial Data Acquisition System and Control) with front-end electronics packed in crates. PETRA II started operation with this system; in 1996 the mini-computers were replaced by Windows PCs using VisualBasic and interconnected via Ethernet. VisualBasic has demonstrated its unique strength as an integrated development environment for powerful graphics and rapid application design. In the meantime, industrial laboratory automation hardware and software, industrial fieldbus systems, embedded CPUs and programmable logic arrays have broken down the strict separation between front-end electronics and the control system software. The performance of modern software development tools and network technologies as well as the available CPU power has grown dramatically during the past few years. Efficient communication patterns such as publish-subscriber mechanisms are becoming standard, component or object oriented software is more maintainable and reusable, and new Web-based technologies provide simple access to all kinds of data and services.
The proposed control system for PETRA III faces two major challenges. First, a reasonable balance must be found between continued use of proven technologies and upgrades using new technologies and ideas. An important consideration here is support for the large number of existing technical components and subsystems, which will be carried over into PETRA III. Second, the novel operation mode of PETRA III as a continuously running high-quality light source with low down time places strict requirements on the availability, stability and performance of the control system architecture, tools, hardware components and user applications.

3.11.2 General properties of the PETRA III control system

3.11.2.1 Overview

The proposed system is based on our experiences with the present PETRA and HERA control systems. It uses a multi-layer architecture consisting of a client tier, a server tier and an integration tier, using TINE (Threefold Integrated Network Environment), a set of communications protocols and services developed over the past 12 years as the core of the HERA control system. Many of the existing components and subsystems which will be used in PETRA III already support TINE interfaces or gateways.
We anticipate several significant changes in the general control system implementation. First, the present VisualBasic-based console applications run only on Microsoft Windows platforms. We intend to move to Java-based applications to remove this limitation. Second, the HERA control system, in particular, shows many signs of its gradual construction. TINE and its associated services are now in a mature state and for PETRA III we will be able to implement features such as archiving, local history records, and naming conventions in a uniform fashion across the control system.

The control system must accommodate a range of users, with varying needs. At the client level, TINE supports the scientific computing software tool MATLAB, which can be used by accelerator physicists for specialized studies. For remote client access, we are developing a TINE-to-SOAP (Simple Object Access Protocol) interface, which could be a generic solution for connection to standardized Web Services.

The server level will include front-end device servers for which the control system group has full responsibility, servers for which the responsibility is shared, in varying degrees, between the control system group and the engineers responsible for the hardware, and gateways to autonomous control systems maintained by other groups. Some of the gateways already exist, for example a software interface between TINE and the EPICS (Experimental Physics and Industrial Control System) control system used by most of the technical infrastructure subsystems at DESY. The servers with shared responsibility raise several issues, for example the need to agree with other groups at DESY on the range of hardware (such as fieldbusses) and software, which will be supported by the control system group.

More generally, the flexibility provided by a modern control system brings with it the danger of excessive fragmentation of both hardware and software solutions, and associated increases in the manpower required for support and maintenance. The old control system philosophy one size fits all is no longer practical or desirable; it is nonetheless important to limit the range of choice, and not unnecessarily throw away the enormous benefits of standardization. The balance must be somewhat different for the various classes of users.

3.11.2.2 Control system architecture and software bus

The architecture of the proposed control system for PETRA III follows the multi-layer approach and consists of Ethernet connected client, integration and server tiers, see Fig. 3.11.1. It must allow for adiabatic updates as well as updates of complete components without major disruption of the remaining system.

The client tier contains the graphical client applications. The server tier houses the device server applications and the adapters to control systems maintained by other groups. The integration tier consists of a software bus and its associated services, as well as control system server applications with system-wide responsibilities (‘advanced server applications’). The software bus is a software library providing an interface to a certain object model for representation of data and devices and handling the communication between clients and servers. All clients or servers attached must feed the interface in conformance with the object model. Foreign systems are integrated through translation layers called gateways or software bus adapters.

The proposed software bus is TINE, originally developed at DESY for the HERA control system. Features supported by TINE include:

- Runs on Windows, Unix, Linux and VxWorks platforms,
- Application Programmer Interfaces for C/C++, VisualBasic, Java, and MATLAB,
- Data exchange via client-server, publisher-subscriber, broadcast, and multicast communication,

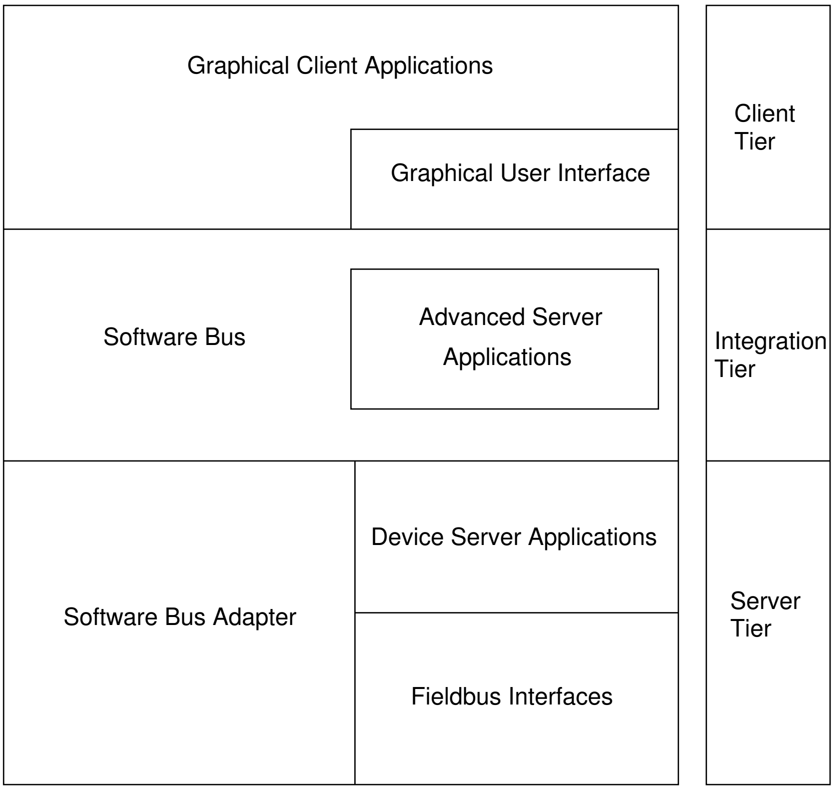

Figure 3.11.1: Standard architecture of the proposed PETRA III control system.

- Supports UDP, TCP/IP, and IPX transport protocols,
- Interfaces to LabView and Agilent Vee environments (i.e. laboratory automation software tools),
- Interfaces to EPICS control system front-end servers (IOCs)

Associated services include:

- Local history and data archiving,
- Alarm generation and processing,
- Name service with plug and play automated server registration,
- Software wizards for generation of skeleton servers and clients.

TINE has been continually developed over the past years. Future plans include implementation of the TINE registry according to the UDDI (Universal Description, Discovery and Integration) specifications, and a TINE-to-SOAP proxy interface to standard Web services. The TINE registry will be the central platform-independent database to store information about all distributed control system services and assets, as well as user access rights. In addition, the conformity with the object models and system databases of other control systems

(e.g. DOOCS at DESY or Tango at ESRF) will be further enhanced.
Tab. 3.11.1 lists the subsystems of PETRA III, together with how they will be interfaced to the software bus. The external controls systems to be interfaced are the technical infrastructure, the pre-accelerators, and HASYLAB synchrotron radiation beam line control. The equipment of the remaining subsystems communicates either directly with the software bus or over a fieldbus connected with a TINE server. The subsystems are described in detail in Sec. 3.11.3.
The interface with the HASYLAB synchrotron radiation beam line controls, which must be developed, deserves special attention. It will be important to read out the detailed status of all beam line devices for control room use and, for later analysis, the machine archive.

Subsystem	Integration Path
General technical infrastructure	EPICS Adapter (adapter exists), SEDAC / TINE Server (interface exists)
Magnet power supplies and magnet control	CAN / TINE Server (interface exists)
RF-system	TINE Server
High voltage power transmitters (RF-system)	EPICS Adapter (adapter exists)
Vacuum system	SEDAC / TINE Server (interface exists)
Injection elements	SEDAC / TINE Server (interface exists) GPIB / TINE Server (interface exists)
Timing and synchronization system	SEDAC / TINE Server (interface exists) VME / TINE Server (interface exists) GPIB / TINE Server (interface exists)
Control of beam parameters	TINE Server
Beam diagnostics	TINE Server
Technical interlock system	TINE Server, SEDAC / TINE Server (interface exists)
Storage ring instrumentation	CAN / TINE Server (interface exists)
Radiation interlock	CAN / TINE Server (interface exists)
Synchrotron radiation beam lines and insertion devices	Adapter (adapter to be developed)
Pre-accelerators	Adapter (adapter exists)

Table 3.11.1: Integration paths for technical subsystems (for details see Sec. 3.11.3)

3.11.2.3 Operation model and distribution of responsibilities

Traditionally, most control systems had a very strict separation between the control system and the underlying front-end electronics. However, following the trend by which analog electronics are increasingly replaced by programmable digital electronics or high-level processors running powerful operating systems, we see that the engineer provides more and

more often not only front-end electronics, but also front-end device server software and hardware. A similar situation exists when accelerator physicists provide either algorithms for the beam control or even application programs.
To avoid an un-maintainable fragmentation of the control system between the various hardware and software platforms as well as programming languages and styles the control system group will define and maintain a restricted set of standards to be followed. The control system group will help and guide the programmers and engineers with the goal of a clean implementation and consistent usage of the standards.
The responsibilities of the control system group will include in any case the computer networks, the core software such as the software bus, application programmer interfaces (API), generators, templates and adapters, the fieldbus interfaces and drivers, the overall system integration and administration, the code repository and other common services. Further, the control system group offers to provide the client applications. For engineers, who implement only the front-end electronics hardware the control system group will provide in addition the corresponding front-end device server applications and the server hardware.

3.11.2.4 Conventions, supported platforms and programming languages

Uniform naming conventions will be enforced. The data attached to server specific properties as well as the methods must be defined and named in an intuitive and human readable format. Every server application must consistently maintain the complete set of stock or default properties of the control system such as engineering units or minimum / maximum limits.
It is important to maintain a clear separation between the tasks to be performed by the client and the server applications. Console client applications should support visualization and user initiated requests, while the data conversion and device-specific logic is encapsulated in the front-end device servers. Automated procedures spanning devices on multiple front-end device servers should be implemented by the advanced server applications in the integration tier. Examples are multi-step sequencing, parameter archiving, alarm handling etc. Exception handling in reaction to software or system errors must be performed in a consistent way.
Well-designed and user-friendly graphical client applications make extensive use of the graphical features of the underlying run-time environment. These so-called rich clients are in contrast to the so-called thin clients usually implemented at present as dynamic Web pages executed with greatly reduced performance by a Web browser. Rich client applications are proposed to be the standard human-machine interface. However, accessing the general control system via the Web by viewing for example certain task specific maintenance pages will also be supported.

The ability to visualize the PETRA III operation across all platforms while keeping a uniform look-and-feel for the users is very important. The graphical user interface ACOP (Accelerator Component Oriented Programming) originally developed for the HERA control system offers an intuitive interface for accessing front-end devices as well as a graphics package for data presentation and online data analyses. Java is proposed as platform independent language for graphical client applications. Desktop PCs running Windows or Linux are well

suited to host the corresponding virtual machine.
Advanced server applications (VisualBasic, Java, C, C++ or scientific computing software such as MATLAB) and device server applications (VisualBasic, Java, C, C++ or laboratory automation software such as LabView or Agilent Vee) must run with high availability. The corresponding computers (Windows, Linux) should be rack-mounted, remotely controllable, well cabled and efficiently air-cooled requiring more reliable computer hardware than mass-market desktop PCs. Crate-hosted computer hardware (cPCI with Windows, VME with Linux or VxWorks) can be chosen in combination with dedicated measurement or fieldbus boards. Boards packed in plug-in modules and housed in crates are superior compared to boards with PC card design, since, for example, hardware changes are facilitated.
For embedded systems, dedicated versions of Windows or Linux with reduced features are available. The software development (VisualBasic, C) can be performed on desktop PCs if the hardware of the embedded system is carefully selected.

3.11.2.5 Tools and services

Integrated development environments enable creation of optimized graphical human-machine interfaces and efficient online debugging. VisualStudio has demonstrated its strength for C++ and VisualBasic. For Java, a handful of tools (Eclipse, NetBeans etc) are available and rapidly improving in their capabilities. The application programmers will decide on a preferred development environment. Reusable operation specific graphical software components must be written for general use.
Software wizards will be provided for generation of server application skeletons fully integrated into the control system. Wizards will also be available for the configuration of simple graphical application clients for data presentation, e.g. for urgent troubleshooting or dedicated measurement series. These skeletons are especially useful for engineers and physicists who are not experts in the controls programming.

The DESY proprietary fieldbus technology SEDAC will continue to be used at PETRA III for many existing systems. The control system group maintains the necessary interface and driver software for Windows, Linux and VxWorks. The controls group will also support a limited number of industrial fieldbusses, definitely including CAN and GPIB.
Experience shows that extensive, but intelligent error logging and parameter archiving is essential for fast fault detection and machine operation at high availability. A central alarm logging facility as well as an archive system for time series and snapshots will be implemented. The relevant parameters and event triggers will be supplied by the server applications by feeding the corresponding interfaces of the software bus.

Automation of multi-step procedures is essential for high-efficiency machine operation. A software tool to load and store parameter set-ups and to execute linear or repetitive automated sequences will be installed. A supervisory server determines the actual machine state and issues information about allowed or forbidden actions according to predefined rules.

3.11.2.6 Network and security

A structured, broadband Ethernet network will connect the PETRA III control system computers allowing for high data throughput e.g. for video frames, efficient network administration and remote fault diagnosis. A well-configured firewall provides network security by separating the control system network from the Internet and DESY intranet. Only authorized hosts will have access to the control system.
TINE communications require open TCP-ports. Therefore, direct remote access from outside could be a risk. A VPN (Virtual Private Network) tunnel connection will allow outside access without this risk.
In addition, user login names are checked against the TINE registry, which keeps the security database maintaining the individual permissions. TINE can allow WRITE access only to specific users, and/or only from specific network, or network addresses.

3.11.2.7 Information services

Various Web-based information services will be provided: documentation pages and templates, electronic logbook and e-mail based notification in case of errors, virtual white board, machine operation overview charts etc. In addition, the control system group will be available for consultation regarding all aspects of the control system.

3.11.2.8 System administration

Many system administration tasks will be necessary for a smooth and reliable operation of the control system. Examples are user administration, creating computer configurations and images, preparing new or spare computers prior to installation, operating the file server and maintaining the code repository, executing updates, supervising running processes etc. The use of a platform-independent administration tool would ease the tasks. Highly automated and fast procedures have to be provided to install security patches or for disaster recovery after major network troubles or mains power blackouts etc.

3.11.3 Technical subsystems and beam control

3.11.3.1 General technical infrastructure

Most of the technical infrastructure (electrical power distribution, cooling water distribution, pressured-air distribution, ventilation) is supervised by a SCADA-like (Supervisory Control and Data Acquisition) control system based on EPICS. It is fully operated by the corresponding technical groups. They plan to integrate the operation of the PETRA III technical installations according to the proven concept of common process visualization, alarm handling and data archiving originally introduced for the HERA operation.
PLCs and other process control equipment communicate via fieldbus (Profibus) and Ethernet connections with the EPICS servers (IOCs). All equipment and process parameters are stored in a database (Oracle). From this repository, all local databases of the individual IOCs and the layout of the operator displays will be generated automatically. All alarm, archive

and logging data will be stored in the database. To a growing extent Web-based tools to visualize and analyze on- and offline data are used. It is not planned to duplicate this control infrastructure within the general control system. The bi-directional interface between both systems already in use at HERA will be used to allow access to EPICS IOCs. Naming conventions and object definitions have to be revised or redefined consistently.

3.11.3.2 Technical interlock system and storage ring instrumentation

The technical interlock system proposed by the instrumentation group will report its status and messages to the central alarm logging facility using the dedicated software bus interface provided by the control system group. The status of the temperature sensors and switches for example attached to the water-cooling tubes of the magnets or vacuum tubes with high synchrotron radiation power absorption are traditionally read and analyzed by SEDAC based electronics. This infrastructure will remain unchanged at PETRA III. The fieldbus connection between the front-end electronics of the movable collimators and slit masks and the corresponding control system device server will be up-graded from SEDAC to CAN technology by the instrumentation group.

3.11.3.3 Magnet power supplies and magnet current control

The power supply group operates many types of magnet power supplies, which are equipped with various regulation and control electronics. The interface modules to the control system are the power supply controllers (PSC) designed and maintained by the control system group. The PSCs are equipped with microprocessors and provide many features. Examples are internal or synchronous current ramping, data recording using internal transient recorder channels and passing status information from and commands to the power supply electronics. The PSCs communicate with the control system via the SEDAC fieldbus system. The SEDAC equipment used for magnet control is the largest and most complicated fraction of the total installed SEDAC electronics. Due to the aging of the electronics involved, lack of replacement parts, the complexity of the PSC software written in assembler, and the complexity of the entire system, the components belonging to the general control system will be completely redesigned. Based on a prototype development for the VUV-FEL Linac, a common modular PSC type will be developed with individual interfaces for the different magnet power supply types. PSCs will be linked together in small groups interconnected by the CAN bus and supervised and controlled by a local magnet server with a TINE interface to the network. These servers will contain local intelligence for alarm processing and executing procedures such as demagnetization cycles. Experience with similar TINE devices shows that the throughput for simple client commands is well over 100 Hz, so that use of this path for the slow orbit feedback should not be a problem.

3.11.3.4 RF-system and high voltage power transmitters

The technical control and data acquisition system as well as the technical interlock system of the RF equipment will be completely redone by the corresponding RF group also maintaining the RF server. The server will be the interface to the general control system and will be fully integrated. The slow-control and fast data acquisition of the high voltage power transmitters is realized by EPICS IOCs. Status information of the transmitters is vital for an efficient operation of the storage ring and in particular the RF system. Therefore, the EPICs IOCs of the power transmitters will also be fully integrated into the general control systems and its services such as alarming or parameter archiving. The biggest challenge will be the handling of the data generated by the extended RF data acquisition system. Transient recorders will permanently digitize more than 200 data channels (12-bit resolution, 10 MHz sampling rate and 16 million samples storage depth per channel). Conceptual details such as central or local archiving, reasonable trigger and filter conditions as well as resulting network load and storage capacity etc have to be worked out.

3.11.3.5 Vacuum system

The front-end electronics of the vacuum system is traditionally based on SEDAC modules and maintained by the vacuum group. Getter pump and total pressure gauge readings or operator requests to close or open valves etc are transmitted through the SEDAC fieldbus system from the control system to the electronic modules and vice versa. Front-end microprocessor boards designed in SEDAC technology handle emergency situations requiring fast response such as unexpected pressure rise. Auxiliary pump stations are operated in local mode and modern mass spectrometers are interfaced with laptop computers. Both types of devices are presently not remotely accessible via the control system. The client and server applications of the control system are maintained by the control system group and provide data visualization, midterm archiving and operator interventions tools, database handling and special interlock features.
It is not planned to change the SEDAC based vacuum system electronics. However, the capabilities to integrate and control remotely pump stations, mass spectrometers or other commercial available equipment with standardized computer interfaces will be provided.

3.11.3.6 Injection elements

The electronics to remotely control and trigger the PETRA III injection elements is realized in SEDAC technology and maintained by the corresponding technical group. Various modules to define gates, to transmit high voltage set-values, to de-multiplex trigger signals delivered by fiber-optic cables etc are used. It is not planned to exchange this equipment. Slow-control of the injection elements is provided by a server application maintained by the control system group.
On the other hand, the group in charge of injection elements provides equipment based on oscilloscopes to digitize measured current pulses of the kicker and septa magnets. The oscilloscopes are locally read out via GPIB. All measured traces are stored by a server running a LabView application and visualized by a corresponding LabView client application. The corresponding technical group will no longer maintain these LabView applications. It is proposed to redo, integrate and maintain server and client applications by the control system group.

EDMS Nr.: D00000000822371 Rev: A Ver: 1 Status: Released - Dat.: 8. Apr 2008

3.11.3.7 Timing and synchronization system

The central elements of the timing and synchronization system are the cycle generator and the trigger generator. The cycle generator specifies and controls the transfer of electrons or positrons from DESY II to its clients. The trigger generator controls the number of bunches transported to the declared target RF buckets in DORIS and PETRA.
The beam control group operates the cycle generator and the trigger generator. The control system group is responsible for the server application and the interface to the timing and synchronization system and for the client applications of the operators. Software changes are expected in particular with the proposed top-up filling mode. The measured traces of the digital scopes used to verify the timing conditions and bunch fill patterns will be captured and distributed via the general control system.

3.11.3.8 Control of beam parameters

Multi-bunch feedback and tune control for the electron machines at DESY is performed by custom DSP (Digital Signal Processing) cards built by the beam control group and interfaced to the control system as bus cards in PCs using TINE for network communications. The system for PETRA III will continue this line of development.
Orbit stabilization feedback will be shared between two systems. A fast feedback system will control oscillations about the mean orbit in the frequency range from several Hz to several hundred Hz. This is the responsibility of the beam control group and will use special connections to position monitors and fast correctors which bypass the Ethernet based communications, and, as for the multi-bunch feedback, use the control system only for a top level interface. The slow orbit feedback, in the range several Hz and below, will have access to the full set of position monitors and correctors via the standard fieldbus or fast Ethernet paths. A single central computer will be responsible for orbit control calculations and for sending the corresponding commands to the correctors.
For machine physics studies, experience at HERA has been that the many of the required software tools require more flexibility than can be provided with hard-coded applications, and that it is preferable that the machine physicists construct their own programs using an interactive environment such as MATLAB. The controls group has been responsible for maintaining the TINE-MATLAB interface, and the physicists for the applications; we expect this arrangement to continue. The controls group will also supply some simpler tools, such as generic programs for stepping set-values and displaying and recording the resulting beam behavior.

3.11.3.9 Beam diagnostics

The beam diagnostics group provides the measurement systems for transverse beam positions, beam current as well as transverse and longitudinal beam sizes. In most cases, the diagnostics experts will also maintain the corresponding device servers.
It is planned to avoid long-distance transmission of video sequences via cables to the end users. Instead, it is proposed to distribute the video frames via the control system network as an integrated software bus service. TINE is able to handle in multi-cast mode captured video data with a rate of 4.5 MBytes/s.

3.12 Power Supplies and Cables

3.12.1 Magnet power supplies and cables

3.12.1.1 Magnet power supplies

Experimental Hall Section

- **Dipole Magnets**
  The power supply for the 18 dipole magnets in the new octant of PETRA will be located in PETRA-hall *Northeast*. The magnets will be fed by a SCR power supply with 750 V/650 A.

- **Quadrupole Magnets**
  The quadrupole magnets will be fed by power supplies that are located between the tunnel and the wall of the experimental hall. For the individual control of the quadrupole magnets, a total of 90 power supplies will be installed. Each of them provides a current of 200 A and a maximum voltage of 40 V. These devices are fed by nine pre-rectifiers with 130 V/2300 A.

- **Correction Magnets**
  For operation of the 150 correction magnets the same number of power supplies is needed with an individual power of 0.5 kW. They will be placed between the tunnel and the wall of the experimental hall.

7/8 PETRA

- **Dipole Magnets**
  The 194 dipole magnets in the remaining 7/8 of PETRA will be fed by a single current circuit. For this purpose, a SCR power supply with 600 V/600 A is required that is installed in PETRA-hall *Northeast*. By that means, the transformers and oil pits of the former dipole power supply of PETRA II can be further used.

- **Quadrupole Magnets**
  For the two serial quadrupole loops in the remaining 7/8 of PETRA III, two SCR power supplies with 450 V/550 A will be installed. The quadrupole magnets, which are combined in 24 groups with 7 magnets each, 24 power supplies with 100 V/550 A are needed. These power supplies are fed by six pre-rectifiers with 130 V/2300 A, to be installed in PETRA-hall *Northeast*
  For the control of the individual quadrupole magnets near the experimental hall, eight power supplies with 20 V/550 A will be installed in PETRA-hall Northeast and eight power supplies with 20 V/550 A will be installed in PETRA-hall East. The power supplies in PETRA-hall East are fed by one pre-rectifier with 30 V/2300 A. The six power supplies with 20 V/550 A for the six quadrupole magnets near PETRA-hall South will be located in PETRA-hall South left. These power supplies are fed by one pre-rectifier with 30 V/2300 A.

- **Sextupole Magnets**
  For the power supply of the sextupole magnets, 4 SCR devices with 300 V/400 A are sufficient. These will be installed in hall *Northeast* as well.

- **Correction Magnets**
  The 200 power supplies (0.5 kW) for the correction magnets of the remaining 7/8 of the PETRA ring will be distributed amongst the PETRA halls, as for the operation of PETRA II.

An overview about the various power supplies and their planned location is given in Tab. 3.12.1 and 3.12.2.

3.12.1.2 Cabling

Experimental-Hall Section

- **Dipole Magnets**
  For the cabling of the dipole magnets in the experimental-hall section, cables with a cross section of 240 mm^2 will be used. This cable will be guided directly from the hall *Northeast* to the series of dipole magnets and back again.

- **Quadrupole Magnets**
  For the supply of the quadrupole magnets, cables with a minimum cross section of 70 mm^2 are required. They will be guided through cable trenches with a cross section of 300 mm $\times$ 150 mm underneath the shielding wall to the magnets.

- **Correction Magnets**
  The correction magnets will be connected to their power supplies with cables of type NYM-J or similar. They will be guided along the same way as the cables for the quadrupole magnets.

7/8 PETRA

For the supply of the remaining 7/8 of PETRA III, aluminum power rails will be used that are already installed in the tunnel along the whole PETRA ring parallel to the accelerator. They have a cross section of 1000 mm^2. Due to space limitations the lower layer will be dismounted and mounted beneath the tunnel ceiling. Along the experimental-hall section, the aluminum power rails are replaced by corresponding cables from hall *East* to hall *Northeast*.

- **Dipole Magnets**
  The dipole magnets will be connected with cables of 240 mm^2 total cross section, running from the power supplies to the power rails.

- **Quadrupole Magnets**
  In a similar way the quadrupole magnets are connected with a cable cross section of 120 mm^2.

Type	Voltage (V)	Current (A)	Power (kW)	Quantity
Pre-rectifier	130	2300	300	10
Pre-rectifier	30	2300	70	3
SCR power supply	750	650	450	3
SCR power supply	350	550	180	7
power supply	100	550	48	30
power supply	40	200	7	100
power supply	20	550	12	24
Correction power supply	20	15	0.5	360

Table 3.12.1: Power supplies required for PETRA III including backup devices.

- **Sextupole Magnets**
  For each of the four circuits that are connecting the sextupole magnets, one cable with a cross section of 185 mm^2 will be used. It will be laid in the same way as for the dipole and quadrupole magnets.

- **Correction Magnets**
  In the same way as in the experimental-hall section, the correction magnets are connected with NYM-J cables. Compared to PETRA II, the cable path remains unchanged. The cables are guided from the PETRA halls into the tunnels. Running along the plank beds, that are mounted above the power rails, they are guided to the correction magnets.

type	**chrst.**	**magnet**	**no.**	**location**	**no. of magnets**	**magnet location**
SCR power supply	750V/650A	B	1	Hall North-East	18	Exp. hall
SCR power supply	600V/600A	B	1	Hall North-East	196	loop circuit
Power Supply	40V/200A	QD1	9	Exp. hall	9	Exp. hall
Power Supply	40V/200A	QF1	9	Exp. hall	9	Exp. hall
Power Supply	40V/200A	QD3	9	Exp. hall	9	Exp. hall
Power Supply	40V/200A	QD4	9	Exp. hall	9	Exp. hall
Power Supply	40V/200A	QF5	9	Exp. hall	9	Exp. hall
Power Supply	40V/200A	QF5	9	Exp. hall	9	Exp. hall
Power Supply	40V/200A	QD4	9	Exp. hall	9	Exp. hall
Power Supply	40V/200A	QD3	9	Exp. hall	9	Exp. hall
Power Supply	40V/200A	QF2	9	Exp. hall	9	Exp. hall
Power Supply	40V/200A	QD1	9	Exp. hall	9	Exp. hall

Pre-rectifier	130V/2300A	-	4	Exp. hall	-	-
Power Supply	20V/550A	Q1KL	1	Hall North-East	1	North-Northeast
Power Supply	20V/550A	Q2KL	1	Hall North-East	1	North-Northeast
Power Supply	20V/550A	Q3KL	1	Hall North-East	1	North-Northeast
Power Supply	20V/550A	Q4KL	1	Hall North-East	1	North-Northeast
Power Supply	20V/550A	Q1KR	1	Hall North-East	1	North-Northeast
Power Supply	20V/550A	Q2KR	1	Hall North-East	1	North-Northeast
Power Supply	20V/550A	Q3KR	1	Hall North-East	1	North-Northeast
Power Supply	20V/550A	Q4KR	1	Hall North-East	1	North-Northeast
Power Supply	20V/550A	Q5NL	1	Hall East	1	East-Southeast
Power Supply	20V/550A	Q6NL	1	Hall East	1	East-Southeast
Power Supply	20V/550A	Q7NL	1	Hall East	1	East-Southeast
Power Supply	20V/550A	Q8NL	1	Hall East	1	East-Southeast
Power Supply	20V/550A	Q9NL	1	Hall East	1	East-Southeast
Power Supply	20V/550A	Q10NL	1	Hall East	1	East-Southeast
Pre-rectifier	30V/2300A	-	1	Hall East	-	-
Power Supply	100V/550A	Q0K	1	Hall North-East	4	loop circuit
Power Supply	60V/550A	Q1K	1	Hall North-East	5	loop circuit
Power Supply	60V/550A	Q2K	1	Hall North-East	5	loop circuit
Power Supply	60V/550A	Q3K	1	Hall North-East	5	loop circuit
Power Supply	60V/550A	Q4K	1	Hall North-East	5	loop circuit
Power Supply	60V/550A	Q5K	1	Hall North-East	7	loop circuit
Power Supply	80V/550A	Q0A	1	Hall North-East	7	loop circuit
Power Supply	80V/550A	QK1	1	Hall North-East	7	loop circuit
Power Supply	60V/550A	Q2A	1	Hall North-East	7	loop circuit
Power Supply	60V/550A	QK3	1	Hall North-East	7	loop circuit
Power Supply	60V/550A	Q4A	1	Hall North-East	7	loop circuit
SCR power supply	350V/550A	QD	1	Hall North-East	63	loop circuit
SCR power supply	350V/550A	QF	1	Hall North-East	63	loop circuit
Power Supply	60V/550A	Q3	1	Hall North-East	7	loop circuit
Power Supply	80V/550A	Q2B	1	Hall North-East	7	loop circuit
Power Supply	80V/550A	Q1	1	Hall North-East	7	loop circuit
Power Supply	80V/550A	Q0B	1	Hall North-East	7	loop circuit
Power Supply	80V/550A	Q9N	1	Hall North-East	6	loop circuit
Power Supply	80V/550A	Q8N	1	Hall North-East	6	loop circuit

Power Supply	80V/550A	Q7N	1	Hall North-East	6	loop circuit
Power Supply	60V/550A	Q6N	1	Hall North-East	6	loop circuit
Power Supply	60V/550A	Q5N	1	Hall North-East	6	loop circuit
Power Supply	60V/550A	Q4N	1	Hall North-East	8	loop circuit
Power Supply	60V/550A	Q3N	1	Hall North-East	8	loop circuit
Power Supply	60V/550A	Q2N	1	Hall North-East	8	loop circuit
Power Supply	60V/550A	Q1N	1	Hall North-East	8	loop circuit
Power Supply	60V/550A	Q0N	1	Hall North-East	3	loop circuit
Power Supply	60V/550A	QG	1	Hall North-East	2	loop circuit
Pre-rectifier	130V/2300A	-	5	Hall North-East	-	-
Power Supply	20V/550A	-	6	Hall South	1	at Hall South
Pre-rectifier	30V/2300A	-	1	Hall South	-	at Hall South
SCR power supply	300V/400A	S1	1	Hall North-East	35	loop circuit
SCR power supply	300V/400A	S2	1	Hall North-East	35	loop circuit
SCR power supply	300V/400A	S3	1	Hall North-East	35	loop circuit
SCR power supply	300V/400A	S4	1	Hall North-East	35	loop circuit
Corrector	20V/10A	-	200	PETRA-Halls	200	7/8
Corrector	20V/10A	-	60	Exp. hall	60	Exp. hall
Backleg	10V/15A	-	18	Exp. hall	18	Exp. hall
Fast corrector	20V/10A	-	70	Exp. hall	70	Exp. hall

Table 3.12.2: Overview of the power supplies for PETRA III including their location.

3.12.1.3 Redundance

For operation with high efficiency , sufficiently high reliability and fast failure handling are required. This will be achieved by having spare units in standby mode. For each group of ten active chopper supplies one spare will be available. One extra SCR will serve as a spare for the seven SCR power supplies. The interlock and permits for the ten units will be combined and fed to the spare power supply. Hence no further cabling for these signals will be necessary. The magnet circuits are equipped with quick connectors. The faulty unit can then be repaired or replaced without disturbing operation. These measures will ensure that operation is interrupted for less than one hour.
Due to their high reliability, the power supplies for the correction magnets are not included in this redundancy concept.
The accelerator availability could be further increased by equipping the power supplies with additional switches. This enables power supply exchange to be automated from the control room. The down time could then be reduced to some 15 minutes in about 80 % of the trips.

Calculation on MeanTime Between Failure (MTBF) The mean time between failure (MTBF) is known from the experience with the power supplies acquired during recent years.

MTBF per chopper power supply	30000 h
Number of devices	152
MTTF for all devices	30000 h/152 = 197 h
MTBF per correction power supply	400000 h
Number of devices	360
MTTF for all devices	400000 h/360 = 1111 h
MTBF per thyristor power supply	20000 h
Number of devices	8
MTTF for all devices	20000 h/8 = 2500 h
MTTF for all power supplies:	
1/(152/30000 h + 360/400000 h + 8/20000 h)	= 157 h

From these considerations one derives a mean time between failure of 157 h = 6.5 days.

3.12.1.4 Accuracy

Different parameters define the accuracy of the power supplies. These are the absolute accuracy, repeatability, stability and the voltage and current ripple. The current settings of the power supplies will be stored in a file system. The final values are found by optimization by the operator. The repeatability has to be high to reach the required set value again.
The stability is defined as short term stability being less than 1 hour and the long term stability in the range from 1 hour to months. The factors determining the stabilities are e.g. aging of components, temperature variation or fluctuation in the mains feed. In general the short term stability is a factor of 10 better than the long term stability. The relative stability and reliability $\Delta I/I_N$ with I_N the nominal current and ΔI the current variation of the power supply is given in Tab. 3.12.3.

	Main magnets	Steering magnets
Repeatability	$< 10^{-4}$	$< 5 \times 10^{-4}$
Long term stability	$< 10^{-4}$	$< 5 \times 10^{-4}$
Short term stability	$< 10^{-5}$	$< 5 \times 10^{-5}$

Table 3.12.3: Accuracy of magnet power supplies.

.

The current ripple depends on the voltage ripple of the power supply, the inductance of the magnet and the frequency spectrum of the power supply. It is given by:

$$I = U \times \frac{1}{j\omega L + R} \tag{3.12.1}$$

$$\frac{I_{ripple}}{I_{nominal}} \approx \frac{U_{ripple}}{U_{nominal}} \times \frac{R}{\omega L} \tag{3.12.2}$$

with $\omega = 2\pi f$, f being the frequency of the ripple and L the inductance of the magnet. In the following we assume pessimistically that the DC resistance R of the different magnet circuits is 1 Ω.

SCR power supplies The current is controlled with a resolution of 16 bit. The typical frequency of the SCR power supplies is 600 Hz. The voltage ripple of the power supplies is specified to be $U_{ripple}/U_{nominal} < 0.01$. The required relative ripple amplitude for the dipole is $< 1 \times 10^{-5}$. With $L_{dipole} = 0.8$H the relative ripple amplitude becomes 3.3×10^{-6}. The required relative ripple amplitude for the quadrupole is $< 5 \times 10^{-5}$. With $L_{quad} = 0.1$H the relative ripple amplitude becomes 2.6×10^{-5}.

Chopper power supplies The resolution of the reference current is 16 bit. The typical frequency of the chopper power supplies is higher than 16 kHz. The voltage ripple of the power supplies is specified to be less than 5 $\%$ of the output voltage. The required relative ripple amplitude for the quadrupole is $< 5 \times 10^{-5}$. With $L_{quad} = 0.1$H the relative ripple amplitude becomes 5×10^{-6}.

Correction power supplies The current is controlled with a resolution of 16 bit. The typical frequency of the steerer power supplies is higher than 16 kHz. The voltage ripple of the power supplies is specified to be less than 5 $\%$ of the output voltage. The required relative ripple amplitude for the steerer is $< 5 \times 10^{-5}$. With $L_{quad} = 0.5$H the relative ripple amplitude becomes 1×10^{-6}.

3.12.2 HVDC transmitter power supply and klystron protection

3.12.2.1 PETRA II status

Two rectifying units exist to power the two double transmitter installations in PETRA II. One unit in hall south/left (building 42a) and the other in hall south/right (building 42b). The DC output power of each installation is 2.1 MW (58 kV DC / 36 A DC). Much of the equipment is over 25 years old and no longer state of the art. An uncontrolled rectifier is driven by a tap changing transformer set. The output voltage is determined by the preselected tap winding but cannot be regulated quickly in the case of load variations or system voltage dips. The tapping switch of the transformer is no longer commercially available and needs intensive maintenance. Control equipment and monitoring are obsolete and susceptible to malfunction. Klystron protection is carried out by triggered spark gaps, which are out-dated and not reliable. The medium high voltage switchgear is state of the art. It has been renewed in 2002 and will stay in operation for PETRA III.

3.12.2.2 PETRA III design

It is necessary to build two new identical high voltage direct current (HVDC) power supplies to feed the RF system for PETRA III. Their design is based upon the specification of the high power klystrons, in particular that they operate at 75 kV and 18 A DC. This results in 2.7 MW of DC power to feed a double transmitter installation. Some flexibility is needed to carry out e.g. klystron tests so we intend to provide an additional power margin of 10 per cent. This results in the required DC output power of 3.0 MW for one HVDC power supply. Similar power supplies are in operation and have yielded good experience. Existing high reliable components will be reused. A schematic of the HVDC transmitter power supply and klystron protection is shown in Fig. 3.12.1 .

Medium High Voltage Switchgear The medium high voltage switchgear consists of one passive incoming feeder panel and three outgoing feeder panels, which are equipped with vacuum circuit breakers. Two outgoing feeder panels are provided to supply each of the HVDC transmitter power supplies south/left and south/right. The third feeder panel is for back up purposes. The incoming supply is accomplished as a dead-end feeder from main switchgear station *A*. It is not planned to establish a redundant feed in. The switchgear is assembled inside a separate substation next to building 42b. Inside this substation additional space is provided to extend the switchgear. Up to two additional feeder panels can be mounted.

HVDC Power Supplies One thyristor controlled HVDC power supply is provided to power each of the double transmitters. The concept is based on the so-called “star point controller” in an intermediate voltage circuit. The thyristor controllers are fed by a medium high voltage transformer set. Continuous regulation of the output voltage is realized by phase angle control of the intermediate voltage (< 1000 V AC). The controlled voltage is transfered to the high voltage transformer set and subsequently converted by diode rectifiers.
Smoothing of the DC output voltage is accomplished by a passive RLC filter. The smoothing

inductance is connected to the DC current star point of the thyristor controller. The inductance is housed in a cabinet located next to the thyristor controller. The RC filter is at high voltage DC level. Therefore it has to be installed inside the modulator room of the transmitter building. All components at voltages < 1000 V AC (thyristor controller, smoothing inductance, control electronics) will be mounted in cabinets for indoor installation. These cabinets will be arranged within an extended area of the transmitter building. All air insulated components at high voltage DC level will be installed inside the modulator room. This room has to be erected inside the transmitter building. All components at voltages > 1000 V AC (main transformer, HV transformer, HV rectifier) will be located inside oil filled tanks for outdoor installation. These tanks will be situated outside the transmitter building close to the modulator room. The main parameters of a HVDC power supply are presented in the following table:

Main parameters of one HVDC power supply:

main input voltage	U_{AC}	10	kV
main input power	S_{AC}	4	MVA
max. DC output voltage	U_{DCmax}	80	kV
max. DC output current	I_{DCmax}	38	A
max. DC output power	P_{DCmax}	3,0	MW
nom. DC output voltage	U_{DCn}	75	kV
nom. DC output current	I_{DCn}	36	A
nom. DC output power	P_{DCn}	2,7	MW
control range output voltage		0...80	kV
operating range at transmitter operation		50...80	kV

Klystron Protection High power klystrons are protected against arcing and other failures (e.g. focus current) by LTT-Crowbars (Light Triggered Thyristor Crowbar). In the case of malfunction in one of the two klystrons a fast bypass is established by triggering the thyristors. Thus the energy is limited to an appropriate value.
The technology of LTT-Crowbars has been developed at DESY. It has been in operation successfully at the DESY II since May 2003. For the operation at PETRA III the voltage level of these crowbars has to be increased from the present 50 kV DC up to 80 kV DC. Such development is under way. The LTT-Crowbar will be installed inside the modulator room.

Modulator room The new modulator room is part of the transmitter building. It serves as a closed electrical operating room to contain all components at high voltage DC level. Each of the two existing transmitter will be extended to serve a new modulator room. It is a significant part of this concept to arrange the outdoor components close to the modulator room. Thus special high voltage DC cables and appropriate cable sealings are no longer required. Losses regarding the intermediate voltage cabling (between thyristor controller and transformer) are reduced. The areas necessary are available and earmarked for extension of buildings, transformer foundations and oil pits.

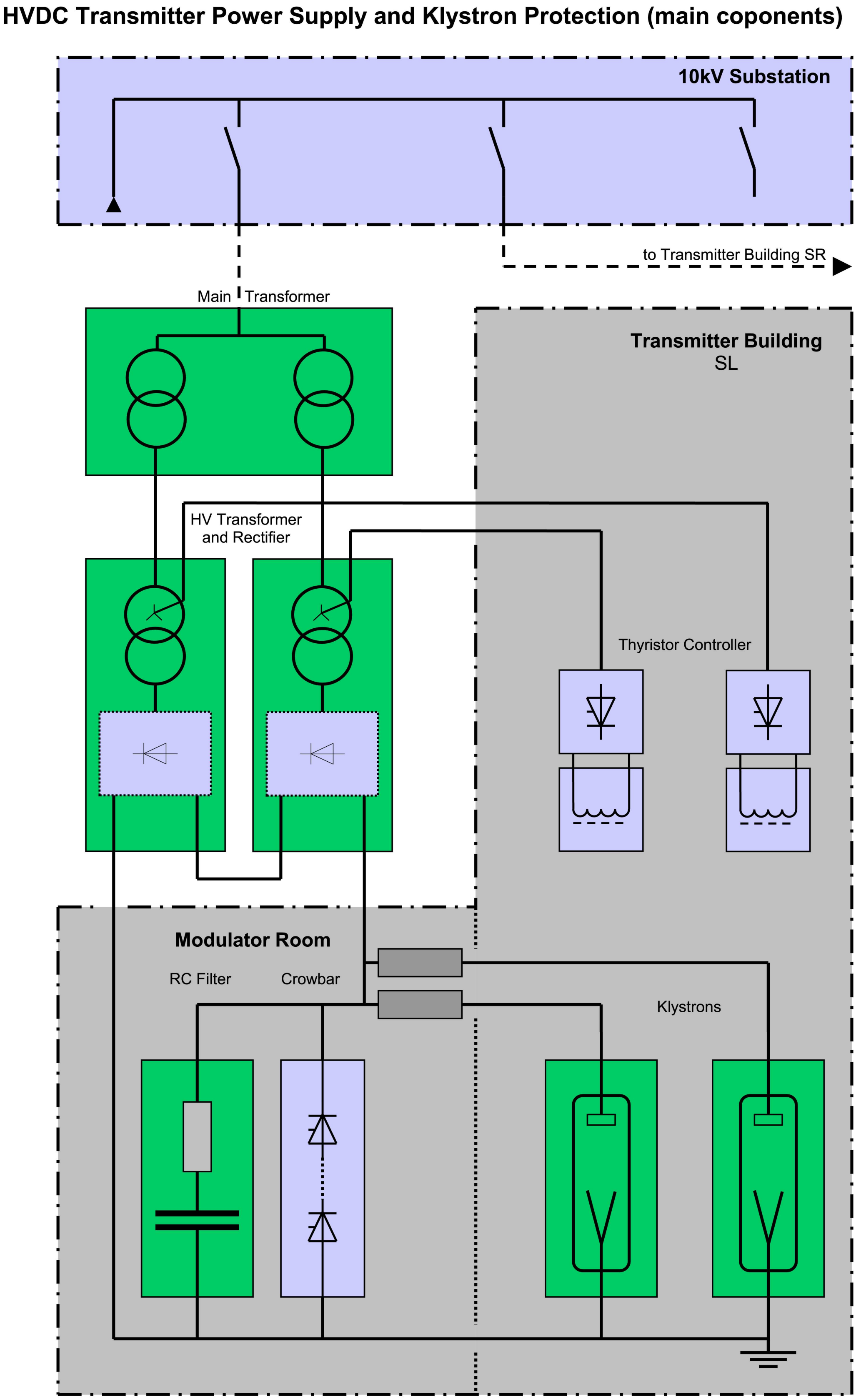

Figure 3.12.1: Schematic representation of HVDC transmitter power supply and klystron protection (main components).

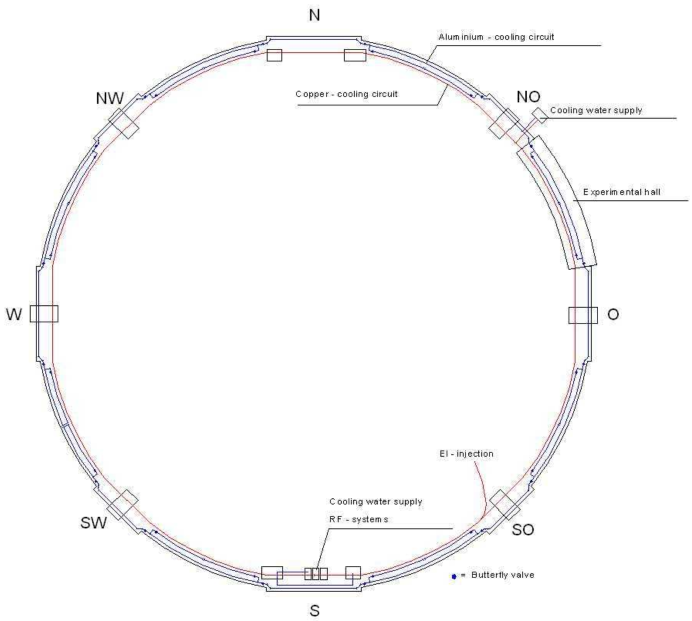

Figure 3.13.1: Overview of the cooling-water supply at PETRA

3.13 Cooling Systems

The cooling-water of PETRA III is supplied from two locations as sketched in Fig. 3.13.1 : To cool the Al- and Cu magnet coils a circumferential cooling pipe of cross section dimension DN 100 is foreseen. Input of the cooling water proceeds from a separate hall near to PETRA-hall *Northeast*. The magnets are connected with hoses. A separate distribution pipe is installed in each octant to cool the dipole-magnet coils. The magnets in the new octant will be connected to the Cu cooling circuit. The draining of individual components can be performed with help of a circumferential bilge suction line.
Chilled water for the experimental hall will also be produced in PETRA-hall *Northeast*. Cooling generators are hybrid dry-cell coolers with a closed cooling cycle. All cooling cycles are operated with fully demineralized water (conductivity $< 1\,\mu$S/cm).

3.13.1 RF cooling systems

PETRA III contain two RF-systems that are fed by a common cooling water supply. Each system consists of two klystrons with the corresponding absorbers, circulators and cavities as sketched in Fig. 3.13.2. The following components of the RF-systems are supplied with cooling water :

- 4 klystrons (2 in each system), consisting of
  collector with Δp = 2.0 bar, inlet temperature, q_e = 38.3°C, and
  4 $\times$ body with Δp = 3.0 bar, q_e = 28°C.
  Cooling power for each system max. 2700 kW

- RF-absorber (hall) with $\Delta p = 4.5$ bar, $q_e = 28°$C. Cooling power for each system max. 750 kW
- RF-absorber (tunnel) with $\Delta p = 4.5$ bar, $q_e = 28°$C. Cooling power for each system max. 700 kW
- Cavities with $\Delta p = 1.0$ bar, $q_e = 28°$C. Cooling power for each system max. 1260 kW
- Circulator with $\Delta p = 3.0$ bar, $q_e = 28°$C. Cooling power for each system max. 40 kW

1. The cooling of the magnets and the experimental hall is provided from PETRA-hall *Northeast*.
2. The cooling of the RF-system is supplied via PETRA-hall *South*.

The the temperature of the cooling water will be reduced in the cooling towers to 28°C and then fed into the cavities and the corresponding absorbers. The return water will be used as supply water for the klystrons. In this way the amount of water to be delivered is significantly reduced.

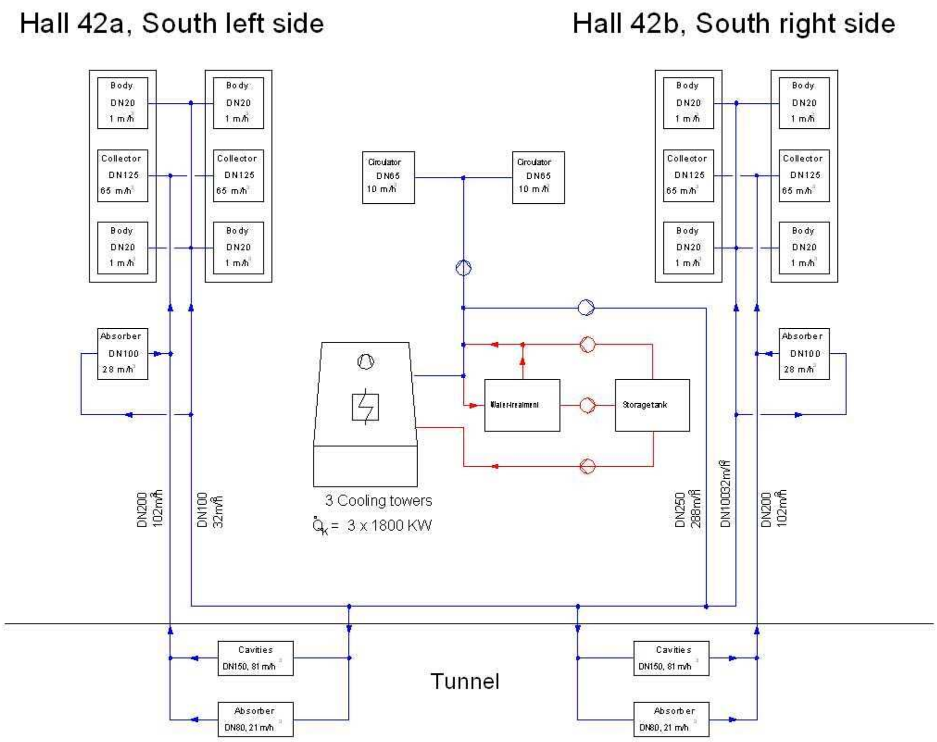

Figure 3.13.2: Scheme of the cooling circuits for the RF-system *South*

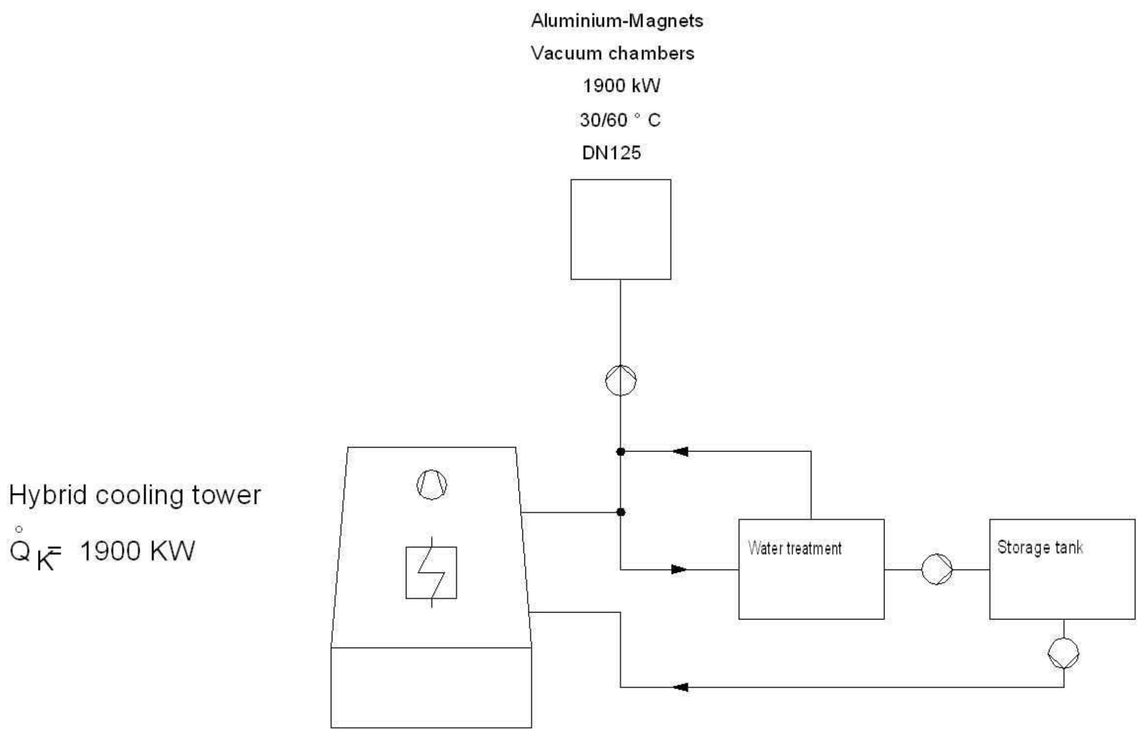

Figure 3.13.3: Scheme of the cooling circuits for the Al - components

Each RF-system is equipped with a circulator. For these devices the supply water line contains an electrically heated buffer tank to keep the water temperature at 30°C. The supply water temperature is controlled by a three-way valve.

At PETRA-location *South*, three hybrid cooling towers with a total power of 5400 kW will be installed. They will be dimensioned to a wet-bulb temperature of 21.5°C which allows for a dry operation up to a temperature of 15.6°C. In this operation mode, the water consumption can be reduced by 75 % compared to conventional wet-cooling. In addition, vapor formation can be almost completely avoided.

For reasons of cost reduction and environmental protection it is intended to operate the cooling water circuit without the addition of anti-freeze. Upon danger of freezing the devices will be drained automatically.

3.13.2 Magnet cooling systems

In the new octant, magnets with copper coils are used, while the magnets in the remainder of PETRA still contain aluminum coils. These two different materials necessitate the use of two separate cooling systems.

For the aluminum components a cooling tower with a cooling power of 1900 kW will be installed at the PETRA-location *Northeast*. Its schematic layout is shown in Fig. 3.13.3.

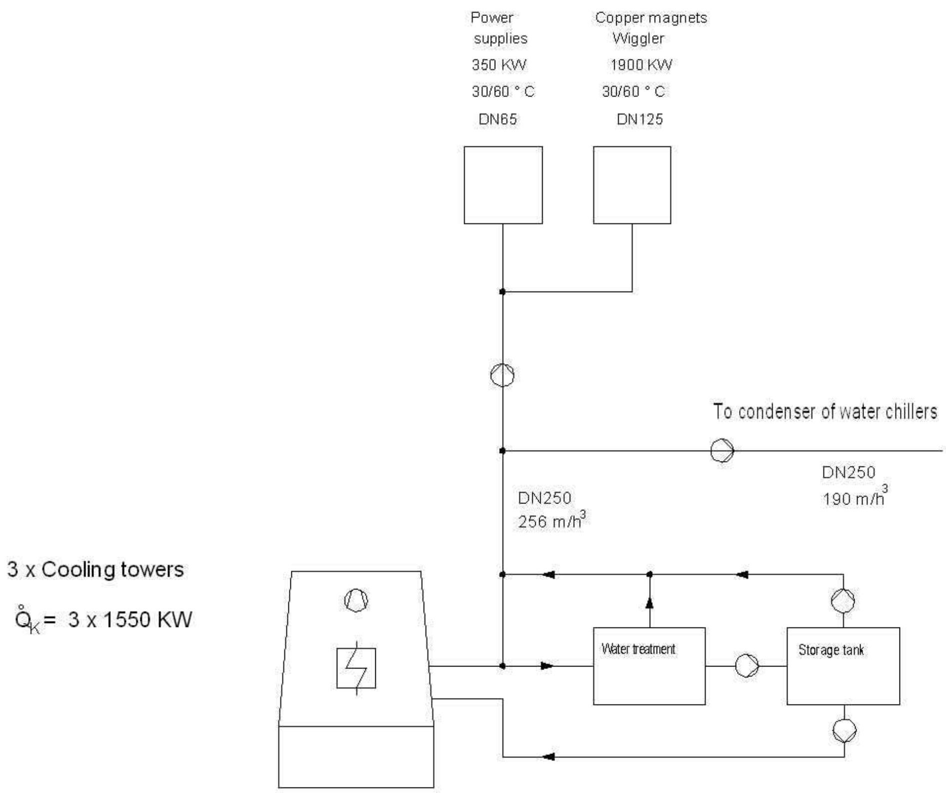

Figure 3.13.4: Layout of the cooling circuits for the Cu - components

The technical basis is the same as described in the previous section. The device is dimensioned for a wet-bulb temperature of 21.5°C so that a dry operation is possible up to a temperature of 14.9°C. At the cooling tower, the water temperature will be initially controlled to 28°C via the speed of the ventilator. The supply water temperature for the magnet coils will then be controlled to 30°C using a 3-way valve.
The copper circuit also cools the rectifiers for the electrical power supplies and the absorbers at the damping wigglers in the long straight sections. The total cooling power of this system is 2250 kW. The principle of operation is the same as described above with the supply water temperature of the magnet coils being controlled to 30°C $\pm$ 0.1°C . Fig. 3.13.4 shows the cooling circuits for the copper components.
The return water temperature from the magnets, of up to 60°C, offers the possibility to use this waste heat to warm the experimental hall. For that purpose a heat exchanger will be included in the return water line. If the waste heat is not sufficient, additional hot water from the central heating system will be fed in.
The heat exchanger can be operated in reverse direction so that the cooling system can be protected from freezing when the storage ring is not operating.

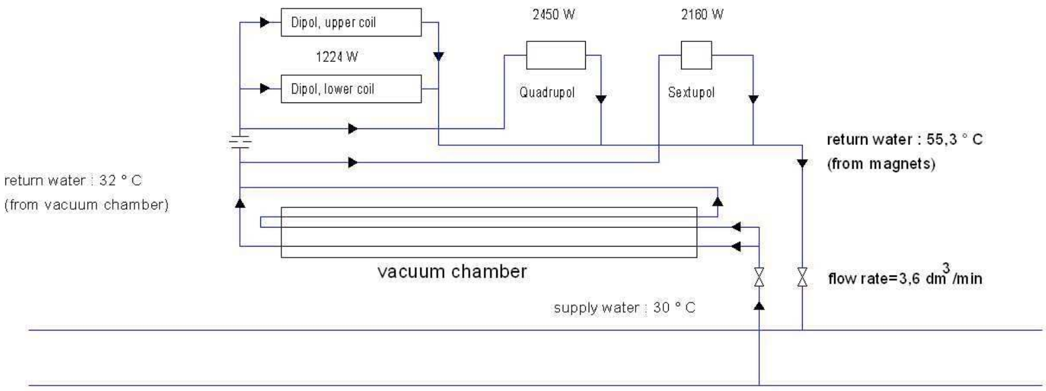

Figure 3.13.5: Scheme of the cooling of the vacuum chamber.

3.13.3 Vacuum chamber cooling system

The vacuum chambers are made of aluminum and will be supplied from the same cooling circuit as the aluminum coils. For this purpose a separate distribution pipe is provided in each octant.

To cool the vacuum chamber a significantly lower pressure is needed compared to that for the magnets. Therefore pressure reducing valves will be installed at each distribution pipe. The synchrotron radiation power density in the old seven octants is about 100 W per m. To avoid deformation the temperature and its gradient across the chamber should vary as little as possible.

The new vacuum chambers for PETRA III are equipped with cooling tubes on both sides. This setup maintains thermal stability by the use of a suitable flow rate on the inside and outside of the chamber with a low amount of cooling water. A similar system is already used successfully at DORIS. The layout proposed for PETRA III is shown in Fig. 3.13.5.

3.13.4 Air conditioning

3.13.4.1 Air conditioning of the tunnel

For the air conditioning of the tunnel four independent climate-control devices working in transverse mode are installed. Fresh air is drawn in through a weather protection barrier in the mixing chamber of the device. Recirculating air can be mixed in upon demand. After filtering and temperature adjustment, this air is blown by a ventilating fan through galvanized steel ducts into the tunnel.

The climate control devices are mounted outside the experimental hall on the southwest side. Water at a temperatures of 12(16) °C (supply / return temperature) and of 50(30) °C is used for cooling and heating respectively. The climate control devices are equipped with fire shutters to fulfil fire protection requirements. The air conditioning system for the tunnel is shown schematically in Fig 3.13.6.

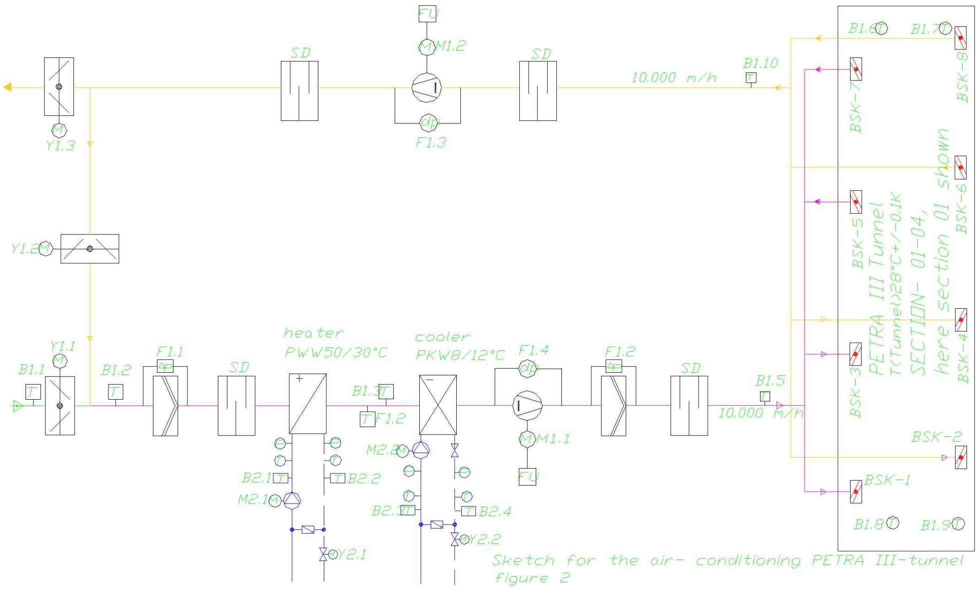

Figure 3.13.6: Air conditioning layout for the tunnel

- **Temperature control:**
  To control the air conditioning process each system is equipped with individual direct digital control (DDC) regulation. Temperature regulation is realized as a cascade control of the intake/interior air. The cascade consists of a guiding regulator and subsequent regulators. The guiding regulator adjust the air supply flow in proportion to the deviation of the temperature in the tunnel. This temperature is defined as the average value acquired from four sensors. No humidification or drying of the air is foreseen for the tunnel.

- **Technical data**

Incoming air flow rate	:	$4 \times 9.000\,\mathrm{m^3/h} = 36.000\,\mathrm{m^3/h}$
Used air flow rate	:	$4 \times 9.000\,\mathrm{m^3/h} = 36.000\,\mathrm{m^3/h}$
Ratio intake/exhaust air	:	0 – 100 % variable
Temperature in the tunnel	:	28 °C ± 0.1 °C

3.14 Radiation Safety System

3.14.1 Safety considerations

The shielding of the synchrotron light source is built to ensure total containment of the primary electrons[1] in the storage ring tunnel. The storage ring shielding is designed to absorb both primary electrons and their secondary radiation. The optical hutch shielding in turn will block bremsstrahlung and its secondary radiation only. Thus primary electron losses in optical hutches must be prevented. Therefore the separation of the synchrotron light/bremsstrahlung from the primary electrons is a key issue of radiation safety. The relevant technical component is the dipole magnet called separation dipole immediately downstream of the insertion device. A malfunction e.g. a short of this element has to be considered for two different operation modes of the storage ring:

a) Stored beam operation:

A field change of approximately 3 % leads to a total loss of the primary beam whereas a reduction of more than 90 % is necessary to direct primary electrons into the synchrotron light beam line. So the separation dipole prevents losses of primary electrons into the optical hutches under stored beam operation.

b) Injection into the storage ring:

If the separation dipole had no magnetic field during injection the primary electron would go straight into the optical hutch. A system called Safe Injection System is needed to avoid this problem.

The existing synchrotron light source DORIS III uses a Save Injection System employing beam shutters: one injection shutter in the transfer line to the storage ring and shutters in each of the synchrotron light beam lines. During transfer the injection shutter is open and all synchrotron light shutters are closed. The synchrotron light shutters can only be opened if the injection shutter is closed.

PETRA III is expected to be operated in top-up mode that means that the synchrotron light shutters stay open during injection. So a shutter based Safe Injection System cannot be used. A different system has to be implemented. There are at least two methods to achieve this: one passive and one active.

The passive solution is a permanent dipole magnet located in the synchrotron light beam line deflecting all primary particles. Advantages are no maintenance effort and no special personnel interlock system. Disadvantages are the need for additional space in the synchrotron light beam line and possible degradation of the magnetic field due to radiation.

[1] In this section the notation “electron” is used for both “electron” and “positron”.

The active solution is based on the fact that the injected beam cannot travel along a synchrotron beam line while there is stored beam in the machine. It consists of a redundant beam current monitor system which triggers a dump, if the current drops below a threshold e.g. 20 % of the nominal value. Although no extra element is required in the beam line disadvantages arise from reliability issues, high maintenance effort and the need for a special personnel interlock system. This solution seems to be the only one for upgrading existing Synchrotron Light Sources to the top-up mode (Emery & Borland, 1999b; Borland & Emery, 1999; Emery & Borland, 1999a; Luedeke & Munoz, 2002; Sanosian, 2002; Berkvens et al., 2002; Job, 2002; Casarin et al., 2002).
For PETRA III the passive solution will be chosen. Each synchrotron beam line will be equipped with a permanent dipole magnet as the Save Injection System. The permanent magnet fields will be measured once a year to ensure their integrity. Note, that this passive solution is also sufficient for start-up injection. So the PETRA III personnel interlock system will be simpler than that of DORIS III.

3.14.2 Basic machine parameters

The main parameters relevant for radiation protection are the electron energy 6 GeV and the maximum current of 200 mA corresponding to 10^{13} circulating electrons. An operation time of 6000 hours per year is assumed. The injector DESY II can deliver 10^{10} electrons at a rate of 6 Hz.

3.14.3 Beam loss scenarios

As we have seen above the primary electron beam is contained and therefore lost only inside the main storage ring tunnel and cannot exit the shielding. In the following, different beam loss scenarios are discussed.

3.14.3.1 Normal continuous beam loss

The total number of electrons injected per year has to be estimated. Two different modes are foreseen, the few bunch mode (high bunch charge) with a lifetime of 1 h and the multi bunch mode (low bunch charge) with a lifetime of 24 h. A simplified assumption of equal operation time in each mode yields 10^{13} * 3000h/1h + 10^{13} * 3000h/24h = $3*10^{16}$ lost electrons per year. If the transfer efficiency is 50 % one finally gets $6*10^{16}$ lost electrons per year.
In the worst case scenario, all electrons are considered to be lost within the new octant of length 300 m (as opposed to being equally distributed around the ring). In order to apply a simple model, this line source is translated into equivalent point sources. This model allows a simple calculation of the dose at a given perpendicular distance from the line source behind the shielding. As a rule of thumb the number of lost electrons over a length of twice the perpendicular distance to the line source is taken as the strength of the equivalent point source. This point source is located in the middle of this segment. To calculate the dose behind the shielding at 2.5 m from the line source a segment length of 5m defines the equivalent **point source with a strength of 10^{15} electrons per year**.

3.14.3.2 Accidental beam loss

Beam loss events can occur for different reasons namely malfunction of machine components or human error. Here two worst case scenarios are described:

a) Start-up injection:

Either there is an obstacle in the electron beam pipe, for instance a closed vacuum valve or a separation dipole trips and the beam is lost immediately downstream the permanent magnet inside the tunnel. In both cases no beam can be stored. One may use additional transfers to diagnose the fault. Suppose this takes an hour then 10^{10} * 6 Hz * 3600 s = $2*10^{14}$ electrons are lost. So the **point source strength is $2*10^{14}$ electrons per event.**

a) Stored beam:

A separation dipole fails due to a short. The magnetic field decays slowly compared to the 8 μs resolution time so the beam gets lost over many turns. Assuming that all the losses occur in one insertion device the **point source strength is 10^{13} electrons per event.**

3.14.4 Shielding calculations

3.14.4.1 Design goal

The experimental hall should be accessible without any restrictions. So the acquired personal dose of 1 mSv/a may not be exceeded according to the German Regulations for Radiation Protection. The shielding will designed such that the personal dose will be at least a factor of two, 0.5 mSv/a, below this limit. The machine is assumed to be operated for 6000 h/a however as an individual works at most 2000 h/a, the local dose could be 1.5 mSv/a without exceeding the goal. A beam loss event as described above is expected to occur less than five times per year. Hence the shielding should restrict the dose to 0.1 mSv per event.

3.14.4.2 Lateral shielding of the Storage Ring

Photons, low energy neutrons and high energy neutrons are the most penetrating secondary particles produced by the primary electrons. Behind thick shielding high energy neutrons mainly contribute to the dose. To minimize the space required in the experimental hall the lateral shielding is made from heavy concrete having an attenuation length of 30 cm for high energy neutrons. The following doses are calculated at a distance of 3 m from the loss point behind a 1 m thick heavy concrete wall:
For the beam loss events a target efficiency of 0.1 is applied. This is an empirical value derived from the comparison of measurements with the simple point model predictions. It takes into account that a real loss is not point-like but is distributed over a longer section of the beam pipe.

Scenario	Personal dose	Design goal	
		Pers. dose	Local dose
Normal continuous loss	0.3 mSv/a	0.5 mSv/a	1.5 mSv/a
Start-up (Dipole fault)	0.02 mSv/event	0.1 mSv/event	
Top-up (Dipole fault)	0.0009 mSv/event	0.1 mSv/event	

Table 3.14.1: Comparison of dose estimates with design goals.

The rest of the PETRA III ring is shielded by 4 m of soil equivalent to more than 2 m of heavy concrete, so it needs not to be considered here.

3.14.4.3 Shielding of an optical hutch

Interaction of the primary electrons with any atom generates bremsstrahlung. Only bremsstrahlung produced in the straight section containing an insertion device can travel along the beam line. This radiation will interact with any material in its path e.g. mirrors. In the following estimates are given for electron beam interactions with the residual gas inside the beam pipe and with its wall.

a) Gas bremsstrahlung:

A 20 m undulator is considered installed in a 61.5 m long drift section at an N_2 equivalent pressure of 5 * 10^{-10} mbar. The bremsstrahlung from this section as well as the synchrotron light from the undulator reaches the optics hutch. When the bremsstrahlung interacts with a mirror neutrons are generated. At a distance of 1 m the dose is estimated to 6 mSv/a. To remain below the design goal an attenuation by a factor of 4 will be required.

b) Wall bremsstrahlung:

Here a scaling to the TTF-II case (Leuschner, 2002) is given. Scaling based upon beam power leads to reliable results at least for the neutron yields. A loss of 10^{16} electrons at 1.6 GeV corresponds to 2.7*10^{15} electrons in our case. It leads to a neutron dose of 1 Sv at 1 m distance from the mirror. For the scenario of normal continuous loss of 10^{15} electrons per year the neutron dose is about 400 mSv/a, therefore, an attenuation by a factor of 250 is needed.

c) Shielding Requirements for the White Beam:

There are different means to reduce the neutron dose around components located in the white beam, for instance collimation (Takahashi et al., 2001) and shielding. Using shielding to attenuate the neutron doses by a factor of 4 to 250 then 20 cm to 70 cm of heavy concrete is needed. Here, heavy concrete is an economic compromise between a low-Z material against neutrons and a high-Z material against scattered electro-magnetic radiation such as bremsstrahlung and γ's. The dose level due to the latter radiation components is not accessible by a simple formula but could be much higher than that of the neutrons. In order to efficiently use the available space the losses in each beam line will be individual modelled and a consistent shielding concept will be developed. The optimization will be done using Monte Carlo codes also giving the dose fields due to the electro-magnetic radiation.

3.15 The Personal Protection Interlock System

3.15.1 Basic technology

Since DESY started to operate particle accelerators in 1962 a personal protection system against ionizing radiation exists, consisting of relays and switches. This technology is still used for the interlock logic for all accelerators. Computers were first connected to the system in 1978 at PETRA I, but only to gain status information and to handle the temporary access procedure from the control room. Here the connection between the door interlock information and the computer was realized with a separate hardware using the DESY long distance field bus system SEDAC (SErial Data Acquisition and Control System), which was developed for the PETRA I control system.
For PETRA III it is planned to replace this system by a new technology developed at DESY. This new system has been installed in 2003 for the door interlocks of the DESY II/DESY III tunnels and the Linac 2 and it is in routine use.

The parts of the new personal protection system, relevant for security are built with relays of a new generation, using forcibly guided contacts which enable a continuous supervision during operation. In comparison to a PLC (programmable logic controller) the use of wire connected relays is more transparent especially for interlock tests and maintenance.
Logic units are housed in modules. The main features of the new technology are the modularity and the integration of a computer interface with a CAN-Bus system inside the modules. Using this technique not only the door interlock (like at PETRA I) will be controlled but also the interconnections required for the beam permit.

3.15.2 Supervision of relays

One improvement of the security is the supervision of all relay functions. Usually it can only be detected, whether a relay is active or not. With forcibly guided contacts also a malfunction can be detected. This makes it possible to have a partial interlock test each time any logic status changes.
Furthermore all contacts of the relays are housed in separate compartments. So if one contact is broken no accidental connection to this contact is possible. Also if one normally open (no) active contact is burnt no normally closed (nc) contact can close and vice versa. This produces the means to detect a malfunction. At all relays in the interlock system opto couplers are used to detect the on or off status by measuring the current. The true status of a relay is determined by surveying one nc contact.

3.15.3 Modules with CAN bus interface

The advantages of computerized control become clear, when the required interface is located near the surveyed relays and all interfaces are connected by i.e. a field bus like CAN Bus to concentrate the transport of information. The logic unit modules have all been developed using the same interface board. Only a few standard modules are required to fulfill many purposes. The interface board is plugged onto the main board which carries all relays and

60V connections. The interface board (see Fig. 3.15.1) consists of two parts: the general interface with the interlock proprietary electronics, and an industrial CAN Bus controller. If this industrial controller would become obsolete, only the interface board would have to be changed to use some other commercial type of controller. Each module has its own CAN address. Each crate containing the modules has its own CAN Bus repeater. This ensures ease of maintenance.

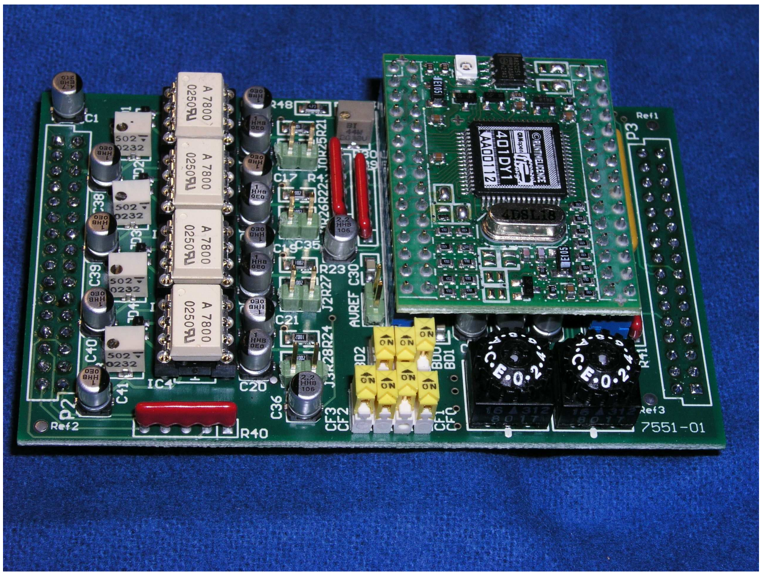

Figure 3.15.1: Interface board with plugged CAN Bus controller

3.15.4 The door interlock

Like all other components of the interlock system also the door interlock has two identical independent logic systems in this case two separate contacts at each door. In addition, the standard modules for the door interlock (see Fig. 3.15.2) have a third system which registers the status of a searched area and the locked door. Only this system has to be jumpered to open the door for a controlled access to a searched area without breaking the interlock. During this procedure the two door contacts remain active.

3.15.5 Logic for the beam permission

Another standard module was created to serve as a logic unit to process all input signals required for the beam permit. It consists of eight inputs with supervised relays and an output matrix with four trees to create logical operands as required for the door interlocks, emergency offs, key boxes, contacts of beamshutters or dumps etc. Additional modules could be easily accommodated to combine more inputs or have more combinations. Operating modes and combinations thereof will be handled with similarly constructed modules (see Fig. 3.15.3)

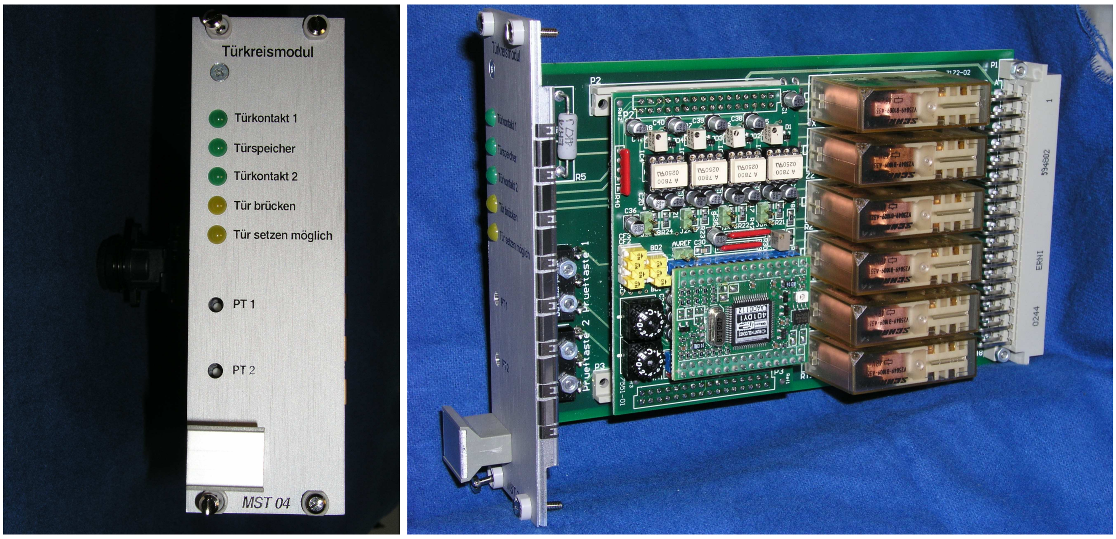

Figure 3.15.2: Door interlock module with inserted interface board

3.15.6 Integration of computer tasks

The hardware components responsible for ensuring security and the supervision and control by the computer are independent. In fact, if the computer were to fail, were to be switched off or the field bus lines were accidentally cut, then all the security logic would continue to act in a safe way. The beam permission would be interrupted given the absence of any logic input signal. On the other hand, it is impossible to set the door interlock or give any beam permission if the computer hardware is not ready.
The computer module consists of one embedded controller board in PC104 format. The module includes a CPU (133MHz) with 16 MB memory, Watchdog, EEPROM, flash disc (96MB), Com ports, Ethernet10/100Base-T, one CAN Bus port and interface for further

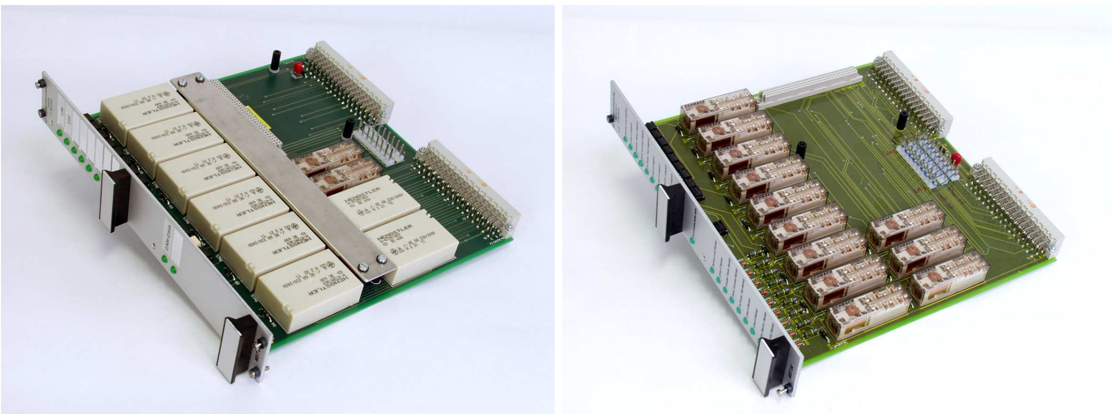

Figure 3.15.3: Logic Modules for the Beam Permit: Input module and selection logic module

plugged interface boards. Here two isolated double CAN Bus boards and one module with four isolated RS232 / RS422 (switchable) ports are used. All these boards are combined into one module with the width of 21 units. (see Fig. 3.15.4)

The operating system is ELinOS , a special Linux OS for embedded systems configurable e.g. to be booted from flash disc, which is used also for event logging. There are running several tasks for communication with the control system of the accelerators, the door interlock, permission logic, video controller, p.a. system etc. Not only the door interlock itself but some components near each door, including displays mounted on the door (e.g. Door Interlock set , Radiation, Prohibited area), the magnet holding the door shut, warning lamps etc. will be controlled by the computer. So near each door a box, the CAN Terminal Box (see Fig. 3.15.5), is installed, which is connected to the computer by the CAN Bus. This bus may be as long as one km or more.
Using this technique a new beam permission interlock has been developed realizing improving security by a combination of relays and computer. It is planned to use the new technology

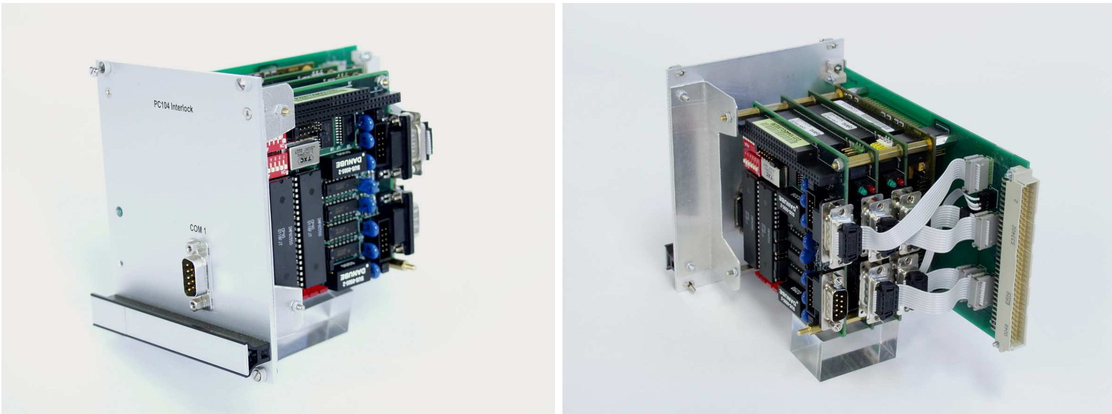

Figure 3.15.4: Computer module with interface boards

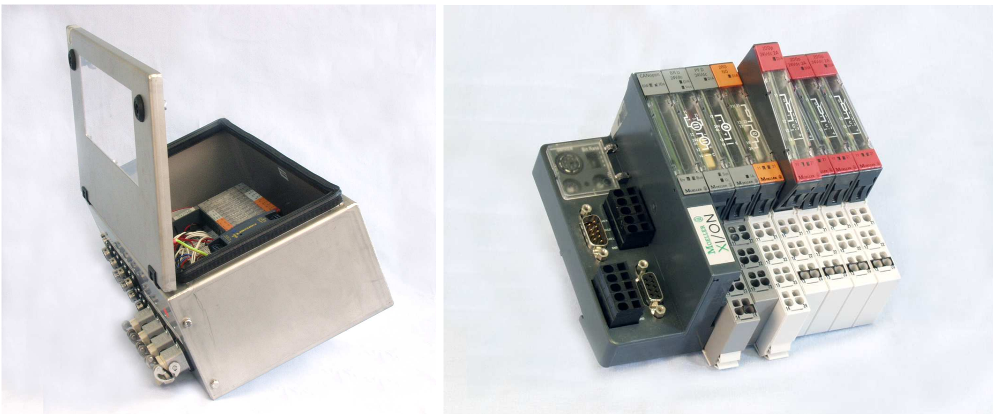

Figure 3.15.5: CAN Terminal Box and some internal components

for the complete interlock system of PETRA III. This includes components of the accelerator tunnel as well as of the photon beamline experiments and the interconnection to the injecting accelerator, the synchrotron DESY II. Further development work for the application of the system at the user controlled experimental areas has to be done.

3.16 Injector

3.16.1 Linac 2/PIA upgrade and modifications for PETRA III

3.16.1.1 Description of the components

The Linac 2 is the first accelerator in DESY's e^-/e^+ accelerator chain. It delivers either 450 MeV electrons or positrons of about the same energy for the injection into the Positron Intensity Accumulator (PIA), which is a small storage ring of 28.8 m circumference. The accelerator is operated with 50 Hz repetition rate and delivers 50 ns, 10 mA, $\Delta E/E \approx 1\,\%$ bunch trains with a bunch to bunch distance reflecting the linac's RF operating frequency of 2.998 GHz. The electron beam's time/current structure differs slightly: 20 ns, 50 mA, $\Delta E/E \approx 0.27\,\%$

The *accelerator* consists of a 150 keV electron source and two groups of 5.2 m long accelerator sections separated by the conversion target for positron production. The total length is approximately 75 m. Many of the components have been renewed during the last years. Part of the infrastructure is still from the linacs commissioned in the late 1960s.

The *injector* is based on a thermionic gun with a specially prepared cathode of 28 cm^2. The cathode is heated by electron bombardment (3 kV, 400 mA). The 150 kV gun voltage is shaped in a pulse forming network. The produced electron beam structure is: 150 keV, 6 A, 30 μs long pulses with 50 Hz repetition rate. The gun is then followed by a chopper / pre-buncher combination which delivers either 2–3 A (positron mode) or 50 mA (electron mode) in pulses of a few 10 ns. In 1999 the complete vacuum system has been rebuilt in order to allow for a quick cathode exchange. All gold wire sealing gaskets were replaced by standard Conflat type gaskets. Chopper and pre-buncher were renewed. New beam optics allows for higher electron current transmission from the gun into the first accelerator section.

The *accelerator sections* are 5.2 m long traveling wave units operated in the $2\pi/3$ mode at 2.998 GHz. The filling time is 0.74 μs, the group velocity varies from 3.5 % down to 1.3% of the speed of light. The typical accelerating gradient is 17 MV/m, corresponding to 100 MW after SLED pulse compression. The first group of accelerator sections consists of 5 units and delivers up to 450 MeV for positron production. The second group of sections has 5 plus 2 units. The additional two are used to optimize the beam energy by opposed phase detuning. Between 1999 and 2003 all 12 sections were replaced using a new design in which the water-cooling tubes have no soldered connections inside the vacuum anymore. The structures were designed, built and commissioned at DESY. The production was successful so that the technology could be transferred to industry. Identical accelerator sections are now used at other accelerators.

Each accelerator section is driven by its own *klystron* (type Thales TV 2002 DoD) and *modulator*. The typical klystron lifetime of 25,000 hours together with the operation time per year leads to a replacement of approximately 4 klystrons per year. The driving RF modulators were all renewed between 2001 and 2003. They got a complete new wiring, new charging power supplies, and new controls. Beside the housing the pulse forming network was kept.

The *positron conversion* between accelerator sections 5 and 6 is based on a 7 mm thick Tung-

sten target which is followed by a 1.8 T solenoid (3 kA, 10 μs, 50 Hz, water cooled). Two targets are available without replacing the converter unit.
Each of the two targets is 17 mm in diameter and has a 5 mm orifice for e^- operation, i.e. the electrons are passing the conversion target without hitting it, using steering coils. Although no problem occurred during the last 8 years, the target unit was replaced together with the neighboring accelerator sections in 2003.

The *Positron Intensity Accumulator* PIA is operated at 450 MeV energy and accumulates typically 1010 positrons for the injection into the DESY II storage ring. At present the ejection takes place with either 6.25 Hz (DORIS mode) or half that frequency, i.e. 3.125 Hz (PETRA mode). The Linac 2 delivers 20 ns long bunch trains.
In PIA a 10.4 MHz as well as a 125 MHz is used to produce the bunch time structure needed for the injection into DESY II. The 10.4 MHz RF system was replaced beginning of 2001 and the old transmitter was reconstructed accordingly. The 125 MHz cavity still needs to be replaced by the new one which was commissioned independent of the PIA operation in fall 2003. Installation is expected for the next shutdown.

3.16.1.2 Required modifications

Until today the Linac 2 as well as PIA are used to produce beam for either DORIS, PETRA, or HERA. The required operation time per day is of the order of hours. The consequence is that simple repair or needed maintenance can often be done between two subsequent runs. Water leaks or aged cables can be replaced whenever needed. For the planned top-up operation of PETRA III a careful check of all components is required. In the following a complete list of action items is given.

The *electron gun* needs either a renewal of the modulator or a complete new design. The modifications of the modulator will be similar to the reconstruction of the modulators driving the accelerator section.

The alternative is a completely new design. A motivation to consider this is the fact that the ceramic used for the 150 kV isolation separates the beam line vacuum from the oil surrounding all the back parts of the gun. At present a study is under preparation which compares the used gun with the much more common triode design. The effort for the modulator modifications is well known. A new gun design requires additional resources in terms of FTE and money. Some spare *accelerator sections* are needed. They must be conditioned and stored under vacuum in order to allow for a quick exchange. Four of these sections are underway.
During the operation of the *modulators* the lifetime of the thyratrons as well as their reservoir voltage needs attention. For PETRA III operation the thyratrons will be replaced by a new long living type which presently is under test. The adjustment of the thyratron voltage will be possible without switching off and opening the modulator.

As long as positrons are foreseen for the operation of PETRA III the quick exchange of the *positron converter* in case of problems (vacuum or water leak) is a problem. After turning down the linac, about 4 weeks decay time are needed before technicians can access the

components. Therefore it is necessary to design a new conversion target which avoids all soldering between vacuum and water cooling. The new design could have a non-movable target inside a ceramic cylinder and the focusing solenoid outside the vacuum system. Local lead shielding could be part of the converter unit. The risk of vacuum problems would be clearly reduced. Due to the local shielding the exchange should be possible in a much shorter time.
Systems like *water pump stations, magnet power supplies, magnets, controls* must be state of the art. Spares must be available wherever longer repair time is estimated. This clearly improves the reliability as well as availability of the Linac 2 and PIA.

3.16.1.3 Needed resources

The resources needed in terms of money and FTE were identified. With an uncertainty of 30 % the Linac 2/PIA modifications need an additional amount of approximately twice the yearly operations budget. The funding profile is known. With respect to the needed FTE the assumption is that most of the modifications could be done together or instead of the anyhow required maintenance and preventions. The re-design of the positron converter and a new gun / injector design will require additional person power.

3.16.2 DESY II

At present, the DESY II synchrotron accelerates single bunches of positrons or electrons from an injection energy of 450 MeV to either 4.5 GeV, for transfer to DORIS, or to 7 GeV for injection into PETRA II and for three internal test beam experiments. The 5 families of synchrotron magnets are powered using resonant circuits, which cycle at 12.5 Hz and include regulation hardware to ensure accurate tracking.

The injection frequency f_{inj} of DESY II is determined by the accumulation time in the upstream intensity accumulator (PIA). Injection nominally takes place at 6.25 Hz in DORIS mode or 3.125 Hz in PETRA mode, for which high single bunch intensities (I_{sb}) of up to 3×10^{10} particles per bunch (ppb) are accumulated with a 50 Hz injection rate in PIA. The flexible timing system would allow the accumulation time in PIA to be shortened to match the 12.5 Hz repetition frequency of DESY II thus allowing maximally efficient injection into PETRA III with single bunch intensities in the range of $I_{sb} = (1...5) \times 10^9$ ppb. Maintaining the currently used intervals for accumulation in PIA, $I_{sb} = (0.1...1.5) \times 10^{10}$ ppb, f_{inj} = 6.25 Hz, and $I_{sb} = (0.1...3.5) \times 10^{10}$ ppb with f_{inj} = 3.125 Hz may be easily accommodated.

Within a measurement accuracy of a few percent, the injection and extraction efficiencies into and from DESY II are $\sim 100\,\%$. Transmission through DESY II typically exceeds $90\,\%$.

The theoretical horizontal beam emittance at extraction from DESY II is presently 860 nmrad at 7 GeV for PETRA II and is 325 nmrad at an extraction energy of 6 GeV for PETRA III. The reduction in emittance results from the lower energy and deactivation of the presently used frequency modulation, which is used at the expense of increased horizontal emittance to detune the cavities to compensate for beam loading at high beam currents. While not considered in the design concept for PETRA III, further reductions in emittance might be achievable using a higher phase advance per cell in DESY II and/or by retuning the cavities and invoking a frequency shift during the acceleration cycle. The implications of these options are under study.

The high level of performance in terms of delivered beam and reliability of the DESY II synchrotron is the result of continual refurbishment and modernization of the accelerator subsystems. The
DESY II and DESY III synchrotrons contribute only a few percent of the overall down time of the existing accelerator facilities (including HERA). In the future, to assist in identifying potential weaknesses, software improvements will be made to detect out-of-tolerance hardware errors and to better automate logging of component failures. Also the RF cavity control systems will be modernized and the 10 kV power transformer station will be renewed. Prior to commissioning of PETRA III, the sections of the vacuum chambers common to the DESY II and DESY III accelerators will be separated to decouple the two subsystems.

To ensure reliable and optimum performance of DESY II over the first decade of PETRA III operation, three major upgrades have been identified (see Sec. 3.13 and 3.12): renewal of the water cooling systems, replacement of the RF transmitter power feed systems, and replacement of the main synchrotron magnet power supplies. Smaller improvements foreseen for the long-term include upgrading of the low voltage switching systems, replacement of the correction magnet power supplies. Minor improvements aimed at higher reliability of the RF systems, and the design and construction of a high dynamic range current monitor for detection of unwanted satellite bunches are planned.

While PETRA III is being commissioned and/or in operation, it is foreseen that DESY II continues to serve as an injector for DORIS. With PETRA III injecting in top-up mode, the presently used option of independent setting of the DESY II extraction energy may not be compatible. In this case, ejection to DORIS will take place during the energy ramp of a 6 GeV PETRA III cycle as has been demonstrated to be feasible in the past.

Preliminary tests of 'top-up' mode injection, as foreseen for PETRA, have been performed in DORIS. Automated transfers at fixed bunch current have yielded so far a uniformity in total current of 0.5 %.

Chapter 4

Radiation Sources

4.1 Insertion Devices

4.1.1 Introduction

The new octant of PETRA III houses 8 straight sections, each providing space for a 5 m long insertion device. As discussed in Sec. 3.2.1 several of these straights will be split into two sections for 2 m long devices with a 5 mrad bent in-between. This scheme of canted undulators, which feed different experimental beamlines and can be operated independently from each other, has successfully been installed also at other facilities (Elleaume, 2002; P. Den Hartog, 2003) in order to enlarge the number of independent undulators within one straight section. At present, 4 straights are proposed to be equipped with altogether eight 2 m insertion devices (IDs). Furthermore, a long straight section upstream of the new PETRA III arc is available to place a 20 m long undulator. In total there will be 13 undulator beamlines in the new arc. Three different planar hybrid undulators and three special devices are planned, namely a helical undulator of APPLE2 type, a quasi-periodic undulator and a long device for the 20 m straight.

The radiation characteristics of undulators and wigglers have been described in detail in numerous publications (e.g. Alferov, Bashmakov & Bessonov, 1974; Walker, 1993; Kim, 1995; Onuki & Elleaume, 2003). Here, only a few fundamental properties and approximations are briefly summarized for easier assessment of the proposed insertion devices.

The peak field B_0 in a periodic magnet structure with period length λ_U strongly depends on the magnetic gap g and can be approximated by (Elleaume, Chavanne & Faatz, 2000)

$$B_0 = a \cdot \exp\left[b\left(\frac{g}{\lambda_U}\right) + c\left(\frac{g}{\lambda_U}\right)^2\right] \tag{4.1.1}$$

with the parameters a, b, c depending on the applied magnet technology (e.g. a= 3.69, $b = -5.07$, c=1.52 for hybrid devices with vanadium-permandur pole pieces). The deflection parameter K is a measure for the interaction strength of the electron beam with the magnetic field B_0 of the insertion device and can be written in practical units as

$$K = 0.934 \cdot \lambda_U\,[cm] \cdot B_0\,[T]. \tag{4.1.2}$$

K/γ describes the maximum deflection angle of the electron, with $\gamma = E/(m_e \cdot c^2)$. The maximum transverse beam excursion for the PETRA III undulators is approximately $x_0 \sim 2\,\mu$m. The wavelength and spectral width of the undulator harmonics n is given by

$$\lambda_n = \frac{\lambda_U}{2n\gamma^2}\left(1 + \frac{K^2}{2} + \theta^2\gamma^2\right) \quad \text{or} \quad E_n[keV] = \frac{0.95 \cdot n \cdot E\,[GeV]^2}{(1 + K^2/2 + \theta^2\gamma^2)\,\lambda_U\,[cm]} \tag{4.1.3}$$

$$\frac{\Delta\lambda}{\lambda} = \frac{\Delta E}{E} \approx \frac{1}{nN} \tag{4.1.4}$$

where θ is the observation angle of the radiation and N is the number of undulator periods. On the other hand, the continuous spectrum of wiggler radiation ($K \gg 1$) is characterized by the critical energy

$$E_c = 0.665 \cdot E\,[GeV]^2 \cdot B_0\,[T] \tag{4.1.5}$$

The total radiation power generated by an insertion device with length L is

$$P_{\text{tot}}\,[kW] = 0.633 \cdot E\,[GeV]^2 \cdot B_0\,[T]^2 \cdot L\,[m] \cdot I\,[mA] \tag{4.1.6}$$

The spectral characteristics of undulators is often described by the brilliance, i.e. the flux F_n within the central cone of the n-th harmonic normalized to the 4-dimensional phase space volume

$$B_n = \frac{F_n}{4\pi^2\sigma_{Tx}\sigma_{Ty}\sigma_{Tx'}\sigma_{Ty'}} \tag{4.1.7}$$

The flux integrated over the central cone of the n-th harmonics can be written as

$$F_n\,[ph/s/0.1\%BW] = 1.43 \cdot 10^{14} \cdot N \cdot I\,[A] \cdot Q_n(K) \tag{4.1.8}$$

where $Q_n(K)$ ranging from 0 to 1 represents a sum over Bessel functions taking into account the angular characteristics of the emitted radiation.

The quantities σ_{Tx} and $\sigma_{Tx'}$ denote the total RMS source size and divergence, and are a convolution of the finite electron beam size (σ_x, $\sigma_{x'}$) and the natural photon beam size (σ_r, $\sigma_{r'}$) caused by a single electron.

$$\sigma_{Tx} = \sqrt{\sigma_x^2 + \sigma_r^2} \quad ; \quad \sigma_x = \sqrt{\epsilon_x\beta_x} \quad ; \quad \sigma_r = \frac{\sqrt{2\lambda L}}{4\pi}$$
$$\sigma_{Tx'} = \sqrt{\sigma_{x'}^2 + \sigma_{r'}^2} \quad ; \quad \sigma_{x'} = \sqrt{\frac{\epsilon_x}{\beta_x}} \quad ; \quad \sigma_{r'} = \sqrt{\frac{\lambda}{2L}} \tag{4.1.9}$$

Different definitions of $\sigma_{r'}$ and σ_r as a Gaussian approximation of the line shape function are used in the literature; the ones used here follow Kim (1995) and others. In low emittance storage rings, two limiting cases of brilliance usually appear: In the VUV energy regime, the radiation is mostly diffraction-limited ($B \rightarrow \sim F_n/\lambda^2$) while for higher X-ray energies the photon beam size is defined by the electron beam emittance ($B \rightarrow \sim F_n/\epsilon_x\epsilon_y$). Also, the brilliance definition does not include the energy spread of the electron beam which is

typically in the order of $\sim 10^{-3}$ in a storage ring and may lead to additional broadening of harmonics, i.e. brilliance degradation, for very long undulators. Apart from the fact that experimentally only the integrated flux F_n or the angular flux density $dF_n/d\Omega$ can be measured, the brilliance describes the figure of merit of a radiation source as it includes important properties like high flux, small source size and divergence, and small bandwidth. Depending on the sort of experimental station, the brilliance or the integrated flux through a certain aperture describe the radiation requirements more appropriate.
All calculations have been done with the codes SPECTRA (Tanaka & Kitamura, 2001) or SRW (Chubar & Elleaume, 1998) using the nominal operation parameters for PETRA III (Tab. 3.1.1) and β functions according to Tab. 2.2.2.

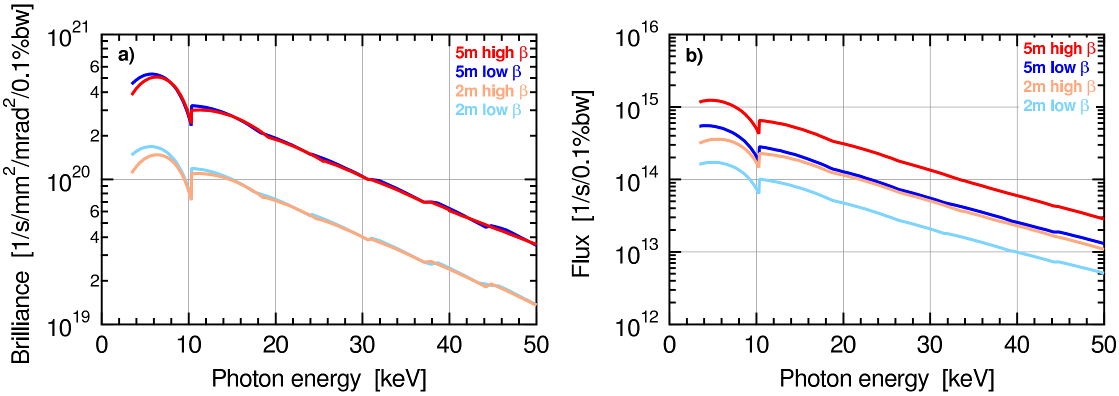

Figure 4.1.1: Effect of undulator length and β-function on a) the brilliance of a standard undulator and b) the partial flux through an aperture of 1×1 mm^2 at 40 m source distance.

The electron optics is very flexible in the new arc of PETRA III. The lattice is of Double Bent Achromat (DBA)-type with one dispersion-free section per cell for installation of undulators (Sec. 3.2.1). The twiss parameters of each DBA cell can be adjusted in two complementary settings according to the requirements of the particular experimental station. Fig. 4.1.1 compares brilliance and flux through an aperture of short and long undulators for low and high β optics at nominal operation parameters. Within 20%, the brilliance is the same for both optics as it is largely dominated by the electron phase space. The partial flux increase with undulator length is roughly linear for energies above 20 keV, only towards low energies the increase is up to a factor $\sim$3.6, i.e. $\sim$N$^{1.4}$, mostly due to the natural divergence $\sigma_{r'} \sim 1/\sqrt{L}$ dominating the total vertical divergence. Typical source size values are given in Tab. 2.2.2.

4.1.2 Design and manufacturing issues

The minimum magnetic gap has been deduced from the vertical acceptance of 2.2 mm mrad intended for the undulator locations. This value corresponds to a minimum vertical inner half aperture of 3.5 mm equivalent to about $10{\cdot}\sigma_y$ of the injected beam which has been confirmed by tracking calculations (Sec. 3.2.1). Considering 1 mm wall thickness of the vacuum chamber and allowing for 0.5 mm tolerances, a minimum magnetic gap of 9.5 mm results for all IDs within the new arc. This value is considered for all the planar hybrid devices. For the soft X-ray APPLE2 undulator as a pure permanent magnet device, a minimum gap of 10 mm has been chosen to provide space for the placement of shims.

Regarding the magnetic field quality, the requirements for the PETRA undulators are stronger to some extent than those of today's 3^{rd} generation sources as the expected gain in emittance has to be preserved in the insertion devices in order to accomplish the expected brilliance. Tolerance limits for the residual field integrals and the integrated multipole errors of the undulators can be assumed to be the same as for the dipole magnets around the ring. A specification for a transverse good-field region has been defined to k_x=0.1 in a generalized case (Sec. 3.2.2) and will be reassessed by tracking calculations in the detailed design phase. The phase error plays an important role for storage ring undulators as it critically determines the quality of the higher undulator harmonics. It has to be kept as small as possible to maintain the spectral purity and intensity of the harmonics which become more and more sensitive to phase jitter. Today's state of the art technology achieves values down to a few degrees.

The permanent magnet technology has been very well elaborated in the past. Pure permanent magnet and hybrid devices are equally established, the latter providing slightly higher fields but requiring more effort in magnetic design and field error correction. While NdFeB magnets are used in conventional devices for the most part due to their large remanence field, SmCo material is usually applied where higher radiation exposure otherwise might possibly lead to a local demagnetization damage, e.g. in small gap in-vacuum undulators.

Sufficient radiation protection of the undulator structures is crucial for a long-term steady state operation of a user facility as any demagnetization spoils the radiation characteristics in an undefined way. This is especially important since top-up operation as a key feature requires injection at closed gap. It is therefore planned to install a dedicated collimator in the storage ring which adequately confines the injected beam (Sec. 3.2.1).

At present, three different types of planar hybrid devices are considered with two different lengths together with a quasi-periodic undulator as a modified fourth type. Standardization of the mechanical support frame, the magnet girders, the gap drive and motion control system are a mandatory design issue. Design studies for a mechanical support structure and magnet girders have already begun. Also here, requirements are somewhat more demanding in terms of stiffness and gap positioning accuracy than for today's facilities in order to cope with the expected emittance. Specifications can be reached with today's technology. The same holds for the motion control system. All these activities are strongly connected to parallel developments for the XFEL project and will mutually benefit from each other.

For the construction and manufacturing of the proposed APPLE2 undulator (Sec. 4.1.6) and an in-vacuum undulator possibly desired for the long 20 m straight section (Sec. 4.1.8), no detailed experience is available in the laboratory at present. Both technologies have been well established in recent years so that both insertion device types are available commercially meanwhile. It is planned to design these devices in close collaboration with well-experienced other laboratories, to assemble them in industry for the most part, and to measure and shim these undulators at DESY.

4.1.3 Standard undulator

The large majority of all experimental techniques demands wavelength tunability of the photon source. Even if the photon energy is constant during an individual scan, a large continuous energy range has to be accessible to develop full strength of the various experimental methods. For PETRA III parameters, a tunability requirement in the X-ray regime essentially fixes all other ID parameters once magnet technology, minimum magnetic gap etc. are defined. Full energy tunability with a smooth transition between 1^{st} and 3^{rd} harmonics is obtained for a maximum deflection parameter K $\gtrsim$ 2.2. Together with the related period length λ_U = 29 mm, the 1^{st} harmonics falls to E_1 = 3450 eV. This complies with the appropriate low energy limit of ≈5 keV for most X-ray techniques. Tab. 4.1.1 shows some relevant parameters of the PETRA III standard undulator.

	Standard ID	Spectroscopy ID
Minimum magnetic gap	9.5 mm	9.5 mm
Period length λ_U	29 mm	31.4 mm
Length L	2 m or 5 m	2 m or 5 m
Peak field B_0	0.81 T	0.91 T
Deflection parameter K_{max}	2.2	2.7
1^{st} harmonic E_1	3450 eV	2400 eV
Total Power P_{tot}	7.5 kW	9.5 kW
On-axis power density	0.19 W/μrad^2	0.20 W/μrad^2
Power in 1×1 mm^2 at 40 m	119 W	125 W
High-β source (10 keV)	140×5.6 μm^2	7.9×4.1 μrad^2
Low-β source (10 keV)	36×6.1 μm^2	28×4.0 μrad^2

Table 4.1.1: Parameters of the X-ray undulators. Power and source size values are given for a 5 m long device and 100 mA beam current.

The expected brilliance of this device is displayed in Fig. 4.1.2 for a 5 m long device in a high-β section. As discussed above, the brilliance of the PETRA III IDs depends only to a small extent on the electron optics in the particular straight section. Brilliance values in the order of 10^{20} ph/(s mm^2 mrad^2 0.1%bw) will be obtained in the energy range up to 30 keV covered by the 1^{st} to 7^{th} harmonics. Higher undulator harmonics will show up throughout the entire energy spectrum though their intensity gradually deteriorates with respect to the ideal magnet structure due to the more affecting phase error for higher harmonic numbers. At energies of ≈100 keV, the undulator can therefore be more regarded as a wiggler-like device with a bumpy but almost continuous spectrum. Fig. 4.1.3 shows the partial flux through an aperture of 1×1 mm^2 at a distance of 40 m corresponding to a solid angle of 25×25 μrad^2 for a high-β section. The spatial flux density for low and high-β optics is compared in Fig. 4.1.4 for the 1^{st} and 3^{rd} harmonics.

A maximum power density of 0.19 W/μrad^2 corresponding to 119 W/mm^2 at 40 m source distance has to be expected for on-axis radiation (Fig. 4.1.5). As also the vertical distribution is nearly uniform over 1 mm^2 on-axis, this value also corresponds to the total power deposited on this area in 40 m distance.

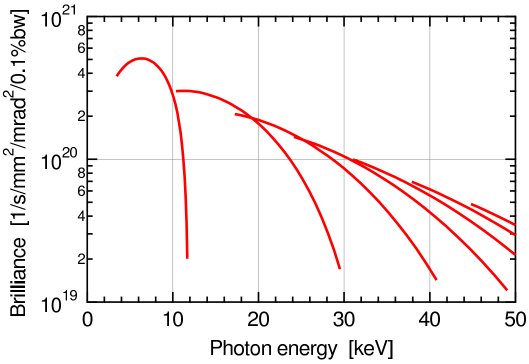

Figure 4.1.2: Calculated brilliance of the standard undulator providing full tunability (K_{max}=2.2). Parameters: 5 m ID length, high β-section, nominal electron beam parameters.

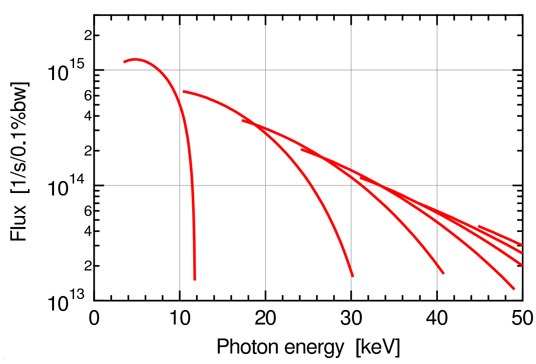

Figure 4.1.3: Partial flux of the standard undulator through an aperture of 1×1 mm^2 at 40 m distance from the source.

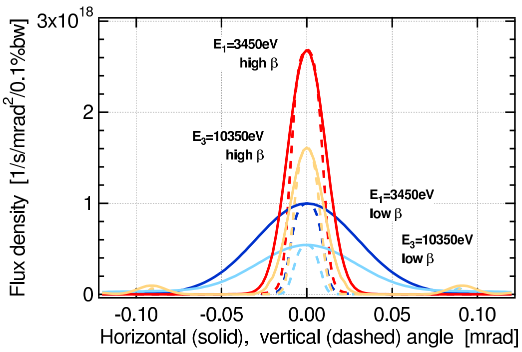

Figure 4.1.4: Angular flux density distribution for the 1st and 3rd harmonics of the standard undulator in case of high and low β-optics, respectively.

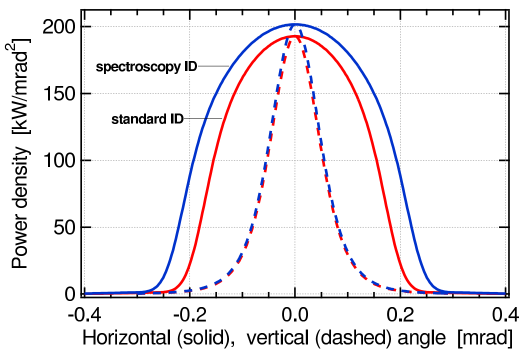

Figure 4.1.5: Horizontal and vertical power density distribution of the standard and spectroscopy undulator. The slightly larger distribution of the spectroscopy ID reflects its somewhat larger K parameter.

4.1.4 Spectroscopy undulator

Although the standard undulator provides radiation down to 3.5 keV, several spectroscopic techniques require photon energies below that. As a user demand an undulator for spectroscopy purposes should be an energy tunable device with the 1st harmonics at E_1 = 2.4 keV, the latter criterion being the more constrictive condition. This undulator needs a period length of λ_U = 31.4 mm corresponding to K_{max} = 2.7 which is comparable to the standard

ID. Undulator parameters are summarized in Tab. 4.1.1. Power density and source size are very similar to those of the standard undulator but the emitted total power $P_{\rm tot}$ scaling with B^2 is 27% higher than that of the standard ID. Figures 4.1.6 and 4.1.7 show brilliance and partial flux through a 1×1 mm^2 aperture at 40 m distance from the source. With respect to the standard undulator, brilliance and flux of this ID are only slightly lower which is mainly due to the 10% smaller number of periods related to the enlarged period length.

In certain experimental techniques like XAFS, the primary photon energy is varied for each data point; a spectrum might cover a scan range of 200 to 1500 eV. For PETRA III undulators with a spectral width of $\approx$1% or below, this requires a combined move of the undulator gap together with the monochromator in order to preserve the high intensity of the particular harmonics. Fig. 4.1.8 shows the relation between gap and photon energy for different harmonics and illustrates the scan speed assuming a constant gap velocity of 1 mm/s. With a scan speed of at least 500 eV/s (depending on gap value and harmonic number), the actual gap move of the undulator will not be the limiting factor in a fast point-per-point measurement. For special time-resolved studies, a point-per-point measurement will be too slow and data have to be taken on the fly. There are two ways to do this for energy scans much wider than the spectral width of the undulator harmonics: The best method to do so is a simultaneous, synchronized gap movement together with the monochromator along a predefined path. The actual path will be a function of the absolute energy, energy range, scan speed, gap, and harmonics number. This scheme requires very stable and precise components, both for the gap drive and the monochromator; appropriate flexibility in motion control systems is state of the art. Alternatively, a taper can be introduced in the magnet structure of the undulator to broaden the energy spectrum artificially. In this case the undulator would be adjusted before and remain silent during measurement.

Introducing a magnetic taper is equivalent to applying a (systematic) phase error to the magnet structure and, therefore, degrades the interference condition for the generated radiation. Because of that a magnetic taper always decreases the spectral intensity of the undulator. On the other hand, tapering is a good means to create a pink beam with distinct properties (Lai

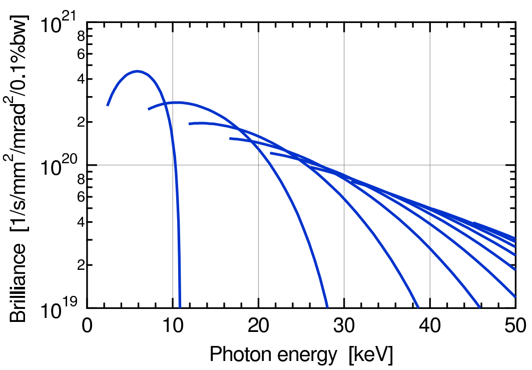

Figure 4.1.6: Calculated brilliance for the spectroscopy undulator designed for a minimum accessible energy E_1=2.4 keV (parameters: 5 m ID length, high β).

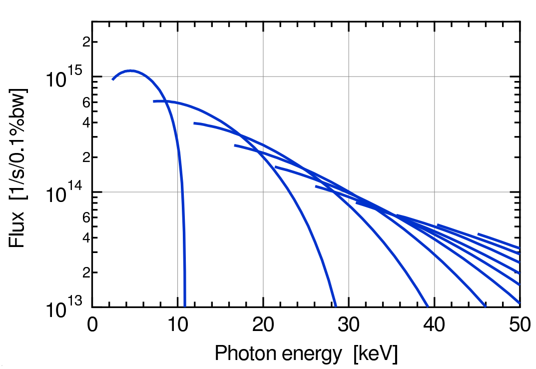

Figure 4.1.7: Spectroscopy ID: Partial flux through an aperture of 1×1 mm^2 at a source distance of 40 m.

et al., 1993). The bandwidth increase due to taper can be approximated by

$$\frac{\Delta E}{E} = \frac{K^2}{1+K^2/2} \cdot \left(\frac{\Delta g}{\lambda_\mathrm{U}}\right) \cdot \left(b + 2c\frac{g}{\lambda_\mathrm{U}}\right) \tag{4.1.10}$$

where E is the energy corresponding to the average K parameter at the mean gap g in the undulator, and Δg is the applied taper (see Eqs. 4.1.1 and 4.1.3). The bandwidth increase is about linear with Δg, and should be convoluted with the bandwidth in the untapered case (Eq. 4.1.4) to obtain the total bandwidth. The spectral intensity decreases according to the total bandwidth increase. In general, a tapered undulator still exceeds a wiggler by at least one order of magnitude in flux density, and only for extreme taper the harmonics will overlap and the spectral properties fade to the frequency averaged wiggler case. Furthermore, the spatial distribution of the undulator harmonics is increased, the opening angle will be determined by the K value of the low gap end of the tapered device.

Fig. 4.1.9 illustrates the spectral distribution of the spectroscopy ID for different taper values. For a gap taper of about 0.6 mm, corresponding to a difference in the resonance energies of 13% between entrance and exit of the undulator, the spectral distribution broadens to roughly 260 eV and 880 eV (FWHM) for the 1^{st} and 3^{rd} harmonics, respectively. An intensity decrease by a factor ≈ 10 has to be accepted for this taper amount. It can also be seen in Fig. 4.1.9 that the spectral distribution contains some fine structure with a variation of $\approx 10\%$ depending on the particular taper setting.

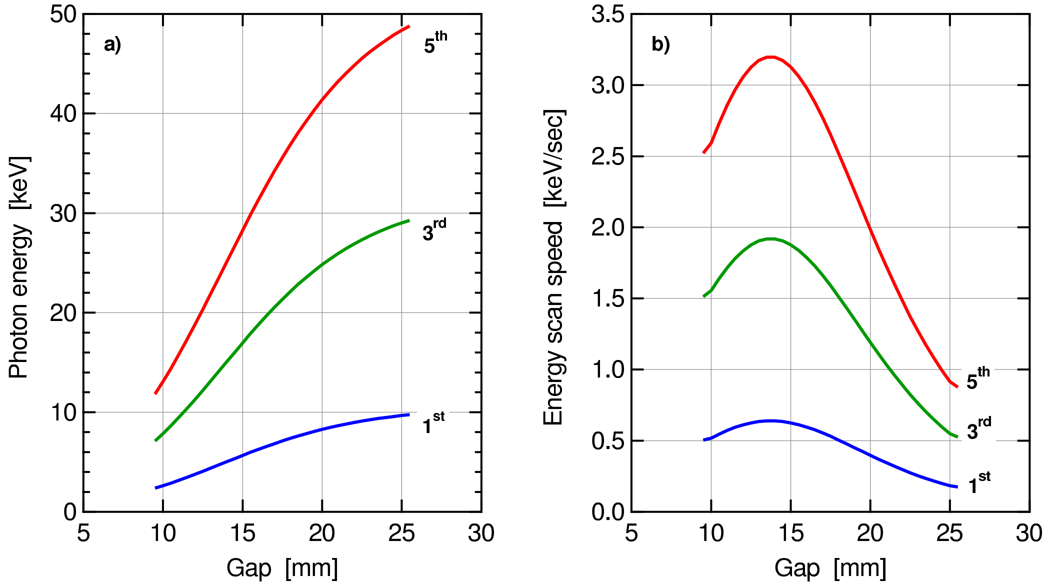

Figure 4.1.8: a) Dependence of photon energy on magnetic gap for different harmonics of the spectroscopy undulator. b) Estimation of the energy scanning speed considering a gap change of 1 mm/s.

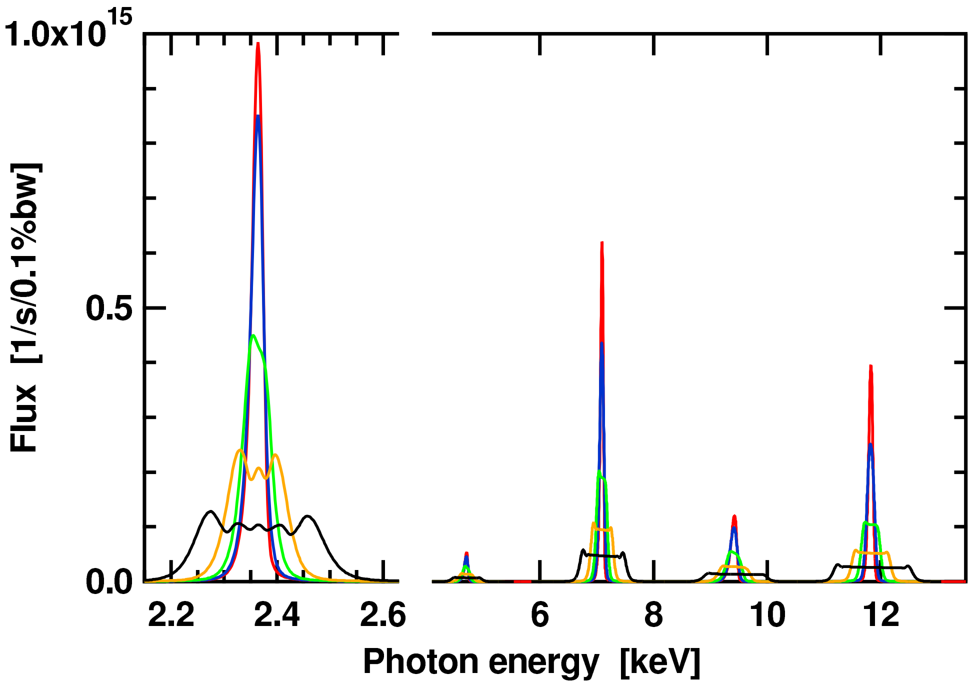

Figure 4.1.9: Spectral flux distribution through $1 \times 1\,\text{mm}^2$ at 40 m source distance for the spectroscopy undulator at different taper settings (0, 60, 150, 300, 600 μm). The line width of 1.1% (0.7%) at the 1^{st} (5^{th}) harmonic in the non-tapered case (red) broadens to about 11% (13%) FWHM for a taper of 0.6 mm (black) corresponding to 260 eV (1500 eV). At the same time, the intensity drops by roughly a factor of 10.

4.1.5 Hard X-ray source

Hard X-ray radiation will be required at PETRA III for various material science applications. The parameter choice for a device optimized for energies of 100 keV and above also depends on the desired beam spot size on the sample. Clearly, a strong wiggler provides the highest total flux, however, it radiates into a huge solid angle which is only of little use for the downstream X-ray optics. Moreover, such a device is not really appropriate for a storage ring trimmed towards lowest emittance. Instead, the insertion device with a given length has to be optimized in terms of maximum flux density through a useful aperture. Fig. 4.1.10 compares the angular flux density at an energy of 100 keV for permanent magnet devices with different period length. A maximum flux density of $7 \cdot 10^{15}$ ph/(s mrad^2 0.1% BW) can be obtained for this particular photon energy with a moderate wiggler with 49 mm period length and K = 7.7 (Tab. 4.1.2).

Fig. 4.1.11 shows the flux through an aperture of $1 \times 1\,\text{mm}^2$ at 40 m source distance as function of energy for different insertion devices under consideration. This comparison is representative for this particular aperture, proportions do change especially for larger apertures (compare Fig. 4.1.10). Here, the standard undulator and the spectroscopy ID are treated as wigglers with their maximum K parameter as the high harmonics at energies above $\approx$70 keV largely overlap and even a small residual phase error will smear the spectral structure for the

	Hard X-ray ID
Minimum magnetic gap	9.5 mm
Period length λ_U	49 mm
Length L	2 m or 5 m
Peak field B_0	1.68 T
Deflection Parameter K_{max}	7.7
Critical energy E_c	40.2 keV
Total Power P_{tot}	32 kW
On-axis power density	0.24 W/μrad^2
Power in 1×1 mm^2 (L=40 m)	148 W
Beam divergence at 100 keV	470×70 μrad^2

Table 4.1.2: Parameters of the hard X-ray source. Power values are given for a 5 m long device at 100 mA beam current.

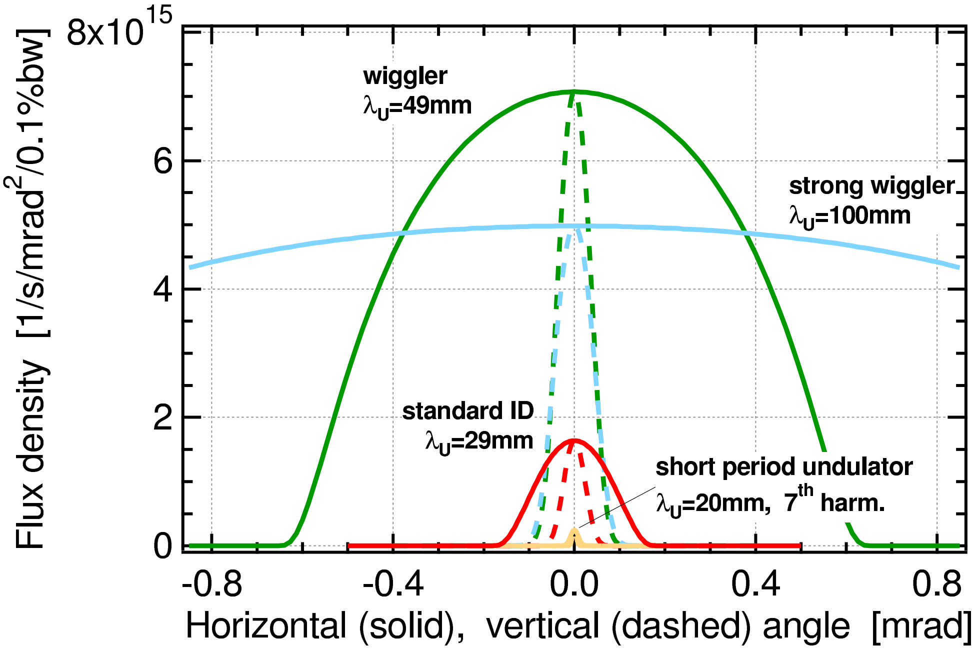

Figure 4.1.10: Angular distribution of the proposed hard X-ray device (λ_U=49 mm) at an energy of 100 keV. For comparison, the flux density is also shown for the standard undulator, a dedicated short period undulator, and a strong wiggler. For operation primarily at 100 keV, the two latter options are inadequate.

most part. On the other hand, a dedicated short period undulator with λ_U = 20 mm will have its 9th harmonics at $\approx$111 keV and will show clear undulator behavior. Such a device will be tunable only at energies above 87.6 keV (7th harm.) but regarding an aperture of 1×1 mm^2,

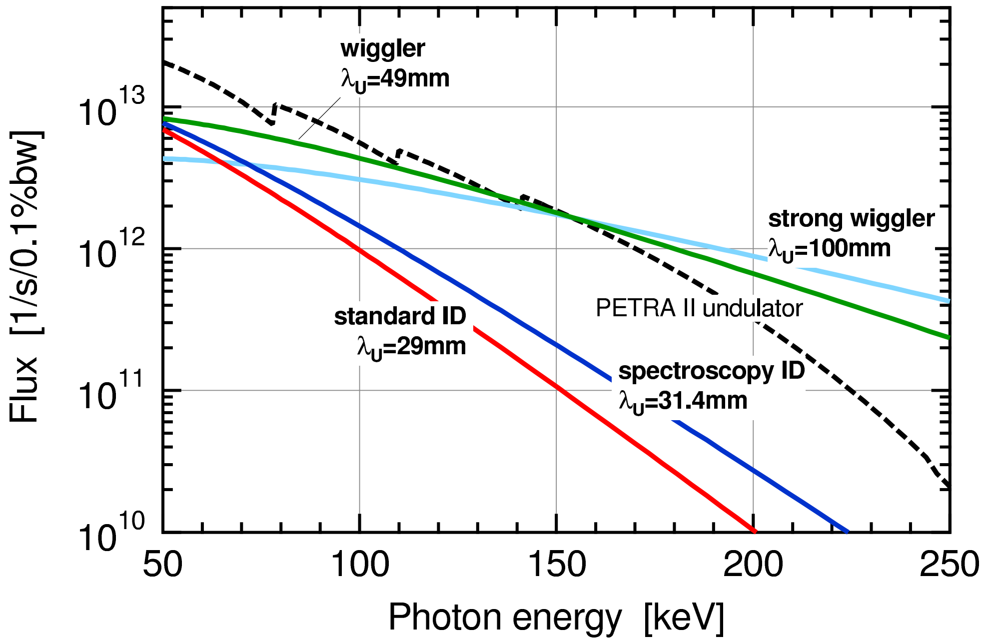

Figure 4.1.11: Spectral flux through $1\times1\,\text{mm}^2$ at 40 m for the hard X-ray wiggler (λ_U=49 mm, K=7.7). Though a stronger wiggler would slightly excel the proposed device above 150 keV it would be unfavorable due to power considerations. The performance of the standard and spectroscopy undulator in this energy range are shown for comparison (here, both devices are treated as wigglers). Finally, the spectral flux of the today's PETRA II undulator is shown for a source distance of 100 m.

it will be superior to a wiggler only at energies below ≈70 keV and cannot compete at higher energies due to the rather low K parameter (0.87). The total emitted power is not more than ≈2.5 kW.
Considering a beam acceptance of $25\times25\,\mu\text{rad}^2$, the optimum PETRA III device for energies around ≈100 keV and above is a wiggler with λ_U = 49 mm and K_{max} = 7.7. It should be noticed that this hard X-ray device will even meet the performance of today's PETRA II undulator which largely benefits from the high electron energy (12 GeV) of this machine.

4.1.6 Variable polarization soft X-ray undulator

A soft X-ray beamline in the VUV regime providing circularly polarized radiation is a very versatile instrument especially at storage rings operating at higher energies (Brookes et al., 1998; Saitoh, Nakatani & Matsushita, 1998). An undulator for this purpose covers the entire energy range of experimental interest by the 1^{st} harmonic which provides complete (100 %) circular polarization. At low energy storage rings devoted to the soft X-ray regime, energies above ≈800 eV can be accessed only by higher (3^{rd}) harmonics which do not exhibit full circular polarization. Instead, a trade-off has to be used between elliptical polarization and the obtained flux. In the energy range above ∼5 keV, circularly polarized X-rays can be produced very efficiently with maximum and constant polarization degree by means of a quarter wave plate (Lang, Srajer & Dejus, 1996) from a linearly polarized beam (Sec. 6.15). Because of strong absorption, however, this scheme does not work in the soft X-ray regime

where the particular polarization has to be imprinted from the very first in the undulator.
A momentous user demand for this soft X-ray undulator is the variability of polarization, i.e. both switching from left- to right-handed radiation and also tilting the linear polarization vector from the horizontal to the vertical plane. Therefore, an APPLE2-type (Advanced Planar Polarized Light Emitter) undulator (Sasaki et al., 1993) is proposed which provides full flexibility in this respect. In such a device the desired polarization is selected by a parallel or antiparallel shift of the longitudinally separated magnet rows. For zero longitudinal shift, the APPLE2 provides horizontal linear polarization and resembles a usual planar pure permanent magnet undulator.
A truly helical undulator has the peculiarity, that only the 1^{st} harmonics radiation falls on-axis while all higher harmonics are emitted in rings. Because of that the on-axis power density is drastically reduced which is very advantageous for the heat load-related properties of high performance optics. One possible option for this beamline could be to split the insertion device into two 2 m undulator segments. Then, circularly polarized radiation with opposite helicity of the two IDs can be superimposed to generate linearly polarized radiation with very little power on the optical elements. A phase shifter, which will be installed in between the segments to match the radiation of the two segments in the helical mode, can be used in this linear superposition mode to adjust the declination angle of the polarization vector from the horizontal to the vertical direction. This scheme has already been used successfully at other SR facilities (Bahrdt et al., 2001a). However, as a drawback of this mode the degree of linear polarization is reduced due to the electron energy spread, the beam emittance, and also the finite beamline acceptance.

Operation mode	Shift	B_{eff} [T]	K_{eff}	E_1 [eV]	P_{tot} [kW]	$dP/d\Omega$ [kW/mrad^2]
Circular	$\lambda_U/4$	1.10	6.5	246	11	0.14
Horizontal linear	0	1.39	8.2	160	17	123
Vertical linear	$\lambda_U/2$	0.94	5.5	333	8.0	82
45° linear	$\lambda_U/4$	0.77	4.6	473	5.5	0.48

Table 4.1.3: Parameters of the soft X-ray APPLE2 undulator. 'Shift' denotes the longitudinal displacement of the magnet rows. The device has a period length λ_U=63 mm and consists of two 2 m long segments separated by an optical phase shifter.

The energy range of this APPLE undulator has been specified by the users to reach from the carbon K-edge over the 3d L- to the rare earth M-edges, i.e. from $\approx$250 eV up to $\approx$2.3 keV. As known, the accessible energy range, in particular the 1^{st} harmonics position, for a given period length of the undulator depends on the longitudinal shift of the magnet rows and is different in the various operation modes. The low energy limit should also be covered in the helical mode to be able to apply the scheme of superimposed left and right polarized radiation discussed above. The period length which results from these considerations is λ_U = 63 mm. This value is related to a minimum gap of 10 mm taking into account that shims which have to be placed on the magnet structure need extra vertical space. Tab. 4.1.3 summarizes the parameters for the different shift dependent operation modes. The lowest

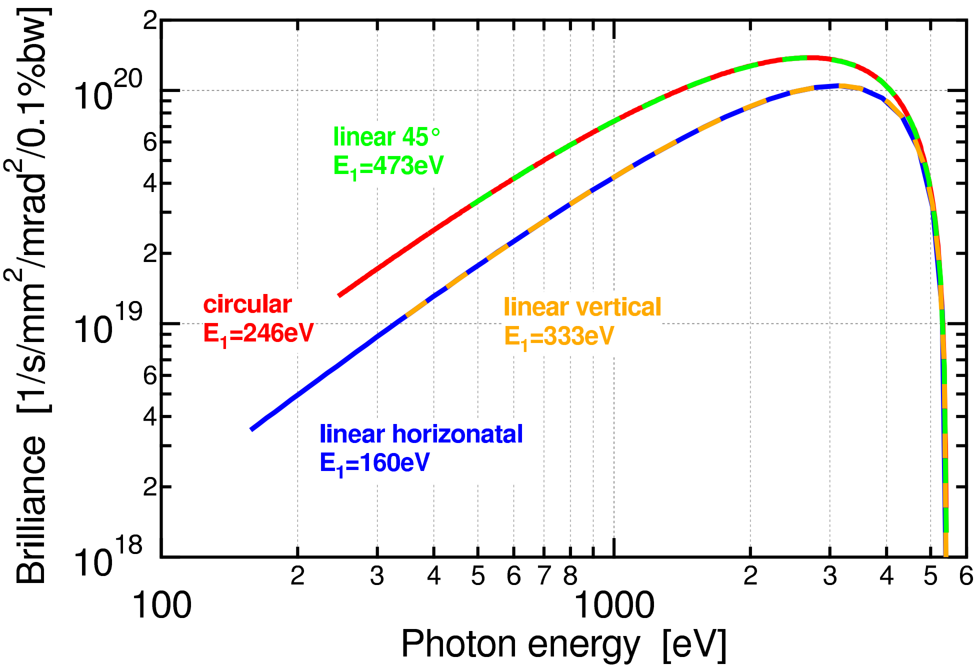

Figure 4.1.12: Brilliance and onset of the 1st harmonics in the various operation modes of the APPLE2 undulator.

photon energy of E_1 = 160 eV can be reached only in the horizontal linear polarized mode while the 1st harmonics onset is at highest energy for 45° tilted linearly polarized light. However, the energy range of the latter can be extended down to 250 eV if the radiation is created by the superposition scheme.

Fig. 4.1.12 compares the brilliance of the APPLE2 undulator in different operation modes. The onset of the 1st harmonic depends on the maximum effective K value which is related to the various operation modes. For a particular energy, i.e. the same K_{eff}, the brilliance is larger in the circularly and 45° linearly polarized mode as the norm of the helical field is constant along the undulator in these cases.

The radiation properties in the different modes can be illustrated in more detail by looking at the spectral distributions in Fig. 4.1.13. In the horizontal linear polarization mode the APPLE device represents a conventional planar undulator (a). Phenomenologically, the same holds for the vertical linear polarization scheme except that the onset of the 1st harmonic is at higher energies there. In the circularly polarized mode (b), the intensity at the 1st harmonic is ≈2 times larger than in the linear case. The calculated spectral width is about 1.6 % in both cases, in agreement with the relation 1/nN (Eq. 4.1.4). When reversing the helicity in one of the undulator segments in order to create linearly polarized light by superposition (c), the spectral width increases while the intensity decreases equivalently because the two segments are partially mis-phased, i.e. there is a destructive interference condition for one field component. This is independent of the adjustment of the phase retarder between the segments so that the same spectral distribution is expected for all orientations of the linear polarization vector. The angular flux density distribution of the 1st harmonics corresponding to the above cases is shown in Fig. 4.1.14. While in the harder X-ray region the spatial

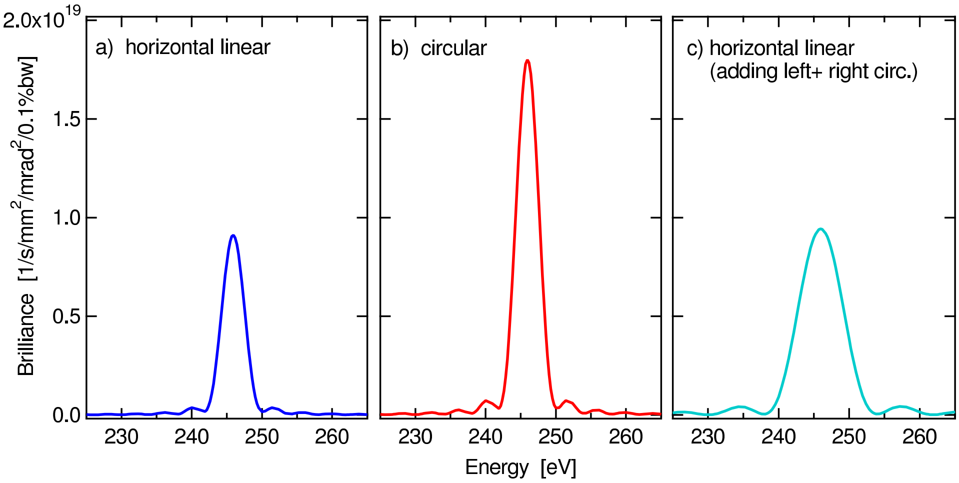

Figure 4.1.13: APPLE2: Spectral brilliance distribution of the 1^{st} harmonic at E_1=246 eV for different operation modes. In case (c) the horizontal linear polarized light is generated by superposition of left and right circular polarized light from the two undulator segments.

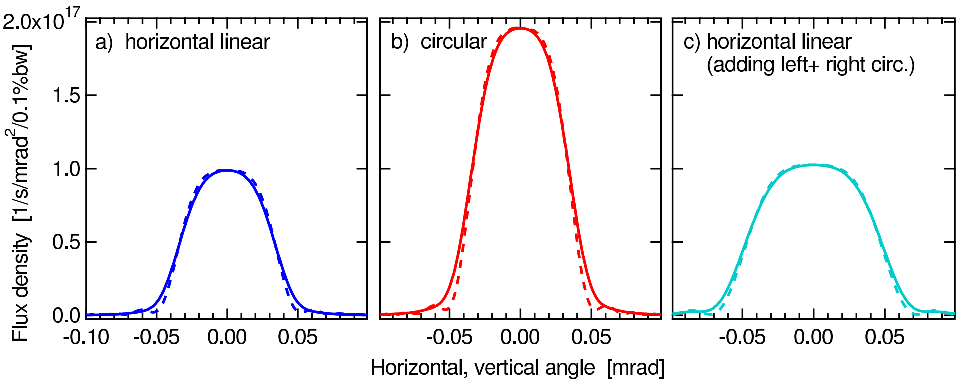

Figure 4.1.14: Horizontal (solid) and vertical (dashed) flux density of the APPLE2 undulator at E_1=246 eV for different operation modes (see Fig.4.1.13).

distribution of the central cone is elliptically, the beam footprint is almost circular in the VUV region because it is limited in both directions by the natural divergence $\sigma_{r'} = \sqrt{\lambda/(2L)}$. In the planar linear (a) and in the circular mode (b) the central cone has an opening angle of $\approx$70 μrad (FWHM) which is very close to $\sigma_{r'}$ fully dominating the angular distribution. In the superimposed linear mode (c), however, the spatial distribution is considerably broadened due to the only partly phased magnetic condition in this mode. Furthermore, the degree of linear polarization at the 1^{st} harmonics is reduced to 0.91 (0.72) for E_1 = 246 eV (2 keV) even for the on-axis radiation while it is 1 in case (a) across the entire central cone. These distinct differences in the spectral and spatial distribution for different polarization modes at the same energy might have to be kept in mind for special polarization dependent studies.
Fig. 4.1.15 compares the angular (a) and spectral (b) power density distribution in the helical and planar linear operation mode. In the low VUV region, i.e. for large K values, the power

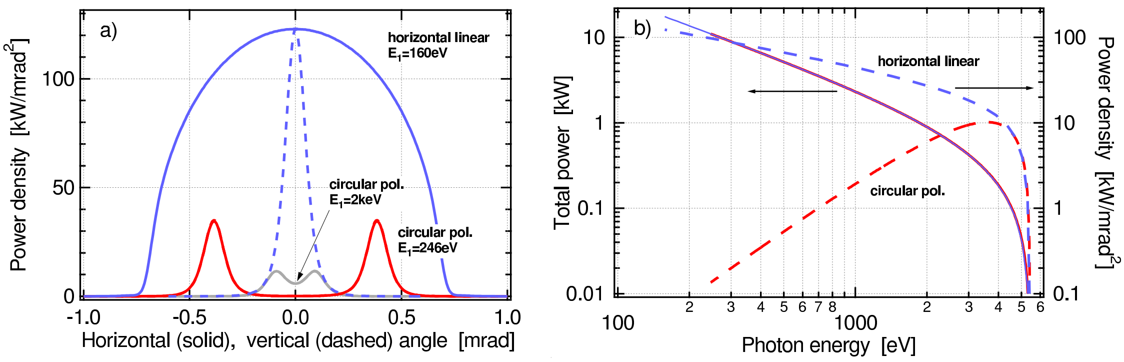

Figure 4.1.15: APPLE2 undulator: a) Horizontal (solid) and vertical (dashed) power density for different operation modes and energies. b) Spectral distribution of total power and on-axis power density (dashed) for horizontal linear and circular polarization mode. Note the increasing on-axis power density for decreasing K value in the circular mode.

density reaches values of only several tens kW/mrad^2 in the helical case. The same low power density is achieved for linearly polarized radiation if it is generated by superposition of left and right circularly polarized light. Then, the on-axis power density will be about two orders of magnitude lower than that caused by the same device if operated in the horizontally linear polarized mode where the high central cone intensity of all higher odd harmonics sums up to a large on-axis power. In contrast to the linear mode, the on-axis power density in the helical case increases with higher fundamental energy, i.e. lower K values, although the total power is reduced.

An electromagnetic helical undulator (Chavanne, Elleaume & Vaerenbergh, 1998; Gluskin, 1998) has not been considered for PETRA III as fast helicity flipping has not been addressed as a central user requirement. Moreover, it has been experienced in the past that electromagnetic IDs are not trivial to operate invisibly for the storage ring and other beamlines; this might hold even more for an ambitious machine like PETRA III. Alternatively, fast helicity switching up to ≈100 Hz can also be realized using a pair of 2 short helical permanent magnet undulators with opposite helicity where the photon beams are slightly tilted (Elleaume, 1994; Sawhney et al., 1997) or displaced (Ingold, 2000) towards each other so that they can be switched by means of a mechanical chopper in the photon beamline.

4.1.7 Quasi-periodic undulator

For the resonant scattering experiments discussed in section 6.15, the suppression of higher harmonics radiation at the position of regular multiples of the fundamental is essential to achieve ultimate sensitivity for the detection of very weak reflections. Besides an energy dispersive detector at the experiment and a mirror assembly in the photon beamline, the use of a quasi-periodic undulator (QPU) additionally contributes to suppress the higher harmonic content, altogether by about 10 orders of magnitude. Most monochromators also transmit perfectly on the 3rd or 5th of the selected energy which always causes a contamination by higher harmonics. In contrast to a periodic undulator, the higher harmonics in a QPU appear at non-rational multiples while at energies of the regular 3rd or 5th harmonic the intensity

can be suppressed by more than one order of magnitude. Higher harmonics are likewise present and provide tunability over a large energy range.
Based on the fundamental principles of a quasi-periodic undulator (Sasaki et al., 1995; Hashimoto & Sasaki, 1995), meanwhile QPUs have been built and operated in various modifications. The quasi-periodic magnet lattice has been applied successfully to pure permanent magnet structures (Chavanne, Elleaume & van Vaerenbergh, 1998; Chavanne, Elleaume & van Vaerenbergh, 2000), to the APPLE2 design (Sasaki, Diviacco & Walker, 1998; Diviacco et al., 2000), and to hybrid magnet structures (Bahrdt et al., 2001b). Usually, the quasi-periodicity in the magnet structure is introduced by a partial retraction of several distinct magnets in the arrays.
The perturbation pattern can be derived (Sasaki, 1998) from a projection of a 2-dimensional lattice (lattice constant ratio r) onto a line (inclination angle α). The parameters r and α are connected with the dislocation series affecting the position of the higher harmonics, and the phase jump driving the relative intensities between harmonics. Using such a scheme, the quasi-periodic magnet structure can be designed according to experimental needs though there is a mutual impact on brilliance and harmonics suppression which therefore cannot be optimized separately. The suppression of the regular harmonics will usually be in a range between 10 and 100 while the flux reduction of the QPU-harmonics regarding those of the periodic structure is in the order of 0.3 to 0.8.
Along with the user requirements for this beamline it is planned to modify a spectroscopy undulator (Sec. 4.1.4) for these purposes. With a period length of λ_U = 31.4 mm this ID has its 1^{st} harmonic at E_1 = 2.4 keV which corresponds well with the specified low energy end of 2.8 keV.
It will be advantageous if preferably the same mechanical design of the magnet structure could be used for the QPU as it is developed for the standard undulator. A vertical adjustment possibility of the magnet keepers can be integrated by simple modifications. Furthermore, the keeper must allow sufficient space to enlarge the retracted magnets in height. It has been pointed out (Bahrdt et al., 2001b) that this modification helps to localize the perturbation and to avoid an oscillation of the phase which leads to a cleaner optical spectrum.

4.1.8 20m undulator

As a further option, the first straight section within the new arc of PETRA III provides space for an undulator of maximum 20 m length. No dedicated ID type for this straight is, however, proposed at present as the individual experiments have not yet been assigned to certain beamlines. Nevertheless as a general remark, it is very obvious that low count rate experiments, e.g. due to a very small band pass or spatial acceptance, will benefit most from a very long undulator. Also, an insertion device for the VUV energy range is unfavorable as a more wiggler-like device, necessary to access the low energies, in conjunction with the full length of 20 m causes an enormous power load on all front end and primary optic components. A reasonable way around this difficulty is the placement of an Figure-8 undulator which considerably reduces the on-axis power density while the brilliance is only moderately decreased as it has successfully been demonstrated at SPring-8 (Tanaka & Kitamura, 1995; Tanaka & Kitamura, 2000). Besides, in the VUV energy range the photon beam spot is still

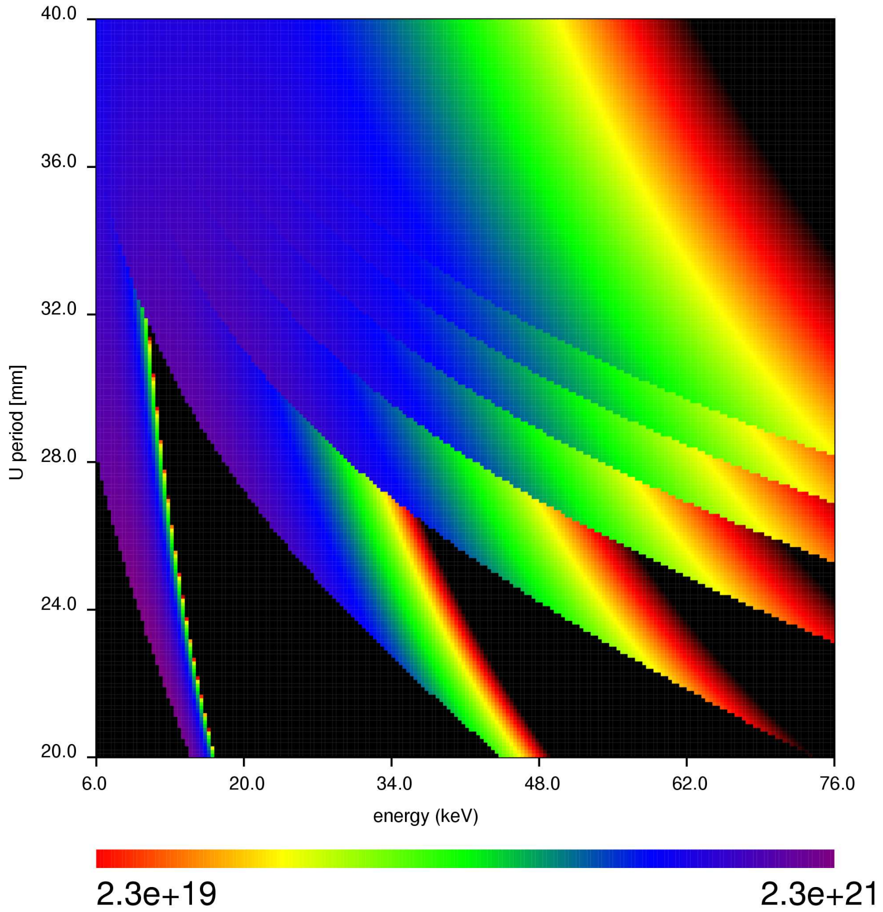

Figure 4.1.16: Brilliance map as function photon energy and period length for a set of 2 incoherently superimposing 10 m long undulators with a minimum gap of 12 mm.

largely diffraction limited and the brilliance gain with ID length would be maximum there while in the X-ray region the increase is less beneficial as discussed in Sec. 4.1.1.

There are two general ID concepts for this 20 m straight section that differ in their focusing scheme: The straight could be filled by several undulator segments separated by quadrupoles. This approach provides the possibility to keep the average vertical β-function rather small which in turn is essential to allow for a small geometrical vertical aperture and magnetic gap. Because of the spatial separation of the undulator segments, also a phase shifter has to be inserted between two ID segments in order to adjust the interference condition according to the particular gap. A phase shifter is a small magnetic chicane for the electron beam made from permanent or electromagnets (Pflüger & Tischer, 2000) and is also a key component in the undulator system planned for the DESY X-ray FEL. In this respect there will be a substantial mutual benefit for design, construction, and operation of such an undulator system for PETRA III and corresponding developments for the XFEL.

Alternatively, the straight section could be filled by a single 20 m long undulator, the β-function spanning over the entire ID length. Due to the parabolic increase of β aside its

minimum value within a cell, the vertical beam size at the ID ends will be considerably larger for a long undulator. Even for an adapted β-function, the minimum vertical beam stay-clear will increase to ensure a similar geometrical beam acceptance as for a short device. Furthermore, it is evident that such an ID has to be built as an in-vacuum undulator since it would not be feasible technologically to build the vacuum chamber of a conventional undulator in one single piece. Then, any interruption of the magnet structure due to a vacuum flange would imply a phase mis-match which has to be compensated by a phase shifting unit; the extra space required for that thwarts the original idea of this undulator and makes an in-vacuum undulator the only appropriate device similar as for the 27 m long undulator at the SPring-8 beamline BL19LXU (Kitamura et al., 2001).
Finally, an intermediate scheme, like e.g. a set of two 10 m long undulators with a focusing triplet in between, has been considered and will be reassessed once the beamline parameters have been specified. The expected performance of such a device can be seen in the brilliance map (Fig. 4.1.16) as function of energy and period length. In this case, the radiation of two 10 m long undulators would add up incoherently. A phase shifter in between the segments would improve brilliance only for the 1st harmonic radiation as e.g. for a fully tunable device ($\lambda_U = 29$ mm) the spectral line width $\Delta\lambda/\lambda$ of the 3rd harmonics approaches the electron energy spread $\Delta\gamma/\gamma = 0.0011$ at about 9 m undulator length.

4.1.9 Future upgrade ideas

The implementation of further beamlines in a future upgrade at the designated positions of the PETRA III storage ring as well as a potential upgrade of beamlines in the new arc will benefit from the progress in the SR optics and especially from the ongoing developments in the insertion device technology.
As practiced at other 3rd generation facilities, vertical apertures and hence magnetic gaps had been lowered without constraint to safe operation once the machine has been running routinely and sufficient experience had been gained. Then, the minimum gap will be in a range where the use of in-vacuum undulators (Chavanne et al., 2002; Hara et al., 1998) will improve the spectral intensity significantly as the gap is again reduced by the vacuum chamber wall thickness. Also, the vertical aperture can immediately be adapted to the needs of a particular operation mode though possibly sacrificing the low energy end of the undulator spectrum. The advantage of the in-vacuum technology is the decrease of period length for a given K value, i.e. the attainment of a larger number of periods for a given undulator length. Therefore, the advantages of an in-vacuum undulator will appear especially for short period devices at high photon energies.
In addition, the development of superconducting insertion devices has made continuous progress in recent years (LeBlanc & Wallén, 2002; Berger et al., 2002; Batrakov et al., 2002). In particular, the recent completion of a short period undulator (Kubsky et al., 2003; Chouhan et al., 2003) with $\lambda_U = 14$ mm and a peak field of 1.3 T shows that superconducting undulators might be technologically feasible also for storage ring operation in several years once the phase error will be in a range of today's permanent magnet undulators. Parallel developments on Nb_3Sn superconductors (Prestemon et al., 2003) will push the performance limit of superconducting devices even higher. Fig. 4.1.17 exemplarily shows the brilliance to

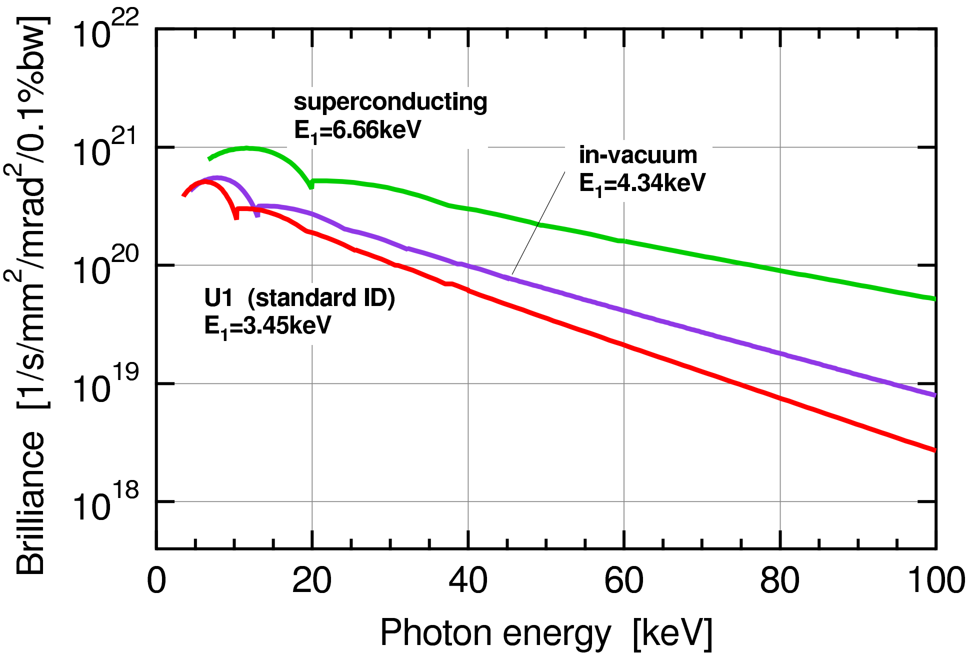

Figure 4.1.17: Performance of an in-vacuum or superconducting undulator as possible devices for a future upgrade of PETRA III.

be expected of a superconducting 15 mm period undulator (L=4 m) with $K_{max} = 2.2$ together with that of a 4 m long permanent magnet in-vacuum undulator $\lambda_U = 23$ mm, also designed for full tunability (K_{max}=2.2). Both devices exceed the brilliance of the standard undulator especially towards higher photon energies.

Finally, a variable period undulator had been proposed (Shenoy et al., 2003b) which once could overcome the inherent limitation of a conventional, fixed-period undulator which is always optimized for only one wavelength, usually the 1^{st} harmonic corresponding to the minimum gap. Such a device will operate much closer to the optimum K value ($\approx$1.2) for all photon energies and exhibit higher brilliance beyond the 1^{st} harmonic.

4.2 Damping Wigglers

Damping wigglers will be installed in two long straight sections of the machine to reduce the emittance of the storage ring to 1 nmrad. Concept and layout of these damping wigglers is discussed in sections 3.2.1 and 3.4. Although not realized in the first stage of PETRA III, the damping wiggler radiation can serve an experimental station making use of a large hard X-ray beam. The synchrotron radiation created in a single damping wiggler segment has a total power of about 20 kW which is emitted within a horizontal opening angle of $\alpha \approx 2K/\gamma \approx \pm 2.4$ mrad. About 340 W will be generated on-axis within a solid angle of 0.1×0.1 mrad^2. The angular power distribution of a single segment has been calculated for the nominal machine parameters (Fig. 4.2.1a). The power density reaches an on-axis peak value of 40 kW/mrad^2. In principle, the damping wiggler radiation can be used in a photon beamline at the end of certain wiggler straights (Sec. 10). With its broad homogeneous spatial distribution it might be an interesting source for certain material science applications. The critical energy of the wiggler is 36 keV, Fig. 4.2.1b displays the spectral flux distribution of a single wiggler segment. As a different option a dedicated undulator or wiggler could be installed as the last device in a damping wiggler straight section. In this case, the various wiggler segments will form a uniform background underlying the undulator spectrum.

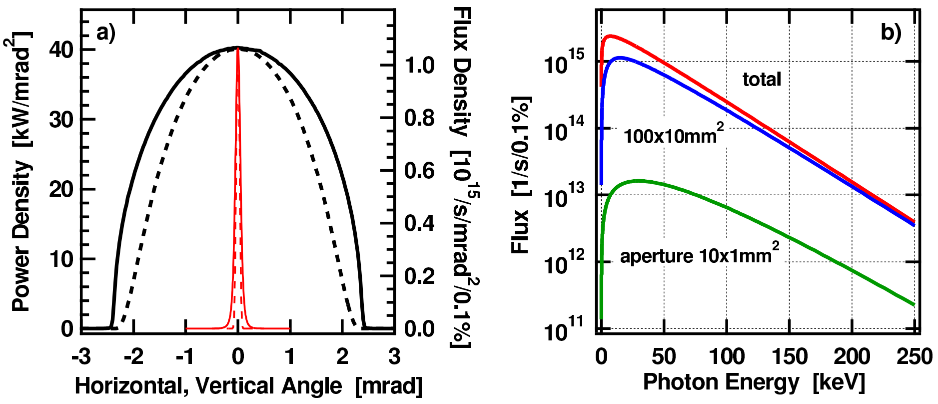

Figure 4.2.1: a) Radiated power density (solid) of a 4 m long wiggler segment together with the spatial flux distribution at 100 keV (dashed). The emitted total power is ∼20 kW, the integrated (0.1×0.1 mrad^2) on-axis power is about ∼340 W. b) Spectral flux distribution of a single wiggler segment through different apertures located at a distance of 40 m from the source.

4.3 Bending Magnets

At the envisaged particle energy of 6 GeV, the field of the bending magnets in the 'old' 7/8 of the PETRA III storage ring will be too weak ($E_c \approx 2.5$ keV) for the production of

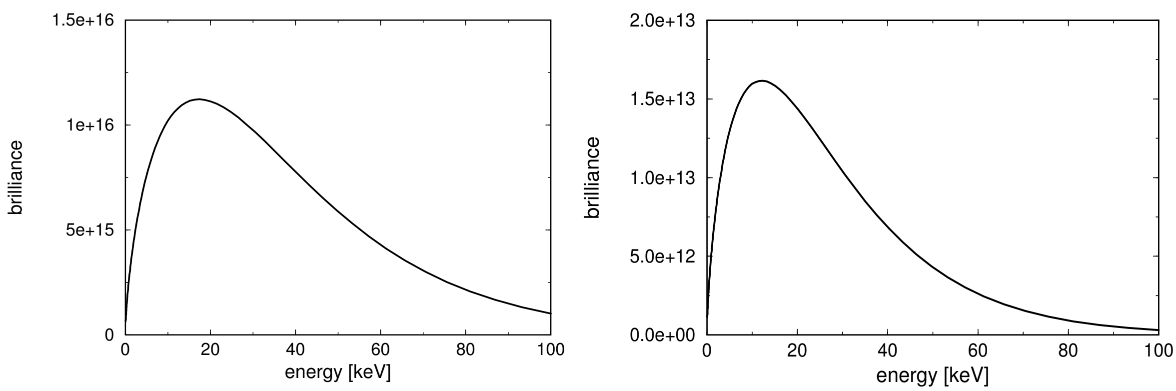

Figure 4.3.1: Comparison of the brilliance in ph/(s mm^2 mrad^2 0.1%BW) of the radiation from a PETRA III (left) and DORIS III (right) bending magnet. All values for DORIS III correspond to a current of 120 mA.

magnetic field	0.87 T
critical energy	20.8 keV
horizontal β	2.62 m/rad
vertical β	38.65 m/rad
horizontal α	0.938
vertical α	0.133
horizontal dispersion	0 m
σ_x	51 μm
σ_y	19.6 μm
$\sigma_{x'}$	27 μrad
$\sigma_{y'}$	0.5 μrad

Table 4.3.1: Characteristic parameters and optical functions in the first part of a PETRA III bending magnet in the new eighth of the storage ring for a particle energy of 6 GeV.

harder X-rays. However, the parameters (see Tab. 4.3.1) of the bending magnets in the new, reconstructed eighth of PETRA III will be comparable to the ones of other hard X-ray 3^{rd} generation synchrotron radiation storage rings like ESRF and are therefore ideally suited for the production of hard X-rays.

In the following, the radiation properties of DORIS III bending magnets will be used for comparison. In Fig. 4.3.1 the brilliance of the radiation from a PETRA III and a DORIS III ($E_c \approx 16$ keV) bending magnet are compared. Due to the about 20 times smaller source size of PETRA III, the brilliance at this source is almost three orders of magnitude higher than for DORIS III.

In Fig, 4.3.2 the flux through a 1 mm^2 aperture in 40 m distance from the source is compared for both sources. Since the radiation characteristics of a single electron $\sigma_{r'}$ is dominating the angular distribution of bending magnet radiation the differences between the two sources are relatively small especially in the lower energy range shown in Fig. 4.3.2. From the results in Figs. 4.3.1 and 4.3.2 it becomes obvious that experiments using radiation from PETRA III bending magnets without any focusing optics will not have significantly more photons on a small sample than at DORIS III. However, the radiation will be significantly more parallel as it is indicated by the higher brilliance. With suitable focussing optics full advantage can be taken from the higher brilliance of PETRA III especially at higher (E>50 keV) photon energies. Possibilities to use bending magnet radiation at PETRA III are discussed in Sec. 10.3.

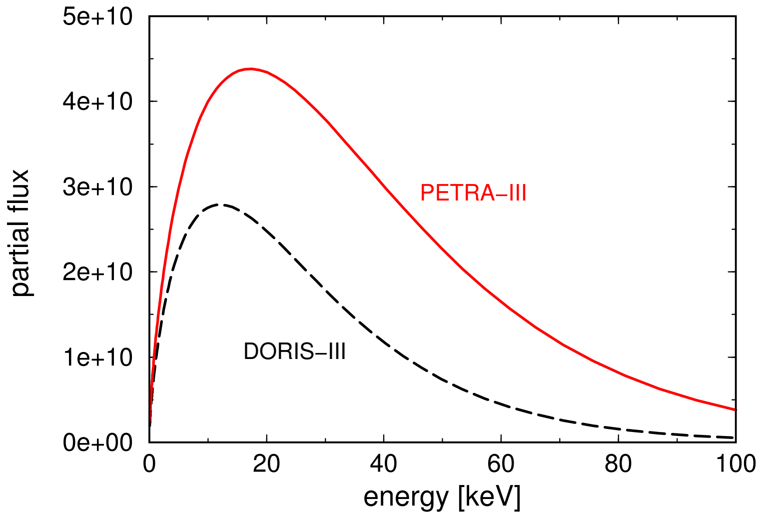

Figure 4.3.2: Comparison of the flux through a $1 \times 1\,\mathrm{mm}^2$ aperture in 40 m distance from the source in ph/(s 0.1%BW) of the radiation from a PETRA III and a DORIS III bending magnet. All values for DORIS III correspond to a current of 120 mA.

Chapter 5

Beamline Front Ends and Optics

5.1 Introduction

For the beam transport between the undulator and the experimental hall a generic beamline is proposed which contains the minimum number of elements which are needed to guide the beam to the experiment. In Fig. 5.1.1 a PETRA III tunnel segment with the undulator and the beamline front end is shown.

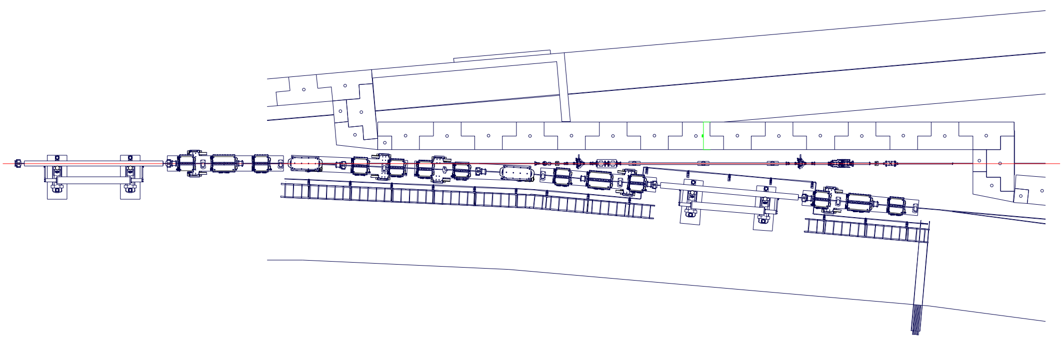

Figure 5.1.1: Overview of the PETRA III tunnel installations with the undulator on the left and the front end components tangential to the storage ring.

Special experimental needs may reduce the number of proposed devices in the generic part and add special optical devices close to the experiment, i.e. for achieving a higher degree of monochromatization or strong focusing. The main tasks of the generic beamline are the following:

- provide a hydrocarbon and dust free vacuum system
- transport the photon beam from the undulator to the experiment, conserving the unique beam properties

- ensure radiation safety by collimation and suitable beamshutters
- ensure equipment protection by an appropriate vacuum interlock system
- monitor the photon beam position
- shape the beam with fixed and movable masks to reduce the power load on optical components
- monochromatize the white beam
- collimate or focus white and monochromatic light by mirrors
- filter the white beam to reduce the power load and suppress harmonics

The layout is split into two parts separated by the storage ring tunnel wall. Inside the ring tunnel no optical components, as mirrors and monochromators, will be placed.

5.2 Ring Tunnel – Beamline Front End Installations

Inside the ring tunnel all components in the photon beamline dealing with radiation safety, beam position and beam collimation will be placed as shown in Fig. 5.2.1. There will be the option for a collimating lens system placed inside the ring tunnel.
Space is also needed for the vacuum protection system, i.e. the fast acting valve. The vacuum failure sensing devices will be installed in the optics hutch. A windowless beam transport system will connect the storage ring and the experimental hutch.

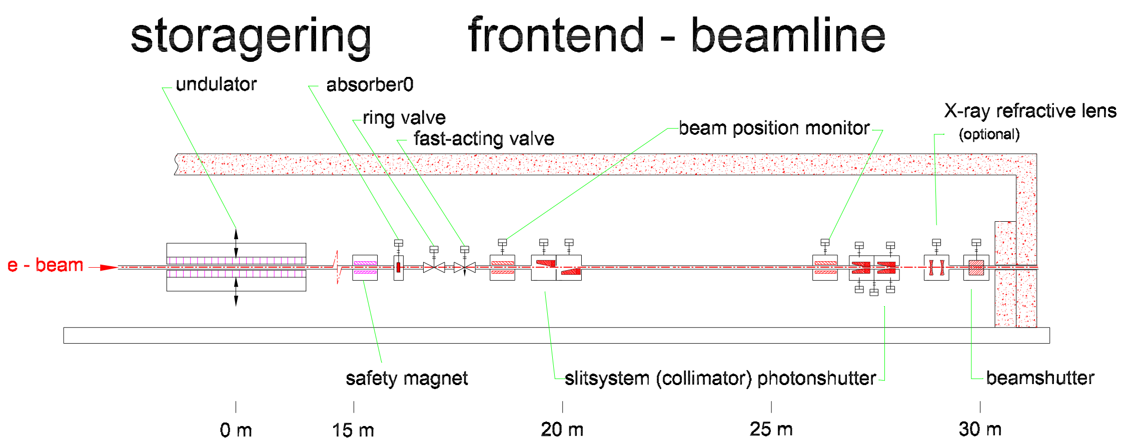

Figure 5.2.1: Schematic layout of the generic beamline components located inside the ring tunnel.

5.2.1 Radiation safety

The radiation safety system allows a safe access to the optical elements and the experiment without interruption of the storage ring operation. PETRA III will run in a continuous filling mode which requires a special arrangement of radiation safety components. For a fail safe particle injection, each beam outlet has to be equipped with a permanent magnet which extracts misguided particles out of the photon beamline.
The beam shutter will be placed directly in front of the storage ring wall. A photon shutter protects the beam shutter absorbing the full photon beam power.
To limit the neutron dose caused by the Bremsstrahlung originating from electron beam losses inside the undulator vacuum chamber, two vertical absorber slits are installed in the beamline at 18 m and 28 m from the source. During normal operation of the storage ring an aperture size of $\approx$1 mm prevents a direct line of sight towards the undulator vacuum chamber. These apertures will be opened for filling during alignment of the storage ring and the set-up of the apertures.

5.2.2 Beam position monitors

Photon beam position monitors (BPM) will be installed in front of the vertical slit systems. At present, the basic BPM follows the 4 blade design (Hahn et al., 1998). In the case of a high brilliance undulator beamline, the performance of these devices suffers from the radiation from adjacent bending magnets and quadrupoles. At PETRA II, the collimation of the bending magnet radiation proved to be feasible, and allowed the use of blade monitor systems.
For PETRA III, a BPM (Schulte-Schrepping et al., 2003) based on the detection and imaging of ionized residual gas is proposed. This device provides a non-intrusive, non-saturable means of detection of the center of mass of the beam position.

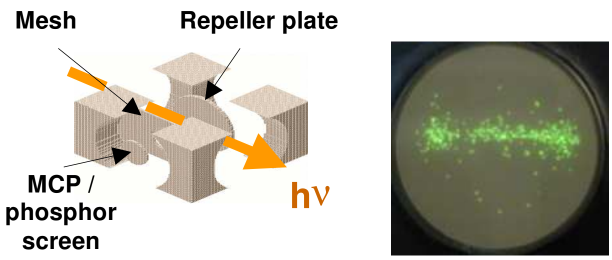

Figure 5.2.2: First results from a photon beam position monitor imaging the photon trace through an ionized gas.

In Fig.5.2.2 the set-up and a first measurement of a photon trace through the detector is shown. The set-up consists of a micro-channel plate (MCP) with fluorescent screen and fiber-optic, a mesh and a repeller plate. Residual gases in the detector will be ionized by the photon beam and accelerated towards the MCP. A proper geometrical arrangement of the plates and the field distribution will image the ions/electrons onto the MCP. The amplified signal is converted to visible light by the fluorescent screen and coupled into a fiber optic window. The image is recorded outside the vacuum chamber by a CCD camera. The speed of the monitor is determined by the gas pressure. A CCD and frame grabber setup working at video frequencies would provide a 25Hz update rate of the position signal.

The BPM in front of the first slit measures the vertical and horizontal position of the full photon beam. The BPM in front of the second slit will be used to center the first slit in the vertical direction and measures the photon beam position in the horizontal direction.

5.2.3 Beam shaping and photon shutter

The design of the two slit systems is shown in Fig.5.2.3. They will absorb off axis radiation of the undulator. The second slit additionally functions as a power absorber to shut off the photon beam. While the first slit collimates only in the vertical direction, the second slit also collimates in the horizontal direction. The total power in the white beam will be as high as 30 kW with a maximum power density of 800 W/mm^2 in 30 m from the source in the case of the 20 m long undulator at 100 mA. Future upgrades to a beam current of 200 mA will be considered and implemented in all designs.

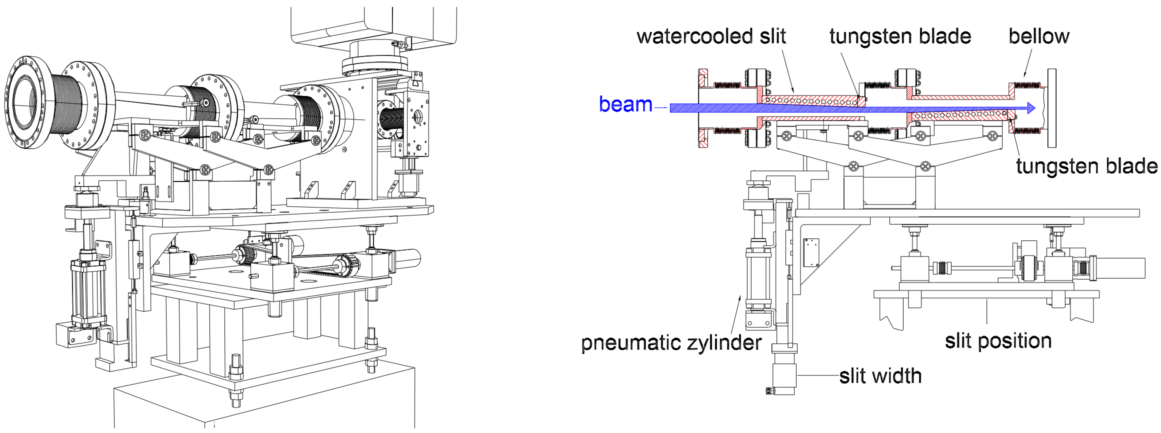

Figure 5.2.3: High power slit system and beamshutter suitable for PETRA III undulator beamlines. (U. Hahn, M. Rüter, Hochleistungsstrahlverschluss- und Spaltsystem für Synchrotronstrahlung, Patent Nr. DE 101 35 307 C2).

The cross-section on the right in Fig.5.2.3 shows the principle of operation of the vertical slit system. The upper and lower jaw consist of an inclined (≈1 degree) water cooled copper absorber (Wang & Hahn, 1996b) to accept the power, and a tungsten blade to stop high energetic radiation. The slit height is controlled by one drive moving both jaws. The vertical slit position is adjusted by moving the whole set-up. The shutter function of the slit is driven by the pneumatic cylinder.

The horizontal slit function is achieved by integrating a horizontal movable absorber (Marion & Zhang, 2003).

5.3 Optics Hutch Installations

All optical elements, except an optional collimating X-ray lens, will be located inside the optics hutch outside the ring tunnel. This scheme allows access to all major beamline optics components without affecting the storage ring operation. The optics hutch will provide proper shielding and suppression of background radiation. A secondary beamshutter allows access to the experiment while the main beamshutter is open. The thermal stability of the optical components benefits from the continuous filling mode and the secondary beamshutter. The layouts of the optics hutches follow the experimental needs. The different beamline options provide a fixed exit photon beam at the experiment, independent of the configuration of the optics:

- monochromatic photon beam, direct or mirrored

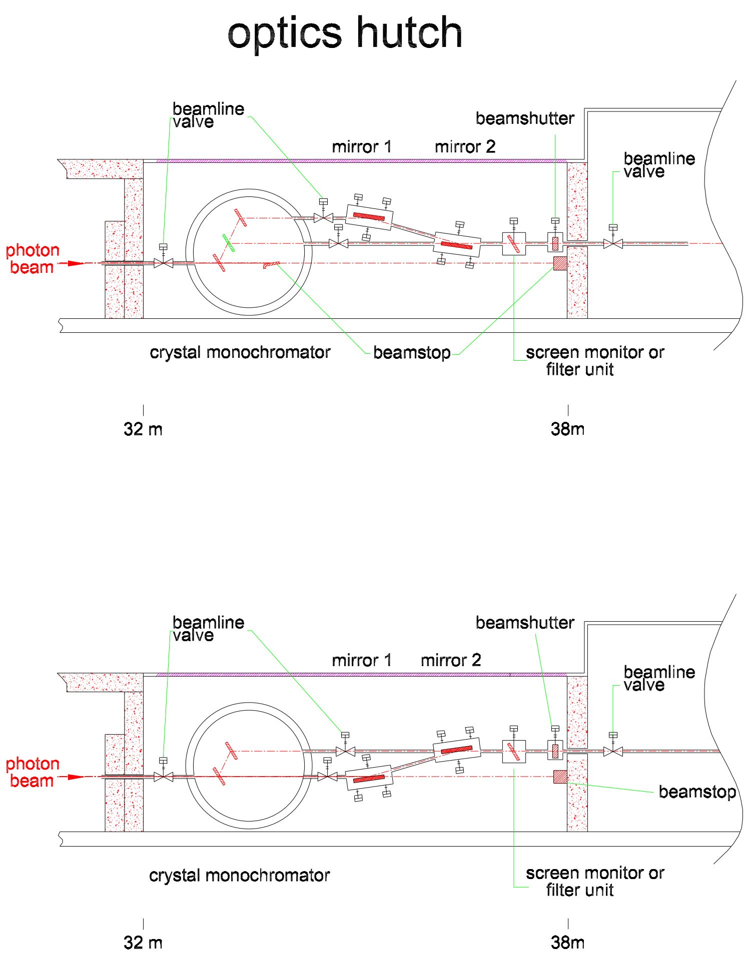

Figure 5.3.1: Top: Schematic layout of the optics hutch providing a monochromatic photon beam. The monochromatic and pink beam offset will be 25 mm relative to the white beam. The mirrors are moveable in the vertical direction. Bottom: Layout of the optics hutch providing a monochromatic photon beam or a mirrored pink beam.

- monochromatic photon beam or pink mirrored beam
- soft X-ray monochromator

In Fig. 5.3.1 options providing a monochromatic photon beam, direct or mirrored, and a pink beam are shown. In Fig. 5.3.2 a monochromator for the soft X-ray regime is presented.

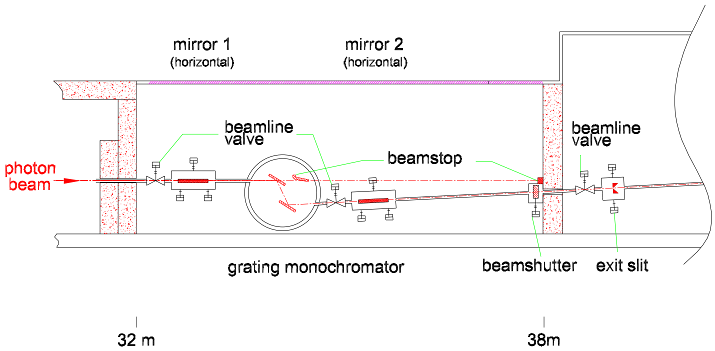

Figure 5.3.2: Soft X-ray beamline with grating monochromator and horizontally deflecting mirrors (design described in this report) located inside the optics hutch.

5.3.1 Crystal monochromator

A fixed exit double crystal monochromator setup in Laue- and in Bragg-geometry will be installed. A monochromator with a common rotation of both crystals is favorable due to the enhanced speed and accuracy in energy scans. If the preservation of coherence properties of the photon beam is mandatory, silicon monochromator crystals will be installed due to the ultimate perfection of single crystal silicon. Cryogenically cooled silicon can accept a total heat load of 400 W at the crystal. The use of apertures in the white beam to select the central cone of the undulator radiation will fulfill this requirement.
For all experiments not depending on the transverse coherence properties of the photon beam, diamond crystals will be used, either at room temperature or cryogenically cooled (Bilderback et al., 2000, Zhang et al., 2003). The decision between the use of Laue-cases and Bragg-cases and possible combinations of both is dependent on the tolerance to chromatic aberrations. Diamond crystals will be used in the Laue case due to the small size of the perfect area of synthetic diamond crystals in the 5x5 mm^2 range.
Other means of beam conditioning like the use of asymmetric crystals have to be explored carefully in order to preserve the quality of the beam.

5.3.2 Mirrors

We propose to use two 1 m long mirrors to provide a fixed offset of the beam. If coherence preservation is mandatory, a projected footprint of the beam should be accepted with 5σ of the footprint to avoid diffraction at the mirror edges.

The mirrors will suppress higher harmonics in the beam and provide the option of focusing or collimation. The focusing range of toroidal and elliptical mirrors will range from 1:1 – 1:20 assuming glancing angles from 1 to 5 mrad.
Si mirror substrates are the best available choice. A special issue for the mirror quality is the source brightness and coherence preservation. The mirrors will be cooled where necessary. The necessary precision of the mirror surface with figure errors in the sub-μrad range is reached by ion beam figuring. The requirement for brightness preservation follows the assumption of a maximum tolerable enlargement of the virtual image of the source by 10% in RMS size (Howells, 1999). Assuming a Gaussian source of width Σ, and a distance r from the source, the allowed slope error σ is given by:

For the tangential plane: $\sigma \leq \Sigma$ / (4r) and the sagittal plane $\sigma \leq \Sigma$ / (4r sinΘ) with the grazing angle given by Θ.

This imposes strict requirements on the mirror quality. The actual value depends on the choice of a low or high beta section in the storage ring and the distance from the source to the mirror (e.g 0.25 μrad and 1 μrad, respectively, at 35m from the source).
Ultra micro focusing schemes in Kirkpatrick-Baez (KB) configuration with bend elliptical mirrors will provide focal sizes below 1 μm. These setups require accompanying metrology effort at the beamline to verify and monitor their properties.

5.3.3 Filters and windows

The design for the filters used at PETRA II (Wang & Hahn, 1996a) will be adapted to the beam sizes and power densities at PETRA III. Special care will be taken to preserve the beam brightness and coherence, i.e. by using polished surfaces and homogeneous and uniform dense materials. The interface to the experiment will be a diamond window or a differential pumping stage for windowless operation.

5.4 Vacuum System

An average pressure in the beamline of 10^{-7} mbar is targeted. This pressure range is determined by the operation and lifetime of the ion-pumps. At the connection to the storage ring a pressure better than 10^{-9} mbar has to be achieved to avoid an additional gas load on to the ring vacuum, which would affect the particle beam lifetime and increase the background radiation. The beamline vacuum system is separated from the storage ring vacuum by an all-metal ring valve combined with a fast acting valve. The fast acting valve is controlled by two pressure sensors, which are placed outside the storage ring tunnel. The ring valve is protected against radiation from the bending magnet by the absorber. These devices may only be closed at a fully opened undulator. In the case of an accidental venting of the beamline and closing of the fast acting valve, the stored beam has to be dumped. A set of water cooled apertures collimates the bending magnet radiation, avoiding distributed gas loads in the beampipe by photon desorption and unwanted heating of beamline components.

The vacuum structure as shown in Fig.5.4.1, the diameter of beampipes and the pumping scheme, of the generic beamline follows the rules as applied to photon beamlines at DORIS III or PETRA II.

Device	Distance from the source [m]	Device length [m]	Beamline Inner diameter [mm]	Remarks
Safety magnet				
Beam outlet	16	0	20x12	Hor.* vert.
Fixed Mask with Absorber	16	0,5	20x12	
Ring valve	16,5	0,072	37	VAT Reihe 48
Beampipe with ion pump	16,572	0,5	37	
Fast acting valve	17,072	0,035	40	VAT Reihe 75
Bellow	17,107	0,15	40	
Beam Position Monitor 1	17,107	0,75	35	
bellow	17,857	0,15	40	
Fixed mask	18,007	1	40	
Beampipe with ion pump	19,007	7,5	37	
Beam Position Monitor 2	26,507	0,75	40	
Photon Shutter with Slit System	27,257	2	37	
Beampipe with ion pump	29,257	0,5	37	
X-ray refractive lens	29,757	0,5	35	
Collimator and Beamshutter	30,257	1	37	
Shielding Wall Crossing	31,257	1	35	

Figure 5.4.1: Layout of the vacuum system and positions of components inside the generic beamline.

In the beamlines viton sealed valves are preferred. This is because of the simplicity, the particle free operation, and the short closing time of these devices.

A dust particle free vacuum system around the optical components is necessary to avoid coherence effects at the surfaces of mirrors and monochromator crystals. Therefore all cleaning and mounting of components has to be done according to class 100 clean room specifications [1]. The design and assembling of the beamline components have to fulfill this demand. The pump down with special oil-free turbo-molecular pumping units has to take care of the particle free operation. Special venting procedures have to avoid a dust particle flow towards the optical components. To avoid carbon contamination of radiation exposed surfaces a hydrocarbon free vacuum (partial pressures of hydrocarbons less than 10^{-3} of the total pressure) is needed. All beamline vacuum components have to fulfill the HASYLAB vacuum specifications (Hahn, 2003).

[1] clean-room classification according to US Fed. Standard 209E

Chapter 6

Beamlines and Experimental Stations

6.0.1 Introduction

The PETRA III upgrade will result in nine straight sections for insertion devices within the new experimental hall. Depending on the applications each straight section can either be equipped with a single 5 m long insertion device or with two 2 m long devices which will be inclined towards each other by 5 mrad (see also Sec. 2.2.1). The distance from an insertion device to the end of the tunnel shielding wall will be about 33 m due to the large radius of the PETRA storage ring. According to the presently planned experimental hall dimensions the maximum source to sample distance will be about 100 m. The angle between neighboring straight sections will be 5°. Due to the very parallel photon beams expected at PETRA III (Sec. 2.2.3), especially in case of a high-β section, it should easily be possible to operate more than one experimental station along the beampath of the same undulator either in a time sharing mode or even simultaneously. Such an arrangement is schematically sketched in Fig. 6.0.1. The space for experiments will be more restricted in case of two insertion devices located in the same straight section. As far as possible the layout will be optimized for minimal interaction of the two corresponding stations during the operation phase. In Fig. 6.0.2 a possible layout of such canted undulator beamlines is shown. In this case, both beamlines will likely share at least the first optical hutch for some of their optical elements. Such an arrangement will leave one of the beams almost unrestricted in space except in the

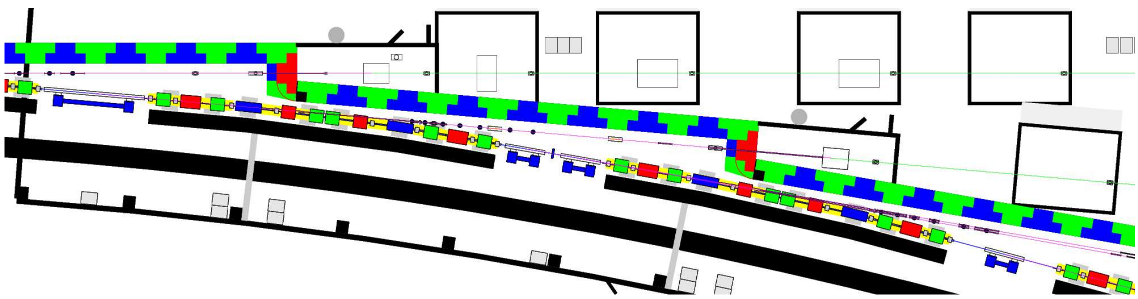

Figure 6.0.1: Schematic drawing of several experimental hutches arranged at a single undulator beamline (top view).

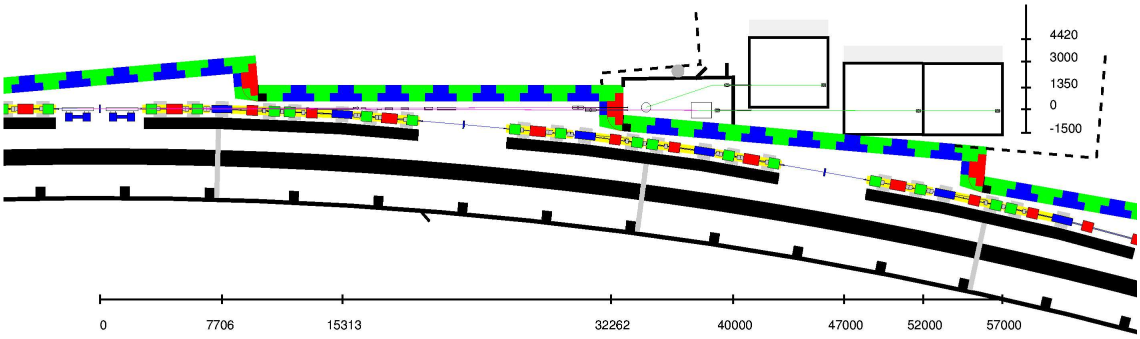

Figure 6.0.2: Schematic drawing of canted undulator beamlines. The exact layout of the hutches will depend on the equipment to be installed in the experimental endstations.

region close to the shielding wall. Depending on the exact layout of the experimental station of the second beamline ("side station") and the energy range that will be used, it has to be discussed if a horizontally or vertically deflecting monochromator is advantageous. The canted undulator beamline with horizontal deflection is shown in Fig. 6.0.2. In either case, a wide energy tunability as well as a very long experimental station will be more difficult to achieve for side stations.

In principle two insertion devices could be placed in every straight section. The difference in brilliance between a 5 m and a 2 m insertion device is a factor of 2.5–3.2 depending on the photon energy (Fig. 4.1.1). According to present plans it is foreseen to split four straight sections. However, this number certainly needs to be evaluated again when the decision on the first beamlines to be built has been made.

Experimental issues that are relevant for almost all experimental stations are described in Sec. 6.0.2. In Sec. 6.18 experimental techniques will be presented for which no dedicated station is proposed. These techniques will either be applied at many stations or can easily be carried out at several different experimental setups with limited additional effort.

This report does not include any proposal for time resolved experiments exploiting a *single bunch mode* operation of the storage ring for two reasons:

1. Due to the small emittance of PETRA III the lifetime for a single bunch with high charge is rather low. If we assume an injection frequency of 0.1 Hz in top-up mode the maximum stored current per bunch will be about 5 mA. For that reason PETRA III is not the ideal source for this kind of experiments.
2. More important: DESY expects the European XFEL laboratory in Hamburg to become operational about 2–3 years after the first beam at PETRA III will be delivered. The pulse intensity of the XFEL will about four orders of magnitude higher compared to PETRA III and the pulse duration will be almost three orders of magnitude shorter.

Keeping these arguments in mind and the fact that with the VUV-FEL, another source with extremely short pulses for time resolved experiments is available on site, specialized fast time resolution experiments have not been considered for PETRA III. However, a bunch timing signal will be provided to all beamlines. In the few bunch mode ($\approx$ 40 bunches, equally distributed, 2.5 mA bunch current) the time window will be 192 ns. This is well suited for pump-probe experiments with few ps time resolution. The number of photons per pulse in 0.1% BW will be about 10^8, compared to about 10^{12} expected for the X-FEL in SASE mode. Presented as an individual beamline, 22 experimental stations are proposed in sections 6.1–6.17. The decision on

- the number of stations to be built in 2008,
- the experiments to be joined at one undulator beamline,
- the distribution of experiments on 2 m and 5 m insertion devices, and
- the assignment of experiments to straight or side station insertion devices

will be achieved with the assistance and expertise of a beamline advisory committee which will be established after publication of this report as already mentioned in Chapter 1.

The estimates for the investment costs given at the end of each beamline proposal are restricted only to endstation equipment. The capital investment and personnel needed for beamline optics, vacuum system and shielding hutches have to be added for the total beamline costs. The later ones amount to about 2 M€ per beamline on average.

6.0.2 General experiment support infrastructure

Computing and experiment control All PETRA III experiments will be controlled by the same software and hardware modules, as far as possible. The experiments will also have direct control of the undulator gap and access to relevant beamline information like beam position, bunch current, bunch timing signals, etc.. A detailed description of the computing infrastructure is given in Sec. 7.3.

Experiment support It is planned to set up an experiment support group for the experimental hall which will take care of specialized equipment that may be used on demand at different beamlines. The instrumentation provided includes:

- high pressure cells and the related infrastructure (Sec. 6.18.1)
- cryo equipment like cryo streamers, closed cycle cryostats, bath- and flow-cryostats (He and N_2)
- furnaces for different temperature ranges
- high field magnets
- detectors, 0–2 dimensional, ...
- electronics such as NIM-modules
- mechanic components such as translation stages and turn tables
- lasers

The provision of a pool of specialized equipment has been very successful at other user facilities. The pool should be allowed to dynamically adopt to the experimentalists requirements. Sufficient staff will be allocated to ensure maintenance and development of the equipment.

6.1 High-Energy X-ray Diffraction

Authors :

U. Hoppe	Universität Rostock, Germany
T. Lippmann	GKSS Research Center, Geesthacht, Germany
H. Reichert	MPI Stuttgart, Germany
R. Röhlsberger	DESY, Hamburg, Germany
S. D. Shastri	APS, Argonne, USA
J. Strempfer	MPI Stuttgart, Germany
M. von Zimmermann	DESY, Hamburg, Germany

6.1.1 Current state of the scientific field

With the development of modern synchrotron radiation sources, high energy X-ray diffraction became a powerful tool for the analysis of bulk materials and buried interfaces. Since the absorption lengths above 100 keV for most materials lie in the range of 0.1 mm to several cm, studies of the bulk behavior of thick samples as applied for materials research become evident. For the same reason, thick window materials for sample environments like cryostats or furnaces are less critical or negligible. In many cases, the surface of a material exhibits complex defect structures. High energies can penetrate through millimeters of material so that contributions from the near-surface region and the sample container become negligible. Moreover, corrections for absorption, extinction and multiple scattering effects can be neglected in many cases.

Another important feature of high-energy X-rays is that reciprocal space can be mapped up to large momentum transfers such as 30–50 $Å^{-1}$ which is crucial for precise structure determination of liquid and amorphous materials. As a result, slightly differing bond lengths in the structure can be revealed, as demonstrated recently in the analysis of the network structure in a glass (Petkov et al., 2000). The analysis of the diffuse scattering provides high-resolution structural information also for crystalline materials. While conventional diffraction yields the spatially averaged crystalline structure, the diffuse scattering reveals local deviations from the average structure (Reichert et al., 2001).

High-energy X-rays have been applied in a variety of areas for structure analysis : defect and diffuse scattering, texture analysis (Bunge et al., 2003), structural phase transitions, charge and orbital ordering (v. Zimmermann et al., 2003), and magnetic scattering (Strempfer et al., 2004).

The application of high-energy diffraction methods becomes particularly attractive if combined with microfocusing techniques. This has been applied to investigate ordering phenomena at the solid-liquid interface which led to the discovery of a five-fold local symmetry in liquid Pb in contact with the Si(1 1 1) surface (Reichert et al., 2000). It is expected that such studies can be extended into new areas by using high-brilliance X-ray beams delivered at PETRA III.

6.1.2 Science at the high-energy X-ray diffraction beamline

The very high brilliance of the undulator beams at PETRA III allows for a significant enhancement of existing experimental techniques: Focusing to micron scale spot sizes will enable the selection of very small gauge volumes and a corresponding differential mapping of the sample properties. The implementation of high-resolution monochromators allows to probe samples with elemental specifity via contrast variation around absorption edges. This is interesting for 5d and 5f elements with K - edges above 40 keV. Element specific investigations involving those elements often suffer from high absorption which leads to unreliable near-surface effects.
Moreover, the extremely high photon flux in these beams permits time-resolved investigations to capture transient events on the sub-second time scale. Among the large number of possible applications, a few will be highlighted in the following sections. These are scientific fields that are not accessible to neutrons (unable to microfocus, low flux) or lower energy X-rays (low penetration capability).

6.1.2.1 Buried interfaces

Interfacial phenomena strongly determine the functionality and properties of complex systems as they occur in nano technology and in nature. Very often one has to deal with deeply buried solid-solid or solid-liquid interfaces which critically determine the function of electrolytes, fuel cells, or nano mechanical devices, see Fig. 6.1.1a-c. Particularly in nature and in biological systems, fundamental phenomena and processes may occur at interfaces between two macroscopic objects. A specific example is the phenomenon of interfacial melting of ice in contact with minerals as sketched in Fig. 6.1.1d. This phenomenon is expected to be of crucial importance for many environmental processes. Access to buried interfaces is obtained in a transmission-reflection scheme using high-energy microbeams, as sketched in Fig. 6.1.2a. Due to the high photon energy, a long path in the sample can be traveled while keeping the absorption losses low. The microbeam enters the sample sideways, thus selecting just the boundary of interest and avoiding signal contamination by surrounding interfaces and surfaces as in the conventional scheme, see Fig. 6.1.2b. Such studies have an enormous potential to investigate dynamical phenomena like melting and phase transitions at buried interfaces. While surface melting has been studied extensively (Frenken & van der Veen, 1985), buried interfaces were hardly accessible due to the strong absorption of low-energy X-rays and the low brilliance of neutron sources. Here, the high-brilliance beams delivered at PETRA III will open new experimental possibilities. High-resolution data are obtained by recording specular reflectivities up to momentum transfers q_z of $1.0\,\text{Å}^{-1}$ or beyond. The use of microbeams confines the specularly reflected signal to a very small region in phase space, so that the background from diffuse scattering is strongly reduced. For that reason, the outstanding brilliance of the PETRA III undulator beams is essential for these studies.

6.1.2.2 High-energy diffuse scattering

Diffraction studies of the structure of condensed matter often suffer from a small scattering cross section, especially when diffuse scattering experiments are required for the investi-

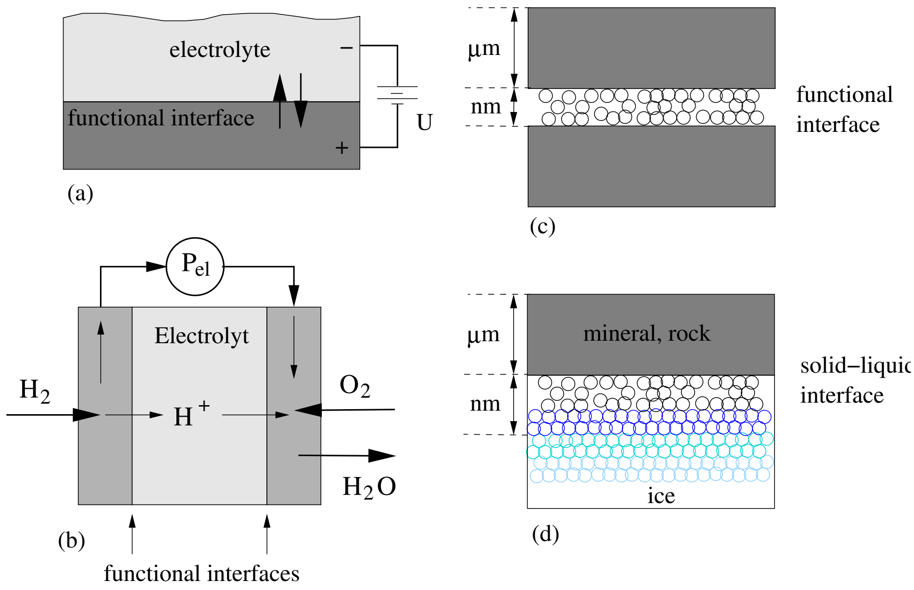

Figure 6.1.1: Examples of deeply buried functional interfaces as they occur in (a) electrolytes, (b) fuel cells, (c) lubrication in nanoscale mechanics, and (d) environmental problems such as interface melting of ice in contact with minerals. (Figure adopted from Reichert et al., 2003a)

gation of local deviations from the average structure. This problem can be overcome by using new techniques based on high energy X-ray diffraction. With this technique a high energy X-ray beam is directed at a well-oriented single crystal in transmission geometry. The scheme combines the advantages of two other scattering methods in diffraction physics. High energy photons penetrate a large sample volume giving a total number of scatterers in the X-ray beam comparable to the neutron case. As in electron diffraction (TEM) the diffraction pattern can then be imaged in a plane that is almost flat due to the large radius of the Ewald sphere. This allows to record diffuse diffraction patterns with unprecedented resolution and statistics on a time scale of seconds. An example is displayed in Fig. 6.1.3 that shows scattering from the spin-glas $Cu_{83}Mn_{17}$ from which strain-induced nonanalytic short-range order was derived (Reichert et al., 2001).
Another example are ordering phenomena in complex oxide materials. The physics of these materials is determined by the competition between spin, charge and lattice degrees of freedom. Particular effects are the formation of charge-ordered clusters in the manganite perovskites, giving rise to the phenomenon of colossal magneto resistance (CMR) (Vasiliu-Doloc et al., 1999) or the formation of stripe phases in high-T_c superconductors (Mook & Dogan, 1999). To obtain a complete picture of the physics of such systems, data from the entire volume of reciprocal space are essential. In contrast to neutron scattering, these data can be collected very quickly if high-brilliance, high-energy X-rays are used in combination with large 2-dimensional detectors. This allows for extensive systematic investigations with unprecedented accuracy.
Using modern focusing techniques (e.g. compound refractive lenses) it has become possible to produce high energy microbeams to probe local deviations from the average structure in

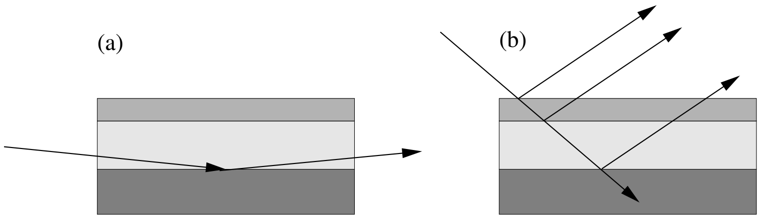

Figure 6.1.2: Access to buried interfaces using a high-energy X-ray microbeam in a transmission-reflection scheme (a), compared to the conventional reflectivity setup (b). This allows one to clearly separate the reflected signal from the interface under study from the surrounding interfaces (Reichert et al., 2003a).

inhomogeneous systems. Kinetic processes like the nucleation of precipitates from a disordered matrix or the ordering/disordering kinetics in structural phase transformations can be followed in-situ and in real time. This opens completely new possibilities to investigate kinetic phenomena on an atomic length scale. It is particularly interesting to extend these studies to systems in confined geometries such as surfaces, thin films, superlattices and nanoparticles.
Successful analysis of diffuse-scattering data requires close interaction with theoretical studies. In recent years, the accuracy of atomistic simulations of oxide materials has significantly improved, as demonstrated for the sequence of phase transitions in $KNbO_3$, for example (Sepliarsky & Phillpot, 2000). The results of such simulations are combined with Monte Carlo modeling of diffuse scattering to determine fundamental properties of materials such as the interaction potential in multicomponent systems.

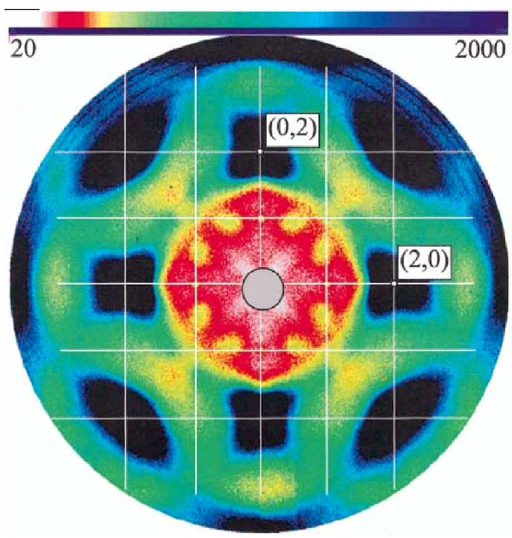

Figure 6.1.3: Measured diffuse intensity pattern with the (0 0 1) surface normal oriented parallel to the beam. The center of the image is blocked by a beam stop to shield the detector from the intense primary beam.

6.1.2.3 Charge - density analysis

In recent years it has been shown that high–energy synchrotron radiation is an excellent tool to perform charge density analysis, see, e.g. (Graafsma et al., 1998; Lippmann & Schneider, 2000a; Lippmann & Schneider, 2000b; Kirfel et al., 2001; Lippmann et al., 2003). Experimen tal charge distributions are often used in comparison with theoretical results in order to test structural models, i.e. precise atomic coordinates, and to reveal details of the chemical bonding in crystals. Moreover, they can be used to derive further physical properties, e.g. electrostatic potentials, electrostatic moments, lattice energies, which can be compared to results obtained by other methods, e.g. spectroscopy or thermodynamic measurements (Coppens, 1997).

Usually, charge densities are calculated after adjustments of an appropriate structure model to a set of structure factors. These are obtained from integrated reflection I_{int} intensities via application of various correction factors: $I_{int} = L \cdot P \cdot T \cdot A \cdot E \cdot |F|^2$, where the Lorentz correction L and the polarization correction P can simply be calculated after the experiment and the thermal diffuse scattering correction T can be minimized by measuring at low temperatures. In contrast, the absorption correction A often cause problems, if the shapes of the samples are irregular. Moreover, the extinction correction E can not be carried out prior to refinement, because the crystal quality is usually a priori unknown. In order to minimize the errors of the last two corrections the best solution is to minimize the corrections themselves, i.e. using high–energy radiation.

In addition to the improvement of the data quality, high–energy radiation opens the gate to a large number of new structures, which contain heavy elements, because the strong absorption of low–energy radiation by these structures prohibited the experimental determination of reliable structure factors in the past. High–T_c superconductors may be considered as an example for these materials (Lippmann et al., 2003).

Most of the experiments have been performed at high–energy wiggler beamlines, e.g. BW5 at DORIS III. Since the sample sizes are typically of the order of a few 100 μm, only a small fraction of the primary radiation is scattered by the sample. In contrast, the use of high–brilliant 3^{rd} generation light sources with small beam sizes should yield an intensity gain of the scattered radiation by at least 1 to 2 magnitudes, which offers the possibility for various new experiments and studies in this field. In combination with fast detectors the performance of time–resolved studies are possible, e.g. structure factor measurements after illuminating the samples with a laser in order to test excited states (Kim et al., 2002). Another benefit of the intensity gain is the enhancement of the data resolution by extending the size of the data sets. Up to now this has simply failed due to a lack of beamtime. An enhancement of the data resolution would offer the possibility to study small structural features in detail and thus to answer open questions. As an example, 30 years ago theoretical considerations lead to the question, whether near–core electron orbitals are spherical, as usually believed, or also affected with small aspherical distortions (Bentley & Stewart, 1974). A proof of this core deformation will be possible, as soon as high–resolution experimental data are available.

6.1.2.4 High-resolution studies of liquids and amorphous materials

X-ray diffraction studies of structures of disordered materials (glasses, melts) are often accompanied by correction problems arising from absorption, Compton scattering, fluorescence, scattering from the sample environment, and finite momentum transfer range. The idea using high-energy photons to overcome these problems goes back to Egelstaff (Egelstaff, 1983). A pioneering experiment using 95 keV photons was performed at wiggler beamline BW5 of HASYLAB for studying the structure of vitreous silica (Poulsen et al., 1995). Since that time a progressing number of such experiments has been carried out. For example, structural studies of oxide glasses were performed, where data at momentum transfers Q up to 300 - 400 nm^{-1} were collected (Petkov et al., 2000; Ohno et al., 2001; Hoppe et al., 2000). The quality of the X-ray scattering data will be comparable with those obtained in neutron scattering experiments at the best sources. Effects of truncation of the measuring range become less significant with increasing Q. Data obtained from X-ray contrast variation and neutron scattering can be combined to reach highest resolving power and precision. This is also valid for samples which are known as highly absorbing for low-energy radiation in conventional experiments such as lead containing glasses (Ohno et al., 2001). Nevertheless, some problems are not properly solved and need optimization: The Compton scattering increases dramatically with momentum transfer and a separation of the elastic line with the structural information from the Compton profile is only possible for large scattering angles at energies significantly below 100 keV (Laaziri et al., 1999). This requires a vertical scattering plane to avoid problems with the beam polarization (Petkov et al., 2000). On the other hand, the use of photon energies clearly beyond 100 keV is optimal to reduce absorption problems to a negligible degree and to obtain high-precision data. However, this means that all structural information will be found at small scattering angles where Compton scattering cannot be subtracted (Hoppe et al., 2000). Except for the use of energy-dispersive detectors for discrimination of fluorescence and other sources of background, also fast 2D-detectors are desirable for series of measurements with short exposure times (Petkov, Qadir & Shastri, 2004).

6.1.2.5 High - energy magnetic X-ray diffraction

Magnetic X-ray scattering results from the interaction of the electromagnetic wave not only with the charge of the electrons in the solid but also with the magnetic moment. The interaction with the magnetic moment is a relativistic effect and is described by first order perturbation theory. Thus, the intensity of the magnetic signal is several orders of magnitudes weaker than the charge intensities. Whereas the magnetic X-ray scattering cross section in the hard X-ray energy range (5–20 keV) involves both spin and orbital magnetic moment, non-resonant high-energy magnetic X-ray diffraction at energies above 80 keV is only sensitive to the spin magnetic moment (Brückel et al., 1993). At these energies, true bulk properties are investigated due to the high penetration depth of the radiation. High-energy magnetic X-ray diffraction is thus complementary to magnetic neutron diffraction, where also the whole sample is penetrated but where the sum of spin and orbital magnetic moment contributes to the magnetic cross section. With both techniques the same samples can be investigated, even with the same sample environment. By combination of the results,

absolute spin and orbital magnetic moments can be determined independently with high accuracy (Strempfer et al., 2004).
The investigation of temperature dependencies of the magnetic order parameter with high energy photons takes advantage of the high momentum space resolution of X-ray diffraction at the synchrotron compared to that in neutron scattering experiments. Because of the narrow rocking curves of the Bragg reflections, the Bragg intensity can be separated from the much wider diffuse scattering background in the critical regime near the Néel temperature. Also, small magnetic satellite reflections can be separated easily from the much stronger charge Bragg reflections.
Non-resonant magnetic scattering of high-energy X-rays provides highly precise and detailed information on the spin density which can serve as test data for density functional theories. So far, only rather simple compounds have been investigated. At PETRA III, this method can be extended to compounds of more complicated structure. Requirements here are high quality crystals, a large magnetic moment and a favorable ratio of the number of magnetic electrons to the total number of electrons. For such investigations, a high-brilliance beam combined with high incident flux and low background is indispensable.

6.1.2.6 High-energy X-ray diffraction from correlated electron materials

Correlated electron materials are a highly interesting class of compounds both from a scientific point of view, but also for applications as functional materials. The strong interplay of spin, orbital, charge and lattice degrees of freedom makes the comparison of model calculations to experimental results highly desirable. A more detailed introduction into correlated electron materials can be found in Sec. 6.15. The hard X-ray diffraction technique is a very sensitive probe for lattice distortions and is thus capable to detect structural distortions associated with orbital ordering (Geck et al., 2002) and charge ordering (v. Zimmermann et al., 1998). Even the spin order can, in principle, be determined with hard X-ray diffraction (see Sec. 6.1.2.5). The technique offers possibilities that are important for the investigation of correlated electron materials, among these are the bulk sensitivity, which makes surface contaminations negligible. Furthermore, the signal from small structural features becomes enhanced by probing larger samples. The Laue scattering geometry allows to access large amounts of reciprocal space. Another important aspect is the complex sample environment that can be used for hard X-ray diffraction experiments. Due to the high penetration depth of X-rays with energies around 100 keV, it is possible to use pressure cells and magnetic fields without compromising the measured signal and the accessibility of reciprocal space. With these external fields it is possible to disturb the balance between the various degrees of freedom in these materials (Geck et al., 2002; Wakimoto et al., 2003). Since the structural distortions are often of diffuse nature, an option to relax the resolution and thus achieve the highest possible photon flux on the sample, would be desirable.

6.1.3 Beamline description

The beamline consists of two optics hutches and two experimental hutches. Optics hutch 1 (OH1) contains a cryogenically cooled double-Laue monochromator. Optionally, this

monochromator could be replaced by a multilayer monochromator if a larger bandpass can be traded in for a higher flux. The optics hutch 2 (OH2) hosts subsequent optics for beam manipulation like collimating or focusing lenses and an optional high-resolution monochromator. For stability reasons we propose two separate optics hutches. OH2 offers some user space for development and testing of special optical components, for example. Experimental hutch 1 (EH1) will be devoted to magnetic scattering, scattering from glasses and amorphous materials etc. It should contain enough user space to accommodate different types of sample environments. Experimental hutch 2 (EH2) will host two experimental setups, i.e., one for microbeam diffraction from buried interfaces and one for diffuse scattering. The former setup consists of a granite plate that carries a specially designed heavy-duty rotation stage with a horizontal axis that allows for adjustment of the incidence angle with nanoradian precision. For maintaining a very high stability, it is mandatory to mount the detector on a separate stage that is decoupled from the sample stage (Reichert et al., 2003a).
The setup for diffuse scattering requires a long baseline to achieve sufficient resolution in q-space. A fast detector system should be implemented so that this method can be extended to time-resolved studies of dynamical phenomena with ms time resolution.

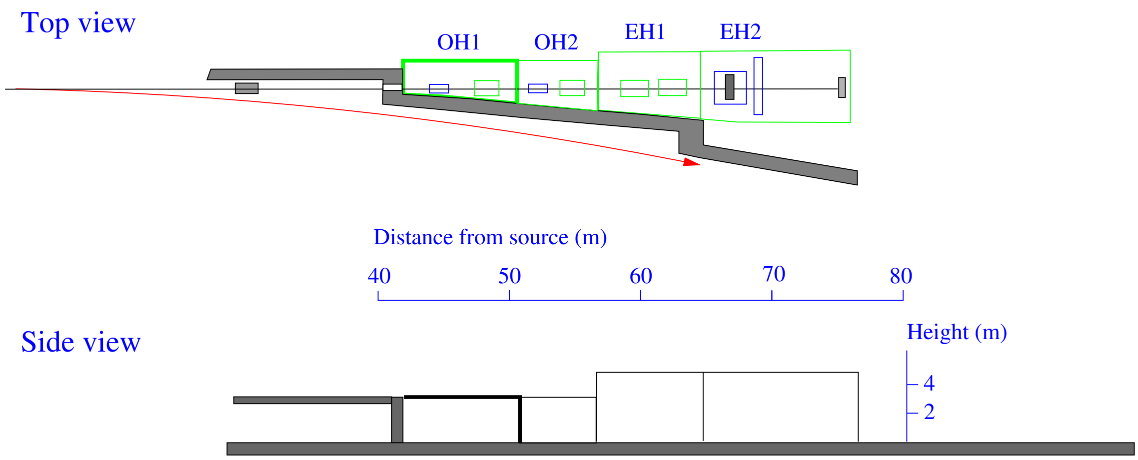

Figure 6.1.4: Layout of the proposed beamline for high-energy X-ray diffraction at PETRA III, consisting of two optics hutches (OH1, OH2) and two experimental hutches (EH1, EH2).

6.1.3.1 Undulator

For this beamline we propose the use of undulators that are optimized for the generation of high-energy X-rays. Very efficient schemes can be implemented, if spectral coverage in the low-energy range (10–40 keV) is not needed. The goal is to achieve maximum brilliance in the range from 50 keV to 100 keV. To achieve a complete spectral coverage from 40 keV upwards it may be necessary to implement two (non-canted) undulators on a 5 m long straight section, that are optimized for different spectral ranges. Details about the undulator design for high-energy radiation can be found in Sec. 4.1.5.

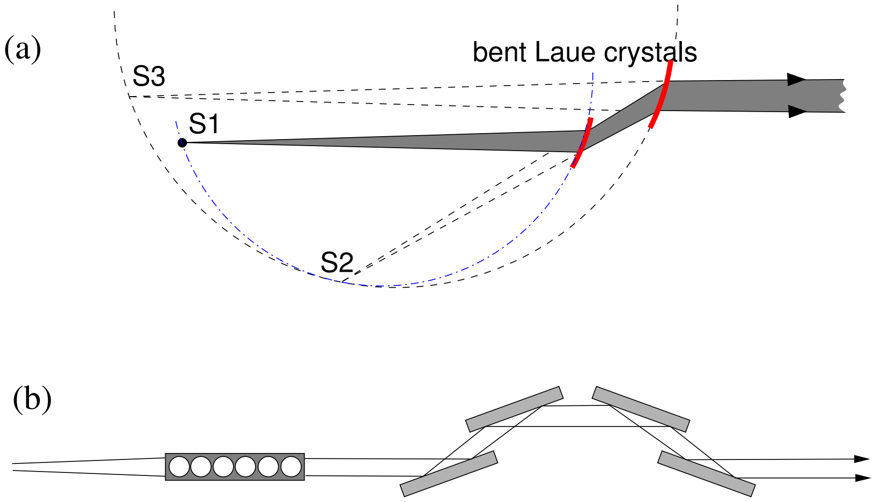

Figure 6.1.5: a) Tunable in-line monochromator for high-energy X-rays, consisting of two vertically diffracting Laue crystals located about 40 m from the undulator source S1. The Rowland circles of both crystals intersect tangentially at the virtual source S2. b) Arrangement for a high-resolution monochromator with a relative energy bandpass of $\Delta E/E \approx 10^{-4}$.

6.1.3.2 Monochromator

At high photon energies, flat crystal optics becomes very inefficient due to a reduced angular acceptance. Schemes to enhance the angular acceptance like mosaic crystals or gradient crystals in general do not preserve the brilliance of the reflected radiation. This, however, is a necessary prerequisite for the implementation of subsequent optical elements like compound refractive lenses, especially if μm - size focal spots are desired. Full brilliance preservation can be achieved by the use of asymmetrically-cut bent Laue crystals (Lienert & Keitel, 2001). The strain broadening of the angular acceptance leads to an increase of the diffracted flux by one to two orders of magnitude (Suortti, Lienert & Schulze, 1994; Suortti & Schulze, 1995). Due to the bending the scattering becomes kinematical so that the scattering volume increases because it is determined by absorption rather than extinction. This approach has been employed to realize a tunable, fixed-exit monochromator for high-energy X-rays (Shastri et al., 2002), as sketched in Fig. 6.1.5a. In this setup, two crystals are cylindrically bent in Rowland geometry so that all rays make the same incident angle with respect to the crystal planes. This leaves the energy bandwidth $\Delta E/E$ at a value of about 10^{-3} in the 60 - 80 keV range which is sufficient for most experiments. Flux values in the range of 10^{13} ph/s are expected in a cross section of $0.5 \times 0.5\,\mathrm{mm}^2$ of the monochromatic beam. This exceeds values at existing sources by about an order of magnitude.
For a number of applications, an energy resolution in the range of $\Delta E/E \approx 10^{-4}$ is necessary. Such values can be achieved by a set of four symmetric Si(1 1 1) crystal reflections that are arranged to resemble two channel-cuts in a dispersive (+−−+) geometry, shown in in Fig. 6.1.5b. Such an arrangement has been successfully tested at beamline 1-ID of the APS (Shastri, 2004). Compared to a single symmetric Si-(1 1 1) reflection, this scheme has the advantage that the beam position on the sample is insensitive to energy and angular fluctuations

of the beam delivered from the first monochromator stage (only the transmitted intensity may drift). As a result, such a monochromator scheme can be ideally combined with subsequent focusing optics and experimental arrangements that demand for highest stability.

6.1.3.3 Focusing optics

For an efficient illumination of buried interfaces, the radiation has to be focused to μm sized focal spots. The use of microbeams significantly enhances the signal-to-noise ratio in evanescent X-ray diffraction and X-ray reflectivity studies. First, the entire beam cross section contributes to the scattered signal at very small grazing angles. Second, the very small phase space volume covered by the detector drastically reduces the contribution from diffuse scattering. Thus, microfocusing is essential to access large momentum transfers where X-ray reflectivities have dropped to the range of 10^{-12}.
At high energies, several options are available to achieve micron-sized focal spots. Compound refractive lenses have been used to yield spot sizes in the range of $10\,\mu$m at a photon energy of 71 keV (Reichert et al., 2003a). Single zone plates cannot be manufactured thick enough to produce a π phase shift between zones. Nevertheless, a 10 micron-sized focal spot has been achieved at 50 keV by precise stacking of several zone plates (Shastri et al., 2001). Another option is the use of Laue crystals that are bent to set the source outside the Rowland circle. Using this method, 90 keV X-rays have been focused to $1.2\,\mu$m (Lienert & Schulze, 1998). Eventually, the most promising candidates for sub-micron focal spots seem to be bent multilayer mirrors, despite the demanding angular stability and slope-error requirements. Point focusing in this case can be achieved by the combination of two multilayers in Kirkpatrick-Baez geometry.

6.1.3.4 Sample stages

The stability of the sample stages plays a crucial role for X-ray scattering experiments involving microbeams. For adjustment of the incidence angle in high-energy grazing-incidence reflection, the accuracy of commercially available stages is not sufficient, in particular if heavy weights like UHV chambers have to be adjusted and kept stable within nanoradian precision. In this area, significant R&D activities have to be carried out to meet these requirements in routine user operation.

6.1.4 Capital investment and personnel

For the development of the scientific program at the beamline, two researchers are required who will run independent activities to accommodate a wide scientific community.
The performance of the monochromators and high-resolution sample stages crucially depends on an engineer that is dedicated to such developments. In particular, experience in nano-radian motion control is required. For installation of the beamline components and their maintenance, two technicians are needed, whereby one of them is specialized installations, including motor control and data acquisition.
The total capital investment for this experimental station amounts to **1990 k€**.

6.2 Coherent X-ray Beamline

Authors and Consultants :

O.H. Seeck	FZ Jülich GmbH, Germany
S. Eisebitt	BESSY, Berlin, Germany
G. Grübel	DESY, Hamburg, Germany
U. Pietsch	Universität Potsdam, Germany
I. Robinson	University of Illinois, Urbana, USA
T. Salditt	Universität Göttingen, Germany
M. Tolan	Universität Dortmund, Germany
E. Weckert	DESY, Hamburg, Germany

6.2.1 Current state of the scientific field

Among the most exciting properties of today's third generation synchrotron radiation sources is the high flux of coherent X–rays provided. It is given by $F_c = (\lambda/2)^2 \cdot B$, where λ is the wavelength and B is the brilliance. Typically, $10^9 - 10^{10}$ photons per second at 1 Å wavelength are delivered at existing sources such as ESRF, APS or SPring-8. The availability of intense coherent X–ray beams has fostered the development of new, coherence based techniques such as Coherent X–ray Scattering (CXS), X–ray Photon Correlation Spectroscopy (XPCS), phase contrast and tomographic imaging and interferometry. Much of the excitement about scattering with coherent X–rays stems from the perspective to perform atomic resolution correlation spectroscopy and/or to reconstruct coherent scattering images to unravel the underlying real space information.
If coherent light is scattered from a disordered system it gives rise to a random–like diffraction or "speckle" pattern. Such a speckle pattern is caused by interference and is related to the exact spatial arrangement of the underlying disorder. The scattered intensity might be quantified by $I(Q,t) \propto |\Sigma_j \exp(iQ \cdot R_j(t))|^2$ where Q is the momentum transfer and $R_j(t)$ are the positions of the scatterers at time t. The sum has to be taken over scatterers in the coherence volume only, spanned by the transverse $\xi_t = (\lambda/2) \cdot (R/\sigma)$ and longitudinal $\xi_l = \lambda \cdot (\lambda/\Delta\lambda)$ coherence lengths. Here, (σ/R) is the angular source size and $(\Delta\lambda/\lambda)$ is the bandwidth of the radiation. If the spatial arrangement of the scatterers changes as a function of time the corresponding speckle pattern may also change and the temporal intensity fluctuations of a single or of equivalent speckle(s) are a measure of the underlying dynamics. Temporal intensity fluctuations can be quantified by Photon Correlation Spectroscopy (PCS) for the visible coherent light case or by XPCS in the X–ray regime.
Static X–ray speckle has first been reported by Sutton et al. (1991), followed by XPCS results (Dierker et al., 1995; Thurn-Albrecht et al., 1996). XPCS has since then matured considerably and Fig. 6.2.1 shows the regime where XPCS experiments have already been performed (outlined in red) compared to areas covered by other techniques. As can be seen from the figure XPCS covers intermediate length scales very well and overlaps with visible light scattering (PCS). It is noteworthy that correlation times below 100 ns have been detected in reflectivity geometry at low Q (Sikharulidze et al., 2002), thus bridging the gap to the energy domain techniques, e.g. Neutron Spin Echo (NSE). Many applications are located at

low Q [surface/capillary wave type dynamics (Seydel et al., 2001; Madsen, Als-Nielsen & Grübel, 2003)] or moderate Q ($< 5 \cdot 10^{-2}\,\text{Å}^{-1}$) addressing mostly questions in complex fluids (Mochrie et al., 1997; Grübel et al., 2000; Lurio et al., 2000). Access to shorter length scales ($Q > 5 \cdot 10^{-2}\,\text{Å}^{-1}$) can be more difficult. The necessary higher temporal coherence implies a higher monochromaticity that can only be provided at the expense of coherent flux. This cannot always be compensated by 2–D detection since fast (ms - μs) 2–D single photon counting detectors with appropriate spatial resolution and quantum efficiency do not exist today. An accompanying R&D effort in 2-D detectors is thus mandatory and engaged e.g. for pixel detectors.

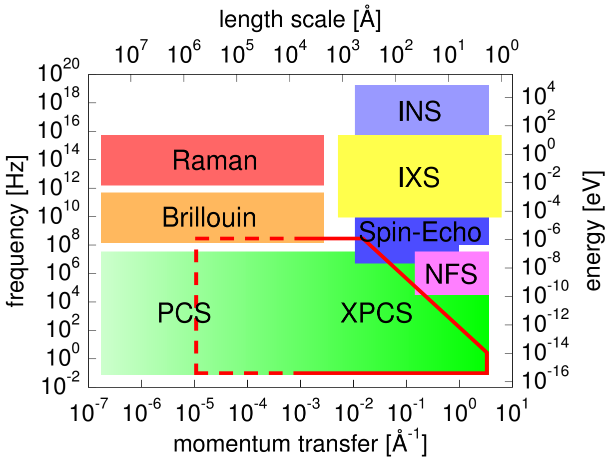

Figure 6.2.1: Sketch of the accessible frequency momentum transfer ranges for different experimental methods. The red outlined area can presently be studied with XPCS.

The inversion of speckle images is complicated by the fact that the necessary phase information is lost during the measurement. There are, however, algorithms that allow to recover this information when speckle images are sampled with fine enough resolution. This has been shown for artificial model structures (Miao et al., 1999) and applied e.g. to nano-crystalline materials (Williams et al., 2003; He et al., 2003). The latter work was successfully carried out on single crystalline material with a typical dimension down to 100 nm. An increase in brilliance would lead here to the possibility to study smaller objects and to eventually investigate granular microstructure in polycrystalline films. Magnetic X–ray speckle has been observed and characterized in a variety of materials (Peters et al., 2000; Eisebitt et al., 2003) without however leading to any successful reconstruction (or dynamic measurement) yet. Novel sources such as PETRA III will enable to reconstruct magnetic speckle patterns and to deduce the exact 3–D spin arrangement in magnetic nanostructures, such as magnetic storage media. Diffraction on single molecules is beyond the scope of storage ring sources. Simulations indicate this possibility for a future FEL source (Miao, Hodgson & Sayre, 2001). It is however already evident today that at novel sources like PETRA III the borderlines between near–field (Fresnel) imaging and far–field (Fraunhofer) diffraction will become increasingly transparent. Thus both, coherence preservation and/or tuning and reconstruction technologies will become more and more important. Smaller sources will also permit the transition from micro– to nano-focusing enabling new applications such as element specific micro– or nanofluorescence correlation spectroscopy (Wang et al., 1998a). It can furthermore be expected that the impressive achievements in measuring source and coherence properties with sophisticated interferometers will continue to flourish in view of the continuous improvements of the existing sources. A dedicated beamline both characterizing and exploiting the coherence properties at the new PETRA III facility is thus mandatory.

6.2.2 Science at the Coherent X-ray Beamline (CXB)

The new PETRA III storage ring will provide an unprecedented high spectral brilliance ($4 \cdot 10^{20}$ (s·mm^2·mrad^2)$^{-1}$ at 8 keV for a 5 m undulator device and 0.1% bandwidth) and more favorable source parameters (about 4 times smaller horizontal source size compared to ESRF). One can thus estimate (for 10 μm transverse coherence lengths) that PETRA III will supersede the coherent flux at ESRF by 1 -2 orders of magnitude. This will directly couple to experimentally accessible shorter time and/or length scales.
The projects related to the Coherent X–ray Beamline at PETRA III (CXB) can basically be split into two parts which will in the following be treated separately: Static (time averaged) experiments such as imaging where the spatial resolution is of importance and time resolved studies where the dynamics of the samples is of interest.

6.2.2.1 Time resolved experiments

In the last years X–ray Photon Correlation Spectroscopy (XPCS) has been developed and established at ESRF (ID10) and APS (IMM–CAT) to investigate dynamical phenomena. There are several advantages over other methods such as photon correlation spectroscopy using visible coherent laser light: a) The accessible Q–range is larger than 10^{-3} Å^{-1}, thus fluctuations on length scales in the sub–micrometer range can be studied. b) The penetration depth Λ of the X–rays can be tuned over a wide range. Illumination under grazing incidence makes XPCS surface sensitive (Seydel et al., 2001). For larger incident angles Λ may exceed several hundred micrometers depending on the wavelength and XPCS becomes bulk sensitive. c) Usually, multiple scattering effects can be neglected which simplifies the data interpretation. d) Optically opaque samples can be studied because they are transparent for X–rays (within the limit of the penetration depth).
The study of bulk dynamics in complex fluids (viscous liquids and glass forming systems, colloidal suspensions, ferrofluids, emulsions, polymeric systems, biologically relevant systems such as blood or milk) by XPCS is well engaged. To study them small angle scattering methods in transmission are used (see e.g. also Fig. 6.2.2). Many of these systems are in a concentrated state and frequently optically opaque which excludes the use of visible coherent light. With today's X–ray sources only the dynamics in the small Q regime with relatively slow correlation times τ from milliseconds down to microseconds are easily accessible. With the higher coherent flux at PETRA III progress in many areas is expected: Dynamics of complex fluids, dynamics in phase–separating and glass forming systems, critical dynamics and surface/interface dynamics. Most importantly however it will be possible to address non–equilibrium dynamics phenomena.
There is a class of experiments that require a maximum of flux at moderate momentum transfers (e.g. dynamics in liquids in the vicinity of the liquid structure factor peak). These

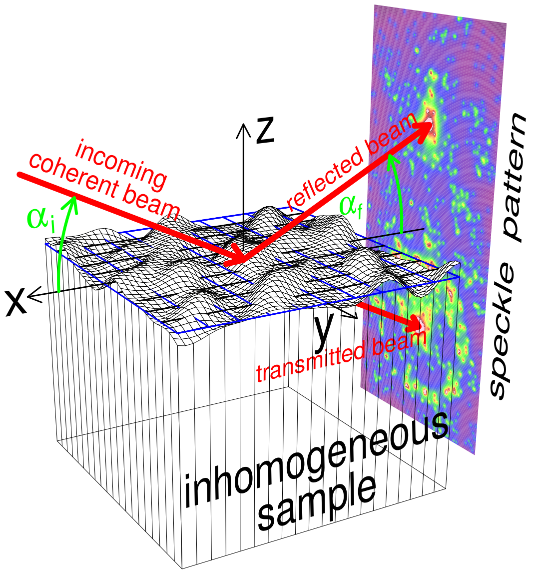

Figure 6.2.2: Sketch of a typical experiment using a coherent X–ray beam. Bulk inhomogeneities of the sample will result in a speckle pattern around the transmitted or reflected beam. Fluctuations in the sample will cause fluctuating speckle patterns. The speckle patterns are measured with a CCD–camera or with point detectors depending on the experimental needs. Correlation functions, derived in space and/or time yield the static and dynamic properties of the sample.

experiments are difficult today because a monochromatic beam with $\Delta\lambda/\lambda = 10^{-4}$ is too weak while a pink beam with $\Delta\lambda/\lambda = 1/nN = 0.01...0.03$ does not provide sufficient longitudinal coherence length ξ_l. Here n is the undulator harmonic (typically 3 at ESRF and 1 at APS) and $N \approx 35$ is the period. The 5 m undulator at PETRA III provides $\Delta\lambda/\lambda \approx 0.006$ on the fundamental (n=1) and the pink beam mode at PETRA III is thus a very attractive option for intermediate Q range experiments.

Many samples, especially those containing organic material, are quite sensitive to radiation damage and the flux and, even more important, the photon energy has to be tuned carefully. Simple polymers can withstand a 10 times higher dose when 16 keV photons are used instead of 8 keV radiation. Unfortunately, operation at higher energies is unfavorable since both, the transverse and longitudinal coherence lengths decrease with increasing energy. That experiments can be carried out with coherent X–rays at high photon energy was recently shown by Thurn-Albrecht (Thurn-Albrecht et al., 2003). The PETRA III source will provide sufficient spatial coherence (because of the small source size) to perform experiments at photon energies above 15 keV as a standard option.

Coherent X–ray scattering can be performed in surface sensitive mode. In this case, the scattering experiment is done in reflection geometry (see Fig. 6.2.2). An example are capillary waves on bulk material (Seydel et al., 2001) or thin films that can be investigated by studying the dynamic surface structure factor S_c as a function of the momentum transfer Q. For propagating waves (limit of small viscosity) $S_c \propto 1/Q^2$ holds whereas overdamped modes show $S_c \propto 1/Q$. This implies that the dynamics becomes faster with increasing Q and shorter length scales. Estimated from the PETRA III source parameters, the Q–range may be extended by a factor of 5 to 10 at CXB depending on the capillary mode characteristics. Thus, the zone of the sub–micrometer scale where finite size effects become important can be reached.

Up to now XPCS experiments have exclusively been carried out in homodyne mode (no photon mixing). Intensity limitations can be overcome by using the heterodyne mixing which is frequently applied in visible light scattering techniques (Langevin, 1992). The weakly fluctuating speckle signal from the sample is coherently superposed with a strong static reference beam. The fact, that the amplitudes of both signals (rather than their intensities) are superimposed results in an amplification of the fluctuating signal, thus dynamics on very short length scales can be investigated. The scattered signal from the sample and the reference beam must be produced within the coherence volume of the light (see Fig. 6.2.3). For X–rays this very difficult to achieve: The reference beam device (such as a beam splitter, a pinhole, a grating or a mesh) has to be located extremely close to the illuminated part of the sample. The increased coherence lengths at PETRA III will facilitate set-ups of this type. This will allow to investigate fluctuating surfaces and interfaces of organic liquids and soft matter.

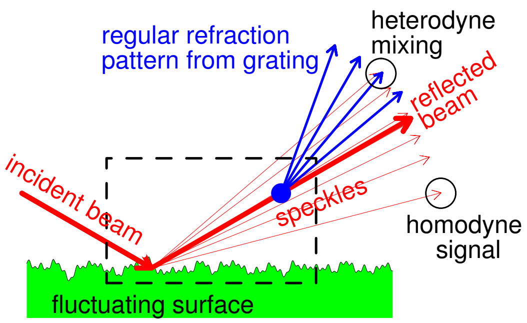

Figure 6.2.3: A possible setup of a heterodyne mixing experiment using a coherent X–ray beam to investigate surface dynamics. The fluctuating speckles (thin lines) are coherently superposed by refraction peaks of a grating which is placed in the static specularly reflected beam of the sample. The dashed area represents the coherence volume of the X–rays.

Further topics which may be investigated at CXB are fluctuating domains close to second order phase transitions (e.g. in magnetic materials or order–disorder transitions). Close to the transition temperature T_c critical slowing down of the fluctuating domains appears with correlation times $\tau \propto \xi^z$ ($z = 2.125$ for the 2–dimensional Ising model) where ξ is the correlation length which diverges proportional to $1/|T-T_c|^\nu$ (Petracic et al., 2002). Correlation times up to 100 ms have been reported which makes many systems accessible at CXB (Shu & Rand, 1997). The PETRA III source will allow to study small τ at small ξ where the photon flux is the limiting factor.
Flux limited up to now are also experiments on magnetic systems. Magnetic X-ray speckle has been observed (Peters et al., 2000; Rahmin et al., 2002) but a measurement of fluctuations has not been successful yet. With the high coherent flux at PETRA III, using a fast CCD–camera and a beam with intermediate energy resolution (multilayer monochromator such as proposed for CXB) the gain in intensity should be around 2 to 3 orders of magnitude which will make experiments on magnetically fluctuating systems possible.

6.2.2.2 Time averaged experiments

The shape and the internal structure of extremely small objects such as nano-crystals or grains can in principle be fully determined by using very high resolution speckle patterns even though the phase information of the object is lost during the scattering process. This is achieved by oversampling (reciprocal space resolution is much higher than necessary to monitor the sample size) and by illuminating a larger volume (compared to the sample volume) completely coherently (Fienup, 1982). A reconstruction of the sample structure in real space is possible by applying an iterative mathematical algorithm on the speckle pattern. The feasibility is shown in Fig. 6.2.4, where oversampled coherent scattering was performed at 3.1 nm wavelength. At this wavelength, the spatial resolution is limited to 100nm by the detector acceptance and the available coherent flux. At PETRA III higher momentum transfer can be achieved due to the accessibility of sub–angstrom wavelength in combination with a coherent flux which is larger than at existing sources. One can estimate a gain in resolution at least by a factor of 10.

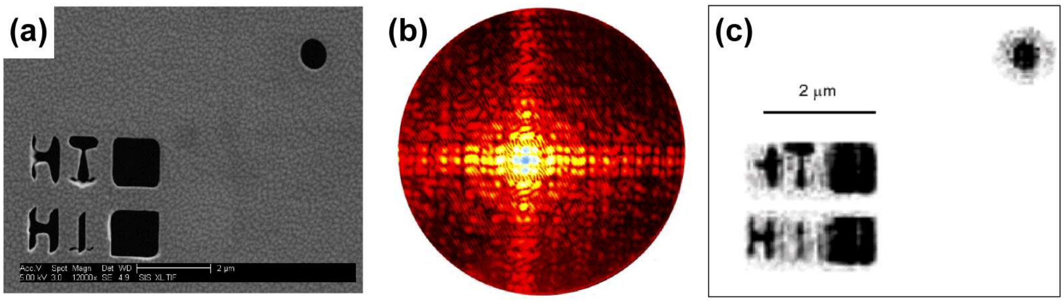

Figure 6.2.4: Example for imaging of a small object (a) via a speckle pattern (b). The reconstruction is shown on the right hand side (c). The spatial resolution is determined by the speckle intensity and the limited Q–space which can be covered (S. Eisebitt, private communication).

The test structure in Fig. 6.2.4 can better be investigated by microscopic methods. X–rays become superior when the objects are buried, if the internal structure is of interest or if material sensitivity is desired. An important example are nano-crystals (crystals smaller than about 100 nm) which may appear in new industrial materials and which show different physical properties compared to larger crystals. For material sensitivity a source with tunable photon energy is necessary. To investigate the internal structure a fully functional diffractometer is needed as it will be set up at CXB to orient the sample in the beam and to cover the full reciprocal space. Again PETRA III as a source is needed: It delivers large coherence lengths even at photon energies above 10 keV which is necessary to completely and homogeneously illuminate the samples.

For some applications a completely coherent point source with nanometer size is of advantage. Nowadays, the focusing is limited by the quality of the optical devices and in some cases by the initial coherence of the synchrotron beam. A new approach is the use of two dimensional waveguides to create a completely coherent wave field at the exit of the device with a spot size of only $(30\times60)\,\mathrm{nm}^2$ (Pfeiffer et al., 2002). The size may be chosen even smaller depending on the incident flux and the amount of photons which can be coupled into the waveguide. If the intensity of the nano-focused beam is sufficiently large holographic experiments with sub–nanometer resolution become possible which could be extremely interesting. With the proposed capabilities of CXB this kind of experiments seems to be feasible.

6.2.3 Beamline description

The crucial parameters for a coherence based beamline are the brilliance and the spatial and temporal coherence lengths. In order to achieve extremely stable and vibration free beam conditions the beamline instrumentation and equipment has to be chosen carefully. Only the proper design of both (the source and the beamline) guarantees a successfully working instrument. This implies first of all maximum beam stability in both position and angle, long lifetime of the stored beam, thermal stability of optical elements and a filling pattern as close as possible to DC conditions. External fluctuations are to be avoided. This refers to environmental noise, instrumentation related noise (pumps, cooling devices etc.,) and electrical noise.
Secondly, extremely important is the choice of a proper detector system. If a point detector is chosen to investigate single speckles an APD (avalanche photo diode) with its high dynamic range is the detector of choice. This is especially important when correlation times become very short. In many cases 2D–detection (CCD–camera) is the only solution to gain scattered intensity by averaging over iso–Q rings in small angle X–ray scattering (SAXS) geometry. In this way the illumination time on the sample can drastically be reduced (by a factor of 5 to 100, depending on the experiment). Therefore, an ultra fast CCD–camera is mandatory to be installed at CXB. This implies compatible set-ups for data transfer, the data storage, the computer hardware and software.
For all experiments with high spatial resolution and for many time correlation experiments a fully functional diffractometer with high accuracy is necessary $(Q > 5 \cdot 10^{-2}\,\text{Å})$. The detector arm should be able to carry a point detector or a CCD–camera. The option to tilt the incident beam (liquid diffractometer) is desirable. All optics and X–ray windows have to be optimized in order to maintain a large degree of coherence.
Key features and essential parameters for the beamline are listed in the following. A sketch of the beamline design is shown in Fig. 6.2.5.

- **Type of undulator and station**
  CXB requires a straight station (no side station) with a 5 m undulator.

- **Energy tunability**
  The full range of 5 keV – 25 keV. The energy will be quickly tunable during the experiment.

- **High β– or low β–section**
  A source with switchable β function is planned. If this is not possible a high β section is preferred.

- **Beamsize and shape at the sample**
  The beamsize and shape depends on the β-function. At a low–β section the FWHM beamsize will be 3 mm horizontally and 0.45 mm vertically for 12 keV radiation and in 50 m distance from the source. For experiments at a high–β section a beam size of $0.9 \times 0.2\,\text{mm}^2$ will be achieved for the same conditions.

- **Divergence of the beam**
  The RMS divergence at a high-β section will be 30 μrad horizontally and 4 μrad vertically for 12 keV photons. At a high–β section the divergence will be (8×4) μrad^2. Focusing will be possible.

- **Stability of the beam**
  The beam will be extremely stable in terms of time and space. The fluctuations will be smaller than 0.5% of the nominal values over 8 hours. External vibrations will be avoided. The beamline runs best with stable filling patterns of the electron/positron–bunches.

- **Flux and bandwidth of the beam, tuning of the coherence**
  The bandwidth of the first (fundamental) harmonic of a 5 m standard undulator at λ=1.5 Å is $\Delta\lambda/\lambda = 6 \cdot 10^{-3}$. The expected coherent flux at λ = 1.5 Å for $B = 4 \cdot 10^{20}$ is $F_c = (\lambda/2)^2 \cdot B$ is 1.4·10^{13}. The nominal transverse coherence length at 50 m from the source is about $40\,\mu\mathrm{m}$ (h) × $580\,\mu\mathrm{m}$ (v) for a high-β section and $110\,\mu\mathrm{m}$ (h) × $510\,\mu\mathrm{m}$ (v) for a low-β section. The longitudinal coherence length for $\Delta\lambda/\lambda = 6{\cdot}10^{-3}$ and λ=1.5 Å is $\xi_l = 0.025\,\mu\mathrm{m}$. Bandwidth tuning and increased longitudinal coherence lengths will be achieved via different monochromator configurations: A Si-(111) double monochromator and a multi layer monochromator will be installed. It will also be possible to guide the pink beam into the experimental hutch. A pair of mirrors will suppress higher harmonics. Focusing is foreseen via mirrors and/or by compound refractive lenses.

- **Coherence preservation**
  All optics will be carefully chosen and adapted under the aspect of coherence preservation and heat load resistance. The number of optical components will be minimized. All surfaces will be polished. Diamond based optics has to be considered.

- **Distances from the source**
  The optical components will be located as close as possible to the source. The distance source–sample will be about 50 m. The experimental hutch will be approximately 20 m long (see Fig. 6.2.5). Some space will be reserved for an optional side station.

- **Supplies at the beamline**
  Cooling water (room temperature), He– and N_2–gas supply, compressed air, supply for other gases. Two–phase and three–phase power outlets.

- **Additional equipment at the experimental station**
  Fast point detectors (avalanche photo diodes), a fast CCD-camera and a digital correlator for the point detectors will be set up. A 6–circle diffractometer for the sample and an x–y stage for the CCD will be assembled with accuracies of 10^{-3} deg in angular space and 0.1 μm in translation. An optical bench in front of the diffractometer will be installed. Pinholes, zone plates mounted on accurate x–y stages will be available. Additionally, temperature controllers, active vibration isolation stages, turbo pumps, ion getter pumps and power supplies will complete the setup.

- **Computing**
  A standard computer will control the beamline. A high performance computer with very fast data transfer lines and very large disk space will be used with the CCD camera.

From the previous sections it is clear that CxB will be designed and equipped to make a multitude of different experiments possible. A straight station is mandatory: For some experiments the pink beam passes to the experimental hutch, for others the energy has to be tuned. A β–switchable source will be favorable: Imaging and CXS experiments can benefit from a low β–section, XPCS works better at a high β–section.

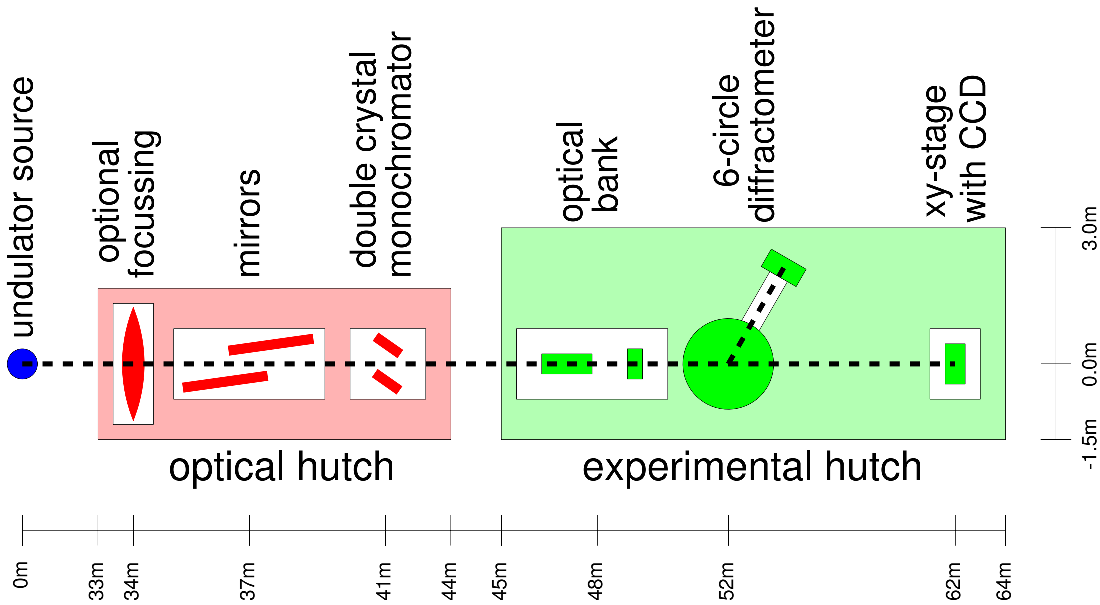

Figure 6.2.5: Generic layout of the coherence application beamline CxB at PETRA III (not to scale). Only the most important devices are shown. The approximate height of the hutches will be 5 m. The whole ground should be as vibration free as possible.

To keep the degree of coherence the number of optical windows in the beamline will be minimized. If the windows are made from Beryllium the surfaces have to be polished. Diamond windows have to be considered, windowless operation has to be studied as an option.

6.2.4 Capital investment and personnel

In order to ensure 24 h operation the minimum staffing consists of 2 staff scientists (1 permanent), 2 postdocs, 1 engineer and 1 technician. Estimated capital costs (excluding the insertion device) comprising experimental instrumentation, detectors, beamline control, and data acquisition are about 2000 k€. The layout of the beamline is highly modular and, based on the experience at ESRF and APS, we have solutions for every component. This will enable us to make the installation of the beamline and the start of commissioning compatible with day one operation of the machine.

6.3 High Resolution X-Ray Diffraction Beamline

Authors and Consultants:

O. Bunk	RISØ, Denmark
J. Falta	University of Bremen, Germany
R. Feidenhans'l	RISØ, Denmark
J. Grenzer	University of Potsdam, Germany
U. Klemradt	RWTH Aachen, Germany
Ch. Kumpf	University Würzburg, Germany
O. Magnussen	University of Kiel, Germany
W. Moritz	LMU München, Germany
B. Murphy	University of Kiel, Germany
M. Nielsen	RISØ, Denmark
D. V. Novikov	DESY, Germany
H. Over	University Giessen, Germany
U. Pietsch	University of Potsdam, Germany
M. Schmidbauer	Humboldt-Universität zu Berlin, Germany
Th. Schmidt	University of Bremen, Germany
O.H. Seeck	FZ Jülich GmbH, Germany
S. v. Smaalen	Universität Bayreuth, Germany
J. Zegenhagen	ESRF, France

6.3.1 Research with high-resolution X-ray diffraction methods

High resolution X-ray diffraction (HRXRD) is very widely used as a standard tool for structural investigations over a wide variety of length scales (see, for instance, the "Advances in X-ray analysis" series, Gilfrich et al., 1993 and following issues):

- At atomic scale: The atomic structure and charge density in bulk, and layers as well as at surfaces and interfaces can be resolved. Diffraction methods are the most accurate probe to determine the positions, occupation factors and displacement parameters of atoms within the unit cell. Well ordered systems allow even charge density studies on the level of binding electrons.

- At nanometer scale: For structures at solid and liquid surfaces and at buried interfaces HRXRD allows to define such parameters as thickness, orientation, chemical composition and interface roughness of layers. By variation of the incidence angle in reflectometry and grazing incidence diffraction/scattering also depth-resolved studies can be carried out. Two-dimensional reciprocal space mapping methods are nowadays standard tools for these applications.

- At mesoscopic scale: Structural parameters of periodic and non-periodic nanostructures and organic/inorganic material systems at mesoscopic scales can be investigated. Also for these techniques reciprocal space mapping is standard.

- High resolution X-ray diffraction methods are traditionally used for precise measurements of lattice parameters. They allow to define important physical parameters of perfect single crystals, for instance thermal expansion coefficients and phase transition parameters. Also precise measurements of strain and stress distribution at the level of relative lattice parameter variations of $\sim 10^{-4} - 10^{-6}$ in the bulk and at interfaces are possible. Lattice distortions induced by various defects can be studied from their influence on the form and the width of reflection profiles.

6.3.2 High resolution beamlines at existing synchrotron facilities

High resolution X-ray diffraction belongs to one of the most demanded basic techniques and involves a very wide variety of modern diffraction methods. Many undulator beamlines dedicated for high resolution measurements are currently operated at ESRF, APS and SPring8. The common design includes a lq. N_2-cooled double-crystal monochromator and a double-mirror harmonics suppression system. This optics provides good angular collimation in one plane, usually in the vertical one. The beam has a relative bandwidth of $\Delta E/E \sim 10^{-4}$. Many of the beamlines are equipped with focusing optics, which however degrades the beam collimation. Such beam parameters suit well to a resolution level, which was demanded at the beginning of the 90's. Since then, the complexity of objects and processes under investigation has immensely grown. To meet the new requirements, the beamlines must provide high flux X-rays with large transversal and longitudinal coherence.

6.3.3 High resolution diffraction at PETRA III

The proposed HRXRD beamline at PETRA III will deliver a beam, highly collimated in both planes and with a controlled bandwidth variable in the range $\Delta E/E \sim 10^{-5} - 10^{-4}$ in the whole wavelength range. The collimation and longitudinal coherence can be tailored according to the demands of the experiment and allow investigations at variable length scales and in a wide energy range. This is especially important for research of modern materials and physical effects at mesoscopic lengths.
The unique combination of very wide wavelength tunability in the range from 4 to 45 keV, ultra-high angular collimation and high monochromatization of the beam, delivered by the proposed HRXRD beamline, will open new possibilities for a wide spectrum of scientific fields:

- A variable longitudinal coherence and a large coherence volume of the beam will provide access to length scales ranging from Ångstrøms up to tens of micrometers.

- The high energies available (25–45 keV) will enable experiments at buried solid/solid and liquid/solid interfaces. This is of special importance, as interface processes are so far mostly studied in model surface experiments.

- High brilliance and high photon flux will allow *in situ* investigations of process kinetics as in diffusion, growth and phase transitions. Research on very small, of the order of nanometers, sample volumes and highly dissolved materials will become feasible.

- Small beam sizes combined with high collimation will be used for combined real- and reciprocal space mapping of samples with complicated lateral structures, such as surface relief gratings or quantum dot arrangements. This is of a special interest for investigation on technologically relevant samples.

- The high brilliance at higher X-ray photon energies will also enable accurate crystallographic studies on extremely small single crystals of compounds that are so complicated in structure that powder crystallographic structure determination methods fail. The extremely parallel radiation is of advantage for the investigation of crystals with satellite peaks very close to main reflections as they occur in some incommensurate structures or in some long periodic super structures.

The list of experimental methods in the field of structural characterizations that will benefit from the high brilliance of PETRA III is large. It includes correlation spectroscopy, GIXRD (SXRD)[1], GISAXS[2], grazing incidence X-ray scattering, magnetic X-ray scattering (MXRD), micro spot X-ray diffraction and scattering, X-ray reflectivity, X-ray standing waves (XSW) employing X-ray fluorescence and X-ray photoelectron spectroscopy as secondary signals. The sensitivity of the scattering methods can be enhanced by anomalous absorption techniques for a wide range of materials.
New prospects in surface and interface investigations, opened by high-resolution diffraction at PETRA III, are of particular interest for the progress in the structural characterization of new materials and will stimulate their development as exemplarily discussed for organic electronics below. Here the main achievement will be the possibility to perform structure determinations for materials consisting of light elements (like carbon) which, due to their very small scattering amplitudes, have remained 'invisible' in conventional surface diffraction and scattering experiments.
The high brilliance combined with very large longitudinal coherence can also bring major advances in liquid surface research, especially in fluctuations at liquid surfaces, liquid metals, surface freezing and layering and in-situ crystallization from solutions (Tolan, 1999).

6.3.3.1 In-vacuum surface research

The high brilliance storage ring PETRA III will enable a wide range of qualitatively new experiments regarding the structure of surfaces and interfaces, like time-resolved measurements of surface and interface processes. Large benefit will be gained from the expected high brilliance of PETRA III. It will allow to collect data at a drastically shorter time scale. The beamtime required to perform a structure determination by means of grazing incidence X-ray diffraction (GIXRD)[3], for example, can be expected to be reduced from many hours to some minutes. This will not only permit to develop GIXRD into a standard tool of surface science, complementing LEED (low-energy electron diffraction) in its role as a work horse for the characterization of surface structures, but also allows structure determination of highly

[1] GIXRD: grazing incidence X-ray diffraction; SXRD: surface X-ray diffraction.
[2] GISAXS: grazing incidence small angle X-ray scattering.
[3] This method is also referred to as SXRD (surface X-ray diffraction).

diluted systems (like promoters in catalysis or dopants in semiconductors), and systems for which only very small sample volumes are available. The most important objects will be mineral and oxide surfaces, with applications in the fields of sensing and catalysis, materials for medical applications like implants, and quantum structures prepared on the basis on conventional and new semiconductors. Time-resolved diffraction experiments will allow to monitor structural changes during surface, interface and 'bulk' processes like catalysis (performed in near ambiance conditions), adsorption and desorption (also intentional contamination), phenomena of epitaxial growth for a wide variety of growth methods such as MBE (molecular beam epitaxy), MOVPE (metal organic vapor pressure epitaxy), HPCVD (high pressure chemical vapor deposition, even up to atmospheric pressures), PECVD (plasma enhanced chemical vapor deposition) and phase transitions of thin films. In combination with a tunable polarization, analogous progress can be achieved in magnetic scattering experiments.

6.3.3.2 Mesoscopic semiconductor structures

Vertical carrier confinement is the basis for the most modern opto electronic devices. A lateral carrier confinement offers another degree of freedom for device design. In some cases, it allows to achieve better parameters, as i.e. a higher modal gain, a better thermal stability, and tunable emission wavelength of laser diodes (Klopf, Reithmayer & Forchel, 2000).
Several concepts are being used to create a lateral confinement. One important approach is to exploit the self-organized growth of heavily strained 3D islands of the active material (Bimberg et al., 1999; Schmidbauer et al., 1998). In a different approach, semiconductor surface wire and/or dot structures are created by a holographic exposure, a subsequent wet chemical etching and in a second epitaxial step the complete planarization of the corrugated surface. Another technology employs the low energy focused ion beam implantation for direct production of buried nanostructures. In case of implantation energies less than 100 keV the penetration depth of ions lies below 1 μm. At a depth up to 500 nm, the implantation induces no significant structural damage, but a periodic strain profile.
The challenge in structural characterization of lateral semiconductor nanostructures is the non-destructive investigation of the shape and strain distribution (Schmidbauer et al., 1998; Roch et al., 2002; De Caro, Tapfer & Giuffrida, 1996; Shen et al., 1996; Grenzer et al., 2000; Grenzer et al., 2004; Zhong et al., 2003). Due to the lateral periodicity on the mesoscopic length scale each fundamental Bragg peak is accompanied by satellites, so-called grating peaks. For the typical lateral periodicity of 500 nm the period of these peaks equals Δq_x= 0.013 nm^{-1}, which requires a highly collimated beam and goniometers with an angular resolution and angle reproducibility better than $0.001°$ for both sample $\Delta(\omega)$ and detector $\Delta(2\Theta)$ rotation axis for peak separation. The large lateral correlation length of modern artificial nanostructures results also in satellite peaks which are extremely narrow in width. This makes the requirement for the parallel beam optics and precise mechanics especially critical in order to achieve that the width of the resolution function is smaller than the intrinsic width of the satellite peaks. In structures obtained by ion implantation, damage and strain profile must be defined. The entire strain lattice can be probed depth-resolved by GIXRD considering the same instrumental demands (Grenzer et al., 2000).

6.3.3.3 Phase transitions in surfaces and thin layers

Research of hase transitions at surfaces is a very important and fast developing field of modern solid state physics. The existing theoretical descriptions of phase transitions at surfaces (Dietrich & Wagner, 1983; Binder, 1983; Diehl, 1986 and others) are yet to be fully verified experimentally. Recent theoretical papers (Landau & Binder, 1990; Milchev et al., 2003) emphasize the importance of measuring critical behavior at the surface as close as possible to the critical temperature.

Using surface X-ray scattering Burandt *et al.* (1993) obtained the first observations of near-surface critical phenomena of a phase transition in a molecular solid (NH_4Br single crystal) showing both an order-disorder and a strong displacive component. In a very interesting experiment Krimmel *et al.* (1997) performed an X-ray scattering study of the continuous B2-A2 order-disorder transition in semi- infinite FeCo(001). They observed that the surface related order parameter persists above the bulk critical temperature for a mesoscopically thick surface sheet. This temperature dependence displays a behavior similar to that of a magnet exposed to an external field. They conclude that the surface layer is not induced by surface coupling but rather by surface segregation. This experiment provides evidence for the presence of a surface field which couples to the surface susceptibility. In a grazing incidence study (Zhu et al., 1998) of the order-disorder transition in $Cu_3Au(111)$, a first order phase transition in the bulk at 665 K was observed as well as enhanced surface ordering to a slightly higher temperature. The strong diffuse scattering from short range order fluctuations in the bulk became much weaker in the surface region. Reichert *et al.*(2003) reported a new type of short-range order correlations at the (001) surface of Cu_3Au proposing that this new surface effect was caused by a dramatic change in strain-induced interactions at the surface.

The physical properties of epitaxial ferroelectric films can be very different from those of bulk crystals, mainly because of the distortion of the film by the substrate and the electrostrictive coupling between polarization and strain, which is characteristic for perovskite ferroelectrics. Size effects in thin ferroelectric films result also from domain-wall contributions and include (a) a minimum thickness for the existence of ferroelectricity, (b) a thickness-dependent increase of the transition temperature and (c) modifications of the spontaneous polarization. In addition, also major qualitative changes of phase diagrams are predicted by theoretical calculations, leading to specific ferroelectric phases that do not exist in bulk crystals. For example, the paraelectric to ferroelectric transition in certain perovskite films is predicted to be of second order instead of first-order as it is in the bulk; in a certain range of misfit strains and temperatures, a heterophase state may be stable, being composed of distorted ca and aa phases. However, since most calculations are based on relatively simple domain models, high quality experimental data are necessary to test these critical issues for the application of thin ferroelectric films and nanostructures. The observation of unusual, complex polarization states in ferroelectric films represents an experimental challenge.
Synchrotron radiation offers the unique possibility to determine lattice parameters and unit-

cell distortions in single-crystalline films, in and out of the plane of growth direction, with high precision. Furthermore, depth-resolved measurements allow access to the strain gradient towards the surface as well.
Such investigations would benefit strongly from a high-resolution beamline at PETRA III owing to the high brilliance of the beam and the high X-ray energies available (to penetrate strongly absorbing electrodes and other components of more complex multilayers). Experiments with small ferroelectric capacitor structures could be envisaged, with samples placed in additional contact to a dielectric spectroscopy setup.

The study of phase transitions in thin layers and especially at surfaces is a far clear case where both high resolution and high intensity are required simultaneously. Intrinsic widths of the Bragg peaks are typically $0.005°$ or less and scattering becomes especially weak close to the transition temperature. To investigate superstructures forming or melting, one will require the very low divergence provided by a high resolution beamline on a high flux high brilliance source.

6.3.3.4 Soft matter systems: organic thin films - organic electronics

A central effort in organic electronics and related fields (notably organic photovoltaic and organic light emitting diodes) is the development of a set of materials with a broad range of optical, optoelectronic, electronic, and sensing functionalities and adapted solution-based additive manufacturing processes (e.g. printing, display), applicable to a range of structural substrates to form composite materials with *designed multi-functionality*. Structural control of multi-functional materials is a key requirement for a solution-based manufacturing approach. The ability to control the structures must extend over many different length scales ranging from the nanometer molecular length scale to the macroscopic length scale on which components and devices will be fabricated.
In the last decade a number of publications have been devoted to inscription of surface relief gratings containing light sensitive moieties (Rochon, Batalla & Natansohn, 1995). The wavelength of the laser should be near the absorption maximum associated with the trans-cis and cis-trans isomerisation of the azobenzene moieties. In case of polymers containing azobenzene units, a sinusoidal surface relief grating is created if the sample surface is illuminated by an interference pattern of two counter-rotating circular-polarized beams of an Ar+ laser (l=488 nm). The absorption of this light induces material flow even at room temperature which is at least 100 K below the glass transition temperature, of the polymers. These properties make the investigated polymer materials very attractive for applications, in particularly for high-density optical storage. Using a laser power of about 250 mW/cm^2 and a film thickness of 400 nm, a surface relief amplitude in the order of 100 nm is generated after a time of about 30 s. The development of this surface relief grating is observed by in-situ X-ray diffuse scattering and reflectivity measurements. The correlation length of these grating structures exceeds several millimeter; therefore the grating peaks are again very narrow requiring an extreme high angular resolution (Kim et al., 1995; Barrett, Natansohn & Rochon, 1996; Jiang et al., 1996; Geue et al., 2003).
The typical length scale of self-organization is much smaller (typically < 10 nm) than the

length scale on which devices and components are fabricated. Therefore, in many cases the potential benefits of self-assembling properties do not translate into enhanced materials performance. If structural control is to be achieved, for example, with the help of a patterned, templating substrate, the length scale of patterns on such templates needs to match the length scale of self-organization (van de Craats et al., 2003; Bunk et al., 2003).

Interfaces formed by solution processing of different materials, such as in inorganic/organic hybrid materials are difficult to control, and are usually not atomically abrupt. Only a limited set of metrology tools for quantitative characterization of interfaces exists, in particular for characterization of interfaces between functional polymers.

Grazing Incidence X-ray Diffraction (GIXRD) is eminently suited for providing information about the molecular arrangements at buried interfaces and therefore also the method of choice for answering these questions. Using GIXRD one obtains detailed information on the orientation and the apparent size of the self-organized domains in poly-3-hexylthiophene (P3HT) films spun on actual FET substrates (see Fig. 6.3.1). This result demonstrated the strong dependence of the macroscopic charge carrier mobility on the orientation of the self-

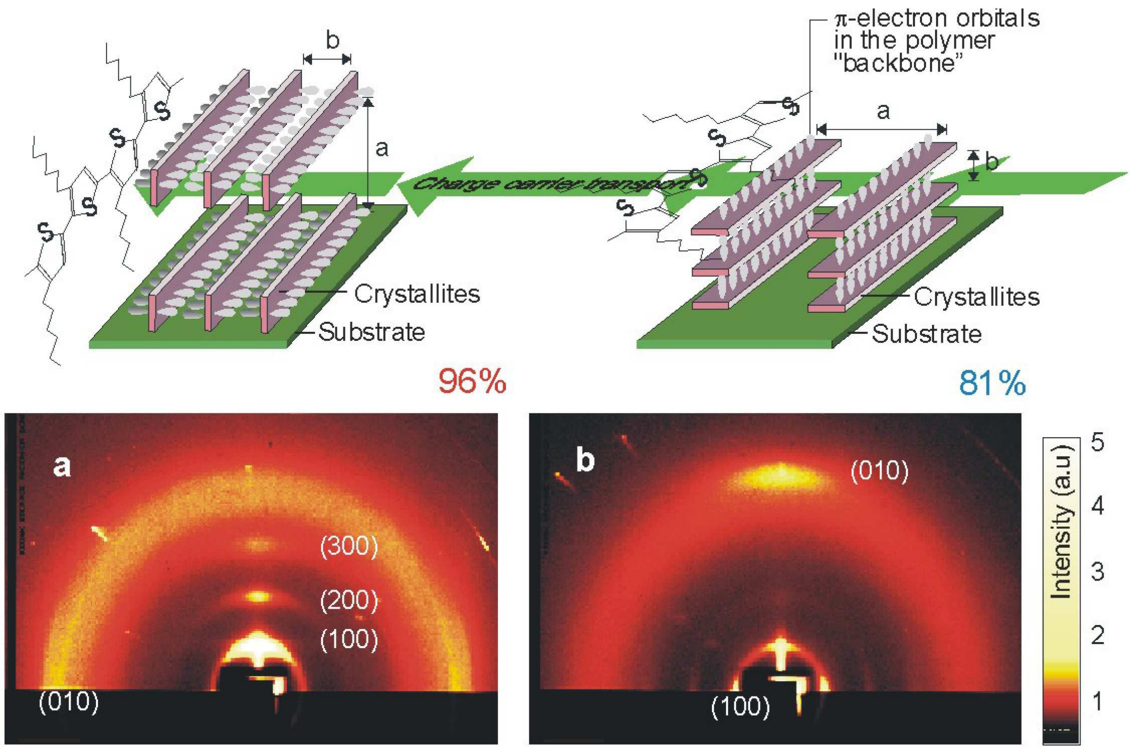

Figure 6.3.1: The two-dimensional distribution of scattered grazing incidence X-ray intensities from spin-coated 70–100 nm thick P3HT films with regioregularity of 96% (a) and 81% (b) on Si/SiO_2 substrates: The vertical (horizontal) axis corresponds to scattering normal (parallel) to the plane of the film. Different orientations of the micro-crystallite grains with respect to the substrate are sketched above, together with the direction of motion probed when measuring the mobility of the charge carriers. The measured charge carrier mobility increases by a factor of 100, from $\sim 0.001\, cm^2/Vs$ to $\sim 0.1\, cm^2/Vs$, going from the situation depicted in (b) to (a).

organized domains (Sirringhaus et al., 1999), and lead to the conclusion that high mobilities reflect effective inter chain transport.
Further, GIXRD investigations have revealed the structures formed at the interface between external alignment layers and a film of discotic molecules. Three epitactic growth modes of the discotic molecules were discovered, demonstrating a direct control of the orientation of the π-stack direction.
A micro focus beamline with a well characterized, high collimated beam at the sample would allow to rapidly explore essential scattering data in one step, using a state-of-the-art CCD camera. For many types of cast films (e.g. most spin-cast samples), the ordering is solely in the direction parallel to the surface normal, hence a single image at grazing incidence would provide the total scattering information obtainable in the diffraction regime.
Combining diffraction analysis with X-ray reflectivity will add tremendously to the power of characterization of buried interfaces. Here the main benefit can again be expected mostly from a small, well defined and first and foremost a well collimated beam. Relating structural characteristics to device properties requires the structure to be investigated under realistic conditions. The power of gaining insight into the structure of material is dramatically diminished if we cannot correlate it to other material properties. For example, the characteristics of FET devices are strongly dependent on the properties of the semiconductor in the channel region between the source and drain electrodes. As typical channel widths are of the order of a few microns, a true microprobe beam would allow us to monitor the structural development in the channel while a real transistor is operating.

6.3.3.5 Liquid surfaces and interfaces

The physics of liquid surfaces involves a wide variety of structural and dynamical properties, including among all capillary waves (Gutt et al., 2003), surface layering (Magnussen et al., 1995), surface freezing (Sloutskin et al., 2002), mixing/demixing, wetting, and the phase behavior of Langmuir films (Magnussen et al., 1996; Kraack et al., 2002). They are investigated at the surface of simple liquids, liquid metals, alloys, molten salts and inter metallic compounds.
Ideally, a dynamic range down to 10^{-10} should be accessible for these measurements, requiring high flux. Since liquid surfaces often exhibit significant curvature, small vertical beam size and divergence, i.e. high brilliance, are required. Furthermore, the possibility of high flux / high energy measurements would allow to extend these studies to liquid-liquid interfaces, e.g., to liquid metal/electrolyte interfaces or model biomembranes.
Liquid surface research will require an additional tilting monochromator/mirror close to the sample and a liquid surface setup on the diffractometer the HRXD beamline.

6.3.3.6 High resolution structural investigation on bulk crystals

The high brilliance of a PETRA III undulator will provide unique possibilities for the investigation of micro crystals, aperiodic compounds and for charge density studies.

- Crystals of a large number of complex materials cannot be grown to large sizes since the corresponding synthesis paths deliver only micro crystalline powders. Crystal structure determination from powders is still limited to relatively simple compounds and also limited in accuracy due to the unavoidable overlap of reflection profiles. However, most of the micro crystalline powders contain crystals from 1 to 10 μm size which is, depending on the exact composition and the radiation dose the crystals can suffer without damage, sufficient for single crystal diffraction studies at a high brilliance undulator beamline even for complex structures.

- Aperiodic crystals like incommensurately modulated crystals or quasi crystals show at least in one dimension no translation symmetry despite the fact that they exhibit sharp Bragg reflections. In general, the diffraction pattern consists of reasonably strong main reflections and of satellite reflections with intensities 10^{-1} to 10^{-8} times weaker than the main reflections. This large difference in intensity requires extremely intense beams for a reliable determination of the satellite reflection intensities. Since these satellite peaks can occur very close to each other or to the main reflections a parallel beam is required in order to separate the different orders. Aperiodic crystals are found in many material classes, e.g. many electronic materials exhibit at low temperatures phase transitions giving rise to incommensurate spin- or charge-density waves. Only the accurate knowledge of the incommensurate structure will enable a thorough understanding of the mechanism of the phase transition and of the physical properties.

- Accurate charge density studies allow to analyze the strength and kind of chemical bonding and other interatomic interactions (Koritsánszky et al., 1998). The experimental determination requires reflection intensities of very high accuracy and high completeness up to a resolution of at least $\sin(\theta)/\lambda = 1\,\text{Å}^{-1}$ or better up to $\sin(\theta)/\lambda = 1.3\,\text{Å}^{-1}$. Especially for more complex organic compounds like pharmaceuticals and small proteins it is extremely difficult to achieve a sufficiently high resolution due to the weak scattering power in this range even at the low temperatures (20–100 K) used in order to minimize the thermal motion of the atoms. Therefore, the high brilliance of an undulator is required for the reliable determination of the intensity of the high order reflections (Jelsch et al., 2000). In many cases X-ray photon energies above 20–30 keV are beneficial in order to reduce radiation damage and to minimize systematic errors like absorption and extinction (see also Sec. 6.1.2.3).

6.3.4 Beamline optics and apparatus

The high resolution X-ray diffraction beamline can use a standard PETRA III undulator in a high-β section of the storage ring and will operate in the energy range from 4 to 45 keV. Due to the wide energy range and the necessity to reach energies as high as 45 keV, the beamline can hardly be placed on a side station. No white or pink beam applications are planned.

6.3.4.1 Beam conditioning optical elements

The first optical element of the beamline will be a fixed-exit double-crystal silicon monochromator cooled to 120 K. The monochromator includes two pairs of crystals, with symmetrical (1 1 1) and (3 1 1) reflections. The former pair can be used for preliminary monochromatization in the energy range from 4 to about 25 keV, while the latter one can be best operated in the higher energy range.
The double crystal primary monochromator is followed by a fixed-exit Bartels type double channel-cut high energy resolution monochromator. A set of interchangeable channel-cut Si crystals with (1 1 1), (1 1 0) and (3 1 1) surface orientations will allow a wide choice of intense reflections. Depending on the combination of reflections employed, the divergence of the beam can vary between $0.5\,\mu$rad to the full $5\,\mu$rad coming from the source. This monochromatization system ensures an energy resolution $\Delta E/E \sim 2 \cdot 10^{-4} - 5 \cdot 10^{-5}$ in the whole energy range. Simultaneously, the same double channel-cut monochromator provides a high angular collimation. Depending on the experimental requirements, the monochromator can be installed in the vertical or in the horizontal plane. In experiments which require small beam cross-sections, the secondary monochromator should preferably be placed near to the sample position.
The higher harmonics are suppressed by the same crystal arrangement (Fig. 6.3.2). As an option for the lowest energy range, a set of two flat mirrors (two stripes, uncoated and Rh coated, with the vertical deflection plane) can be used.

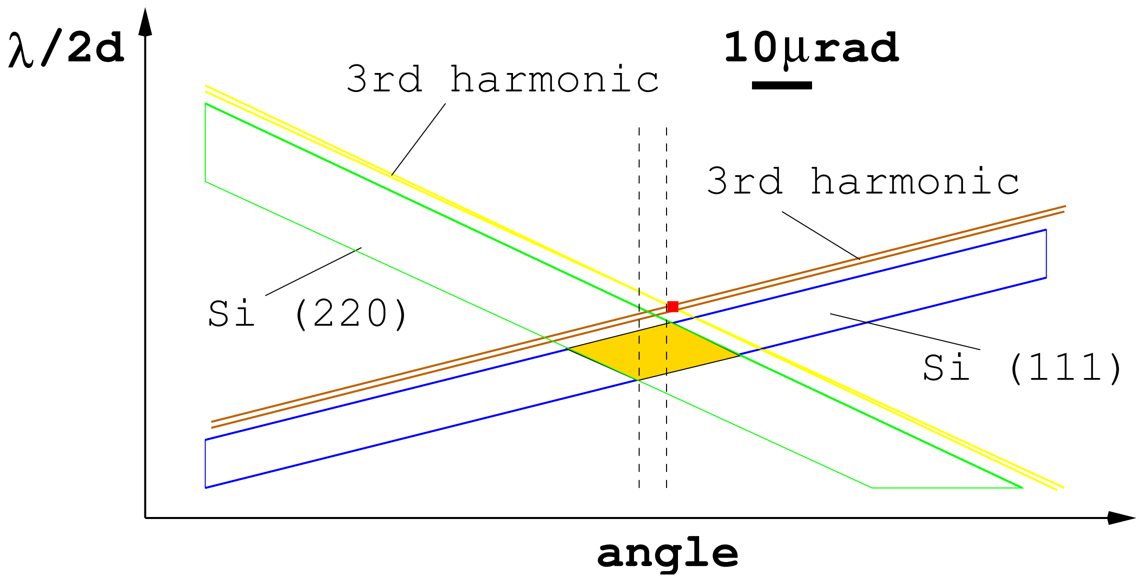

Figure 6.3.2: Suppression of higher harmonics by Bartels type monochromator. The DuMond diagram presents, as an example, a case of Si(1 1 1)/Si(2 2 0) reflection pair at 8 keV, with the third harmonic at 24 keV. The higher harmonics are visible only in a narrow angular interval, marked by the red spot. Already a minor detuning of crystals allows to suppress the harmonics by a factor of 10^{-4} or better. The dashed lines mark the angular interval, where the transmitted 8 keV beam will pass without a loss of intensity.

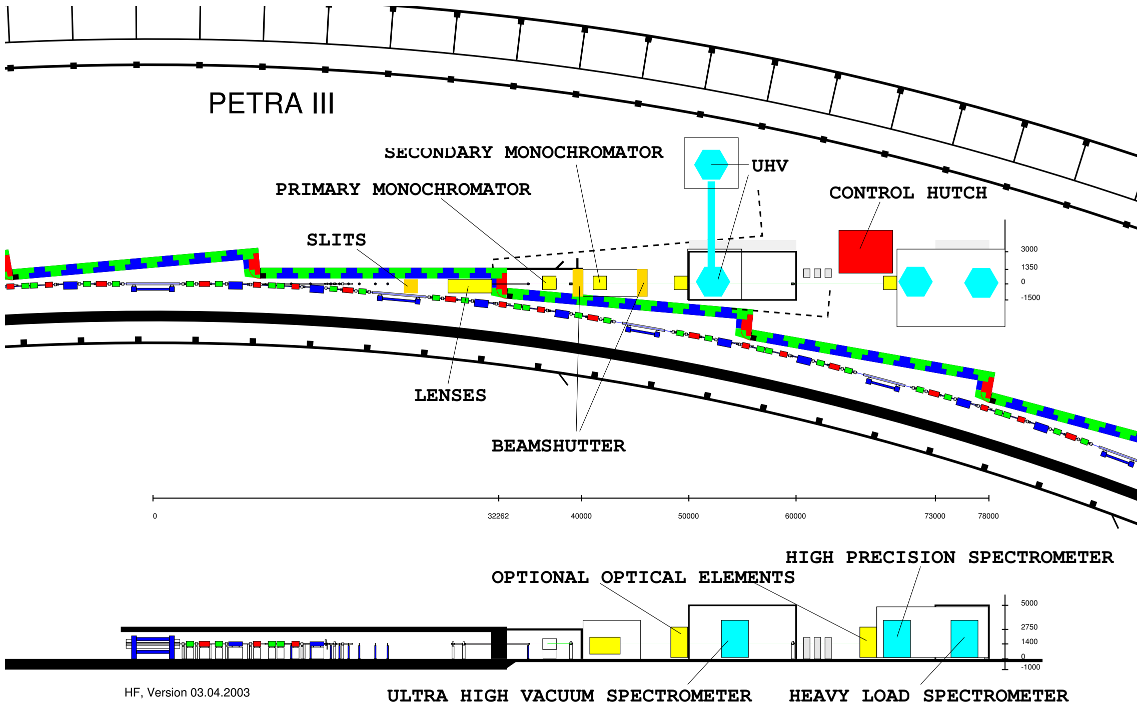

Figure 6.3.3: General beamline layout.

6.3.4.2 Experimental hutches

The proposed beamline includes two experimental hutches (Fig. 6.3.3).

- Ultra-high vacuum chamber hutch
  Hutch 1 is dedicated to research in ultra high vacuum (UHV). The main element of the equipment is an ultra-high vacuum chamber, directly connected via a differentially pumped line to the monochromator. The chamber is equipped with a 3-circle sample goniometer with precise sample rotation axis.
  Due to the high beam collimation in both planes, the UHV experiments become very tolerant to a possible misalignment of the diffracting planes. With the beam collimated in one plane, a misalignment leads to information loss due to widening of the curves. With the beam collimated in both planes, the misalignment leads to non-coplanar scattering geometry, which can be easily accounted for at the data evaluation stage. Because of the high monochromatization, the experiment is also extremely insensitive to the lattice mismatch between the sample and monochromator. Independent of the material under investigation and the chosen reflections, the measurements can be carried out effectively in non-dispersive mode. The UHV experimental chamber will

be equipped with an energy-dispersive electron detector, mass spectrometer and sample heating appliance. The X-ray experimental chamber is directly connected via an in-vacuum sample transfer line to an external UHV sample preparation and characterization facility. The facility can be operated independently from the experiment. It will include a comprehensive set of equipment for different film growth (MBE, HPCVD, MOVPE) and surface analysis (LEED, RHEED, STM, etc) techniques. The samples are delivered to the X-ray experimental chamber through an in-vacuum transfer line. This combination enables complex studies of interface processes. Focusing elements as refraction lenses and Fresnel plates can be inserted between the UHV experimental chamber and the monochromators for better localization of the experimental area.

- Diffractometry hutch
  The high resolution diffractometry hutch is designed for two separate diffractometers: one precise 6-circle diffractometer and one heavy-load diffractometer. The exit window of the high-vacuum part of the beamline will be made of polished Be or diamond to preserve the beam coherence. As an option, windowless layout could be realized in future.
  At the first stage, only the precise spectrometer will be installed. The sample rotation stages of the spectrometer will provide four degrees of freedom, with a precision on the main rotation axis better than $0.5\,\mu$rad. The opened Eulerian cradle will allow installation of light sample chambers to control the sample environment during experiments. The possibility to use non-coplanar diffraction schemes will be provided by a detector arm with two degrees of freedom. The detector arm will rotate in a wide angular range and can be additionally equipped with an analyzer crystal setup or a 2D detector.
  For liquid surface experiments, the precise spectrometer will be used for installation of an additional monochromator for beam inclination. The high precision and availability of multiple degrees of freedom will allow continuous incidence angle variation with fixed beam spot at the sample. A vibration-free user appliance for liquid samples will be provided additionally.
  As in the UHV hutch, an optical bench for focusing optics and/or Bartels-type double channel-cut monochromator can be placed in the front part of the hutch.

The monochromator and experimental hutches will be built on a vibrationally isolated foundation. The temperature in this hutch will be kept stable within 0.5K.

6.3.4.3 Further experimental equipment

- Optical and mechanical elements, media supplies.
  The standard beamline equipment consists of Fresnel and refraction lenses, slits, and precise translational stages. A set of pumps and power supplies will be available. Cooling water, helium and nitrogen gas supplies as well as a cabinet for gas flasks

with possibly short connection lines to the sample will be integrated into the hutch layout.

- Detectors
  Ionization chambers, scintillation counters and PIN- and avalanche photo-diodes will be available for X-ray registration. For energy dispersive measurement, the beamline will be equipped with Si(Li) and/or multi-pixel silicon drift detectors. For 2D mapping and for crystallographic data collections an accurate, fast readout 2D CCD camera, diode or pixel array detector will be available.

- Electronics, computers and software
  The beamline will be operated locally, including a possibility to vary the undulator gap during the measurements. The electronics in modular NIM standard will allow the most fast and flexible way to optimize the data acquisition for any user experiment.

- Beamline control room and workshop
  The beamline control room will be built adjacent to the diffractometry hutch. A general purpose workshop can be shared with several other beamlines. A separate vacuum workshop is needed.

- Cryogenics
  A variety of cryostats will be available including lq.-N_2 and He cryo-streamers for low temperature experiments.

6.3.5 Research and development challenges

In the optical and mechanical parts, all proposed components have already been tested in numerous applications and can be built and operated routinely.
Some very limited R & D effort is necessary to construct an in-vacuum optical bench for interchangeable double channel-cut monochromator, switchable between vertical and horizontal diffraction planes. Test experiments can be carried out to ensure the high harmonic suppression in combination with angular stabilization operation.
The bottleneck for high resolution diffraction experiments - just as for most modern SR techniques - will the problem of fast signal detection, especially the lack of fast high-resolution 2D imaging detectors. Their development requires a coordinated effort of the whole synchrotron radiation community.

6.3.6 Capital investment and personnel

The beamline will be staffed with 2–3 scientists/postdocs and 2 technician/engineers.
The estimated total capital investment of this experimental endstation amounts to about **1900** k€.

6.4 Micro- and Nanotomography

Author :

F. Beckmann GKSS - Research Center Geesthacht, Germany

6.4.1 Introduction

Microtomography (μCT) using synchrotron radiation became a valuable tool for the non-destructive three-dimensional investigation of specimens in fields of e.g. medicine, biology and materials science. Employing highly brilliant and collimated X-rays of second and third generation synchrotron sources new contrast techniques including phase, fluorescence and enhancement by diffraction were developed. Existing schemes were optimized to yield more sensitivity to structural changes at less burden afflicted to the specimen.

At DORIS III absorption- and phase-contrast μCT techniques were developed and applied at photon energies in the range of 8 to 150 keV. At the wiggler-beamlines BW2, W2, and BW5 the present user experiment for microtomography makes use of the large, intense, and incoherent X-ray source. The present setup is optimized for performing absorption-contrast microtomography on large samples. Due to the divergence of the source the spatial resolution, which can be achieved in the tomogram, is limited to about 2μm. At PETRA III the excellent X-ray source will allow for new absorption- and phase-contrast techniques which make use of the coherence of the X-ray beam. Furthermore the spatial resolution will be increased into the 50 nm regime.

6.4.2 Current state of the scientific field

The standard application of microtomography at current third generation synchrotron radiation facilities makes use of the low divergence and high intensity of the source to record parallel 2-dim. projections of samples using monochromatic X-rays. By rotating the specimen, typically in steps of 0.1 to 1 degree, and repeating the measurement over the range of 0 to π the tomographical scan is performed. The tomographical reconstruction then yields the 3-dim. spatial description of the projected property of the sample. Several different absorption- and phase-contrast techniques were developed in recent years (Bonse & Busch, 1996).

6.4.2.1 Methods

The experimental setup consists of a 2-dim. X-ray detector and a high-precision sample manipulator. The distance between detector and manipulator can be changed not only to allow to introduce sample environment or an X-ray interferometer, but also to exploit the coherence effects of the X-ray beam of 3rd generation sources.

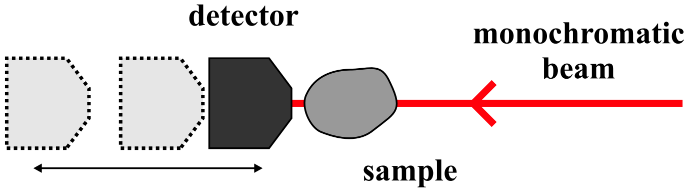

Figure 6.4.1: Schematic setup for absorption-contrast μCT.

Absorption-contrast μCT

To perform absorption-contrast μCT radiograms are taken at a minimal detector-sample distance. A single projection is obtained by recording the primary intensity $I_0(x,z)$ and the attenuated intensity $I(x,z)$, where x denotes the horizontal and z the vertical dimension (see Fig. 6.4.1). The attenuation projection $P(x,z)$ can be determined by

$$P(x,z) = \int \mu(x,y,z)\,dy = -\ln\left[\frac{I(x,z)}{I_0(x,z)}\right] \ . \tag{6.4.1}$$

Using the atomic number Z, photon energy E and mass density ρ the attenuation coefficient μ except close to absorption edges can approximately be expressed by

$$\mu \propto \frac{Z^4}{E^3} \cdot \rho \ . \tag{6.4.2}$$

The photon energy E is matched to the sample characteristics in order to obtain sufficient contrast in the tomogram. Therefore only the structure of the most absorbing material of the specimen can be investigated well by absorption-contrast μCT.

Phase-contrast μCT

X-rays are not only attenuated by the specimen, they are also shifted in phase. This behavior is described by the complex index of refraction

$$n = 1 - \delta - \mathrm{i}\beta \ , \tag{6.4.3}$$

where the real part δ corresponds to the phase shift due to refraction and the imaginary part β to the absorption. Depending on the type of the X-ray source different phase-contrast imaging techniques were developed which are suited for different types of sample composition. At incoherent X-ray sources of second generation synchrotron radiation facilities multiple crystal reflections or X-ray interferometer have to be used. At third generation sources phase-enhancement can be achieved by varying the sample-detector distance (Snigirev et al., 1995; Cloetens et al., 1996) due to the partial coherent X-ray beam. In Fig. 6.4.2 the coherent image formation of a transmission image is shown. Using sample dimension d and wavelength λ four regions of sample-detector distance y can be distinguished:

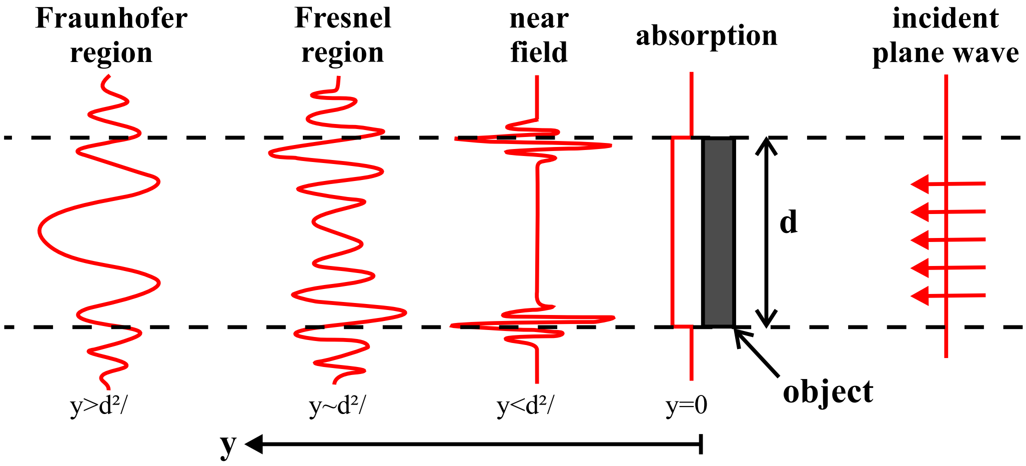

Figure 6.4.2: Coherent image formation with partially coherent X-rays depending of the object-detector distance y, sample dimension d and wavelength λ.

$y = 0$	**absorption**	The intensity is a pure absorption image.
$y < d^2/\lambda$	**near field**	Contrast is given by sharp changes in the refractive index, i.e. at interfaces.
$y \sim d^2/\lambda$	**Fresnel region**	The image loses more and more resemblance with the object.
$y > d^2/\lambda$	**Fraunhofer region**	The image intensity is the Fourier transform of the object transmission function.

Phase-enhanced μCT

Using a partial coherent beam, images are taken in the near field (s. fig. 6.4.2). Rotating the sample and performing a tomographical scan emphasizes the sharp changes in the refractive index of the sample. This is called phase outline contrast (Raven et al., 1996; Spanne et al., 1999).

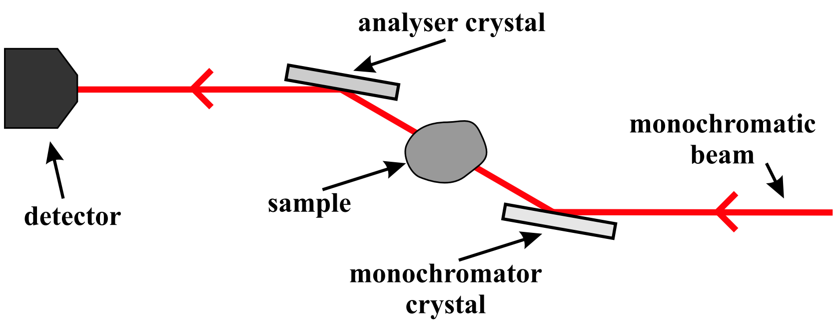

Figure 6.4.3: Setup for diffraction-enhanced imaging. A monochromator and analyzer crystal is used to record images at different positions of the rocking curve of the analyser crystal.

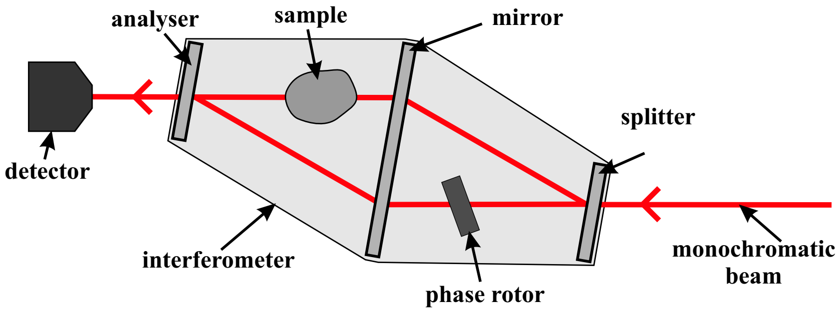

Figure 6.4.4: Experimental setup for interferometric phase-contrast. A monolithic X-ray interferometer is used to divide the monochromatic beam into two coherent beams. The phase rotor introduces a defined phase shift and the direct phase projection can be obtained.

A more sensitive technique makes use of multiple crystal reflections. In Fig. 6.4.3 the schematic setup is shown. Images at different positions of the rocking curve of the two crystals are recorded. From these images an absorption image and a phase enhanced image can be obtained (Bravin, 2003; Pagot et al., 2003). Using this as the contrast method in tomography again results in mapping of borders of changes in the refractive index.

Interferometric phase-contrast μCT

To be able to obtain the refractive index in the tomogram, phase projections of the sample have to be measured. A direct technique makes use of an X-ray interferometer which allows for the measurement of a phase projection modulo 2π. The principle setup is shown in Fig. 6.4.4. For one phase projection interference patterns, with and without the sample, are obtained at different overall phase shifts introduced by the phase shifter (Momose, 1995; Beckmann et al., 1997; Momose, 2002). Using the electron density σ, the phase shift ϕ is given by

$$\phi \propto \frac{\sigma}{E} \quad . \tag{6.4.4}$$

Holotomography

An indirect method to measure the phase projection makes use of the partial coherence of third generation SR beams. By varying the sample-detector distance and recording images different spatial frequencies in the projected phase images vanish (Talbot effect). The so-called holographic reconstruction procedure then determines the phase projection. (Cloetens et al., 1999)

X-ray imaging detector

The different microtomographic techniques described in the previous paragraphs make use of a 2-dim. X-ray detector. This device consists of a single crystal fluorescent screen and a

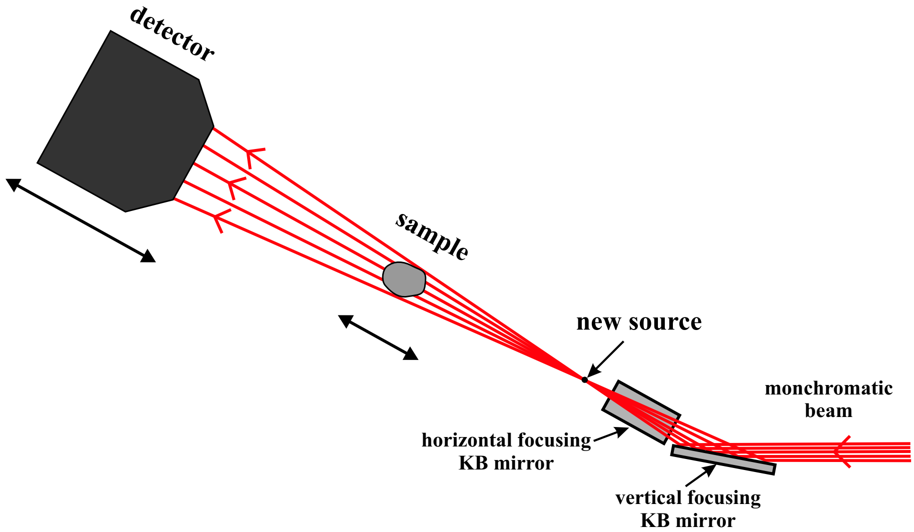

Figure 6.4.5: Experimental setup for cone-beam nanotomography. Two KB mirrors are used to produce a divergent X-ray beam. Depending of the distance source-sample-detector the magnification of the system can be altered. A spatial resolution in the tomogram in the order of the source size is possible.

lens-coupled CCD-camera. In standard applications a spatial resolution of about 0.7μm is achievable.

Nanotomography

To increase the spatial resolution to the nanometer regime, X-ray magnifying techniques have to be applied. One approach is to magnify the transmission image behind the sample and performing tomography in parallel beam geometry. For this purpose asymmetric crystal reflection (Stampanoni et al., 2002) or compound refractive lenses (Rau et al., 2001; Schroer et al., 2002b) can be used. A different approach is given by generating a divergent X-ray source and performing cone-beam tomography (see Fig. 6.4.5), which is a standard technique for microtomography at conventional X-ray tubes. Currently a source size of about 100 nm can be achieved by the use of Kirkpatrick-Baez (KB) mirrors.

Pink- and white-beam μCT

For very high spatial resolution the exposure times of the detector are in the seconds range. By the use of a multi layer as a monochromator the resulting larger bandwidth and intensity allows for a faster μCT. In some special application the use of pink- or white-beam is also reasonable.

6.4.2.2 Applications

The described imaging techniques are not all available as a standard user application. Only the setup for absorption-contrast μCT and phase-outline μCT fulfill the requirements for becoming a user experiment. One approach to setup a high-throughput x-ray μCT system was done by a group at the Advanced Photon Source (Wang et al., 2001). In the following section a few current examples of application of μCT at different synchrotron radiation facilities are given.

Medical science

First applications of μCT using synchrotron radiation in the field of medical science were the investigation of bone. Here, mainly the structural parameters and the comparison to conventional methods were of interest (Bonse et al., 1994; Delling et al., 1995). Current applications put emphasize on the process of regrow and remodelling of bone.
Many experiments were performed to characterize new biocompatible materials which can be used as an implant for bone defects (Müller et al., 2002; Weiss et al., 2003; Schiller et al., 2004). Furthermore, phase contrast techniques were applied to soft tissues to find new techniques for tumor detection (Takeda et al., 1998; Beckmann et al., 1999).

Materials research

In materials research the microstructure of a variety of different types of samples are studied. Starting from low absorbing carbon-carbon composites (Coindreau, Vignoles & Cloetens, 2003) up to high absorbing metal foams and concrete samples (Maire et al., 2003).
The behavior of materials under compression can be studied (Salvo et al., 2003). Furthermore by tracking marker particles in Al alloys, the measurement of the plastic displacement gradient component in three dimensions becomes possible (Nielsen et al., 2003). Another application is the study of the interaction of short fatigue cracks with the grain boundaries in cast Al alloys (Ludwig et al., 2003).

6.4.3 Science at PETRA III

The extraordinary source characteristics of PETRA III will allow for all the different techniques described in the previous section. Furthermore, these techniques will be combined to simultaneously map different features of specimens. This will give new impact to the understanding of the 3-dim. composition and behavior of samples from a variety of different research communities. Therefore it is necessary to provide for a user experiment allowing for an automatic scanning and data evaluation.
In combination with the tomography setup at DORIS III the following beamlines will be available for users at DESY:

	DORIS III		Petra III	
	BW2	HARWI II	100 m beamline	200 m beamline
energy range	6–24 keV	20–250 keV	6–150 keV	6–150 keV
beam width	10 mm	80 mm	5 mm	10 mm
beam height	4 mm	8 mm	1 mm	2 mm
coherent image	no	no	yes	yes
spatial resolution	2 μm	3 μm	0.7 μm / 50 nm	0.7 μm / 50 nm

Exploiting the characteristics of the different beamlines for tomography the types of samples investigated at PETRA III can be divided into:

- *large samples*: Ø $>>$ 5 mm, typical 20-150 keV
  In combination with the knowledge of a coarse tomography, region of interest tomography can be performed (sample larger than size of the beam).
- *medium-size samples*: Ø $\approx$ 3 mm, typical 8-60 keV
  This type of sample will become the standard application of performing absorption-contrast and phase-enhanced μCT showing a spatial resolution of about 0.7 μm.
- *small samples*: Ø $<$ 1 mm, typical 6-30 keV
  For very small samples, a spatial resolution of $\approx$ 50 nm can be achieved by applying cone-beam nanotomography.

Furthermore a variety of different sample environments and combination with other techniques e.g. diffraction experiments is foreseen.

6.4.4 Beamline description

The standard user experiment for microtomography at PETRA III will require a large monoenergetic, parallel and intense beam. The photon energy range will be from 6 to 150 keV with a beam size of about 5 x 1 mm^2. The schematic beamline layout is shown in Fig. 6.4.6.

6.4.4.1 Insertion device and monochromator

As insertion device a tunable standard undulator at a low β section will be used. Inside the optics hutch the standard monochromator will be installed. Mirrors can be added to suppress higher harmonics especially for low photon energies. To be able to select photon energies in

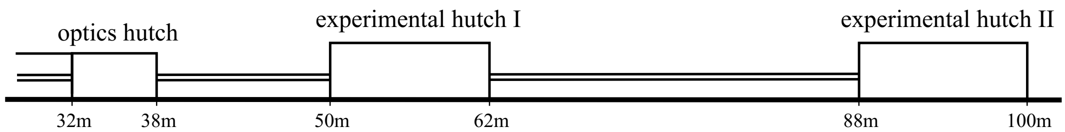

Figure 6.4.6: Schematic layout of the beamline for micro- and nanotomography.

the total energy range of 6 to 150 keV different sets of crystals are foreseen. To achieve a smooth beam profile, the beamline will have as few optical elements as possible.

6.4.4.2 Experimental hutch I and II

The experimental hutches will allow for a variable sample detector distance up to 10 m. Experimental hutch II will house the user experiment for absorption-contrast and phase-enhanced microtomography. The experiments in hutch I will focus on nanotomography applications. There different optical elements, e.g. KB-mirrors, CRLs, asymmetric Bragg-magnifier, will be added to achieve a X-ray magnified image of the sample. Using KB-mirrors, a nanometer divergent X-ray source will allow for performing cone-beam nanotomography.

6.4.4.3 Environment

To provide for a user experiment for tomography, laboratory space for sample preparation is required. Furthermore an automatic sample changer will allow to effectively exploit the assigned beamtime. Gigabit ethernet infrastructure is needed to process and backup the expected data.

6.4.5 Capital investment and personnel

Two different setups specialized for microtomography (hutch II) and nanotomography (hutch I) are needed.
The total investment costs for these experimental stations account for **2130** k€.
The costs for central data backup and computer power to provide for on-line reconstruction are not included in this estimate.

The beamline for micro- and nanotomography will be run as a user facility for short term and very fast experiments. New experimental and data evaluation techniques have to be developed. Furthermore the user operation requires continuous improvement and maintenance of the beamline hardware and software. Therefore two scientists, one software engineer, one mechanical engineer, and one technician should be employed on a permanent basis.

6.5 Inelastic Scattering

Authors:

H. Franz	DESY, Hamburg, Germany
M. Krisch	ESRF, Grenoble, France
M. Müller	Universität Kiel, Germany
H. Requardt	ESRF, Grenoble, France
R. Röhlsberger	DESY, Hamburg, Germany
Yu. V. Shvyd'ko	Universität Hamburg, Germany
H. Sinn	Advanced Photon Source, Argonne, USA

Consultant:

A. Q. R. Baron SPring-8, Harima, Japan

6.5.1 Current state of the scientific field

One of the most successful areas in science which has emerged from the advent of third-generation synchrotron radiation sources is inelastic X-ray scattering (IXS) with meV energy resolution. Starting from the pioneering work performed at HASYLAB in the 1980s (Dorner, Burkel & Peisl, 1986; Dorner et al., 1987), the technique is now established and has proven to be a powerful spectroscopic tool in the study of lattice dynamics, complementing the previously unique inelastic neutron scattering (INS) technique. The impact and the maturity of the technique is documented by numerous high-level publications in fields of research ranging from materials science over geophysics to biology, see, e.g. (Sette et al., 1998; Burkel, 2000) and references therein. IXS constitutes the perfect complement to INS in areas where INS is difficult, and often impossible, to apply:

1) The study of collective excitations in disordered systems, where well defined excitations are typically only existing up to momentum transfers Q of a few nm^{-1}. In particular for disordered systems with a high speed of sound ($>$ 2000 m/s), the low-energy and low-momentum transfer regime, it is difficult, or even impossible, to access by neutron scattering due to kinematic limitations (Sette et al., 1996; Burkel, 2000).

2) The small source size and beam divergence of modern synchrotron sources opens the possibility to study materials available only in small quantities down to 10^{-5} mm^3. This is of particular interest for the study of matter under high pressure, since it allows one to employ diamond anvil cell techniques, and therefore access pressure regimes up to 100 GPa and beyond.

The extensive IXS studies on liquid water are probably the best example for the wealth of new insights which could be gained in its mesoscopic dynamics (Ruocco et al., 1996; Ruocco & Sette, 1999), but as well the large body of studies performed on other liquids and glasses has allowed one to answer many open questions related to the nature of the high-frequency excitations, relaxation phenomena and the interplay between structural and dynamical properties (Sette et al., 1998). A more recent emerging field is high pressure research, where studies on single crystals are currently performed up to 400 kbar (Occelli

et al., 2001; Raymond et al., 2002; Loa et al., 2003), and the megabar regime has been entered using polycrystalline samples (Fiquet et al., 2001). The determination of sound velocities and, in the case of single crystals, of the full elasticity tensor as a function of pressure is one of the key inputs for geo- and planetary science, but of course not restricted to this specific field of research. More generally, the possibility to map out the phonon dispersion allows one to evidence pressure-induced anomalies, thus gaining detailed insight into precursor effects and the nature of phase transitions. As for the very high pressure studies, IXS is unique in the study of small sample quantities, and we cite as examples here the work on highly correlated electron systems (Astuto et al., 2002; Shukla et al., 2003; Fukuda et al., 2003; Manley et al., 2003; Wong et al., 2003).
At present there are four IXS beamlines operational: ID16 and ID28 at the ESRF (Verbeni et al., 1996; Masciovecchio et al., 1996; Sette et al., 1998), 3-ID at APS (Sinn et al., 2001; Sinn et al., 2002), and BL35XU at SPring-8 (Baron et al., 2001b), and at least two further projects are in progress. All operating beamlines are heavily overbooked, and a large amount of excellent science proposals have to be rejected.

6.5.2 Science at the inelastic scattering beamline at PETRA III

The PETRA III project provides the opportunity to build a scientifically unique IXS beamline, extending the existing possibilities worldwide and responding to the high demand of the international user community. The outstanding brilliance of undulator radiation will allow for the combination of high-resolution inelastic X-ray spectroscopy with microfocusing techniques. This has a major impact in the following areas:

a) The radiation can be focused to dimensions of a few μm, so that sample volumes in the range of 10^{-6} mm^3 become accessible. As a result, the vibrational behavior of single crystallites in polycrystalline materials can be investigated. In this sense, the polycrystals of today will become the single crystals of tomorrow. Moreover, materials can be studied where the growth of large single crystals is not possible like certain kinds of quasicrystals or superconductors. The use of high photon energies allows one to study high-Z materials. This is particularly interesting for the study of electron-phonon interactions in new materials like high-T_c superconductors or heavy-fermion systems. The application of microfocused beams allows one to study phonons in confined geometries and at surfaces.

b) A small beam size at the monochromator position allows for a very effective implementation of sub-meV spectrometers. This applies in particular if multi-bounce monochromators are used to achieve a very steep resolution function. Since the corresponding optics relies on the utilization of highly asymmetric reflections, a small vertical beam size allows one to keep the size of the monochromator crystals small.

The design goal for this beamline is an energy resolution of the inelastic spectrometer of 0.5 meV. Together with the above mentioned features, this will open new experimental possibilities in many areas of condensed matter research. A few of these exciting applications will be highlighted in the following sections.

6.5.2.1 Disordered materials

In contrast to crystalline systems, disordered materials are characterized by the absence of translational order. The discrete inter particle distances are replaced by a correlation function that describes the topological disorder. It is obvious that dynamical properties are strongly influenced by the type and degree of the disorder. Moreover, the disorder leads to additional degrees of freedom like diffusion and relaxation in liquids and melts as well as hopping and tunneling processes in glasses. The interplay of these phenomena on different time and length scales introduces a rich phenomenology of dynamical properties. Due to kinematical limitations of neutron scattering, a comprehensive picture of the high-frequency collective dynamics in disordered materials is still missing. In particular, the following questions on the mesoscopic dynamics are still to be answered:

- How do the collective excitations observed in glasses relate to the anomalous thermal conductivity observed at low temperatures ?
- What is the relation between the structural properties and the spectrum of excitations ? How do the different atomic species of a multi-component melt contribute to these excitations ?
- What is the origin of the excess specific heat at low temperatures and the excess density of vibrational density of states ?
- How are short wavelength excitations affected by relaxation processes compared to those at long wavelengths and how is the high-frequency dynamics affected in the vicinity of the glass transition ?

Vibrational spectra of disordered materials are dominated by a very strong elastic line. An unambiguous resolution of low-energy spectral features requires an energy resolution of the spectrometer that is in the range of 0.5 meV.

6.5.2.2 Collective excitations in low dimensions

Phonons are a good example for quasi particle excitations that can be significantly modified by interfaces and multilayered structures. Since the functionality of future micromechanic devices will depend on phase transformations and their underlying dynamics, the tailoring of phononic spectra to specific purposes will be of increasing importance in the future. In this field, basic research and applications are intimately related. Key roles are anticipated for the following fields of materials physics:
Functional materials like shape memory alloys are based on structural phase transitions, which allow the material to modify its domain structure. The underlying physics of these phase transitions is intimately related to lattice instabilities with soft phonon modes (Shapiro et al., 1989). In the future, materials with new transformation behavior based on strongly modified dispersion relations will emerge. Fig. 6.5.1 shows different types of such phonon anomalies for a hypothetical material. Structural distortions associated with ferroelectric phase transitions can be used to generate actuator effects in conjunction with the permanent

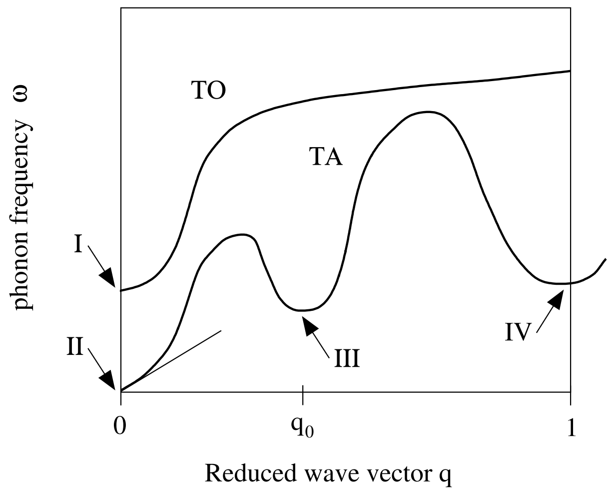

Figure 6.5.1: Phonon branches of a hypothetical material that exhibits soft phonon modes associated with lattice instabilities (Krumhansl & Barsch, 1992). Phonon anomalies of type I and II can be observed in ferroelectric and ferroelastic transformations, respectively. Phonon anomalies of type III and IV are typically found in shape memory materials and amorphous metals. TO and TA denote transverse optical and transverse acoustical branches, respectively.

electric polarization. The ferroelectric transition depends on the phonon behavior, which has already been demonstrated to exhibit unexpected strong modifications in thin films (Akimov et al., 2000). The envisaged application of nanostructured ferroelectric materials in high-integration on-chip devices (Xu et al., 1999) will necessitate detailed basic research on ferroelectric transitions in thin films and dots in particular (Alexe et al., 1999).
Moreover, critical phenomena at surfaces (Binder, 1983) are a topic of basic research currently receiving a lot of attention from the theoretical point of view (Pleimling, 2002). X-ray techniques in grazing incidence geometry are very surface–sensitive, however, the scattering volume is greatly reduced. The high flux and the microbeam at the PETRA III IXS beamline would allow to experimentally investigate the modification of lattice excitations at the surface.

6.5.2.3 Quasicrystals and amorphous metals

Quasicrystals and amorphous metals have in common that electronic correlations play an important role to stabilize their structure. For example, quasicrystalline phases are found to be stable when $2k_F \approx k_p$ where k_F is the Fermi wave number and k_p is the value of the structure factor maximum. In amorphous metals, electronic Friedel oscillations around the atoms give an important contribution to the pair potential. The total energy of the system is minimized if the atoms are effectively bound in the minima of the Friedel potential. It seems to be a generic feature of disordered metals that the electron-electron interaction leads to a strong enhancement of these oscillations (Kroha, 2000). This mechanism has important implications for the vibrational dynamics of non-crystalline materials. Around the wavenumber k_p of the structure factor maximum one finds energetically low-lying vibrational excitations (Suck et al., 1983; Häussler, 1992). This is similar to the roton-like modification of the phonon dispersion in quantum liquids, comparable to the type-III phonon anomaly in Fig. 6.5.1. The energy ω_0 of these excitations scales with the inverse of the structure factor, i.e., $\omega_0 \sim 1/S(k_p)$. Therefore, upon transition into the crystalline state, these modes approach zero energy. This transition is particularly interesting to be observed near a (quasi) crystalline-amorphous transition. To reveal the nature of these low-energy excitations, investigations with sub-meV energy resolution in the presence of a strong elastic peak are necessary.

Also quasicrystalline order leads to new kinds of collective excitations like phasons and other non acoustic localized modes at very low energies (Bak, 1985). Many quasicrystalline systems cannot be studied by inelastic neutron scattering because single crystals are available only in very small sizes or they contain elements that are detrimental to neutron scattering. Amorphous metals very often can only be produced by vapor quenching in the form of thin films. Therefore, the proposed IXS beamline at PETRA III with 0.5 meV energy resolution and the option for a microfocused beam will be ideally suited for the study of such systems.

6.5.2.4 High-pressure studies

As already mentioned before, the small source size and beam divergence of modern synchrotron sources opens the possibility to study materials available only in small quantities down to $10^{-5}\,\text{mm}^3$. This is of particular interest for the study of matter under high pressure, since it allows to employ diamond anvil cell techniques, and therefore access pressure regimes up to 100 GPa and beyond. For disordered and polycrystalline materials orientationally averaged information is obtained, whereas the use of single crystals allows to map out the full dispersion scheme of the acoustic and optical branches. Recent examples are the phonon anomalies in Cesium metal (Loa et al., 2003) and SmS (Raymond et al., 2002). Furthermore, the complete set of elastic moduli can be straightforwardly determined from the initial slope of the acoustic branches, therefore allowing to study elasticity under pressure (Antonangeli, 2004). Current challenges lie in the preparation of these tiny single crystals (with a typical diameter of 50 mm and a thickness of 20 mm or less), and the preservation of a sufficient crystal quality to high pressures. The coupling of high pressure with low/high temperatures is a natural extension, and the corresponding instrumentation such as cryostats and heaters is well developed. The highest attainable pressure is intimately linked to the sample volume, and therefore continuous efforts have to be made in order to match the lateral beam dimensions with the sample size. In this respect the expected performances of PETRA III promises to further reduce the minimum sample volume needed, or to record IXS spectra more rapidly (in cases where extreme conditions of temperature and/or pressure can only be maintained for a few hours).

Another important field of research concerns the determination of sound velocities in materials under geophysical conditions. This necessitates the use of anvil cells that allow for pressures in the Mbar range and temperatures up to 2000 K. For that purpose a laser heating system has to be installed at the beamline. Such systems allow one to selectively heat the samples in diamond anvil cells. Interesting systems are metallic melts under high pressure at high temperatures as they are extremely relevant to understand the properties of planetary cores, for example. In these studies, an important quantity to be derived from the data is the velocity of sound. Under conditions of high temperature and high pressure, this is hardly possible with any other method. However, an accurate determination of sound velocities is only possible if the excitation spectrum can be measured at low momentum transfers and low energy transfers, i.e., very close to the elastic line.

6.5.3 Beamline description

The main components of the spectrometer for inelastic X-ray scattering are a monochromator selecting hard X-rays with a spectral width of $\Delta E < 1$ meV and an analyzer performing energy analysis of the inelastically scattered X-rays. The required momentum resolution $\Delta Q < 0.5\,\mathrm{nm}^{-1}$ limits the solid angle $(\Delta\alpha)^2$ from which the scattered photons can be collected. Typical values are $\Delta\alpha < 10$ mrad. To obtain sufficiently high count rates in these energy/momentum intervals, a very high incident photon flux is mandatory. The design goal at this beamline is to exceed a flux of 10^{10} photons/s/meV at the sample position. Therefore, the beamline proposed here is located at the position of the 20-m undulator.
The operating energy has to be above $\sim$ 22 keV where the Darwin width of Si-Bragg reflections is below 1 meV. The use of high photon energies has significant advantages. First, one obtains access to strongly absorbing samples or samples in strongly absorbing environments. Further important aspects are the fact that photo absorption along the beam path is low and radiation damage in the sample becomes much lower at higher energies.
A very high energy resolution is mandatory to study collective excitations at low energy- and momentum transfers in disordered materials. For the study of lattice dynamics in single crystals, however, the requirement for high energy resolution can be relaxed. For that reason, the beamline should host two different instruments that are specially designed for these applications. The instrument for 0.5 meV energy resolution requires a long distance between the sample and the analyzer (10 – 15 m). This instrument is operated in a horizontal scattering plane covering a moderate range of momentum transfers up to $60\,\mathrm{nm}^{-1}$. Investigation of single crystals requires the access to high momentum transfers ($100 - 200\,\mathrm{nm}^{-1}$). Thus, the analyzers should be mounted on a vertical spectrometer arm so that high scattering angles can be reached without suffering from the polarization factor. In the following we describe how these design goals can be met in the beamline proposed here. The general layout of the beamline is shown in Fig. 6.5.2. The individual components are described in the following sections.

6.5.3.1 Undulator

In order to surpass the performance of present IXS instruments, the highest possible brilliance has to be achieved. The optimum device in this respect is the 20 m undulator being located in a high-β section of the storage ring. The choice of the undulator period is strongly dependent on the choice of working energies. The greatest flexibility in choosing the working energy is achieved by an PETRA III undulator with a fundamental in the range of 3–7 keV, as described in Sect. 4.1 of this report. Energies up to 35 keV are then reached in the 5^{th} harmonics. This approach, however, imposes a significant heat load on the first optical elements so that a very efficient cooling scheme has to be implemented. Otherwise, the high heat load may be detrimental for the overall stability of the whole beamline. On the other hand, a short-period undulator with a fundamental at the desired energy could be used that leads to a significantly lower heat load and increased stability. This, however, goes on the expense of the tunability of the working energy. Thus, the ideal solution would be the combination of both schemes in a revolver-type undulator.

6.5.3.2 Passive optics

These components comprise X-ray beam monitors and high-heatload slit systems which can cope with the high incident heatload of the undulator beam. In particular, high-resolution X-ray beam monitors are indispensable for the reliable and reproducible operation of the beamline, considering that stability at the μm level has to be achieved.

6.5.3.3 Beam transport and hutches

In order to optimize the efficiency of the inelastic spectrometer, various collimating and/or focusing elements have to be installed along the beam path. The first element of this type

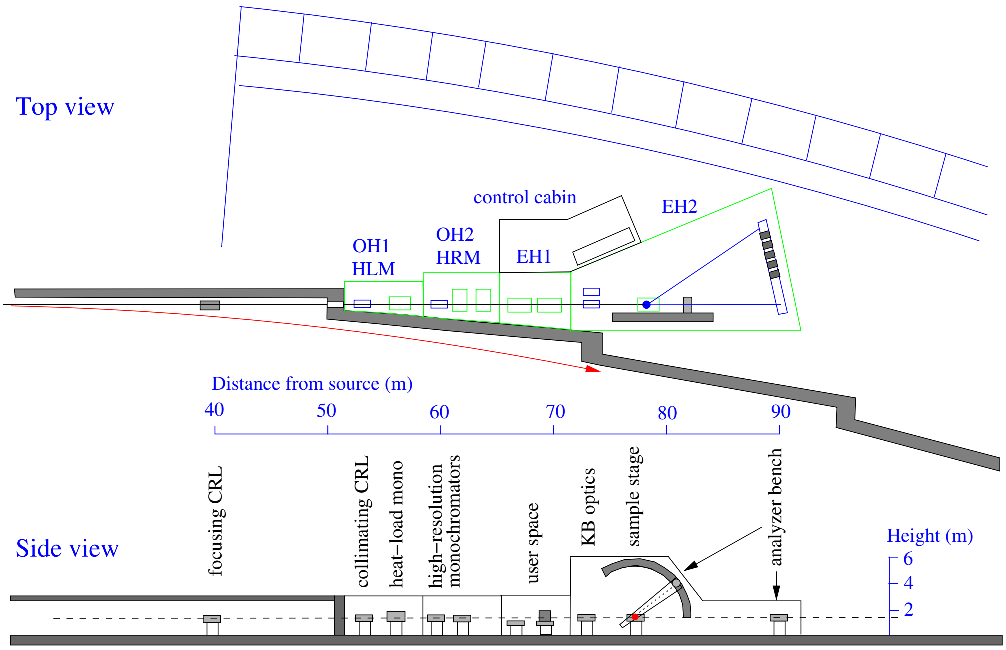

Figure 6.5.2: Layout of the proposed beamline for inelastic X-ray scattering at PETRA III. The optics hutches OH1 and OH2 contain the heat-load monochromator (HLM) and the high-resolution monochromators (HRM), respectively. The experimental hutches EH1 and EH2 contain instruments for various inelastic spectrometers as explained in the text. The height of the hutches EH1 and EH2 (partly) is raised to about 6 m to accommodate the operation of top-loading cryostats and a spectrometer with a 4.5 m vertical arm in EH2. The CRL in the front end focuses the beam to the position of the HRM.

should be a focusing compound refractive lens (CRL) that is installed half-way between the center of the undulator and the high-resolution monochromator. This preserves the low divergence of the undulator beam while providing a small beam cross section at the first crystal. As a result, highly asymmetric reflections can be used while keeping the size of the crystals small. The proposed location of the CRL is within the front end of the beamline.
To achieve micron-size focal spots on the sample, we propose the use of Kirkpatrick-Baez (KB) mirror optics. To allow for sufficient flexibility selecting the focal spot size (which determines the beam divergence on the sample), there should be enough room in front of the sample for placement of the focusing optics.
To accommodate the experimental needs and to allow for a high flexibility, we propose an arrangement of hutches as sketched in Fig. 6.5.2. The optics hutches OH1 and OH2 contain the heat-load monochromator and the high-resolution monochromators, respectively. The first experimental hutch EH1 is a hutch that is devoted to the test of optical components, development of new experimental schemes, testing of equipment etc. Hutch EH2 contains two inelastic spectrometers that are centered around the same sample position that coincides with the focus of the KB mirror optics. One spectrometer has a vertical arm for IXS with medium energy resolution in the range of 2–3 meV, while the other one is a horizontal spectrometer for sub-meV inelastic scattering.

6.5.3.4 Heat-load monochromator

The first monochromator has to be capable to absorb the high power density of the undulator beam and to preserve the brilliance. A suitable solution for this purpose is the use of two diamond (111) reflections that comprise a fixed-exit double-bounce monochromator. At the expected power loads of about 500 W/cm^2 a cryogenic cooling scheme is recommended, even though the proper mounting of diamond crystals under these conditions still has to be developed.

6.5.3.5 High-resolution monochromators

The basic layout of an IXS beamline is significantly determined by the high-resolution monochromator. Presently, there are two approaches realized at existing instruments. The original design uses a backscattering reflection from a single Si crystal where the energy is tuned by a temperature scan of the crystal with mK precision. It is currently implemented at the IXS beamlines of the ESRF and SPring-8. Another approach is the use of multi-bounce high-resolution monochromators, as they are employed at the IXS beamline of the APS. The energy can be scanned very fast by the motion of a single stage that is equipped with a nano radian angular encoder. While the first approach requires a transfer tube for the white beam that extends all along the beamline to the back reflecting crystal, the monochromator in the second case is mounted in-line and just introduces a parallel offset of the beam. Here we propose to implement the latter design with an in-line 4-bounce monochromator in (+−−+) arrangement as shown schematically in Fig. 6.5.3a. Such a design is characterized by a higher throughput compared to the (++−−) monochromators (Ishikawa et al., 1992; Mooney et al., 1994) or (+ +) monochromators (Chumakov et al., 1996; Toellner et al., 1997) of the

same energy resolution, which are routinely used presently. Moreover, a much higher energy resolution can be achieved (Yabashi et al., 2001; T. S. Toellner, priv. commun.). Another approach is the use of a double-backscattering monochromator, as shown in Fig. 6.5.3b.
In contrast to a single backscattering reflection, the in-line design offers a number of advantages:

- The intensity in the tails of the resolution function is significantly reduced. This is crucial for the extraction of weak low-energy modes in disordered materials like amorphous metals where the elastic line is typically very strong.

- Energy scans are performed by the movement of a single motor and can thus be done very fast, if required. Consequently, energy regions without any structure in the phonon spectrum can be scanned with a larger step size. Such a flexibility is hardly possible in a thermal scan.

- The beamline is not obstructed by the white-beam transfer tube that extends all the way to the backscattering monochromator. An in-line monochromator does not impose any constraints on the design of the sample environment. Moreover, one can still use the beam from the high heat-load monochromator for convenient adjustment of the analyzer and the sample, where even weak reflections can be monitored.

Due to the low divergence of undulator beams from PETRA III, very efficient in-line monochromators can be employed. To achieve energy resolutions in the sub-meV range, the operating energy should be above 25 keV. These energies are determined by the back reflection analyzers as discussed in the next section.
An important aspect to be considered is the heat-load that is imposed by the eV beam from the heat load monochromator. At present sources this amounts to total powers in the range of 100 - 200 mW. The thermal gradients induced by this power may strongly deteriorate the performance of the high-resolution monochromator. A way to alleviate the thermal problems is cryogenic cooling of the monochromator crystals at 123 K where the thermal expansion of silicon is zero. In addition, the throughput increases due to the increase of the Debye-Waller factor with decreasing temperature, especially for high-order reflections. (However, it should be noted that the energy resolution degrades due to the enlarged Darwin width at low temperatures.) This concept has been successfully realized by the APS group (T. Toellner, E. Alp) recently. They achieved a vibration-free operation by cooling with He gas flowing through a lq. N_2 heat exchanger.
Besides these schemes, there is a recent proposal for reaching sub-meV resolutions in the range of 5–10 keV (Shvyd'ko, 2004). This idea relies on the wavelength dispersion in highly asymmetric back reflection. The basic layout is sketched in Fig. 6.5.3d. It consists of three crystals acting as collimator (C), dispersing element (DE) and wavelength selector (WS), respectively. The relative spectral bandpass of this configuration is given by $\Delta E/E = \Delta\theta/\tan\eta$, where $\Delta\theta$ is the angular emittance of the collimator and η is the asymmetry angle of the dispersing element. Although this approach is not compatible with the in-line design as pursued here, it offers a number of advantages : The absolute bandpass ΔE scales linearly with the photon energy E, in contrast to the monochromators discussed

before. Moreover, ΔE can be simply changed via the asymmetry angle η without affecting the angular acceptance and the throughput of the arrangement. Finally, the demands for temperature stability and angular control are not as serious as at high photon energies. To convert this approach into an in-line monochromator, one could envisage an arrangement as in Fig. 6.5.3b with the back reflecting crystals being cut highly asymmetrically. The corresponding energy analyzer that relies on the same principle is shown in Fig. 6.5.4b.

6.5.3.6 Inelastic spectrometer

The analyzers for the scattered radiation will be spherically-bent silicon pixel analyzers made from dicing of Si wafers. The scattering geometry introduces an additional broadening of the resolution function of such a spectrometer. This contribution is given by $\Delta E/E = (a^2 + p^2)/L^2$, where a is the size of the illuminated area on the sample, p is the pixel size of the analyzer, and L is the distance between sample and analyzer. For the horizontal spectrometer one should aim at $L \approx 10\,\mathrm{m}$ to allow for sub-meV resolution around 25 keV. To enhance the efficiency of this spectrometer, multiple analyzers of this kind are foreseen. In case of the vertical spectrometer that is planned for the study of phonons in new materials, we aim at an energy resolution of 2–3 meV. To reach this goal, a long arm with $L > 4.5\,\mathrm{m}$ has to be implemented, hosting a single Si pixel analyzer. This arm can be constructed in a

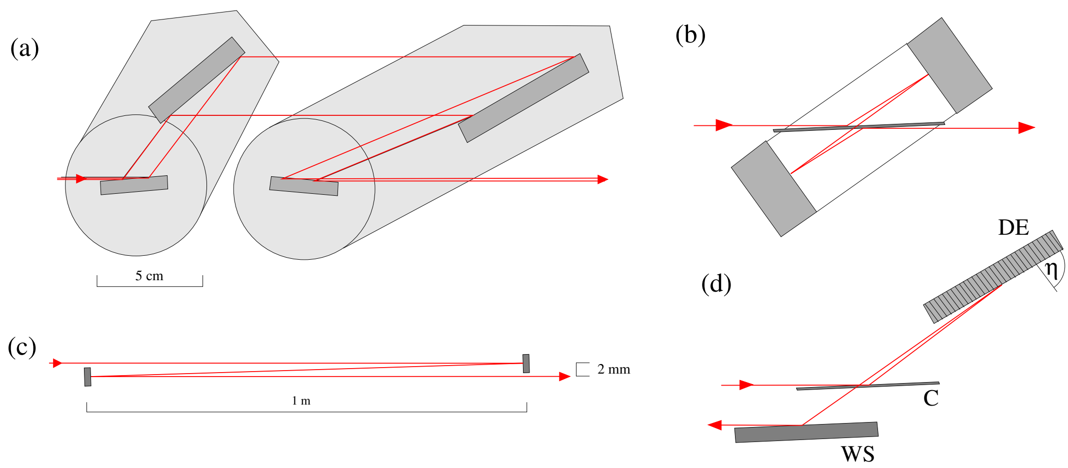

Figure 6.5.3: Possible schemes for high-resolution in-line monochromators to achieve sub-meV energy resolutions at photon energies above 20 keV. a) In this four-bounce arrangement, the two sets of crystals are mounted on a weak-link mechanism (shaded areas) for ultra precision motion control (Shu, Toellner & Alp, 2001), sometimes referred to as 'artificial channel-cut'. Similar schemes in combination with cryogenic cooling allow for a high-throughput monochromator at 25.7 keV with an energy bandwidth of 0.7 meV (T. S. Toellner, priv. commun.). b) A very compact optical design for Bragg reflections near backscattering (Baron et al., 2001a), using a very thin coupling crystal within a backscattering channel cut. c) Double - backscattering monochromator. This design combines a high throughput with narrow tails of the resolution function, as already successfully tested (H. Sinn, priv. commun.) d) The wavelength dispersion in highly asymmetric back reflection can be exploited to design monochromators with sub-meV resolution in the 5–10 keV range (Shvyd'ko, 2004).

lightweight manner were the counterweight is replaced by a driving mechanism to move the arm to the desired momentum transfer. Such an instrument would be unique worldwide to complement the experimental programs at facilities like APS and SPring-8.

For the Si pixel analyzers there are presently no demonstrated alternatives for energy resolutions in the range of 1 meV. However, an improvement of the existing analyzer schemes can be realized by employing *exact* backscattering (Shvyd'ko, 2004). Due to the large angular acceptance in this geometry, larger pixel sizes compared to the conventional scheme are possible. This allows for an easier fabrication and enhances the analyzer efficiency. On the other hand, to realize this scheme, a ring-shaped detector has to be developed. This is sketched schematically in Fig. 6.5.4a. On the first sight, a disadvantage of this concept is the excitation of multiple reflections due to the high symmetry of the Si crystal structure, reducing the efficiency of the analyzers. This can be lifted by the use of crystals with lower symmetry like sapphire or silicon carbide. Presently, however, the quality of these crystals does not allow for the construction of large-scale analyzers. Nevertheless, their development

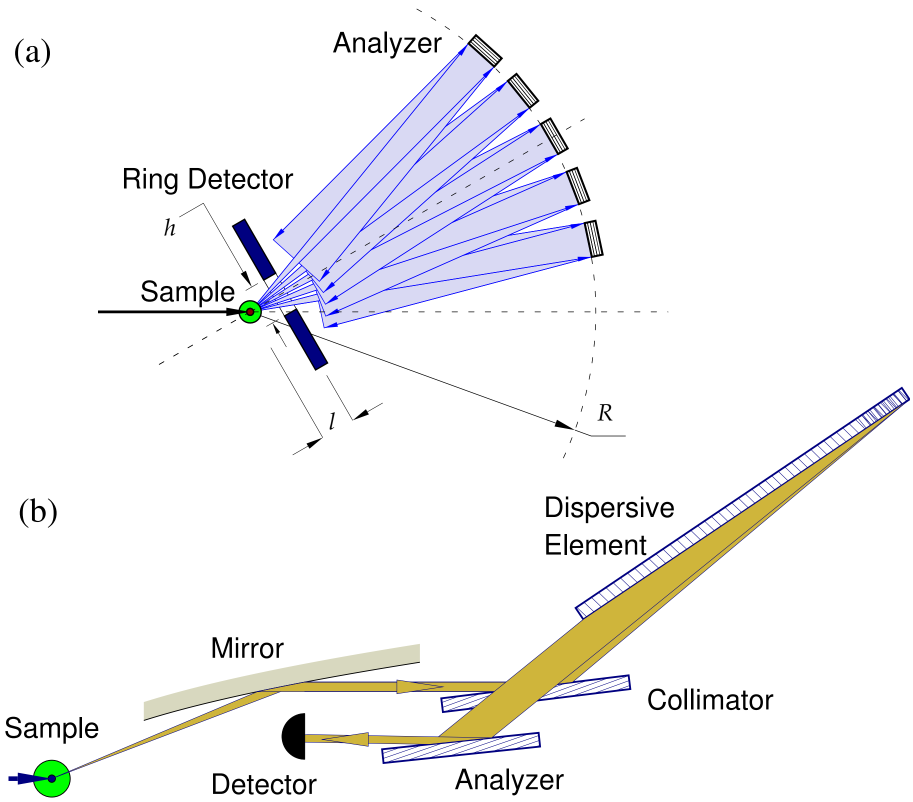

Figure 6.5.4: Schematic layout of a new backscattering analyzer for inelastic X-ray scattering (Shvyd'ko, 2004). a) Si-pixel analyzer working in exact backscattering geometry. The detector has a ring-shaped geometry so that the scattered radiation at a certain momentum transfer can pass through. Typical values are $l = 0.3$ m, $h = 3$ mm, thus selecting a 10-mrad interval of scattering angles. b) Two-crystal arrangement with a highly asymmetric reflection very close to backscattering. This design has the potential to reach sub-meV resolution in the range of 5–10 keV.

should be pursued during the R&D process for this beamline. Another way to enhance the efficiency of Si backscattering analyzers is the use of reflections that are less degenerate than the widely used ones. While the (13 13 13) back reflection at 25.7 keV is a 26-beam case and the (15 15 15) back reflection is a 56-beam case, other cases like the Si (2 2 20) and the Si (10 12 18) back reflection are only 6-fold degenerate, respectively.
Accordingly, a very small illuminated spot size on the sample allows for a larger pixel size at a given value for ΔE. This is another argument for using a microfocused beam. Moreover, in this case it will also be possible to illuminate thin films in grazing incidence geometry while maintaining a sufficiently small spot size on the sample.

6.5.3.7 Sample environment

For the investigation of single crystals or for adjusting samples in grazing incidence geometry, a goniometer with four circles is required. The goniometer should as well support heavy equipment such as cryostats. It is also desirable to have considerable free space at the sample position. For quick checks of sample orientation and/or quality, the mounting of a two-dimensional CCD detector behind and close to the sample has to be foreseen.

6.5.4 Capital investment and personnel

For the development of the scientific program at the beamline, two researchers are required who run independent activities to accommodate a wide scientific community.
The special crystal optics for the high-resolution monochromators and the analyzers should be made in-house. The performance of these devices crucially depends on an engineer that is dedicated to such developments. In particular, experience in nano-radian motion control is required. For installation of the beamline components and their maintenance, two technicians are needed, whereby one of them is specialized in mechanical problems, including operation of the analyzer fabrication, and the other one is specialized on electrical installations, including motor control and data acquisition.

The total capital investment for these experimental stations is **4060 k€**.

6.6 Nuclear Resonant Scattering

Authors :

H. Franz	DESY, Hamburg, Germany
R. Röhlsberger	DESY Hamburg, Germany
R. Rüffer	ESRF, Grenoble, France
B. Sepiol	Universität Wien, Austria
Yu.V. Shvyd'ko	Universität Hamburg, Germany
M. Sladecek	Universität Wien, Austria
G. Vogl	Universität Wien, Austria
G. Wortmann	Universität Paderborn, Germany

6.6.1 Current state of the scientific field

Nuclear resonant scattering (NRS) of synchrotron radiation was first demonstrated at HASYLAB in Hamburg almost 20 years ago now (Gerdau et al., 1985). First experiments were done at a bending magnet beamline (F4 at DORIS III). But only the advent of high energy third generation synchrotron sources like ESRF and APS has allowed to turn this method into a routine technique. Due to the sharpness of the nuclear resonances (typically some neV to μeV) NRS experiments are extremely flux hungry. For the same reason they require sophisticated monochromatization with a resolution in the meV or even sub-meV region. This is why NRS would profit most from the planned 20 m ID. Already now, ID18 at ERSF uses the equivalent of a 5 m long device, optimized for the ^{57}Fe transition at 14.4 keV. This reflects the fact that ^{57}Fe is the working horse for NRS due to it's favorable transition energy and life-time. However several other isotopes (^{161}Dy, ^{151}Eu, ^{61}Ni, ^{149}Sm, ^{119}Sn,....) are used for investigations mainly in the field of magnetism.
Experiments using NRS can be divided into three classes:

- Hyperfine spectroscopy via elastic NRS. In this field NRS has been used to study magnetism in thin films (Röhlsberger et al., 2003), high pressure (Lübbers, Wortmann & Grünsteudel, 1999) and biophysical applications (Trautwein & Winkler, 1999). Quasi-elastic forward scattering gives information about jump–diffusion (Vogl & Sepiol, 1999), structural relaxation in disordered (bulk and confined) systems (Sergueev et al., 2002; Asthalter et al., 2001) and also spin relaxation (Shvyd'ko et al., 2001).

- Vibrational spectroscopy via nuclear inelastic scattering (NIS). In experiments on thin films (Ruckert et al., 2000), protein dynamics (Parak & Achterhold, 1999) NIS has proven to be superior to inelastic neutron scattering, be it due to the small beam size, the element specifity or the larger scattering cross-section (0.13 Mbarn).

- Synchrotron radiation-based perturbed angular correlation SRPAC. This new technique (Sergueev et al., 2003) can be used to gain information about rotational dynamics in systems which display a vanishing Lamb–Mössbauer–factor.

NRS experiments take advantage of the large cross–section of nuclear resonances. Thus in spite of the narrow bandwidth the signal from the sample may be rather strong. In addition the isotope selectivity and the time discrimination help to reduce the background to a level close to zero. Sample environments like high pressure cell, cryostats, furnaces or matrices do not contribute to the measured signal. That is why in NRS minute amounts of sample material is sufficient. Of course, also the small beam at third generation SR sources helps to minimize the sample volume. This is often a big advantage compared both to neutron scattering and conventional Mössbauer spectroscopy.

6.6.2 Science at the NRS beamline at PETRA III

In the following we will sketch some scientific fields where we expect NRS at PETRA III to deliver a unique contribution.

6.6.2.1 Magnetism and dynamics of low-dimensional structures

The investigation of nanoscale structures by means of advanced X-ray scattering techniques will be an important contribution of PETRA III to the field of artificially structured materials. In particular, elastic and inelastic nuclear resonant scattering will offer unique opportunities for the investigation of magnetic and dynamic properties that lie at the heart of novel functional materials. Due to the use of hard X-rays, buried interfaces will be accessible, for which currently no alternative technique is available.

Lattice dynamics with nanoscale spatial resolution
Propagating excitations like phonons can be significantly modified by interfaces and artificial superlattices. The tailoring of phononic spectra to specific purposes will be of increasing importance in the future. Since only a fundamental understanding of vibrational properties under the influence of interfaces will ensure full tunability, basic research and applications will be intimately related. Due to its isotopic specifity, NIS opens the possibility to selectively obtain the vibrational properties of nanoparticles and thin films that contain the resonant isotope. There is no need to discriminate against inelastic signals from surrounding materials. The sensitivity of the method to thin films has been proven already in a number of experiments (Röhlsberger, 2001). However, the statistical quality of the data that can be obtained at present-day sources is not sufficient to allow for investigations of single monolayers. On the other hand, flux estimates for the 20 m undulator beamline at PETRA III indicate that a vibrational spectrum from a single monolayer of ^{57}Fe can be obtained in a few hours. This opens the possibility to selectively introduce isotopic probe layers in the sample and obtain vibrational properties with atomic resolution. It is a distinct advantage of this technique that such probe layers do not disturb the chemical integrity of the system.
A very interesting research area are low-energy excitations in nanoparticles and clusters (Fultz et al., 1997). The nature of these modes is far from being understood. NIS at PETRA III will allow one to selectively probe, e.g. different parts of such structures to locate their spatial origin (grain boundaries, surface or core). The application of focusing techniques will allow one to probe smallest amounts of material and thus facilitate, for the first time, experiments on thin films in high-pressure cells, for example. Such investigations are mandatory

to pinpoint the origin of the anomalous dynamical properties in low dimensions.

In-depth speckle metrology of magnetic thin films

Ultrathin probe layers can be employed to determine the in-depth magnetic structure of stratified media (Röhlsberger et al., 2002). At PETRA III, this technique can be combined with the outstanding coherence properties of the beam to perform a new type of speckle metrology. In this case one records the delayed resonant photons that are diffusely scattered from the magnetic domain structure within the probe layer. With probe layers placed in various depths of the sample, an in-depth image of the domain structure in the film is obtained. There is currently no other technique available through which such information can be obtained. This method requires the use of a 1D or 2D detector with the capability of ns temporal gating. Such a development based on APD arrays is underway and should be available when PETRA III becomes operational.

It is the virtue of nuclear resonant scattering, that elastic and inelastic spectroscopy can be performed in basically the same experimental setup. Thus, in a direct combination of both spectroscopic methods one can envisage detailed studies of the magnetoelastic coupling in magnetic nanostructures. While such investigations have been performed recently for FeO single crystals (Struzhkin et al., 2001), it would be very interesting to extend such experiments to magnetic nanostructures as well. This is particularly interesting in the case of metal/oxide heterostructures where unexpected magnetic properties resulting from the coupling of metal and oxide have been found (Beach et al., 2001). The comparison with previous experiments at existing sources shows that only the estimated flux delivered from the 20 m undulator beamline at PETRA III will allow for systematic studies in this field.

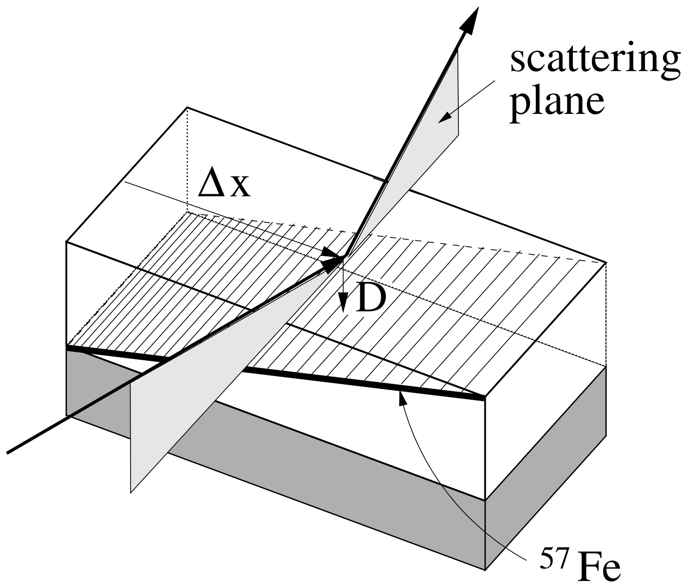

Figure 6.6.1: Use of an ultrathin probe layer of ^{57}Fe to determine the depth dependence of magnetic and dynamical properties in thin films by transverse displacement Δx of the sample.

6.6.2.2 Magnetism and lattice dynamics at extreme conditions: high pressure and high temperature

The knowledge about the properties of matter under extreme conditions, here high pressure and high temperature, is of utmost importance for solid state physics, material science and geophysics. Using diamond anvil cells (DAC), ultra-high pressures up to 4 Mbar (400 GPa), which compares with 3.5 Mbar at the Earths inner core, can be reached. Since the size of the pressurized samples above 1 Mbar is in the 1 - 10 μm range, such high pressure experiments benefit from the high brilliance of third-generation synchrotron sources as well as from the recent developments of focusing optics. Both NFS and NIS techniques have been already used for studying magnetism and lattice dynamics in the Mbar range, for instance the suppression of Fe band magnetism in RFe_2 Laves phases (Lübbers, Rupprecht & Wortmann, 2000) and the lattice dynamics in the hexagonal high-pressure phase of iron (Lübbers et al., 2000; Mao et al., 2001). Future NFS and NIS experiments at higher pressures and smaller samples will profit from the increased brilliance and flux of the envisaged NRS beamline at PETRA III enabling also experiments which combine two extreme conditions, e.g. high pressure and high temperature, possible for instance with Laser heating, or, as mentioned above, high pressure/low temperature experiments on nano-scaled magnetic systems (e.g. layers).

Magnetism at extreme conditions

Beside iron magnetism which is already investigated routinely at high pressures and high/low temperatures (Lübbers, Rupprecht & Wortmann, 2000; Rupprecht et al., 2002), the rare-earth magnetism at extreme conditions is a wide field with new challenges, which can be tackled with sensitive Mössbauer resonances like Sm^{149}, Eu^{151} and Dy^{161}, all of them already employed successfully for various problems. Eu(II)-chalcogenides are presently studied with an enormous variation of the magnetic ordering temperature, for instance in EuS from 16 K (0 GPa, NaCl-phase) to 280 K (77 GPa, CsCl-phase)(Lübbers, Rupprecht & Wortmann, 2000; Rupprecht, Ponkratz & Wortmann, 2003). In Eu and Sm systems, magnetism and valence transitions are often closely related, as demonstrated recently by a study of SmS (Barla et al., 2004). Of current interest are strongly correlated 4f- and 5f-systems (Heavy Fermion systems) exhibiting magnetism and superconductivity with pressure as an important parameter. Here probe atoms like Sn were used successfully (Barla et al., 2002). Future work at PETRA III may approach new frontiers in 4f magnetism, for instance delocalization of 4f-electrons in Sm and Dy metal at ultra-high pressures. A related topic is, as for Fe in magnetic layers, the investigation of the phonon-magnon coupling in systems with strong 4f magnetism, e.g. $SmCo_5$ and $DyFe_2$, by using NIS.

Phonon spectroscopy at extreme conditions

The actual geophysical interest in the hexagonal high-pressure phase of iron as the most relevant phase of the Earths solid inner core has triggered the first high-pressure phonon studies of this phase (Lübbers et al., 2000), reaching 1.53 Mbar in a second attempt (Mao et al., 2001). At ESRF, recent progress in the focusing optics (compound refractive lenses and K-B mirrors) allow to concentrate the whole monochromatized beam to a spot of less

than 10 μm diameter and to record a NIS spectrum of iron at 130 GPa in 12 h with a much better statistical accuracy and spectral resolution than in the first studies (Giefers et al., 2002). The texture in the pressurized sample, here ϵ-Fe, is used to extract from the NIS spectra the phonon density-of-states (DOS) as seen in different crystallographic directions. This allows for a mode-specific analysis of the phonon spectra, for instance an identification of the two optical modes and provided the first experimental proof of an anisotropy in the sound velocity parallel and perpendicular to the hexagonal c-axis (Giefers et al., 2002). It should be remembered that the observed anisotropy of the sound velocities in the Earths core is attributed to highly textured ϵ-Fe in the core (Creager, 1997), the reason for this texture is presently discussed with various models (Jephcoat & Refson, 2001; Steinle-Neumann et al., 2001; Buffet & Wenk, 2001).
To approach the inner Earths conditions, one needs beside high pressure also high temperature. The thermodynamic properties of iron at ultrahigh pressures and temperatures are therefore of utmost geophysical interest; the same holds for the minerals building up the upper and lower crust, all containing iron, e.g. the olivine (Mg, Fe)SiO_3. Their dynamic properties and phase transitions at high pressures and temperatures, also sound velocities, can be sensitively monitored by measuring the phonon DOS at the Fe sites. Temperatures up to 1000 K can be easily reached with "intelligent" diamonds (diamonds with integrated heaters) or with simple ovens (Rupprecht et al., 2002), temperatures up to 3000 K can be reached with resistance heatings of the gasket, even higher temperatures up to 4000 K with Laser heating. Such NIS studies at elevated temperatures can prove (or disprove) recent theoretical predictions about the temperature dependence of the anisotropy of elastic parameters and sound velocity in ϵ-Fe (Jephcoat & Refson, 2001; Steinle-Neumann et al., 2001; Buffet & Wenk, 2001). The option to compare thermodynamic parameters derived at elevated temperatures with the ones at ambient temperature to improve estimates of important properties such as melting temperatures beyond the Mie-Grüneisen approximation is one more reason for combined high-p,T NIS experiments.

6.6.2.3 Glass dynamics

The narrow bandpass makes NRS an ideal tool to study dynamics. In time resolved mode the nano- to μ-second region is accessible. This is the relevant time scale to study the glass transition in the light of mode-coupling theory (Bengtzelius, Götze & Sjölander, 1984; Sergueev et al., 2002). In particular the recent advances using single nucleus scattering (SRPAC) allows one to study the range from fast β-relaxation (several 10 ps) to the α-relaxation even below T_c (Sergueev et al., 2003). Following the pioneer-experiment at ESRF a systematic study of glass-formers of different strength will help to unravel the mechanism underlying the glass transition. In particular the option to separate translational and rotational motion by NFS and SRPAC will shine light on the origin of discrepancies found when combining results from different techniques like dielectric relaxation, light scattering or inelastic neutron scattering.
In the energy resolved mode even faster dynamics in the ps-time scale are accessible. This is the domain of phonons. In this area the so called boson peak is still a puzzle waiting to be solved. The boson peak is an excess density of states found in the vibrational spectra of

all disordered systems around several meV. The following question may be addressed with inelastic scattering experiments:

- are the excess exitations propagating or localized
- if they are propagating, how does the dispersion look like, is it of acoustic or optic type

In combination with non-resonant inelastic scattering nuclear resonant experiments with very good energy resolution (below $0.5\,meV$) can help to get answers to these points.

6.6.2.4 Diffusion

Diffusion plays a key role in the kinetics of structural changes that occur during the processing of metals, alloys, ceramics or semiconductors. The atomic migration in crystalline solids consists of jumps of individual atoms. The variety of atomic jump mechanisms is closely connected with defects.

Diffusion in solids is usually investigated on a macroscopic scale following the inter-penetration of two atomic species across an interface (tracer technique). This method deduces atomic events from macroscopic effects as, for instance, the concentration gradient of diffusing isotopes. In contrast to this macroscopic, classical methods diffusion can be studied at the microscopic level also. I.e. in a way which can reveal the jump vectors and the jump rates of the atoms. Nuclear resonant scattering of synchrotron radiation is one of the most successful methods for this kind of dynamics studies (Sepiol & Vogl, 2003; Vogl & Sepiol, 1999).

Scattering of X-rays in grazing incidence geometry has become an established technique for studying the structure of thin films and multilayers. The special goal of this method is the depth profile analysis. Combining grazing-incidence reflection with nuclear resonant scattering results in the depth-selective investigation of diffusion and of the hyperfine parameters of resonant nuclei. Combination of diffusivity studies with ab-initio calculations will allow the quantitative estimate of the diffusion rates and mechanisms at surfaces and in thin films. This is a challenging project, but should now be within the reach of the most performant synchrotron sources and ab-initio simulation tools.

Recently we have indeed gained the first preliminary results on diffusion in iron layers close to the surface (Sladecek et al., 2001) and in ultrathin iron films on a tungsten (110) surface (Sladecek et al., 2003), see Fig. 6.6.2. In the most challenging case a sub-monolayer is scanned for diffusion and relaxation. Until now these studies suffer from the limited brilliance of presently available sources. Higher brilliance as expected from PETRA III will enable to perform such studies in decent measuring time and thus result in detailed understanding of the kinetics of phase formation and transformation in thin films and multilayers by in-situ investigation.

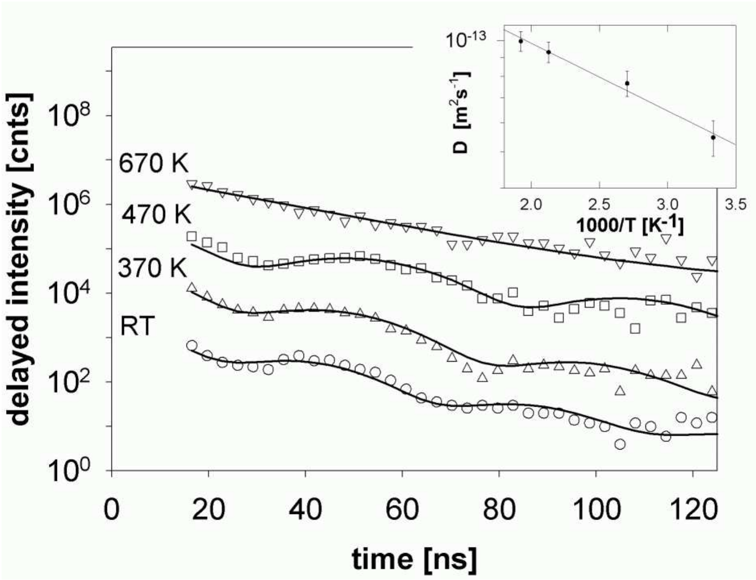

Figure 6.6.2: NRS spectra of an iron sub-monolayer on W(110) substrate. The quantum beats are a result of a quadrupole interaction. At higher temperatures the beat period increases and the beats disappear completely at about 670 K. This reversible effect is explained by a relaxation of the EFG. The inset shows the diffusion coefficients estimated from increase of the beat period.

6.6.2.5 Time domain interferometry

Besides the established and widely used resonant techniques where a “Mössbauer” isotope is needed as part of the sample, the increased spectral flux available at PETRA III could make time-domain interferometry (TDI) (Baron et al., 1997) a more widespread technique. TDI uses resonant filters, for example stainless-steel foils, as nuclear monochromators and analyzers. This offers the option to investigate also samples without resonant isotopes and to vary the momentum transfer in the scattering process by changing the scattering angle. Using APD-pixel detectors currently developed in different laboratories will open the way to study the q-dependence of relaxations in a very efficient way.

6.6.2.6 Metrology

The ”Physikalisch Technische Bundesanstalt” (PTB) has expressed their interest to maintain an experiment at the nuclear resonance beamline at PETRA III. The scope of the project is to define a new length-standard based on the Mössbauer radiation from ^{57}Fe (Shvyd’ko et al., 2000). Using a combined visible – X-ray Fabry–Perot interferometer (Shvyd’ko et al., 2001) the wavelength of the Mössbauer radiation can be directly (without the use of a transfer standard) measured in units of a well define laser line. The latter is usually a iodine stabilized He-Ne laser achieving a reproducibility of the wavelength of 3 parts in 10^{11}. Compared to this the uncertainty of the lattice constant of Si is orders of magnitude larger (some 10^{-8}). The main advantage of the Mössbauer wavelength standard is the independence of the wavelength on temperature or pressure. Even if the chemical environment and hence the hyperfine interactions are not known the relative uncertainty of the ^{57}Fe transition energy is of the order 10^{-11}. If a chemically well defined sample is used, the uncertainty is two orders of magnitude better. The stability of the Mössbauer line is even higher, 10^{-15}, comparable only to the Cs atom fountain clock.

6.6.3 Beamline layout

The following layout and the specifications of a NRS beamline are discussed under the assumption that it will be a user friendly beamline for highest performance of dedicated applications. These comprise hyperfine spectroscopy and dynamics under extreme conditions as high pressure, high and low temperatures, external magnetic fields and confined geometry. Confined geometry comprises nanostructured material, thin films, surfaces etc. In all applications highest brilliance and a proper timing mode are mandatory.

6.6.3.1 X-Ray source

In order to be competitive or even surpass the performance of existing synchrotron radiation sources highest brilliance is mandatory. In general this can be achieved with an undulator operating in the fundamental with smallest magnetic gap. In practice this will not always be possible. Therefore, taking the envisaged machine parameters into account, the 20 m undulator option with a revolver like system would be beneficial in order to optimize the flux in two energy regimes. (1) ^{57}Fe seems to be still the most important isotope. It would require an optimized magnetic structure of the undulator for 14.4 keV in the fundamental. This choice would give highest brilliance as well as less heat-load which would also be beneficial for the overall stability. (2) The second magnetic structure should be optimized for X-rays between 21.5 keV and about 30 keV in the third harmonics for the other Mössbauer isotopes which would cover in the fundamental also Tm and Kr. The Ta resonance at 6.2 keV would not be accessible.

6.6.3.2 High heat-load optics

High heat-load monochromator:
Due to the distinct energies of the Mössbauer transitions a scanning option for the high heat-load monochromator (HHLM) is not necessary. However, long term stability is mandatory. Here the ESRF design has proven to be the most simple and stable choice. A big offset of the crystals is beneficial for space considerations and heat-load from scattered radiation. Preferably the X-ray beam should be scattered up in order to leave the synchrotron radiation orbit avoiding the cone of the Bremsstrahlung. The downstream crystal is by definition the more stable one as it does not see 'real' heat-load. It also should become the most stable one with respect to the mechanics. The optics should be located in a separate hutch with beam shutter to allow for a continuous and stable operation of this unit. The angular resolution needed is $0.5 \cdot 10^{-6}$ rad, the size of the tank must be large enough to cover an energy range of 6–70 keV with Si (111). Of course lN_2 cooling is mandatory.

Compound refractive lens:
A compound refractive lens (CRL) is required upstream of the HHLM in order to collimate the beam for best performance of the HHLM. Especially at higher energies a better matching of the beam divergence and the crystal acceptance is achieved.

Beam position and intensity monitors:
A beam position monitor as the first element, i.e. before any optical element will be beneficial. Furthermore, intensity monitors are required after each optical element.

Slit systems:
The estimated high power of the synchrotron radiation will need a high power slit system upstream of the HHLM. A beam defining slit system downstream of the HHLM should be highly precise and easily scanable.

6.6.3.3 Focusing

Focusing optics are mandatory for most of the applications in NRS. There are two options: (1) a moderate focus (e.g. $100\,\mu\text{m} \times 100\,\mu\text{m}$) utilizing CRLs for vertical and horizontal focusing; (2) for e.g. a $10\,\mu\text{m} \times 10\,\mu\text{m}$ or smaller focal spot utilizing a Kirkpatrick-Baez (KB) optics system based on graded multilayers. Option (1) has the advantage that the beam stays straight and the focal length is big allowing for large sample environment and a permanent set-up somewhere in the beamline. Furthermore the alignment is very simple. Option (2) has a shorter focal length (approx. 500-700 mm) and deflects the beam out of the straight, i.e., the sample environment has to be chosen accordingly and the optics has to move to the corresponding experimental station. The alignment is more challenging.

6.6.3.4 High energy resolution optics

The high resolution monochromator (HRM) is the 'main' monochromator in NRS applications. It needs most development and alignment efforts. So far HRMs for the energy regime up to about 30 keV have been developed on the basis of multi-bounce arrangements. At least two HRM mechanics should be foreseen, one hosting the crystals for the ^{57}Fe resonance energy and one hosting alternative crystals for other isotopes. If one cannot afford more systems right from the beginning, space should be provided for at least two to four other systems. Collimating CRLs upstream of the HRM should be foreseen in order to ease the design and to improve the performance of the HRM. Options for HRMs which also cover higher energies should be considered as 'true' back-scattering arrangements. Permanent stations for monitoring the resonance up- and downstream of the HRM would ease the operation.

Further space should be kept for polarization shifter and further upgrades or new ideas e.g. the nuclear lighthouse effect. The HRM optics will be located in a highly temperature and mechanical stabilized hutch with a separate beamshutter. This ensures low-vibrational noise to maintain a good short- and long-term stability.

The HRM will be preferably a four bounce type with fixed exit. Recently good results have been obtained with $(+,-,-+)$ monochromators (Yabashi et al., 2001; Toellner & Shu, 2001; Toellner et al., 2002). The energy range will cover the Mössbauer transitions between 7 keV and 30 keV. We will aim for a very good energy resolution in the sub-meV range (0.5 meV or better) for NIS and reduced load on the detector for NFS. The required angular resolution and stability is 20 nrad. Requirements for thermal stability are 0.01 K. Alternatively new setups can be used with three or four independent crystals (see Fig.6.6.3). Some of these new ideas are discussed in Sec. 6.5.3 (for a thorough review of high resolution monochromators see (Shvyd'ko, 2004)).

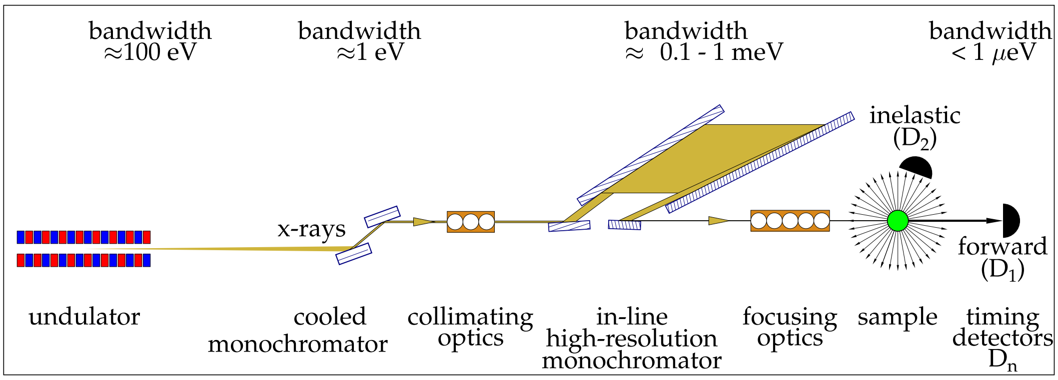

Figure 6.6.3: NRS beamline with resolution optics base on an advanced design with four independent crystals.

6.6.3.5 Detectors

Detector requirements can be divided in three classes: (1) monitoring, (2) main detectors and (3) auxiliary detectors.

(1) Monitors are mandatory for surveying beam intensity and beam position. There are various designs available, e.g. ionization chambers, PIN diodes, etc.

(2) In the case of the main detector a fast detector system (ps to ns resolution) with wide dynamic range, high efficiency and big area for NIS would be the detector of choice. So far detector systems based on APDs are used in NRS applications. Experience shows, however, that there is a need for further development. Further, for several applications a 1D or 2D fast detector system would improve the scientific output.

(3) Auxiliary detectors are e.g. image plates which are readily available.

It has been proven that separate hutches for each of the various sample environments make the operation much more efficient and reliable. Therefore, at least three independent experiments hutches are proposed (see Fig. 6.6.4).

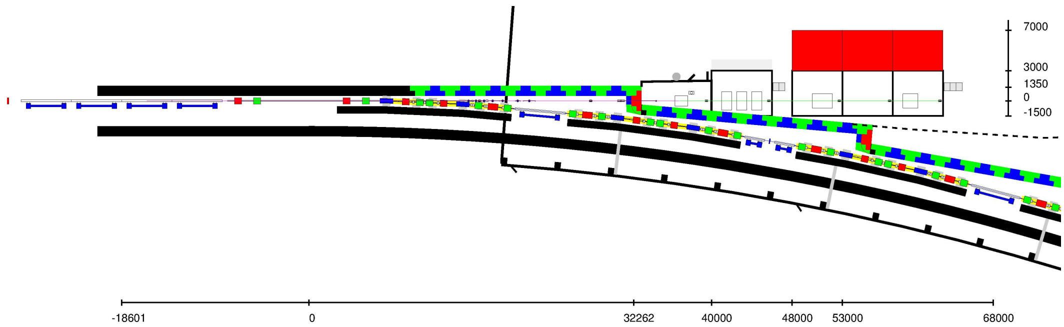

Figure 6.6.4: Schematic layout of the proposed NRS beamline.

6.6.3.6 Sample environment

Four types of sample environments will be used in NRS experiments at PETRA III.

(1) A cryo-magnet system for nuclear forward scattering (NFS) and nuclear reflectometry (NR), hyperfine spectroscopy and small-angle scattering

(2) A UHV system for NR, hyperfine spectroscopy and dynamics

(3) Cryo-systems and furnaces for hyperfine spectroscopy and dynamics

(4) High pressure cells.

Cryo-magnet system

A cryo-magnet system (specifications see below) is used in NFS geometry mainly for high-pressure work (hyperfine spectroscopy and diffraction) and in NR geometry for surface investigations (hyperfine spectroscopy and small-angle scattering). Other investigations which need low temperature and external magnetic fields are possible as well. An option for in-situ X-ray diffraction would be an asset. This could be accomplished in the simplest case by an image plate detector or a separate 2Θ detector system. Of course much more efficient would be an on-line 2D detector. The cryo-magnet system will be top-loading and sufficient vertical space is required (approx. 5 m).

Requirements for the cryo-magnet system

We should head for a temperature range from 1.5 - 500 K with an additional option to achieve mK temperatures. The horizontal magnetic field will have a maximum value of about 10 T. The sample volume will be at least $(50\,\mathrm{mm})^3$ delivering enough space for high pressure cell and thin film samples. It turned out that the sample holder needs to be vertical motorized with position feedback on the sample, a rotation around the vertical axis will also be provided. The entire set-up will be mounted on a two circle element for Bragg and tilt angle alignment. For the translational (vertical and horizontal) alignment of the samples μm resolution is mandatory. The system will allow in-situ pressure calibration and change of pressure.

UHV environment

There are two options for an UHV system: (1) UHV chamber with a load-lock system to carry out NRS experiments and a characterization option (LEED, AES, ...) in order to monitor the sample quality, (2) UHV chamber for preparation, characterization and NRS experiments.

In both cases a vertical $\Theta\,/\,2\Theta$ geometry for small angles ($\Theta < 5°$) is needed. The operation temperature regime should cover at least lN_2 temperature to highest temperature. This will allow for hyperfine and phonon spectroscopy as well as for diffusion studies. Specialized staff is needed to operate the system and keep it functional at high performance level.

Cryo-systems and furnaces

These systems are employed for temperature dependent studies in NIS, SRPAC or NFS e.g. diffusion studies. Typically the systems are small in size and easily movable, i.e. they can be exchanged as needed. Furthermore, the same hutch might be used for 'unforeseen' set-ups. There are different user friendly solutions to reach He-temperatures, i.e. closed-cycle cryostats, flow cryostats or bath cryostats with cold finger. Since some set-ups, e.g. for the determination of isomer shifts and inelastic scattering with resonant energy analysis, are highly sensitive to vibrations, vibrational damping and mechanical stability will be guaranteed. For the high temperature range a mirror-furnace will be available.

6.6.3.7 Infrastructure

For an efficient operation of the instruments discussed above the following infrastructure would be desirable.

High pressure

Provided the users bring their own high pressure cells the necessary high pressure infrastructure can be kept low. However, minimum equipment to load high pressure cells (e.g. DAC), to change and to determine pressure (e.g. Ruby fluorescence) is mandatory. Depending on the choice for the position sensitive detector for diffraction work the necessary infrastructure should be provided. This equipment should be closely located to the beamline.

UHV environment

From the scientific point of view it is clear that a full UHV system with preparation option is the proper choice. Preparation of samples is the most crucial part which needs experienced personnel and sufficient test and preparation time. Therefore, the system should also be kept operational in a separate laboratory outside the actual beamtime.

Control cabin

In order to ease the operation of the experimental stations and to make it efficient as possible, control cabins attached to each experimental station are mandatory. They should be organized such that independently to the other stations set-up and operation is possible. Otherwise the down time of the beamline will become unacceptable.

6.6.4 Capital investment and personnel

The beamline will be staffed with 2–3 scientists and 1–2 engineers.
The total costs for the nuclear scattering beamline amounts to about **2400** k€.

6.7 High Energy Materials Science

Authors:

F. Beckmann	GKSS - Research Center Geesthacht, Germany
T. Lippmann	GKSS - Research Center Geesthacht, Germany
K.-D. Liß	Technical University Hamburg - Harburg, Germany
R.V. Martins	GKSS - Research Center Geesthacht, Germany
J. Metge	GKSS - Research Center Geesthacht, Germany
A. Pyzalla	Vienna University of Technology, Vienna, Austria
A. Schreyer	GKSS - Research Center Geesthacht, Germany

6.7.1 Current state of the scientific field

6.7.1.1 Introduction

Diffraction methods are well established in Materials Science and Engineering. From the 1930s on X-rays from laboratory sources have been used for non-destructive characterizations of the phase composition of various materials (Hauk, 1997). One of the early and still important applications regarding **phase analysis** in engineering materials is the determination of the retained austenite content in steels, which has a strong influence on steel properties (e.g. Wang et al., 2003a).
Texture analysis by diffraction enables the determination of the orientation distribution of the crystallites. Important technical applications of texture analysis, for instance, are optimizations of the directional properties of semi-finished material for forming processes, e.g. sheet materials, and optimizations of the directional properties of components (e.g. Juul Jensen & Kjems, 1983).
The development of methods for the analysis of **residual (internal) stress** by neutron diffraction started in several groups in parallel (e.g. Allen et al., 1981). The residual stress state of materials and of components is of high importance, since their stress state under working conditions is a superposition of the load and the residual stress state. Thus, for instance, in case of fatigue loading, in most cases compressive residual stresses in the component's near-surface zone proved to be beneficial while tensile stresses were detrimental for the component's lifetime. Reflection profile analysis reveals additional information about residual micro-stresses and, in general, about inhomogeneities of the crystal lattice (e.g. twinning, stacking faults). Engineering applications of profile analysis include e.g. the determination of solute nitrogen in high nitrogen steels and solute carbon in case-hardened steels as well as the determination of the effective depth of surface treatments such as shot peening.

6.7.1.2 Neutron diffraction

Neutrons have been widely used for phase, texture and residual stress analysis, applying well established techniques. Compared to laboratory X-rays the essential advantage of neutrons is their higher penetration depth. This enables phase, texture and internal stress analyses in the bulk of materials and components. For instance the three-dimensional residual stress state of the matrix and the particles of composite materials can be determined non-destructively (e.g.

Al - Si, Ti + SiC, Al + SiC) (e.g. Fiori et al., 2000). The application of neutron diffraction in materials science suffers from the comparatively low neutron flux and the high divergence of neutron beams. Due to the low flux the gauge volume element has a minimum size of app. 1 mm^3, which limits the achievable spatial resolution. Furthermore, the necessary data acquisition times, which are usually in the range of minutes, restrain the application of neutron diffraction for in-situ experiments. In addition, the high divergence of the neutron beam often leads to blurred volume element boundaries. This has also a strong influence on the reflection profiles and, thus, often rules out an accurate reflection profile analysis. Nevertheless, well established and standardized techniques are commonly used for texture and strain analyses and several dedicated instruments exist at various neutron sources. The complementarity of these techniques to X-ray diffraction techniques is of particular interest for the proposed project due to the vicinity of the neutron source at GKSS, Geesthacht.

6.7.1.3 Synchrotron X-ray diffraction

The availability of synchrotron radiation has opened up a broad new field for the application of diffraction techniques in materials science (e.g. Liss et al., 2003). This is due to the extremely high photon flux, the high parallelism and the large range of photon energies available.
The high parallelism of the synchrotron radiation has opened up the possibilities to determine phase composition, texture, lattice defects, and strains / stresses in new materials such as nano-crystalline materials, nano-composites, and crystalline fractions of partially amorphous materials. Due to the high photon flux strain and texture scanning as well as in-situ experiments are possible. Within the area of materials science and engineering a distinction between experiments using monochromatic low and medium energy (<40 keV), monochromatic high energy, and white high energy synchrotron radiation is useful.

Monochromatic low and medium energy synchrotron radiation

As a result of the low penetration depth bulk investigations with low and medium energy radiation are limited to materials with low absorption such as polymers (e.g. Swartjes et al., 2003; Terry et al., 2003) or thin samples. An example from the field of energy storage is the in-situ investigation in transmission geometry of thin battery electrodes under operation (Morcrette et al., 2002a).
In the case of highly absorbing bulk materials, characterizations of the very-near-surface zone (penetration depths of a few hundred nanometers, e.g. in multi-layer-systems) and in the near-surface zone (penetration depths of a few hundred μm, e.g. in surface treated components) are commonly performed. Various techniques addressing these questions were developed in the past (e.g. Van Acker et al., 1993; Ruppersberg, Detemple & Krier, 1989; Genzel, 1994; Leverenz, Eigenmann & Macherauch, 1996).
A technique for three-dimensional structural microscopy with sub-micrometer resolution has been developed by Larson and co-workers (Ice & Larson, 2000; Larson et al., 2002). It is based on the Laue technique, the use of polychromatic low energy radiation and a scanning approach. It allows a micro structure and strain mapping in the near surface zone (Larson et al., 2003). Another method is due to Wroblewski and co-workers (Wroblewski et al.,

1999). It uses an 8 keV synchrotron beam and the setup consists of a 4 - circle diffractometer and a micro-channel plate in front of a CCD. The micro-channel plate serves as a 2D array of collimators. This so-called MAXIM setup provides extended maps with a reported resolution of 12 µm, e.g. of the position of various fine-grained phases (Pyzalla et al., 2001b) or the strain state (Wroblewski, 2002).

A number of so-called micro-focus beamlines, working at low photon energies, exist today. The focusing to 0.1–1 micrometer is achieved by a variety of optical components, such as focusing multi-layers (Ice et al., 2000), zone-plates (Tamura et al., 2000; MacMahon et al., 2003), refractive lenses (Snigirev et al., 1996; Lengeler et al., 1999b; Schroer et al., 2002a), and waveguides (Pfeiffer et al., 2002).

Monochromatic high energy synchrotron radiation

Due to the high photon flux and the penetration power of hard X-rays bulk investigations are commonly done in transmission geometry. The sample thickness ranges from several centimeters in case of Al samples to several millimeters in the case of samples containing large amounts of heavy elements like Ag, W or Pb. Three main fields where hard X-rays are used for the macroscopic characterization of materials can be identified. The first one is a powder diffraction approach where an average, macroscopic information about the full specimen is obtained. The works reported comprise e.g. the structure solving from polycrystalline specimens (Schmidt, Poulsen & Vaughan, 2003), high temperature powder diffraction (Kramer et al., 2002), and the processing of bulk metallic glasses (Yavari et al., 2002). A second field is the investigation of the local texture, initiated at HASYLAB (Garbe, Poulsen & Juul Jensen, 1996; Mishin et al., 2000) which later has led to a dedicated setup there (Wcislak et al., 2002). Thirdly, high energy X-rays have been applied by numerous groups for the characterization of the local strain state, mostly in transmission geometry, hereby integrating over the sample thickness or defining a fixed volume element for depth resolved investigations (e.g. Withers et al., 2002; Webster et al., 2001; Hanan et al., 2002).

The development and implementation of micro-focusing optics for hard X-rays (Lienert et al., 1998; Lienert et al., 1999) has opened the gate for the bulk characterization of the micro structure, texture, and strain on the mesoscopic length scale. Combined with optical elements such as a conical slit cell (Nielsen et al., 2000) or a spiral slit small gauge volumina down to $1.2 \times 6 \times 250\,\mu m^3$ are realized. 2D CCD detector systems provide in combination with the high photon flux a fast data acquisition (about one image acquisition cycle per second). Dynamic studies of the local texture and strain state in torsion samples during deformation were reported (Martins et al., 2002), using a slit imaging technique (Lienert et al., 2000) with a microfocused beam in combination with a conical slit cell and a large area CCD with fast readout. Non-destructive depth resolved phase and strain characterizations, e.g. of friction stir welds (Martins & Honkimäki, 2003), are possible with setups comprising a spiral slit and a large area detector. The development of the 3 Dimensional X-Ray Diffraction (3DXRD) microscope (Lienert, Poulsen & Kvick, 1999) has paved the way for investigation of mesoscopic phenomena such as e.g. the kinetics of individual bulk grains during recrystallization (Lauridsen et al., 2000), in-situ observation of the rotation of deeply embedded individual grains (Margulies, Winther & Poulsen, 2001) or the in-situ determination of the strain tensor in individual bulk grains (Margulies et al., 2002). The 3DXRD method is based on a ”tomographic” (meaning here a data acquisition at a series of different angular sample positions) approach in combination with a microfocused beam and area detectors. The use of high resolution detectors and appropriate data reconstruction routines leads to a spatial resolution down to 5 µm. The data acquisition in the ”tomographic” approach is considerably faster than in other 3D techniques, based on ”scanning” approaches. A fast data acquisition is the basis for the in-situ observation of dynamic processes.

A first experiment combining diffraction and a tomography data (acquired at two different beamlines), was reported by Preuss and co-workers (Preuss et al., 2002). In this combined experiment the progressive fragmentation process of a single SiC fibre embedded in a Ti-6Al-4V matrix was studied.

White high energy synchrotron radiation

In contrast to experiments with monochromatic X-rays, where the intensity of the diffracted photons is measured as a function of the Bragg angle (i.e. angle dispersive), the experiments using white radiation are energy dispersive. Usually an energy dispersive point detector with a sufficient energy resolution is placed at a fixed Bragg angle and the intensities of the energy spectrum are recorded. Residual stress analyses using white high energy synchrotron radiation were first reported by Reimers and co-workers (Reimers et al., 1999). Due to the short data acquisition times, in the order of seconds, in-situ investigations of particle reinforced Al alloys under tensile load at elevated temperatures became feasible (Pyzalla et al., 2001a). Another common application is the residual strain analysis of ceramics, e.g. of thermal barrier coatings (e.g. Gnäupel-Herold et al., 2000).

Limiting factors

Limitations in the applications up to now depend on the length scale the experiments are aiming for.

In the case of investigations on the macro scale, which usually means a powder diffraction approach, the limitations are given by the graininess of the material. To achieve a high spatial resolution parallel to the incident X-ray beam, slit systems are usually inserted in the diffracted beam and the incident beam has to be confined or focused horizontally and/or vertically. In the case of a coarse grained sample micro structure, macroscopic information is not ensured, because only a few grains are illuminated. (Due to the larger sampling volumes this problem usually does not occur in neutron diffraction experiments.) To maintain the high spatial resolution along the beam the samples can be, in some cases, oscillated or rotated perpendicularly to the beam to obtain a better grain sampling.

In the case of investigations on the mesoscale, i.e. on a level, where the aim is to obtain information about individual grains, the problems are different. The aim here is to observe simultaneously as many individual (possibly nano sized) grains as possible, in certain cases (e.g. grain boundary mapping) with a high spatial resolution. This is until now hampered by diffraction spot overlap, detection limit, and low detector resolution. Solutions to these problems are ,e.g. the development of detectors with higher spatial resolution (i.e. much better than 5 µm), a smaller beam size (<1 µm), new experimental approaches, and modified or new reconstruction algorithms. In-situ observations are up to now mostly limited to model cases. Characterizations of complex and highly dynamic processes are still limited by factors such as data acquisition rate and photon flux.

6.7.2 Science at PETRA III

Synchrotron radiation has gained an increasing interest in the materials science community within recent years. It has been shown that substantial new insight into material and component structures and relations between structures and properties can be obtained using synchrotron radiation. In particular materials science with hard synchrotron X-rays has been developing fast during the last 5 years and shown to be promising for investigations of bulk materials and components. Most experiments so far have been carried out at the ESRF (beamlines ID11, ID15A, ID15B, ID30, and ID31), at HASYLAB (beamline BW5 and PETRA II), and at the APS (beamline 1IDB). In principle, both angle and energy-dispersive measurement setups with monochromatic and white radiation, respectively, are possible. The materials science beamline at PETRA III will initially focus on angle-dispersive setups and take advantage of the small beamsize achievable there. The realization of an energy-dispersive setup will be highly emphasized at the HARWI-II beamline, projected by GKSS Geesthacht at the DORIS III storage ring (Beckmann et al., 2003). The HARWI-II beamline avails of the large beam size provided by the wiggler source (e.g. tomography).
The experiments performed up to now in materials science were, to a large majority, focusing on two fields: The investigation of engineering materials and components and fundamental studies in the field of metallurgy and crystallography. In both areas in-situ studies became more and more established. These studies were mostly comprising the (in-situ) investigation of thermally activated processes and / or the material behavior under different basic deformation modes such as tension, compression, shear, and torsion.
The experiments projected for the new beamline will focus on three main topics, which are partly intersecting and for which the instruments will be optimized for (discussed in detail in the following subsections):

- Experiments targeting the industrial user community which will be based on well established techniques with standardized evaluation routines.
- Applied research such as the investigation of power systems (e.g. fuel cells) or process optimization (e.g. manufacturing processes).
- Fundamental research where engineering, metallurgy, physics, chemistry, biology etc. are merging.

Large scientific progress in these fields will be ensured by three particular and unique features of the new beamline:

- Emphasis on complex in-situ studies, e.g. of highly dynamic processes
- Submicron spatial resolution at high energies for high resolution bulk investigations
- Merging of different analytical techniques such as diffraction, tomography, and small angle scattering

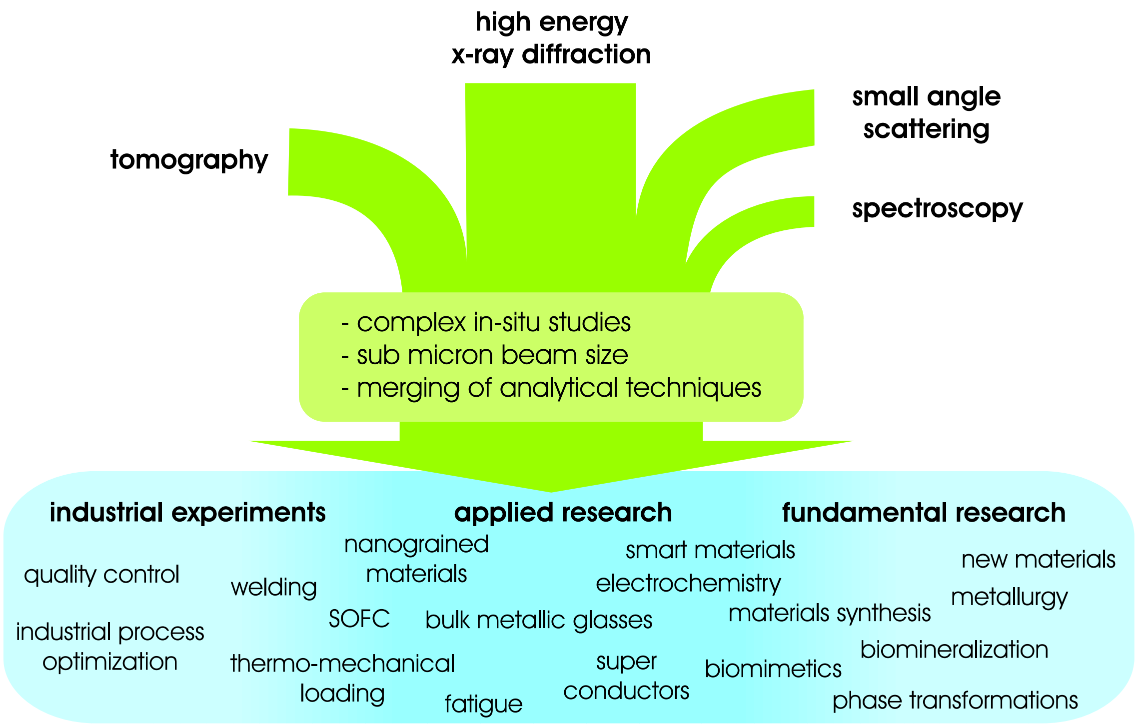

Figure 6.7.1: Overview of the main beamline features, analytical techniques, and research topics projected. (see subsections for details)

Fig. 6.7.1 summarizes the main beamline features, analytical techniques and research topics projected.

By providing the possibility to use this large range of different analytical techniques in parallel, this beamline will be the first one fulfilling one of the main requirements for future research in materials science as expressed in the *European White Book on Fundamental Research in Materials Science* (Rühle et al., 2001).

6.7.2.1 Industrial user community

The intention is to respond to the increasing demand for ”full service” measurements. In other words, the industrial user wishes to send his samples and to receive the results in form of a report, without the need to have a deep understanding of the experimental details and the data evaluation. Moreover, industrial users often prefer measurements to be performed for a large number of samples. These investigations could concern, e.g. a process optimization or a process quality control. This type of experiment will be optimized for high sample throughput. It requires dedicated setups with fast data acquisition based on well established and robust experimental techniques for phase, strain, and texture analysis, and standardized online data analysis routines. They will be complying with the VAMAS standards (Versailles Project on Advanced Materials and Standards). Another type of industrial experiments is the non-destructive investigation of complete structural components or components in operation. This can be, e.g. the strain mapping in critical components of an engine in operation. The new beamline will provide the necessary infrastructure for heavy load sample and sample environment positioning (up to 1 t) and the operation of ”specimens” (e.g. dedicated air outlet for an engine investigated in-situ; cooling).

6.7.2.2 Applied research

The experiments in this field will e.g. focus on the in-situ investigation of liquid / solid processes such as the melt spinning of bulk metallic glasses (e.g Yavari et al., 2002) or welding. These experiments will benefit from the high flux in combination with ultra-fast detector systems. In the field of power system development and optimization, which partly reaches into the field of electrochemistry, experiments of high importance are the investigation of the strain field and interface kinetics of operating Solid Oxide Fuel Cells (SOFC) or the in-situ phase monitoring of battery electrodes (Morcrette et al., 2002a).

The rapidly advancing miniaturization of components and the development of nano-materials will require powerful tools for the optimization of interface-engineering processes. Examples are the non-destructive micro structural analysis of nano-grained metals and ceramics or high resolution strain maps in functionally graded materials. These applications will benefit from the sub-micrometer focusing and the nano-detection capabilities of the new beamline. Furthermore, ”classic materials” (e.g. steel, Al-alloys), ”advanced materials” (e.g. metal matrix composites, Mg base alloys, TiAl), and new materials such as ”smart materials” (e.g. materials with embedded strain monitoring devices or ”self healing” materials), can be investigated. These investigations will excel in the new parallel design of the experiments. It enables e.g. the monitoring of the crack propagation by tomography and the development of the strain field by diffraction within a self healing component or a fiber reinforced material under thermo-mechanical loading. In addition, the installation of the proposed flight tube permits to characterize by small angle scattering *for the first time at high energies and simultaneously to diffraction* e.g. polymers, precipitates, voids, and phase separation (e.g. Fratzl, 2003; Kostorz, 1991) in bulk materials and complex components under thermo-mechanical loading. The use of high energy radiation will permit to perform these investigations in bulk samples of several millimeters to centimeters thickness of technologically important materials such as steel, Ni-base, and Al-base alloys. On a nanometer scale the technique will also allow to gain information on the internal grain microstructure (Fratzl, 2003) which is then directly related to the diffraction data from this specific volume element (cf. 6.7.2.3). Diffraction experiments employing different strain scanning techniques will allow to examine the complete strain state of a sample, from the very-near-surface region down to the bulk. Sample environment for thermo-mechanical loading will cover uni-, bi-, and triaxial deformation modes. The infrastructure will allow an easy accommodation of user provided equipment (e.g. for the in-situ monitoring of processes like friction stir welding). A unique feature of the projected beamline will be an external materials testing laboratory which will contain mechanical testing devices, furnaces, cryostats etc. so that samples during long-term mechanical, thermal and thermo-mechanical testing can be frequently studied using high energy synchrotron radiation.

6.7.2.3 Fundamental research

A large number of experiments will be related to metallurgy and the investigation of polycrystalline materials. The macroscopic properties of polycrystalline materials crucially depend on the behavior and interaction of the individual grains along the complex network of interfaces. The grain boundaries are the glue that hold polycrystalline materials together. Three-dimensional X-ray diffraction (3DXRD) microscopy provides a means for non destructive characterization of the internal structure of polycrystalline materials (Poulsen et al., 2001, Schmidt, Poulsen & Vaughan, 2003). The method is illustrated in Fig. 6.7.2. A monochromatic point-focused beam selects a local gauge volume that contains a sufficiently small number of grains for individual observation. Rotation about the ω axis is used to excite multiple reflections from each individual grain, from which the orientations of all grains in the gauge volume can be determined. Measuring the same reflection spot at different distances of the 2D detector, the position of the grains can be determined by backtracking. Finally, a complete map of the grain boundaries within the volume can be reconstructed (Lauridsen et al., 2001, Poulsen & Fu, 2003). The types of grain boundaries in a material and the way in which they are connected affect a wide range of material properties. The tailoring of these properties has triggered the emerging technology of 'grain boundary engineering'. Fundamental research in this field is essential to specify and produce the desired micro structures. High-energy X-ray microbeams provide a unique opportunity for the determination of internal structures. A scientifically very active area is the study of grain growth. The final micro structure of a material, for example, depends on the grain growth during thermal processing. For a direct engineering it is essential to understand the driving forces behind the change in grain size. The instrument proposed here offers a unique capability to access all

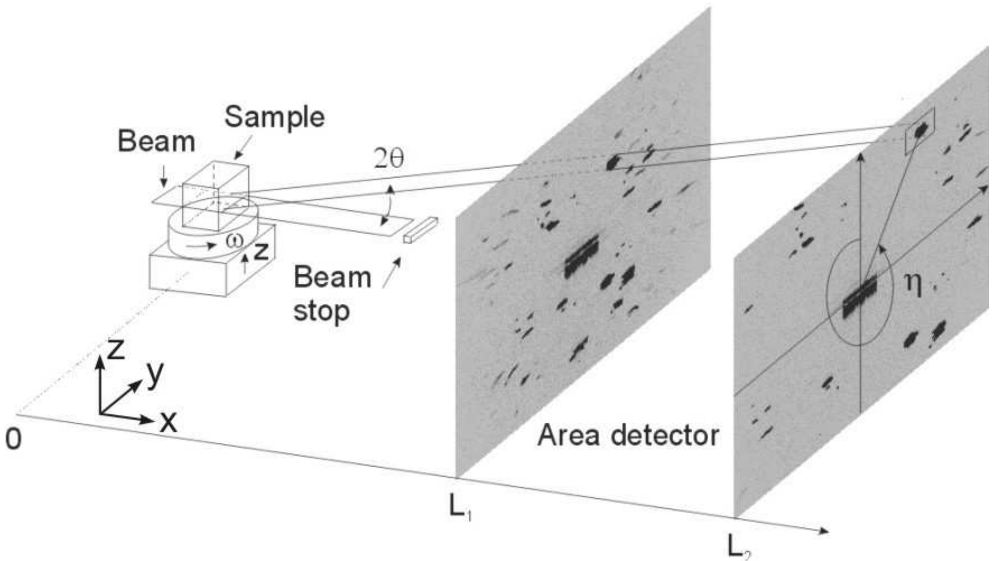

Figure 6.7.2: Grain mapping of a polycrystalline material by 3DXRD (courtesy H.F. Poulsen)

quantities to study grain boundaries and their dynamics (Poulsen & Schmidt, 2003). The development and numerous applications of 3DXRD have shown that a tremendous insight into mesoscale phenomena is possible with high energy X-rays. Up to now most of these experiments were related to model materials such as pure Cu or Al. Moreover, each experiment was focusing on one phenomenon at a time (deformation induced lattice rotation or plastic strain or elastic strain etc.). The aim is to fully characterize samples non-destructively in one experiment, i.e. to analyze all the aspects of deformation induced phenomena in parallel experiments, hereby merging different techniques (plastic strain measurement by tomography; elastic strain and lattice rotation measurement by diffraction, using a large area detector; grain mapping by diffraction, using a high resolution area detector; precipitation and void characterization by small angle scattering; spectroscopy (in the limits of the instrumentally given energy range) e.g. on single intermetallics or precipitations). The availability of a sub micrometer focus combined with high resolution detectors and optical elements like spiral and conical slits (see Fig. 6.7.3) will push this kind of non-destructive in-situ investigations to the subgrain and nano crystalline level.
The beamline will provide the necessary infrastructure to perform experiments in the field of physics under extreme conditions (high pressures, high magnetic fields, low / high temperatures) to investigate e.g. phase transitions at high pressure or extreme temperatures. This is of particular interest in the field of high temperature superconductors.
Furthermore, the beamline design permits an easy accommodation of sample environments

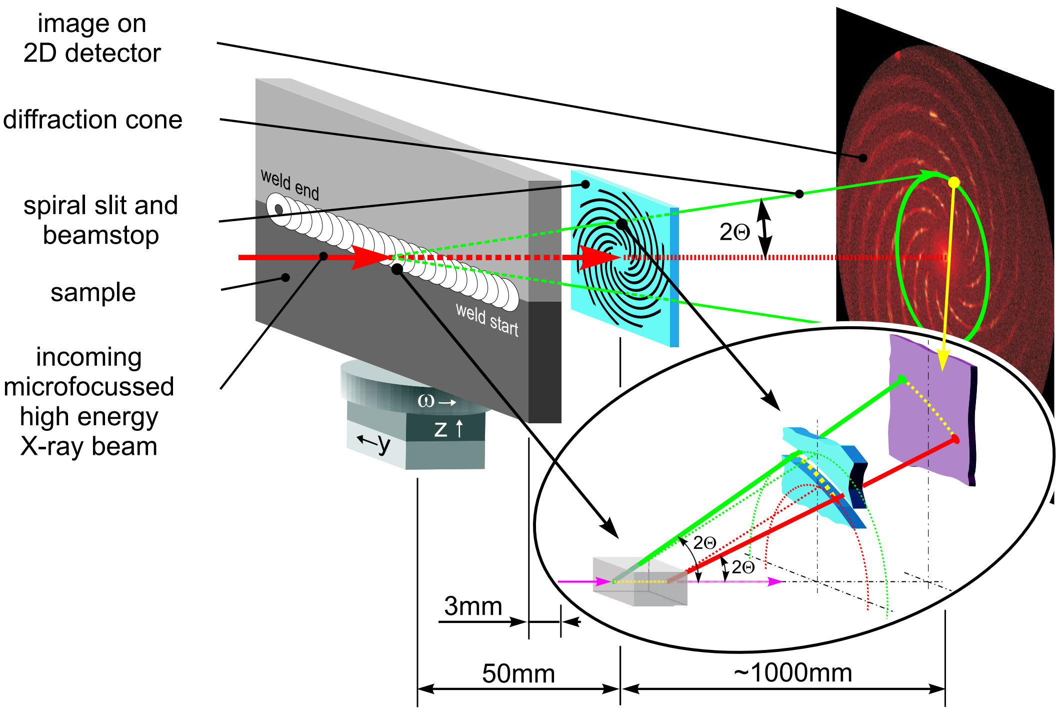

Figure 6.7.3: Schematic of setup with spiral slit system for non-destructive depth resolved phase and strain investigations. The inset visualizes the principle of the beam path which leads to the spatial resolution.

and optical components (e.g. monochromator) provided by the user, such as e.g. setups for the investigation of solid / solid and solid / liquid interfaces and diffuse scattering from binary systems (Reichert et al., 2000; Reichert et al., 2001). The beamline will be a powerful tool for analyses in rapidly emerging fields like biomimetics. Biomineralization and synthesis processes (e.g. nano crystalline bone material) can be investigated on a nanoscale due to the high resolution capabilities and low detection limit. The future development of new materials and materials processing will largely benefit from the high flexibility of this beamline.

6.7.3 Description of the beamline

The beamline layout as proposed at the moment is shown in Fig. 6.7.4. Characteristics valid for the whole beamline are:

- Temperature stability: experimental floor: 1 K, hutches: 0.1 K
- Beam height: 1.4 m above floor in order to accommodate heavy sample environments
- Pits with elevators in the experimental hutches to accommodate large diffractometers, samples, and sample environment
- Hutch height: experimental hutches: 5 m (cryostat), optics hutch 4 m
- Access to experimental hutches from the roof
- Manual cranes (> 1.5 t) below the ceiling in every hutch
- Media: biologically clean cooling water (15 °C), dry N_2, compressed air, He recovery line

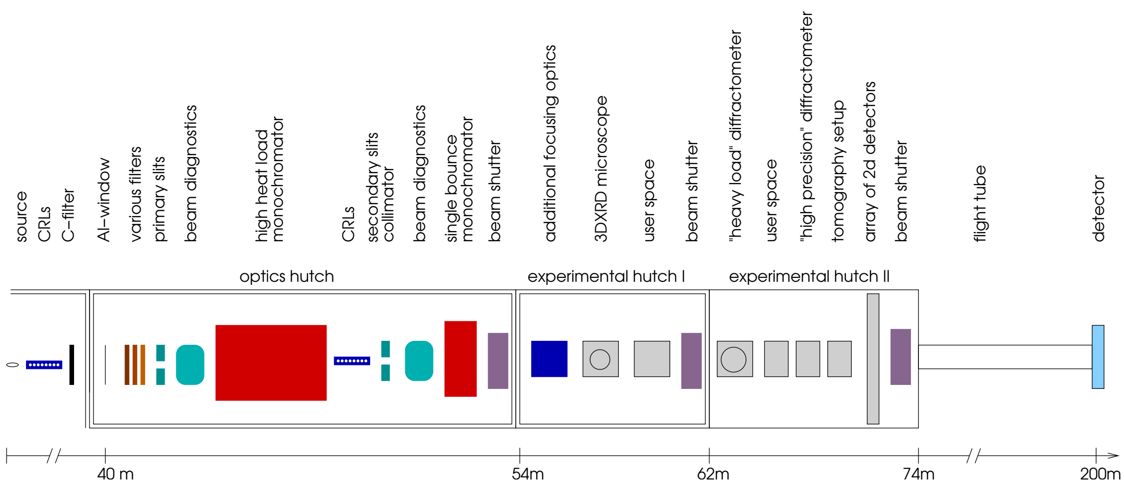

Figure 6.7.4: Schematic layout of the high energy materials science beamline.

- Special air outlet for engines (cf. 6.7.2.1), for experimental hutches only
- Decoupling of all hutches from PETRA hall floor
- Large hutch doors without barriers on the floor
- Network and power connections in every hutch

Besides the beamline itself, 40 m^2 for laboratory plus a storage area are needed. The lab has to be located in the direct vicinity. Office space for 4 scientists, 1 technician, and several students and postdocs is needed.

6.7.3.1 Insertion device

The insertion device has to meet the following three high priority requirements of the beamline (discussed in detail below):

- Main energy of 120 keV
- Source suitable for sub-micron focusing at high energies
- Minimized heat load for optical elements

With an energy range between 50 and 300 keV the accessible energy range for hard X-rays will be substantially larger than for most of the existing beamlines. The X-ray energy is a compromise between the penetration depth necessary for bulk studies in most engineering materials (Al-, Fe-, Ni-, Co-base alloys) and the scattering angle respectively the angular resolution. Therefore, a main energy of 120 keV is proposed for the design of the insertion device.
The sub-micron focusing requires mainly a small source size, a small source divergence. Therefore the insertion device should have a source size below 57 x 10 μm^2 (H x V) FWHM (incl. source broadening) and a source divergence below 88 x 5 μrad^2 (H x V) FWHM.
A high flux is desirable for this device, but is of lower priority than the main energy, the source size, and the low heat load.
Typically a primary beam of about 1 mm^2 will impinge on the focusing optics, but in particular for fast grain mapping applications and tomography a primary beam with a substantially larger width (about 3mm) is favored.
Studies will be undertaken to examine the feasibility of a superconducting device.
Experiments using energies below 50 keV have to be performed at other beamlines.

6.7.3.2 Beamline optics

Filters are foreseen to strongly suppress the energies below 50 keV and thus reduce heat-load problems on the optics. They will allow to operate all monochromators in air ambiance.
A unique specialty of the proposed beamline at PETRA III will be the high flexibility in shaping the high-energy X-ray beam, depending on the particular needs of the experiment. The beam type will range from a sub-micron focused pencil beam (e.g. for the investigation

of individual nanosized grains), over a line focus (e.g. for fast grain tracking) to box shaped beams with a homogeneous beam profile (e.g. macroscopic texture and strain analyses, tomography), hereby benefitting from the high photon flux, the small source size, and the very small beam divergence.
Beam focusing will be achieved with conventional bent monochromator and bent multilayer setup and with X-ray lens systems such as refractive X-ray lenses. The development of lens systems is currently progressing strongly and focusing spot sizes smaller than 1 µm are envisaged for hard X-rays. An important feature will be the availability of a fixed-exit focusing monochromator, thus allowing e.g. phase analyses with high spatial resolution using a conical slit cell. Compound Refractive Lenses (CRLs) that improve the parallelism of the beam will be installed in the front end, close to the source. For large beam sizes the shaping of the beam will be performed using slit-systems.
Optical elements that are part of the setups in the experimental hutches are conical and spiral slit cells, glas capillary arrays, and micro-channel-like plates made from tungsten. They ensure a high spatial resolution, within the sample, parallel to the beam (better than 50 µm). Further developments in this area are expected. Furthermore, refractive lenses can be used as analyzers in the diffracted beam.
Such a comprehensive system of beam types, slits and lenses for the different applications in materials science is so far not available at a single high-energy beamline.

Summarizing, several optics have to be considered:

- Slit optics: This is the simplest either in a white beam or through a monochromator setup.

- Scanning fixed-exit monochromator: The second crystal defines the incident beam condition by rotation to the appropriate Bragg angle only. The first crystal rotates and moves on a long translation stage and is fed back to the maximum transmitted intensity, thus eliminating the influence of rotational errors of the first crystal. The fixed-exit monochromator tunes through the whole energy range as defined above. Due to the small scattering angles, reflection condition is in asymmetric Laue geometry. A simple rotation of the inclination switches from the (111) to the (311) and eventually more reflections.

- Scanning fixed-exit focusing monochromator, maintaining focus size and position over a range of several keV, realized with bent Laue crystals.

- Several sets of crystals will be available such as perfect or oxygen precipitated and bent crystals. Different monochromators, placed besides each other, can be moved into operation by lateral translation.

- Single-bounce monochromator: This monochromator type in horizontal geometry will be foreseen for special purposes and the monochromatic beam will only go to the white beam hutch (experimental hutch I), allowing a high flexibility in the arrangement of the experimental setup in the hutch space as well as in focusing.

- Space will be foreseen for compound refractive lenses in the front-end, improving beam parallelism.
- For focusing purposes compound refractive lenses will be foreseen after the monochromator.

6.7.3.3 Experimental hutch I

The first experimental hutch will be a white beam hutch with a space of $5 \times 8\,\mathrm{m}^2$. It will permit the installation of user provided monochromators, increasing the flexibility for beam focusing and experimental setup design. All experiments using white beam can be carried out here. The main components of this hutch are:

- 3DXRD microscope.
- Additional focusing optics close to the 3DXRD microscope.
- A cooled beam stop at the end of the hutch.
- Beam available from single-bounce monochromator (see optics hutch).
- Space e.g. for a “user monochromator” and for user provided setups.

The single-bounce monochromator (situated in the optics hutch) will be operated in horizontal geometry. Its distance to the beam shutter has to be small in order to reduce the size of the horizontal shutter opening. The experiment itself can be set up in the first experimental hutch.
Even if the white beam hutch is initially not built at once, it has to be foreseen in the design for the static load for the whole beamline since from experience at the ESRF for safety reasons a radiation shielding thickness of at least 50–200 mm Pb is necessary which results in a significant floor loading. Preferential to the Pb shielding would be a concrete shielding of the white beam hutch, but the concrete shielding requires more space.

6.7.3.4 Experimental hutch II

The second experimental hutch will have space for four experiments:

- A heavy load diffractometer which can carry a load up to 1000 kg for big samples and different sample environments (cryo magnet, press, tensile testing machine, furnace, etc).
- A smaller high precision diffractometer for micro beam applications.
- Space for user supplied experimental setups.
- A tomography setup which goes preferably to the end of the hutch using the largest possible beam size. The possible implementation of the flight tube (see fig. 6.7.4 and 6.7.3.5) will, therefore, also be of great advantage for these applications.

The heavy load goniometer will be optimized for materials science investigations. For analysis with a spatial resolution in the sub-µm range a high precision translation and rotation system will be installed. Until now (2003) there is no such instrument available at a synchrotron beamline. This device is supposed to enhance the precision in movement for larger samples and especially for large sample environments such as furnaces, devices for mechanical testing and thermo-mechanical testing. A further unique feature will be the combination of the synchrotron radiation laboratory with the above mentioned external materials testing laboratory (mechanical testing devices, furnaces, cryostats etc.).
The second hutch will be at least 12 m long in order to achieve high angular resolutions and to accommodate all experiments. At the very end of the hutch 2-dim position sensitive detectors will be mounted. A novel multi-detector concept will enable simultaneous data collection for different diffraction angles.

6.7.3.5 Flight tube

A unique and particular feature of the projected beamline will be the possibility to perform small angle scattering experiments at high energies on bulk samples, simultaneously with diffraction experiments. The feature distances in the micro structures to be investigated by small angle scattering typically range from 1 to 1000 Å (e.g. porous media, polymers, precipitates). To achieve a minimum angular resolution at 120 keV the area detector needs to be placed at least 200 m away from the source, i.e. at a distance of about 150 m from the first possible sample position. The detector chamber will be connected to the experimental hutch by a flight tube (see Fig. 6.7.4). Because of the resulting space constraints outside the experimental hall the beamline should occupy the third or fourth position in the experimental hall. Even if the flight tube is not part of the first construction phase the space required outside the experimental hall should be taken into account when decisions are made on the position inside the experimental hall.
With the option to perform on the same sample and the same volume element, parallel to diffraction experiments, in particular cases analyses by small angle scattering, tomography, and spectroscopy, the proposed beamline will be the first, where the boundaries between these analytical techniques are gradually disappearing.

6.7.3.6 Detectors

The wide variety of experiments for this beamline is reflected in the particular need of various special detectors. In most cases the use of area detectors will be favored to realize the high data acquisition rates required for dynamic in-situ studies and to fully benefit from the high photon flux. Mainly three different types of area detectors for diffraction experiments can be distinguished:

- Large area detectors, allowing the monitoring of complete Debye-Scherrer-rings at large sample-detector distances (at least 2000 mm) for ultra fast strain and lattice rotation analyses.

- Array of large area wire-detectors which can be translated over a long range along the beam for high angular resolution, comparable to the HARWI II setup. In contrast to the other large area detector they can only monitor sections of Debye-Scherrer-rings.

- High resolution detectors (around 1 μm resolution) which, as a consequence, are placed close to the sample, e.g. for subgrain mapping.

For the small angle scattering experiments area detectors with an efficiency optimized for high energies are required Standard point detectors are required in case of spectroscopy analysis. Improvements in the field of detector development are expected within the next years.

6.7.3.7 Redundant-beamline concept

The beamline will be equipped based on a ”redundant-beamline concept”, meaning that critical spare parts or a complete replacement exist for all crucial components of an experimental setup in case of failure. This concept relates to components such as critical sample translation and rotation units, detectors, fast beam shutters, sample environment, electronics etc. This spare pool does not necessarily need to be exclusively accessible to this one beamline. However, many of the critical parts will certainly be beamline specific such as detectors for high energy X-rays. The financial investment will be low in comparison to the loss of beamtime, considering the amount of lost manpower for several months of experiment preparation.

6.7.3.8 Beamline control and data collection

To attract user communities, especially from the engineering sector, who are not familiar with synchrotron radiation, the concept for instrument control software and data evaluation will strongly involve the aspect of user-friendliness. Measurement techniques and analysis routines according to the VAMAS standards will be implemented, which will be of particular interest for industrial users. For scientists familiar with the techniques interfaces between the basic instrument control and data acquisition will be provided for the development of novel measurement and evaluation techniques. The use of SPEC as beamline control software is strongly favored. It ensures an easy compatibility of software and will facilitate the collaboration on this sector with other synchrotrons, e.g. the ESRF.

6.7.4 Capital investment and personnel

6.7.4.1 Capital investment

The total investment costs for this beamline sum up to **5350** k€.

6.7.4.2 Personnel

The projected beamline will be highly versatile in its application, merging different analytical techniques. This necessitates and justifies the employment of four scientists, one software engineer, one mechanical engineer, and one technician on a permanent basis.

Ideally the scientists are complementary in each others competences. Particular skills and knowledge are required in the fields residual strain analysis, texture analysis, powder diffraction, tomography, and high-energy X-ray optics.
A software engineer is a prerequisite for the smooth and efficient operation of the beamline. Most experiments carried out will highly rely on complex software for high-speed data acquisition and on-line data analysis. Furthermore, the beamline control requires a continuous improvement and maintenance.
The continuous improvement of beamline hardware, development and realization of new components and setups will be carried out by the mechanical engineer together with the technician, in close collaboration with the scientists.
The technical staff might be part of a pool for beamline software and hardware support. However, particularly in the start up phase of all the beamlines it is clear that these pools have to be sufficiently large (one engineer and technician per beamline) to avoid bottlenecks. It is emphasized here that dedicated PETRA groups of significant size will be highly appreciated for optics, metrology, detector support, computing, and beamline specific engineering tasks.

6.8 Powder Diffraction

Authors and Consultants :

H. Ehrenberg	Darmstadt University of Technology, Germany
Th. Wroblewski	DESY, Hamburg, Germany

6.8.1 Current state of the scientific field

The low divergence of synchrotron radiation (SR) together with its high intensity permits powder diffraction (PD) with much higher angular and time resolution than at conventional laboratory X-ray sources. The resolution function of a powder diffractometer operated in parallel beam geometry is given by the sum of three angular dependent terms which are proportional to the acceptances of monochromator, receiving slit or analyzer crystal and the divergence of the incident beam, respectively (Wroblewski, 1991). At a powder diffractometer situated at a bending magnet of a 2^{nd} generation synchrotron source, for example the B2 powder diffractometer (Knapp et al., 2003), the latter term is dominant due to the high divergence of the radiation from DORIS. To reduce this divergence a collimating mirror must be used, limiting the accessible energy range (Knapp et al., 2001). At a PETRA III undulator all three terms will be in the same range of a few μrad yielding an instrumental resolution function with two orders of magnitude smaller half widths without collimating elements.

In contrast to single crystal diffraction in PD the reciprocal space is projected from three dimensions to one dimension frequently leading to severe overlap of reflections. Additional information can be obtained by measurements at different temperatures because of a partial peak separation due to anisotropic thermal expansion. High resolution is, therefore, essential for the structural characterization of polycrystalline materials.
The refinement of crystal structures by the Rietveld method is a very well established standard technique in PD (Rietveld, 1969; Young, 1993; McCusker et al., 1999) and with the advantages of synchrotron radiation now even applied in protein crystal structure analysis (von Dreele, 2003). However, the most significant progress in crystallographic applications of PD over the last decade was the improvement of structure determination strategies (David et al., 2002). Although structure solution from PD data is not yet a routine task, further progress in available software packages will allow their use for an expanding scientific community and push the successful application to more complex structures (David, 2003). Present limitations are radiation damages, especially in beam-sensitive organic samples, and the availability of beam time at appropriate experimental stations to collect data with sufficient counting statistics over a wide enough range of diffraction angles at several temperatures.

Crystal structure analysis on polycrystalline samples is a complementary tool to diffraction from microcrystals (Harding, 1996; Serda, Grochowski & Duddeck, 2004). The advantages of microcrystal diffraction in general are a more straightforward unit-cell determination and structure solution. In both cases the accuracy of the final structure model is limited by the restricted amount of diffraction data that is possible to record. It depends on the specific situation whether PD or single-microcrystal diffraction is the method of choice. PD is the only applicable method whenever not even microcrystals are available or reconstructive phase transitions or chemical reactions prevent single-crystal techniques. This is by far the most frequent case for applications in materials science, where structural analyses of inhomogeneities and anisotropies of multi-phase and composite materials are requested over a wide range on length scale from nano-size domains, crystallites and grains up to micro devices. The properties of many materials result from the anisotropy of individual crystallites, their locations and orientations. High-resolution PD does not only provide bulk-representative averages; more and more sophisticated methods have been developed during the last years to separate the effects of grain size and residual strain but also to analyze the effects of dislocation densities or inter-growth distributions (for example in ceramic superconductors) on the profile shape (see for example the Size-Strain III conference, Trento, 2001 or (Mittemeijer & Scardi, 2004)). This progress in data evaluation entails a further increased demand for high-resolution PD data.

Especially the response of materials to external fields and the changes during aging and fatigue are in the center of interest of materials science. Such investigations require dedicated sample environments, which allow conditions of real operation mode compatible with PD. At present, about 90% of all diffraction experiments at the high-resolution PD beamline B2 at HASYLAB are performed in flexible sample environment with at least one variable parameter. The recent development of a new position sensitive detector for highly efficient data collection (Knapp et al., 2004) allows for sample environments with higher absorption and smaller beam or sample size (Knapp et al., 2003).

The demand for powder diffraction using high-energy SR with low divergence will further increase in the next years because of qualitatively new opportunities offered by dedicated sample environments for in-situ characterization of polycrystalline materials and the expanded capabilities of established methods at enhanced radiation sources. The existing and already planned experimental stations cannot serve the expected beam time request.

6.8.2 Science at the high-energy powder diffraction side station

Dedicated high-resolution PD beamlines belong to the working horses at all synchrotron facilities operating in the hard X-ray regime. The following applications are proposed for a side station with a fixed photon energy of about 56 keV.

6.8.2.1 Crystal structure determinations from PD data

In cases where no suitable single crystals are available, crystal structure solution and refinement depends on high-resolution PD. The use of high-energy SR ($>$ 50 keV) is of primary importance: Radiation damage in beam-sensitive materials like organic, biological or pharmaceutical samples, is significantly reduced. Furthermore shorter exposure times will reduce the effects of secondary processes, following the primary radiation damages, that lead to further degradation of the structure. The high intensity of the primary beam will allow for time-efficient data collection at different temperatures. Compounds with heavy elements can be studied in capillary mode due to the much smaller absorption of high-energy SR. The temperature dependent formation of complicated superstructures in ordered intermetallic compounds from disordered alloys is an example for new opportunities. Such phase diagrams, especially of air-sensitive systems with intermediate phases, are very often incomplete. The application of halogen-mirror furnaces offering temperatures up to about 2200°C is often limited by the lack of appropriate sample holders. In addition to solid ceramics or powders in Al_2O_3- or MgO-tubes also air-sensitive samples, sealed in welded for example Pt/Rh-tubes, can be studied with high-energy SR.

Another set of novel experiments is based on newly designed in-situ cells for the investigation of polycrystalline materials under real operation conditions. Hereby, the high penetration capability of high-energy SR through pressure-stable shieldings and the smaller exit windows, sufficient for short wavelength diffraction, are exploited.

6.8.2.2 In-situ studies of chemical reactions

Besides investigations of temperature induced phase transitions there is an increasing demand for in-situ studies of crystalline phases during chemical reactions with gases or liquids and as solid catalysts for heterogeneous catalysis (Norby, 1997; Andersen et al., 1998; Parise, Cahill & Lee, 2000; Chupas et al., 2001). Examples for reactions of interest are oxidation or reduction processes in dilute oxygen and hydrogen atmospheres, respectively (Rodriguez et al., 2002); for example the latter reaction is used for preconditioning of noble-metal catalysts to remove inactive oxide layers from surfaces (Campbell, Daube & White, 1987). Other examples are dehydration processes using dry noble-gas atmospheres (Reisner et al., 2000) and gas-solid reactions like the adsorption of molecules into zeolites and their thermal stabilities under real catalytic conditions. An example for diffraction studies on solids within liquids is the ion exchange in zeolites (Lee et al., 2000).

Such experiments require controlled and well defined atmospheres at elevated temperature and pressure in mechanically stable reactors. High-intensive and high-energetic SR with sufficient penetration capability is essential for time-resolved diffraction studies under these conditions. Both the degradation and intermediate states of catalytic active materials can be investigated, providing information about the optimum working point and the underlying processes like amorphization, crystal growth or phase transitions. The expected results will elucidate the working mechanisms and help to improve heterogeneous catalysts, components in low-temperature membrane and high-temperature solid oxide fuel cells and catalysts for automobile exhausts. A possible extension in future might be the investigation of reactions under supercritical conditions, but at present it is not clear how supercritical in-situ conditions can be realized.

6.8.2.3 Electrochemical intercalation in battery materials

Rechargeable batteries, especially for notebooks and mobile phones, are often based on the reversible exchange of lithium between two electrodes. In the charged state lithium atoms are situated in the anode host material, most commonly graphite, and in the discharged state as lithium ions in a cathode host like $Li(Co,Ni)O_2$ or $LiMn_2O_4$. The lithium transfer is possible via an electron insulating but Li-ion conducting electrolyte. The high economical interest in secondary batteries has triggered numerous research activities including in-situ diffraction (Richard, Koetschau & Dahn, 1997; Bergström, Gustafsson & Thomas, 1998; Cras et al., 1998; Mukerjee et al., 1998; Meulenkamp, 1998; Morcrette et al., 2002b; Braun et al., 2003; Li et al., 2003). An in-situ cell for user's applications is already in operation at beamline B2 (Baehtz et al., 2004). This design is shown in Fig. 6.8.1 on the left hand side and allows experiments with sample rotation in transmission mode. Diffraction data are collected simultaneously with the electrochemical characterization of the battery, shown in Fig. 6.8.1 on the right. Hereby, phase transitions have been studied during charging and discharging, resulting in phase diagrams for $Li_{1-x}Mn_2O_4$, $Li_{1-x}(Co,Ni)O_2$ and $Mg_xMo_3S_4$.

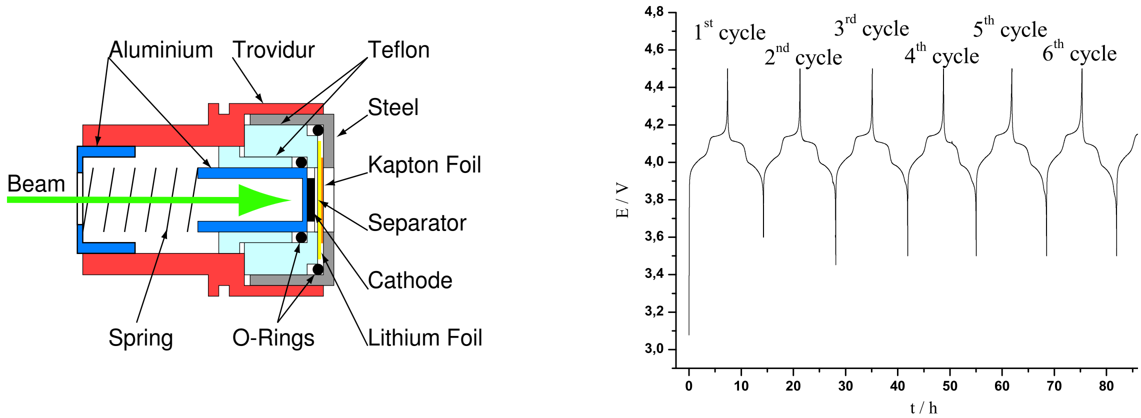

Figure 6.8.1: Schematic drawing of the available in-situ cell for characterization of battery materials (left). The corresponding cyclovoltamogram of more than 6 charge and discharge cycles of $LiMn_2O_4$ (right) proofs the correct electrochemical behavior.

The long-time stability of capacity is the crucial criterion for applications, and in-situ studies are needed after more than 1000 charge-discharge cycles to reveal information about degradation mechanisms. All existing in-situ cells are designed to minimize absorption effects from current collectors, electrode materials, electrolyte, separator and shieldings. As a consequence, the cells are not perfectly sealed and fail after about 10 cycles. Furthermore, the active electrode areas are rather small so that much higher current densities are used for in-situ studies than in actual technical applications. Both limitations are overcome with high-energy SR as electrode stacks in ideally closed shieldings can be used.

6.8.2.4 Piezoelectric ceramics with applied external fields

A significant drawback in the investigation of PZT ceramics by X-ray diffraction is the huge absorption of lead. For energies below 20 keV only surface-near regions can be studied (linear absorption coefficient $\mu > 50\,\mathrm{mm}^{-1}$) instead of the representative response of the bulk material. High-energy synchrotron radiation (e. g. $\mu \sim 3.4\,\mathrm{mm}^{-1}$ for 55 keV) is of primary importance for significant progress in this field. Bulk experiments in transmission geometry with sputtered electrodes on both sides will become feasible with a sample oscillation for better statistics of crystallite orientation. In addition to DC fields in-situ studies with AC fields appear possible. The synchronization of a chopper or the detector electronics with the applied alternating field will allow to sum up data from successive periods in the same polarization state of the piezoceramic. For such stroboscopic studies the time structure of the PETRA ring (7.7 μs in single bunch mode) might be of interest. Temperature and frequency dependent studies can provide information about domain wall dynamics and the effects of sintering conditions, doping, ageing and fatigue. High-resolution PD data are essential for a sophisticated profile analysis, especially for samples near the morphotropic phase boundary, where different crystal structures can coexist.

6.8.2.5 Shape-memory alloys under external load

Behavior under mechanical stress is a common scientific problem for constructional materials and becomes particularly interesting in relation to smart materials, actuators and sensors, such as piezoelectrics or shape memory materials, and most importantly in relation to fatigue in any material. In the international scene, beamlines for materials research with mechanical loading frames have been constructed for neutrons and synchrotrons. In particular, the SMARTS neutron beamline at LANL has been constructed around a loading frame equipped with a graphite heater to achieve 2000 K (Bourke, Dunand & Ustundag, 2002), similar, but so far without heater is the new ENGIN-X beamline at RAL. At ESRF, ID11 is equipped with a 5 kN loading frame, and the beamline has the capability of investigations of single grains in the polycrystalline matrix and of 2D mapping of the microstructure (Margulies, Winther & Poulsen, 2001). The main advantage of the synchrotron, and in particular of high-energy synchrotron beam lines is the capability of true sub-mm space resolution (i. e. combine the advantage of spatially resolved information (Schmahl et al., 2004) with bulk information (Sittner et al., 2002; Sitepu et al., 2003). Most important, a synchrotron experiment is able to follow the stress state of selected single crystallites in a polycrystalline matrix (Gundlach et al., 2004), a capability with enormous potential for understanding the mechanical strength of materials.

These are only selected examples for advanced characterization techniques of polycrystalline materials under real operation conditions. The exploration of materials response with respect to a more dimensional parameter space, e. g. with respect to combinations of temperature, pressure, stress, frequency and amplitudes of external fields, etc., is the key issue for a newly established high-resolution PD beamline.

6.8.3 Beamline description

From the above mentioned instrumental and experimental demands the following characteristics of beamline and instrumentation can be deduced :

The beam should be highly parallel in the vertical direction. In the horizontal direction, however, a more divergent beam is required. This results from the demand of having sufficient orientational statistics of the grains in a powder. To achieve random orientation the sample is usually filled in a capillary and rotated. Nevertheless, the illuminated region of the capillary should be as long as possible to increase the number of diffracting grains. The photon energy will be fixed to about 56 keV. In this case the powder diffractometer could be operated at a 'side station'. For highest resolution analyzer crystals must be used. This should be done with a multiple analyzer stage to reduce the measuring time. This circle should have a reproducible resolution of $0.0001°$ in 2Θ, matching the resolution function. For experiments not needing ultimate resolution a one-dimensional position sensitive detector (PSD) is needed, which can be mounted in a fixed position, facing the analyzer arrangement. A two-dimensional PSD in the low-angle region with flexible sample-detector distance is needed for texture analyses and orientation-resolved diffraction.

The operation with fixed photon energy imposes only minor restrictions, because most of the proposed experiments benefit from higher energies (limited by the monochromator specifications for high-resolution PD). The overall demand for resonant diffraction studies is rather low and can be served elsewhere. On the other hand, a significant improvement in efficiency can be obtained by optimizing the detector systems for a small energy range. The standard detector systems for synchrotron powder diffraction, scintillation counters, image plates and CCDs, are working over a wide energy range with similar good performance. By restriction to a narrow energy window the detector efficiency can be improved considerably by optimization for this specific energy.
For the various in-situ studies appropriate sample environments (furnaces, cryostat, in-situ cells, etc.) must be available, which can be easily changed. Operation at fixed energy will ensure better compatibility between different set-ups.

A special environment is that for high pressure studies. It employs the anvil-type of high pressure apparatus. This option does not require bulky equipment, whereas it makes it possible to generate the largest pressure range and provides large variety of experimental options. The high pressure environment includes diamond anvil cell, large-volume Paris-Edinburgh cell, sapphire-anvil Kurchatov Institute cell. The cells can be combined with cryostats for low temperature studies as well as with the laser heating system to achieve high pressure - high temperature conditions. The small sample volume due to the high pressure and/or laser heating requires a micro beam. It is therefore recommended to have a kind of table top experiment at a micro focus beamline instead of a high-resolution PD beamline.
The powder diffractometer will be operated at a low beta (high divergence to obtain a broad beam) section. No mirror will be used because of the required high energies. Depending on whether the whole wavelength range will be used or only a fixed wavelength a double (cryogenic Si 111 or Si 311) or single crystal monochromator (Diamond 111) is needed.

6.8.4 Capital investment and personnel

An important component is a high precision diffractometer including encoder, multi analyzer stage and control system. The PSD should have a spatial resolution of 0.1 mm corresponding to the projection of a thin capillary. The readout time should be in the millisecond range.

Possible electronic detectors matching these specifications are diode arrays, strip detectors or CCDs (spectroscopy mode), covering an angular range of $\approx 30°$. For certain applications modified commercial detectors applied in non-destructive testing may be applied. (In this field even detectors covering a wide angular range are available. Presently, however, no detector covering this angular range is available from the shelf. Detector development is, therefore, as for many other beamlines, of paramount importance. Open questions are whether a curved detector is needed or a linear one is sufficient and whether it must be monolithic or can be composed of several elements (blind areas between elements). It should also be investigated whether relatively cheap detectors as they are used in check-in applications at airports can be applied.
Various sample environments like cryostat, furnace, in-situ cells are foreseen.

The total cost of the powder diffraction station will be about **1200 k€**.

Two scientists and two engineers will be needed during construction and commissioning. After commissioning one engineer may be sufficient provided that there is support from central services (computing, electronics, workshops).

6.9 Unfocused ASAXS Beamline

Author :

G. Goerigk IFF, FZ Jülich GmbH, Jülich, Germany

6.9.1 Abstract

Due to the low emittance of PETRA III the beam parameters at a high-β section are in a high degree suitable for the design of an unfocused **S**mall-**A**ngle **X**-ray **S**cattering (**SAXS**) beamline with high q-resolution. Additionally the energy spectrum covered by a PETRA III standard undulator will allow one to make use of the element-selective **A**nomalous **S**mall-**A**ngle **X**-ray **S**cattering (**ASAXS**) technique and to extend the classical energy range of this technique (5–35 keV) up to energies of about 90 keV. The extension to higher energies will give access to the K-absorption edges of the heavier elements (Z > 53). The energy range in combination with the high flux of a 3rd generation source offers the opportunity to address numerous challenging scientific objectives in solid state physics, catalyst research, chemistry and biology, which are not accessible by the existing state of the art (A)SAXS-experiments.

6.9.2 Current state of the field

Small-Angle X-ray Scattering experiments average over a large sample volume and give structural and quantitative information of high statistical significance on a mesoscopic length scale between one and hundreds of nanometers, which can be correlated with macroscopic physical and chemical parameters of the analyzed materials (alloys, semiconductors, glasses, macromolecules in solution, metal nanoparticles, composites).
In the past Synchrotron Radiation (SR) provided the SAXS-technique with four major improvements:

1. The photon flux, which is many orders of magnitudes higher compared to classical X-ray sources allows one to study samples, which show only weak small-angle X-ray scattering.

2. The continuous energy spectrum of SR allows for the energy tunability of the technique. Beside the possibility to adapt the X-ray energy to the sample under investigation (e.g. thinning of samples with internal stress is limited and SAXS analysis should be done at higher energies to minimize absorption) the further advantage is the energy tunability in the vicinity of the K- and L_{III}-absorption edges of most of the elements. This technique - known as Anomalous Small-Angle X-ray Scattering (ASAXS) – is based on the anomalous variations of the atomic scattering factors near the absorption edges and allows for the element-specific characterization of the samples under investigation on the mesoscopic length scale. After the exploratory studies of the 1980s (Stuhrmann, 1985; Simon, Lyon & de Fontaine, 1985), ASAXS became a standard technique, which is nowadays used to address numerous challenging scientific objectives in solid state physics, materials science, catalyst research, chemistry and biology

(Goerigk et al., 2003), where classical SAXS experiments (with fixed energy) are not able to provide decisive information. As a consequence it appears desirable to design a SAXS beamline at a 3^{rd} generation source with an unfocused, energy tunable beam, with the goal to fully exploit the scientific potential of this technique. For this reason, this proposal addresses the more general subject of an unfocused ASAXS beamline.

3. The very small beam divergence in both the horizontal and vertical directions. The spatial resolution of a SAXS experiment depends strongly on the beam parameters and benefits crucially from low divergence and high collimation. This determines the size scale of the topological or chemical inhomogeneities, which can be observed.

4. The extension of the X-ray spectrum to energies higher than 30 keV at the 3^{rd} generation sources with sufficient machine energy (ESRF, APS, SPring-8).

In Europe, three beamlines have been optimized for the ASAXS technique: JUSIFA at HASYLAB, D2AM at ESRF and D22 at LURE (the latter being upgraded and reinstalled at the French synchrotron radiation source SOLEIL). Two of these beamlines (JUSIFA and D22) are using fixed exit double crystal monochromators, which turned out to allow far easier operation compared to focusing optics (at D2AM). As a consequence, an “easy-to-use“ ASAXS beamline should abandon focusing optics if possible (Goerigk et al., 2003).
Scientific examples for key applications of the ASAXS technique are :

- Polyelectrolytes with counter ion distributions (Guilleaume et al., 2001; Guilleaume et al., 2002; Goerigk et al., 2004; Das et al., 2003),
- amorphous semiconductor alloys (Goerigk & Williamson, 1998; Goerigk & Williamson, 2001a),
- metal nanoparticles (for instance used as catalysts) (Polizzi et al., 2001; Rasmussen et al., 2000; Bota et al., 2002; Haubold et al., 2003),
- membranes from biology (Richardsen et al., 1996) and from technical applications (Prado et al., 2003).

Three examples are shown in Figs. 6.9.1–6.9.3. The examples have in common, that only the ASAXS technique is able to provide the essential information.

Numerous materials were analyzed by ASAXS in the last decade and the concerned fields of research are solid state physics (amorphous alloys, glasses, semiconductors, bulk metallic glasses, ceramics), materials science (membranes in fuel cell techniques, nanostructure caused by welding processes in alloys), catalyst research (metal nanoparticles on various support structures, zeolites), chemistry (polyelectrolytes) and biology (liposomes, proteins, DNA). The samples under investigation are solids, liquids, gels, aoregels, compound-materials, powders, crystals or thin layers studied under various process parameters (gas flow, gas mixture, temperature, external electric or magnetic field, electrolytes of different mixture, pressure).

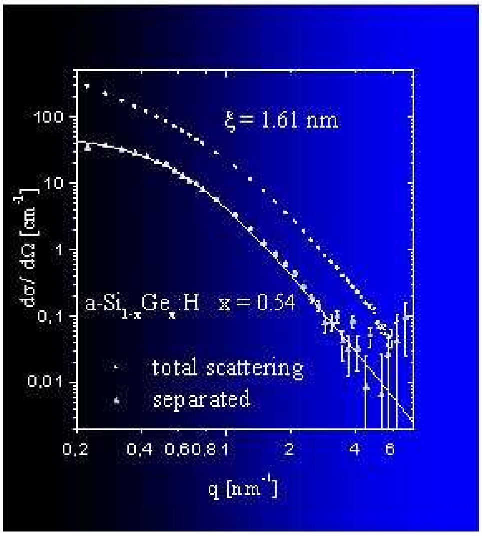

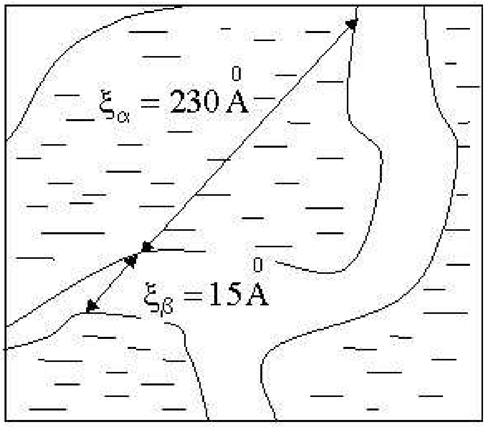

Figure 6.9.1: This first example shows results from ASAXS measurements obtained from amorphous hydrogen containing Silicon-Germanium alloys, which are used in solar cell techniques. The ASAXS-measurements were carried out in the energy range of the K-absorption edge of Ge at 11.1 keV and the specific scattering, originating from Ge-containing inhomogeneities was separated (triangles) from the scattering of other inhomogeneities, mainly hydrogen containing voids. The solid line passing through the separated scattering curve is a fitted model function, representing a two-phase mixture (right side), one phase covering 90% of the volume with a correlation length of about 20 nm surrounded by a second phase with reduced density and reduced Ge-concentration and a correlation length of about 1 nm (Goerigk & Williamson, 2001b). From the analysis of extended ASAXS measurements at 16 X-ray energies in combination with densitometric measurements the volume fractions, densities and Ge-concentrations of the inhomogeneities were deduced and correlated with the materials opto-electronic properties.

Future scientific objectives for ASAXS studies at a 3rd generation source will be the analysis of the conformation of polyelectrolytes and other macromolecules in solution, DNA with counter ion condensation, membranes from biology, colloids, characterization of metal nano particles, catalysts on various support structures, time-resolved measurements on catalysts with in-situ cells under process parameters, membranes from fuel cell techniques, bulk metallic glasses, amorphous semiconductors alloys, crystalline semiconductors, quantum dots, porous glasses, magnetic alloys and others. Additionally to the fields of research many classical SAXS studies (at fixed energies) will use a SAXS beamline with unfocused beam.

Beside the ASAXS applications mentioned above additional scientific objectives, which make use of the anomalous dispersion corrections but employ different experimental techniques, may use the unfocused beam. Such a technique is (anomalous) grazing incidence small-angle X-ray scattering (GISAXS) on magnetic multilayers (Laidler et al., 1996), for example. Using a diamond phase retarder, optional applications are, especially at the X-ray energies of the L-edges (up to 22 keV) : magnetic anomalous grazing incidence X-ray scattering and magnetic anomalous small-angle X-ray scattering (MASAXS) with circular polarized X-rays (Fischer et al., 1998).

6.9.3 Design of the beamline

Beam parameters and location: The large majority of (A)SAXS studies need a suitable beamsize, high photon flux and a suitable X-ray energy (range). Sometimes a high q-resolution is required. PETRA III will meet this requirements at a high-β section.
Beam size: As already mentioned in the beginning, SAXS experiments average over a large sample volume. This is a big advantage, when comparing for instance with TEM or other microscopic methods. Especially when dealing with ASAXS, suitable beam sizes

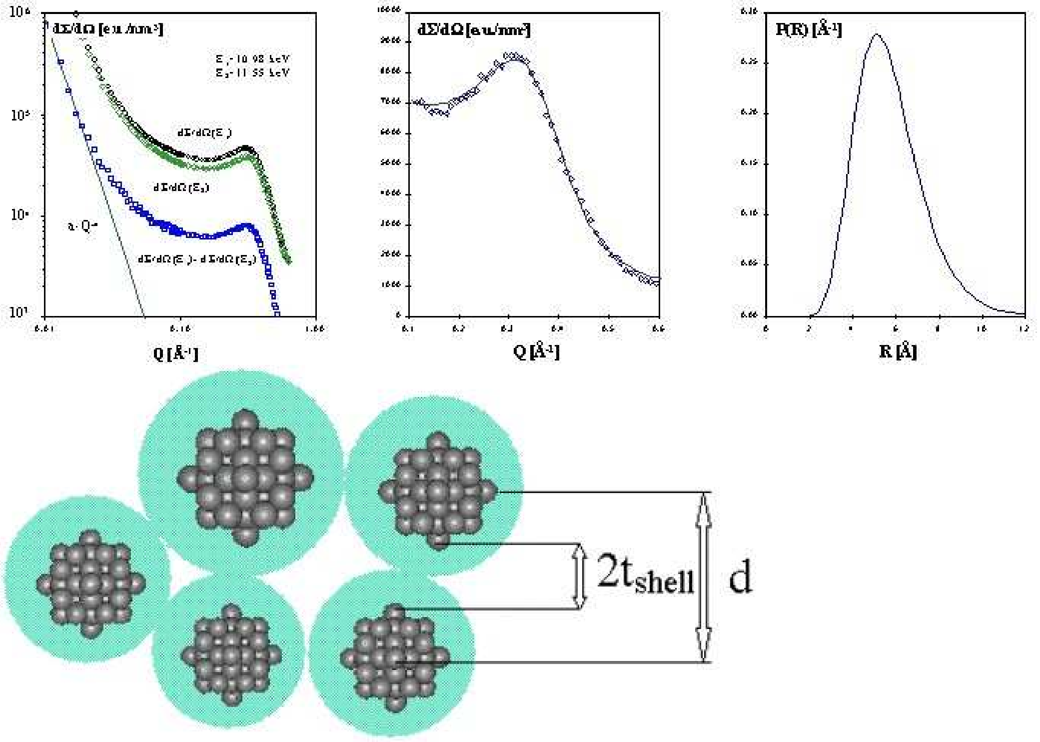

Figure 6.9.2: Metal nanoparticles play an important role e.g. in fuel cell technology and catalysis or in the development of novel synthetic pathways to nanostructured metal colloids (1-50 nm). Further objectives are to organize these materials into 2- and 3-dimensional arrays (e.g. by using organic spacer molecules) and to examine potential applications in catalysis and material science. Employing the ASAXS-technique the specific scattering contribution of the metal colloids can be separated from those of the spacer molecules or other support structures. The Figure summarizes results obtained from ASAXS-measurements on platinum nanoparticles with organic spacer molecules in the energy range of the Pt-L_{III}-absorption edge at 11.56 keV. The separated scattering curve of the Pt-particles (blue squares left diagram) is shown in more detail plotted on linear scales in the central diagram. The solid line represents a model function of Pt-particles with a size distribution around 1 nm (right diagram) and a correlation distance between the particles of about 2 nm (Vad et al., 2002).

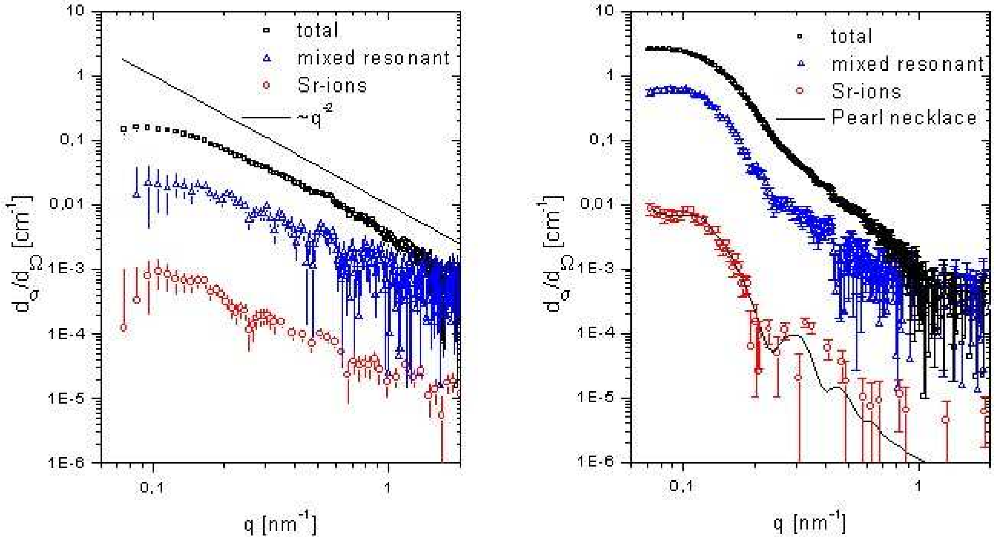

Figure 6.9.3: Polyelectrolytes are highly charged macromolecules. The density of charges along the polymer chain may cause a wide variety of conformations. A large variety of polyelectrolytes is found in nature, where the role of electric charges is essential for the proper functioning of nucleic acids, the numerous enzymes and proteins. The Figure summarizes the results obtained from ASAXS measurements on Na-polyacrylate (NaPA) surrounded by Sr-counter ions in aqueous solution. Different ratios of the concentration of $SrCl_2$ /[NaPa] reveal dramatic changes in the scattering curve. At the lower ratio (left) the scattering curves indicate a coil like behavior, while at the higher ratio (right) the scattering curves are contracted to smaller q-values, caused by the collapse of the NaPA coil to pearl-like subdomains. The separation of the pure resonant scattering contribution (red circles) yields the form factor of the distribution of the Sr-counter ions around the polymer chains, which shows a lot of structural details like a maximum at 0.1/nm and a maximum at 0.3/nm. The solid line passing through the red circles is the model function of a pearl necklace model (Goerigk et al., 2004).

are necessary (not smaller than 100 μm) because otherwise the transmission measurement, which represents one of the most crucial parameters in the ASAXS technique, is strongly influenced by the local structure of the sample. For most applications a beam size between 300 and 800 μm appears desirable. At 10 keV a beam size of about 800 μm (horiz.) times 500 μm (vert.) can be achieved with an unfocused beam at a distance of about 40 m at a high-β section. Tab. 6.9.1 summarizes the beam size for different energies at a high β-section at a distance of 40 m (without monochromator).

Energy [kev]	5 (Ti)	10 (Zn)	15 (Rb)	20 (Mo)	90 (Bi)
x [mm]	0.5	0.46	0.45	0.44	0.43
y [mm]	0.22	0.17	0.15	0.13	0.10

Table 6.9.1: RMS-beam size depending on the energy at a high-β-section at 40 m distance.

Photon flux : High flux is needed for SAXS studies on weak scatterers. The photon flux of the 3rd harmonic (K=1.5) through a pinhole of 0.8 x 0.4 mm^2 amounts to about 10^{13} ph/sec for a bandwidth of 0.01$\%$ at 15.1 keV, which will reduce the measurement time for ASAXS sequences on highly diluted solutions or amorphous alloys from several days to several hours, with a clear improvement of the statistical significance of the data.
q-resolution : The q-resolution due to the beam divergence at a high-β section amounts to $\Delta q = 3 \cdot 10^{-5}$ Å^{-1} (again at 10 keV). In comparison to this, with a distance of 10 m between sample and detector at the 40 m location, the q-resolution calculated from the beam size at 10 keV is $1.9 \cdot 10^{-4}$ Å^{-1}, which corresponds to a length scale of 3.3 μm. The q-resolution is limited by the beam size and the smallest q-value is about a factor 6 larger compared to the minimum q-value limited by the beam divergence. Though this resolution is hard to achieve with a conventional SAXS equipment, in principle the vanishing beam divergence at the high-β section will allow to improve the q-resolution up to this theoretical value in the future (for instance at the expense of flux by reducing the beam size). Especially the SAXS studies of highly correlated large particles (colloids > 100 nm) will benefit from a high q-resolution.
Energy range : The classical energy range of ASAXS between 5 and 35 keV can be accessed by harmonics up to the 7th order by tuning the K-parameter. In principle making use of the 7th harmonic a future option may be to extend the energy range up to the energy of 91 keV giving access to the K-edges of the heavier elements like **Ba, Nd, Os, Ir, Pt, Ta ... Bi**. Barium is an important counter ion in polyelectrolyte research. Neodymium is of high interest in the research of amorphous alloys with magnetic properties. A lot of the heavier elements are used for the development of electrode materials in fuel cell techniques. The access to the K-edges of these heavy elements would offer to extend the ASAXS-technique to compact cell structures of large thickness. This kind of in-situ experiments could be performed so far only by small-angle neutron scattering experiments (SANS). The photon flux at 90 keV is between 2 and 3 orders of magnitude lower compared to 10 keV but is still considerably high. At lower energies (< 5 keV) the fundamental and the 3rd harmonic provide considerable photon flux giving access to the K-edges of Ca at 4.04 keV.
Beam stability : For the anomalous dispersion applications beam stability and precise energy calibration are of great importance. A beam stability of 1$\%$ with respect to the beam size is required.
Monochromator and optics : The energy range between 5 and 35 keV can be assessed by a Silicon (3 1 1) fixed exit double monochromator with flat crystals. For the energies up to 50 keV a Silicon (5 1 1) can be used. If the energy range is extended to energies beyond 50 keV a Laue monochromator must be employed. Due to the high flux and the very small beam divergence at the high-β section no focusing optics are required. Higher harmonics (3rd) are rejected by detuning of the 2nd crystal (JUSIFA). To reduce the heatload a cooled pinhole with a variable size should be implemented before the 1st crystal. Only the central cone is passing through the pinhole and the expected heatload of about 5 kW can be reduced by more than 90$\%$.
Vacuum : To avoid background scattering from air the secondary vacuum section of the beamline is designed as a high vacuum beamline (p $\sim 10^{-4}$ mbar). The secondary vacuum must be separated from the ultra high vacuum of the monochromator section by a beryllium window.

Slit system : A minimum of three slits are needed. The 1st slit is placed as an entrance slit to the monochromator reducing the fluorescence background originating from upstream components. The 2nd slit is located behind the 2nd crystal and the 3rd just before the sample, with the distance between the last two slits of several meters.

Experimental setup : The experimental setup is expected to reproduce the JUSIFA standard of fast, precise and automated change of detector position with sample detector distances between 0.5 and 10 m. Larger distances should be attainable.

Sample environment : A sample chamber of sufficient size is needed, which can be easily accessed and will allow the easy adaption and the implementation of complex sample manipulators (sample orientation by tilting and rotating) and complex sample environments (heaters, cryogenics, electric and magnetic fields, electro-chemical cells, in-situ reactors applying special gas mixtures plus temperature, capillary systems).

Beam-detectors : Suitable beam monitors for beam alignment (before 1st monochromator crystal and downstream the 2nd crystal), and further monitors for the precise measurement of the primary flux coming to the sample (normalization) and transmitting the sample (transmission measurement) must be implemented.

XAFS measurements : The reliable uncomplicated performance of XAFS measurements is mandatory for an ASAXS beamline (JUSIFA).

SAXS-detectors : Probably a collection of different detector types will be needed for the different applications. For applications requiring high position resolution CCDs or online image plate scanners may come into operation for fast measurement sequences (membranes, layers). Long term measurements on highly diluted systems (polyelectrolytes) or highly homogeneous alloys (bulk metallic glasses) will need devices with low noise. In the last years pn-CCDs with energy resolution have been developed for X-ray astronomy. This detector type would offer access to various materials, which so far are not accessible to the ASAXS technique due to a strong fluorescence background from one of the elements in the material. Examples are bulk metallic glasses of the composition $Cu_{60}Zr_{20}Ti_{20}$ at the Zr-K-edge at 18 keV, where the SAXS is superimposed by the Cu fluorescence or pressure reactor vessel steel with Cu-carbides at the Cu-K-edge at 8.9 keV with a overwhelming fluorescence from Fe. Though the size and the maximum count rate up to now are not sufficient (position and energy resolution are already fully sufficient), future developments will improve these devices and make it suitable for synchrotron radiation applications and open new horizons especially for the ASAXS technique (Goerigk et al., 2002).

Measurement sequences : The measurement programs are expected to reproduce the JUSIFA standards of highly automated, flexible and user-friendly (easy programming) algorithms, which are able to process complex measurement sequences (including SAXS-pattern of the samples, background measurements, energy dependent detector sensitivity, dark current, calibration and sample transmission at different energies, different samples, different sample orientation). All measurements are calibrated into absolute units of macroscopic scattering cross sections. Suitable reference standards for the different energy ranges must be calibrated and can be assessed by the measurement sequences on a different sample holder.

Data processing : The data are subsequently processed by the fast JUSIFA data evaluation algorithms (correction for background, dark current, detector sensitivity, transmission, calibration into absolute units, combination of the scattering curves obtained from different q-ranges, calculation of scattering curves at pre-defined q-bins). Today the JUSIFA algorithms typically process several 100 2d-patterns into scattering curves within a few minutes.

6.9.4 Conclusion

An unfocused (A)SAXS beamline at a high-β section at PETRA III will combine the high photon flux of a 3rd generation source with an exceptional low beam divergence, which offers the possibility to improve the experiment to a very high q-resolution. Thus an expensive focusing optic can be omitted with the result, that the beamline will be easy to use, especially when dealing with the ASAXS technique, where a monochromator of sufficient energy resolution is mandatory, which can be operated fast and reliable over a large energy range. An additional future option will be, to extend the classical ASAXS range to higher energies up to 91 keV giving access to the K-edges of the heavier elements.

6.9.5 Capital investment and personnel

For the operation of the beamline a minimum of manpower of two scientists and two engineers will be needed. Costs for infrastructure are not included.
The total costs for investment amounts to **1570 k€**.

6.10 A Microfocus Beamline for Soft Matter Science

Authors:

R. Gehrke	DESY, Hamburg, Germany
M. Müller	Uni Kiel, Germany
P. Müller-Buschbaum	TU München, Germany
N. Stribeck	Uni Hamburg, Germany
A. Meyer	Uni Hamburg, Germany
O. Paris	MPI Golm, Germany

6.10.1 Introduction

Small-angle and wide-angle X-ray scattering (SAXS and WAXS) are extremely important tools in soft condensed matter science. Phase separation, aggregation, or nanostructuring lead to ordered structures on various length scales ranging from a few up to several thousand nanometers. Often these structures are hierarchically organized, i.e. structures formed on a given length scale compose superior domains ordered on a larger length scale. At surfaces and interfaces special structures can be formed which can be investigated by grazing incidence scattering techniques while the bulk structures are observed in transmission geometry. All SAXS techniques have common requirements concerning the incident X-ray beam at the sample position. These are :

- **Low Divergence**
  The divergence has to be as low as possible. The resolution in terms of the largest electron density correlation distances which can be observed in a SAXS experiment depends on this quantity.

- **Small Beamsize**
  The beam cross section has to be sufficiently small. If the sample is homogeneous on length scales far beyond the investigated correlation distances then the beam size could be in the order of the sample size. In the case of hierarchically organized samples, however, the beam size must not be larger than the domains which are investigated. These domains can have dimensions down to the sub-micrometer range. Thus, a submicrometer focus is required to selectively scatter from single domains or to scan across different domains. Systems of this kind have increasingly become subject of SAXS investigations during the last years. Important representatives are composite materials and biological materials like wood, bones, or even biological tissue.

- **High Intensity**
  The flux in the incident beam has to be as high as possible. Most samples in soft condensed matter science are extremely weak scatterers. They contain mainly light elements like hydrogen, carbon, oxygen, and nitrogen with small numbers of scattering electrons, the phase contrast between the scattering phases is very often extremely low, and finally the number of scattering entities in the irradiated volume is small. The latter is especially true for experiments with very small focus size in relation to the size of

the scattering units, and for investigations of surfaces and interfaces. In addition, many experiments are carried out time resolved in-situ during structural changes caused by the application of external fields or forces or by temperature changes. If these changes take place on a time scale of a few seconds, then accordingly fast subsequent measurements with proper counting statistics are necessary in order to get the desired temporal resolution. For soft materials in combination with high photon flux radiation damage can be an issue. Its influence depends strongly on the chemical and physical structure of the investigated material and one has to address this problem in each type of experiment individually. In many cases degradation takes place as a consequence of radical formation, followed by diffusion controlled rearrangement of the structures. In many cases the involved processes are slow compared to the data acquisition time, therefore the measurement can be completed before significant changes occur. In some cases sample cooling can reduce the degradation effects.

- **Energy Tunability**
  The photon energy should be tunable. Energies around 10 keV are well suited for soft matter samples, because the typical absorption coefficients of this kind of materials lead to an optimum sample thickness in the order of a few millimeters at these energies. However, if special techniques like anomalous scattering are going to be used, the energy has to be tuned to the absorption edges of the interesting atoms.

- **Coherence**
  For standard scattering experiments the coherence properties of the beam will not be used. However, if a high degree of coherence is available at the sample position one could record speckle patterns in a SAXS experiment to perform photon correlation spectroscopy and study the dynamics of the sample. Moreover, oversampling techniques could be applied to directly reconstruct the spatial shape of the scattering entities.

It is immediately obvious that high-brilliance undulator sources at 3rd generation synchrotron radiation machines fulfill the above requirements by far better than all other X-ray sources including wigglers presently used at DORIS III. Using an undulator at a high emittance machine leads to much better quality of conventional SAXS data which is essential for more sophisticated data analysis techniques presently under development. More important, new experiments become feasible which only can be done with undulators. These include measurements using a focus of micrometer size and even below, thereby still maintaining a good angular resolution and high photon flux. This part of the TDR proposes a versatile SAXS/WAXS beamline at a PETRA III undulator for high resolution measurements using incident beams with very small cross section in normal and grazing incidence. It supports scanning techniques as well as time resolved measurements.

6.10.2 Current state of the scientific field

6.10.2.1 Small- and wide-angle scattering (SAXS/WAXS)

SAXS experiments with moderate resolution below 100 nm, WAXS experiments and the simultaneous combination of SAXS and WAXS have been performed at synchrotron radiation sources for many years. They cover the time-resolved observation of crystallization and melting processes in polymer materials as well as orientation processes upon elongation of polymers (Stribeck et al., 2003; Barbi et al., 2003a; Barbi et al., 2003b) with temporal resolution down to the range of a few seconds. Other examples are phase separation processes in block copolymers, phase transitions in liquid crystalline polymers and lipids (Funari, Barcelo & Escriba, 2003), and gel formation in polymer systems.

6.10.2.2 Ultra small angle scattering (USAXS)

Ultra small-angle scattering using pinhole collimation is currently performed at the ESRF undulator ID02 and at the HASYLAB wiggler BW4. Both instruments reach a maximum resolution of about 500 nm, with a total photon flux of 10^{13} photons/s at ID02 and of 10^{11} ph/s at BW4. Examples of present state-of-the-art experiments include the observation of the formation and orientation of nanostructures in polymer systems during elongation or thermal treatment of the sample (Stribeck et al., 2002b; Stribeck et al., 2002a; Wang et al., 2003b). High quality scattering data allow the application of new sophisticated data evaluation schemes. An example of a USAXS experiment with an extremely weak scattering nanostructured sample is shown in Fig. 6.10.1. It addresses particle track etched polymer membranes which serve as templates for the creation of nanotubes and nanowires. Thin polycarbonate films were irradiated with argon ions, the particle tracks were etched to produce nanometer sized pores which then could be filled with other materials like metals or polymers. The figure shows scattering diagrams which reveal information about size and orientation distribution of the formed nanotubes and wires (Hermsdorf et al., 2003). Fig. 6.10.2 shows the development of USAXS during the formation of crazes upon elongation of a polycarbonate sample (Karl et al., 1999; Minko et al., 1999; Lorenz-Haas et al., 2003). Information about craze formation is important as crazes are the precursors of cracks which finally cause the breaking of the sample upon elongation.

6.10.2.3 Grazing-incidence small-angle scattering (GISAXS/GIUSAXS)

Scattering experiments with grazing beam incidence and high resolution in reciprocal space are at present carried out at the HASYLAB beamline BW4 (Müller-Buschbaum, 2003; Müller-Buschbaum et al., 1998). A typical example is shown in Fig. 6.10.3 which illustrates GIUSAXS measurements on dewetting of thin copolymer films on a Si/SiO$_x$ surface (Müller-Buschbaum et al., 2000). The out-of-plane intensity distribution parallel to the surface (q_y-scan) reveals information about lateral correlations. In contrast to transmission SAXS the maximum resolution is not limited by the size of the primary beam on the detector but mainly by the distance between sample and detector. Thus a maximum resolution of more than 1000 nm can be achieved at BW4. With sufficiently high photon flux time resolved GISAXS measurements can be performed. This is illustrated in Fig. 6.10.4, where

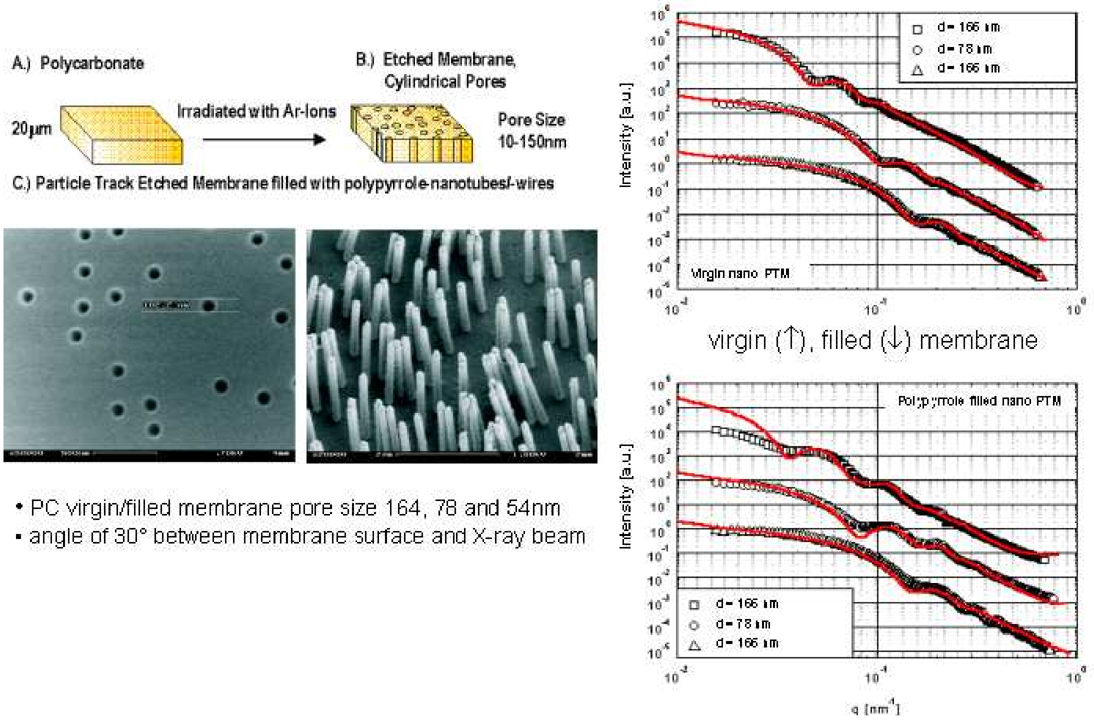

Figure 6.10.1: Combined SAXS and USAXS measurements of particle track etched polycarbonate membranes before and after filling of the pores with polypyrole *(A2 and BW4 at HASYLAB).*

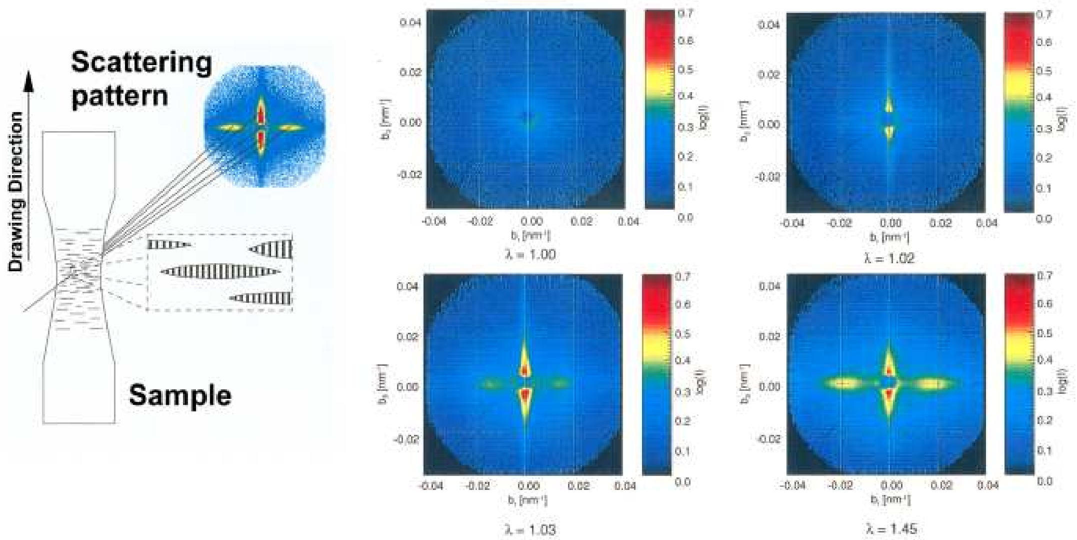

Figure 6.10.2: Formation of crazes during elongation of polycarbonate. USAXS scattering patterns obtained at different draw ratios λ *(BW4 at HASYLAB).*

structural changes in a thin film of a copolymer on a Si/SiO$_x$ surface were followed which were caused by application of a solvent vapor (Müller-Buschbaum et al., 2003a). The time between two subsequent scattering patterns was 30 minutes in this experiment. The observation of significantly faster processes would require a higher photon flux in the incident beam than available today.

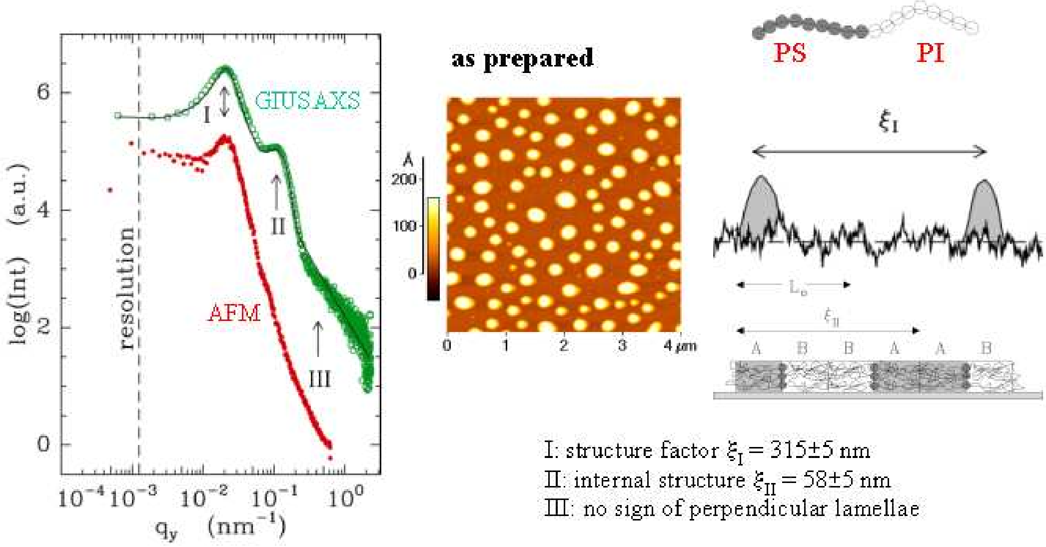

Figure 6.10.3: GIUSAXS investigation of the dewetting process of a spin coated polystyrene-polyisoprene block copolymer film on a Si/SiO$_x$ surface *(BW4 HASYLAB)*.

6.10.2.4 Microfocus scattering (μWAXS, μSAXS, μGISAXS)

Position resolved diffraction and scattering using a microbeam is done presently at a few synchrotron radiation facilities (Riekel, Burghammer & Müller, 2000; Müller, Burghammer & Riekel, 2001). The microbeam setup at ELETTRA, Trieste, is located at a wiggler. It uses a toroidal mirror and slit collimation and achieves a beam of 20 μm diameter. The maximum resolution is 100 nm with a total flux of about 10^7 photons/s. The microfocus beamline ID13 at the ESRF is located at an undulator. With focusing mirrors and collimation a beamsize of 10 μm can be reached with a photon flux of 10^{11} photons/s. The maximum resolution is 50 nm. With capillary optics this focus can be further demagnified down to 2 μm, the flux decreases by one order of magnitude to 10^{10} photons/s and due to the increased divergence the maximum resolution is now limited below 10 nm. By using a waveguide the beamsize can be reduced to 0.2 μm in one direction, thereby reducing the usable flux to 10^9 photons/s while keeping the maximum resolution still at 10 nm (Müller et al., 2000a). A typical application for a 2 μm beam at ID13 is illustrated in Fig. 6.10.5. Wood represents a nice example for hierarchically structured systems, it shows different structural ordering on a wide range of length scales, starting with molecular composites in the nanometer range, followed by lamellar and cellular structures in the micrometer range. In the experiment the orientation of the cellulose fibril helices in a wood cell wall was measured with spatial resolution (Lichtenegger et al., 1999). A total area of 40 μm side length was scanned with a 2 μm focus, and for each position a complete diffraction pattern was obtained. From the orientation of the diffraction maxima the local orientation of the helix could be derived. Other typical experiments investigate the internal structure of single thin fibers like cellulose fibers (Müller et al., 2000b; Moss et al., 2002) or spider silk (Riekel, Müller & Vollrath, 1999). An experiment of this kind is illustrated in Fig. 6.10.6 which addresses the cross sectional texture of carbon fibers (Paris et al., 2001). A 12 μm thick single fiber was scanned laterally using a 3 μm beam. The intensity course of the (002) and (100) reflections was compared with the theoretical one calculated for different texture models.

Using a 5 μm microbeam with a GISAXS experiment leads to a beam footprint of only 300 x 5 μm^2 on the sample surface. This allows to obtain position resolved GISAXS data as shown in Fig. 6.10.7. The experiment studies the formation of complex nanostructures in thin polystyrene films on a Si/SiO$_x$ surface (Müller-Buschbaum et al., 2003b). At certain given temperatures dewetting processes lead to a coexistence of large micrometer sized drops and nanodroplets. With scanning GISAXS the different domains can be clearly distinguished.

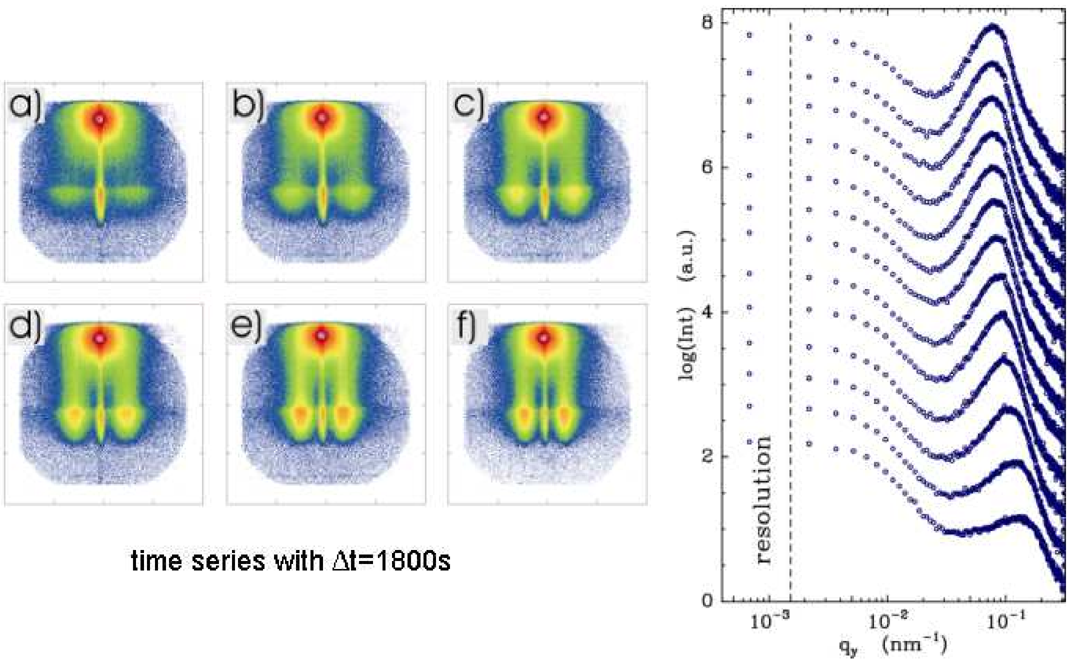

Figure 6.10.4: Time-resolved GISAXS measurement of a nanostructured polystyrene-polyparamethylstyrene block copolymer film on Si/SiO$_x$ during treatment with toluene vapor *(BW4 HASYLAB)*.

6.10.3 Scientific case for the proposed instrument

It should be noted that at PETRA III compared to the ESRF beamlines for each given focus size a markedly higher maximum resolution at higher photon flux can be reached. This is mainly caused by the smaller beam divergence at the PETRA III undulator. The state-of-the-art experiments illustrated with the above examples form the basis of the scientific case for the proposed new instrument. Present experiments in the field are limited by the beamtime available at existing instruments and, more important, by technical restrictions in terms of smallest achievable focus size and corresponding resolution and photon flux. Many scattering investigations utilizing a beam of small cross section will clearly benefit from having a smaller focus and simultaneously higher resolution and flux than available today, and many new experiments will only be possible with this. Generally, it will allow time resolved measurements on a shorter time scale and/or spatially resolved scattering experiments using a microfocus especially in hierarchical systems where the observation of structural domains down to the 100 nm range is desired. Present attempts to reach this region suffer from flux and/or resolution limitations and each step forward to improve this will be of great value.
Also data quality in classical SAXS and USAXS experiments can be markedly improved by using a high flux microbeam with a high degree of collimation, because the measurements

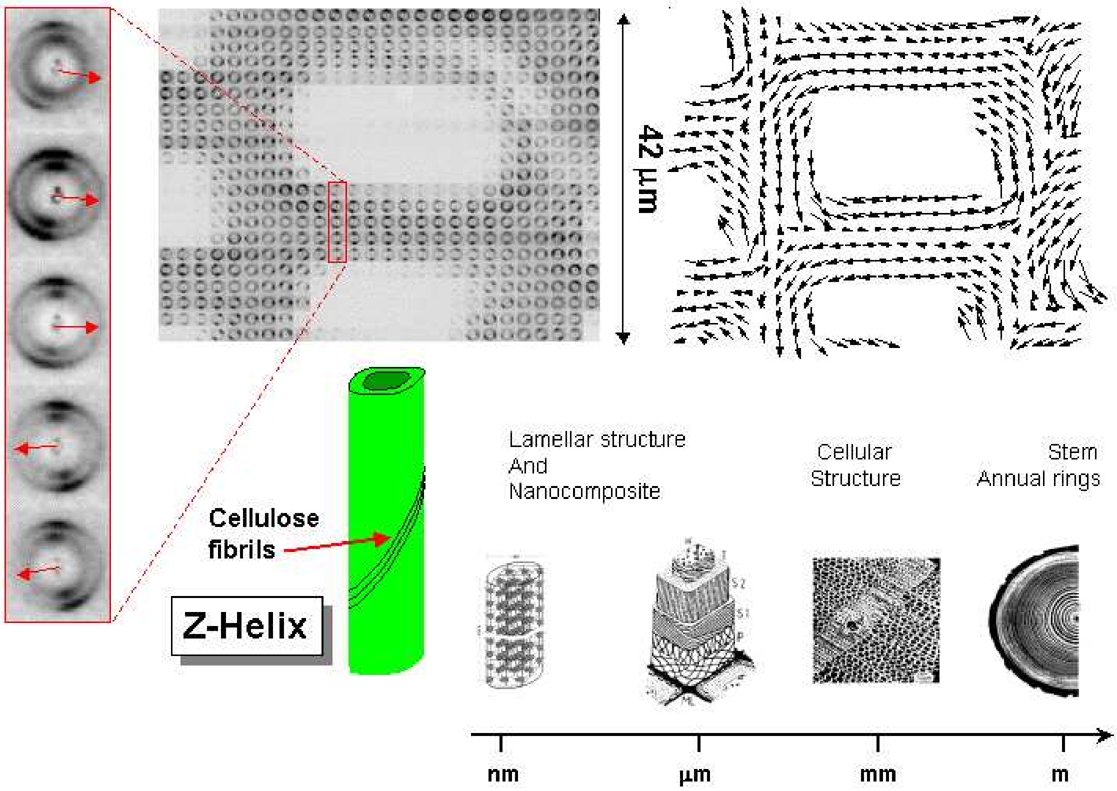

Figure 6.10.5: Determination of the helical arrangement of cellulose fibers in the cell wall of wood by means of scanning micro-diffraction using a 2 μm focus *(ID13 ESRF).*

will be much less affected by the beam profile and therefore much better allow the application of more elaborate data evaluation techniques developed recently.
New techniques are opened if the achieved maximum resolution becomes comparable to the cross section of the incident beam. Instead of observing periodical electron density fluctuations within the irradiated domain the formfactor of the irradiated domain itself will be measured similar to single particle SAXS in dilute solutions. Additional experimental options are possible if the high degree of coherence in the source is maintained in the focus. This is mainly a question of the quality of the optics, especially of the mirrors. Making use of the coherence could help to solve the phase problem in this kind of scattering experiments.

6.10.4 Beamline layout

The proposed beamline uses a standard PETRA III X-ray undulator installed at a high-β section. The first optical element is a fixed exit silicon (111) double crystal monochromator, tunable from 4.5 keV to 20 keV. It can be placed as close as possible to the source. It is not planned to use the white or a pink beam. Downstream of the monochromator there is a pair of Kirkpatrick-Baez (KB) mirrors for subsequent vertical and horizontal focusing. The standard photon energy is going to be 10 keV. The overall length of the instrument from the source to the end of the experimental area is about 95 m. The focus is going to be at 85 m

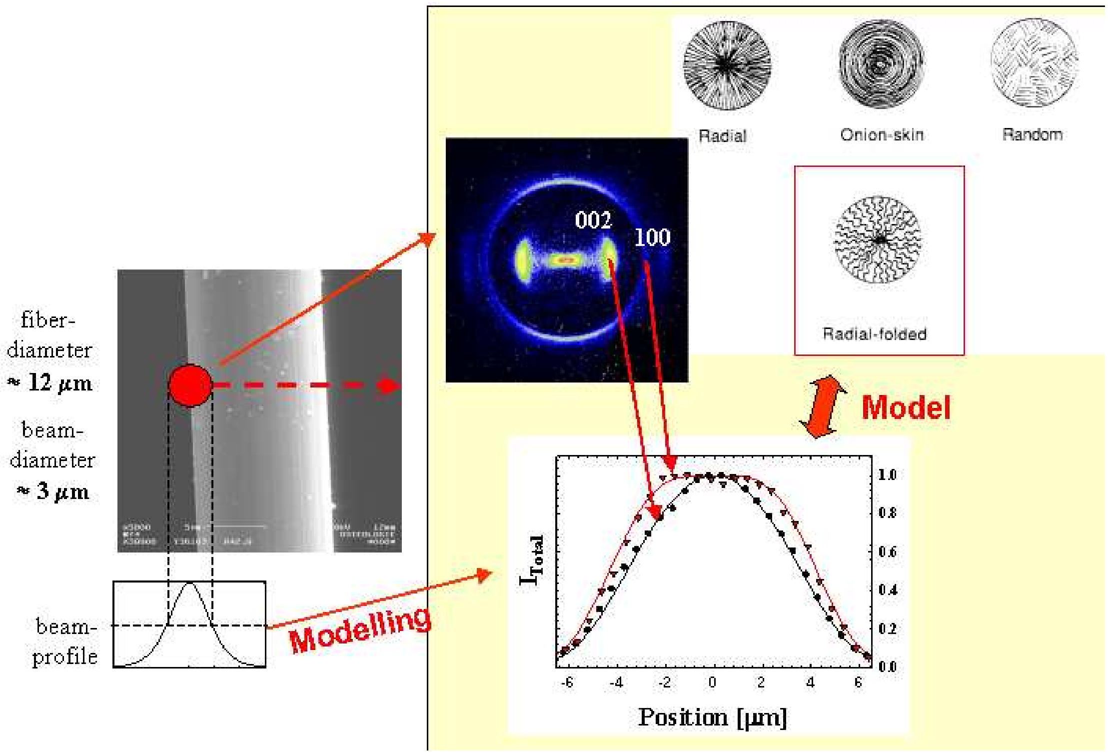

Figure 6.10.6: Determination of the cross sectional texture in a single 12 μm thick carbon fiber by means of scanning microdiffraction using a 2 μm focus *(ID13 ESRF)*.

behind the source. Finding the best positions for the two mirrors means to find an optimum compromise between the desired focus size and the desired maximum resolution in terms of the largest observable electron density correlation distances. Generally, decreasing the focus size in a given direction by placing the corresponding mirror closer to the focus position is accompanied with an increase of the divergence in that direction, thus causing a decrease of the achievable maximum resolution. Aiming for a maximum resolution of at least 10000 nm in the vertical and 1000 nm in the horizontal direction the source properties of the standard undulator tuned to 10 keV lead to a focus size of 7 μm vertically and 40 μm horizontally direction (FWHM). In this case the first mirror has to be placed 57 m behind the source and the second one at 75 m. The beam divergence is then 13 μrad in the vertical and 120 μrad in the horizontal direction (FWHM values). The layout of this arrangement is schematically shown in Fig. 6.10.8. Ray tracing calculations for this setup result in a total photon flux of $3{\cdot}10^{13}$ photons/sec at 10 keV in the 85 m focus point.

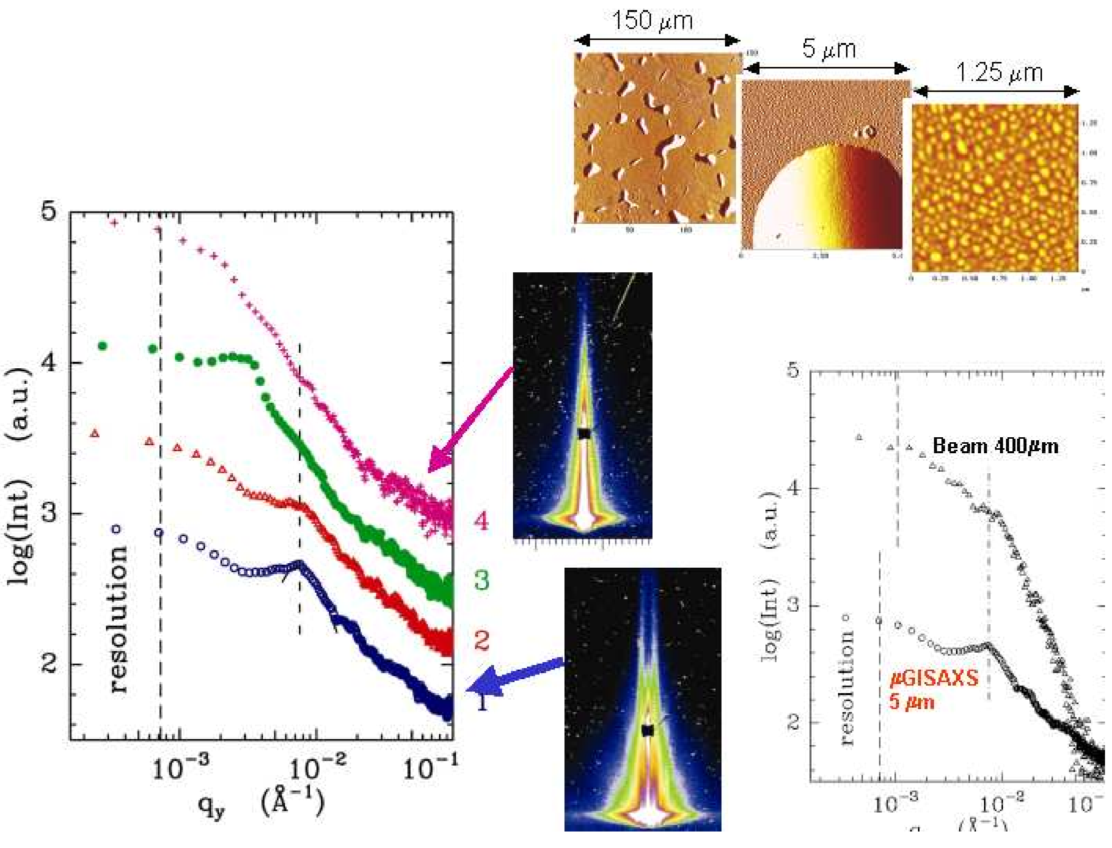

Figure 6.10.7: Investigation of heterogeneous surface structures formed by polystyrene on Si/SiO$_x$ upon dewetting at low temperatures. Spatially resolved GISAXS measurement using a 5 μm incident beam. The thickness of the oxide layer is 2.4 nm, with a 0.9 nm thick oxide layer the dewetting leads to a homogeneous structure *(ID13 ESRF)*.

6.10.4.1 Layout of the experimental area

The focus provided by the KB optics allows for a maximum resolution in transmission SAXS experiments of about 1800 nm in the horizontal and about 15000 nm in the vertical direction using a focus to detector distance of three meters. This is the theoretical limit in terms of largest observable electron density correlation distances and it gives sufficient leeway to perform high resolution scattering experiments from WAXS to SAXS within the angular range required for present and future investigations.
The basis of all experimental setups is a 15 m long optical bench on which all necessary equipment can be mounted and positioned in the beam. Looking downstream this bench starts five meters before the focus position and extends to 10 m behind it. The sample position is at the focus location. For normal transmission SAXS/WAXS measurements a two-dimensional detector with about 200 μm spatial resolution and 2000 x 2000 pixel can be used in a distance of up to three meters from the sample. If an experiment demands for a particular high angular resolution, a detector with about 40 μm pixel size can be placed in the focal plane with the sample position up to four meters in front of it. Another scenario foresees simultaneous measurements in the WAXS and SAXS regime using the 40 μm pixel size detector for the WAXS range and the 200 μm pixel size detector for SAXS.
Concerning the sample environment the design is very flexible. A variety of different sample holders will be provided including a universal goniometer, furnace chambers, stretching devices, high pressure cells, temperature controlled cuvettes for liquid samples, etc. Sample equipment already existing for measurements at A2 and BW4 can also be easily adapted to the new instrument. Other, more specialized sample environments will be provided by the users of the instrument if required.

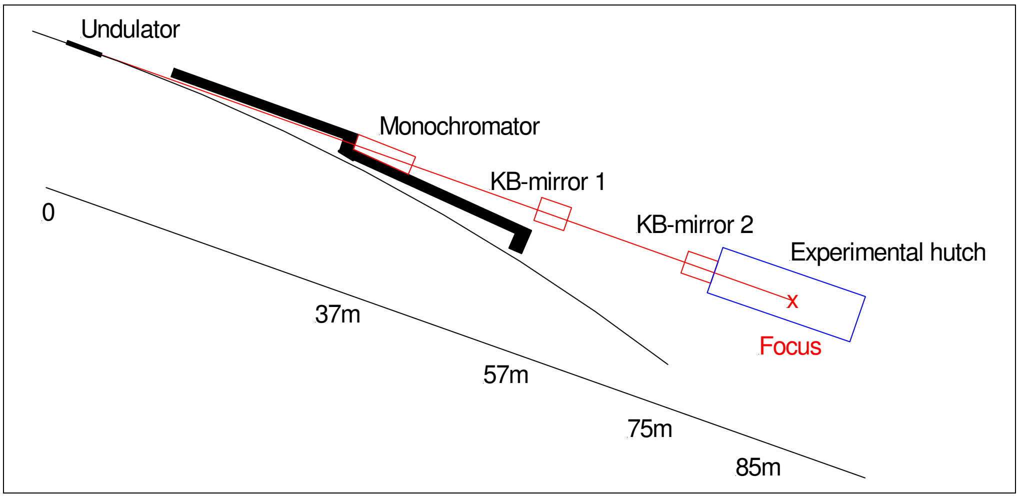

Figure 6.10.8: Sketch of a possible SAXS/WAXS setup in the PETRA III experimental hall. First focusing mirror at 57 m, second at 75 m, focus at 85 m. The red rectangles indicate the optics hutches, the blue outlines the microfocus hutch.

For grazing incidence measurements a special goniometer will be installed which allows to adjust the sample orientation and the position of the focus on the sample with very high precision. The design shall allow to do scanning experiments along the sample surface. If required, the distance between sample and detector can be increased up to 10 m to observe lateral ordering on a very large length scale.
The focus produced by the KB mirror system can be used as a prefocus for additional focusing elements to produce an extremely small focus down to the nanometer range. Depending on the progress of various developments which are presently under way these elements could be capillary optics, Fresnel lenses, compound refractive lenses, or waveguides. Calculations for a glass capillary which uses the prefocus to produce a 100 nm size beam spot show that a 100 mm long capillary with 4 μm entrance diameter could produce such a focus with a efficiency of 4% . This implies a total flux of $9{\cdot}10^{11}$ photons/s in a focus of 100 nm diameter. The beam divergence would be around 2 mrad which still allows to perform SAXS measurements with a resolution up to 50 nm. In general one can state that due to the properties of the prefocus, i.e. small beam cross section and low divergence, it will be well suited for each kind of subsequent nanofocusing optics. To use the nanofocus for scanning microdiffraction applications a positioning unit has to be provided which allows to align the sample precisely relative to the beam and to perform the scanning operation. The basic concept of alignment is to define a position on the sample by means of an optical microscope and then to transfer this point to the position of the nanobeam.

6.10.4.2 Stability issues

In order to make proper use of the small focus, its position must be fixed at least within 10% of its corresponding dimensions. Thus, special attention must be paid to thermal and mechanical stability of the beamline and decoupling of vibrations from grounding, cooling liquids and devices like pumping units etc. Stability considerations also serve as arguments against the design of this instrument as a side station at a canted pair of undulators. The monochromator has to be constructed as a compact unit to avoid independent motions of the first and second crystal relative to each other. Therefore, a large distance of both crystals as envisaged in the side-station concept will surely have a negative impact on the stability of the focus. Finally, one should note that the planned top-up mode operation of the storage ring will improve the overall stability of the experiment.

6.10.4.3 Infrastructure

Because the proposed instrument involves many different experimental options, sufficient space must be available in the experimental hutch in order to keep the different experimental modules in place and to facilitate changing from one setup to another in an efficient and fast manner. Also user specific sample equipment like stretching devices, cryostats, etc. might require larger space. Therefore, the width and height of the experimental hutch shall not be significantly below five meters. Envisaging the frequent setup changes, sufficient laboratory space in the vicinity of the experimental hutch is also required. An area of 16 m^2 will be the minimum.

6.10.4.4 Detectors and data handling

Two area detectors shall be available at the instrument. A large one with 2000 x 2000 pixel of 200 μm^2 size and a small one with 2000 x 2000 pixel with 40 μm^2 or less. The pixels shall be integrating with a signal to noise ratio of 10^4 or better and for time resolved measurements the readout time shall be in the order of seconds. As a first approach CCD detectors can be used which are already commercially available, but it would be highly desirable to have semiconductor pixel detectors with parallel pixel readout. However, such detectors are presently not available and would have to be developed outside the scope of the proposed instrument.
The beamline shall be equipped with two PC workstations, one for the instrument control and data acquisition, the other for data evaluation. The beamline control shall be performed via VME electronics. The amount of data obtained in an experiment depends strongly on the experiments. For instance, a typical scanning experiment using the nanofocus would lead to 30 x 30 scattering patterns each with up to 2000 x 2000 pixels and a depth of 24 bit per pixel. This amounts to about 10 Gigabyte of data which are typically acquired within two hours. Similar amounts of data could be generated in a typical time resolved experiment.

6.10.5 Capital investment and personnel

The many experimental options of the instrument require to construct and to operate it by a team of two scientists who are full time in charge of this project. They shall be assisted by two full time engineers, one with major skills in electrical engineering and electronics, the other in mechanical engineering. The team should start working on the project about two years before the beginning of the construction of the instrument in order to design and purchase major components. Thereby, the construction of the experimental setup could start in parallel to the construction of the beamline and after one year of construction work the main parts of the setup could be ready for test operation. Another year later the major components of all experimental setups can be finished. This amounts to a total main construction period of four years. The work might be supported by postdocs and PHD students who take care of the construction of user specific sample environments. They could be delegated by external user groups, and they should start working on the project when it can be foreseen that they can make practical use of their facilities within the time of their stay. As soon as the optics and main parts of the experiments are going to be installed, an expert with skills in software engineering and programming shall join the project for three years. The task of this person is to design and implement software to control the instrument. This work shall be based on the laboratory wide concept how to control various hardware components and shall implement software which not only performs the task of moving motors and acquiring data but which also assists the workflows of changing setups and adjusting the instrument in a user friendly manner. The aim is to help to make setup changes as efficient and fast as possible.

The total investment cost for this beamline amounts to **1020 k€**.

6.11 Absorption Spectroscopy

Authors and Consultants :

M. Denecke	FZK, Karlsruhe, Germany
R. Frahm	Bergische Universität Wuppertal, Wuppertal, Germany
M. Fröba	Justus-Liebig Universität, Giessen, Germany
J.-D. Grunwaldt	ETH Zürich, Switzerland
D. Lützenkirchen-Hecht	Bergische Universität Wuppertal, Germany
J. Röhler	Universität zu Köln, Germany
E. Welter	DESY, Hamburg, Germany

6.11.1 Current state of the scientific field

X-ray Absorption Fine Structure Spectroscopy (XAFS) is a well established method for investigations of the local atomic and electronic structures of matter. Because absorption edges are intrinsically element specific, XAFS yields unique insight into matter, especially in small atom aggregates (clusters, nano-particles), surfaces and dilute systems. Thus it extends structural research beyond X-ray diffraction methods, and in combination with it in a novel method named DAFS (diffraction anomalous fine structure) both methods join their strengths. Synchrotron radiation based XAFS is nowadays routinely used in nearly all areas of fundamental and applied research. More intense or more brilliant sources can shift the limits to currently inaccessible applications.

While studies of the electronic structure using X-ray Absorption Near Edge Structure (XANES) spectroscopy require a high energy resolution, better than $10^{-4}(\Delta E/E)$, in a relatively narrow energy range of about 150 eV, studies of the local atomic structures by the Extended Absorption Fine Structure (EXAFS) rely on a very high momentum transfer of the scattered photoelectrons, corresponding to typically 1–1.5 keV - in special cases up to 3 keV - photon energy above the edge. Both types of measurements need very high monochromatic photon flux to achieve a high signal-to-noise ratio $> 10^4$, particularly in the case of dilute samples, surfaces, μm-sized samples, or data collection in reflectivity or fluorescence modes. To cover an appropriate energy range, a tapering of the undulator or gap scans of the untapered undulator are mandatory. For XANES-measurements just a small tapering is necessary (if at all), for EXAFS an energy range of typically 1.5 keV has to be covered for high quality data of one absorption edge.

The high flux *and* brilliance of 3^{rd} generation sources do open new horizons for XANES and EXAFS experiments. Among the new possibilities are investigations of μm-sized samples, tiny samples confined in strongly absorbing environments, fast measurements of highly diluted species and spectroscopic investigations with spatial resolutions down to the μm or even nm scale. As a consequence all 3^{rd} generation facilities run XAFS beamlines at undulators. Tab. 6.11.1 lists the undulator XAFS beamlines at the three major high energy 3^{rd} generation sources in the world. Except ESRF ID 24, that uses a very specialized dispersive set-up, none of the beamlines is exclusively dedicated to XAFS spectroscopy. Many beamlines share an XAFS set-up with set-ups for X-ray fluorescence (beamlines dedicated to geochemistry / environmental sciences) and/or X-ray diffraction (beamlines dedicated to

Beamline	Applications	Energy range (keV)	Spot Size (μm H x V)	Source
ESRF				
ID24	Dispersive XAFS	5 - 28	20 x 200	tapered undulator
ID 21/22	μ-Fluorescence			
ID26	High brilliance spectroscopy	3.2-30	200 x 80	scanable undulator stepwise/continuous
APS				
1ID	Materials Science Physics	4.2-30	6 x 2 (with CRL)	scanable/tapered undulator
9ID	Materials Science	3.1-22.5		scanable undulator
10ID	Materials Science Environm. Science	4.8-32	5 x 5 (with KB)	
11ID-D		4-50		(wiggler)
13ID	Geoscience Env./soil Science	4-45		
16ID	High pressure			
18ID	Biology	3.5-35	40 x 200	
20ID	Material Science Env. Science	4 - 50	400 x 100 1 x 1 with KB	scanable undulator
32ID	Material Science			
SPring-8				
BL10XU	Material Science	6-35	500 x 1000	scanable undulator

Table 6.11.1: XAFS beamlines at ESRF, APS and SPring-8

material science).

The working range of these beamlines starts at E $>$ 3.5 keV. Mirrors are used up to E $\approx$ 30 keV for focusing and/or rejection of harmonics. This energy range comprises the most important absorption edges for XAFS spectroscopy. The upper limit of the working range is given by the mirrors which have to be operated at reasonable glancing angles of a few mrad. A standard set-up with at least one focusing mirror achieves spots with diameters between some 10 μm and $\approx$ 200 μm. At some beamlines smaller spot sizes (1 - 25 μm^2) are reached by additional Kirkpatrick-Baez (KB) mirror systems which are placed close to the sample. Alternatively, compound refractive lenses are used for μm-scale foci. The undulator beam is monochromatized by a cryogenically cooled Si double-crystal monochromator with fixed exit. In some cases (for instance 20 ID at APS) the monochromator is installed in front of the first mirror.

All of the listed beamlines use scanable undulators to perform EXAFS scans covering an energy range of 1000–2000 eV. The design parameters of these undulators are close to those of the PETRA III spectroscopy undulator.

6.11.2 Science at PETRA III

The experiments at the PETRA III undulator XAFS beamline will take advantage of the unique properties of the source, namely the high brilliance, the high intensity and the wide energy range extending into the very hard X-ray range. The high brilliance allows to focus a large number of photons into a $\mu\mathrm{m}$-sized spot. Many of the applications using an XAFS beamline at PETRA III will come from fields which have successfully profited from XAFS spectroscopy in the past. These are mainly condensed matter physics, physical chemistry, catalysis research, material sciences, and environmental/geochemical sciences. Below some proposals for future research at the PETRA III undulator XAFS beamline will be given.

6.11.2.1 Electronic and structural inhomogeneities in strongly correlated electron systems

In research on strongly correlated electron systems, a realization is growing that their "abnormal" electronic structure - experimentally explored, e.g., by high resolution electron spectroscopy - is intrinsically connected to complex atomic structures on varying length-scales from atomic to macroscopic. Most of the these metals are thermodynamically meta-stable and exhibit non-stoichiometries of one or more atomic constituents. Many of the existing techniques for studying a material's structure quantitatively reveal only average properties such as the crystal structure. What is needed in addition are bulk probes that provide quantitative information about deviations from this average picture, i.e. measurement of atomic (or local) structures in disordered systems. Of particular interest are nano-phase separation and multi-scale structures generally developing with the growth of the strongly correlated electron system through carrier doping into a parent Mott insulator.

Nano-phase separation, however, requires new technical approaches to study intermediate length-scale (100 nm) structures. Sub-micrometer focusing of the X-ray beam in an XAFS-spectrometer at a high brilliance source will allow for a new imaging technique, revealing different local atomic structures in the phase separated topology of strongly correlated electron systems. Another new possibility for research on strongly correlated electron systems, which would be available using sub-micrometer focusing of monochromatic X-ray beams, is EXAFS spectroscopy of sub-millimeter sized single crystals from strongly correlated electron systems. Due to their intrinsic electronic inhomogeneity even sub-millimeter sized "single crystals" of these systems are usually multi-phased (Kaldis, 2001).

6.11.2.2 Tomography and reaction engineering

Solid materials and heterogeneous catalysts are presently characterized *in situ* by X-ray absorption spectroscopy, often in combination or even simultaneous with X-ray diffraction accessible on the same beamline. However, the element-specific analysis of the structure in a tomographic manner in the different catalyst particles or crystalline solids is important as well, but difficult to achieve. One of the few techniques available for this is electron microscopy combined with elemental mapping. But the structure is difficult to extract, and *in situ* studies are not possible. Most catalysts are, however, composed of different components and thus tomographic images are an important issue. Moreover, the use of hard X-rays offers the advantage of large penetration depths and allows *in situ* investigations.

A great challenge at the PETRA III undulator XAFS beamline for such investigations will be the scanning of catalyst particles with the micro focused beam, both *ex situ* and *in situ*. An image achieved on a Cu/ZnO catalyst with the help of beryllium compound refractive lenses is shown in Fig. 6.11.1 (Schroer et al., 2003a). Both an X-ray beam of high brilliance and fast scanning of the energy is necessary for this purpose. Presently no other method can provide both tomographic and element specific information on such particles at the same time. In solid state chemistry, gradients during solid-solid reactions or solid-gas reactions often occur, and tomography can help to obtain microscopic insight into the reaction mechanism.

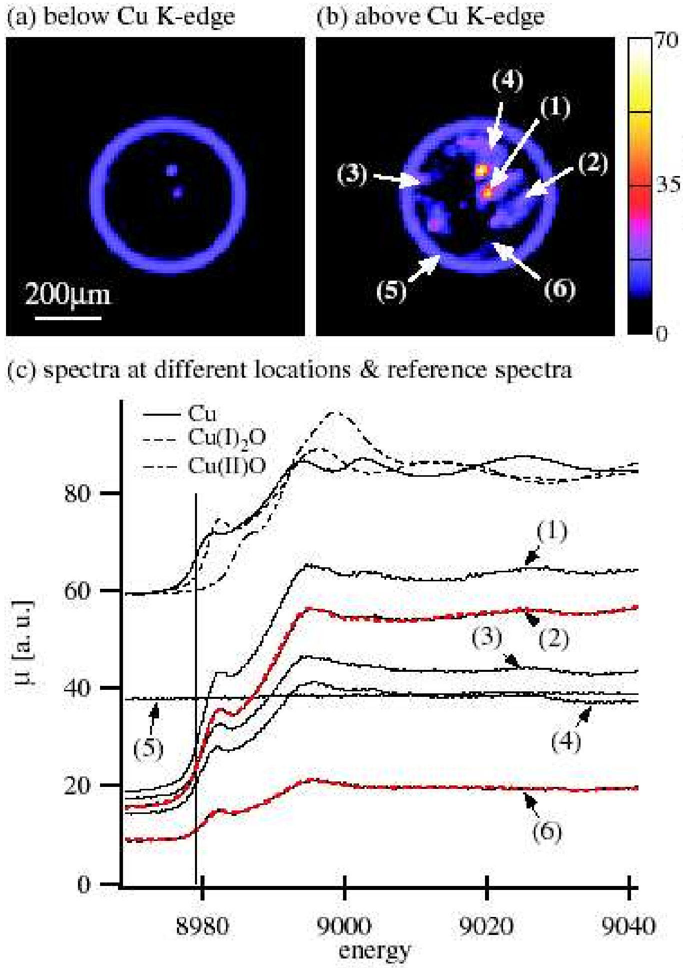

Figure 6.11.1: Reconstructed tomogram of a capillary filled with a CuO/ZnO catalyst (a) below (E=8970 eV) and (b) above the Cu K-edge (E=8995 eV). Reconstructed XANES spectra at different locations marked in (b) and offset reference spectra of metallic Cu, Cu(I)$_2$O, and Cu(II)O. The dashed red curves in (c) represent two fits using the reference spectra. Measured at the APS, beamline 1ID (Schroer et al., 2003a).

Another important topic in heterogeneous catalysis is the study of catalysts in their working environment. Engineering of reactors (avoiding hot spots, etc.) is an important issue. In continuous fixed-bed reactors, large concentration gradients occur along the reactor bed. One of the great challenges is to unravel how such gradients affect the structure of the solid catalyst, a question of tremendous industrial importance. Tomographic changes along the axial and radial distribution in the catalyst bed can greatly support modeling studies. Such information can be gained for both solid-catalyzed gas reactions as well as liquid phase reactions.

6.11.2.3 High pressure studies (*in situ* and *ex situ*)

Various technical processes such as methanol or ammonia synthesis are performed at high pressure. More recently, high pressure technology has gained renewed attention, mainly spurred by the beneficial features reported for reactions performed in supercritical media. There is a strong need to gain information on the structure of catalysts under such reaction conditions (Grunwaldt, Wandeler & Baiker, 2003). X-ray absorption spectroscopy and attenuated total reflection infra-red spectroscopy are presently the most promising *in situ* techniques for heterogeneously catalyzed reactions giving information on the structure and the surface of the catalysts.
Recently, *in situ* EXAFS studies have been performed at the Pd K-edge during aerobic oxidation of alcohols in supercritical carbon dioxide (150 bar, $^{\circ}$C), which show the potential of high pressure studies (Grunwaldt et al., 2003). Small beam sizes will facilitate these studies because the use of rather thin windows is especially important for absorption edges below 10 keV. The potential of such high pressure studies has been recently outlined in different publications (Grunwaldt, Wandeler & Baiker, 2003; Topsøe, 2003).
Not only *in situ* investigations will benefit from the small spot size. The small focal spot size combined with the high flux of a PETRA III undulator beamline will allow for studies of the electronic and atomic structure under extreme conditions in high-pressure devices, such as diamond anvil cells (Bassett et al., 2000). Applications are expected to be in the areas of condensed matter physics, physical chemistry, geochemistry and geophysics.

6.11.2.4 QEXAFS investigations of fast structural transformations

The high brilliance of the PETRA III undulator beam will also be advantageous for quick EXAFS (QEXAFS) studies (Frahm, 1989a), also in combination with lateral information on the sample. In recent studies (Grunwaldt et al., 2001; Lützenkirchen-Hecht et al., 2003), the data quality of QEXAFS *in situ* studies could be improved using undulator beamlines at present 2^{nd} and 3^{rd} generation synchrotron sources. A further step forward is expected with the PETRA III upgrade. The higher photon flux on the sample directly corresponds to a better time resolution, especially in the case of dilute samples (Lützenkirchen-Hecht, Grundmann & Frahm, 2001; Lützenkirchen-Hecht & Frahm, 2001). A μm-sized focal spot allows e.g. to investigate individual grains in a catalyst sample during an *in situ* reaction, or to perform EXAFS measurements in the reflective mode on small sample areas. Currently, in many cases the atomic reordering during fast chemical reactions like combustions and decompositions is still unknown. For the understanding of such processes it is also important to look for intermediate, short lived structural phases. Additional applications for measurements with μm-size lateral resolution and high time resolution are manifold, e.g. the investigation of localized corrosion phenomena such as pitting corrosion (Lützenkirchen-Hecht & Strehblow, 2003).

6.11.2.5 High energy XAFS

The energy range of the L-edge XAFS in most elements is strongly limited by the relatively small energy differences within the L-multiplet. K-edges do not have such a limitation. The problem is demonstrated in Fig. 6.11.2 (Borowski, Bowron & de Panfilis, 1999), comparing the EXAFS and their corresponding Fourier transform (FT) spectra of Eu in Eu_2O_3 from the L_3 and K-edges. The gain in resolution of bond distances through the extended momentum range in the K-edges EXAFS is clearly visible.

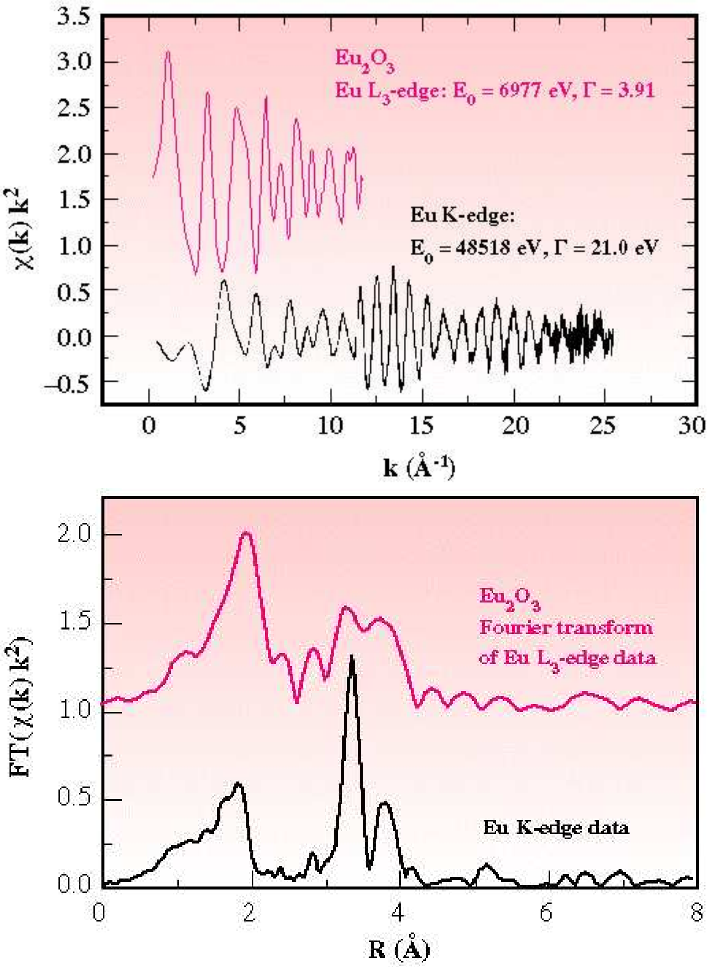

Figure 6.11.2: Comparison of Eu K-edge and L_3-edge XAFS spectra (top) and the corresponding Fourier transformed spectra (bottom) measured on a Eu_2O_3 sample at the ESRF.

A further advantage of high energy XAFS is the high penetration depth of the X-ray photons. It minimizes the ubiquitous problems arising from strongly absorbing matrices (Mavrogenes et al., 2002) and/or sample containers. The spectroscopy undulator (Sec. 4.1.4) of PETRA III emits a spectrum, intense enough for high quality XAFS measurements even at $E \gg 50\,\mathrm{keV}$. The beamline design will take account of this property and enables measurements of K-edge XAFS up to $Z \approx 83$.

It is important to develop an experimental system to improve the energy resolution of the XAFS-spectra beyond the lifetime broadening visible in simple absorption measurements, which is significant at high energy edges. Usage of a high resolution detector system (e.g. a crystal analyzer in Rowland geometry) enables to overcome the lifetime broadening caused by the very large broadening of the 1s core level that is observed in transmission measurements. This is done by choosing the wavelength of the detected photons so that only those electrons that decay from the sharp 3p level into the 1s hole are detected (de Groot, 2001 and references therein). A further application for which high precision spectra are indispensable is the investigation and modeling of multiple shell excitations (Kodre et al., 2002) in the high energy range.

6.11.2.6 Extremely small sample volumes

An advantage of the highly brilliant beam is that small sample volumes can be investigated. This is not only important for the aforementioned studies under extreme conditions (high pressure, temperature). Applications are in the fields of materials science, geochemistry, mineralogy and environmental chemistry. Due to safety and ecological aspects, it is important for toxic or radioactive samples to use small sample volumes. For example, experiments on plutonium, whose nuclides play the dominant role in long-term radio-toxicity of high level nuclear waste, can be down-scaled to a level of activity below the exemption limit. Fluorescence XAFS experiments on a solution containing $^{242}\mathrm{Pu}$ are typically performed on 400 μL solutions with Pu concentrations of 1-2 mmol/L contained within 5 mm diameter polyethylene tubes. A single sample in such an experiment contains an activity near 25 kBq. This value exceeds the exemption limit for $^{242}\mathrm{Pu}$ (10 kBq). If the beam is focused and the impinging number of photons high, the same experiment can be performed in capillary cells, thereby reducing the sample volume to 0.5 μL and less. A sample with this volume, having the same expected signal, has an activity near 350 Bq. This is well below the exemption limit and allows leeway for volume errors and additional activity due to the presence of other nuclides in the $^{242}\mathrm{Pu}$ nuclide vector actually used.

Geochemical understanding of the reactions between rocks and natural fluids in geological processes is important for many research areas (search for economically relevant deposits, performance assessment of waste repositories, etc.). The high chemical and physical heterogeneity of natural systems requires investigation using techniques with high sensitivity, high spatial resolution and/or surface specificity. All these techniques will benefit from the high brilliance of the PETRA III undulator beamline. One specific example in this field is the analysis of fluid- inclusions in minerals, where samples of small volume are of interest (Anderson, Mayanovic & Bajt, 1995).

6.11.3 Beamline description

6.11.3.1 General remarks

The XAFS beamline at PETRA III cannot be installed on a side station, because the energy has to be scanned over a wide range in a short time. A minimum spot size of less than 1 μm seems to be achievable. The high technical demands of such a nano-focus station and the resulting complexity of operation require two experimental stations: one for measurements with the sub-μm focus, and another for measurements with a moderately focused or unfocused beam. This proposal describes a beamline suited for measurements with focal spot sizes between 1 and 100 μm. XAFS measurements at E > 30 keV have to be carried out without any mirror optics, resulting in a spot size of $\approx 1\,\mathrm{mm}^2$. Fig. 6.11.3 shows sketches of the set-up for E < 30 keV and E > 30 keV. A design proposal for a (spectroscopy) beamline

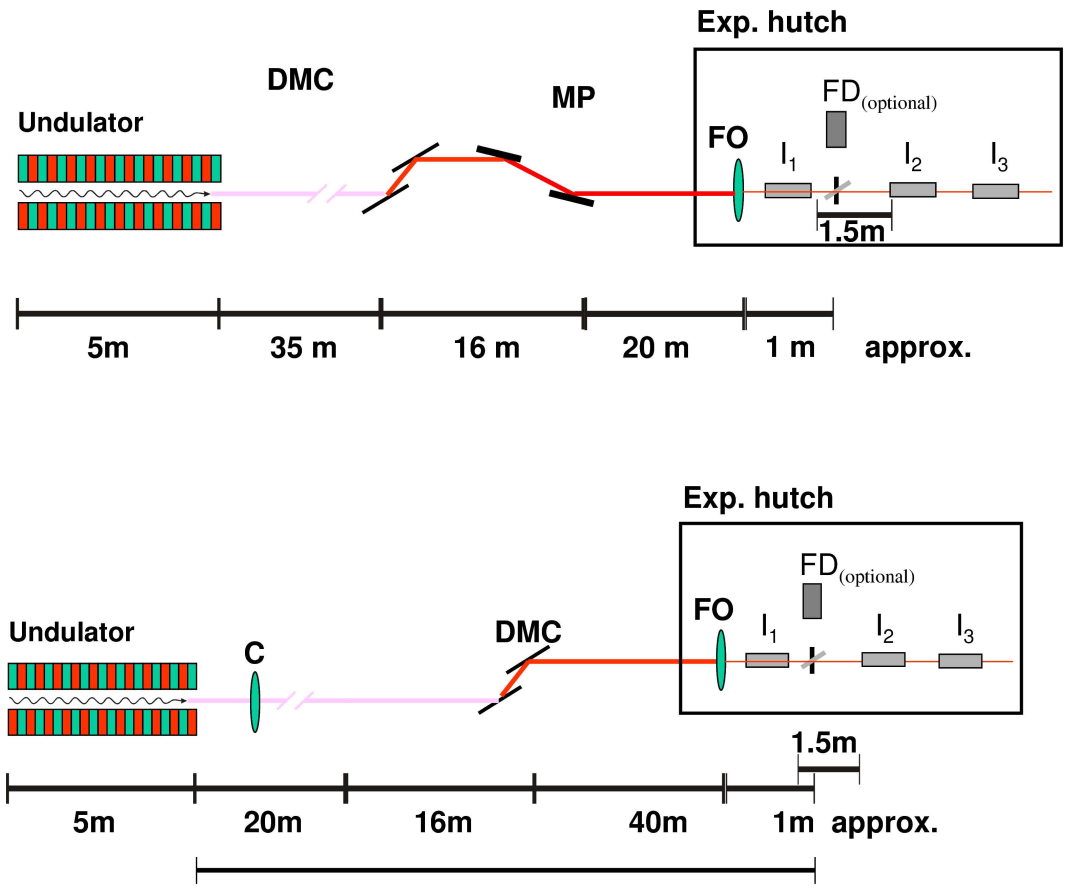

Figure 6.11.3: Schematic drawing of the PETRA III XAFS beamline showing the different set-ups for energies < 30 keV (top) and for energies > 30 keV (bottom). The drawing is not to scale and all distances are only given to illustrate the overall spacial demand. (C = collimating lens, MP = mirror pair, DCM = double crystal monochromator, FO = focusing optics, FD = fluorescence detector, I = ionization chambers)

capable of focusing down to 100 nm and smaller will be given in Chapter 6.13. For specific applications however the XAFS-beamline will enable focusing down to spot sizes of $\approx 1\ \mu\mathrm{m}$ using Kirkpatrick-Baez mirror systems or X-ray lenses.

6.11.3.2 Undulator

The emission spectrum of the undulator must cover the energy range from 2.4 up to 80 keV. The first harmonic will cover the energy range between 2.4 and ≈ 9 keV. A complete description of the undulator parameters can be found in Tab. 4.1.1. Since the energy range used during an XAFS scan is much larger than the natural width of the undulator peak, it is necessary to taper its gap to cover the EXAFS range close to the selected edge.
An undulator line width of 15 % ΔE/E can be achieved by a taper of 1 mm over the entire undulator length for a 2 m insertion device. The effect of different tapers is shown in Fig. 4.1.9. An undulator line width of about 1500 eV is possible for the 3^{rd} harmonics at energies in the range of the Cu K-edge (Lai et al., 1993). The brilliance under these conditions is still higher than the one of a wiggler at PETRA-III.
Alternatively, if the highest obtainable brilliance must be used, the gap of the untapered undulator will be scanned parallel to the monochromator. A reasonable maximum scan speed for a continuous scan is of the order of 500 eV/sec (see Fig. 4.1.8). This method is applicable to single experiments, but it is obviously impossible to scan the undulator gap with the high repetition frequency requested e.g. for XAFS-tomography applications. A high β position for the undulator is preferable for the majority of applications. The option to shift the β-function of the storage ring is particularly interesting, because all applications requiring focal spot sizes smaller than some $\mu\mathrm{m}$ will benefit from an undulator positioned in a low β region.

6.11.3.3 Beamline optics

The beamline optics consists of three major units, the monochromator, two plane mirrors for higher harmonic suppression and optional KB-mirror or lens systems for beam focusing. It will be possible to move both, the mirrors and the monochromator, into a position that allows the white beam to pass. This will allow the use of specialized optical components such as very fast scanning piezo driven monochromators in the experimental hutch. The ensemble of monochromator and mirrors will allow to work with a fixed exit for the mirrored monochromatic beam (2.4–30 keV) and the white beam. The monochromatic beam with E > 30 keV will enter the hutch 2.5 cm higher than the mirrored beam.

6.11.3.4 Monochromator

It is planned to use a fixed exit double-crystal monochromator (DCM) with cryogenic (LN_2) cooling of both crystals. It will be equipped with an angle encoder on the Θ-arm and a MOSTAB feedback loop. For the desired energy range from 2.4 to 80 (100) keV more than one crystal pair is necessary. Three pairs of crystals, Si(111), Si(311) and Si(511), will be mounted in a common housing and will be exchangeable by remote control. The mechanics of the DCM must be compatible to fast (500 eV/sec) scans. The monochromator will be operated with two different distances between the two crystals. This is necessary because sufficiently small cut-off energy of the mirrors is only possible if the incident angle of the beam on the mirrors is changed. On the monochromator side this means that the height of the second crystal must be remotely adjustable. Fig. 6.11.4 shows the necessary movements of crystals and mirrors.

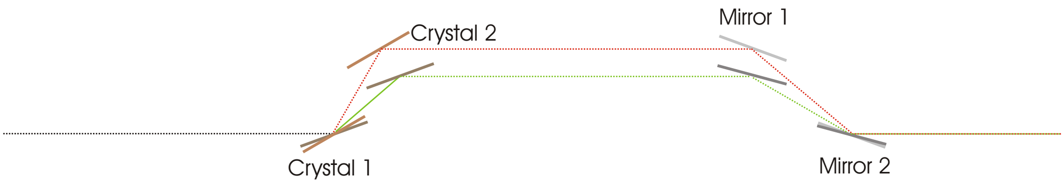

Figure 6.11.4: Scheme of the movements of monochromator crystals and mirrors necessary to fulfill the fixed exit condition for different glancing angles of the mirrors.

6.11.3.5 Mirrors

The mirrors shown in the schematic drawing (Fig. 6.11.3a) serve one main purpose: the rejection of higher harmonic radiation. Because of the large energy range, an effective higher harmonic rejection can only be achieved by using more than one coating of the mirror surface combined with different incident angles. It is planned to coat three stripes on both mirrors with different materials (Si, Rh, Pt). Incident angles of 2.5 mrad for energies between 8 and 30 keV and 5 mrad for energies less than 8 keV will be used. The resulting reflectivities in the energy range 2–30 keV are shown in Fig. 6.11.5. The monochromatic beam will have a fixed exit height. The mirrors compensate the vertical offset caused by the monochromator, so that the beam exits the optics hutch in the ring plane. In this geometry, it is necessary to block the very high energy background photons (Bremsstrahlung, etc.) with a massive beam stop between monochromator and the first mirror.

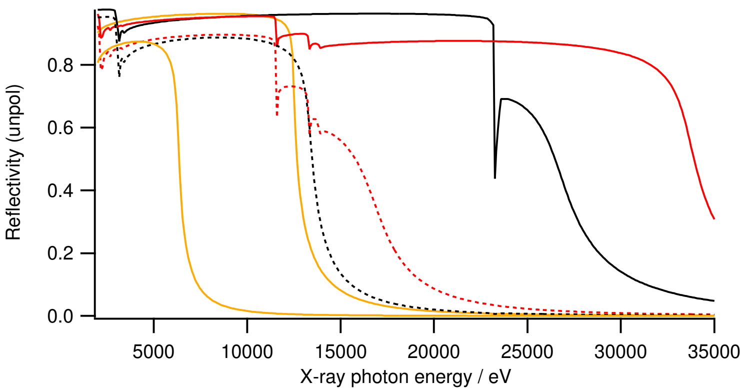

Figure 6.11.5: Reflectivity of the X-ray mirrors coated with Si (yellow), Rh (black) and Pt (red). Shown are the reflectivities at glancing angles 2.5 (solid) and 5 mrad (dashed).

The need of a fixed exit height, despite the necessary change of the incident angle for higher and lower photon energies, forces to change the exit height of the monochromator by changing the height of the second crystal and to change the height of the first mirror accordingly, see Fig. 6.11.4. Both adjustments can be done mechanically by linear movements. Like all other moveable optical components the mirrors must be equipped with angle and linear encoders. Thus it will be possible to restore once aligned settings with sufficient precision and to enable fast changes of the beamline set-up.

6.11.3.6 Focusing optics

In the energy range 2.4–30 keV beam spot sizes between $1\,\mu\mathrm{m}^2$ and the size of the unfocused beam will be achieved using Kirkpatrick-Baez (KB) mirror systems near the sample. For reasons of stability, it is advantageous to install the final focusing elements (KB-mirrors or lenses/lens systems) on the same desk as the samples. The KB-mirror systems will be designed such that the mirror pairs for different focal spot sizes may be rapidly exchanged. Because focusing mirrors are not usable at $E > 30$ keV, it is planned to use alternative focusing optics such as compound refractive lenses (CRL), Fresnel zone plates, 2-D waveguides and parabolic planar or kinoform lenses for focusing at $E > 30$ keV. All refractive optics suffer from chromatic errors. Therefore, they are currently not used for EXAFS experiments. For short scans (100–200 eV) these errors are negligible so that at least XANES scans are possible with refractive optics (Schroer et al., 2003a). Use of the unfocused beam for measurements on larger samples will be an option.

6.11.3.7 Detectors

Ionization chambers are the preferred type of detector for transmission XAFS experiments. The broad energy range of the beamline requires a variety of gases including the noble gases Ar – Xe. For lower energies it will be possible to work with reduced pressure in the ionization chambers. For fluorescence detection XAFS experiments, multi-pixel solid state detectors must be available. The high expected flux can only be handled by a detector with a large number of relatively small pixels. An energy resolution of ≈ 300 eV (FWHM @ Mn K_α) is under most circumstances sufficient for EXAFS measurements. The critical point is to attain a ≈ 300 eV resolution at high count rates $\gg 100$ kcps. At present, these requirements are best fulfilled by detectors such as the currently optimized Si-drift diode detectors (Hansen & Tröger, 2000).
A bent Laue analyzer detection system can be an interesting alternative to energy dispersive solid state detectors for fluorescence XAFS measurements. Especially at sources with very high flux, the background photons can saturate the detection system while the number of analyzed photons is still very small in experiments using an energy dispersive detector (Zhang, Rosenbaum & Bunker, 1999).

6.11.3.8 Experimental hutch / sample environment

A hutch size of 4 x 3 x 8 m^3 (H x W x L) is needed to accommodate the experimental set-up. Directly behind the beam entrance into the hutch space additional optical components can be installed. This can be either KB- mirror systems for different focal spot sizes, or lens systems. Alternatively, it will be possible to install a very fast scanning monochromator at this position (Richwin et al., 2001). For larger *in situ* applications, the distance between the I_0 and the I_1 detector must be adjustable. A maximum distance of 2 m is sufficient. For measurements at lower energies a vacuum chamber will be installed between the first and the second ionization chamber. The large number of *in situ* experiments foreseen make it mandatory to have all the necessary infrastructure for the use of toxic and/or corrosive gases in the experimental hutch, this includes an exhaust system for toxic and/or corrosive gases. Furthermore standard media such as cooling water, pressurized air and gases like N_2, He and Ar, which are needed for the operation of ionization chambers and for some sample environments, will be available. A chemistry lab equipped with a glove box, a fume exhaust and all before mentioned media supplies will be available in the vicinity of the beamline. The sample will be mounted on a high precision sample manipulator. An optical microscope with CCD camera is necessary for the adjustment of the sample position relative to the beam. A sample holder with He-cryostat and heating coils will be available for measurements at temperatures between 4 and 300 K. A closed cycle He-cryostat is desirable for measurements with an unfocused beam, when a certain amount of vibration can be tolerated. A diffractometer and a position sensitive detector are useful for combined XAFS/XRD measurements, which are highly demanded for many investigations (Clausen, Topsøe & Frahm, 1998; Grunwaldt & Clausen, 2002; Clausen et al., 1993; Grunwaldt et al., 2000).

6.11.4 Capital investment and personnel

The investment costs for the XAFS beamline sums up to about **1830 k€**.

Manpower requirement:
1 Staff scientist (from beginning of 2004) 1 Engineer (6 month after the scientist) 1 Postdoc (not later than start of building/ordering phase) 1 Postdoc (Start of commissioning)

6.12 High-Energy Photoelectron Spectroscopy

Authors and Consultants :

R. Claessen	University of Augsburg, Germany
W. Drube	DESY, Hamburg, Germany
L. Kövér	ATOMKI, Debrecen, Hungary
P. LeFèvre	LURE, Orsay, France
V. N. Strocov	SLS, Villingen, Switzerland
J. C. Woicik	NIST/APS, Argonne, USA
J. Zegenhagen	ESRF, Grenoble, France

6.12.1 Current state of the scientific field

Photoelectron spectroscopy (PES) techniques are key methods in solid state physics and material science, providing unique information about chemical composition and electronic structure, both of the atomic core and the valence states (Kevan, 1992; Hüfner, 1996). PES is also an ideal experimental probe to study aspects of electronic correlations and other atomic many-body effects, which are among the most fascinating topics of modern solid state research (Imada, Fujimori & Tokura, 1998). This includes very fundamental problems such as correlation-induced metal-insulator transitions in 3d-metal oxides or heavy-fermion behavior in 4f-metal compounds, but also novel phenomena like high-temperature superconductivity in cuprates or colossal magnetoresistance in manganites, which hold high potential for possible device applications. A thorough understanding of these materials requires a detailed determination of their microscopic electronic structure. Here PES has been established as a fundamental experimental probe, because the signal can be directly compared to the single-particle excitation spectrum of the corresponding theoretical models used to describe these interacting electron systems (Hüfner, 1996).
In conventional PES, here defined as h$\nu < 2$ keV, the information is primarily obtained from the topmost atomic layers ($\approx$ 1 nm) because of the strong Coulomb interaction of electrons traveling through a solid (Ley & Cardona, 1979). This is a great advantage for surface studies, but it seriously limits the capability to yield reliable information on the electronic structure in the bulk, which often is different. Novel materials of interest today are ternary, quaternary or even more complex compounds, with large unit cells whose spatial dimensions are comparable to or even exceed the probing depth of conventional PES (Fig. 6.12.1). Likewise, technologically relevant buried interfaces and nano-structures cannot be accessed at all. As a consequence, the application of PES has at present little impact in material science. The extreme surface sensitivity can be overcome using hard X-ray excitation ($h\nu \gg 1$ keV) which produces energetic electrons with a correspondingly larger escape depth. It is then possible to "look" much deeper into the sample, $\approx$ 10 nm, a range which is already interesting for modern nano-technology and future devices.
To date, only few PES studies have been made at hard X-ray energies because the experiments are highly demanding. A high photon flux is required to compensate for low signal rates: photoelectric cross-sections are decreasing rapidly above the excitation threshold σ_{nl}(E) $\propto$ E$^{-3.5-l}$ (Bethe & Salpeter, 1957) and the transmission of electron analyzers

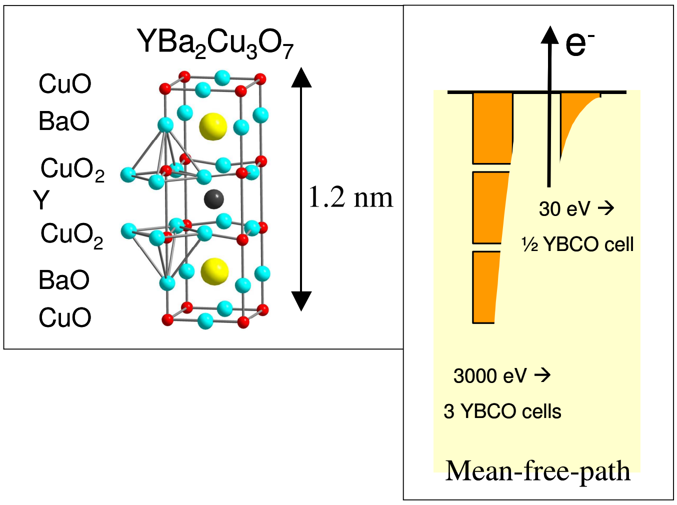

Figure 6.12.1: The unit cell of YBCO (left) and the mean free path of electrons with different kinetic energies relative to the YBCO unit cell (right).

strongly drops at high retardation ratios, which are required to measure fast electrons with high energy resolution. Also, suitable spectrometers are not readily available.

To study atomic inner-shells, a moderate resolution is usually adequate to match the intrinsic hole lifetime broadening. Experiments of this kind are now routinely performed at DORIS combining the high flux from the BW2 X-ray wiggler in the range 3–8 keV with a parallel detecting high-energy electron analyzer. Here, the achievable resolution (≈ 0.5 eV) is strongly limited by the low source brilliance. Nevertheless, interesting novel results were obtained e.g. for resonant excitation of inner-shell Auger transitions in solid metals (Drube, Treusch & Materlik, 1995). Recently, it was demonstrated that high-energy resonant Auger spectra allow to discriminate dipolar from quadrupolar transitions at the K-absorption threshold in TiO_2 because excitations into localized final states differ in energy (Danger et al., 2002).

Core level spectroscopy provides unique information on elemental composition, chemical bonding and also electron correlation phenomena involving the atomic core. However, in order to fully understand material properties, it is essential to study the valence states as well. Here, excellent energy resolution is a key ingredient to resolve the subtle features which carry the information needed to characterize the electronic structure and to put theoretical predictions obtained by state-of-the-art computational methods to a stringent test.

State-of-the-art PES in the XUV-regime achieves meV energy resolution at energies < 100 eV where the surface sensitivity is extreme. At energies of ≈ 1 keV a resolution < 100 meV is already challenging and grating monochromators become very inefficient at higher energies. In the hard X-ray range, perfect Si crystals are used instead where the resolving power and the achievable *absolute* resolution is *improving* with energy (using high-index reflections). A bandwidth < 10 meV is obtained above 10 keV, well suited for high-resolution spectroscopy as needed e.g. for correlated electronic systems. Clearly, this requires a brilliant source which is capable of delivering the highest possible photon flux into this narrow spectral bandwidth to cope with low signal rates. Such demanding experiments have not been realized so far.

Hard X-rays offer the additional possibility to excite X-ray standing waves (XSW) in crys-

talline materials (Zegenhagen, 1993). If XSW is combined with PES, electronic and structural information is obtained in parallel and can thus be directly correlated. This approach has been recently used to identify local adsorption geometries exploiting the chemical shift sensitivity of PES (Jackson et al., 2000). The combination of XSW with valence band spectroscopy even enables unique site-specific investigations of hybridization and bonding as has been demonstrated very recently (Woicik et al., 2002).
In summary, photoelectron spectroscopy using hard X-rays is a novel technique with interesting prospects for electronic structure investigations of solid materials. However, the full potential of this method can only be explored at a high-flux and brilliant source. At present, strong attempts are being made to implement this promising technique at $3^{\rm rd}$ generation X-ray sources (ESRF, SPring-8).

6.12.2 Science at PETRA III

6.12.2.1 Introductory Remarks

Hard X-ray PES with high energy resolution is extremely challenging and requires an intense and brilliant source as well as highly sophisticated electron detection. The instrument proposed for PETRA III specifically utilizes the low source emittance. The low divergence beam from a high-β undulator is ideally suited for high-resolution monochromatization preserving a high monochromatic flux ($\approx 10^{11}\mathrm{s}^{-1}$ into $\Delta\mathrm{E} \approx$ 10 meV around 10 keV) which is needed to compensate for small cross-sections. Furthermore, the achievable resolving power of the electron analyzer is linked to the spot size on the sample which can be as small as about 10 μm with suitable X-ray optics. It is, however, not planned to aim at sub-μm X-ray focusing for spatial resolution in a scanning mode. It seems that for spatial resolution, where the main focus is on elemental analysis, electron beam excitation is more powerful. It is possible already today to perform e.g. scanning Auger measurements with 10 nm spatial resolution which is unlikely possible with hard X-rays. However, there are currently interesting novel developments in electron spectroscopy instrumentation. Lower energy PES spectromicroscopy using a combination of a photoemission electron microscope and a hemispherical energy analyzer has already reached a level of about 20 nm resolution. This concept used at somewhat higher energies is an option also for PETRA III since this approach clearly requires a sufficiently small X-ray focus and a high flux density.

6.12.2.2 Strongly correlated systems: states near the Fermi level

The proposed instrument is ideally suited to study strongly correlated systems which are most interesting, fascinating, and also promising for device applications. Novel magnetoresistance materials are already frequently used for data storage and they are also candidates for other advanced applications, such as spin-valve transistors. High-temperature superconductors are still of moderate industrial use, but they display puzzling properties, which are still lacking comprehensive theoretical underpinning. Their theoretical understanding is mostly aided by (a) macroscopic transport measurements, (b) analysis of atomic and nano-scale structure and, most importantly here, (c) high resolution spectroscopic analysis of the electronic structure and excitation spectrum.

As outlined above, the information obtained from conventional high resolution PES is strongly influenced by surface effects. The high-energy technique proposed here is designed to overcome this problem since it allows highly bulk-sensitive studies. The planned X-ray range up to 25 keV with electron detection energies up $\approx$ 15 keV yields unprecedented PES probing depths. At the same time, the targeted energy resolution ($<$ 200 meV in the standard mode and 10-50 meV in the high-resolution mode) will facilitate detailed measurements of correlation effects in the valence band, i.e. specifically for states near the Fermi energy. Note that these values are obtained at *high* X-ray energies with the simultaneous advantage of bulk sensitivity.

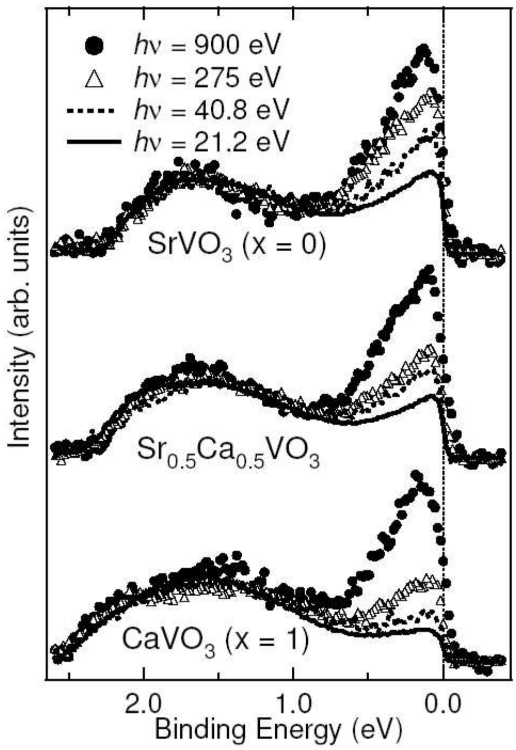

Figure 6.12.2: Valence band spectra of $Ca_{1-x}Sr_xVO_3$, measured at different photon energies. With increasing photon energy the quasi-particle intensity (peak near 0 eV) is seen to grow relative to the “lower Hubbard band” (feature around 1.7 eV). This reflects reduced electronic correlations in the bulk as compared to the surface (from Sekiyama et al., 2003b).

Another benefit of the PETRA III brilliance is the achievable small photon spot because correlated electron materials are often available only as rather small single crystals. The detrimental effect of decreasing photoexcitation cross-sections towards high photon energies will be compensated by the high flux of the PETRA III “spectroscopy undulator” in combination with the high throughput of high-resolution post-monochromators (HRM) which can only be achieved in a brilliant beam. For efficient high-resolution photoelectron measurements, an electron spectrometer will be used which is specifically designed for ultimate performance at high kinetic energies, including a parallel detection capability.
The specifications of the proposed beamline will facilitate direct measurements of the intrinsic bulk electronic structure. As a consequence it will become possible to establish direct connections between spectroscopic information and data extracted from integral volume-sensitive probes such as specific heat, magnetic susceptibility, or conductivity, allowing for a most comprehensive experimental characterization of such materials. Furthermore, despite

the volume-sensitivity of high-energy PES it will still remain possible to vary the probing depth and even detect surface effects by using a grazing electron emission geometry.
Today, first steps are already being made to increase the information depth in high-resolution valence band spectroscopy in the soft X-ray regime up to $\approx 1000\,\mathrm{eV}$ using sophisticated grating monochromators and powerful undulators at 3^{rd} generation facilities, such as beamline BL25SU at SPring-8 (Saitoh et al., 2000). Recent experiments (Sekiyama et al., 2000; Mo et al., 2003) have already revealed dramatic surface effects in PES spectra of complex correlated electron materials. As an example, Fig. 6.12.2.2 shows valence band spectra of $\mathrm{Ca_{1-x}Sr_xVO_3}$ at different photon energies (Sekiyama et al., 2003a). The crucial information contained in these data is the ratio of the quasi-particle peak and the "lower Hubbard band" intensity, which is directly linked to the quasi-particle mass renormalization. This ratio is seen to increase with photon energy and hence with probing depth, confirming that the effective mass previously obtained from low energy PES is strongly distorted by surface effects. These observations helped to resolve a long-standing discrepancy between PES results and thermodynamic data and led to a comprehensive and even semi-quantitative understanding of the electronic structure of these vanadates (Sekiyama et al., 2003a).
Finally, it is noted that valence band studies using energetic photoelectrons might retain angular information if the angular resolution of the spectrometer is high enough. At a kinetic energy of about 10 keV, the whole Brillouin zone collapses into a small angular cone of about 2° for a 0.3 nm unit cell. Thus, using 2D detection, the 1D-angle versus energy distribution can be obtained in parallel. The feasibility of performing angular resolved PES in this way in the soft X-ray range has already been demonstrated (Brookes, 2003).

6.12.2.3 Material Science: buried interfaces and nano-structures

The achievable bulk sensitivity will also enable true material science applications where the relevant properties are mostly determined by interfacial regions well below the surface. Note that a modified surface region, generally not of interest, covers *any* material under *ambient* conditions, incompatible with the need for surface "cleanliness" in low energy PES experiments. Here, it will be possible to "look through" these dead layers. This opens many possibilities which are crucial to material science studies: the bulk chemical state of a compound can be determined, buried interfaces and/or nano-structures become accessible. Moreover, the information depth can still be tuned from bulk to surface to some extent, e.g. by varying the electron emission angle and/or the excitation energy ("depth profiling").
At a kinetic energy of $\approx 10\,\mathrm{keV}$, the inelastic mean free path of photoelectrons is surpassing $\approx 7\,\mathrm{nm}$ (cf. Fig. 6.12.3) and chemical and electronic information can be retrieved from regions buried deeper than 10 nm. It was recently demonstrated, that an AlAs layer in a GaAs/AlAs/GaAs quantum-well structure can be analyzed through 10 nm of covering material (Dallera et al., 2003) with kinetic energies of 6 keV. This is a length scale which is relevant for the developing field of nano-electronics. High-resolution spectroscopy using this instrument at PETRA III will hence be a uniquely sensitive probe to study electronic material properties in future nano-science and technology, provided the samples of interest are sufficiently conducting.
The range of materials which comprise buried interfaces and/or nano-structures to tailor elec-

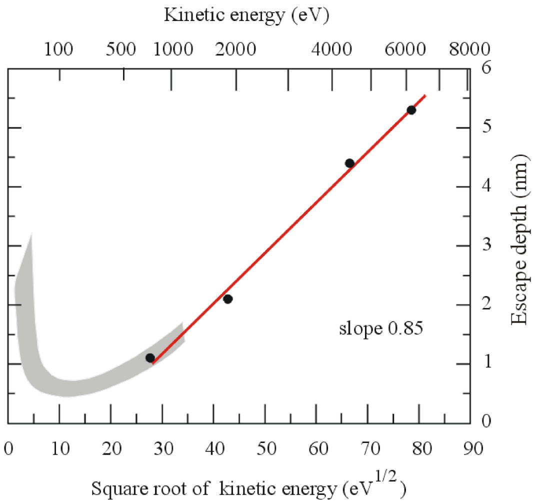

Figure 6.12.3: New measurements of the electron escape depth in GaAs (dots) in comparison with the “universal curve” (shaded curve). Measurements were carried out at ID32, ESRF.

tronic properties for specific device applications is enormous and will not be elaborated here. So far, high-energy PES has already been used to characterize interesting, but comparatively simple interface systems such as SiO_2/SiC (Virojanadara et al., 2001) and high-k insulators on Si (Kobayashi et al., 2003). Another example of high current interest in microelectronics is the incorporation of light-emitting devices into Si, which would allow the integration of optoelectronics into the established Si device technology. Recently, intense room temperature photoluminescence originating from Ge quantum dots (QDs) embedded in Si was reported (Cirlin et al., 2002; Zakharov et al., 2003). The photoluminescence from the QDs occurs due to quantum confinement effects. Structural aspects of the Ge/Si systems, including Ge/Si intermixing at the interface, have been extensively studied by electron microscopy and X-ray techniques. However, very little is known about their electronic structure. Of particular interest are band offsets at the Ge/Si interface, which promote accumulation of electrons and holes in the QDs, and - of course - the local electronic structure near the interface.
Since the QDs structures are usually buried a few nm, they are accessible to PES with this instrument. Furthermore, there is no need for *in situ* sample preparation which requires additional special instrumentation and is time consuming. Samples can be grown *ex situ* and protected by cap layers which would still be “transparent” in the experiment.
In general, the valence band region contains contributions from the entire elemental manifold within the probed sample volume. For a clear chemical contrast, it may therefore be advantageous to measure shallow core electrons (e.g. Ge 2p in the example above) which also can be made highly energetic owing to the high excitation energy available at the PETRA III beamline. Measuring the exit-angle dependence of the peak intensities, it will be possible to characterize the elemental intermixing near the interface and the diffusion of QD atoms into the matrix. If the selected levels are sharp enough, bulk and interfacial chemical shifts can be separated. Indications for different electronic environments and/or disorder of the interface atoms can in principle be obtained from a detailed line shape analysis, provided the data are of high statistical quality. Again, a high X-ray flux density is essential also for this type of experiment. Finally, valence band offsets at the interface can be derived from the relative energies of core level lines in the bulk.

6.12.2.4 Deep inner-shells

An obvious benefit of the wide energy spectrum available at this instrument is the ability to access tightly bound inner-shell levels which are largely unexplored so far. It becomes possible to study atomic resonance phenomena involving purely inner shells but also outer shells for a large range of materials which provide unique information on electron correlation and the nature of (localized) unoccupied states near the Fermi level. Also here the energetic electrons allow to probe true bulk properties. This was utilized in a resonant 3d photoemission study at the Ce $\mathrm{L_3}$-edge of $\mathrm{CeRh_3}$ (Ogasawara et al., 2000), a mixed-valent intermetallic compound where the 4f hybridization is weaker at the surface than in the bulk. By measuring the intensity modulation of the different $\mathrm{3d\,f^{(0,1,2)}}$ final states around the Ce $\mathrm{L_3}$-edge (constant initial state) the three resonances could be unambiguously identified and related to the profile of the corresponding X-ray absorption spectrum which only exhibits two distinct structures.

Unoccupied states may also be probed by resonantly exciting inner-shell Auger transitions which are very sensitive to the local electronic structure around the absorbing atom. If the core electron is excited into localized empty orbitals, the corresponding Auger final states often differ in energy and can be resolved in the experiment. This was recently exploited to discriminate dipolar and quadrupolar transitions at the K-absorption threshold in rutile $\mathrm{TiO_2}$ (Danger et al., 2002). In the absence of strong resonances, sub-threshold excited inner-shell Auger spectra carry information on the local density of unoccupied states (Drube, Treusch & Materlik, 1995; Kövér et al., 2003). The threshold behavior of inner-shell Auger satellites provide valuable information on multi-electron excitations involving the outer local orbitals (Drube et al., 1999).

The strength of photoemission spectroscopy is its "chemical" sensitivity to composition and local bonding. However, the "chemical shift", i.e. the kinetic energy difference of a specific core level line of an atom in different chemical environments, is generally only used as a fingerprint. It cannot be directly related to the dependence of the (initial ground state) potential in the atomic core of the atom on the local environment because of the additional (final excited state) contribution which arises through inner- and extra-atomic relaxation in response to the core hole creation. The so-called "Auger parameter" (Wagner, 1975), i.e. the combined kinetic energy shift of a core level and an Auger line, is often used to discriminate initial and final state contributions. However, this concept relies on the assumption of core level independent energy shifts, which is generally not justified (Cole, Macdonald & Weightman, 2002). It has been shown, however, that the final state relaxation contribution is directly related to the quantity $\Delta\beta(\mathrm{i}) = \Delta\mathrm{E_A}(\mathrm{kii}) + 2\Delta\mathrm{E_B}(\mathrm{i}) - \Delta\mathrm{E_B}(\mathrm{k})$ which combines the energy differences $\Delta\mathrm{E_B}$ of two *inner-shell* core levels, (i) and (k), and the kinetic energy $\Delta\mathrm{E_A}$ of the connecting Auger transition (kii) (Hohlneicher, Pulm & Freund, 1985). Generally, level (k) is tightly bound and inaccessible to ordinary photoemission. At PETRA III, the available large energy range offers the possibility to apply this concept on a broad basis. Very recently, it has been demonstrated for $\mathrm{SiO_2/Si(100)}$ that initial and final state contributions to the Si 2p "chemical shift" can be quantitatively separated (Eickhoff, Medicherla & Drube, 2004). The results are in good agreement with recent state-of-the-art first-principles calculations.

6.12.2.5 Site-specific photoelectron spectroscopy

In conventional PES, the intensity of the plane-wave-like X-rays is essentially constant over the dimensions of a crystalline unit cell. As a result, the emitted photoelectrons are coming from anywhere within the information depth of the sample. No spatially resolved data, that would provide electronic and chemical information on an atomic scale, is obtained. Varying the electron take-off angle and/or the exciting X-ray energy only changes the integral depth weighting according to the effective electron attenuation length (including elastic scattering), but gives no atomic resolution.

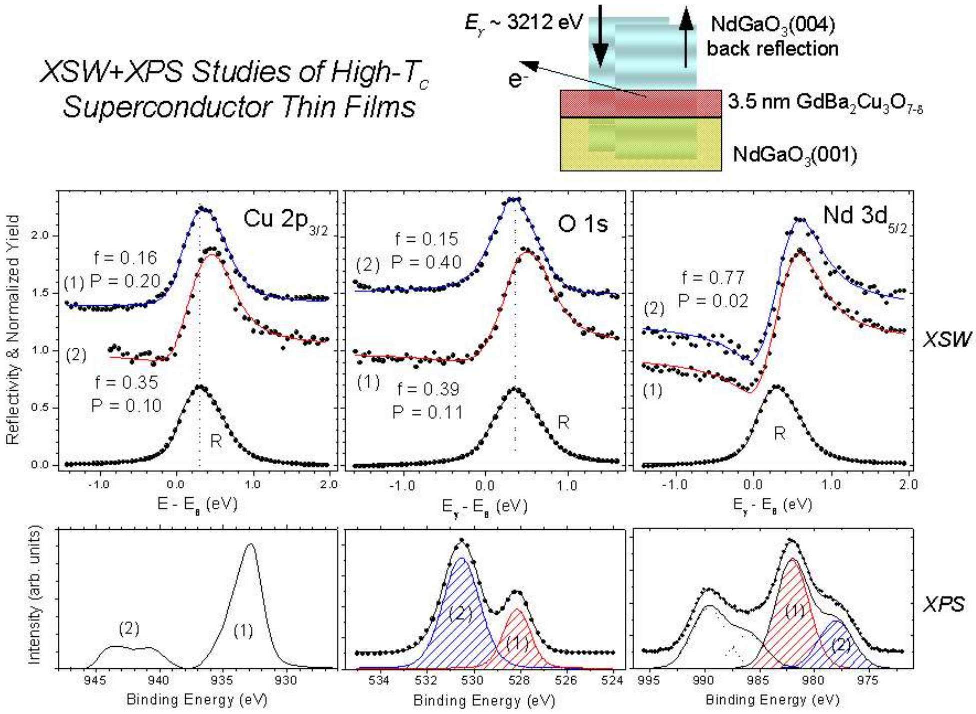

Figure 6.12.4: XSW/PES data of a 3.5 nm superconducting GBCO film on NGO-(0 0 1). All elemental components of the film can be analyzed. The result of the XSW analysis of Cu and O is shown. The PES signal from the substrate (Nd 3d) can be recorded as well. Measurements performed at ID32, ESRF.

This limitation can be overcome for single crystalline materials at short wavelength excitation, as proposed here. It is achieved by using the spatial variation of an X-ray standing wave (XSW) in the vicinity of a crystal X-ray Bragg reflection. The XSW approach is been frequently used for surface structure determination (Zegenhagen, 1993) where the high element specificity of core level photoemission can be effectively utilized to identify adsorbate species. Recently, using high energy resolution to resolve chemically shifted components of the same element, it was possible to track local adsorption sites through surface chemical reactions (Jackson et al., 2000).

Analyzing photoelectrons excited by an X-ray standing wave permits to directly correlate structural with chemical and electronic properties, even in complex systems. As an example, Fig. 6.12.4 shows the XSW/XPS analysis of a superconducting $\mathrm{GdBa_2Cu_3O_{(7-\delta)}}$ (GBCO) film on the (001) surface of $\mathrm{NdGaO_3}$ (NGO), exposed to normal ambient. The PES lines of Cu and Oxygen can be decomposed in an intrinsic, clean part and a component, which can be assigned to the degraded portion of the film. The XSW analysis of the latter reveals a lower coherent fraction and a different coherent position compared to the intrinsic part. The Nd 3d signal from the substrate peak is split into several components, a shake-up satellite and a shifted component due to a charging effects. The analysis of the Cu XSW yield allowed to deduce the bonding *geometry* at the GBCO/NGO interface (Lee et al., 2003).
Going one step further, the site-specificity of XSW combined with valence photoemission allows to obtain quantitative "partial photoelectron spectra" which reflect the valence charge distribution of the constituent atoms (Woicik et al., 2001). This was demonstrated by comparing data obtained for the heteropolar GaAs and the homopolar Ge (Woicik, Nelson & Pianetta, 2000). It is emphasized that unlike in resonant photoemission, the sensitivity to different species is *not* obtained from (uncontrolled) sensitivity differences, but rather from geometrical structure of the material.
In a recent combined experimental and theoretical study of rutile $\mathrm{TiO_2}$ it was possible to observe experimentally, and confirm theoretically, the unequivocal trace of σ and π covalent bonds, and even non-bonding π orbitals associated with the O atoms alone (Woicik et al., 2002). Neither the positive identification of the physical origins for the spectral line-shape nor the observation of the detailed chemical hybridization can be obtained from conventional PES.
These studies show that site-specific PES is a powerful tool that affords a unique combination of element-, space- and electron-initial-state sensitivity. In conjunction with first principles theory, it provides insight into the spatial extent of electron states and into chemical bonding. It can be applied to a variety of materials that are of interest to the materials and physics communities from both a fundamental and an applied point of view. The key goal is to provide the most direct evidence as to the nature and degree of chemical bonding and to provide a definite, and as quantitative as possible, analysis of electronic structure in terms of orbital hybridization.

6.12.3 Beamline description

6.12.3.1 General Remarks

Hard X-ray photoelectron spectroscopy, in particular with high energy resolution ($\Delta E/E$ down to 10^{-6}), requires a highly brilliant X-ray source to obtain a high flux density within a narrow spectral bandpass in order to cope with small photoelectric cross-sections.
The total photon energy range is determined by two basic aspects: 1) The low energy regime should connect to the range still accessible by XUV-beamlines using grating monochromators. Considering a reasonable Bragg angle limit for Si(1 1 1) crystal monochromatization, the energy range will extend down to 2.4 keV. This allows to access the Sulphur K-edge for resonant excitation. Also, energies around and below 3 keV are often necessary to excite

X-ray standing waves in back-reflection geometry. 2) A high energy limit, of course, is not strictly defined but a practical limit around 20 keV may be assumed, given by the working range of electron spectrometers and photoelectric cross-section considerations. For inner-shell studies, kinetic electron energies are lower. Therefore it seems wise to aim at an upper photon energy limit of about 25 keV to access the L-edges of *all* elements for resonant studies. In any case, continuous tunability in the entire range is mandatory. This requirement is not compatible with the operation at a side station.
The beamline will provide maximum flux also at low energies which excludes the use of Be-windows in the beam path. A windowless operation up to the sample, however, is not necessary. The use of ultra-thin low-absorbing windows as vacuum separators, such as carbon foils in the white beam or Mylar foils in the monochromatic beam, is advantageous to operate the UHV system up to the experiment especially if the vacuum conditions and/or requirements in the PES analysis chamber differ from those in the other parts of the beam path.

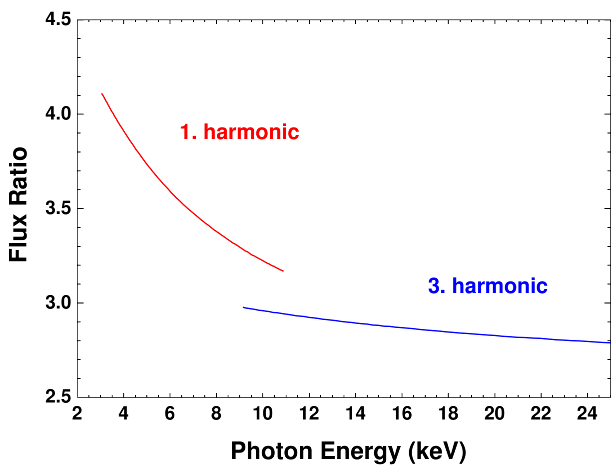

Figure 6.12.5: Flux ratio of a 5 m vs. 2 m undulator ("spectroscopy device") for a high-β source. Shown is the ratio of the partial flux into a 18 (vert) $\times$ 25 (hor) μrad^2 angle which corresponds to the FWHM of the full beam.

6.12.3.2 Undulator and Source

The photon energy ranges from 2.4 to 25 keV and the undulator will *continuously* cover the entire regime using the 1^{st} and 3^{rd} harmonic. The necessary undulator parameters are well matched by the "spectroscopy device" as described in Sec. 4.1.4. The 1^{st} harmonic can be tuned from 2.4 to 10 keV which is foreseen as the main working range for many applications. Except for energies below $\approx$ 10 keV, the photon flux scales linearly with the device length. The gain factor of a 5 m device compared to a 2 m device is 3–4 in the 1^{st} harmonic ($<$ 10 keV) and $\approx$ 3 in the 3^{rd} harmonic ($>$ 10 keV) (Fig. 6.12.5). It must be recognized that, in general, high-energy PES experiments are photon flux limited. The reduced intensity at a short undulator scales the measurement time but is - in many cases - not critical for the signal-to-noise ratio. If there is a necessity to operate a side station in parallel, a short undulator may be used, although this is not a preferred mode of operation.
A high β-source is best suited for an efficient monochromatization using high-resolution post-monochromators. Also, it is desired to minimize the horizontal beam size at larger

distances to cope with the limited acceptance of e.g. KB-focusing optics near the experiment. Close to the source pre-collimation using compound refractive Be-lenses (CRLs) is not applicable at low energies.

6.12.3.3 Beamline optical elements

The principle optical elements are a high-heatload monochromator, a pair of mirrors in the monochromatic beam, one or more high-resolution post-monochromators (HRM), which can be optionally placed into the beam, and a focusing optics (Fig. 6.12.6). While the high-heatload monochromator and the mirrors are located in the primary optics hutch, post-monochromatization and focusing will be done further downstream, close to the experiment. For an optimum throughput of the HRM, which is only used at energies above $\approx$ 6 keV, collimating CRLs may be used in the white beam. They must be removed for work at low energies. The combined monochromator and mirror arrangement will allow fixed beam exit conditions for the entire energy range (2.4–25 keV).

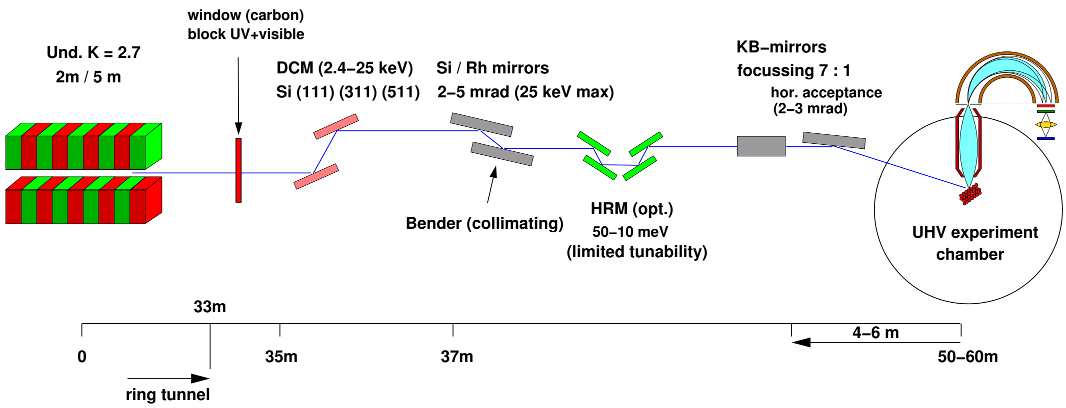

Figure 6.12.6: Schematic layout of the high-energy XPS beamline.

6.12.3.4 Monochromatization

Because PES is a highly energy resolving technique, the achievable energy resolution is a key parameter. The most important issue is the optimization of the throughput of the beamline at all desired energy resolutions in particular at higher energies ($> \approx 6$ keV) since cross-sections are decreasing rapidly. For a range of applications, especially core level spectroscopy, monochromatization of the order 200 meV will be adequate.

It is planned to use a fixed-exit Si double-crystal high heatload monochromator with three different crystal pairs. Cryogenic (LN_2)-cooling of both crystals in each pair is mandatory. For practical considerations, a maximum Bragg angle of 60^o is chosen which corresponds to minimum energies of 2.3 keV for Si (1 1 1), 4.4 keV for Si (3 1 1) and 6.9 keV for Si (5 1 1). The achievable energy resolution without pre-collimation is shown in Fig. 6.12.7. Using Si (3 1 1) and Si (5 1 1) crystals in their respective energy ranges, a resolution below 200 meV is obtained between 4.4 and about 10 keV as a direct benefit from the PETRA III source brilliance. At lower energies, Si (1 1 1) crystals have to be used where the intrinsic bandwidth is broader but still sufficient for many core level studies. The monochromator will

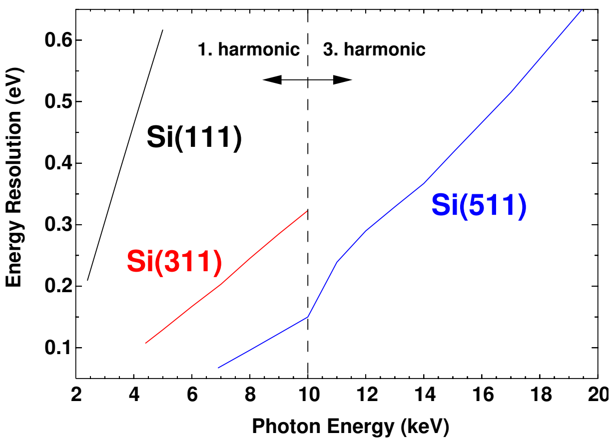

Figure 6.12.7: Energy resolution (FWHM) of Si double crystal monochromators for the uncollimated undulator beam (2 m device, high-β source) using the 1st and 3rd harmonic. The effective divergence is larger in the 3rd harmonic leading to a “kink” in the resolution for the Si (5 1 1) crystal pair around 10 keV. The Si (3 1 1) values are only plotted up to 10 keV.

be equipped with precision angular encoders on both rotation stages. Although mechanically challenging, because of the space requirement of cryogenic cooling, the three Si crystal pairs, (1 1 1), (3 1 1) and (5 1 1), have to be mounted in a common vacuum vessel. They must be exchangeable remotely by the experiment control system. A monochromator stabilization feedback loop (similar to the HASYLAB MOSTAB design) is necessary for continuous scans over larger energy intervals such as for edge-scans and/or constant initial state (CIS) measurements. Otherwise, the feedback system will be deactivated in order not to degrade the effective energy resolution.

For very high-resolution studies < 100 meV, Si post-monochromators utilizing higher-order diffraction planes will be used. At higher energies, white-beam collimating CRLs may serve to keep the angular divergence of the beam incident on the HRM below $\approx 5\ \mu\mathrm{rad}$. If absorption losses and/or chromatic aberrations cannot be tolerated, the beam will be collimated in the vertical direction by bending one of the mirrors. Because of the beam quality at PETRA III, is not absolutely essential to operate the HRM in close back-reflection geometry for high energy-resolution at close to 100% throughput. This ensures a certain range of energy tunability which is needed. A two-axes HRM is planned, with crystal optics utilizing asymmetric reflections. The energy resolution will ultimately reach down to 10 meV at energies around 12 keV while still providing a photon flux of the order $10^{11}\ s^{-1}$. A detailed design will be worked out to compromise high energy resolution and tunability. It will be possible to remotely move the HRM in and out of the beam.

6.12.3.5 Mirrors

The mirrors in the monochromatic beam (Fig. 6.12.6) serve to reduce the higher harmonic contribution and to provide vertical collimation for HRMs. Although higher harmonics are not generally a problem for PES, valence band studies at lower excitation energies (where HRMs are not used) may suffer from a reduced signal-to-background ratio. Therefore, it is planned to operate the mirrors at different glancing angles to tune the cut-off energy. This

implies that the vertical crystal offset in the high heatload monochromator must be adjustable to maintain fixed beam exit conditions.
The lowest cut-off energy is about 8 keV and the highest energy to be reflected is about 25 keV. The glancing angle will be > 2 mrad in any case to accept the full beam while keeping the mirror length reasonable (< 1 m). Therefore, two pairs of mirrors with different coatings, e.g. Si and Rh, will be used. Si is necessary to obtain high and structure less reflectivity down to 2.4 keV (noble metals like Rh, Pt exhibit absorption edges around 3 keV). The glancing angle will be tunable in a range from 2–5 mrad. It is necessary to bend the second mirror for beam collimation in cases where CRLs are not suitable.

6.12.3.6 Focusing optics

Focusing of the beam is necessary to match the acceptance of electron spectrometers. It is, however, not planned to aim at sub-μm focusing for spatial resolution (see 6.12.2.1). Since the maximum photon energy is < 25 keV, beam focusing will be accomplished using Kirkpatrick-Baez (KB) mirror systems. This has the advantage of non-chromaticity as opposed to CRLs, which also are not applicable at low energies. Assuming a practical demagnification ratio of about 7:1, the beam can be focussed down to about $50\,\mu\mathrm{m}$ horizontally and a few $\mu\mathrm{m}$ vertically which directly translates into an increased electron spectrometer performance at very high energy resolution, i.e. retardation ratio. A moderate demagnification ensures that the KB-mirror system does not intersect with the complex and large UHV-equipment at the experiment (at 50–60 m from the source, see Fig. 6.12.6).

6.12.3.7 Experiment Hutch, Endstation and Instrumentation

The experiment needs a radiation shielded hutch for the endstation, post-monochromators and focusing optics ($\approx 4\,\mathrm{m(H)} \times 3.5\,\mathrm{m(W)} \times 8\,\mathrm{m(L)}$), and a control hutch ($\approx 2.5\,\mathrm{m(H)} \times 3\,\mathrm{m(W)} \times 4\,\mathrm{m(L)}$) for the electronics, computing and work space for users.
The endstation consists of a UHV-chamber arrangement with a μ-metal shielded main chamber housing the electron spectrometer, a sample manipulator with the necessary degrees of freedom for positioning and alignment (also for XSW), etc. Sample preparation and characterization facilities will be available in separate preparation chambers which can be accessed through a sample transfer mechanism.
The high-transmission electron analyzer will be a specially designed instrument with high-stability, high-voltage power supplies. It will reach retardation ratios up to 1000 which are necessary to measure electrons up to ≈ 15 keV with an energy resolution down to 10 meV. A parallel electron detection scheme will be implemented for an efficient operation of the spectrometer. Such novel types of analyzers are currently being developed by several companies and also in the framework of an EU-project (VOLPE). They will be put to first tests at X-ray beamlines at SPring-8 and ESRF in 2004. Temperature stabilization down to $\pm 1°\mathrm{C}$ at the endstation and the post-monochromators/focusing optics is necessary to achieve high energy and spatial stability.
The analyzer is a large and heavy device and it has to be aligned relative to the X-ray beam with great precision in order to match the acceptance of the electron zoom lens and the focal

spot on the sample. Therefore, the entire UHV-system will be mounted on an adjustable support which can be positioned with high accuracy ($< 10\,\mu$m) under remote control from the experiment. The setup will also provide high mechanical stability and flexibility to allow precision XSW experiments. All movements needed for positioning and alignment will be stepper-motor controlled.
In order to pass to the monochromatic beam on to other experiments further downstream, it will be possible to move the endstation out of the beam path without breaking the beamline and the experiment vacuum. A rail system will allow to translate the complete setup perpendicular to the beam (after disconnecting the vacuum systems) by about 2 m into an "off-line" position. Additional transverse space must therefore be available implying the need for a position of the experiment hutch not too close to the source ($\approx$ 50-60 m). It will thus be possible to maintain the instrument and prepare experiments while the beam is used for other work further downstream.
The experiment control system (hardware plus software) will allow a fast and simultaneous operation of the electron analyzer, the X-ray optics, in particular the monochromator, and the motor controlled movements of the endstation. This is essential to achieve the highest degree of flexibility for the experiments.

6.12.4 Capital investment and personnel

The total investment cost amounts to **1485 k€**.

Manpower (construction phase):
1 scientist (planning/construction/commissioning)
1 engineer (planning/construction/commissioning)
1 postdoc (ordering/construction/commissioning)
1 postdoc (construction/commissioning)

Manpower (operation phase):
1 scientist, 1 engineer, 2 postdocs

6.13 Hard X-ray Microprobe

Authors and Consultants :

G. Falkenberg	DESY, Hamburg, Germany
K. Rickers	DESY, GeoForschungsZentrum Potsdam, Germany
K. Janssens	University of Antwerp, Belgium
L. Vincze	University of Antwerp, Belgium
M. Wilke	Universität Potsdam, Germany
C. Schmidt	GeoForschungsZentrum Potsdam, Germany
M. Lankosz	University of Science and Technology, Krakow, Poland
M. Szczerbowska-Boruchowska	University of Science and Technology, Krakow, Poland
J. Chwiej	University of Science and Technology, Krakow, Poland

6.13.1 Current state of the scientific field

At various beamlines at the ESRF, APS and SPring-8, hard X-ray microprobes are currently in operation (e.g., Somogyi et al., 2001; Susini et al., 2003; McNulty et al., 2003; Suzuki et al., 2003; Hansel et al., 2002) that combine the non-destructive elemental micro-analysis capability of μ-XRF (microscopic X-ray fluorescence analysis) with the ability of performing complementary μ-XAS (X-ray absorption spectroscopy) and/or μ-XRD (X-ray diffraction) measurements. These instruments provide simultaneous, correlated information on the local elemental composition, chemical state, the local structural environment of specific elements and/or the local crystallographic structure of the examined materials.
The most advanced synchrotron microprobes use undulator sources at 3^{rd} generation, high-energy storage rings, since the fundamental characteristics of these instruments in terms of achievable beam size and flux density are directly related to the outstanding properties (small source size, high brilliance and degree of polarization) of these sources. Depending on the type of focusing device and energy range used for the experiment, beam sizes in the low micron- and even sub-micron range are routinely achieved providing 10^9–10^{12} photon/s intensity with limited divergence (typically ≤ 1 mrad). The high flux results in low limits of detection (LLD) for trace element analysis in the parts-per-billion range (or attogram) for μ-XRF and parts-per-million (or femtogram) for μ-XAS measurements. Both at ESRF ID22/ID18F and at APS 13-ID-C, beside local and two-dimensional micro-analysis by means of combined μ-XRF, μ-XAS and μ-XRD, also absorption/phase-contrast and fluorescent tomography measurements can be realized, allowing the 3D-visualization of the internal structure and/or composition of small samples. The high sensitivity of the spectrometers allows investigations in multiple dimensions by fast scanning: full 3D imaging by fluorescence tomography, confocal μ-XRF, XANES 2D-imaging, XANES- tomography, 3D micro-diffraction and diverse in-situ experiments.
Hard X-ray microprobe techniques are mostly applied in materials, geological, bio / biomedical, and environmental sciences, as well as in archeology and arts. Studies on a variety of scientific problems and materials performed at these beamlines have been published, including :

- the localization and speciation of As and Se in plant roots (Hansel et al., 2001)

- the speciation of Cd in fly-ash particles (Pinzani et al., 2002)
- the characterization of the micro-heterogeneity of reference materials (Kempenaers et al., 2002)
- interplanetary dust particles (Flynn et al., 2003)
- the chemical environment of the uranyl-ion in calcite (Kelly et al., 2003)
- the distribution and microbial reduction of Cr in soil (Tokunaga et al., 2003)
- the sorption and biomineralization of Pb(II) in biofilms (Templeton et al., 2003)
- the three-dimensional analysis of individual fly-ash particles (Golosio et al., 2003)
- the compression behavior of nano-crystalline anatase (Swamy et al., 2003)
- the crystallographic phases present in ancient Egyptian make-up (Martinetto et al., 2001)
- changes in the structure of archaeological bone samples (Wess et al., 2002)
- the dislocation density analysis in single grains of steel (Castelnau et al., 2001)
- the three-dimensional elemental analysis of single cells (Bohic et al., 2001)

A recent review on the (combined) use of μ-XRF and micro-tomography can be found in Sutton et al., 2002.
Hard X-ray microprobe beamlines at third generation synchrotrons are found both at high and low-β sections and make use of undulator insertion devices. In addition, microprobes are installed at some bending magnet sources because of considerable overbooking of the undulator beamlines. Fixed-exit, cryogenically cooled monochromators, equipped with Si(111) (in addition Si(311)) crystals work in the energy range 4–45 keV (72 keV). At ID22 the Si monochromator can be moved out of the beam to enable pink beam operation with 1% band pass by separation of a single undulator harmonic using filters and cut-off mirrors. Various optical systems have been in use at microprobe beamlines: Kirkpatrick-Baez (KB) mirror systems, compound refractive lenses (CRL), Fresnel zone plates (FZP) and capillary concentrators have been used to generate monochromatic or pink micro-beams. Apart from the X-ray sources themselves, many of the capabilities of the above-mentioned beamlines are directly related to the performance, stability, flexibility and robustness of the micro-focussing optics that is employed.
Tab. 6.13.1 summarizes some of the analytical characteristics recently recorded at ESRF beamlines with CRL and a KB-mirror systems in "routine" monochromatic mode. Both optical systems provide a suitable micro-beam for combined μ-XRF, μ-XANES and μ-XRD measurements. The experience at ID22 showed that CRL are very convenient and robust optical systems, requiring little or no (re)alignment and long focal distances (20 cm – 2 m). They can also be removed quickly and effortlessly from the beam, allowing to alternate between focused and unfocussed beam operations. However, their small solid angle does not allow to capture many photons prior to focusing. In addition, these optics are not achromatic, limiting their use for μ- EXAFS experiments. On the other hand, KB systems require a much more elaborate alignment procedure, tend to gradually lose their alignment over time and are not that easily removed from the optical axis of the beamline. The most prominent advantage of KB mirrors is the ability to capture unfocussed photons in a large collection angle and focus them with high transmission in an achromatic manner down to μm or sub-μm diameters.

	Optics (Beam line)			
E = 13 - 14 keV	CRL (ID22)	CRL (ID18F)	KB (ID22)	KB (ID13)
Photon flux (Ph/s)	10^{10}	10^{10}	1-4 10^{11}	$\sim 10^{11}$
Beam size (H×V μm^2)	14×2	3 - 10×1	3×1	0.7×0.7
LLD (Mn-Cu) (fg)	0.3 - 0.5	0.1 - 0.4	0.03	N.A.

Table 6.13.1: Experimental beam parameters at the ESRF ID22, ID18F and ID13, corresponding to compound refractive lens (CRL) and Kirkpatrick-Baez (KB) mirror optics.

A significant evolution is currently taking place in the performance of CRL. Schroer et al. (Schroer et al., 2003c) have combined magnified imaging with tomography to obtain the three-dimensional structure of materials at a resolution well below 1 μm. Using an aluminum lens to record a magnified tomogram of a test sample (microprocessor), a resolution of slightly above 400 nm was found for the three-dimensional reconstruction. CRL made of beryllium (Lengeler et al., 2003) provide better resolution and higher transmission for lower energies. Parabolic refractive X-ray lenses with short focal distance can generate intense hard X-ray micro-beams with lateral extensions in the 100 nm range even at a short distance from a synchrotron radiation source. Planar parabolic lenses made of silicon were fabricated that have a focal distance in the range of a few millimeters at hard X-ray energies. In a crossed geometry, two lenses were used to generate a micro-beam with a lateral size of 380 nm by 210 nm at 25 keV at a distance of 42 m from the synchrotron radiation source (Schroer et al., 2003b). By means of CRL, also XANES tomography was demonstrated, providing information on the oxidation state, the local atomic structure, and the local projected free density of states (Schroer et al., 2003a). Already in use for several years at various American synchrotron micro-focus beamlines, KB mirror systems also have recently been used to generate sub-micrometer beams at ESRF (Hignette et al., 2003). Reflective optics systems, with their high efficiency and achromatic nature are promising approaches towards this goal. At ESRF ID19, the Kirkpatrick-Baez (KB) technology, being developed at the ESRF, has achieved a measured spot size of 0.16×0.21 μm^2 at 20.5 keV. Despite non-perfect optics, an X-ray beam size close to the diffraction limit has been achieved in one direction. Examples of projection full field and micro-fluorescence scanning imaging were reported. Next to providing a higher photon flux than "standard" CRL, this technology therefore also allows, after due alignment of the mirrors, to achieve nm-range focusing of hard X-ray beams.

6.13.2 Science at PETRA III

6.13.2.1 General considerations

It is planned that the scientific problems addressed at the PETRA III hard X-ray microprobe beamline will be tackled by the combined use of different X-ray (micro-) beam methods during one experiment, depending on the nature of the problem and the type of material to be investigated. It is expected that with most problems and materials, micro-beam X-ray fluorescence measurements (Janssens et al., 2000) in combination with broad beam radiography imaging, providing information on the (variation of the) local elemental composition and density, will be the first and most straightforward experiments to perform in the exploratory phase of an experiment. Based on these first observations, information of higher quality (with respect to quantitative character, spatial resolution, structural content) can then be obtained by the use of more elaborate sample manipulation and data acquisition modes and strategies.

6.13.2.2 Examples of applications

In order to provide an idea on the type of generic experiments that are envisaged at the PETRA III microprobe beamline, a selected list of representative problems is outlined below. These specific cases, based on the literature and results of recent feasibility studies, are either being studied today by means of the currently operating X-ray microprobes at the 3^{rd} generation synchrotrons in Europe, the US and Japan or are border-line cases for the 2^{nd} generation X-ray microprobes.

A. *Mapping of composition, chemical state and rheological properties in heterogeneous geological samples*
Geological processes are often "conserved" in mineral reactions in rocks: the chemical composition and the chemical state of a specific metal in two coexisting minerals render valuable information on the pressure-temperature-oxygen fugacity (P-T-fO_2) conditions during the rock-forming process and may be heterogeneous on the micrometer scale. Elements of interest range from S (Z = 16) to U (Z = 92) depending on the geological question. A spatial resolution in the (sub-) μm-range will allow the measurement of short diffusion profiles and the separate analysis of small adjacent minerals. K-shell excitation of elements up to U with LLD in the sub-ppm range for all elements will be useful, together with variable excitation conditions in order to optimize measurement conditions for the element of interest.
Similarly, X-ray micro-diffraction with a spatial resolution in the 0.1 to 1 μm-range will permit to study the deformation of polycrystalline materials, in which the stress distribution is very heterogeneous (Castelnau et al., 2001). Combined with diamond anvil cells (Swamy et al., 2003), a monochromatic micro-beam with high flux in the energy range between 25 and 30 keV allows such studies even at the extreme P-T conditions of the deeper portions of the Earth's interior, which would provide valuable information about fundamental geological processes such as mantle convection and deep earthquakes.

B. *Analysis of fluid, melt and mineral inclusions*
Mineral, melt and fluid inclusions in minerals are formed during crystal growth and may record the conditions present during formation. The quantitative analysis of single melt and fluid inclusions facilitates the study of the chemical evolution of a rock-forming system, which is extremely valuable for the study of rock and ore-forming processes and element transport in the Earth's crust. A high spatial resolution in combination with a confocal setup and high excitation energies would be the set-up of choice. Detection limits in the sub-ppm range for precious elements such as Au will be very important. A CCD camera with an

optical resolution of 0.2 μm or better is needed for the alignment of micron-size inclusions in the beam. The exact quantitative analysis of such inclusions is often difficult because they are heterogeneous (Vanko et al., 2001; Ménez et al., 2002). One way to overcome this problem is to measure rehomogenized inclusions. This would be possible by using a heating stage mounted on the sample stage during inclusion analysis. This set-up would would also allow for the study of chemical state at different temperatures.

An almost unexplored field is the study of sub-micron sized inclusions in Earth and Planetary materials. The study of such inclusions in diamonds using synchrotron XRF/XRD will provide unique direct chemical and structural information about the Lower Mantle and deeper portions of the Upper Mantle. It adds considerably to this knowledge not only by identifying the mineralogy and the structural state of the included high pressure phases, but also any deformation of the surrounding diamond lattice, which, in turn, may allow estimates of the P-T conditions in the source region (Nasdala et al., 2003). Such analyses require the application of an in-situ technique that can be applied to obtain information from well below the diamond surface in order to prevent the complete pressure relaxation of an high pressure inclusion due to its exposure during the preparation of polished microprobe mounts. The synchrotron XRF/XRD microprobe is very well suited for such analysis.

Recently performed in-situ 3D elemental mapping by confocal micro-XRF at the ESRF ID18F XRF/XRD microprobe (see Fig. 6.13.1) and structural analyzes (by micro-XRD and Raman micro-spectroscopy) show the feasibility for obtaining detailed elemental / mineralogical information of poly-phase diamond inclusions, leading to exciting conclusions with respect to the Earth mantle dynamics and tomography (Brenker et al., 2003).

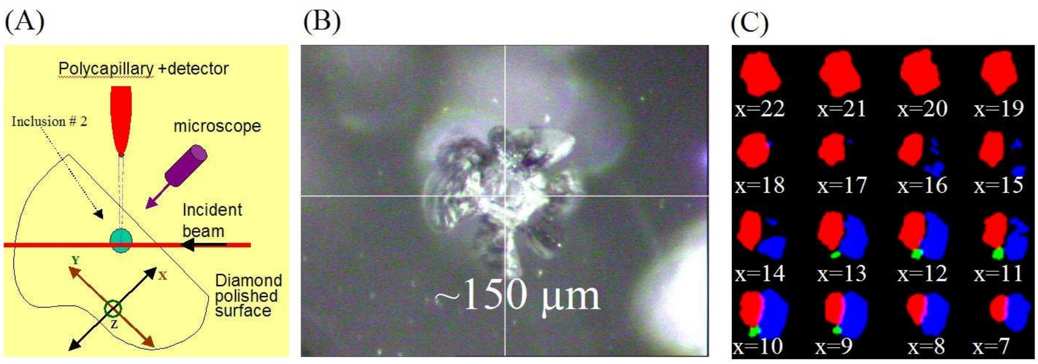

Figure 6.13.1: (A) Schematic drawing of a novel polycapillary based confocal XRF experiment at the ESRF ID18F microprobe applied to 3D-XRF mapping of diamond inclusions. (B) Optical image and (C) reconstructed slices at different depths x (measured in steps of 5 μm) of the inclusion based on trace-level Sr (red), Zr (blue) and Th (green) fluorescent signals. Voxel size: 5x5x6 μm^3. See further details in Brenker et al., 2003.

C. *Determination of mineral solubilities and chemical state in model systems in a Diamond Anvil Cell (DAC)*

The use of a DAC allows for in-situ determinations of mineral solubilities in aqueous solutions and in-situ chemical state mapping at high pressures and temperatures. With the current set-up of the cell, XRF experiments at temperatures of up to 800°C and pressures of up to 1.5 GPa are possible (Schmidt & Rickers, 2003). A rearrangement of the geometry of the sample chamber with the mineral grain being located inside the sample volume enables studies at higher experimental pressures. However, this set-up is applicable only if a primary beam in the micrometer range is available. Due to the absorption of the synchrotron beam and the fluorescence in the diamond this application will take advantage of the highest achievable photon flux. The geometry of the cell requires a focal distance longer than 50 mm and focusing must be possible also at energies significantly above 30 keV in order to facilitate the determination of rare earth elements (REE) at the ppm level via K-shell excitation.

A valuable extension of the solubility studies is the structural characterization of a given element in the coexisting phases by the use of μ-XANES and μ-EXAFS measurements. As natural silicate melts usually contain considerable amounts of water that is only soluble at elevated pressures, XANES/EXAFS studies on the local structural environment of elements using a DAC will provide important insight into the nature of hydrous melts. XANES and, especially, EXAFS measurements rely on high photon flux and, at least of similar importance, on a very stable, achromatic optical system, if focusing to a micron-sized beam spot is necessary.

D. *In-situ localization and speciation of As, Se and other redox-sensitive trace metals in phyto-remediating plants*

In the industrialized parts of the world, and especially in Eastern Europe and Russia, an increasing number of areas are discovered that are polluted with heavy metals such as lead, cadmium, copper, chromium, mercury, arsenic and selenium (Foster et al., 1998). In the specific case of Se, it replaces sulphur in thiol-group containing proteins, hereby significantly altering/reducing their functionality (see e.g. Lemly, 2002). An environmentally friendly and cost-effective measure for soil cleanup is to employ phyto-remediation. Specific plant species can be grown in soils polluted with heavy metals so that the plants: (a) will concentrate the heavy metals in their tissues (up to several hundreds to thousands of ppm in the roots), (b) can change the chemical form of the metals, usually by reduction of inorganic (toxic) forms of the metals and (subsequent) incorporation into biomolecules. Also for clean-up of radioactively polluted soils (e.g. in the 30 km zone around Chernobyl), phyto-remediation is a technique that is being evaluated at present.

A recent study (Wierzbicka et al., 2003) demonstrated that the take-up and effective toxicity of Se for Allium Cepa L. (common onion) strongly depends on the chemical form of Se to which the plants are exposed. In order to understand these differences in response better, microscopic in vivo determinations of total Se and various Se species in various parts (e.g., the roots, the bulb, the leaves) of this and other plants are very relevant. A recent feasibility study performed at HASYLAB using a confocal μ-XRF and μ-XANES setup showed very promising results (see Fig. 6.13.2).

E. *Study of ion-channels and long range ion transport through plants: investigation of structure-function relations by combined XRF microtomography and scanning micro-XRD*

Plant physiologists and microbiologists are trying to link the macroscopic appearance to the molecular biology of a plant, especially with a view to understanding the influence of single genes on a plant's large scale structure. This includes the study of ion channels and

Figure 6.13.2: Confocal μ-XRF and μ-XANES analysis of a Allium Cepa L plant. (a) Photo of a root tip of plant exposed to a selenite (Se 4^+) solution (dia. $\approx$ 1 mm); (b) Se distribution in the plane shown in (a) ; (c) photo of a leaf-tip of a plant treated with a selenate (Se 6^+) solution (dia. $\approx$ 1 mm); (d) Se-distribution in a virtual cross-section perpendicular to the axis of the leaf; (e) Se 6^+ distribution in the tip of the leaf; (f) Se- methyl-seleno-cysteine distribution in the tip of the leaf. Image resolution: $\approx$ 25 μm.

their influence on the long range transport of ions through the plant (Schröder et al., 1999; Schröder & Fain, 1984), for which SR-based XRF microtomography combined with scanning micro-XRD offers a uniquely sensitive/non-invasive tool with the potential of in vivo studies. Fig. 6.13.3 shows recently obtained results from the ESRF ID13 beamline for a combined micro-XRF/XRD experiment on an Opuntia cactus spine having a diameter of about 80 μm.

F. *Trace element analysis of fossils*

Foraminifers are micro-organisms of some 100 μm diameter that are living in the water column. In equilibrium with sea-water they build their carbonate shells. Trace elements such as Cd, Ba, and the REE in these shells are proxies for the palaeoclimate and palaeoproductivity during the living period of the foraminifer. Since the shells are only $\sim$ 10 μm thick, a spatial resolution about 0.5 μm is crucial to discriminate between shell carbonate and secondary coatings.

G. *Trace elements in mineralizing bone-tissues of renal disease patients*

In patients with chronic renal failure, serum phosphorus levels increase due to insufficient renal excretion. To control serum phosphate levels, phosphate-binding agents are given orally, in order to reduce gastro-intestinal phosphate uptake. Until recently, aluminum hydroxide was widely used, but accumulation in bone results in aluminum-related bone disease, characterized by a mineralization defect. Using micro-analytical and histochemical techniques, aluminum was localized at the mineralization front, a region in bone critical for proper mineralization. Lanthanum carbonate has been proposed as a new phosphate-binding agent. However, being also a trivalent cation, and having some chemical similarities with aluminum, deposition of this element in bone cannot be excluded. Due to the extremely low concentration of lanthanum in bone, conventional micro-analytical techniques are not sensitive enough to localize the element so that SR-XRF based determinations are more appropriate. Recent studies at ESRF-ID21 by means of a 1 μm diameter beam have shown La to be enriched at

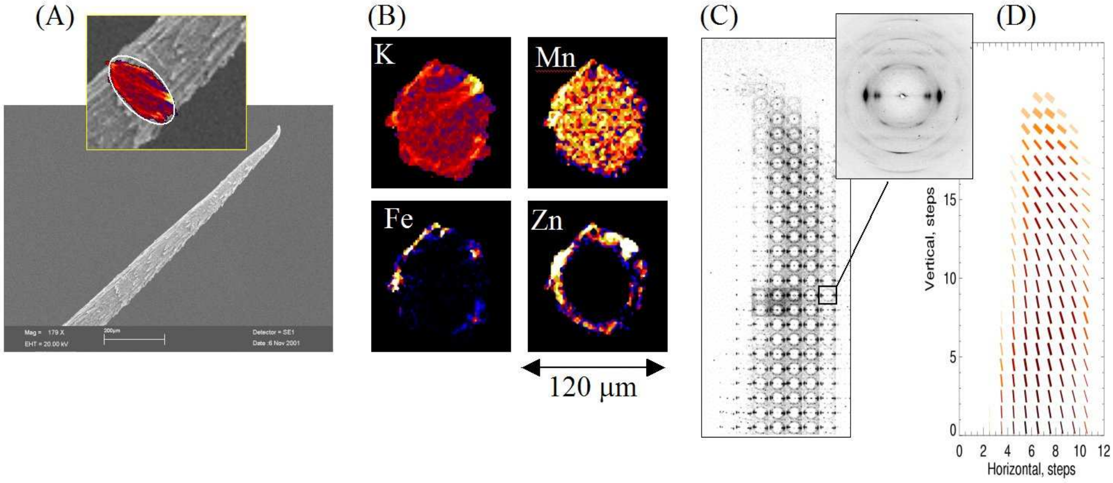

Figure 6.13.3: XRF microtomography and scanning micro-XRD analysis of a single spine collected from an Opuntia ficus indica leaf at the sea promenade in Rapallo (Italy). (A) scanning electron microscopy (SEM) image of the spine, (B) reconstructed distributions of K, Mn, Fe, Zn across an 80 μm diameter cross-section, (C) composite image from the individual XRD- patterns along the 2D-scan and (D) vector field display of the fitted 200 reflection parameters (intensity, azimuthal position and width). Experiment performed by L. Vincze (UA), M. Burghammer and C. Riekel (ESRF ID13).

the edge of the calcified bone (D'Haese et al., 2001). This observation indicates the potential for using trace-level mapping for monitoring the effects of various metal-containing drugs on the formation of dense biomaterials.

H. *Effect of trace levels of Sr on mechanical strength of human bone*

An element that plays an important role in the study of bone and bone diseases is Sr, which is believed, when present in sufficient amounts in blood, to induce the distortion of the crystallographic structure of hydroxyapatite in bone, thereby reducing the mechanical strength of the bone. This disease, known as osteomalacia (D'Haese et al., 2000), can also be induced by renal failure. In Sr-loaded chronic renal failure rats, Sr could be identified at the osteoid/calcification front, a critical site in bone mineralization. However, as in dialysis patients, the bone Sr concentration are 10 to 30-fold lower so that conventional techniques appear to be not sensitive enough to allow a spatial localization of the element in bone sections. The mechanism by which Sr impairs mineralization is not yet clear. This might either be due to a pure physicochemical process or an indirect interference by affecting osteoblast function. A combination of μ- XRF and μ-XRD was employed to (i) visualize the distributions of Ca and Sr in bone-cross sections, indicating the enrichment of Sr in specific areas and (ii) to measure the increasing degree of lattice-distortion in cell cultures grown in solutions with increasing Sr levels (D'Haese et al., 2002). This study has shown that X-ray micro-beams of ≈ 1 μm that allow to perform scanning μ-XRF and μ-XRD measurements on complex biomaterials consisting of several dense and diluted phases, allow to obtain relevant information on the effect of trace constituents on the structural properties of the dense phases in these materials.

I. *Elemental analysis and oxidation-state mapping of single cells in neuro-degenerative research*

The localized elemental analysis of human central nervous system (CNS) tissues and individual cells is essential for the investigation of biochemical processes that lead to neuro-degenerative disorders. The main goal of the research is the investigation of the role of elements, mainly metals, in processes leading to degeneration and atrophy of nerve cells in cases of two neuro-degenerative disorders e.g. Parkinson's disease (PD) and Amyotrophic Lateral Sclerosis (ALS). A common pathological hallmark of these pathologies is the loss of neurons in selected parts of the brain or the spinal cord (Bains & Shaw, 1997). The pathogenesis of PD and ALS is still not known but the most frequently cited theories of the degeneration and atrophy of neurons are oxidative stress, excitotoxicity, protein aggregation, and mitochondrial dysfunction, all of which may be caused in part or enhanced by the presence of metals such as Ca, Mn, Fe, Co, Cu or Zn in the nerve cells (Robberecht, 2000; Mattson et al., 2000; Bush, 2000; Cassarino & Bennett, 1999).

In recent years, increasing experimental evidence was found for the generic relation between the presence of metals and these disorders. For example, experiments performed at HASYLAB and ESRF revealed that neurons in substantia negra in patients suffering from Parkinsons's disease show a significantly higher accumulation of S, Ca, Fe, Cu, Zn, Se and Br in comparison to control cases. Increased Cl, Ca, Zn and Br abundances were observed in tissues from patients of Amyotrophic Lateral Sclerosis (Lankosz et al., 2002; Szczerbowska-Boruchowska et al., 2003). Because of the low content of Mn in CNS tissue (i.e., up to 10 mg/kg), a micro-beam of high intensity and polarization is necessary for the analysis of this element. Moreover, to study the role of trace elements in neuro-degenerative processes the elemental micro-analysis of single neurons is required. The differences in the distribution of metallic elements within a neuron, for example between nucleus and cytoplasm (if visualized) may lead to conclusions on the mechanism of potential action of these elements. Furthermore, in order to study the role of selected elements in pathogenesis of PD and ALS it is also necessary to know if a modification of oxidation states of these elements takes place in infected parts of the brain and spinal cord in comparison to the control tissue areas.

J. *Mobility assessment of polluting and radio-active heavy metals in coarse and fine particles.*

A number of sites in the world are polluted with particles containing high concentrations of heavy metals such as As, Pb, Ni, Cd etc. Usually, the source of pollution are nearby industrial metal-refining or fossil-fuel burning plants that have released pre-concentrated metal-rich slags, dust or other reaction products into the environment. In a number of specific cases, the polluting metals (U, Pu) are radioactive as a result of intentional or accidental military or civilian release of these materials.

When the heavy metals are present in the coarse ($> 10\,\mu$m diameter) particulate fraction, a relatively insignificant fraction can be blown up by prevailing winds so that the major interaction takes place by contact with the ground water (leaching out of soluble ionic forms). Fine particles, on the other hand, may easily become air-borne and, e.g., become deposited in the nose, thorax and lungs where some metallic species may induce cancer (e.g., Ni in metallic form, as produced in Ni-refineries).

In order to assess the effective danger on the short, mid and long term associated with the mobilization of these heavy and/or radio-active metals and their spread into the hydro- and biosphere, apart from the composition, also knowledge on the chemical state and crystallographic phases in which the metals are present, is very important. These investigations need to be carried out on particles of various sizes and porosities. Various X-ray micro-beam investigations techniques (such as μ-XANES, μ-XRD and μ-computed tomography) can be used together to determine a number of different properties of such materials (Salbu et al., 2001; Lind et al., 2002; Salbu et al., 2003; Vincze et al., 2002a; Vincze et al., 2002b).

The availability of X-ray micro-beams of variable diameter, ranging from 1 to 10 μm will allow to characterize individual particles of various sizes by means of μ-XANES and μ-XRD in order to study the interrelation between particle size and the abundance of e.g., Ni species and phases and the dependence of this on the release scenario of the particles.

6.13.3 Beamline description

A hard X-ray microprobe beamline at PETRA III will enable different complementary X-ray (micro-) beam methods to be performed simultaneously or sequentially during one experiment. Scanning X-ray fluorescence microscopy measurements in combination with broad beam radiography imaging will be the most straightforward to characterize heterogeneous samples in terms of (variation of the) local elemental composition and density. Microscopic X-ray absorption spectroscopy (μ-XANES, also μ-EXAFS) and microscopic X-ray diffractions will provide information on the local speciation and structure. Tomographic methods (fluorescence microtomography, XANES microtomography) and confocal arrangements of X-ray optics give access to quantitative three-dimensional measurements.

High demands are made on the accessible range of beam sizes and photon energies and on the flux of the primary beam in order to realize the experiments introduced in the scientific case. The hard X-ray microprobe beamline will provide beam sizes down to the 100 nm range utilizing the outstanding small source size and high brilliance of PETRA III, but also larger beams of 1–10 μm and an unfocused beam for flat field imaging will be available. The accessible energy range covers the K-edge energies from sulfur to uranium (E= 2.4–116 keV) and the flux is maximized by the use of KB mirrors and pink beam option.

Stability, flexibility and robustness of the beamline will be of major importance for the practical use of a microprobe beamline and will therefore guide its design. The key components of the setup are the undulator source, the monochromator system, plane mirrors for high-energy cutoff, the focusing optics and the experiment including scanning unit and detector system. A schematic sketch of the setup indicating the positions of the components is shown in Fig. 6.13.4. The experimental hutch including the focusing elements is placed at 90 m close to the end of the beamline in order to achieve a high demagnification of the X-ray source. The first optical element is located as close as possible to the focusing optics in order to minimize the effect of vibrations. A beam shutter between optics hutch and experimental hutch provides high beam stability by continuous irradiation of optics (e.g. during sample change).

6.13.3.1 Undulator

The hard X-ray microprobe beamline is equipped with the spectroscopy undulator described in Sec. 4.1.4. The undulator is placed in a low-beta section in order to facilitate the smallest possible horizontal beam size. Source size and divergence of the photon beam and other basic parameters of the spectroscopy undulator are listed in Tab. 4.1.1. A device of 2 m length will be sufficient for the majority of the proposed experiments, although microscopic X-ray absorption measurements in ultra-dilute systems would benefit from the increased brilliance of a 5 m undulator device (see Fig. 4.1.1 for comparison). The spectrum of the undulator covers the energy range 2.4–120 keV and higher. In the high energy range, the undulator works like a wiggler, but the intensity in the hard X-ray region is still sufficient as shown in Fig. 4.1.11. A side station is not appropriate for the beamline because of the large energy range of the experiment and the pink beam option.

6.13.3.2 Monochromator system

The monochromator system is composed of a double crystal monochromator (DCM) as described in Sec. 5.3.2 and, additionally, of a double multilayer monochromator (DMM). Both monochromators work in fixed exit-geometry and crystals are cryogenically cooled. The DCM covers the energy range 2.4–120 keV and the DMM the range 6–80 keV. Both monochromators will be operated with variable beam offset. For broad bandpass monochromatization of higher energies ($>$ 60 keV) different approaches have been discussed including the mounting of gradient $\mathrm{Si}_{1-x}\mathrm{Ge}_x$ crystal pairs or mosaic crystal pairs in Laue geometry, and the deposition of multilayer structures on the plane mirrors (see 6.13.3.3) or KB mirrors (see 6.13.3.4). The monochromator system is located as close as possible to the focusing optics in order to minimize the effect of vibrations of the monochromator crystals on the position of the focused beam.

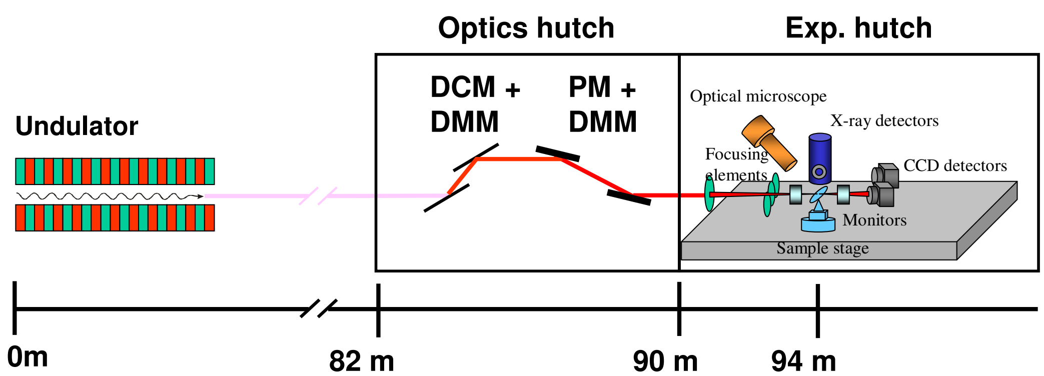

Figure 6.13.4: Schematic illustration of the hard X-ray microprobe beamline proposed for PETRA III. The monochromator system is comprised of a double crystal monochromator (DCM) and a double multilayer monochromator (DMM). Plane mirrors (PM) are coated with different materials and with a multilayer structure.

6.13.3.3 Plane mirrors

A pair of plane mirrors is used for the rejection of higher harmonics radiation. In order to cover the range of cutoff energies from 6 to 35 keV, the mirrors will be coated with different materials (Si, Rh, Pt) and operable at variable incident angles. As mentioned in section 6.13.3.2 one stripe of the plane mirrors may be coated with multilayer structures for high-energy broad bandpass monochromatization. For the preservation of the micro-focusing capability, the mirrors have minimal slope errors (less than 0.25 μrad). The mirrors are cryogenically cooled, because they are exposed to the white beam in pink beam mode and multilayer mode.

6.13.3.4 Focusing optic

The focusing optics are the key element of a hard X-ray microprobe beamline. Today, different concepts for focusing optics exist which are subject of rapid advancements (see 6.13.1). From today's view the beamline will be equipped with two KB-mirror systems, one providing beam sizes down to the 100 $\times$ 100 nm range for ultimate spatial resolution, and one providing beam sizes in the low micrometer range for high flux and low divergence applications. The KB-mirrors are applicable in the low to medium energy range (2.4–30 keV). Especially μ-EXAFS experiments will benefit from the achromaticity and efficiency of KB mirrors. The mirror systems are placed on a linear stage and can be exchanged easily under remote control.
A third position of the linear stage is used to include a CRL unit. CRL are known to generate a stable micro-beam and are capable of focusing X- rays of higher energy (5–50 keV for Be lenses, 15–120 keV for Al lenses). Several sets of CRL optimized for different ranges of energy, and focal sizes will be available. Nanofocusing lenses (NFL) composed of two crossed parabolic planar lenses will be chosen for extremely small beam sizes close to the diffraction limit. Beam parameters calculated by Chr. Schroer for a PETRA III undulator (5 m) and Si(111) monochromator at 20 keV are given in Tab. 6.13.2. Note, that the fluxes are two orders of magnitude higher in pink beam mode.

Lens type	Position	Focal distance	Demagnification	Spot size (mm) Vert.	Hor.	Flux ph/s	Gain
CRL (Be)	100 m	308.5 mm	323	80	258	5.4 10^{10}	3.5 10^{6}
NFL (C)	100 m	7.18 (h) 13.35 (v)	13900 (h) 7500 (v)	24.4	15.5	3.6 10^{8}	

Table 6.13.2: Beam parameters of CRL and NFL focusing optics calculated by C. Schroer for a PETRA III undulator source using a Si(111) monochromator at 20 keV.

6.13.3.5 Experiment

The stability of the setup will be of major importance for the practical use of the microprobe beamline and will therefore guide its design. The sample stage is coupled rigidly to

the focusing optics unit and includes three orthogonal translations and (at least) one rotation. The repeatability of the translations will fall significantly below the smallest achievable spot sizes, i.e. $< 10\,\mathrm{nm}$, at a travel range of 25 mm. In a standard experiment the sample will be mounted in air environment on a goniometer head, which is fixed onto the sample stage. The sample stage can carry also small and light chambers that provide various environments, such as vacuum and helium chambers, diamond anvils cells, heating and cooling stages, reactors, etc. A long distance optical microscope coupled to a CCD camera serves for the adjustment of the sample in the X-ray beam and for documentation. A high-resolution CCD camera, which is placed behind the sample, is used for the same purpose and also for absorption tomography. Optionally, the radiography CCD camera can be replaced under remote control with a large field CCD camera for X-ray diffraction. (Micro-) Ionization chambers are used for normalization and for transmission XAFS experiments. They can be loaded with various mixtures of gases, also at reduced pressures. Several different detector types are provided for the measurement of X-ray fluorescence and will be optionally installed. Multi element silicon drift detectors (SDD) are applied for fluorescence XAFS and fast scanning fluorescence microscopy experiments which are characterized by count rates $\gg 10\,\mathrm{kcps}$. A wavelength dispersive detector is employed for samples providing very high count rates and measurements of fluorescence lines suffering from high background. High quality Si(Li) detectors are well suited for quantitative multi-element analysis and germanium detectors are needed for the measurement of K-lines of heavy elements. It is feasible to place a polycapillary optics in front of any energy-dispersive detector for spatially resolve detection and adjust it with an accuracy of $5\ \mu\mathrm{m}$ (e.g. confocal setup).
Data reduction for scanning micro-XRF/XRD techniques is becoming increasingly a limiting factor as the data rate is growing due to faster detectors and scanning systems and a further increase in source brilliance. In particular the possibility of "data mining" may have an important influence on the outcome of an experimental period at a high-brilliance SR- source. Initial data treatment for scanning micro-XRF/XAS/XRD will be available online and provide an "image" of the microscopic sample structure at the end of a raster-scan. Micro-XRF data will require in particular fast spectral deconvolution and standard-less quantitative analysis techniques, which are applied recursively to individual spectra to determine and visualize the variation of elemental concentrations on-line (Vekemans et al., 2003).

6.13.3.6 Experimental hutch and infrastructure

A size of the hutch of 10 m in length, 4 m in width and 4 m in height is sufficient to accommodate the experimental setup and focussing elements. The sample stage is placed 4 m behind the hutch wall proving space upstream for low divergence focusing optics with large focal distances and downstream for CCD detectors. The levels of dust and other contaminations inside the hutch are minimal and limited only by the free access of the user to the experiment. Care is taken to avoid air flow and vibrations induced by the air condition of the hutch. Standard media such as cooling water, compressed air and gases (N_2, He, Ar) are available. A calm control room providing space for 4 users and a microscopy room equipped with various optical microscopes adjoin the hutch. A chemical lab with glove box and fume exhaust is placed in the vicinity.

6.13.4 Capital investment and personnel

The investments for this beamline sum up to about **1850** k€.
The required personnel is: 2 scientists, 1 engineer, 1 postdoc.

6.14 Variable Polarization Soft X-Ray Beamline for Photon Energies 50–2500 eV

Authors and Consultants :

J. Bansmann	Universität Rostock, Germany
U. Becker	Freie Universität Berlin, Germany
R. Denecke	Universität Erlangen-Nürnberg, Germany
R. Dörner	Universität Frankfurt, Germany
P. Fischer	MPI Stuttgart, Germany
R. L. Johnson	Universität Hamburg, Germany
L. Kipp	Universität Kiel, Germany
M. Martins	Universität Hamburg, Germany
T. Möller	DESY, Hamburg, Germany
A. Müller	Universität Gießen, Germany
R. Reininger	SAS, Madison, Wisconsin, USA
J. E. Rubensson	University of Uppsala, Sweden
H. Schmidt-Böcking	Universität Frankfurt, Germany
C. Schüßler-Langheine	Universität zu Köln, Germany
G. Schütz	MPI Stuttgart, Germany
P. Steinrück	Universität Erlangen-Nürnberg, Germany
L. H. Tjeng	Universität zu Köln, Germany
J. Ullrich	MPI Heidelberg, Germany
W. Wurth	Universität Hamburg, Germany

6.14.1 Introduction

Soft X-rays are ideal for investigations ranging from magnetism in nanostructures to studies on biological systems. Key absorption edges of practically all important elements lie in the soft X-ray range (100 eV to 2.5 keV) which opens up the possibility to uniquely determine the element-specific local electronic structure in complex materials by exploiting atomic resonances. Experiments at the latest third generation synchrotron light sources are now beginning to demonstrate the enormous scientific potential of this spectral region. At present, investigations are still limited by the light source and improved sources will immediately produce new science. In the future polarization-dependent studies with soft X-rays will play a key role in enhancing our knowledge of the structure of matter.

High-energy storage rings are excellent soft X-ray sources and suitable insertion devices can provide very high brilliance circularly polarized light in the energy range 500–2000 eV as has been demonstrated at both the ESRF and SPring-8 (Saitoh et al., 2000). Helical undulators operating in the first harmonic provide the highest flux and complete polarization, but require machine energies greater than 3 GeV. Radiation from higher harmonics of helical undulators is normally not used because it is emitted off axis in a broad cone. The soft X-ray beamlines presently providing circular polarization are heavily oversubscribed (ID 08 at ESRF, BL17SU, BL25SU and BL27SU at SPring-8). Insertion devices on lower energy machines like BESSY II, ELETTRA, and ALS only produce circularly polarized light up to about 500 eV in the first harmonic (see Fig. 6.14.1) and newer machines like SLS and SOLEIL will extend this limit to 700–900 eV. The variable polarization soft X-ray beamline at PETRA III will be unique and by providing the highest brilliance and flux in the important spectral region from 500 eV to 3 keV will open up completely new scientific opportunities. With current technology it is possible to achieve a spectral resolution of 10000 at 1 keV with an extremely high flux (more than 10^{12} photons/sec) focused on the sample. Compared to the best present day sources the PETRA III soft X-ray beamline will provide one to two orders of magnitude higher flux at photon energies above 1 keV. This beamline will promote significant progress in fields ranging from surface science to molecular and cluster physics, magnetic studies, condensed matter physics and nanotechnology.

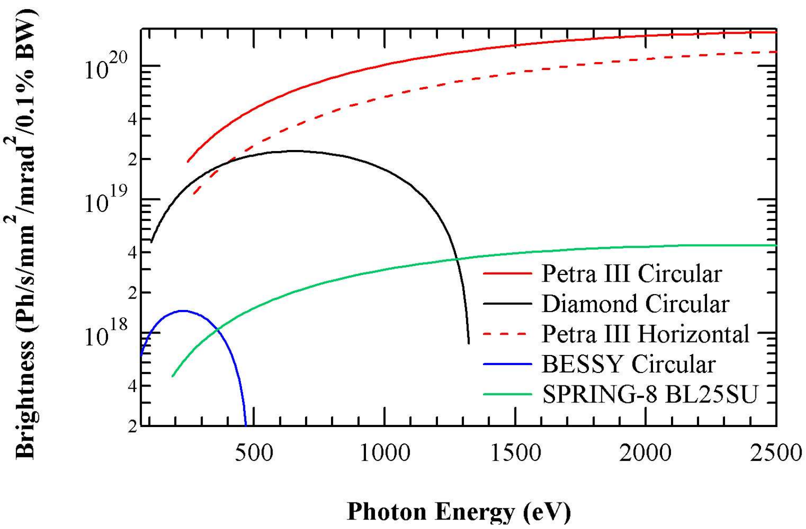

Figure 6.14.1: Brilliance of the first harmonic in the circular and linear mode at PETRA III and circular for the (double) U64 at Diamond, BL25U at SPring-8, and U56 at BESSY. The higher brightness compared to the SPring-8 beamline results from the larger number of undulator periods at the PETRA beamline and from the smaller emittance of PETRA.

6.14.2 Scientific applications of soft X-ray radiation with variable polarization

This section of the report contains contributions from the soft X-ray working groups with specialists in the following fields:

1. Gas phase studies on atoms, molecules, clusters and ions
2. Surface chemistry
3. Surface studies with soft X-ray spectromicroscopy

4. High resolution photoelectron spectroscopy in a wide energy range
5. Magnetic spectroscopy
6. Resonant soft X-ray scattering
7. Anomalous soft X-ray diffraction for spectroscopically-resolved structural studies

Despite the great diversity of the individual fields there is a unanimous consensus on the specification of the soft X-ray beamline at PETRA III described in the final section.

6.14.3 Gas phase studies on atoms, molecules, clusters and ions

Spectroscopic studies on atoms and molecules using photoionization and photoelectron spectroscopy have recently undergone dramatic changes. New synchrotron radiation light sources together with new experimental techniques have greatly enhanced the range of questions that can be answered (Becker & Shirley, 1996; Snell et al., 1996; Björneholm et al., 2000). One current theme is the problem of electron correlation in its various forms. Specific electron-electron interactions play a dominant role in a variety of many-body problems and determine fundamental quantities such as binding energies and partial cross sections. A thorough understanding of electron correlation in atomic and molecular systems provides a basis for understanding electron correlation in solids. While many aspects of the static electronic structure of atoms are well described by current theory, the understanding of dynamical processes in atoms and molecules is still in its infancy. This is even more true for ions, radicals and clusters, where experimental investigations have been seriously impeded by the low particle density. A high resolution, high flux soft X-ray beamline with variable polarization at PETRA III will be an important step forward for many studies in this field.

6.14.3.1 Photoionization and Auger decay in atoms and molecules

Studies of double Auger processes in rare gases will be important at the XUV beamline on PETRA III since they complement the current work on double photoionization. The long time-interval (192 ns bunch separation) between adjacent bunches will be a great advantage for such experiments using time-of-flight electron spectroscopy. With the new beamline it will be possible to study Auger decay from dissociating molecular systems. For these experiments both Doppler marking of the emitter atoms and resonance detuning as alternative methods to achieve time resolution on the scale of molecular dissociation and core-hole relaxation require a high photon energy resolution. Going to larger systems, e.g. the study of fullerenes, the relation between core-level photoelectron emission and subsequent fragmentation in coincidence experiments is of great importance. In these systems the connection between collective excitations, such as plasmons associated with core-level ionization, and multi-electron relaxation, for example double Auger decay (Viefhaus et al., 2004), remains to be investigated.

6.14.3.2 Ionization dynamics studied with multi-coincident techniques

Cold-target recoil ion momentum spectroscopy (COLTRIMS) is a novel momentum space imaging technique for the investigation of the dynamics of ionizing ion, electron or photon impact reactions with atoms or molecules. These studies yield kinematically complete pictures of the correlated motion of the fragment process for atoms and molecules with unprecedented resolution and completeness. Momentum space imaging of all ions and all electrons from photoionization and/or excitation is one of the most sensitive probes for molecular structure and chemical dynamics. With the high resolution of the photon source a highly selective excitation of the molecules can be achieved and imaging all the fragment momenta with multi-hit detectors allows the internal dynamics in the molecule after ionization/excitation to be determined. Kinematically complete measurements of single and double ionization by Compton scattering between 0.5 and 3 eV will give insight into the strength of non-dipole effects. Multi-coincidence studies offer a unique way to explore inner shell ionization of oriented small molecules (Jahnke et al., 2002; Landers et al., 2001). These studies need variable polarization and the time structure of PETRA III with a pulse separation on the order of 100 ns. The large separation is needed in order to correlate electrons and ions. As shown in Fig. 6.14.2, the angular distribution of photoelectrons is extremely sensitive to the shape of the intra molecular potential. With the help of multi-coincidences the dissociation dynamics and the multi-dimensional potential surface can be studied in great detail.

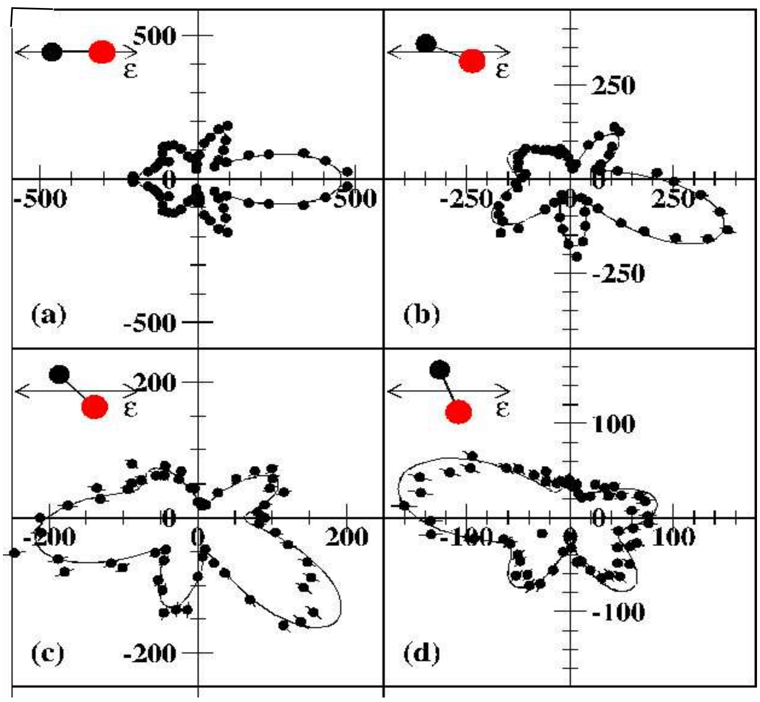

Figure 6.14.2: Angular dependence of electrons emitted from a core excited carbon atom in an oriented CO molecule (Landers et al., 2001).

6.14.3.3 Photoabsorption of free, mass-selected cluster ions

Research on clusters has become a very important and active field in recent years. Core-level spectroscopic studies on mass selected clusters have been limited until recently to small clusters deposited on surfaces. First measurements on free, mass-selected clusters with synchrotron radiation were performed by N. Berrah and coworkers on clusters with up to n=3 atoms at the B 1s ($\simeq 200eV$) edge and the Si 2p edge ($\simeq 100eV$) (Bilodeau et al., 2003). Photoionization studies at inner shell edges will combine for the first time element-specific excitation with cluster size selection. PETRA III will make it possible to perform experiments on free, mass-selected clusters of 3d, 4d and 4f transition metals in the whole XUV region from 50 eV up to 2500 eV exploiting resonances at the $L_{2,3}$ (3d), $M_{2,3}$, $M_{4,5}$ (4d), and $M_{4,5}$ (4f) edges.

6.14.3.4 Photon-ion merged-beams experiment

Data on ionic species are required in many areas, such as technical plasmas, atmospheric science and astrophysics. The study of matter in ionic form is a challenging experimental task. Intense third generation light sources have facilitated remarkable progress in the field of photoionization of ions (Schippers et al., 2003; Müller et al., 2003). Combining state-of-the-art particle sources with the brightest available photon beams will enhance the experimental capabilities. At present only total absorption cross sections can be measured on atomic ions and experiments on molecular and cluster ions are at the detection limit. At PETRA III an experimental set up is planned in which the intense X-ray photon beam interacts with an ion beam of about 2 mm diameter over a length of 1 m. The ideal photon beam would be parallel with a diameter of 1 to 2 mm. The ion beam is prepared in a small electrostatic accelerator with all the necessary mass analysis and beam transport systems so the photon-ion experiment should be an end station. The proposed experiment extends spectroscopic measurements to negatively or positively charged atoms, molecules and clusters. Suitable ion sources (e.g. ECR sources for multiply charged atomic ions or electro-spray sources for highly charged bio-molecules in the gas phase) will provide ions with high charge states and useful beam intensities.

6.14.3.5 Requirements for gas phase studies

A common feature of all gas phase experiments is the need for a photon flux of greater than 10^{12} photons/sec/0.1 %. For many experiments a bunch separation of at least 100 ns is needed since time-of-flight techniques are essential for coincidence experiments. The planned XUV beamline would cover the whole range of important inner-shell excitation and ionization of atoms, ions, molecules and clusters. It would be of great help for these experiments if there is overlap to lower photon energies. The carbon K-edge region is of scientific importance and it is necessary to calibrate the apparatus at well-known cross-sections and angular distributions in order to measure these quantities at higher, unexplored energies. For energies from 200–2400 eV circularly polarized light with a high degree of polarization and the possibility to switch easily between left-and right-handed radiation is required. This is particularly important because many experiments in the field of spin polarization and circular dichroism remain to be performed in the soft X-ray regime. A resolving power of better than 10^4 would serve most experiments with high resolution requirements. But there are experiments in the field of multi-coincidence where a lower resolution would be acceptable. Concerning the spot size the requirements are very different, they vary from 0.01- 0.1 mm in diameter depending on the type of experiment. The space requirements are more or less the same for most of the experiments, a square of $5\mathrm{m} \times 5\mathrm{m}$ is sufficient for the majority of experiments. The K-shell ionization studies on oriented molecules require variable linear polarization as well as circular polarization. All COLTRIMS experiments would profit from a focus of $100\mu\mathrm{m}$ times $100\mu\mathrm{m}$ or smaller. For experiments on clusters a flux larger than $5 \cdot 10^{12}$ photons/s at moderate resolution ($E/\Delta E > 2000$) is best. Lower energy storage rings (BESSY II, ELETTRA, ALS, MAX II) simply cannot compete with the photon flux that will be available at the XUV beamline on PETRA III running at 6 GeV. The experiment on free clusters will be a part of the free ion experiments. Therefore, a 0.5-1 m section with a collimated beam will be needed. The cluster sources will need approx. $1.5 \times 3.0\ m^2$ floor space without electronic equipment. For the experiments on ions there are special requirements: The space, power and cooling requirements can be characterized by typical numbers for existing laboratory setups of similar nature: Area (including control racks, work place, space to access the hardware, etc.): 10m x 8m, Electrical Power: 250 kW, Cooling Water: 180 kW cooling power (high pressure circuit 10 bar for high-power electron-cyclotron-resonance heated -ECR- ion source, low pressure circuit with e.g. 4 bar for pumps, power supplies etc.)

6.14.4 Surface chemistry

Surface chemistry deals mainly with the gas-surface interactions observed in processes relevant to heterogeneous catalysis. Given the complexity of real catalysts, studies are frequently performed on model systems using well-defined single crystal surfaces. Due to the rather long acquisition time of most spectroscopic techniques in surface science, such studies are performed on an ex-situ basis, i.e. after a certain reaction step has been finished. Dynamical processes and parameters, such as adsorption or reaction rates, are not readily available from these experiments which only give integrated results. The use of high-intensity and high-resolution synchrotron radiation has enabled a new quality of research in surface chemistry. Both time-dependent X-ray photoelectron spectroscopy (XPS) (Baraldi et al., 2003; Denecke et al., 2002; Kinne et al., 2002) and time-dependent X-ray absorption (quick extended X-ray absorption fine structure, QEXAFS) (Frahm, 1988; Frahm, 1989b) became available on second and sub-second time scales, allowing in-situ studies on realistic macroscopic time scales (a few ms). The PETRA III upgrade and the planned XUV beamline would substantially enhance the possibilities of these approaches. A main shortcoming of present facilities like BESSY II or MAX-lab is the limited flux and resolution at higher photon energies which are necessary to study deeper core-levels and absorption edges, such as the 2p levels of metals (Cu, Ni) in more detail and also in a time-dependent fashion. This would open up new options to study adsorption and reaction processes on surfaces by monitoring the substrate levels. High-resolution time-dependent studies on dynamic processes at surfaces will become possible with PETRA III. Together with an improved experimental system, which includes a pulsed molecular beam source for gas dosing and multichannel detection for the photoelectrons, highly resolved XPS with measurement times of less than 1 ms per spectrum will be possible. If this is accompanied by a high spectral resolution (even at higher photon energies), the usable temperature range to study activated processes, such as surface reactions, can be expanded to higher temperatures where reactions occur on shorter time scales. The subsequent Arrhenius analysis would be much more reliable and informative, especially in the determination of the pre-exponential factors, which show the largest uncertainties today. In addition, for most reaction systems a significant increase in temperature would bring this important parameter closer to realistic process conditions.

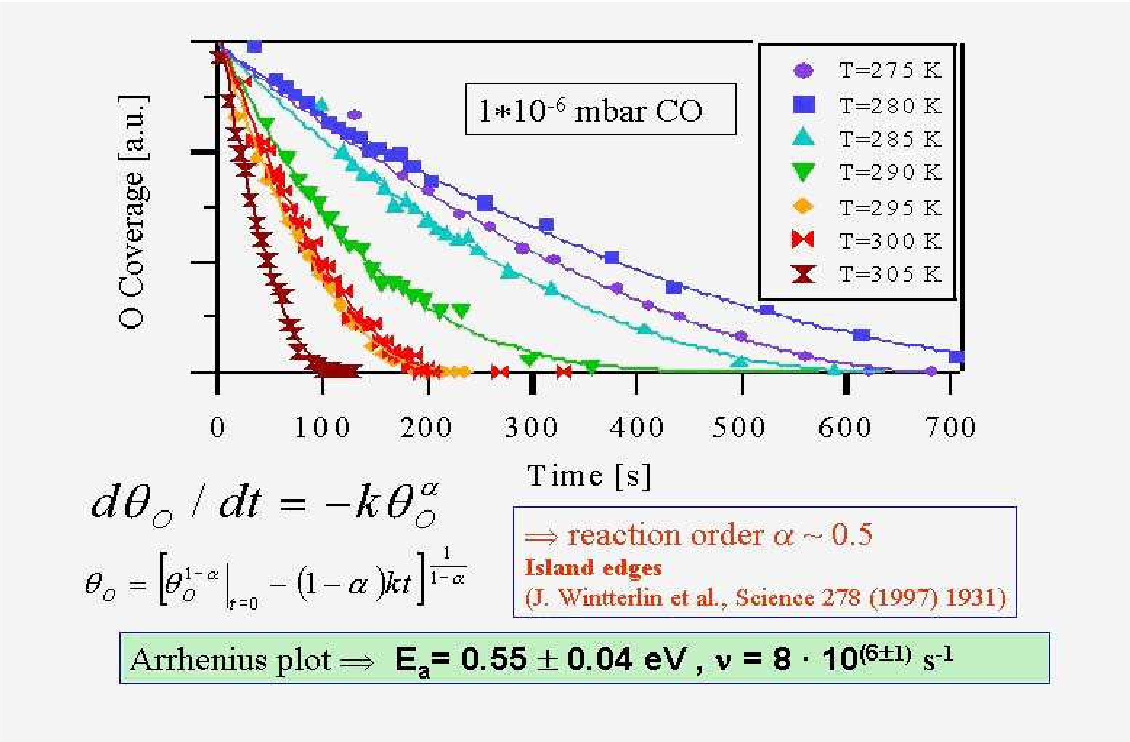

Figure 6.14.3: Time dependence of oxygen coverage for CO oxidation on Pt(111)

Fig. 6.14.3 shows the results of a study of the CO oxidation on Pt(111) recently obtained at BESSY II (Kinne et al., 2004). Here, the decay of the O 1s signal of preadsorbed atomic oxygen with reaction time is studied for various sample temperatures in presence of a CO gas phase. The data analysis yields the activation energy of the reaction between CO and atomic O. Due to the limited time-resolution the reaction temperatures have to be kept below 305 K. With higher photon flux (and an improved detection system) this range could be increased to more than 470 K. In addition, due to the higher photon energies, substrate core-level shifts for a large number of different substrates can be used to identify adsorbate sites. On the other hand, short-lived intermediate species (transition states in reactions) could be detected, which are not seen on longer time scales. The spectroscopic identification of intermediate species is crucial for the improvement of theoretical calculations depending on these transition states. Another technique would be time-dependent QEXAFS measurements which can already be performed at sub-second time scales in the hard X-ray region (Frahm, 1989b). Similar measurements are feasible in the XUV region and will open up new fields of research provided fast scanning of the monochromator and undulator are implemented. QEXAFS can give information about orientational changes of molecules on surfaces taking place during reactions. Studying magnetic dichroism in adsorbate systems is a rather new field (May et al., 1996; Yokoyama et al., 2000). Both the influence of magnetism on adsorption and reaction as well as the influence of adsorption on the magnetic properties of various systems are of great interest, since a large number of metals used for catalysis are magnetic. Measuring magnetic circular dichroism in X-ray absorption (XMCD) or in photoemission (magnetic circular dichroism in angular distribution, MCDAD) gives information about the magnetic moments of the respective entities. Photo-induced surface reactions will be another interesting field which requires a high photon fluxes. By comparing the flux dependent product distributions excitation mechanisms could be resolved.

6.14.4.1 Experimental requirements for surface chemistry

The energy range needs to start at around 100 eV and extend up to about 2500 eV. High resolution together with high flux, especially at higher energies, is more important than the highest photon energies. An ultimate resolution of better than 100 meV at 1000 eV ($E/\Delta E > 10000$) would be desirable, possibly extending to even higher energies (up to 1500 eV). If no spatially resolved microscopy with scanned light spot is considered and if usual sample sizes of diameters of some millimeters are used, the spot size need not be much smaller than $500\mu\mathrm{m}$. For some applications, like diffusion measurements a small light spot of some $50\mu\mathrm{m}$ would be desirable. The best solution would be a variable spot size, achieved with bendable refocusing mirrors. The photon flux needs to be high, but the situation has to be adaptable to the systems studied. Some adsorbate systems are very sensitive to radiation damage. A photon flux on the sample of about $10^{12} - 10^{13}$ photons per second in a medium size ($100\mu\mathrm{m}$) is required. Variable polarization will permit symmetry selection rules and matrix element effects to be exploited in photoemission with linearly polarized light and permit dichroism experiments using circularly polarized light.

6.14.5 Surface studies with soft X-ray spectromicroscopy

Spectromicroscopy combines the power of spectroscopic analysis to determine chemical composition and bonding configurations with imaging techniques to reveal the sample morphology and provide magnified pictures of the sample (Susini et al., 2002). The strength of the method is that it provides information simultaneously in both the spatial and spectral domains. Future technologies will rely on our ability to accurately measure, analyze, and characterize the complex multicomponent systems used in semiconductor devices, industrial catalysts, polymeric systems, and even health care products. The currently planned activities in the field of nanotechnology exemplify the demand for spectromicroscopy to satisfy the common needs of the diverse disciplines involved in this new endeavor. Over the past decade our knowledge of the chemical bonding, electronic structure and vibronic properties of a multitude of systems have been greatly enhanced using high resolution spectroscopies with synchrotron radiation. These studies have been performed on representative macroscopic samples because the brilliance of existing synchrotron light sources is insufficient to obtain simultaneous high spatial and high spectral resolution. Next generation light sources such as PETRA III will change this situation and will open up the field of high resolution spectroscopy on microscopic sample volumes. For the first time it will be possible to investigate laterally structured functional materials with high-resolution electron spectroscopies using synchrotron radiation.

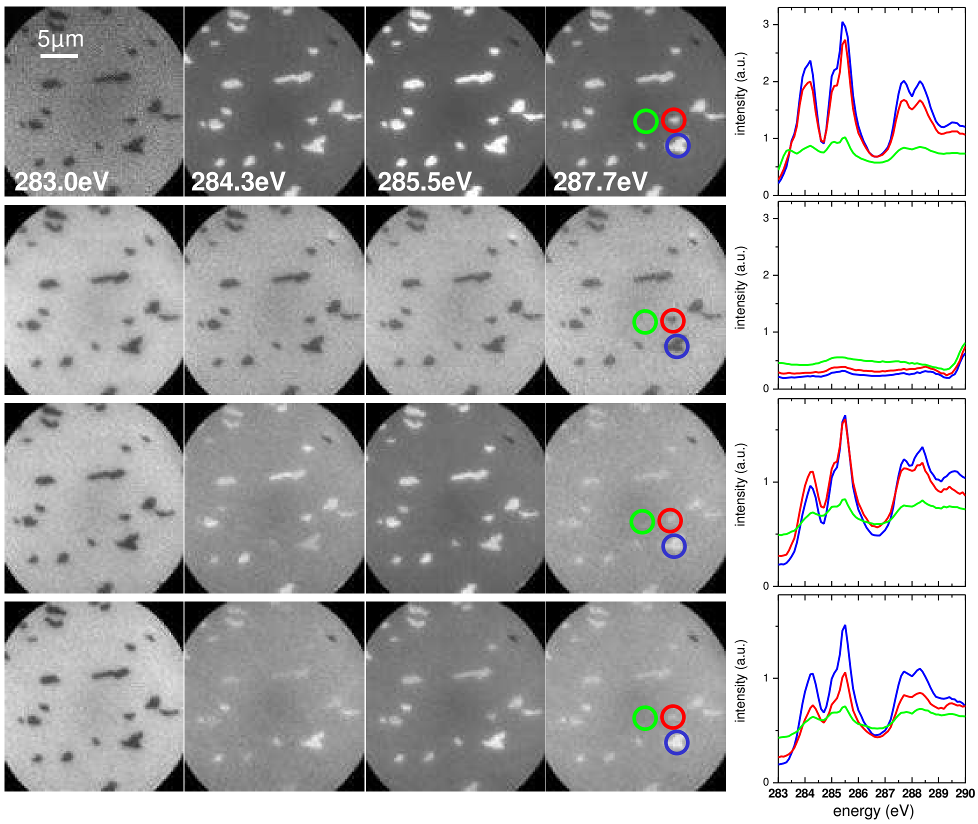

Figure 6.14.4: Polarization-dependent NEXAFS-PEEM images near the C 1s edge from a 5 ML PTCDA film on Ag(111) consisting of islands on top of a bilayer. Row 1 – linear polarization at 70°; row 2 – linear polarization parallel to the surface; row 3 and row 4 left- and right circular polarization. The spectra on the right were recorded from the marked areas corresponding to the bilayer (green) and two different types of islands (red and blue).

Modern high performance materials and devices are intrinsically heterogeneous on length scales ranging from nanometers to micrometers. Silicon semiconductor technology relies on the fantastic chemical purity and crystalline perfection of the initial silicon single crystals yet the microprocessors and memory chips that come off the production line are highly complex nanostructures. Similar demands for spatially-resolved chemical and compositional analysis are found in many industries and applications for spectromicroscopy are envisaged on magnetic materials, polymers, biomaterials, chemical composites and in environmental analysis.

Spectromicroscopy on magnetic materials is particularly interesting to simultaneously image domain structures and reveal whether the magnetic order is compensated or uncompensated using magnetic circular and linear dichroism with polarized light. Light in the soft X-ray region is strongly absorbed by matter and practically all elements have characteristic electron energy levels (absorption edges) that provide unique chemical analysis and in addition reveal the bonding configuration. Fig. 6.14.4 shows the type of information that can been obtained with PEEM spectroscopy at the carbon K-edge. The angular dependence observed with linearly polarized light proves that the PTCDA molecules lie parallel to the substrate. The measurements with right- and left circular polarized light reveal that individual 3D PCTDA islands yield a large dichroic signal of $\pm 15\%$, whereas the bilayers exhibit no dichroism. The dichroic signal from the islands can be either positive or negative which means that spatial resolution is essential to be able to quantify such effects (Schmidt, 2003). By recording the energy and momentum of the emitted photoelectrons a direct determination of the occupied electronic band structure of crystalline samples can be performed.
Undulators that provide variable polarization will revolutionize spectroscopy in the soft X-ray region. The provision of circular, elliptical and variable linear polarization from horizontal to vertical is particularly exciting for spectromicroscopy. Variable linear polarization enables the full dielectric tensor describing the interaction of the electromagnetic radiation with the sample to be determined. Samples that exhibit linear dichroism have very different polarization-dependent absorption spectra due to the orientation of the different bonding orbitals. For angle-resolved photoemission experiments the full polarization control allows a precise determination of the symmetry of the initial states involved in the optical excitation process. User control of both the photon energy and polarization from the undulator places special demands on the orbit stabilization in the storage ring and requires feedback and fast feed-forward control systems.

6.14.5.1 Requirements for spectromicroscopy

Spectromicroscopy experiments demand stringent beam stability so the possibility of varying the source polarization with a fixed experimental geometry is particularly attractive and will enable a variety of new experiments. The energy range of the soft X-ray beamline is a key consideration particular with respect to the variable polarization capabilities of the undulator. From a spectroscopic point of view the spectral region must cover the energy range from 100 eV to 1500 eV to include the K shells of all the light elements and the L shells of the transition metals. The lower limit should include the Si 2p core level at 99 eV. A particularly exciting possibility is high resolution spectroscopy at the sulfur K-edge (2.5 keV). Sulfur is of central importance in a wide range of chemical, pharmaceutical and industrial processes. The combination of chemical analysis, imaging and high-resolution spectroscopy is clearly very attractive, but extremely demanding on the brilliance of the light source. Several spectromicroscopy projects using photoelectron emission microscopes (PEEM) have been initiated around the world. Probably the most ambitious project is the SMART instrument being developed by a consortium coordinated by T. Schmidt and E. Umbach at Würzburg University shown in Fig. 6.14.5 (Schmidt et al., 2003).
The instrument has a highly optimized electron optical system incorporating higher-order

aberration corrections and a high performance OMEGA energy filter. It is currently in the test phase and it will certainly set the standards for spatial resolution and transmission by which other systems will be measured. The spatial resolution will be less than 2 nm with an energy resolution of the imaged electrons below 100 meV. (The theoretical limits are significantly better with a spatial resolution of 0.5 nm). The optimization and aberration correction enhance the transmission by a factor from 50 to 1000 compared to conventional PEEM systems. The combination of the new PETRA III undulator with its variable polarization capabilities with a SMART-type instrument will represent the state-of-the-art for high spatial resolution spectromicroscopy with polarization analysis.

6.14.5.2 Specification of the beamline

Photon flux at the sample; 10^{12} photons/s in an illuminated area of $10\mu\mathrm{m} \times 10\mu\mathrm{m}$ to achieve a spatial resolution better than 10 nm. Polarization variable linear and circular (both helicities); photon energy range from 100 to 1500 eV. Photon energy resolution below 100 meV since the energy resolution of the OMEGA Filter is below 100 meV. The influence of the time structure in ns-ps range has not yet been investigated, but it would be interesting to investigate reaction and diffusion processes on surfaces in real time.

6.14.6 High-resolution photoelectron spectroscopy in a wide energy range

High resolution electron spectroscopies provide direct information about the chemical bonding and electronic structure of surfaces and interfaces of complex new materials. The ma-

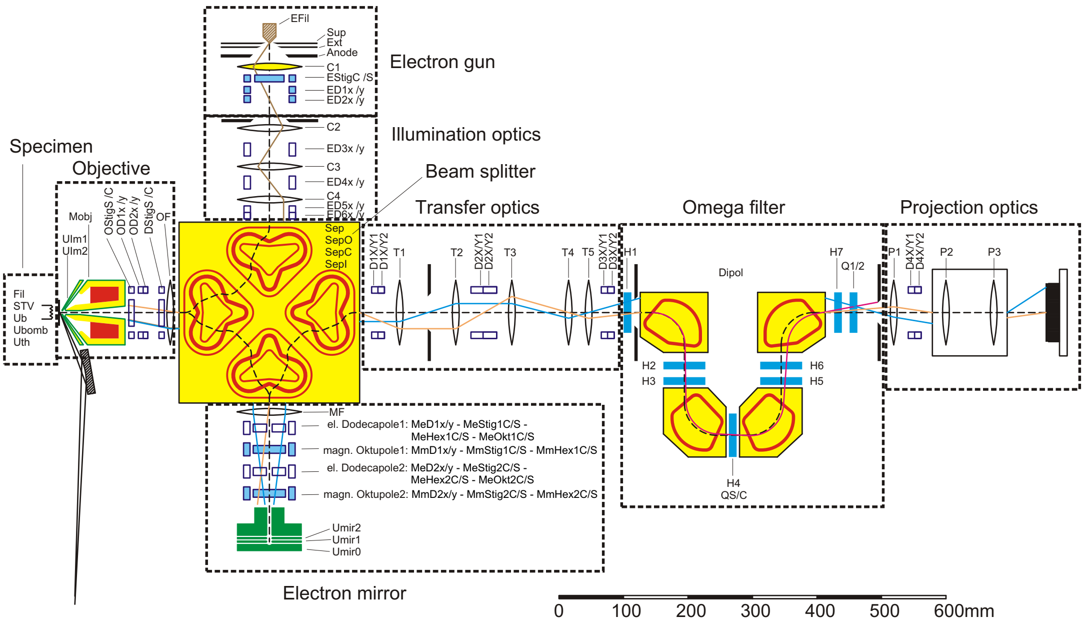

Figure 6.14.5: Schematic of the SMART Instrument (Wichtendahl et al., 1998; Schmidt et al., 2003)

jority of existing beamlines only provide a narrow photon energy range either for studying valence bands or core levels and absorption edges. At PETRA III it will be possible to achieve high flux and spectral resolution over a wide range of photon energies permitting investigations on a single sample with a variety of high resolution spectroscopic techniques.

6.14.6.1 Bulk and surface sensitive momentum-resolved photoemission

Photon energies between 10 and 100 eV are frequently used to directly measure the momentum-resolved electronic band structure of solids with angle-resolved photoelectron spectroscopy. The technique is extremely surface sensitive because of the low kinetic energy of the emitted photoelectrons. For kinetic energies above 1 keV the information depth is no longer restricted to the topmost surface layers and photoemission becomes more bulk sensitive (Sekiyama et al., 2000; Saitoh et al., 1998). With high resolution state of the art electron spectrometers momentum resolved simultaneous investigations of both the surface and bulk electronic structure of materials become feasible. First results indicate that in many materials there are significant differences between bulk and surface sensitive data (see e.g. Refs (Irizawa et al., 2002; Iwasaki et al., 2000).

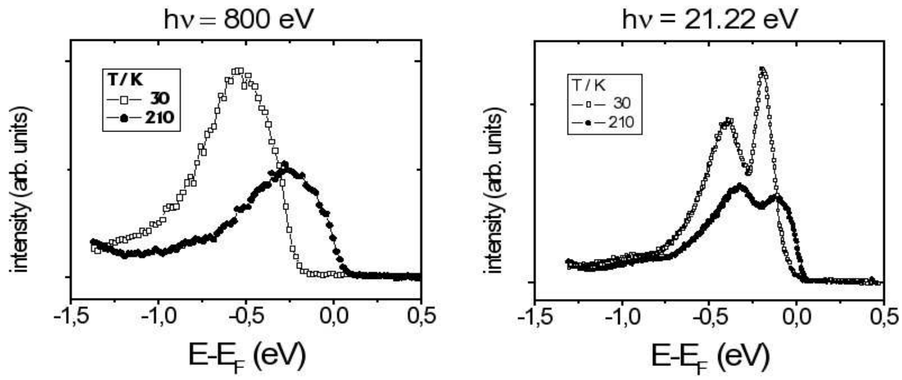

Figure 6.14.6: Angle resolved photoemission spectra of TaS_2 showing the opening of the charge density wave gap upon cooling. Left: Bulk sensitive ($h\nu$=800 eV) and right: surface sensitive ($h\nu$=21.2 eV) spectra.

Fig. 6.14.6 shows bulk- (left) and surface- (right) sensitive spectra of the charge density wave (CDW) gap of 1T-TaS_2 recorded with photon energies of 800 and 21.2 eV. For the bulk sensitive spectra a large gap of about 250 meV is evident while at the surface only a relatively small pseudo gap is observed. This example demonstrates the importance of performing bulk *and* surface sensitive measurements on the same sample. It is worth noting that the high angle resolution of current electron spectrometers permit momentum-resolved bulk electronic structure measurements even at photon energies above 1 keV.

It should be mentioned here that over 90% of the experimental photoemission data on high-temperature superconductors have been recorded with extremely high surface sensitivity at photon energies well below 100 eV. Due to large lattice constants in direction perpendicular to the cleavage planes of these materials not even one complete unit cell is accessed in a standard photoemission experiment. To investigate the changes in the electronic structure with sampling depth a high performance soft X-ray beamline covering a photon energy range from $\sim$ 100 eV up to 2 keV is required.

The ongoing miniaturization of electronic devices means that their performance is increasingly determined by surface and interface effects. It is thus extremely important to be able to tune the information depth of the spectroscopic technique on individual samples in situ.

6.14.6.2 Requirements

A high resolution electron spectrometer in conjunction with a wide energy range, high flux, high brilliance XUV beamline is required. Much progress has been achieved on the electron spectrometer side, but a high resolution XUV beamline covering a photon energy range from 100 eV up to 2 keV in the first harmonic with linear and circular polarization capabilities is still lacking. The circular polarization available over a wide photon energy range will be extremely interesting for studying magnetic interfaces. High flux and brilliance are required to obtain a high resolution focused monochromatic beam with spot sizes in the range of several microns in order to measure small samples, individual domains and microstructures. The proposed beamline will extend the applicability of high-resolution photoemission to laterally nanostructured samples by exploiting microfocusing and will also provide depth information via photon energy tunability.

6.14.7 Magnetic spectroscopy

Magnetic properties of nanoparticles and low-dimensional metallic systems are currently of great interest for high density magnetic data storage, magnetic memories and sensors. Small metallic nanoclusters, i.e. agglomerates with a well-defined number of atoms, are especially promising. For isolated clusters it has been shown that they have magnetic properties that differ both from those of the constituent atoms and from the corresponding bulk material. Since quantum size effects play an important role in small clusters particular properties can be tailored by deliberately choosing a specific particle size. Soft X-ray spectroscopic techniques are ideal for investigating magnetism in small particles in a local element-specific way. The undulator beamlines at third generation synchrotron facilities have demonstrated the strengths of polarization-dependent measurements to determine independently the local atom-specific spin and orbital moments. The variable polarization soft X-ray beamline at PETRA III will provide unique opportunities for X-ray magnetic circular dichroism (XMCD) measurements because the energy range covers all the important transition metal edges. The unprecedented photon flux will permit studies on highly diluted magnetic systems. Using XMCD the magnetic structure of thin layers can be studied layer by layer. Magnetization studies on the PETRA III XUV beamline will include the investigation of magnetic nanostructures, X-ray microscopy, and the study of magnetization dynamics.

6.14.7.1 Magnetism in nanostructures

Due to the low coverages of the samples most XMCD experiments on magnetic nanostructures have employed photoabsorption to investigate the unoccupied states. Using sum rules, spin and orbital moments of the nanostructures can be obtained and it has been shown that the magnetic properties are strongly size depended (Lau et al., 2002). Fig. 6.14.7 shows the ratio of orbital and spin moments for small and large Fe clusters deposited on a thin Ni-film (Lau et al., 2002; Edmonds et al., 1999; Kleibert et al., 2003); small Fe clusters exhibit a strong variation of the ratio and a strongly enhanced orbital moment.

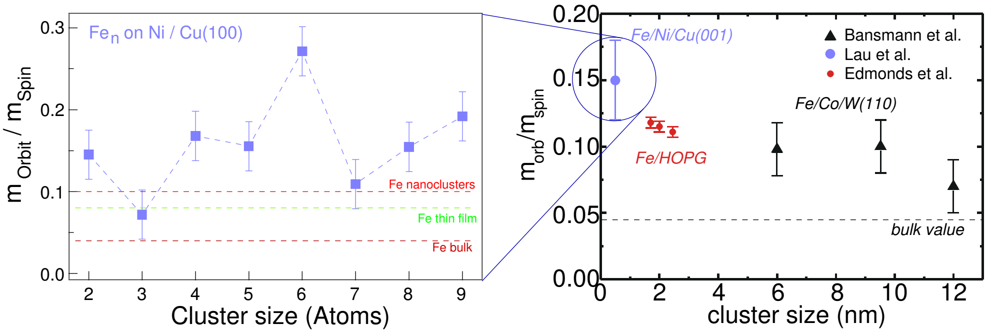

Figure 6.14.7: Size dependence of the ratio of orbital and spin moments for small (Lau et al., 2002) and large (Edmonds et al., 1999; Kleibert et al., 2003) Fe clusters deposited on a thin Ni film.

There is little experimental data available on the magnetic properties of nanostructures. In future experiments on deposited nanostructure and clusters with sizes ranging from a few atoms to several thousand atoms are necessary. Investigations of the occupied and unoccupied electronic states using both photoemission and fluorescence spectroscopy will be performed on the XUV-beamline at PETRA III. Measuring the X-ray fluorescence has the big advantage that the experiments can be performed in high magnetic fields.

6.14.7.2 Requirements

Because of the low fluorescence yield in the XUV region a large photon flux $> 5 \cdot 10^{12}$ photons/s is needed. The spot size at the sample should be from 0.1×0.1 to $1 \times 1\,\mathrm{mm}^2$. The energy resolution should be around 100 meV or better at the L-edges of 3d elements (400-900 eV). The experimental equipment is usually quite large, so a floor space of at least $2\mathrm{m} \times 4\mathrm{m}$ is needed for the experiment (without electronics).

6.14.7.3 Microscopy and magnetization dynamics

The high contrast and the element specificity of XMCD can be used for magnetic transmission X-ray microscopy (M-TXM) on nanostructures. Fig. 6.14.8 shows as an example the magnetization of a small circular dot. Using the pulsed time structure of the synchrotron in this experiment the spin dynamics of the vortex structure was studied using M-TXM and a pump-probe technique (Fischer et al., 2003). A major advantage of the photon based M-TXM technique is the potential to record domain structures in applied external magnetic fields. Imaging can be performed in transmission or using the reflected intensity. Although the signal in reflection is much smaller than the transmitted intensity the flipping ratio, which determines the contrast, is just as high (Geissler et al., 2002) and in addition the lateral distribution of the magnetic roughness at surfaces and interfaces can be investigated. The future potential to be exploited by M-TXM is magnetic microspectroscopy to address the lateral distributions of spin and orbital moments on a sub-10nm length scale and achieve complete information on the spatio-temporal magnetization behavior in low-dimensional systems.

6.14.7.4 Requirements

For these experiments the time structure of the storage ring is important. The ring should run in a few bunch mode with $t = 200 - 300$ ns between the electron bunches. The length of the light pulse should be in the order of $10 - 30$ ps.

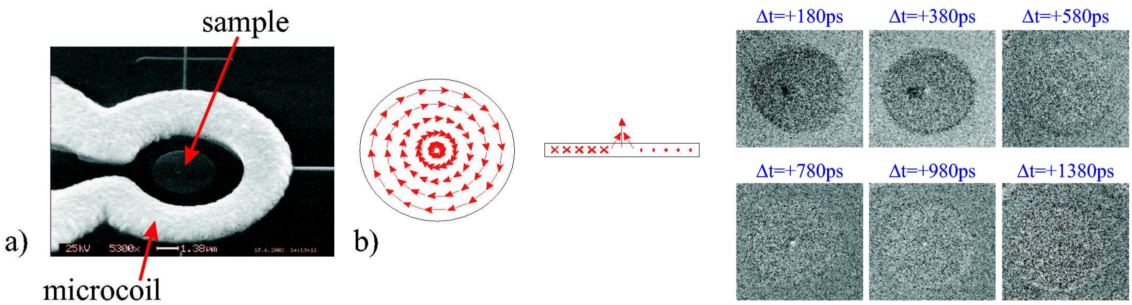

Figure 6.14.8: Microscopy and magnetization dynamic of nanostructures on a ps timescale.

6.14.8 Resonant soft X-ray scattering

Soft X-ray emission (SXE) spectroscopy has several advantages over competing techniques for studying the dynamics and electronic structure of matter. To exploit these advantages very high brilliance soft X-ray sources are required and SXE spectroscopy has recently undergone a renaissance at third generation synchrotron radiation sources. However, the flux at presently available beamlines is the limiting factor, making both counting statistics and the energy resolution inferior to what can be reached in electron spectroscopy. Increasing the spectral resolution is especially valuable, because the absorption-emission event constitutes a resonant inelastic scattering (RIXS) process, where the lifetime broadening of the core-hole state does not contribute to the spectral broadening; hence, the information inherent in the spectra is only limited by the instrumental resolution. The resolution can be improved significantly with the high brilliance of the soft X-ray beamline on PETRA III.
The energy region 1-2.5 keV is comparatively unexplored and very few resonant X-ray scattering experiments have been performed to date. The K-edges of Na, Mg, Al, Si, P, S, the

L-edges of Zn, Ga, Ge, As, Se, Br and the L-edges of the early 4d elements all lie in this energy range. These elements are particularly important for semiconductor technology and are key constituents in many novel correlated materials with unusual superconducting and magnetic properties. This energy range has been little exploited due to the lack of sources with appropriate brilliance, and to some extent also by the erroneous presumption that the core hole lifetime width would smear out the spectral features. The soft X-ray beamline on PETRA III will open the door to this 'new' energy range, where RIXS experiments have enormous potential.
Important features of RIXS include (Kotani & Shin, 2001):

- *Large photon penetration lengths* -True bulk properties are probed. This is especially important in complex materials with large unit cells, and in non-conducting samples where charging effects render electron spectroscopy difficult. Semiconductor (nano)structures, impurities, interfaces, magnetic (nano)structures and buried structures can be probed in a non-destructive way. -Liquids can be studied (separated from UHV by thin windows). Recent results reveal new important information about liquid water (Guo et al., 2002), and hydrogen bonded solutions (Guo et al., 2003). This is a new field with applications in electrochemistry, environmental science, pharmacy and biochemistry. - Gas-phase samples can also be studied using thin window cells and this is of importance for exploring fundamental aspects of the scattering process.

- *Independence of external fields* Since the photons are not perturbed by external magnetic and electric fields, any spectral field-dependence can be directly related to the physical process under investigation.

- *Local electronic properties* Transitions to localized states reveal the density of electronic states at specific local atomic sites. The data from various edges in complex materials are complementary and together can give a detailed picture of the electronic structure.

- *Dipole selection rules* Dipole transitions are sensitive to angular momentum symmetry and orbital geometry. This can be further exploited if the incoming radiation has a well-defined and variable polarization state. Dichroic effects are particularly important in studies of magnetic systems.

- *k-resolution* Momentum conservation in the scattering process makes band mapping feasible. This will become increasingly important in the range above 1 keV, where the momentum transfer in the scattering process is far from zero: Scattering at variable and controlled momentum transfer can be studied.

- *Femtosecond dynamics* The intermediates core hole states have lifetimes on the order of femtoseconds. Any rearrangement on the same time scale is reflected in the spectra. The lifetimes generally become shorter with increasing binding energy, making the 1-2.5 keV energy range particularly interesting.

Resonant elastic scattering in the soft X-ray range has recently been used to identify the spectral features corresponding to various local electronic states in complex compounds and

the geometrical distribution of the states were determined from accurate measurements of the angular dependence of the elastic cross section. Resonant elastic scattering at the oxygen K edge has been used to measure the distribution of doped holes in several cuprate superconductors (Abbamonte et al., 2002). This method has great potential, which can be further exploited at the soft X-ray beamline on PETRA III.
In addition, the large energy-range available at such a beamline would facilitate completely new types of experiments. For the first time it would be possible to measure anisotropic EXAFS in the Raman mode (Gel'mukhanov, Plashkevych & Ågren, 2001), a method that can yield bond-lengths and bond angles in non-ordered samples. For this the tunability over a large energy range and polarization control are crucial.

6.14.8.1 Requirements

For most of these experiments it is very important that the brilliance of the beam can be fully exploited to achieve a high flux of photons with controllable energy and polarization state, in a small spot on the sample. The end-station must be equipped with a refocusing optics that gives a spot size of less than 0.1 mm in diameter. For the spectral analysis a grating spectrometer for the energy range below 1 keV, and crystal spectrometer for the 1-2.5 keV energy range is needed. There are standard instruments designs available which can be adapted. For elastic scattering, k-resolved inelastic scattering, and dichroism experiments, the sample and detector must be able to rotate with high precision around an axis perpendicular to the primary beam.
The heart of the set-up will be a refocusing optics which can focus on the sample to be analyzed in a grating spectrometer, covering the energy range below 1 keV, or direct the beam onto a sample to be analyzed in a crystal spectrometer (1-2.5 keV). As the polarization direction can be varied the spectrometers do not have to rotate around the beam (as is common today). Instead a rotation around an axis perpendicular to the beam is necessary for elastic scattering, k-resolved inelastic scattering, and dichroism experiments. In addition the usual sample preparation equipment is needed, including arrangements for heating, cooling and application of external fields. Moreover, it must be possible to accommodate cells for liquid and gas-phase studies, with associated differential pumping.

6.14.9 Anomalous soft X-ray diffraction for spectroscopically-resolved structural studies

Recent theoretical and experimental studies on doped strongly correlated insulators (Birgenau & Kastner, 2000; Tokura & Nagaosa, 2000; Orenstein & Millis, 2000; Khomskii & Sawatzky, 1997) have demonstrated that the intriguing material properties are due to the strong interplay between spin, orbital, and charge degrees of freedom (Khomskii & Sawatzky, 1997) leading to the formation of new superstructures in the crystal. At length scales of 1-30 nanometers, new phenomena like orbital ordering and phase separation can occur. For example, the existence of phase separation and stripes in nickelates and high-T_c cuprates was predicted theoretically (Zaanen & Gunnarsson, 1989) and confirmed experimentally (Tranquada et al., 1994; Tranquada et al., 1995) as illustrated in Fig. 6.14.9.

These examples strongly suggest that atomic and electronic ordering on a nanometer scale are quite common in doped strongly correlated systems and that such phenomena may govern the unusual low energy properties of the materials. Anomalous soft X-ray diffraction is a unique tool for studying such ordering phenomena since a dramatic enhancement of Bragg peaks is observed when scanning through the relevant inner-shell absorption edges. This technique can be used for the study of magnetic films (Dürr et al., 1999). The excitation is highly sensitive to the oxidation state, orbital occupation and spin state of the ions (Castleton & Altarelli, 2000; Wilkins et al., 2003a; Wilkins et al., 2003b). The assignment of multiplet components to particular electronic states is well established and provides the basis for the interpretation of the experimental data. The period of the ordered phases is usually larger than the lattice constant and matches nicely the wavelength of soft X-ray photons. The resonant enhancement of the scattering cross section for inner-shell excitation is extremely large: An enhancement of six orders of magnitude at the M_5 resonance observed in Ho metal makes feasible investigations of ultra-thin films that are not possible at conventional X-ray energies (Schüßler-Langeheine et al., 2001). Resonant soft X-ray diffraction will greatly advance the understanding of order/disorder phenomena in correlated-electron systems. The energy-dependence of the scattering cross section provides insight into the ordering mechanism (Castleton & Altarelli, 2000).

6.14.9.1 Requirements

The energy range required for such experiments is 250 eV up to 2500 eV, covering the carbon, nitrogen and oxygen K, the transition-metal $L_{2,3}$ and the lanthanide $M_{4,5}$ resonances. To make use of the strong polarization dependence of the scattering cross section, the undulator should provide variable circular and linear polarization. A well focussed beam with a spot size on the sample not larger than 0.05 x 0.05 mm^2 is needed to study inhomogeneous samples.

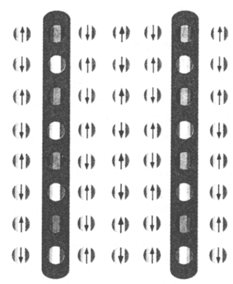

Figure 6.14.9: Stripe ordering in a CuO_2 lattice. Charge is largely confined in the dark regions; the arrows indicate the orientation of the magnetic moment. The stripe is an antiphase boundary of the antiferromagnetic order. Oxygen ions are not shown (from Ref. (Orenstein & Millis, 2000).

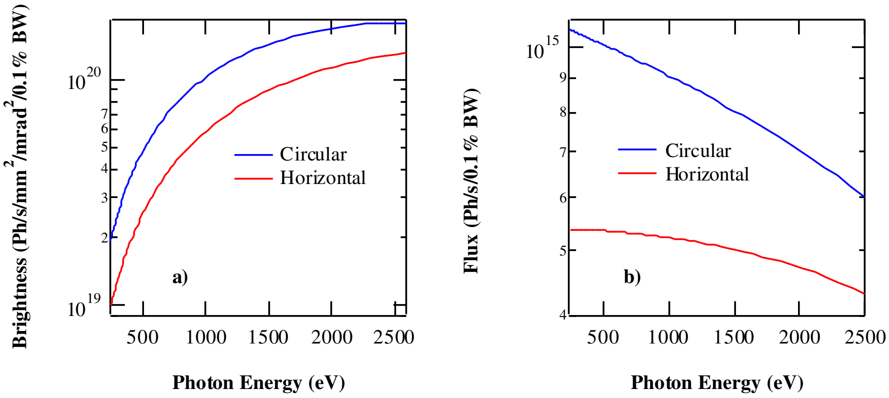

Figure 6.14.10: a) Brilliance and b) flux of the APPLE II insertion device for circular and horizontal polarizations.

6.14.10 Beamline description

The 6 GeV energy of PETRA III and its very low emittance of 1 nm rad makes it an excellent source for a very high resolution and high flux beamline optimized for the energy range 250–2500 eV.

The source for the proposed beamline is a 5m APPLE II device (Sasaki, 1994) with a magnetic period of 63 mm. This device generates 100% horizontally polarized and circular polarized light in the first harmonic over the full energy range of the beamline. In the vertically polarized mode, the lowest photon energy in the first harmonic is 470 eV. The brightness and flux emitted by the insertion device in the first harmonic for circular and linearly polarized radiation are shown in Fig. 6.14.10a and Fig. 6.14.10b. The excellent performance can only be achieved with a full length undulator (5 m, 80 periods, or two 2 m undulator segments, see Sec. 4.1.6) because the brilliance at a side station is approximately five times lower.

A schematic drawing of the beamline is shown in Fig. 6.14.11. The monochromator is basically a collimated PGM developed at BESSY (Follath, Senf & Gudat, 1998) and in use at the ALS (Warwick et al., 2003) and the SLS (Flechsig, Patthey & Quitmann, 2001). The first optical element is a cylindrical mirror collimating the photon beam in the vertical (dispersive) direction and deflecting it horizontally by 2°. The use of a cylindrical mirror instead of a toroid provides a larger demagnification in the horizontal direction. The next optical element is a plane mirror that diverts the central ray to the grating pole.

To achieve a higher reflectivity in its tuning range, the angle of incidence on the mirror is chosen to be $(\alpha - \beta)/(2 + 0.5)$, where α is the angle of incidence on the grating and $\beta(< 0)$ is the angle of diffraction. The angle between the central ray of the selected energy after the grating and the beam incident on the plane mirror is $0.5°$. A toroidal mirror, diverting the beam horizontally by 2°, focuses in both the horizontal and vertical directions onto the exit slit. The final focusing at the sample position is achieved with two plane elliptical mirrors arranged in a Kirkpatrick-Baez (KB) configuration. To achieve a larger demagnification in the horizontal direction, the first mirror in the KB pair focuses in the vertical direction and the second in the horizontal direction. The total demagnification in the horizontal direction is a factor 28.

The monochromator "resolving power", calculated with a 1200 l/mm grating, an exit slit width of $10\ \mu\mathrm{m}$, and a c value of the monochromator $(\cos(\beta)/\cos(\alpha))$ of 2.2, is given in Fig. 6.14.12. Slope errors of 0.05" were assumed on the illuminated area of the plane mirror and on the grating and 0.5" along the sagittal direction in the cylindrical mirror and the toroid. The limiting contribution to the resolving power at low photon energies is the astigmatic coma of the toroid and at high photon energies, in decreasing importance, the contribution from the exit slit, figure errors on the grating, and figure errors on the plane mirror. As seen in the figure, a resolving power greater than 10000 can be achieved up to 2320 eV. A higher resolving power could be obtained in the high-energy range if the monochromator were operated with higher c values, as shown in Fig. 6.14.12.

Fig. 6.14.13 shows ray traces at the exit slit plane for 400 and 400.02 eV when the monochromator is tuned to 400 eV and $c = 2.2$. The optical elements were assumed to have the figure

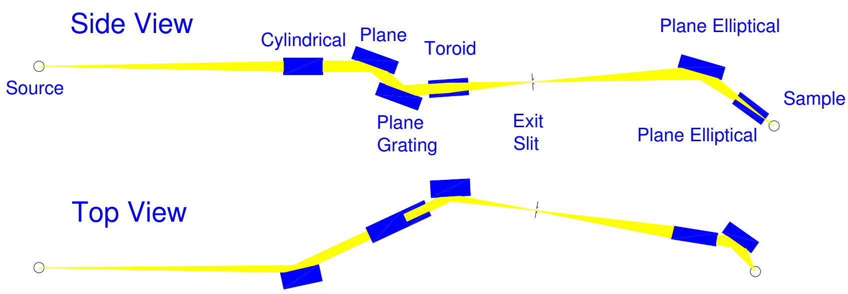

Figure 6.14.11: Schematic drawing of the beamline

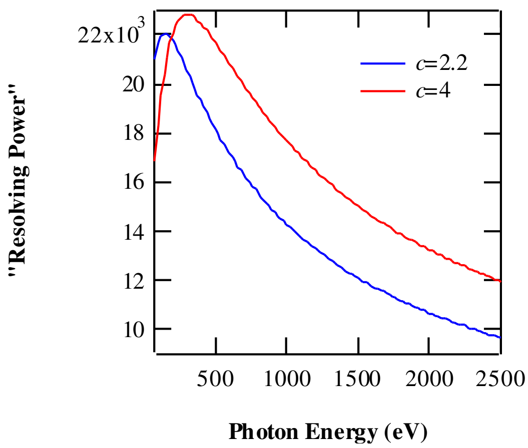

Figure 6.14.12: "Resolving power" obtained with an exit slit width of $10\ \mu\mathrm{m}$ and with $c = 2.2$ and 4.0

errors mentioned above. The ray tracing confirms that a resolving power larger than 20000 is expected at 400 eV.

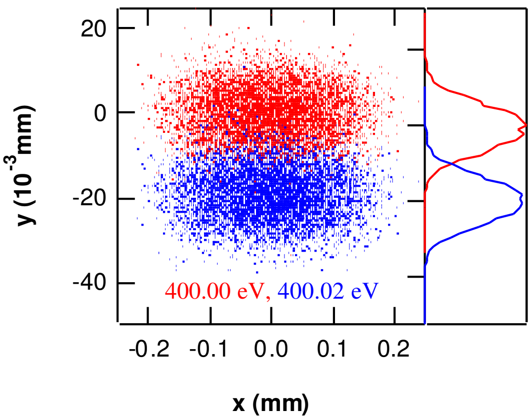

Figure 6.14.13: Ray traces at the exit slit for 400 and 400.02 eV.

The spot at the sample position for 400 eV photons has a FWHM of $23\ \mu\mathrm{m} \times 6\ \mu\mathrm{m}$ $(\mathrm{h} \times \mathrm{v})$ and it slightly decreases with increasing photon energies. It is actually dominated by the assumed figure errors on the optical elements, $0.5''$ along the tangential direction on the collimating mirror and on the toroid and $0.2''$ on the plane elliptical mirrors (Snell et al., 1996; Jahnke et al., 2002). The flux at the sample position when using a $10\ \mu\mathrm{m}$ exit slit was calculated after multiplying the values shown in Fig. 6.14.10b) by the grating efficiencies and mirror reflectivities including a 1 nm RMS surface roughness, and the slit band pass. The calculations were performed for two 1200 l/mm blazed gratings, one Au-coated with a 1.4° blaze angle and the second Rh-coated with a 1° blaze angle. The plane pre-mirror used with each grating is coated with the same material as the grating. The circular and horizontal polarized flux expected at the sample position with $10\ \mu\mathrm{m}$ slits is displayed in Fig. 6.14.14. Within a bandpass of 0.01% typically 10^{12} photons/sec can be expected at the sample position. As seen in the figure, the Au-coated grating and plane mirror combination is advantageous below 680 eV. It is worth pointing out that the monochromator preserves the source polarization.
The beamline is designed to provide also photon energies down to 50 eV by collecting off axis radiation emitted by the insertion device. A movable cylindrical mirror will be inserted after the primary cylindrical mirror to collect the off-axis radiation and send it along the original optical path. Between 60 and 200 eV a flux of $2 \times 10^{10} - 2 \times 10^{11}$ photons/s can be obtained in a bandpass of $0.01\ \%$ at the sample position.
The power absorbed by the first mirror when the ID is tuned to deliver horizontally polarized light at 250 eV is 1560 W and the absorbed power density is $2.3\ \mathrm{W/mm^2}$. The worst case for the plane pre-mirror is 31 W and $0.16\ \mathrm{W/mm^2}$. The power absorbed in the grating is significantly smaller. In order to maintain the beamline performance, internally cooled single crystal mirrors will be required for the first two mirrors as well as a cooling arrangement for the grating.

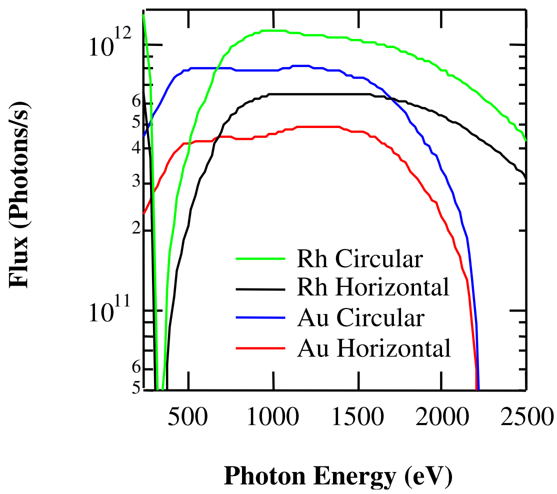

Figure 6.14.14: Circularly and linearly polarized flux (10 μm slit) expected at the sample position for the "resolving power" (20×10^3 @ 500 eV - 10×10^3 @ 2500 eV) given in Fig. 6.14.12.

6.14.11 Capital investment and personnel

The XUV beamline differs considerably from the X-ray beamlines since a plane grating monochromator is used for energy selection. All optical elements have to be installed in UHV-tanks in order to reduce contamination and losses to a minimum level. End stations and experimental methods for the proposed experiments are rather different amongst each other. All interest research groups are expected to bring their own experimental set up and with them.
The total costs for the beamline are estimated to be **1600 k€**.

Two beamline scientists, two postdocs, one engineer and one technician are needed for the construction and operation of the beamline. The construction should be started in 2004.

6.15 Resonant Scattering Beamline in the Hard X-Ray Regime

Authors and Consultants :

Th. Brückel	Institut für Streumethoden, FZ Jülich GmbH, Jülich
D. Lott	GKSS Forschungszentrum, Geesthacht
J. Strempfer	Max-Planck-Institut für Festkörperforschung, Stuttgart
M. Tischer	DESY, Hamburg
P. Wochner	Max-Planck-Institut für Metallforschung, Stuttgart
M. v. Zimmermann	DESY, Hamburg

A resonant scattering beamline is proposed for experiments taking advantage of absorption edges in the hard X-ray regime between 2.8 keV and 30 keV. These experiments include resonant magnetic scattering of both ferro- and antiferromagnets, Templeton scattering and reflectivity measurements. While resonant magnetic scattering and Templeton scattering are well established techniques, the combination with a microfocus in the nanometer regime and the large coherence of the beam obtainable at the PETRA III source give access to new types of experiments that are not possible today.

Many resonant scattering experiments, in particular XMCD experiments, are nowadays carried out in the soft X-ray range, especially due to the large enhancements at the L-edges of the technologically and scientifically interesting 3d transition metals. Soft X-ray studies of magnetic nanostructures have huge scientific potential. However, by using soft X-rays for bulk studies the experiments suffer from high absorption and a limited Q-range due to the long wavelength. Here, hard X-rays could be used to overcome these drawbacks with much higher penetration depths on the order of several micrometers and a wider accessible range in reciprocal space. With X-ray energies from 2.8 keV to 30 keV the whole range of interesting magnetic elements from the K-absorption edges of the 3d transition metals, the K- and L- edges of the 4d elements, the L-edges of the 4f to the L- and M-edges of the 5d and 5f elements is covered.

6.15.1 Introduction: correlated electrons

In condensed matter systems, electrons provide the "glue" which holds the atoms together. Their Coulomb interaction together with the fermionic quantum character leads to correlation phenomena, which are largely not understood. Examples are provided by unconventional magnetism, non-Fermi liquid behavior, superconductivity, integer and fractional quantum Hall effect etc. Research on electronic correlations is at the forefront of condensed matter physics today. On the experimental side, probes are needed that provide detailed space and time resolved information with additional distinction with respect to electronic band states, spin, charge, orbital and lattice degrees of freedom as well as to the atomic species. Such information can be obtained from sophisticated scattering and spectroscopy experiments at undulator beamlines of third generation synchrotron radiation sources. Examples for major challenging issues concerned with electronic correlations, which can be tackled by modern synchrotron radiation experiments, can be summarized as follows:

1. **Complex systems and nano-scale magnetism:** While in the past mainly homogeneous magnetic materials have been studied, the focus is now shifting to composite materials consisting of structural and electronic and magnetic phases in close spatial proximity. The discovery of interlayer coupling and the giant magnetoresistance effect in layered magnetic systems has triggered the field of magneto-electronics or spintronics, where in addition to the electron charge, the electron spin is used to transport, store and process information. As a consequence, the field of magnetism enjoys an unusually strong technological pull, second in condensed matter physics only to that of semiconductors. However, more complex systems not yet used for applications pose many unresolved fundamental puzzles. In a top-down approach, artificially patterned structures consisting of different materials (metals, half-metals, semiconductors, insulators) in close proximity are produced by physical methods such as MBE or sputtering combined with lithography, while in the bottom-up approach self organization is exploited. Understanding the complex magnetic and electronic phases, the ordering phenomena and the proximity effects occurring in these materials is a major intellectual challenge. Experimental evidence can be provided with resonant magnetic X-ray scattering and dichroism experiments, spatially resolved on a sub-micrometer scale.

2. **Highly correlated electron systems:** Heavy-fermion systems, colossal magnetoresistance materials and high temperature superconductors are posing difficult problems despite intense research since more than two decades. The strong electron correlations lead to unusual quantum phenomena such as spin, orbital and charge ordering, metal-insulator transitions, non-Fermi-liquid behavior, or magnetism in close vicinity to superconductivity. Nanoscale phase separation can occur, leading to complex nanostructures by self-organization. Many of these systems have in common a competition of various degrees of freedom and interactions, leading to an extreme sensitivity to external parameters such as magnetic or electric fields, pressure, composition, etc. This nonlinear response to small disturbances renders these systems extremely attractive for applications e.g. as sensors. To resolve the main intellectual problem of understanding the strong electronic correlations one needs to disentangle the various ordering phenomena. Anomalous scattering of synchrotron radiation is ideally suited to study charge order, spin order (resonance exchange scattering), orbital order and lattice distortions (anisotropic anomalous scattering or Templeton scattering). Since many of these scattering channels are rather weak compared to conventional charge scattering, a dedicated undulator beamline with full polarization handling is essential.

6.15.2 Resonant magnetic scattering

The worldwide investment in magnetic devices is 100 billion US-Dollars per year. One of the areas with the most rapid development is data storage media. Both the storage medium and the data read out are based on magnetic phenomena. The rapid progress in this area is demonstrated by the fact that the areal density of data storage grows exponentially in time. Clearly, materials properties on nano-scale dimensions become increasingly important for functional devices.

While it has to be realized that the development of magnetic materials is relatively independent of basic research, the understanding of the phenomena is still critical for further progress. Among these are currently

- magnetic exchange bias
- superparamagnetism and spin dependent tunneling which are both nanoscale phenomena
- non-equilibrium thermal assisted switching

Neutron and X-ray scattering are the only two probes for the magnetic correlation function of bulk material. For neutrons the magnitude of the magnetic scattering cross section is comparable to the nuclear one, leading to similar intensities of magnetic and structural reflections. Despite the relatively low neutron flux, experimental studies of magnetic nanostructures are possible today in grazing incidence geometry. However, in contrast to X-rays, neutrons cannot provide element specific information.
The magnetic X-ray scattering cross section in the non-resonant limit away from absorption edges is well understood (Blume, 1985). In contrast to neutron scattering, where the total magnetic moment is accessible, magnetic X-ray scattering allows one to determine the two individual contributions of L and S to the magnetic moment. While the intensity of magnetic scattering is more than 6 orders of magnitude smaller than the one from charge scattering, enhancements of the magnetically scattered intensity can be observed near an absorption edge, termed resonant exchange scattering (Gibbs et al., 1988; Hannon et al., 1988). Since the resonant scattering process involves transitions from a core level into an empty state above

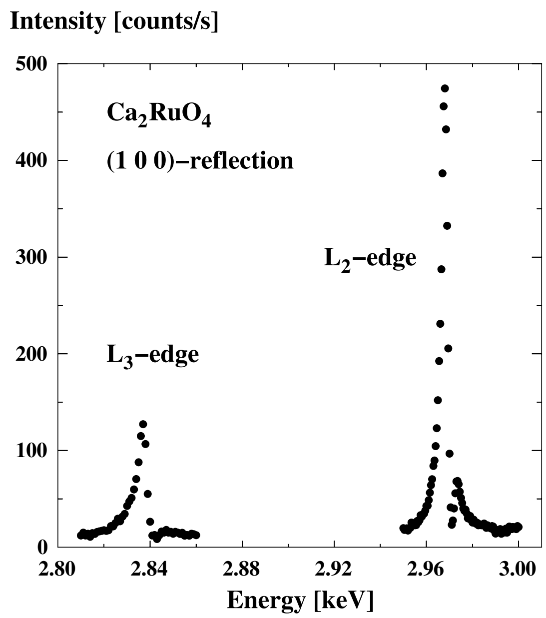

Figure 6.15.1: Intensity of the (1 0 0) reflection of Ca_2RuO_4 as a function of energy at the L_2 and L_3 edges of Ru.

the Fermi level, valuable information is obtained about the electronic structure. The scattering cross section depends on the polarization of the incident and scattered beam, making a well defined polarization of the incident beam and a polarization analysis of the scattered beam necessary. The main strength of resonant magnetic X-ray scattering is the element-specificity. The combination of element and band sensitivity allows one to obtain detailed information on the mechanism of interlayer exchange and proximity effects (Voigt et al., 2004). Utilizing the resonant scattering technique it has been possible to investigate the surface magnetism of UO_2 and how it differs from the bulk magnetism (Watson et al., 2000). Compared to neutron scattering the X-ray scattering technique generally offers a high momentum space resolution, provides element sensitivity and in combination with a micro focused beam, structures on a nano-scale can be investigated. It is thus an excellent tool for studies of functional materials as mentioned above. Beyond that, taking advantage of the large coherence length at PETRA III it will be possible to perform speckle studies to resolve domain shapes or study the dynamic behavior of glassy systems on a μ-second time scale employing the time correlation spectroscopy technique.

The L-edges of 4d transition metals as well as the M-edges of the actinides are located at energies below 4 keV. They are of great interest for the investigation of magnetic properties of compounds containing these elements, since in both cases large resonance enhancements are obtained at the respective absorption edges. At the $L_{2/3}$-edges, the initial states are the $2p_{1/2}$ and $2p_{3/2}$ states. Dipole transitions probe the d-states, where the electrons responsible for the magnetic ordering are located. Because of the large overlap integrals between the p and d levels the scattering amplitude is expected to be similar to the one of the M-edges of the actinides, where in addition the polarization of the f level is stronger.

The M-edges of Uranium with energies above 3.6 keV can be accessed by several beamlines at third generation synchrotrons around the world already. Resonance enhancements of up to 3 orders of magnitude are obtained for uranium and neptunium (Lidström et al., 2000). The 4d transition metal L-edges can only be accessed by one beamline at the APS, where the insertion device has been modified accordingly to reach this energy. There, first measurements have shown recently that indeed a resonance enhancement of more than a factor of 50 is obtained from Ru L-edges (Strempfer et al., 2003) (see Fig. 6.15.1). This opens a new perspective in investigating compounds containing 4d-transition metals.

6.15.3 Magnetic circular dichroism (XMCD) experiments

Research in the field of magnetic materials has largely benefited from the use of polarization-modulated X-ray diffraction and spectroscopy techniques. XMCD is an important effect that is widely used to explore ferro- , ferri- and paramagnetic contributions in a large variety of materials. XMCD describes the difference in the intensities measured with left and right circularly polarized light when the X-ray energy is tuned across an absorption edge of a magnetic site (Schütz et al., 1987). It provides unique information not readily available via other methods enabling a quantitative determination of element-specific spin and orbital magnetic moments. Using XMCD in X-ray scattering geometry, the element-specific sensitivity to the magnetic moments can be combined with the depth sensitivity of X-ray scattering giving information about the magnetic spatial spin contributions from different magnetic sites (Chen

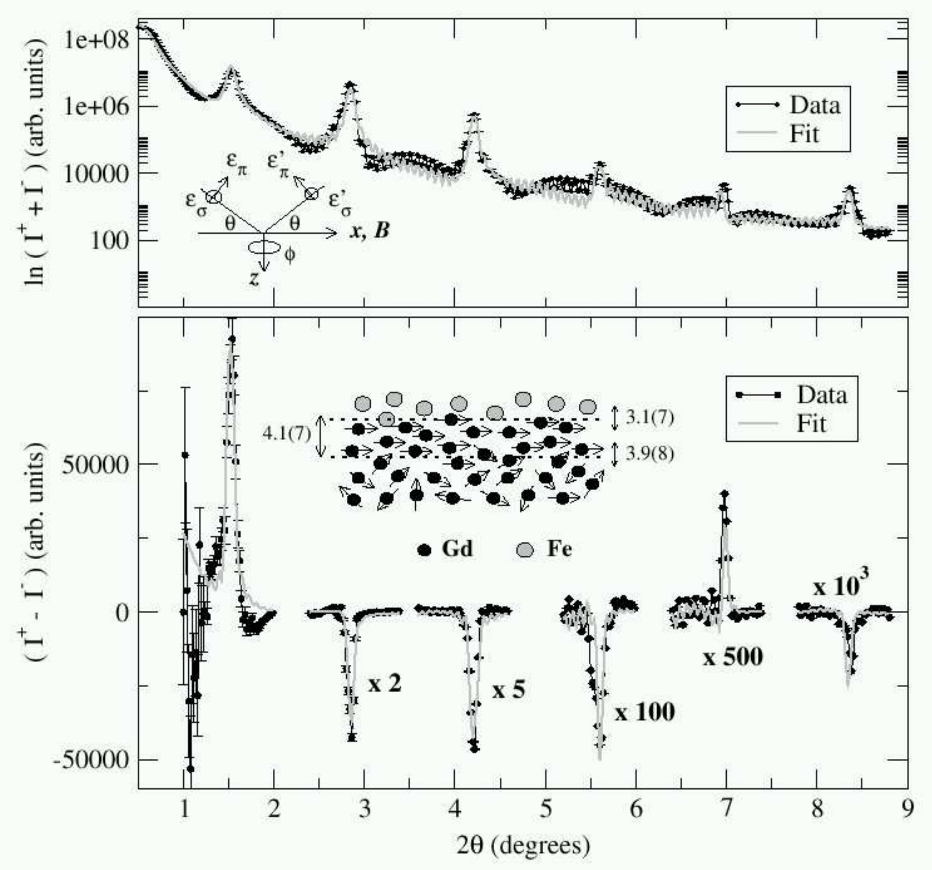

Figure 6.15.2: Charge reflectivity (upper panel) and magnetic reflectivity (lower panel) on a [Gd(50Å)/Fe(15Å)]15 multilayer. The bottom inset shows the derived interfacial structure (Figure taken from (Haskel et al., 2001)).

et al., 1990; Kao et al., 1990; Kao et al., 1994; Chakarian et al., 1996; Stöhr, 1999).

The feasibility of XMCD experiments is strongly dependent on the quality of the X-ray beam: high photon flux with high degree of circular polarization and high beam stability. Circularly polarized X-rays produced by application of phase plates show close to 100% circular polarization (Pizzini et al., 1998; Varga et al., 1999; Maruyama et al., 1999). In addition, the possibility of fast switching between left and right circularly polarized light by variation of the reflection angle at the phase plate enables one to use lock-in amplifiers to further reduce the background noise. Effects with maximum XMCD ratios - the difference in the measured intensities for left and right circularly polarized light divided by its sum - of smaller than 10^{-4} will be easily detectable. Thus, measurements of very small magnetic signals in short data collection times will be possible as e.g. at the K-edges of the 3d transition metals.

The key scattering techniques taking advantage of the XMCD effect are magnetic X-ray reflectivity and diffuse magnetic scattering. Magnetic X-ray reflectivity uses the XMCD effect in the setup of specular X-ray reflectivity and therefore allows to study the magnetiza-

tion profile by distinguishing between different magnetic sites and their spin configurations (Sève et al., 1999; Jaouen et al., 2002). Fig. 6.15.2 shows an example of a magnetic reflectivity curve near the Gd L_3-edge (Haskel et al., 2001). From the magnetic reflectivity signal the spin configuration of the Gd atoms at the Gd/Fe interface can be determined. Due to the excellent properties of the X-ray beam at PETRA III in combination with the proposed design of the beamline providing sensitivity to very small XMCD effects, a powerful tool for the characterization of magnetization profiles of magnetic thin films and multilayer structures will be available. Another important feature is the ability to measure element specific hysteresis loops to examine the switching behavior in magnetic materials, e.g. when consisting of two different magnetic sites as it is the case in exchange bias materials. By variation of the incident angle, different depths can be probed. This can be important if bulk and surface magnetic states should be separated (Haskel et al., 2003).
One of the most intense discussed questions in the field of magnetic thin films and multilayers is the spin ordering at interfaces, e.g. how the magnetic roughness and correlation lengths are related to the chemical counterparts (Nelson et al., 1999; Osgood III et al., 1999; Freeland et al., 1998; MacKay et al., 1996; Kelly IV et al., 2002). Here, diffuse magnetic scattering is an ideal technique to tackle the task, combining the XMCD effect with standard rocking curves or other diffuse scattering techniques (Sinha et al., 1988; Salditt, Metzger & Peisl, 1994). Since the magnetic signal decreases rapidly with increasing parallel momentum transfer, high photon flux and high sensitivity to the XMCD signal become very important.
Another interesting aspect for using the XMCD effect in the hard X-ray regime is the accessible large Q-space. In principle XMCD measurements in high angle diffraction mode are possible to access atomic Bragg reflections of magnetic sites and thus probe the ferromagnetic contributions even down to the atomic level. Finally, one of the outstanding properties of magnetic X-ray techniques is the possibility to distinguish between orbital and spin moments by applying sum rules to the measured MCD spectra (Thole et al., 1992; Carra et al., 1993; Chen et al., 1995; Wu & Freeman, 1994).

6.15.4 Templeton scattering

Resonant X-ray scattering (RXS) at absorption edges not only provides access to the subtleties of microscopic magnetism. In recent years many experiments have shown, that RXS allows the investigation of charge, spin and orbital degrees of freedom even in a single experiment (Paolasini et al., 2002; Caciuffo et al., 2002). Especially for systems where the ground state properties reflect a delicate balance between several different correlated processes, this technique can be of crucial importance.
In a resonant scattering experiment the photon energy is tuned to an absorption edge so as to excite virtual electric multipole transitions between a core state and an intermediate bound state above the Fermi level. If the symmetry of the intermediate state is lowered and aligned by interactions (chemical bonding, Jahn-Teller effect, magnetic, multipolar etc.) the scattering becomes dependent on the polarization of the incident and scattered beam, and the atomic scattering factor is no longer a scalar but becomes a tensor and the diffraction may exhibit birefringence (Templeton scattering). In addition, when the resonating atoms exist in an anisotropic crystalline environment and they occur with more than one molecular

orientation, glide-plane and screw-axis forbidden reflections may become observable, since crystallographically equivalent atoms do not have exactly the same scattering power. Experimentally, the symmetry of the form factor can be efficiently probed with an azimuthal scan, a rotation around the scattering vector. For a direct determination of the origin of the anisotropic chemical environment, the intermediate state probed by the resonance should ideally be the same as the states which directly drive the order. If this condition is satisfied, RXS is the only method to probe directly orbital order, e.g., in 3d transition metal oxides (Wilkins et al., 2003b), or quadrupolar ordering, e.g., of 5f U moments in UPd_3 (McMorrow et al., 2001). Conventional probes, like neutron scattering or non-resonant X-ray scattering etc., do not couple to quadrupole moments and, therefore, quadrupole order can be revealed only indirectly (e.g., via accompanying lattice distortions). To determine orbital order conventionally, in principle a full structural refinement is required with the resolution of a fraction of an electron unit. The observation of Templeton scattering in 3d transition metal oxides, e.g. $LaMnO_3$ (Murakami et al., 1998a), $La_{1.5}Sr_{0.5}MnO_3$ (Murakami et al., 1998b), $YTiO_3$ (Nakao et al., 2002), $KCuF_3$ (Paolasini et al., 2002; Caciuffo et al., 2002) or V_2O_3 (Paolasini et al., 1999), generated appreciable excitement, especially with the prospect as a promising new tool for the study of orbital order in these highly topical systems. In these experiments the K-edge resonance was excited. Therefore, the 4p intermediate states probed by the resonance were not the same as the 3d states which directly drive the order. Up to now it is intensely discussed if the observed anisotropies are caused by a direct or an indirect mechanism. Only in the case of V_2O_3, based on symmetry arguments, there seems to be a consensus that the observed resonances are directly related to orbital order. But generally, there are no doubts that orbital order is driving most of the observations and that Templeton scattering is a valuable tool for the determination of the orbital order configuration, correlation length and temperature dependences. Similarly, experiments on quadrupolar order in 4f systems have relied mainly on investigating the induced order in the 5d bands and not directly as in the 5f system UPd_3.

In many doped 3d transition metal oxides, charge order develops in which the transition metal ions become crystallographically non-equivalent due to valence fluctuations. Using the resonant scattering technique, the valence contrast can be greatly enhanced. Often charge and orbital order are strongly coupled giving also rise to anisotropic anomalous scattering on charge order reflections.

The utilization of the anisotropic anomalous dispersion of the Templeton scattering can also enhance the power of the MAD-method to solve the phase problem in crystallography. Using azimuthal scans, phase information can be obtained from a single wavelength experiment by a change of the effective anomalous scattering.

As mentioned above, the anisotropic anomalous dispersion leads to an anisotropic index of refraction, energy-dependent birefringence and dichroism, which can be used, e.g., for the study of ferroelectrics.

On the other hand, high resolution diffraction has been used to observe correlation effects of a sliding charge density wave (Danneau et al., 2002). Combining the resonant scattering technique with coherent scattering and time correlation spectroscopy would give new insights in such phenomena and are of great technological interest for electro-optical switches and memory (Ogawa & Miyano, 2002).

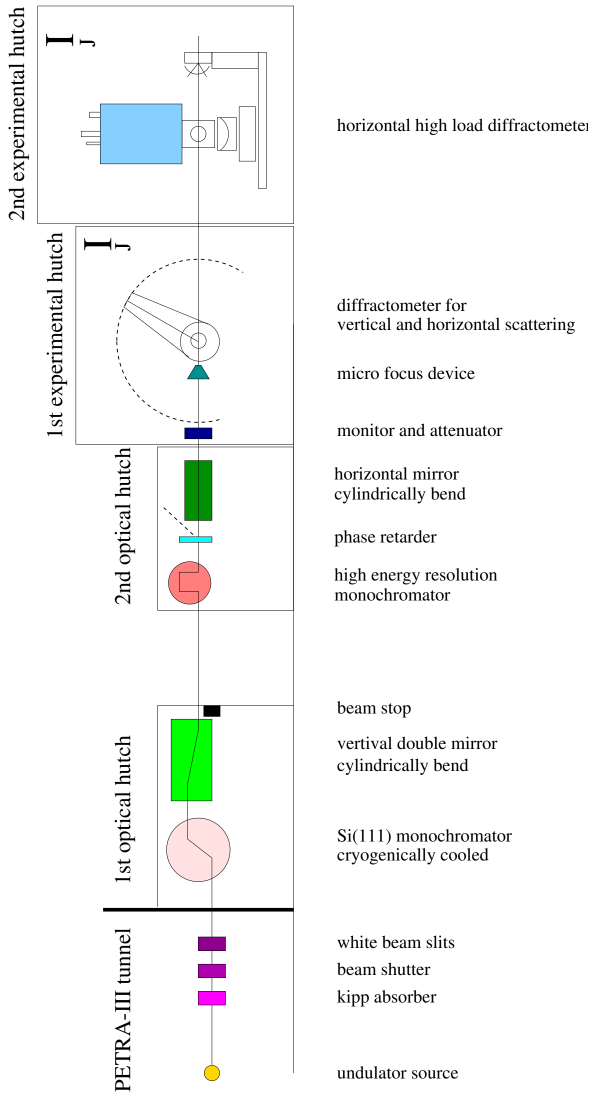

Figure 6.15.3: Schematic layout of the resonant scattering beamline at PETRA III.

6.15.5 Beamline design

The beamline requires a 5 m long undulator to bring a photon flux of at least 10^{13} photons/s/0.01%BW within a spot of below 100 μm in diameter, while preserving the high degree of horizontal polarization and rejecting photons from higher harmonics. The instrumentation should be optimized for diffraction type experiments. A sketch of the proposed beamline is shown in Fig. 6.15.3. Examples for similar existing experimental stations on other sources are ID20 and XMAS at the ESRF, X22-C and X-25 at the NSLS, 9ID-B, 6ID-B and 4ID-D at the APS, 4C and 16A2 at the Photon Factory, KEK, BL39XU and BL22XU at SPring-8. The design of the resonant scattering beamline at PETRA III is guided by the following criteria :

6.15.5.1 Energy tunability

The energy tunability should be from 2.8 keV - 30 keV, covering most of the absorption edges in the hard X-ray regime. This includes the K-edges of transition metals, the L-edges of the rare earth elements and the M-edges of the actinides. The beamline shall be optimized for the range of 3.4 keV - 16 keV. The energy resolution of the incident beam should match a typical core hole life time, which is around ΔE = 1 eV. That will be achieved with a liquid nitrogen cooled Si(111) double crystal monochromator. The Darwin width of this reflection (26 μrad at 10 keV) is significantly larger than the vertical divergence of the incident beam of 5.2 μrad. For high resolution spectroscopic applications a high resolution monochromator with an energy resolution of around 0.2 eV can be added in the monochromatic beam on demand. This will be a fixed exit four-bounce monochromator.

To access the low energy range down to 2.8 keV the beamline should be designed windowless. To avoid absorption, the beam-paths to the sample and from the sample into the detector have to be evacuated.

6.15.5.2 Harmonic rejection

Crucial for the performance of the resonant scattering beamline will be the reduction of higher harmonics in the monochromatic beam. The intensity of the smallest measurable reflections can be 10^{10} times smaller than the main reflections, thus the number of photons in the higher harmonics I_h should compare to the number of photons of the fundamental wavelength I_0 like $I_h/I_0 \sim 10^{-10}$. This high harmonic suppression will be achieved by a combination of energy dispersive devices :

First, the use of a quasi periodic undulator (Sasaki et al., 1995) would reduce the intensity at harmonic wavelengths by two orders of magnitude compared to a conventional undulator device (Sec. 4.1.7). In the ideal case the higher harmonics of a quasi-periodic undulator appear at non rational multiples of the fundamental wavelength. However, in combination with a monochromator tuned to the fundamental wavelength, the wavelength at non rational harmonics are not reflected and thus highly suppressed. Only the residual intensity at rational multiple wavelength will be reflected, which is, however, two orders of magnitude smaller than the fundamental wavelength.

Second, a mirror tuned to just below the critical angle reduces the harmonic contamination by a factor between 10^{-2} and 10^{-3}, while having a high reflectivity for the fundamental of about 95 %. A pair of vertical mirrors and a single horizontal mirror (which will be also used to focus the beam on the sample, see below) would reduce the harmonic contamination to 10^{-6} to 10^{-9}.

Third, an energy dispersive solid state detector is able to discriminate harmonic contamination by a factor 10^{-1} to 10^{-2}. Combining the quasi-periodic undulator with three mirrors and an energy dispersive detector a harmonic suppression of a factors of $10^{-9} - 10^{-10}$ is obtained. Further possibilities for the reduction of higher harmonics would be the detuning of one of the monochromator crystals or the use of a multilayer mirror. Neither of these methods is taken into account since both of these result in a reduced intensity on the sample.

6.15.5.3 Polarization

For polarization resolved measurements the degree of polarization of the incident beam on the sample is of critical importance. This concerns both the linear polarization and the circular polarization. An undulator source at PETRA III will provide a 99.99 % σ - polarized beam. To preserve the linear polarization all optical elements like mirrors and monochromators should scatter in the vertical direction, except for one horizontal focusing/harmonic rejection mirror.
Circular polarization will be obtained by the use of a quarter wave plate (Golovchenko et al., 1986). In the hard X-ray range, the use of quarter wave plates has proven to be superior to a variable polarization insertion device (Lang, Srajer & Dejus, 1996). With quarter wave plates a degree of circular polarization of 99 % percent can be obtained at third generation sources. Generally, the smaller the incident beam divergence, the better the degree of polarization. To minimize the horizontal and vertical divergence (note that the scattering plane of the phase plate is tilted by 45°, therefore both vertical and horizontal divergences need to be minimized) a high-β section will be required. Furthermore, switching rates of a few kHz between left and right circular polarization are possible with these devices (Pizzini et al., 1998). In contrast, typical switching rates for variable polarization insertion devices are in the order of a few Hz, and the efficiency for circular polarization is rather small. Finally, the source point for left- and right-circular polarization of a switching insertion device might be different, which, combined with the high Q-space resolution, makes XMCD-measurements in diffraction geometry impossible.
The phase retarder can also be used as a half wave plate providing a linear π-polarized beam (Ishikawa et al., 1992). This is of importance when the sample environment (e.g., a cryogenically cooled high field magnet) requires a horizontal scattering geometry.

6.15.5.4 Focus and divergence

Without compromising the intensity, the polarization properties and the harmonic rejection, a vertical and horizontal focus of about 10 μm each should be achieved by mirrors. A vertical double mirror in a 1:1 focusing scheme provides a fixed exit and does not increase the vertical divergence. This double mirror is also used for harmonic rejection. A single horizontal focusing mirror with a mapping ratio of 20:1, about 3 m in front of the sample is used to limit the horizontal offset to a few centimeters. Here a horizontal spot size of 10 μm with a divergence of 0.3 mrad will be achieved. This horizontal mirror can be removed if a small horizontal divergence is required.

6.15.5.5 Diffractometer

Two experimental stations are envisioned, such that one experiment can be prepared in one hutch while another one is running in the other hutch. To accommodate the diffractometers with 2 m arms in the hutches, the hutch length should be 7 m. A height of 5 m is required to be able to change samples in liquid He cooled cryostats. Each hutch contains one diffractometer. The first hutch hosts an 8-circle diffractometer for vertical and horizontal scattering. A horizontal scattering diffractometer will be placed in the second hutch. This horizontal diffractometer will be able to carry high loads up to 500 kg and has to be fabricated out of non-magnetic material so that a high-field magnet can be operated. Both diffractometers are equipped with polarization analyzers and shall be capable to perform ψ-scans (scan around the scattering vector). Various detectors will be needed, i.e., an area detector to survey large parts of reciprocal space, a solid state detector with sufficient energy resolution (see Sect. 6.15.5.2) and a detector optimized for a large dynamic range. For the detection of modulated signals lock-in amplifiers are foreseen.

6.15.5.6 Further options

Instrumentation well suited for studies of magnetic materials and correlated electron systems are:

- A high field magnet. Split pair magnets are able to achieve persistent fields of 15 T.
- An ultra low-temperature ^{3}He cryostat to access the temperature regime down to milli-Kelvin, which is unexplored by X-rays. The combination of high magnetic fields with ultra low temperatures would be ideal.
- An option to micro focus the beam with KB mirrors or lenses close to the sample.
- An option to use the large transverse coherence of the PETRA III source for coherent scattering experiments, like speckle or time correlation spectroscopy.

6.15.5.7 Environments

Stability is generally a critical issue, thus a temperature stability of better than 1° is required in all experimental and optical hutches. A topping up injection mode with a current variation less than 10 % would enhance the stability of the optical components. For the preparation of samples and sample environment laboratory space with direct access to the beamline is needed. The sample to source distance is uncritical.

6.15.5.8 Implications of side station

In order to preserve the high degree of polarization it is essential that the sample is located in a straight line to the undulator source and that the reflections of all optical components utilize a vertical scattering plane. The only exceptions are the phase retarder and the removable horizontally focusing mirror. A horizontal deflection of the beam would affect the polarization properties negatively. The instrumentation in the experimental hutches, i.e., both diffractometers, do not allow another beam pipe passing through the hutch within the radius of their respective two-theta arms of approximately two meters from the sample. The undulator gap needs to be adjustable to experimental requirements which are given by the absorption edges of the studied compounds. The reduced intensity provided by a 2 m undulator, about a factor of three smaller compared to a 5 m undulator, could be compensated only by an increase in the data acquisition time of the same amount provided a sufficient stability of the machine and the optical components. However, for the proposed time dependent studies this is not possible and the accessible dynamic range will be more limited.

6.15.5.9 Combination with other end stations

In order to extend capabilities and broaden the user community for the proposed beamline, a combination with resonant inelastic scattering experiments with an energy resolution in the range of 0.1 eV for both monochromator and analyzer is suggested. The additional instrumentation for such experiments will be a high energy resolution analyzer.
Studies of electronic excitations by means of inelastic X-ray scattering experienced tremendous progress in recent years. This technique probes the dynamic structure factor $S(q,\omega)$. Unlike Raman scattering, which is bound to zero momentum transfer, the whole Brillouin zone can be accessed. Thus it is complementary to electron energy loss spectroscopy. However, the resonance process is not yet completely understood. The first experiment employing this technique was performed on NiO and resonant enhancements of the charge-transfer excitation of two orders of magnitudes were found (Kao et al., 1996). The technique allows one to study the dispersion of the charge transfer gap and the propagation of holes (Hasan et al., 2000). Orbital excitations, d-d transitions which are forbidden in the non-resonant case, have been studied in manganite compounds (Inami et al., 2003).
The resonant inelastic X-ray scattering requires the energy tunability foreseen for the proposed beamline and would gain from the high degree of polarization and the high rejection of higher harmonic contamination. Furthermore it would benefit from circular polarized light, an option that is not available on any other source presently.

6.15.6 Capital investment and personnel

The total capital investment for the experimental endstations amounts to **2110 k€** not including 800 k€ for a 15 T magnet.
Personnel: 2 Scientists, 1 Engineer, 1 Technician

6.16 Integrated Proposal by the European Molecular Biology Laboratory for Beam Lines at the PETRA III Storage Ring

6.16.1 Introduction

Authors: Matthias Wilmanns, Christoph Hermes, Victor Lamzin, Wolfram Meyer-Klaucke, Dmitri Svergun & Paul Tucker
Address: EMBL c/o DESY, Notkestrasse 85, D-22603 Hamburg, Germany

6.16.1.1 Summary

The European Molecular Biology Laboratory (EMBL) presents a proposal to build and operate synchrotron radiation beamlines and/or experimental stations in life sciences at the dedicated PETRA III storage ring. The document comprises detailed proposals for beamlines in Biological Macromolecular X-ray Crystallography (MX) in Biological X-ray Scattering (SAXS) and Biological X-ray Absorption Spectroscopy (XAS).

6.16.1.2 Past achievements in provision of synchrotron radiation beam line facilities at the DORIS storage ring

The EMBL-Hamburg Outstation has thirty years of experience in the provision of synchrotron radiation beamlines in life sciences at the DORIS storage ring and in research activities that are associated with the experiments at these beamlines. The basis of these activities has been the provision of synchrotron radiation by the Deutsches Elektronen-Synchrotron (DESY) free of charge. The experimental end-stations including all beamline optics 'behind the beryllium window' (i.e. proximal to the end-stations) have been designed, built and are being maintained by EMBL.
While during the first two decades the amount of activities in MX, SAXS and XAS was comparable, the reconfiguration of the DORIS ring into a dedicated source and the addition of the bypass with seven wiggler stations in 1992 permitted a massive increase of experiments, particularly in MX. During the last ten years three additional MX beamlines (BW7A, BW7B, X13) were completed bringing the total number of EMBL beamlines to seven, in addition to the already existing ones (X11 and X31, MX; X33, SAXS; EXAFS; XAS). An eighth, energy-tunable beamline (X12, MX) is currently being commissioned.
The infrastructure of these beamlines is complemented by the EMBL building (25A) that has been extended by an additional floor in 2002. It hosts a molecular and biochemistry laboratory with about 40 experimental benches, a scientific library, a computer department, an administrative section and office space for about 80 staff and fellows, including some limited facilities for external users. The locally available EMBL infrastructure is integrated into the unique multiple-site structure of EMBL with its head quarters in Heidelberg (Germany) and further units in Hinxton Hall / Cambridge (UK), Grenoble (France) and Monterotondo / Rome (Italy). Various research opportunities and services from these units are directly available to the EMBL-Hamburg Outstation.

While the EMBL-Hamburg facilities were typically used by about 50-100 users per annum during the first two decades these numbers boosted during the late 90ties to 400-500 user visits per year. During these years, in MX more than 10 % of the X-ray structures of biological macromolecules world-wide that were collected using synchrotron radiation and deposited in the Protein Data Bank (PDB) originated from experiments at EMBL-Hamburg beamlines - this is the largest contribution from an European synchrotron facility. We estimate that the world-wide share of SAXS and XAS data from EMBL-Hamburg, although no systematic statistics are available, are within comparable range. More recently, the two new 3^{rd} generation synchrotron facilities in the US (APS) and Europe (ESRF) are generally taking the lead.

At present, the EMBL-Hamburg facilities are used for about 300 external research projects per annum, of which most are from countries in Europe. While in biological MX most of the external research groups are applying for beam time at more than one synchrotron radiation facility in parallel and their projects are generally not in collaboration with EMBL-Hamburg scientific staff, most of the external SAXS and XAS experiments are in collaboration with the respective research teams at EMBL-Hamburg. In response to the flexible needs for experiments in MX, an electronic beamtime booking system was introduced in 2001. Most of the present efforts are directed towards improvements of user friendliness, inter-operability, automation and increase of throughput at the available EMBL beamlines. Recent and present highlights are the provision of software packages for automatic data interpretation in MX and SAXS and the implementation of a robot for sample changing at one of the MX beamlines.

Core resources for the present operation of the EMBL-Hamburg beamlines come from general funding of EMBL by its member states (Austria, Belgium, Denmark, Finland, France, Germany, Greece, Ireland, Israel, Italy, The Netherlands, Norway, Portugal, Spain, Sweden, Switzerland, United Kingdom). They primarily cover the provision of required infrastructures and staff devoted to the scientific and technical support of these activities. During the last decade, access of external users was supported by schemes set up by the European Union for transnational access to infrastructures within its member and associated states. The present infrastructures have also benefited from several research project grants that have been associated with specific beamline activities. At present, the EMBL-Hamburg Outstation participates in / coordinates three major structural proteomics grants (two from the European Union, one from the German Ministry for Science and Education). For the last two years, some beamtime at the EMBL-Hamburg beamlines were used by industrial users. An academic consortium, formed by the Institute for Molecular Biotechnology (IMB) Jena, Germany, and the University of Hamburg, Germany, have substantially invested into the most recent MX beamline X13 at the DORIS storage ring.

6.16.1.3 Future life science oriented synchrotron radiation beamlines and experimental stations at the PETRA III storage ring

Having the opportunity to build state-of-the-art synchrotron radiation beamlines for applications in life sciences will be central and essential for future activities of the EMBL-Hamburg Outstation. Our proposal is guided by the aims to tightly integrate the provision of complementary structural biology techniques that are associated with synchrotron radiation and

interdisciplinary research opportunities. The present proposal is limited to techniques that have been established in Hamburg (MX, SAXS, XAS), however, keeping options open to move into novel research methods and areas allowing the determination of structures, shapes and images of biological entities and their structural dynamics associated with biological processes. A key component of the future PETRA III beamline research activities in structural biology will be the establishment of an experimental platform to accumulate expertise and to develop novel experiments for the X-ray Free Electron Laser facility that DESY is planning to set up, exploiting its expected unique specific properties such as coherence, time structure and intensity.
The EMBL-Hamburg Outstation proposes to make use of the last two straight sections at the dedicated PETRA III storage ring (sections 8 and 9) and to build experimental stations in biological SAXS and MX (Fig. 6.16.1). For biological XAS, we propose a flexible experimental station, which may be combined with related beamline activities by HASYLAB/DESY or other research institutes. We wish to have this station at section 7, thus allowing usage of facilities shared with biological SAXS and MX. In order to make effective and synergistic use of these facilities and to promote their integration we are proposing a joint research area for life sciences. In essence, such joint facility could provide an integrated format for biological sample preparation, on-line data processing and interpretation, and common service logistics (see below). It may serve as a common platform to promote combined approaches using different and complementary structural biology techniques associated with the availability of synchrotron radiation.

Common area for biological sample preparation

There is wide consensus that today the rate limiting step in structural biology is in the preparation of biological samples suitable for subsequent experiments using synchrotron radiation. In X-ray crystallography, in addition the availability of crystals with sufficient diffraction properties is an essential requirement. Achieving these goals becomes even more demanding when moving to large multi-component assemblies and integral membrane proteins. Common to all suggested experimental structural biology techniques, is the availability of biological samples that are homogeneously associated and can be obtained in concentrations in the mM range. Therefore, it will be essential to interface the future EMBL beamline facilities with a common area for sample preparation, characterization and crystallization.
Sample purification: The proposed infrastructure will provide facilities that will allow purification steps that lead to pure samples with measurable feasibility for structural biology experiments. These steps will require equipment primarily suitable for affinity and size exclusion chromatography. Any preceding steps for initial sample preparation (cloning, heterologous expression in prokaryotic and eukaryotic hosts as well as cell free expression systems, initial purification steps) are expected to be carried out elsewhere, either in laboratories of external visitors or within the existing infrastructure of the EMBL-Hamburg Outstation building 25A.
Sample characterization: The proposed infrastructure will provide equipment to characterize the purity and the biophysical status of biological samples by electrophoretic methods (SDS-PAGE, native electrophoresis, isoelectric focusing), by scattering methods (dynamic

light scattering), by sedimentation methods (analytic ultracentrifugation), spectroscopy methods (absorption, fluorescence emission, circular dichroism) and by the application of diagnostic tools for precise identification of probe compositions such as mass spectrometry. In addition, we are proposing to provide specific equipment for the analysis of protein-ligand interactions (proteins, DNA/RNA, lipids, other biological molecules), considering the anticipated increasing demands to provide structural biology solutions for biological complexes as opposed to single molecules. For this, we are proposing to provide equipment for isothermal micro-calorimetry measurements and plasmon resonance measurements.

High-throughput crystallization: It is proposed to interface the biological MX beamlines with the high-throughput crystallization facility which is currently being planned to be initially set up in a separate building that is owned by DESY (Building 3). The major components of this facility will be robotics for solution mixing and drop dispensing, storage of crystallization trays, automated visualization of experiments, interpretation and scoring. We are planning to offer this novel facility to the external user community comparable to the present offer of synchrotron radiation beamline facilities. Once the crystallization facility moves into the vicinity of future PETRA III MX beamlines, we plan to establish an interface

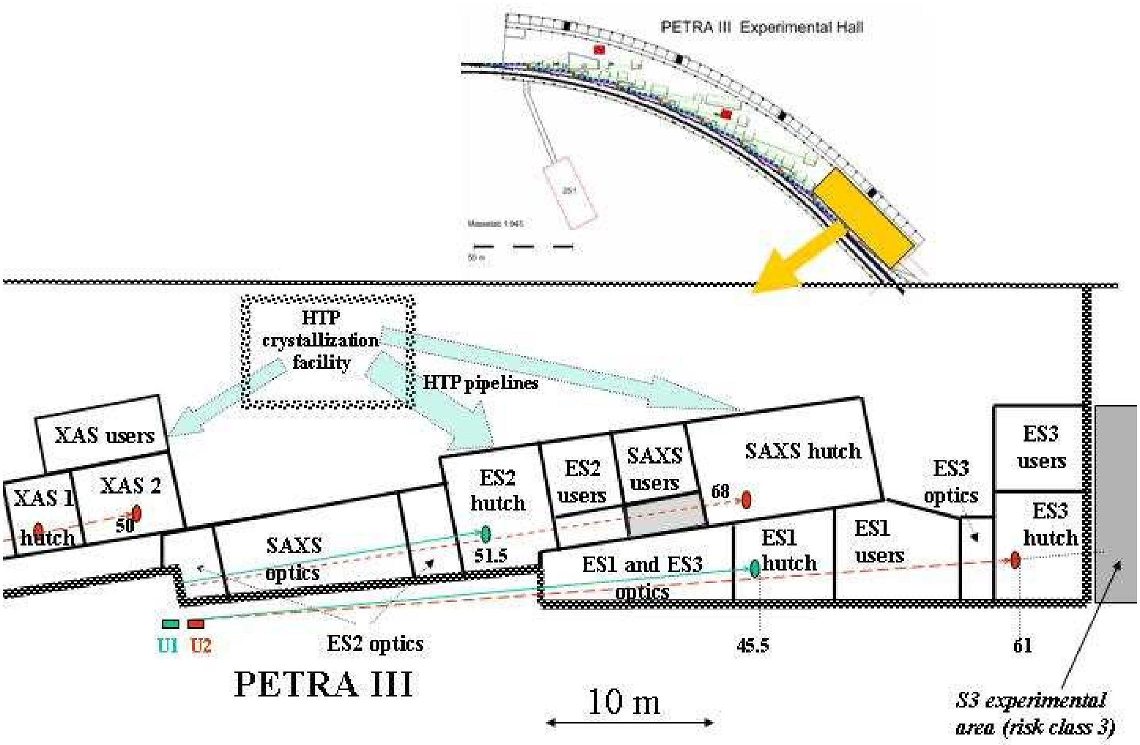

Figure 6.16.1: Schematic layout of proposed EMBL experimental stations on PETRA III.

for automatic crystal transfer to those beamlines to perform test diffraction experiments as the second step of crystal 'visualization' determining their feasibility for X-ray structure determination. Given that for the presently most complex experiments in X-ray crystallography such as the ribosome or multi-component signalling complexes often thousands of crystals needed to be tested, such automated pipeline for crystal feasibility assessment may become a pivotal element in future experiments.
There will be 50 m^2 laboratory space available for each sample purification, sample characterization and for high-throughput crystallization.

On-line data acquisition, processing and interpretation

It is anticipated that packages for the automatic interpretation of experiment data acquired at the PETRA III beamlines will be available, based on past and present developments such as ARP/wARP (MX) and ATSAS (SAXS). We propose a joint infrastructure with sufficient work space to carry out simultaneous work by ten scientists. The working area may also be used for training and teaching purposes. It will be equipped with computers suitable for graphics based data processing and interpretations and document processing. About 80 m^2 of office space is foreseen.

General services

Although we do expect to keep most of our current central services within the present building (25A), there will be limited requirement for the provision of a computer infrastructure, safety instructions and administration. For this purpose about 50 m^2 of office space will be allocated.

Facility for sample handling and X-ray measurements at the S3 security level (future extension)

We propose to keep an option for one of the proposed MX beamlines to make it available for biological samples requiring S3 safety level. Although the actual construction of such facility is not a part of this proposal we wish already at this stage to make an allowance for an extension of a beam pipe into an S3 containment building where diffraction experiments on pathogenic organisms could be performed under the required safety regime. For this facility about 200 m^2 of additional laboratory space outside of the experimental hall but close the the protein crystallography beamlines is foreseen.

6.16.1.4 Support for present operation and proposal for future support

The EMBL-Hamburg proposal for PETRA III beamlines is based on the consideration that, after an intermediate phase of parallel operation of beamlines at DORIS and PETRA III, future operation of PETRA III beamlines will be possible with a funding scheme that is comparable to the present one. However, the design and the construction of these beamlines

will require capital investments that are estimated to be in the order of 16.3 M€.
In the context of a recent application to the European Union in spring 2003, the EMBL-Hamburg Outstation has received written support from a total of 83 research institutes that are situated in Europe and Israel. These institutes constitute a large fraction of the EMBL-Hamburg user community. Given the superior parameters calculated for beamlines at the PETRA III storage ring, we anticipate that there will be even wider interest, including research groups that are not yet part of the EMBL-Hamburg user community.
Building on previous models and experience from partnerships associated with the present DORIS beamlines, the EMBL-Hamburg Outstation is also keen to establish new partnerships with academic and industrial consortia for future beamlines at the PETRA III storage ring. At present, research centers from the Helmholtz Society and Aventis Pharma have expressed interest to become putative partners. We anticipate, that once a formal proposal has been made, more opportunities for partnerships will emerge. EMBL-Hamburg will develop own activities for seeking such partnerships.

6.16.2 Biological macromolecular X-ray crystallography beamlines

Authors: Victor Lamzin, Christoph Hermes, Santhosh Panjikar, Ehmke Pohl, Alexander Popov, Andrea Schmidt, Paul Tucker, Manfred Weiss, Matthias Wilmanns

External advisors:

Zigniew Dauter	BNL, Upton, USA
Andrew Leslie	LMB Cambridge, UK
Sean McSweeney	ESRF, Grenoble, France
Uwe Müller	BESSY, Berlin, Germany
Gerd Rosenbaum	APS, Chicago, USA
Andrew Thompson	SOLEIL, Gif-sur-Yvette, France

6.16.2.1 Present and future challenges for biological crystallography

Over the last fifty years (Dennis & Campbell, 2003 further references within), biological X-ray crystallography has evolved into an advanced field of life sciences and has provided unprecedented structural insight into three-dimensional molecular information of complicated biological processes such as oxygen transport, muscle contraction, replication of genes, immune response, biological energy conversion, photosynthesis, viral assembly, protein synthesis and signal transduction. Knowledge of spatial structures has allowed to delineate the molecular origins for diseases such as cancer, autoimmune diseases and microbial infections. The performance and contribution of biological X-ray crystallography can be readily assessed by the number of new structures being deposited in the PDB, which is increasing at a nearly exponential rate. Coupled to this, the growth in a demand for synchrotron radiation beamlines for macromolecular crystallographic experiments has risen substantially both in absolute numbers and in overall proportion. More than 80 % of PDB depositions quote the use of synchrotron beamlines thus reflecting the superiority of X-ray data from synchrotron sources (Minor, Tomchick & Otwinowski, 2000).

Our aim is to provide synchrotron radiation beam time for macromolecular crystallography (MX) at the future PETRA III storage ring to the international user community, by offering state-of-the-art beamlines both for already established technologies (small crystals requiring microfocusing, phasing requiring energy tunability) and emerging or even novel applications (time resolved studies, novel phasing methods, ultra-high resolution, remote and high-throughput operations). Clearly, the provision of such new beamline facilities at PETRA III will require developments in X-ray structure analysis methods at a comparable scale. We intend to adapt the currently used successful model of independent assessment of the scientific quality of the applications and performed experiments. As a complement to this, we aim to maintain our tradition in training and teaching that are primarily targeted towards young researchers from the community. We also anticipate that the ongoing and future advances in technology and increased throughput in structure determination will create an unprecedented demand of remote operation of the experiments (Smith, 2003). A number of important areas of biology, representing the most demanding challenges in X-ray crystallography and providing a framework for future applications at PETRA III MX beamlines, are outlined below.

Molecular machines and large assemblies: In recent years, crystal structures of large biological complexes have unravelled some of the most fundamental processes in biology, such as transcription (polymerase) and translation (ribosome), import and export across membranes, and the degradation machinery by the proteasome (further citations, see: Huber, 1989; Johnson & Chiu, 2002; Yonath, 2002; Saenger, Jordan & Krauss, 2002; Harrison, 2003). Some of these complexes are integrated into biological membranes, such as photosystems I and II, the light harvesting complexes, the photo reaction center and some of the complexes of the respiratory chain. At present, the largest structures, though bearing internal symmetry, are from - in part complete - viral assemblies. Some of these structures have imposed unprecedented challenges in terms of the size of available crystals, which may be low as a few microns only (Gluehmann et al., 2001; Abola et al., 2000) and unit cell dimensions, in a few cases even exceeding 1,000 Å (Stuart et al., 2002). Many of these projects have only become feasible with the recent availability of the highest brilliance beamlines at 3^{rd} generation synchrotron sources.

Structure based drug discovery: Rational drug design is a process that bases the development of a drug upon the structure of its protein target (Kuhn et al., 2002). Most pharmaceutical companies and some specialized biotech companies such as Astex, Syrrx and Structural GenomiX are employing this approach for their drug discovery pipelines and have become a significant part of the synchrotron user community. A prototype example has been the work on inhibitors of the HIV protease for finding new drugs against AIDS (Wlodawer, 2002). Although most of these approaches have been focused on small, soluble protein targets, recent advances have extended them to targets of much higher complexity, such as the ribosome (Knowles et al., 2002).

Structural Proteomics: The availability of a rapidly increasing number of genome sequences from a wide range of organisms has revolutionized research in life sciences and has ultimately allowed to study biological processes at complete genomic (or proteomic) scale. During the last five years a number of large-scale structural proteomics initiatives has been formed. The common aim of these initiatives is to advance parallel, high-throughput technologies in experimental structural biology and to use them for a large number of structure determinations of a proteome. While some of the early structural proteomics initiatives have have been aiming for a complete knowledge of the "fold space" (Heinemann et al., 2000), more recent projects attempt to make the structures useful for unravelling the molecular basis of biological processes (Burley & Bonanno, 2002; Sali et al., 2003) and to apply them for structure-based drug discovery screening approaches (Buchanan, 2002). A novel direction in structural proteomics oriented research emerges from recent developments and applications of experimental high-throughput methods to systematically identify and to characterize protein-ligand complexes within the proteomes of living organisms (Gavin et al., 2002). Some recent attempts to utilize this novel information, initially for a systematic low resolution imaging of these protein-protein complexes (Aloy et al., 2002), have displayed its large potential for structural proteomics on protein-ligand (protein) complexes.

Time-resolved X-ray studies and structural dynamics: In order to use the structures of the biological macromolecules as tools to understand their functions in biology, it is essential to investigate the dynamic changes of their structures associated with these processes. Over the last two decades, an arsenal of crystallographic methods has been developed, ranging from monochromatic to polychromatic Laue applications (Hajdu et al., 2000; Moffat, 2001). These methods require high intensity and energy tunable synchrotron radiation, permitting an experiment time regime that synchronizes with the reaction kinetics associated with, and the complementary application of spectroscopy and laser techniques, triggering and terminating reactions with at precise time intervals. Proof-of-principle case studies have demonstrated that experiments addressing specific biological questions are feasible in the nsec and even psec regime (Schotte et al., 2003; Bourgeois et al., 2003; Adachi et al., 2003). The expected time structure and optical properties of the PETRA III beamlines will provide ideal opportunities and an experimental set-up for future applications. As a spin-off, there could be also the possibility to use a pink beam option, also known as the narrow band-pass Laue data collection technique, for ultra-fast data collection. Such techniques may allow rapid exposure times in the range of 10^{-4} to 10^{-5} sec per frame, an improved signal-to-noise ratio, the absence of harmonic overlaps and reduced radiation damage effects. Ultimately, time resolved experiments at PETRA III could provide a basis to acquire sufficient expertise to plan and to design novel time-resolved experiments on single particles (Neutze et al., 2000) for the planned X-ray Free Electron Laser facility at DESY campus.

Biological structures at atomic and sub-atomic resolution: The number of X-ray crystal structures at atomic resolution (allowing visualization of atoms) and ultra-high resolution (visualization of electronic features), currently available from the PDB, is steadily increasing (Schmidt & Lamzin, 2002). A protein structure determined to such resolution offers a unique and extremely valuable tool by essentially closing the gap between biology and chemistry via establishing structure-function relationships in unprecedented detail in terms of accurate location of atoms (including hydrogen atoms), accurate inter-atomic distances as well as providing valuable information on the mobility and flexibility of the protein molecule even in the crystal lattice (Dauter, Lamzin & Wilson, 1997; Harata & Kanai, 2002). At ultra-high resolution, as demonstrated for crambin as a proof-of-principle case (Jelsch et al., 2000), even atomic detail of bonding electrons and free electron pairs can be obtained. Some of the specific properties of the PETRA III ring, such as the delivery of X-rays at high energies (defining the maximum reachable resolution) and high intensity will be ideally suited for future developments and applications of atomic resolution methods for a broad variety of crystallized biological macromolecules.

Experimental structure determination methods: Since in MX there is an inherent need to obtain the phase component for structure determination, techniques are required to derive this information experimentally. A major source of such information can be derived from the anomalous and the dispersive signals at energies close to the absorption edge of specific elements built into the structures of biological macromolecules. While traditionally, ‘heavy atoms’ were used by soaking or co-crystallization, more recently the arsenal has been extended by the routine incorporation of heavy-atom substituted amino acids (selenomethionine), heavy-atom derivatised DNA and RNA (iodine, bromine), soaking with halides (Dauter & Dauter, 2001) and even the exploitation of the anomalous signals of ‘light’ atoms such as sulphur and phosphorus that are generally found in biological macromolecules (Micossi, Hunter & Leonard, 2002; Ramagopal, Dauter & Dauter, 2003; Uson et al., 2003). The use of a wide energy spectrum in the range of 5 - 35 keV, which can be offered by PETRA III, will provide an unique opportunity, to offer an experimental setup for a broad range of established phasing methods and to develop novel techniques, particularly aiming for exploiting the anomalous signal properties of atoms that compose biological macromolecules.

6.16.2.2 Instrumental considerations for X-ray stations

General aims

The specifications of the planned MX beamlines at PETRA III will be largely governed by the challenges emerging from the research directions presented above. Biological crystallographic experiments require an intense and very stable X-ray beam tunable in energy with small, adjustable focus and low divergence. The end-stations will be automated to a level that minimizes (and eliminates wherever possible) the need for user intervention. The X-ray beam has to be conditioned by various sets of slits and attenuators and observed by a series of viewers and beam position monitors. Our aim is to provide adequate facilities that can cope with the most demanding requirements:

- State-of-the-art tunability in terms of a broad energy range, energy band pass and excellent beam stability to provide opportunities for carrying out a variety of experimental phasing methods that are available, under development or planned.
- High brilliance coupled with small focus size to allow measurements on extremely small crystals (in the range of a few μm), structures of large biological assemblies (up to the MDa range) and crystals with long unit cell dimensions (> 1000 Å).
- A high degree of automation, user-friendliness and parallelism that will allow high-throughput structure determination, notably in the fields of structural proteomics and drug-discovery oriented structural biology.
- To provide the experimental conditions for measurements and structure determination at extremely high resolution (< 1 Å).

- An experimental environment to allow time-resolved measurements matched to the time structure of the PETRA III ring with the intention of revealing the dynamics of biological processes.

- To allow adaptations in order to meet specific demands (lighting, data collection temperature, use of lasers, etc.).

Specific requirements

The instrumentation requirements are outlined as follows:

1. **Beam divergence**. The divergence of the beam has to be smaller than 0.5 mrad to resolve the diffraction spots of crystals with unit cell dimensions of up to 1,000 Å.

2. **Beam size**. In order to provide the best signal-to-noise ratio in the diffraction pattern, the beam focal size has to be adjustable and made consistent with the specimen size (from 0.3 mm down to 0.02 mm).

3. **Intensity**. The X-ray intensity delivered to a sample will be about 10^{13} ph/sec. Such intensity will allow collection of data from a typical protein crystal with an exposure time of about 0.1 sec per frame (0.5° of oscillation). With sufficiently fast detectors (readout time of about 0.1 sec), appropriate goniometers (rotation speed of about 100-200° per second) and fast beam shutters the total data collection from a crystalline sample will take only minutes.

4. **Energy range**. Experiments utilizing anomalous dispersion properties require X-rays tunable in energy range from 5 to 35 keV (2.5 to 0.36 Å). The higher energy limit is set by the Xe K edge; the lower energy limit is defined by transition-metal K edges and will also allow recording considerably improved anomalous signals from sulphur and phosphorus atoms.

5. **Energy resolution**. The incident spectral band pass $\Delta E/E$ will be less than 2×10^{-4} to resolve specific features in absorption spectra.

6. **Beam stability**. The relative position of sample and X-ray beam must be kept constant to within 5% of the beam size or sample size (whichever is smaller).

Instrumental design

Tab. 2.2.2 recalls the principal beam characteristics of PETRA III undulators. Very small photon source sizes, low divergence and extremely high brilliance (Fig. 2.2.2) will be ideally suited for the tasks of biological crystallography.

6.16.2.3 Proposed end-stations and optics

Overall scheme

In view of the increasing demand for structural information several important factors will be taken into consideration. Firstly, recent improvements in methodologies have provided non-specialists with the ability to carry out macromolecular structure determination. Secondly, the application of high-throughput technologies for protein production and crystallization will have a direct follow up in terms of the number of structures to be determined. Thirdly, industrial research in medicine, pharmacology, food and agriculture is poised to reap the benefits of the high throughput technologies.
To cope with the anticipated categories of experiments and with the diversity of the future user community we propose the construction of three MX beamlines. These beamlines will be in conjunction with one biological SAXS beamline (see Chapter 6.16.3) and are proposed to be situated on the last two high-β straight sections (section 8 and section 9[4]) using two 2 m long undulator sources (U1 and U2) per section (Fig. 6.16.2). The SAXS station will utilize the beam from undulator U2 of the second last straight section (section 8), while the three MX stations will use U1 from the same section and both U1 and U2 undulators from the last straight section. The initial 5 mrad horizontal separation of the U1 and U2 undulator beams (i.e. 170 mm in horizontal direction at 33 m distance from the undulator) will be increased to 300 mm in the vertical direction using vertically deflecting double crystal monochromators. Thus the beam centers at the location of the downstream optics hutches and experimental stations will be separated by more than 350 mm. This vertical separation will be sufficient to permit simultaneous operation of all four experimental stations and will allow the installation of a large area detector and other bulky end-station equipment.

X-ray optics

The objective of the optical set-up is to deliver a monochromatic beam at a fixed position of the sample with easily and quickly adjustable X-ray energy and maximized photon flux. Ideally, both focal spot size and beam divergence will be adjustable to meet the requirements of each individual experiment.
Tab. 6.16.1 summarizes the principal characteristics of the proposed beamlines. The optics of all MX beamlines will be designed to be similar, thus allowing standardization of components design and know-how transfer, particularly during the commissioning stage. The main optical elements are liquid nitrogen cooled double-crystal monochromators and Kirkpatrick-Baez (KB) mirrors, which will be used as focusing elements and high-energy filters. The KB arrangement with two individual mirrors allows independent and tunable focusing in both the vertical and the horizontal directions.
In order to estimate the beam size, divergence, band pass and flux on the sample, ray-tracing calculations were performed using the programs XOP and SHADOW with the input parameters described in Appendix A.1.1. Some examples of these calculations are given below for the station ES3.

[4]These are the two last sections close to building 48, see also Fig. 2.2.1.

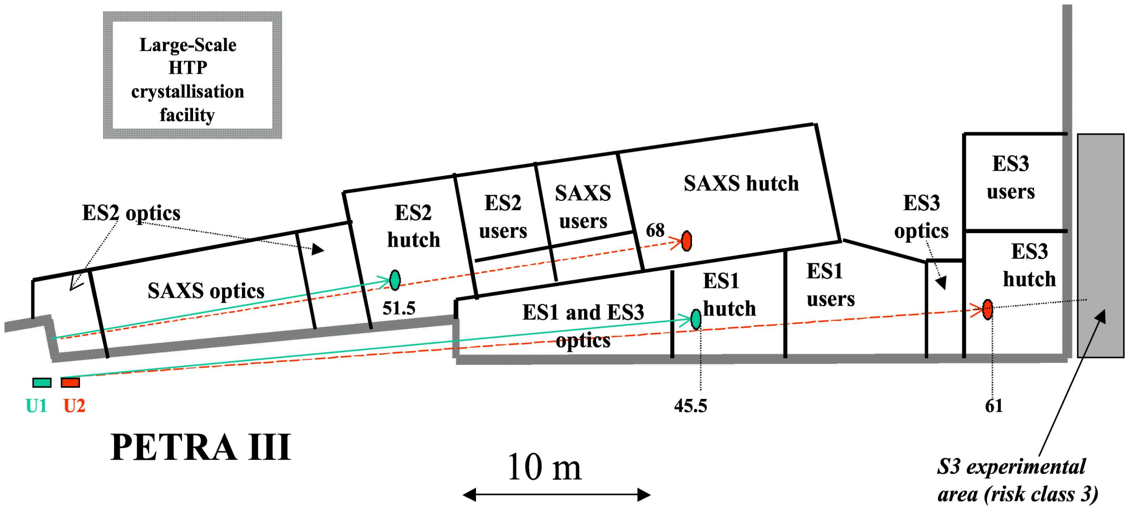

Figure 6.16.2: A schematic floor plan of the PETRA III experimental hall showing the proposed layout of the EMBL MX and SAXS beamlines.

Beamline	ES1	ES2	ES3
Main purpose	Wide range tunability	High-throughput structure production	Microfocus and special application
Energy range, keV	5.0 –35.0	6.0 – 16.5	6.0 –18.0
Bandpass (after monochr.) ΔE/E	Si(111): 1.4 –2.3·10^{-4} Si(311): 4 – 9·10^{-5}	Si(111): < 1.6·10^{-4}	Si(111): < 1.7·10^{-4}
Min. focus size, μm^2 (horizontal x vertical)	25 x 6	24 x 6	14 x 4
Divergence of the focused beam, $mrad^2$ (horizontal x vertical)	0.3 x 0.2	0.3 x 0.2	0.5 x 0.25
Intensity, ph/sec	$3\cdot10^{13} – 1\cdot10^{12}$	$2\cdot10^{13}$	$2\cdot10^{13}$
Pink beam option, (ΔE/E = 1.5·10^{-2}) Intensity, ph/sec	Possible $\sim10^{15}$	No	No

Table 6.16.1: Parameters of planned MX beamlines / end-stations on PETRA III.

Beamline control

The degree of automation controlling the alignment of optical components of a beamline has to be as high as possible with the final aim of a fully self-aligning system. To achieve this goal a sufficient number of monitors distributed along the beam path is a necessary pre-requisite. As a minimum requirement these monitors will be located before and after individual optical components and provide the shape as well as intensity information. They could be based on PIN diodes and fluorescence screens and TV-cameras with frame grabbers. A robust and fast bus system for the various analog and digital signals coming from these monitors and from the encoders of various motor axes will be linked to a dedicated control computer. If not fully automatic in the first instance, the control program must enable the inexperienced user to adjust the beamline for his specific requirements.

MX station 1 – wide range of tunability

ES1 will use the U1 undulator of the last straight section (section 9), Fig. 6.16.2. Fig. 6.16.3 shows the proposed layout of the station components.
The most important parameters for this end-station are the wavelength range (5-35 keV) and the narrow band pass (ΔE/E $\sim 2{\cdot}10^{-4}$) over the whole wavelength range. The focus does not have to be exceptionally small - about 200 μm seem appropriate - although there will be a possibility to achieve a focus size of the order of tens of microns (Tab. 6.16.1). The specific requirements for the detector are good DQE over the entire energy range and a sufficient size to cope with the larger scattering angles at both lower X-ray energies and in high-resolution measurements.

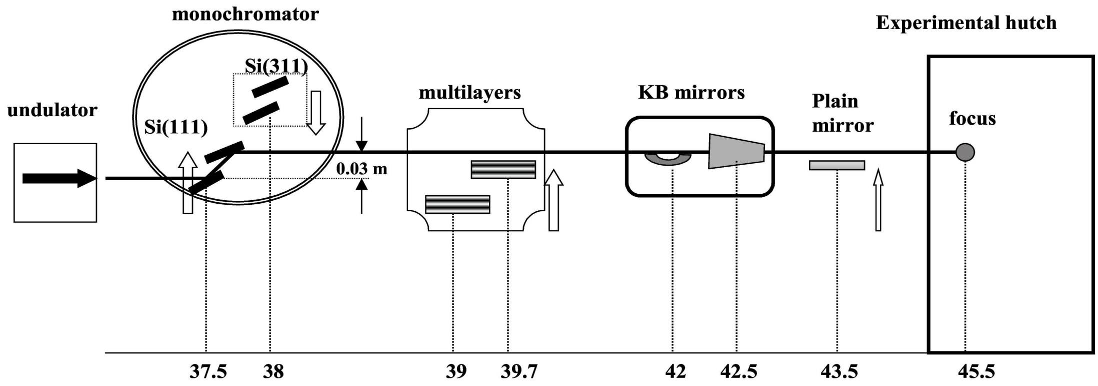

Figure 6.16.3: Layout of the optical components for ES1.

The first optical element is the fixed exit double crystal monochromator. It will be situated 37.5 m from the source point. Two monochromator crystals will be available, a high resolution Si (311) and a lower resolution Si (111). The former will be used for precise white line measurements and the latter for the softer X-ray region (below 10 keV). The Si (111) monochromator will also be used for routine measurements where high intensity is more important than energy resolution.
For high flux studies with "pink beam", the crystal-monochromator would be replaced by a cryogenically cooled double multilayer monochromator. Due to the small incidence angle of

multilayers, the available energy range in 'pink beam' mode will be 8 to 13 keV.
A pair of elliptically bent mirrors in the KB configuration will be used for harmonics rejection and focusing. The first mirror positioned at 42 m from the source will provide focusing in the vertical direction (1:12 demagnification). The second mirror will reduce the horizontal beam size (1:14 demagnification). The rather broad X-ray energy range makes it necessary to coat each mirror with two different metal stripes, rhodium and platinum. Rhodium coating will be used in the energy region between 5 to 18.5 keV at a fixed incident angle of 0.2°. In order to provide harmonic rejection at energies below 8 keV, we propose to use an additional plain silicone mirror positioned at 2 m from the focus. The platinum coated mirror will be used at a fixed incident angle of 0.15° in the energy region from 18.5 to 30 keV and at a fixed incident angle of 0.10° in the region from 30 to 35 keV.
The focal spot size will be variable in both directions (from 25 to 300 μm horizontally and from 6 to 300 μm vertically). In order to achieve this, the image of the source provided by each individual mirror must be adjustable.

To our knowledge, ES1 would be the first MX-station to allow high-energy resolution MAD (SAD) experiments with very high intensity over such a wide range of X-ray wavelengths and at the same time serving as reliable high-energy beam line for ultra-high resolution crystallography.

MX station 2 - high throughput structure production

ES2 is intended for high throughput structure production. It will use undulator U1 from the straight section 8 and will be located near to the Large-Scale crystallization facility, Fig. 6.16.2. Fig. 6.16.4 shows the proposed layout of the optical components. The fixed exit Si (111) double crystal monochromator will lift the beam in vertical direction by 300 mm to separate the beams from undulators U1 and U2. The large distance between the monochromator crystals will restrict the available energy range to an upper limit of 16.5 keV (0.75 Å) but maintaining a certain degree of tunability over the common absorption edges is required to allow high throughput SAD or MAD experiments.

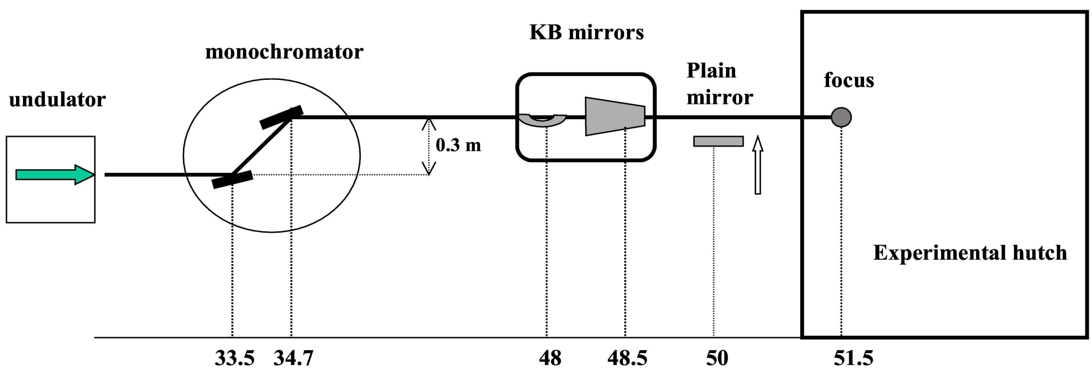

Figure 6.16.4: Layout of the optical components for ES2.

Over the last two years 80 % of the experiments at EMBL beamlines requiring tunability exploited the anomalous signals from selenium, mercury, bromine, platinum and iron. Therefore the station will be tunable over the range 6 to 16.5 keV (encompassing most absorption edges of these elements) with a band pass of $2\cdot10^{-4}$ and adjustable focus. Focal spot size will be variable from 24 to 300 μm in the horizontal direction and from 6 to 300 μm vertically.
Both KB mirrors will have rhodium coating. In the energy range from 6 to 8.5 keV an additional plain mirror either made from Si or SiO_2 or coated with a low-Z material like aluminum will be used for harmonic rejection. The first KB mirror positioned at 48 m will provide focusing in the vertical direction (1:14 demagnification), the second mirror will focus in the horizontal direction (1:16 demagnification). The mirrors will work at a fixed incident angle (0.2°).
A large and fast area detector and state-of-the-art systems for sample mounting and centering as well as automatic data evaluation are indispensable features for the end station of this beam line.
The end-station will be close to the high-throughput crystallization facility being established at the EMBL-Hamburg Outstation. In addition to the "standard" mounting-type experiments we are planning to develop a protocol for direct X-ray scanning of the free interface diffusion plates or even standard vapor diffusion plates to characterize the diffraction properties of the crystals in the trays directly. This option will be combined with the use of the microfocused beam described below.

MX station 3 - microfocus applications

This station will use undulator U2 from the last straight section (section 9), Fig. 6.16.2. The proposed layout for ES3 is shown in Fig. 6.16.5, some of the result of ray tracing in Fig. 6.16.6. The end-station will cover the photon energy range from 6 to 18 keV with the focus size smaller than 15 μm and a divergence of 0.5 mrad in the horizontal direction at the position of the protein crystal.
A fixed exit Si (111) double crystal monochromator will lower the beam in vertical direction by 300 mm to separate the beams from undulators U1 and U2. A plain silicone mirror positioned at 1 m distance from the focus will be used for the harmonic rejection in the energy range of 6 to 8.5 keV. Both KB mirrors will have rhodium coating and will work at a fixed incident angle (0.2°). The first KB mirror positioned at 58.5 m will provide focusing in the vertical direction (1:23.5 demagnification), the second mirror will focus in the horizontal direction (1:30 demagnification). In special cases, focusing to 1x1 μm^2 or smaller will be achieved by the addition of refractive lenses after the KB mirrors.
Given the downward trend in crystal size, reflecting the increasing sizes and complexities of the samples investigated, and the frequency with which initial crystallization conditions yield very small crystals, means of characterization will become critical to determine if the crystallization conditions warrant optimization. Large plate-like crystals susceptible to radiation damage can be exposed in different places to allow complete data sets to be collected, as demonstrated, for instance, for the nucleosome core particle (Luger et al., 1997). In addition, diffraction properties often vary as a function of the way a particular part of the crystal

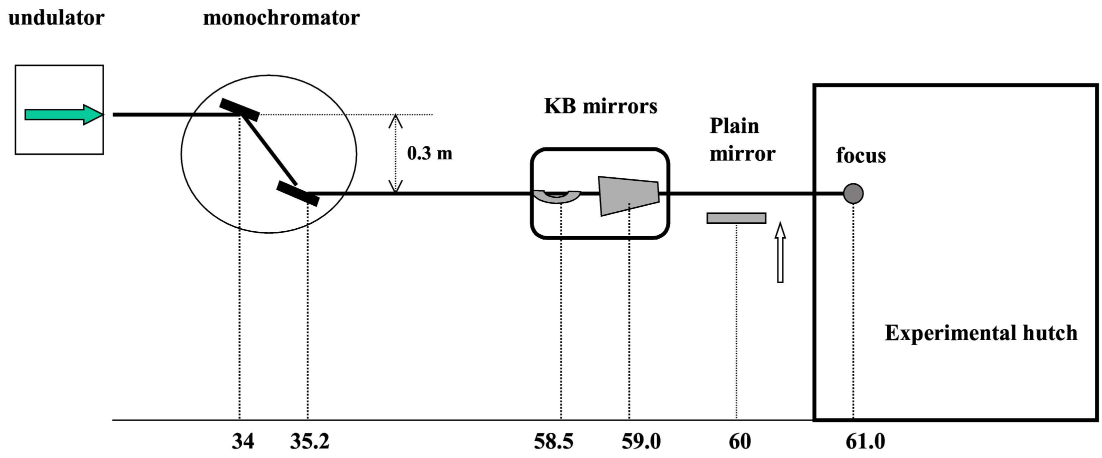

Figure 6.16.5: Layout of the optical components for ES3.

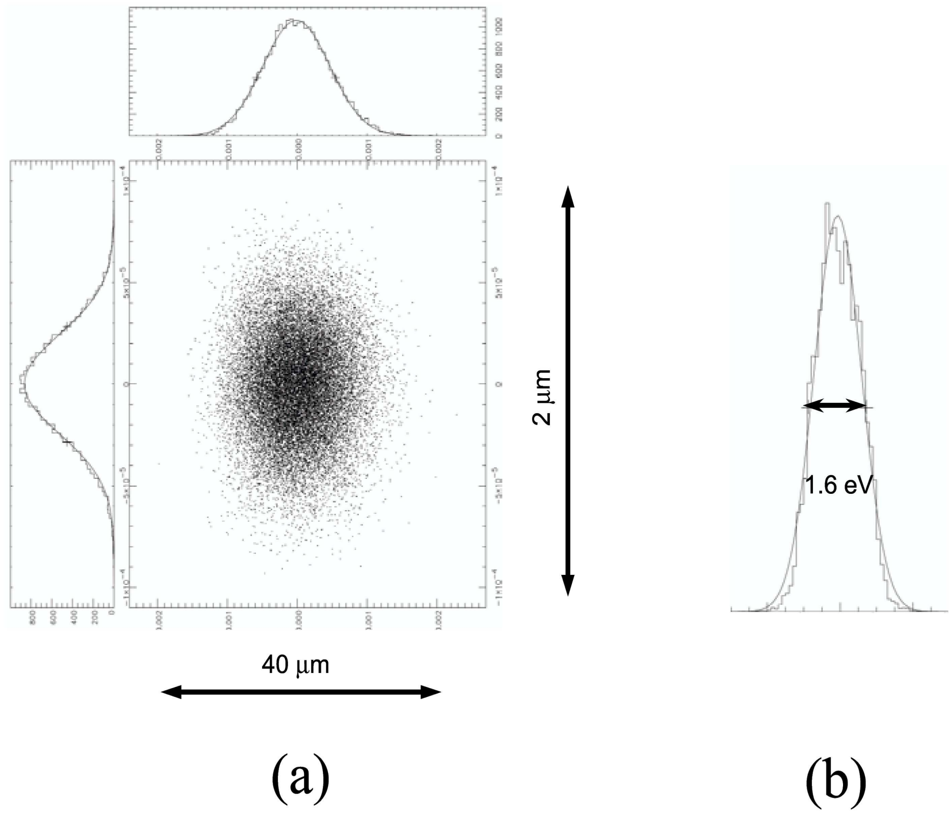

Figure 6.16.6: Ray tracing for the station ES3: (a) spatial distribution of the beam at the focal point and (b) the energy resolution as simulated by SHADOW at an energy of 12 keV.

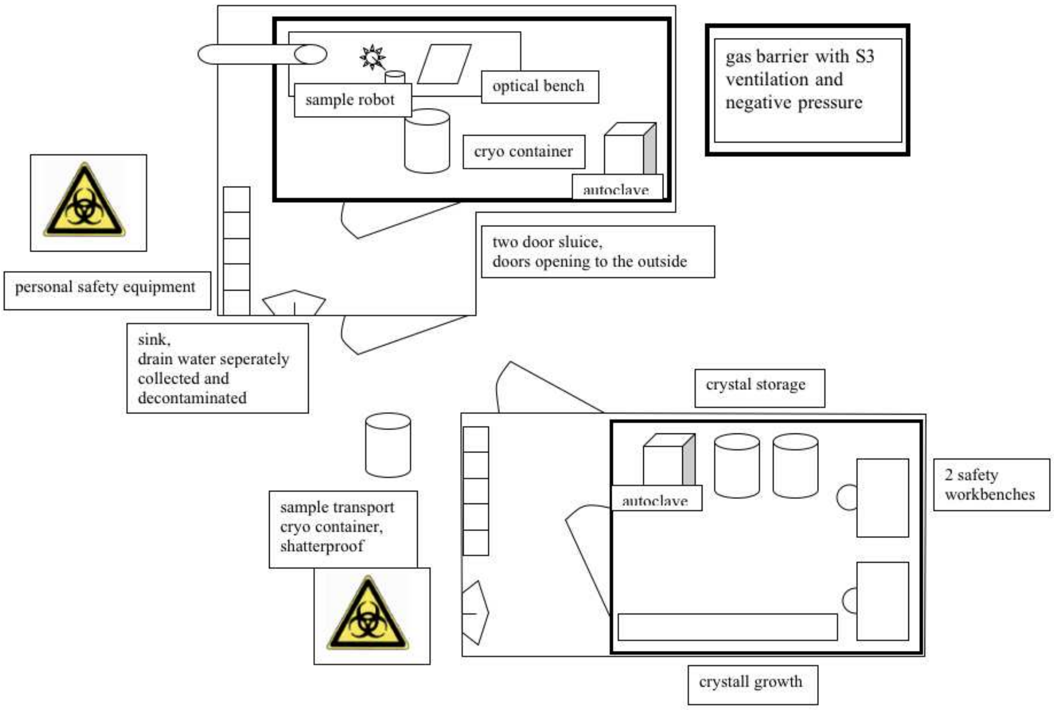

Figure 6.16.7: Layout of the future S3 X-ray facility.

has grown. The beamline ES3 will allow to screen different parts of the crystal allowing focused measurements of the “best” part that may be single or may diffract to the highest resolution.

A key feature of this end-station will be a micro-goniometer with advanced optics and a very small sphere of confusion for the rotation axis. Many of the concepts being used for the micro-goniometer at the ESRF could be adapted. Given the small volumes of the diffracting material the most important parameter for the choice of the detector will be the sensitivity.

MX station 3 - future expansion

Given the above listed specifications for ES3 it would be the obvious choice for measuring “difficult” crystals. A further option is then to expand into a field for which currently no facility exists. Handling of certain viruses, prions and other hazardous compounds underlies strict safety rules, ranging at the level of S3. This imposes certain restrictions on the end-station construction, as it has to be ensured that the entire experimental hutch is well separated from the surroundings and can be chemically and biologically decontaminated. Also, it will be directly linked to an S3 lab for sample preparation and handling. A schematic layout of the S3 facility for applications in biological crystallography is shown in Fig. 6.16.7.

Although actual construction of an S3 facility is not a part of this proposal, allowance will be made already at this stage for the beamline ES3 to have a beam pipe, which could exit the planned experimental hall and lead to an S3 containment building where diffraction experiments on pathogenic organisms could be performed under the required safety regime. It seems essential to offer the users an opportunity to access a facility that would allow handling and measurements of samples at an S3 safety level. Topics and potential applications that currently are of high scientific interest include the following: *prions* causing bovine spongiform encephalopathy (BSE); human Creuzfeld-Jakob disease (CJD), kuru; *retroviruses* human immunodeficiency virus (HIV), T-cell leukemia virus (HTLV) and *hepatitis viruses* A to E.

6.16.2.4 End-station design: specifications for the basic end-station

EMBL will implement a novel design of the crystallographic end-stations where one basic model can be extended to the particular technical demands of each beamline. A number of technical specifications will be similar on all beamlines. Accessory equipment (e.g. a laser for experiments in time resolved crystallography or a high-pressure cell for high-energy applications) can be added when necessary. The end-stations will be designed to operate in a fully automated manner with a possibility of remote control.

Fast Shutter

Due to the high photon flux of the synchrotron radiation extremely short exposure times per frame can be anticipated. Given the prospect of pixel detectors with read-out times in the range of milliseconds that are currently being developed at various laboratories it is considered that diffraction data can be collected in a continuous rotation mode or with very fine slices (less than $0.1°$). This requires an extremely fast and accurate shutter-system that is able to close and open the X-ray beam within less than 1 msec.

Microfocusing and collimation

An accurate slit system is required to match the beam size optimally to the crystal size. The ES3 station will be specifically designed for applications with very small crystals down to 5 μm or even smaller. The accuracy of the slits system thus has to be better than 1 μm. Commercially available systems can already provide the required accuracy.

Beam viewer

A beam viewing system is an integral part of modern end-stations, e.g. the micro-goniometer at the ESRF, as mentioned above. In order to ensure that the synchrotron beam actually hits the sample at a required position, a high-accuracy beam viewing system is required. This can be accomplished by a single crystal scintillator or by a small CCD camera that is moved into the beam in order to determine the center of the beam experimentally. Should the beam be misaligned, an automatic feedback system to the optical instrument (i.e. the final mirror) will move it into the desired position. Alternatively, the entire setup could be placed on an optical bench that is positioned into the beam.

Visible and fluorescence light coupled to a high-resolution video microscope

In order to identify single crystals of biological macromolecules frozen in a cryo-loop there is a need for image recognition in visual light and, possibly, in UV ranges. The idea of utilizing the inherent UV fluorescence of biological macromolecules has been originally suggested by G. Rosenbaum (Rosenbaum, unpublished) and research exploring the feasibility is currently underway at the EMBL-Hamburg Outstation and elsewhere. Whereas two images taken at 0 at 90 degrees will be sufficient to center the crystal a series could be used for shape determination. The precise determination of the shape of the sample could then be used for various applications including an empirical absorption correction for long-wavelength data collection.

Phi-goniostat and kappa goniometer

The end-stations will be equipped with a fast and accurate direct drive phi-goniostat that would also allow the collection of continuous rotation data. Due to the small beam aperture and crystal size the accuracy of the crystal position as well as the sphere of confusion has to be within 5 μm for the standard operation and within 1 μm for the microfocus ES3 beamline. The rotation speed required is 360° per second or even faster.
The end-station ES1 will be equipped with a kappa-axis goniostat, which will allow exact crystal alignment and re-orientation for completion of blind regions in high-resolution data collection. It will be particularly useful in a critical phasing experiment or for semi-empirical absorption correction using psi-scans. The specification for the accuracy will be slightly lower for a kappa goniometer with sphere of confusion of 5 μm.

Motorized beamstop

Motorization of a beamstop is an integral component of the overall automation of the end-station. A versatile beamstop with an integrated X-ray sensor developed at SSRL has proved reliable for a variety of applications including the rapid alignment, exposure control, examination of the direct beam profile, characterization of the shutter timing and energy calibration (Ellis, Cohen & Soltis, 2003).

Robotic sample mounting

A high degree of automation including robotic sample mounting is mandatory. Full software control is needed not merely to accelerate the mounting process as such, but to provide robustness in sample handling and screening and to allow complete remote control of the experiment. The vast majority of the samples will be frozen in cryo-loops on standard magnetic caps in plastic vials and supplied in standard sample containers. A sufficient-size storage container for several sample pucks will be installed at each end-station. We anticipate that by the time of the construction of the PETRA III beamlines the sample container and shipping systems will be standardized

Detector gantry

Given the fast rate of the development of X-ray detectors it is not clear which type of detector will be available by the time of construction of the beamlines at PETRA III (see Tab. A.1.2 for the current anticipations). Therefore, we will stick to a framework that will be able to account for spatial demands and accommodate very large and heavy detectors (optionally even two different detectors). A sufficiently wide range of the sample-to-detector distance will be made available. In order to decrease air scattering at longer wavelengths an option of a helium cone covering the space between the crystal and the detector will be allowed.

6.16.2.5 End-station area

Beamline operators

Each MX beamline will contain sufficient space for the beamline operators and provides easy access to electrical connections, computers for motor controls, monitors for temperature of optical elements, vacuum and beam position. Ideally this area will be close to the beamlines optical hutch and will be enclosed (4 to 6 m^2 is the minimum). Regular beamlines users will not have access to this area.

User area

The user area for each beamline will be quiet (and therefore insulated from the main experimental hall), will provide the necessary control, processing and graphics computers (the future is likely to see the majority of structures being processed and solved "on-site") and will be in close proximity to the experimental hutch. Local experience at DORIS and at other synchrotron facilities will suggest an area of no less than 4x5 m^2 for each of the three user control areas. Given the likely shortage of space one could think of placing these user areas on top of the respective end-stations.
Indispensable components of the user area are: event-monitors for crystal, cryo-system, spindle axis, detector distance, slits, ring current, ion chamber readings, sample changer, fluorescence detector, table alignment and space for the overall set-up, desks for up to four scientists, wardrobe, safe, computers for: monitoring beamline and end-station status, data collection, data processing, computer graphics, PC for word processing and data backup facilities.

Sample storage facility

In order to meet the demand which is likely to arise from the "crystal in the mail"-type data collection, a facility will be installed in close proximity to the experimental hutches, in which samples received from users and ready to be mounted on the end-station, will be stored at liquid nitrogen temperature until they are scheduled for X-ray measurements. Such a storage facility will be adapted to the to be agreed standards with respect to shipping containers, carousels and mounting robots.

The facility will include the following components:

- entry gate,
- barcode reader for sample tracking,
- robotic arm to receive and store the samples,
- storage space under liquid nitrogen temperature,
- automated nitrogen refill through a turbulence-free system,
- computer and data base for sample tracking,
- exit gate.

The facility will need to be accessible from both the outside (entry gate) and the inside of the hutch (exit gate). For practical and space reasons some elements of the manual transfer between the facility and the end-station hutches will have to be accounted for. A room of the size of minimum 2 x 3 m^2 will be sufficient. Efficient ventilation must be insured to cope with the use of large amounts of liquid nitrogen.

Sample preparation laboratory

A single laboratory area no less than 20 m^2, equipped with benches, balance, fridge, deionised water, simple chemicals and basic tools for crystal handling, as well as room and tools for crystal mounting (individually or into carousels), will be in the vicinity. An additional area of 10 to 20 m^2 or a separate enclosure for working with gases (for example for pressure derivatization of crystals with xenon or krypton), including a fume hood for derivatization with possibly toxic chemicals with a high vapor pressure and handling of heavy atom compounds (including waste containers) will also be close by. This enclosure must be ventilated to the outside and must therefore be at the edge of the experimental hall. It will also be possible to temporarily store crystallization plates in this room, which makes air conditioning / temperature stabilization necessary. Liquid nitrogen supply and equipment for cryo-freezing of crystals are absolute requirements and a dewar for storage of crystals at 100 K must be available.

Large-scale crystallization facility

The large-scale crystallization facility will be installed in the vicinity of the beamline ES2, Fig. 6.16.2. It will comprise a fully automated facility involving robotics preparation of solution cocktails for crystallization, drop dispensing, plate sealer, bar-code readers, transport system to and from storage cabinets, optical crystal visualization system and supporting computer environment for full sample tracking. The facility is planned to be installed by EMBL on a DESY side in 2004 and will be moved into the PETRA III hall in 2008. The

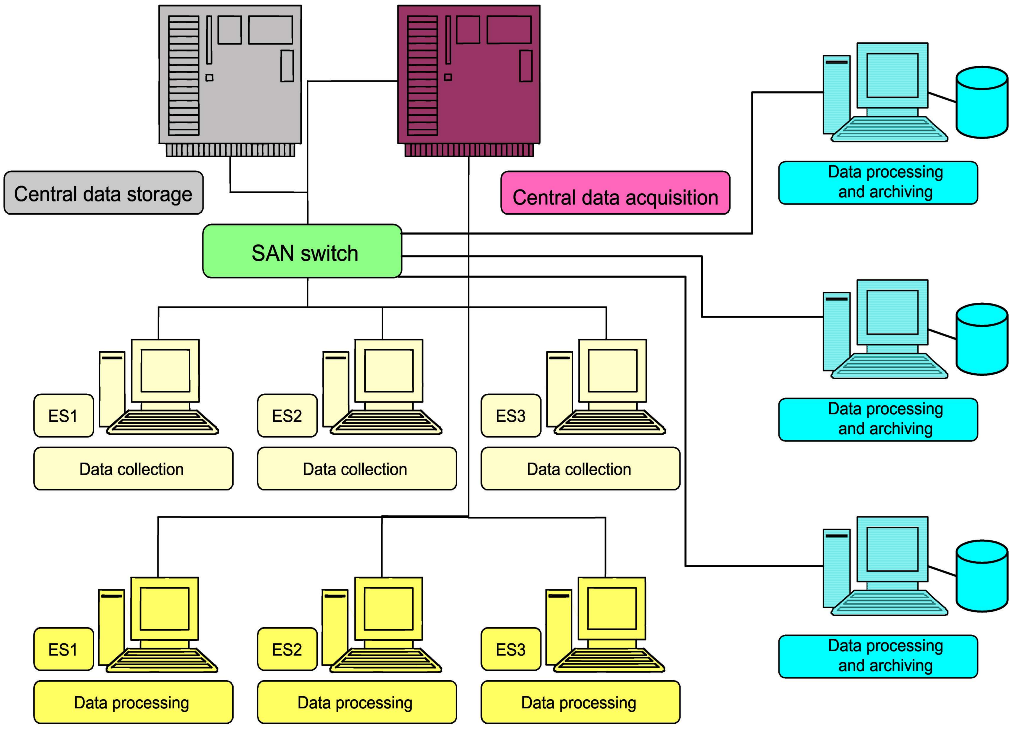

Figure 6.16.8: Schematic representation of the planned computing infrastructure for MX.

minimum space requirements are of an order of 7x8 m^2.

Computer environment

For data collection and processing each beamline will be equipped with three computers, one for data collection, one for data processing and one graphics machine, Fig. 6.16.8. The data collection machine together with the central storage and data processing unit will form a storage area network (SAN) via fiber channel, where central storage device is connected via multiplexed FC uplinks. This will allow the fastest possible data transmission and will be completely independent from the normal network traffic.

The planned data storage unit can be an intelligent fiber channel RAID running RAID level 5 plus hot spare disks and a snapshot functionality so that a normal tape backup will no longer be needed. The needed capacity of the central storage device is related to the image size and the read-out speed of the detectors. The capacity will be high enough to keep data files for at least 10 days, so that users can verify that the data were successfully archived. For data archiving a fiber channel compatible tape device (LTO, SuperDLT) can be connected to the SAN switch, which will then be available from all machines in the SAN. Another possibility for data archiving is the transfer to user laptops via normal network connection.

Data processing machines are basically terminals connected to the central data processing

unit via normal network connection. The central unit will consist of a cluster of machines, which can upscaled and extended when needed.
In MX, data processing and archiving frequently still extends beyond the allocated experimental time. A major reason is within the large time-requirements, and with the small control stations advocated above, the parallel handling of two sets of experiments in this area becomes impossible. Therefore a second area containing the necessary computing and archiving facilities will also be available and common for all crystallographic end-stations. This could be placed almost anywhere in the experimental hall and will have minimum dimensions of $3x10\,m^2$. This area will be equipped with at least three computers connected to the SAN so that fast data transfer to those machines is ensured. They will also be connected to archiving devices. For the type of those archiving device one may consider DVD burners, tape devices or transportable disks or whatever else that will be appropriate at the time of installation.

6.16.2.6 Resource requirements

We have made estimates for the costs of the construction of three MX beamlines, see Tab. A.1.3 for details. Expenses for construction of insulated hutches have not been accounted for. The estimates for the optical and vacuum components, X-ray detector, end-station and computer environment are based on the currently available quotes. We estimate that 9 person-years of a technical position and 3 person-years of a scientists position are required to construct each of the MX beamlines.

6.16.3 Biological small-angle X-ray scattering

Authors: M.V. Petoukhov and D.I. Svergun

External advisors:

Peter Boesecke	ESRF, Grenoble, France
Tetsuro Fujisawa	RIKEN, SPring-8, Himeji, Japan
Guenter Grossmann	SRS, Daresbury Laboratory, Daresbury, UK
Tom Irving	BioCAT, Illinois Institute of Technology, Chicago, USA
Javier Perez	Synchrotron Soleil, Gif-sur-Yvette, France
Ritva Serimaa	University of Helsinki, Finland
Hiro Tsuruta	SSRL, Stanford University, USA
Maria Antoinetta Vanoni	University of Milan, Italy
Regine Willumeit	GKSS Research Center, Geesthacht, Germany

6.16.3.1 Introduction

During the last decade, small-angle X-ray scattering (SAXS) has become an increasingly important tool for the study of biological macromolecules. The method allows one to study native particles, from individual proteins to large macromolecular complexes, in solution under nearly physiological conditions. SAXS not only provides low resolution models of particle shapes but in many cases answers important functional questions. In particular, kinetic SAXS experiments allow one to analyze structural changes in response to variations in external conditions, protein-protein and protein-ligand interactions, and to effectively study equilibrium and non-equilibrium processes like assembly/dissociation of (macro)molecular complexes or folding/unfolding. Fundamental biological processes such as cell-cycle control, signalling, DNA duplication, gene expression and regulation, some metabolic pathways, depend on supra-molecular assemblies, and their changes over time. There are objective difficulties to study such complex systems, especially their dynamic changes by other structural techniques like spectroscopy, NMR and macromolecular X-ray crystallography (MX). Furthermore, for macromolecules with molecular masses of a few hundred kDa - too large for NMR and too small for cryo-electron microscopy (EM) - SAXS remains effectively the only method to obtain their shape in solution. Current trends in the life sciences point to a phase of integrated systems biology, which aims to understand living systems across the different levels of biological organization. Here, SAXS together with cryo-EM will provide the framework for the analysis of complex structures in which the high resolution models from MX and NMR can meaningfully be fitted.

The recent resurgence in biological SAXS is attributed to the synergy of software and hardware development. New powerful data analysis methods have become available (Svergun & Koch, 2002), which tremendously improved resolution and reliability of models deduced from SAXS data, and the new possibilities have significantly enlarged the user community. Simultaneously, SAXS instruments have been built on high brilliance 3rd generation synchrotron sources (Irving, 1998; Fujisawa et al., 2000; Narayanan, Diat & Boesecke, 2001). As the SAXS pattern is collected in the vicinity of the primary beam, the data quality depends critically on the beam size and divergence. SAXS is therefore among the techniques which profit most from the low emittance undulator radiation on 3rd generation sources. Furthermore, the high flux of these sources is extremely important for the analysis of weakly scattering biological samples. Currently, high quality scattering patterns can be collected in less than a second using sub-mm beam sizes on the undulator SAXS beamlines like ID02 (ESRF, Grenoble, France), BL45A (SPring-8, Himeji, Japan), and BioCAT (APS, Argonne, USA).

The high brilliance undulator beamlines are revolutionizing biological SAXS in several ways. Firstly, they permit studies using limited amounts of material (sample volumes down to a few μl and solute concentrations below 1 mg/ml) thus significantly widening the range of applications. This advantage of the high brilliance sources is comparable to the use of small crystals in MX. Secondly, kinetic experiments to measure full solution scattering patterns in the millisecond range have recently become possible (e.g. Schmolzer et al., 2002; Akiyama et al., 2002; Russell et al., 2002). Moreover, the new sources will permit one to revive earlier and potentially powerful approaches like anomalous SAXS (ASAXS) for the analysis not only of counter ion distributions (Guilleaume et al., 2002; Das et al., 2003) but also of bound biologically relevant metals and ions.

The parameters of the major present and planned SAXS beamlines partially used for life sciences on third generation sources are summarized in Tab. 6.16.2. None of these beamlines is dedicated to biological SAXS, except for BL45A at Spring-8, designed for high pressure and time-resolved experiments on solutions. The high flux beamline BL40XU (Spring8) utilizing pink beam is largely used for fluorescence and diffraction studies. The 8-ID IMMW-CAT beamline at the APS, which permits coherent scattering studies with pink beam and time-resolved SAXS experiments, is largely devoted to material science. The 18-ID BioCAT beamline at the APS, designed for non-crystalline biological objects, is shared between three techniques (fiber diffraction, EXAFS and SAXS). The ID02 beamline at the ESRF optimized for the use at 0.1 nm wavelength in wide range of scattering vectors is primarily dedicated to soft condensed matter research. The ASAXS ID1 beamline yielding wide energy range is mostly used for materials research. The planned instruments at Soleil (France) and Diamond (UK) are multipurpose beamlines for research in the areas of condensed matter, materials and the life sciences.

6.16.3.2 Main features of the biological SAXS (BioSAXS) beamline

The present proposal aims at the construction of an undulator beamline for biological small-angle scattering at PETRA III. The main idea is to utilize the low emittance of the PETRA III source and the high brilliance of undulator radiation for providing the user community with a beamline, where the combination of the hardware and data analysis software opens the possibilities for high throughput (HTP) experiments and for cutting-edge research. This beamline will be built in the framework of the general EMBL concept for structural biology at PETRA III, but will also provide options for non-biological studies. The main features of the BioSAXS beamline are:

- The beam quality provided by the PETRA III undulator will be fully exploited to obtain a stable beam of high flux, small size and divergence yielding scattering patterns in the resolution range from about 2000 to 0.1 nm.

- The beamline will be tunable over a broad energy range allowing for ASAXS experiments on biologically relevant atoms or ions, from Ca to Mo (K-edges 4.038 and 19.99 keV, respectively). A high flux mode utilizing a multilayer monochromator is envisaged for the analysis of fast kinetics.

- A pink beam option will be provided for sub-ms kinetic studies, coherent scattering and pilot experiments for future XFEL applications.

- The beamline will share the infrastructure for biological sample preparation and handling with other planned EMBL beamlines and endstations. A pipeline will be envisaged to rapidly analyze proteins and protein complexes purified for the HTP crystallization facility.

- The sample environment will provide possibilities for performing HTP measurements with minimum amounts of material and for kinetic studies. An option will be included to collect crystallographic diffraction patterns from macromolecular assemblies with large unit cells.

- A data acquisition and analysis system will be installed at the beamline for automated data processing and interpretation allowing in particular large scale studies of biological macromolecules and three-dimensional model building.

6.16.3.3 Expected user community and collaborations

The construction of the proposed BioSAXS beamline responds to the rapidly increasing number of biological systems being studied and amenable to SAXS. EMBL runs the SAXS beamline X33 at DORIS III, and the number of biological projects at this beamline has grown annually by about 20% during the last four years. The BioSAXS beamline, combining excellent beam properties provided by PETRA III with the expertise in methods and automated data analysis developed at the EMBL, will make SAXS one of the major methods for the analysis of biological macromolecules. The current user community of the X33 beamline is expected to grow further, and the samples for the solution scattering analysis will come not only from individual research projects but also from systematic HTP protein production facilities.

A SAXS beamline with the proposed parameters (dynamic range, flux and beam size/divergence) will also be useful for soft condensed matter and material science applications (analysis of polymers, colloids and micro-emulsions, liquid crystalline phases, nanomaterials, fiber diffraction studies). Although the main priority of the BioSAXS beamline will lie in biological applications, the short measurement times and automation of the data processing/analysis will leave about 25% beamtime also for non-biological experiments. As a competent partner in this field, GKSS Research Center (Geesthacht, Germany) expressed interest in participating in the construction and operation of this beamline in collaboration with EMBL.

Instrument	Application	Monochromator	Mirrors (H)oriz / (V)ert. Focussing	E range, keV	Source-sample, m	Sample-detector, m	Flux	Spot, mm^2	Divergence, μrad^2
Operational	**beamlines**								
BL45A SPring-8	SAXS	$2\times$flat diamond (111) DCM	KB, V+H Rh coated	6.6-16	56	0.5-10	1×10^{13} @12keV	0.6×0.4	80×30
BL40XU SPring-8	High flux	none, $\Delta\lambda/\lambda=2.0\times10^{-2}$	KB, V+H Si, Rh coated	8-17	48	0.5-4.5	1×10^{15} @12keV	0.25×0.04	Not given
8-ID, ANL	Coherent, time resolved SAXS	none(for pink beam) $\Delta\lambda/\lambda=2.6\times10^{-2}$	Flat Si, No focussing (slits)	7.7	55	4.5	3×10^{12}	0.05×0.05	56×25
18-ID ANL	SAXS, EXAFS, Fiber	$2\times$Si(111) or $2\times$Si (400) DCM (Flat + sagitally bent)	V: ULE/Pd/Pt coated	3.4-34	63	0.5-5.5	1-2×10^{13} @12keV	0.15×0.04	190×160
ID-02 ESRF	SAXS / USAXS	Si (111)	Toroidal coated	8-17	56	0.5 – 10	5×10^{13} @12keV	0.6×0.2	70×25
ID1 ESRF	ASAXS	$2\times$Si (111), $2\times$Si(311) (Flat + sagitally bent)	V: Si/Rh/Pt Rh coated	2.1-42	46.1	0.5 – 5.0	4.4×10^{13} @8keV	0.2×0.06	500×70
Projected	**beamlines**								
Beamline 11 Diamond	NCD (“life + physics”)	Flat/bent crystal Si(111) or multilayer	Focussing mirror (+microfocus)	4-20 ($\Delta\lambda/\lambda = 10^{-4}$)	49	0.5-10	5×10^{12}	0.10×0.01 (normal) 0.02×0.02 (micro)	200×20
SWING Soleil	SAXS / WAXS (“bio + soft”)	Flat crystal $2\times$Si (or Ge)	KB V+H Pd - Si/Pd	5-15 ($\Delta\lambda/\lambda = 10^{-4}$)	32	0.5-10	3×10^{12}	0.40×0.13	$\sim75\times20$

Table 6.16.2: Parameters of SAXS beamlines used for life sciences on 3^{rd} generation sources.

6.16.3.4 Instrument design

Overall scheme and implantation

It is proposed to build the BioSAXS beamline on the second 2 m undulator U2 of a split straight section. The first 2m undulator of this section will be used by the HTP EMBL MX beamline (ES2) and the users of the two beamlines (as well as of the XAS experimental station) will have direct access to the HTP crystallization facility (Fig. 6.16.9). The optical beam path of the MX beamline will be lifted by 30 cm by a double crystal monochromator (DCM), which will be positioned in the first ES2 optical hutch. The optical elements of the BioSAXS beamline will be positioned inside the optics hutch at a distance 35–47 m from the source, and the beam path will be diverted down and to the right to allow for sufficient separation from the ES2 beam pipe (Fig. 6.16.10A). The vacuum tube with the focused SAXS beam will pass through the second optical hutch of ES2 and its experimental hutch (47–60 m), and the SAXS user room (60–65 m). The experimental hutch of BioSAXS will occupy the space at 65–75 m.

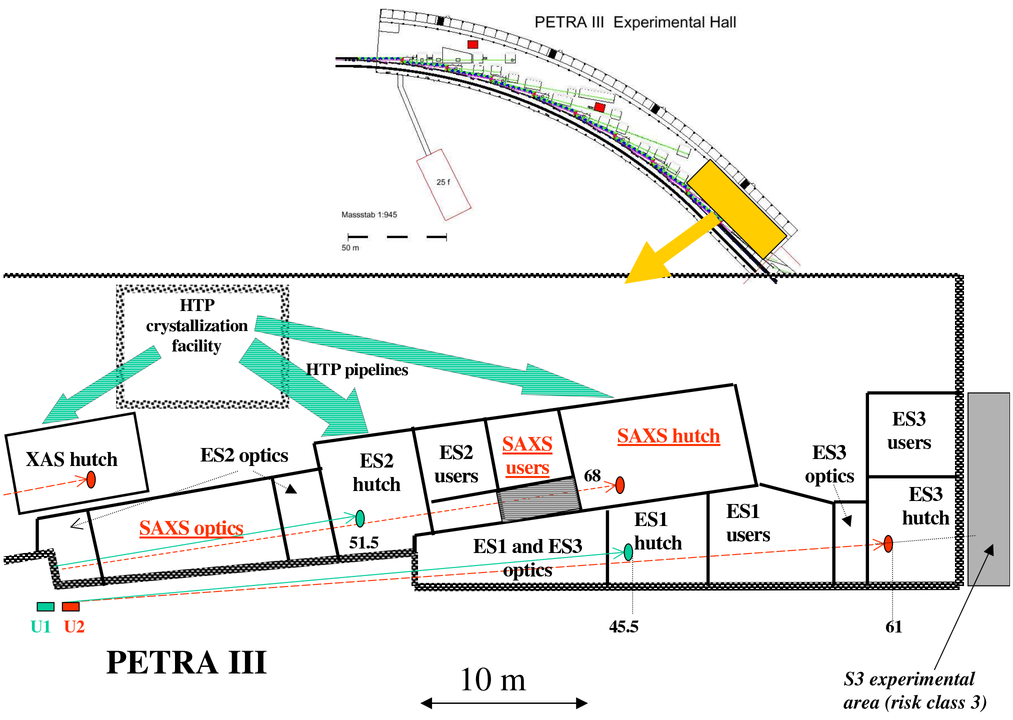

Figure 6.16.9: Overall scheme of the EMBL structural biology area with BioSAXS beamline components in red. Top: implantation of the EMBL area into the PETRA III experimental hall.

Optical elements

Several possible options have been considered for the BioSAXS optics setup to optimize the beam size/divergence, stability and convenience of use. It was decided to use a flexible setup separating monochromatizing and focussing elements and to employ a moderately focussing configuration with small demagnification to minimize the beam divergence at the focus. Given the extremely low emittance of the PETRA III undulator, such a setup permits one to obtain a clean low divergence beam and to reach the scattering vectors corresponding to more than 2000 nm resolution.

The major elements of the beamline presented in Tab. A.1.5 and Fig. 6.16.10 are:

1. **Beryllium window and pinhole.** To reduce the absorption at low energies, a beryllium window of reduced thickness (250 μm) is proposed (at 4 keV, this window yields transmission T=67% *vs* T=44% of a 500 μm window). The position of the undulator beam will be detected by white beam monitors WBM (tungsten wire scan and/or slit scan, the latter detecting also the central cone). A cooled slit system (P) with variable size will select the most intense portion of the white beam thus reducing the heat load onto the subsequent optical elements.

2. **Monochromators**. A flat cryogenically cooled Si(111) fixed exit DCM is positioned at 37 m distance. We suggest the DCM to be the first optical element as it is relatively easy to adjust and monitor its position and orientation in the white beam by observing the Bragg reflection from the first crystal. The DCM will provide $\Delta\lambda/\lambda$=1-2$\times10^{-4}$ for possible ASAXS applications in the relevant energy range (from 4 to 20 keV). For high flux studies, the DCM will be replaced by a cryogenically cooled Mo/C double multilayer monochromator (MLM) at a distance of 38 m yielding two orders of magnitude gain in flux at the expenses of a broader bandpath (from $\Delta\lambda/\lambda$=1.5$\times10^{-2}$ at 7 keV to $\Delta\lambda/\lambda$=2.0$\times10^{-2}$ at 15 keV). Due to the smaller incidence angle of the MLM, the distance between the two multilayers will be larger than that between the crystals in the DCM (up to 0.7 m).

3. **Slits and beam monitoring.** Three pairs of cylindrical horizontal and vertical slits will be used (Fig. 6.16.10). Slit S1 will select the central cone of the undulator and define the beam size. Slit S2, located at about 5 m before the sample, will reduce the background from the optical elements, and the guard slit S3 in front of the sample will reduce the parasitic scattering from S2. The position of the monochromatic beam will be monitored by the removable fluorescent screens and pin diodes (beam monitors, BM). The intensity of the incoming beam will be measured by a removable pin diode and/or by a non-removable device like ionization chamber or glassy carbon placed after S3 in front of the sample and the transmitted intensity by the diode mounted onto the beam stop.

4. **Focussing mirrors.** A pair of cylindrically bent mirrors in Kirkpatrick-Baez (KB) configuration will be used for harmonics rejection and focussing (Fig. 6.16.10). The

first vertically focussing mirror (VFM1), positioned at 40 m, slightly reduces the vertical beam size (1:1.2 demagnification). The horizontally focussing mirror (HFM) at 45 m will reduce the horizontal beam size (1:1.6 demagnification). When used with the DCM and MLM, the water-cooled mirrors will work at a fixed incidence angle (0.18°) and fixed curvatures (11.5 km for VFM1 and 11 km for HFM) to focus the beam at 73 m. Each mirror will have two coatings (Si and Rh) to work in the energy ranges 4-9 keV and 9-20 keV, respectively (Fig. 6.16.11A).

5. **Pink beam mode**. For extra high flux (three times more than for MLM) and coherent scattering applications, a pink beam option will be provided with $\Delta\lambda/\lambda$=2×10^{-2}. This mode will be used for the energies around 8 keV, near the maximum brilliance of the fundamental undulator line. In this mode DCM and MLM will be removed from the optical path, and the first optical element will be a vertically focussing nitrogen cooled mirror VFM2 at 43.2 m (1:1.4 demagnification). This Si coated mirror will have the same focal point and grazing angle as VFM1 to keep the beam trajectory unchanged, so that there will be no need to adjust the focussing of the HFM.

The above configuration will ensure easy and rapid change of mode of operation between the DCM, MLM and pink beam options. The mirror inclinations will be fixed in normal modes of operation but could be changed if additional focussing elements like beryllium lenses will be introduced. All the optical elements will be positioned in the SAXS optical hutch to work under ultra-high vacuum conditions. Differential pumping will be employed to ensure that this portion of the beamline operates in ultra-high vacuum.

6.16.3.5 Beamline performance

To estimate the beam size, divergence and flux on the sample in the proposed configuration, ray tracing calculations were performed. The parameters of the 2 m long U2 PETRA III undulator were: period 2.9 cm, K_{max}=2.2, yielding the source size 330×13 μm^2 and divergence 26×21 μrad^2 (both horizontal×vertical FWHM). The simulations were done using the programs XOP (ESRF) and SHADOW (University of Wisconsin) for the three modes of operation: (i) DCM in the range 4-20 keV; (ii) MLM @ 8 keV; (iii) pink beam @ 8 keV. The position of the focus was at 73 m from the source, and the offset of the beam center with respect to the initial beam direction at the focus point was 17.6 cm (horizontal) and -18.7 cm (vertical) (Fig. 6.16.10A). All the computations were made for the partial flux through the aperture of 1.2×0.7 mm^2 (horizontal×vertical) at 35 m distance (the pinhole size corresponding to the central cone). A 0.5 μrad mean slope error of the mirrors was assumed; mirror surface roughness up to 1 nm did not change the size and divergence significantly.
The beam size and divergence obtained by the ray tracing are presented in Fig. 6.16.10B,C. The materials, positions and orientations of optical elements are given in Tab. A.1.5 and the computed properties of the beam in Tab. 6.16.4. Fig. 6.16.11B presents the energy distributions in the partial flux for the configurations with DCM, MLM and pink beam. From comparison with the existing and planned SAXS beamlines on 3rd generation sources (Tab. 6.16.2) it can be concluded that the BioSAXS beamline will provide the overall widest

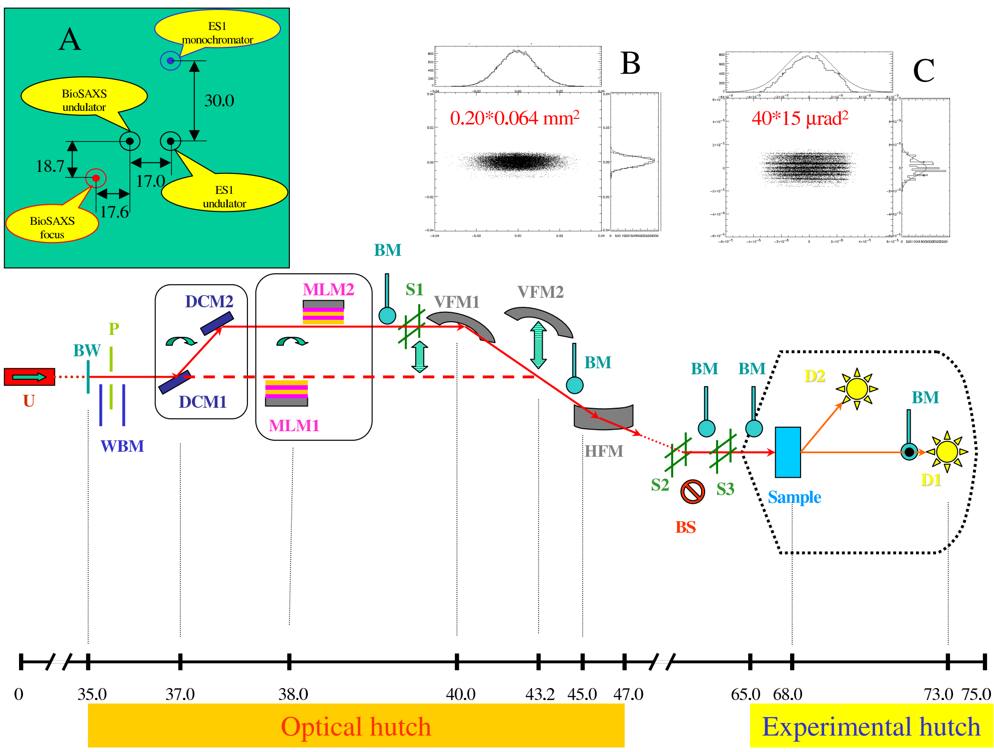

Figure 6.16.10: Schematic design of the BioSAXS beamline. The bottom scale displays distance from the source in meters; for explanations, see text. Insert A displays the cross section perpendicular to the beam direction at the focal point at 73 m from the source (distances are shown in cm). Inserts B and C present spatial and angular distribution of rays at the focal point simulated by SHADOW for a DCM setup at 8 keV.

experimental flexibility simultaneously yielding, thanks to the unique properties of the PETRA III beam, the best divergence for the given beam size.

Allowing for a beamstop size five times larger than the beam size (FWHM), the first useful experimental point in the vertical direction could be measured at about 0.3 mm. For a sample-detector distance of 5 m and the wavelength λ=0.15 nm (E=8 keV), this yields the minimum scattering vector s_{min}=2.5×10^{-3} nm where $s = (4\pi/\lambda)sin(\theta)$, 2θ being the scattering angle. This yields the resolution up to $d=2\pi/s_{min}$= 2500 nm, comparable with that provided by USAXS (Ultra Small Angle X-ray Scattering) in Bonse-Hart geometry. This resolution of the setup is also justified by the ultra-small beam divergence at the sample: over a 5 m sample-detector distance, the effect of beam deterioration (smearing) due to the divergence does not exceed 0.1 mm.

If required for future applications (e.g. for observation of a few particle scattering from flash-frozen samples) the beam size could be further reduced (i.e. with beryllium lenses) at the expenses of divergence. The space for positioning the microfocussing lenses will be

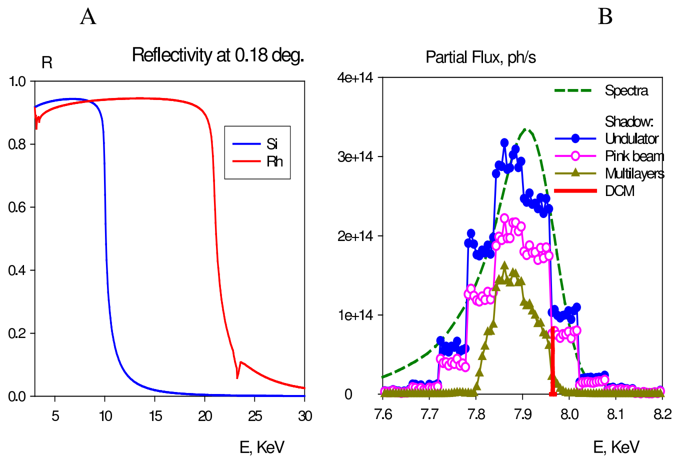

Figure 6.16.11: Reflectivity of the Si and Rh mirrors at the grazing angle of 0.18 degrees as a function of photon energy (A) and the partial flux (in 0.1%BW) of the U2 undulator at 8 KeV through a 2.0×1.5 mm^2 slit at 73 m calculated by SPECTRA (broken line), together with appropriately scaled SHADOW histograms of energy distribution in the beam using different monochromatization options.

available in the small hutch adjacent to the SAXS user room (gray shaded in Fig. 6.16.9; 60–65 m from the source).

6.16.3.6 Experimental hutch

The experimental hutch will have dimensions 10×5 m^2. A motorized table (with a platform of 1×1 m^2 size able to accommodate pre-mounted sample holders of different types) will be positioned between the slits S3 and the entrance of the evacuated detector tube. A second copy of the table platform will be available for mounting another type of sample holder during the current experiment. The sample environment will contain the following options:

- thermostated automated changer of vacuum-tight cells for HTP studies
- thermostated setup with sample circulation to diminish radiation damage
- thermostated stopped-flow apparatus for fast kinetic studies
- cryo-cell to measure flash-frozen samples
- high pressure cell
- a coherent scattering spectrometer
- a triple axis goniometer for measuring crystals with large unit cells.

In most configurations, the sample will be kept in vacuum so that the detector tube will be connected to the vacuum tube containing the optical elements. This will allow to avoid extra windows and to minimize the background scattering and will also be useful for anaerobic experiments. Configurations to measure liquid and solid samples in open sample containers in air will be foreseen as well. A mechanical shutter (MS) will be installed between slits S2 and S3 for fast time resolved experiments.
The beam alignment at the sample position will be monitored by a position sensitive ionization chamber. Two detectors will be used to register the scattering at small and wide angles, whenever possible, simultaneously (SAXS and WAXS detectors D1 and D2, respectively). The sample-detector distances will be variable (SAXS detector: from 1 to 6 m, WAXS detector: 0.3 to 1 m). Off-center positions of the detectors will be foreseen to cover wider angular range, which requires a large diameter (about 1.0 m) detector tank (displayed in dashed line in Fig. 6.16.10). The SAXS detector will provide high count rates at low noise and cover wide dynamic ranges without spatial distortions. It is expected that the further development of hybrid pixel detectors (Berar et al., 2002) will lead by 2007 to the detectors of sufficient size to be effectively used for SAXS data registration. Another option would be e.g. a flat panel solid state selenium detector (MAR Research), which could also be employed for data collection at wide angles.
The user room ($3\times5\,\mathrm{m}^2$) will be placed before the experimental hutch for monitoring the experiment, on-site sample preparation and mounting. In addition to the acquisition system interface, the room will contain minimum sample storage and handling equipment like refrigerator, balance, centrifuge, etc. For specialized biochemical work the users may use the EMBL on-site facilities. Two offices for four persons (personnel, users) will be required in the office block of PETRA III.

6.16.3.7 Data analysis system

As the present beamline is designed for HTP studies, adequate real-time data processing and model-building techniques are indispensable. An integrated software system covering all the analysis steps from data reduction to automated modelling methods will therefore be installed at the beamline. It could be run either interactively via a menu-driven graphical user interface launching the data analysis modules or automatically for which a decision-taking block will be included to select proper analysis actions and to compare concurrent models. This system will be primarily oriented towards the analysis of biological macromolecules, but could also be used for non-biological isotropic and partially oriented objects (inorganic, colloidal solutions, polymers in solution and bulk).

The major components of the system will be:

- **Primary data processing and reduction package** based on the recently developed program package PRIMUS (Konarev et al., 2003) will employ standard data storage formats like Nexus (Maddison, Swofford & Maddison, 1997) and sasCIF (Malfois & Svergun, 2000). Major data processing steps will be performed automatically to compute characteristic functions and overall structural parameters.

Mode/property	Size (H), mm	Div. (H), μrad	Size (V), mm	Div. (V), μrad	Flux, ph/s
DCM 4 keV	0.21	43	0.061	20	1.2×10^{13}
DCM 8 keV	0.20	40	0.064	15	2.1×10^{13}
DCM 12 keV	0.21	38	0.067	10	1.6×10^{13}
DCM 20 keV	0.21	35	0.066	10	0.7×10^{13}
MLM 7.9 keV	0.21	45	0.060	26	3.0×10^{15}
Pink 7.9 keV	0.21	45	0.051	28	9.0×10^{15}

Table 6.16.4: Beam properties at the focal point calculated by SHADOW. Fluxes are computed accounting for transmission of a 250 μm beryllium window.

- **Ab initio three-dimensional modelling suite** containing advanced and further developed *ab initio* programs (Svergun, 1999; Svergun, Petoukhov & Koch, 2001), will utilize the accurate scattering patterns in wide angular range (which can be reliably collected on the high brilliance BioSAXS beamline) to build macromolecular models with resolution to 1-0.5 nm. In large scale studies, these methods will be used to characterize proteins, which could not be crystallized at the HTP crystallization facility.
- **Rapid classification of proteins** will be performed using a database of scattering patterns computed from known high-resolution structures available in the Brookhaven Protein Data Bank (PDB). The prototype of the database is currently being developed Sokolova, Volkov & Svergun, 2003)). Links to Web-based fold prediction sites will be provided with subsequent screening of the predicted models against the scattering data and against the *ab initio* models.
- **Addition of missing fragments and rigid body modelling** will be employed to further characterize proteins and protein complexes solved at high resolution using the HTP crystallographic pipeline. The recently developed methods (Petoukhov et al., 2002; Konarev, Petoukhov & Svergun, 2001) will be further developed and amended for the automated generation of structural models in large scale studies. Additional information from other methods (e.g. XAS data for metal-containing proteins) will be incorporated.
- **Quantitative analysis of interacting systems and mixtures** will be done using parametric linear least squares and non-linear fitting procedures and singular value decomposition (Konarev et al., 2003; Svergun et al., 2000) for time-resolved and titration experiments in the studies of processes like assembly, protein crystallization and (un)folding, as well as in the analysis of non-biological systems.

A functional prototype of the analysis system will be developed by 2007 and tested at the

EMBL beamline X33 at DORIS. It is planned to incorporate a training block into the system employing neural networks for advanced decision-taking and possible user-less operation.

6.16.3.8 Conclusions

The proposed BioSAXS beamline will adequately exploit the exceptionally high brilliance of the PETRA III source to provide an experimental SAXS station with excellent parameters (dynamic range, flux and beam size, divergence) and broad capabilities. The BioSAXS beamline, linked to a HTP protein crystallization facility and equipped with a comprehensive data analysis system will comprise a unique environment for large scale SAXS analysis of biological macromolecules, and, in particular, for simultaneous MX/SAXS/XAS analysis. The beamline will also be available for soft condensed matter and material science applications. The construction of this beamline will further improve the efficiency of structural analysis using the small-angle scattering technique, and the expertise gained at BioSAXS will be shared with other large scale facilities in Europe and worldwide.

6.16.3.9 Cost estimates

The total investment costs of the BioSAXS beamline is estimated to **2.7 M€**.

Personnel (minimum requirement assuming efficient support structure): 4 staff×3 years, 60 k€/person/year **0.7 M€**

Total construction costs: 3.4 M€

Running costs: 4×staff + maintenance: **about 0.5 M€/Year**

6.16.4 Biological X-ray absorption spectroscopy (BioXAS)

Author: Wolfram Meyer-Klaucke

External advisors:

Isabella Ascone	LURE, Orsay, France
Holger Dau	FU Berlin, Berlin, Germany
Gerald Henkel	Paderborn University, Paderborn, Germany
Keith Hodgson	SSRL, Stanford, USA
James Penner-Hahn	University of Michigan, Ann Arbor, USA
Stefano Mangani	Siena University, Siena, Italy
Robert Scott	University of Georgia, Athens, USA

6.16.4.1 Present and future challenges for biological X-ray absorption spectroscopy

X-ray absorption spectroscopy (XAS) determines the electronic structure of probe atoms and their structural vicinity. Experiments are independent of sample state, providing flexibility for the combination with a variety of experimental setups. Thus this spectroscopy is performed on small volumes as well as on bulk material, on frozen material or on a continuous flow of solution. The technique also structurally characterizes dynamic processes, such as catalytic or light driven reactions.

In biology typical probe atoms are metals (e.g. Fe, Zn, Mo) or other elements of limited occurrence (e.g. Br, Se, I). In proteins metals fulfill a variety of essential functions: They stabilize the secondary protein structure, they serve as binding partners in transport processes, they define the pathway for electron transfer, and they act as key elements in catalytic reactions.

Every year an increasing number of proteins is isolated. In at least 30% of these gene products, metals are believed to play a key role; these are classified as metallo-proteins. Some of them, the metallo-enzymes, are catalytically active. The metal ions can serve as probe atoms in spectroscopy. X-ray absorption spectroscopy (XAS) is the only element specific technique that can utilize all metals as probe atoms and determine their metal binding motif. It can thereby identify the metals function in the protein (e.g. Dau, Liebisch & Haumann, 2003; Pohl et al., 2003; Scott et al., 1982). In biocatalysis XAS characterizes the active site depending on physico-chemical parameters, like temperature, pH, substrate or inhibitor concentration, metal content etc. (e.g. Carrington et al., 2003).

In addition to these well-established experiments more and more research activities focus on dynamic processes. In these experiments reaction intermediates are generated by rapid mixing devices (Kleifeld et al., 2003) or by light driven reactions (Dau & Haumann, 2003). The later experiments include pilot experiments for future XFEL applications. Increasingly BioXAS data are measured with high spatial resolution. Researchers obtain two or three dimensional maps of metal coordination and oxidation state. In the upcoming system biology projects research is no longer limited to isolated proteins. It is the interaction between proteins and the influence of external conditions that comes into play now. The so-called Metallome, reflecting the role of metals on the cellular basis, will have an important role. It is likely that again XAS will be the method of choice to provide element specific information on distribution, oxidation state and environment of metal ions in entire organisms and subsets.

Current state of the scientific field

In the past decades X-ray absorption spectroscopy (XAS) has become a widely used technique in biology and biochemistry. The element specific characterization of electronic states and local environment has illuminated the role of metals in many catalytic reactions. Moreover, it identifies functional metal binding sites. Such detailed information on metal oxidation state and metal coordination with subatomic resolution can be obtained by no other method on samples of any state, like solutions, crystals, cell extracts, or organism tissues. The independence of the sample state is a key feature of XAS. Entire organism tissues (e.g. bone, corals) are transparent for X-rays with more than 6 keV. The local environment of probe atoms in such organisms helps to understand general biological and geological processes (Greegor, Pingitore Jr. & Lytle, 1997). In order to illuminate the structure-function relation of the metal centers the effect of physico-chemical parameters on such samples is studied (e.g. Pufahl et al., 1997; Wang et al., 1998b). The higher the number of different sample states analyzed, the more detailed will the catalytic mechanism be understood.
The role of BioXAS in molecular biology has changed in recent years. In the early days, the synergism with techniques like NMR (Banci et al., 2003) and protein crystallography (Scott et al., 1982; Hasnain & Strange, 2003) was not widely exploited. This has changed dramatically. Excellent scientific achievements could in many cases only be achieved due to joint efforts of scientists from different fields (Arnesano et al., 2003; Pohl et al., 2003).
At present for most BioXAS experiments, metal concentrations of about 1 mM are required, except at the most intense synchrotron sources. Although this value represents the lower concentration limit for data collection it is at the same time a very high concentration for proteins. Frequently, proteins precipitate at such concentrations. Increasing the maximum concentration of protein in solution is time consuming and frequently fails. Thus BioXAS experiments require a tunable high-flux source of synchrotron radiation. At present the only spectrometer in Europe fully dedicated to BioXAS is the EMBL Hamburg bending magnet beamline. All other spectrometers in Europe capable of performing BioXAS applications share the experimental facilities with non-biological applications and are not embedded in a molecular biological research environment. Therefore, many of these facilities (Asone, Meyer-Klaucke & Murphy, 2003) are not optimized for BioXAS experiments or will no longer be available in future (like DCI, France or SRS, UK). The EMBL Outstation Hamburg plays a central role in European BioXAS as a provider of experimental facilities dedicated to biological experiments, a host for advanced training courses and a nucleus for methods development. This key role has to be maintained in future.

6.16.4.2 Science at PETRA III – scientific case summary

High-throughput BioXAS

A BioXAS undulator station at PETRA III will provide a unique opportunity for molecular biology in Europe. Experiments, like the ones summarized above, will be performed in a high-throughput mode. Compared to present data collection the amount of protein will be reduced by a factor 100 to 1000, down to about 5 μg of protein. Under such conditions typical BioXAS experiments can be performed in a high-throughput mode. This opens up new fields for the characterization of metal binding sites in genomics and metallomics.

The advantage of high-throughput XAS is realized by examination of individual components of an expressed proteome. The metal sites found in proteins expressed *in vitro* are expected to retain biological relevance. Distribution of metals and relative expression levels of metalloproteins as a function of environment (e.g. microbial growth conditions) could be determined readily. But the promise of metalloproteomics goes beyond the usual expression profiling; this is accessible by standard proteomics techniques, in which the polypeptide chain of a given metalloprotein is quantified and related to environmental influences. Formation of biologically relevant metal sites often requires a set of post-translational events, including metal transport, trafficking, metallocenter assembly, cluster exchange, etc., any of which could be influenced by environmental changes. These metal-based, post-translational events are invisible to standard proteomics analysis and are therefore the sole purview of metalloproteomics (Scott, 2004).

The set-up is also used for the characterization of steady states. By variation of the physico-chemical environment and by rapid freezing of reaction intermediates, a variety of protein states can be prepared and stabilized at cryogenic temperatures for the high-throughput XAS analysis. The much lower threshold for sample volume and concentration will allow to expand the application of XAS in molecular biology to many metallo-proteins that can either not be produced in the quantities required at present or not be concentrated up to the mM metal concentrations, because the protein precipitates. A third advantage of lower concentrations is that these are more relevant to *in vivo* conditions; high protein concentration can lead to aggregate formation (Ralle, Lutsenko & Blackburn, 2003; Penner-Hahn, 2004) that is not representative of the *in vivo* structure. Therefore, such a station is a breakthrough in the characterization of metallo-proteins. Due to the unique environment to perform molecular biology experiments offered by the EMBL Outstation Hamburg, the characterization of metal oxidation state and metal environment might even become a standard part of most biochemical work on metallo-proteins performed in Europe.

Specific requirements and design criteria result from the irradiation sensitivity of the biological sample. Exposure of metallo-proteins to high-intensity X-rays leads to changes in redox state (photoreduction) and structure that typically precede the damage to the amino acid matrix. For very sensitive samples the onset of discernible photoreduction requires at 20 K an integrated X-ray exposure of 10^{12}-10^{14} photons/mm^2. Irradiation by $\sim 10^{13}$ photons is required for the collection of artefact-free data. This corresponds to scan durations of ~ 1 s and an irradiated sample area of 1 mm^2 or greater. At the high-throughput station the potential photoreduction of protein and metal will be minimized by four means. First of all the sample will be cooled down to 5 K in a closed cycle cryostat. Second the solid angle for gathering of fluorescence radiation will be increased compared to present set-ups. An optimized ratio between incoming photons and collected fluorescence radiation lowers the number of photons on the sample required for a defined data quality. Third the experiment will have full control over the undulator gap. The EXAFS signal decays with k^3. In order to achieve a constant signal to noise ratio over the entire data range of about 1.5 keV the acquisition times at higher energies must rise in an appropriate way. By joint movement of undulator gap and monochromator this optimizes the time for data acquisition, which effectively reduces the photoreduction. Fourth the photon flux can be spread over an area of 2 - 5 mm^2 by bending mirror 2 depending on the sensitivity of the metal center.

Cutting-edge experiments

By cutting-edge experiments new kind of information on the function of metals in biology will be revealed that is mostly inaccessible to other experimental techniques.

(a) Time-resolved BioXAS experiments facilitate insights in reaction dynamics/kinetics and structural characterization of intermediate states (Dau, Liebisch & Haumann, 2003; Penner-Hahn, 2004). The proposed time-resolved experiments represent an exciting new approach towards understanding of biological function (catalysis) at the atomic level.

The following types of **time-resolved BioXAS experiments** are planned:

Continuous flow-and-mixing. In combination with rapid mixing intermediate states can be identified and characterized at a ms time scale (Kleifeld et al., 2003; Penner-Hahn, 2004). Even for experiments that do not require high time resolution, there is still a significant advantage in making measurements under flow conditions. This setup allows one to make measurements in fluid solution without the danger of radiation damage. Room-temperature fluid solution measurements are essential for studies of thermochromic materials (Whittaker & Whittaker, 1996); such measurements require the small beam and high flux density that will be possible at PETRA III, but are not feasible using sources such as DORIS.

Voltametry and temperature cycling. The electrochemical potential (or temperature) is varied and a spectrum is taken, say, every 100 ms by piezo-QXAFS (Richwin et al., 2002).

Triggered reactions with Δt > 10 ms–100 s. The reaction is initiated by a light pulse (phototrigger, release of caged substances), temperature pulse or jump, potential jump, or stopped-flow techniques. Then a time series of spectra is collected either by piezo-QXAFS (10 ms>Δt < 1 s) or by rapid scanning of monochromator and undulator gap (Δt > 1 s).

Laser-triggered reactions with time resolutions of Δt > 1 μs. Employing either the photochemical reactions of the investigated metalloprotein itself or of suitable caged compounds, the investigated process is initiated by a ns laser pulse. For each flash-experiment a specific excitation energy is chosen and the time course of the excited X-ray fluorescence is monitored. By carrying out this time scan experiment at 20-50 excitation energies, complete XANES and EXAFS spectra of high quality can be constructed (H. Dau, personal communication). The practical limit of time resolution is estimated to fall in the range of 1-20 μs. For the (unfortunately rare) processes that can be repetitively triggered on the same sample, also ns-experiments may become practicable. [microfocus of about 50 μm x 50 μm to minimize sample consumption; plus ms beam shutter to prevent radiation damage]

(b) **Spatially resolved XANES (tomography)** facilitates spatially resolved speciation with respect to oxidation state and ligand environment (Schroer et al., 2003a). Most experiments on tissue will require reference spectra collected under similar conditions. Rapid scans covering several edges will be one of the new experimental strategies to counteract the radiation damage problem. Thereby 3-dimensional maps on metal oxidation state and environment will visualize metal accumulation and distribution, providing new insights into detoxification processes and metal utilization. Even in the absence of spatial resolution such experiments receive more and more attention (Harris, Pickering & George, 2003)). [microfocus with spot size of 70 nm–1 μm depending on scientific demands].

(c) Beyond the importance of **high-resolution fluorescence** for site-specific measurements, these experiments have the advantage that they provide greatly improved experimental resolution for XANES studies (de Groot, Krisch & Vogel, 2002; Kivimäki et al., 1998; Hämäläinen et al., 1991). Improved energy resolution is critical for resolving small features on the edge, and thus for deducting details of the electronic structure of the absorbing site. Another advantage of high-resolution experiments is that they offer, for the first time, the possibility of distinguishing directly between different ligation types. In conventional EXAFS like in most structural methods, it is impossible to tell the difference between, for example, N and O ligands. However, in high resolution fluorescence it is possible to resolve cross-over bands (core-electron charge transfer transitions) such as the $K\beta''$ transition, that can be used to distinguish between N and O ligands (Bergmann et al., 1999). [expanded beam to prevent photoreduction or small spot if continuous flow cell is used].

(d) **XAS on protein crystals** merges protein crystallography (MX) and X-ray absorption spectroscopy for the determination and differentiation of active site ligands as CN and CO or sulfide and oxide (Hedman, in prep.). [focused beam to match crystal size].

Recent publications have illustrated the potential of the experiments mentioned above. A flexible set-up is required to fulfill the demands of the complex instrumentation. Therefore in the second hutch user groups will find a modular experimental area consisting of five main parts: (a) rapid mixing device for time resolved experiments, (b) a laser system for pump and probe experiments, (c) a system of X-ray lenses for spatial resolved experiments with a resolution of about 100 nm, (d) a goniometer with xy table for XAS tomography and (e) a fluorescence analyzer with meV energy resolution. A goniometer for mounting protein crystals will be transferred from present DORIS stations. In order to minimize set-up periods all equipment will be mounted on individual honeycomb tables so that components can be easily exchanged depending on the scientific demands.

6.16.4.3 Experimental considerations for the BioXAS station

The K- and L- edges of most important probe elements in biological material are covered by the energy range from 5 keV to 35 keV. Thus all elements from Vanadium up to Iodine will be accessible at this station. Moreover heavy elements such as Tungsten will be accessible via their L-edges. For high-throughput and cutting edge BioXAS applications an insertion device is the only photon source generating a sufficient photon flux. According to the ring specifications the 2 m PETRA III undulator U2 described in Sec. 4 will fulfill the requirements. For the energy dependent EXAFS scans over about 2 keV obviously gap scanning is required. Actually this requirement is met by insertion devices at the operating 3^{rd} generation synchrotrons (e.g. Tanida & Ishii, 2001). Further key parameters in the station design are stability and reproducibility of scans and adjustments. The sub-μm stability of the PETRA III ring will result in a corresponding stability of the spot on the sample. This is essential in order to eliminate interference with sample inhomogeneities.

The photon source

In order to make use of standardized components we favor at present the use of a 2 m long undulator with a maximum K value of 2.7 (see Sec. 4). Its first harmonic covers the energy range from 2.4 to 10.6 keV, the 3^{rd} harmonic can be tuned from 10 to 23 keV and the fifth harmonic will be used for experiments between 23 and 35 keV. The resulting beam size and divergence depends on the β-function of the storage ring. For a high-β section it is supposed to be 127 μm and 5.3 μm at 12 keV photon energy, for a low-β function 37 μm and 5.7 μm, respectively. For tomography experiments for low beta a demagnification below 100 nm is possible with parabolic refractive Be-lenses (Lengeler et al., 1999a), whereas in the high beta section a spot size of 300 nm defines the absolute limit for the source-spot distance of 50 m and a photon energy of 12 keV. With KB mirrors similar spot sizes can be achieved. This alternative setup has the advantage of a wider energy range for EXAFS scans.

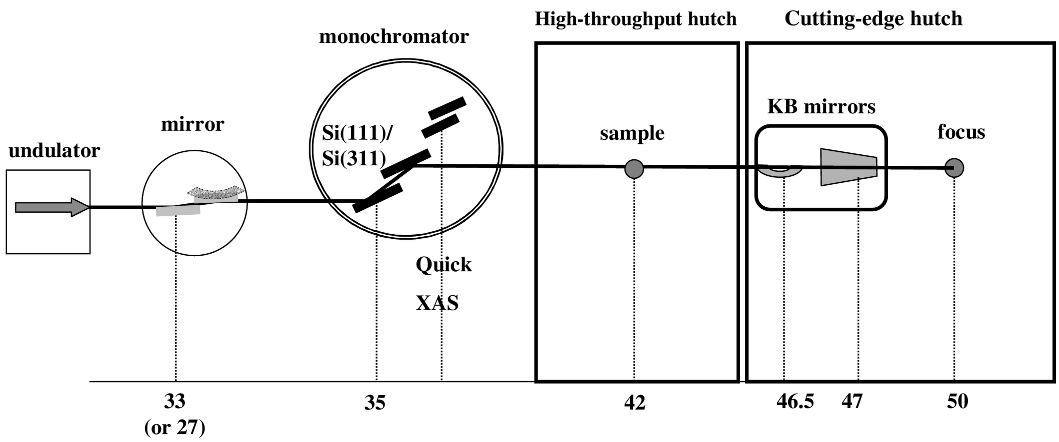

Figure 6.16.12: Layout of the optical components for the proposed BioXAS station. The second mirror demagnifies the spot size as defined by the photon sensitivity of the sample under study. The monochromator tank houses two different monochromator setups: (i) a conventional fixed exit monochromator and (ii) a quick XAS monochromator for fast scans with tapered undulator. KB mirrors or refractive lenses will produce a focus smaller than 100 nm for spatial resolved experiments.

It is important that the energy width of the undulator flux can be broadened. By tapering a gain of up to 200 eV in the harmonic width will be achieved at the expense of a reduced spectral flux. This will enable XANES scans to be easily obtained and ensures compatibility of the source with the piezo-QEXAFS monochromator used for tomography.

Optics

The first optical element takes most of the heat load produced by the insertion device. Here it will be a flat double mirror, which can vary the cut-off energy so that higher harmonics contributions can be minimized. Two different coatings will be available covering the energy range 5–13 keV and 12–35 keV, respectively. Details on the coatings will depend on ongoing international R&D. Variations of the double mirror angle will result in changes of the beam offset between incident and outgoing beam by less than 5 μm. The second mirror will be horizontal bendable in order to spread the photon flux over a larger area.
A monochromator with two plane crystals is the dispersive element. The first crystal will be cooled by liquid nitrogen. The energy range defined above will be covered by two double monochromators, Si(111) and Si(311). An additional Si(511) monochromator for high-resolved XANES at higher energies is under discussion. Beam stability is one of the most important issues to be considered for the station. Thus a fixed exit height design is preferred. The design is aiming at very high stability over the spectral range and especially over the typical scan ranges of about 2 keV. Avoidance of radiation-induced modifications to the biological sample require (1) the capability of scanning simultaneously the monochromator and the undulator gap over 500–1000 eV in $\sim$2 s; and (2) an adjustable focus size (irradiated area on the sample of 1–10 mm^2).

The high-throughput BioXAS applications in the first hutch will be performed with these stable and easily adjustable optical components. The cutting-edge experiments in the second hutch require further optical elements. This includes focusing and a fast monochromator. The fast monochromator is essential for XANES tomography, because conventional systems can not scan at the required high frequencies. Therefore a piezo-QEXAFS monochromator will be mounted as an alternative monochromator with repetition rates of 10 Hz (Richwin et al., 2002). Again the first crystal will be cooled by liquid nitrogen.
A full assessment of microfocussing options will take place in the design phase. Refractive lenses achieve focal sizes of less than 100 nm combined with easy handling at the price of limited flexibility in the energy range. In contrast Kirkpatrick-Baez mirror pairs come with the greatest flexibility for EXAFS measurements, but are more complex in handling and limited in focusing.

Detectors

Three main detector systems are used in BioXAS presently. The standard at low intensity stations is a Ge-multi-element detector. Recent developments in fast digital electronics and detector design result in potential signal throughput of up to 800.000 cps per detector element. In order to cope with the expected fluorescence generated by the sample a multi-element Ge-detector with more than 100 elements would be required for this station. Present research on Si-drift diodes make it likely that such a device again would require a multi-element design with a similar number of individual detector elements. An alternative are systems based on energy separation by Laue diffraction (Zhong et al., 1999) or multilayers (Zhang, Rosenbaum & Bunker, 1998). In that case systems with several scintillator-photomultiplier units are used for photon counting. At present the later system seems superior, but future development has to be awaited. For example, 32-channel boards for digital signal procession are under development and might be available at attractive prices in 2007.

Fluorescence analyzer (RIXS)

Resonant inelastic X-ray scattering (RIXS) looking at the decay of excited elements is a powerful tool in determining site sensitive information on probe atoms as well as in understanding electronic structure of probe atoms and their ligands. Due to the limited spherical angle that is covered by analyzer crystals this technique requires high flux. An arrangement of at least 6 analyzer crystals will be mounted on a honeycomb table for fast exchange of components in the second hutch. Arrangements on such tables have proven in other experiments that they can be removed and reinstalled without further adjustment. For RIXS measurements the sample will flow continuously through a small capillary in order to prevent any photo-reduction or the beam will be widened to lower the radiation dose. In the latter case cryogenic sample temperatures will be obtained by means of a cryo-stream system.

Tomography

A focusing system, either KB or refractive lenses, will be used for tomography applications. Samples will be mounted on a xy table or a goniometer. In both cases the sample can be kept at cryogenic temperatures by the cryo-stream system. As a fluorescence detector the system used in high-throughput BioXAS is installed.

Sample environment for high-throughput BioXAS

Present cryostat systems allow mounting of up to 25 samples. This could easily be extended to 50 or 100 samples without much increase in sample temperature. Such a high-throughput setup would allow automated data collection for long periods. Data collection on samples with low concentration still might require about ten hours of beamtime. On the other hand a tray with up to 100 samples can be quickly screened and then only on the interesting hits EXAFS data will be collected. Given that these processes will be performed in a highly automated fashion, users will have sufficient time for sample preparation and preliminary data analysis.

Energy calibration

A BioXAS experiment typically requires several scans on an increasing number of samples.

Thus scan reproducibility and accurate energy calibration are essential. Therefore, all motors will be equipped with encoders and the transmitted beam will be used for absolute energy calibration (Pettifer & Hermes, 1985).

6.16.4.4 Data acquisition and data reduction software

Data acquisition will be performed in two modes: fully and partially automated. Full automation will allow unattended operation for the determination of metal content of about 100 samples in high-throughput mode and measuring their EXAFS or XANES when appropriate. Demanding applications will be performed in partially automated mode, considering the experimental requirements. For automated XAS data reduction statistical criteria have been defined (Lippold, submitted). Further development along these lines will ensure that when PETRA III becomes available suitable program packages are available.

6.16.4.5 Offline laboratory provision

For the highly specialized BioXAS research an adequate laboratory must be available. This will include a clean *sample preparation area* (filtered air). This area will be linked to a molecular biological laboratory (see above). Essential is equipment for enzyme activity determinations and a glove box for oxygen sensitive operations. For light sensitive proteins space in a dark room has to be available. Space will be dimensioned such that for routine sample preparation two or three user groups can work in parallel.
For data analysis two working places will be available that do not interfere with the groups collecting data. This will ensure that the user groups can refine their data on site, where sufficient BioXAS specific knowledge is available. This is an essential requirement to support projects from non-XAS experienced groups.

6.16.4.6 Resource requirements

Costs for the construction the BioXAS station have been estimated and given below. Expenses for construction of insulated hutches have not been accounted for. The estimates for the optical and vacuum components, fluorescence detector, flexible end-stations and computer environment are based on the currently available quotes. We estimate that 9 person-years of a technical position and 3 person-years of a scientist position are required to construct an entire BioXAS beamline. If a beamline will be shared with other activities less investment and man-years are required. Accounting for limited infrastructure of the EMBL Hamburg initially only the hutch 1 for high-throughput BioXAS is supposed to be operational from 2008 onwards. The second hutch for cutting-edge experiments will be constructed at the same time. Different experimental setups will be implemented iteratively, starting with equipment for time and spatial resolved experiments.

6.16.4.7 Cost estimate

The total investment costs for a BioXAS station is estimated to **2.0 M€**.

Detector type	Costs	Comments
Monolithic Ge-multi element	Very-high	Reliable, but number of elements goes beyond 100
Si-drift diodes (multi element)	high	not yet proven under such conditions
Scintillator/photomultiplier with Laue X-ray energy separator	moderate	not yet used
Scintillator/photomultiplier with Multilayer X-ray energy separator	moderate	Tested at APS, works for limited number of probe elements

Table 6.16.6: Overview of possible fluorescence detectors to be installed on the BioXAS station.

Personnel (minimum requirement assuming efficient support structure):
4 staff×3 years, 60k€/person/year **0.7 M€**

Total construction costs: 2.7 M€

Running costs: 4×staff + maintenance: **about 0.5 M€/Year**

In case that BioXAS will operate an undulator jointly with another application, running costs, personnel and hardware will reduce considerably. For a station being operational 50% of the beamtime the following numbers are estimated. Details strongly depend on overlaps in investment with the second application.

50% Scenario:
Hardware: 1.2 M€ - 1.6 M€
Personnel: 0.4 M€
Total construction costs: 1.6 M€ - 2.0 M€
Running costs: 2.5×staff + maintenance: about 0.35 M€/Year

6.17 Protein Crystallography at PETRA III, Proposal for a Sector With Two Beamlines

Authors:

H.D. Bartunik	MPG-ASMB c/o DESY, Hamburg
G. Bourenkov	MPG-ASMB c/o DESY, Hamburg
E. Mandelkow	MPG-ASMB c/o DESY, Hamburg
Ch. Betzel	Universität Hamburg
R. Hilgenfeld	Universität Lübeck

Aiming to provide a basis for efficient and competitive exploitation of the potential of PETRA III for biological structural research with synchrotron radiation, we propose the construction of a sector comprising two beamlines and infrastructure for sample preparation and data processing. It is intended that the facility will be constructed and used by a consortium, following a suggestion made by the University Hamburg and the University Lübeck to the MPG. Other institutions are invited to join the consortium.

6.17.1 Scientific aims

The development of protein crystallography using synchrotron radiation during all its phases has been substantially influenced and advanced by research activities on the DESY campus, which started at the EMBL Outstation in the late seventies and were later joined by the MPG-ASMB. This led to the solution of many important crystal structures. Outstanding examples of supramolecular structures include the reaction center of photosynthesis, the 26S proteasome (Fig. 6.17.1), and ribosomal 30S (Fig. 6.17.2) and 50S particles. Crystal structure analysis in many cases formed the basis for investigations of dynamic aspects of structure-function relationships, as in the example of the motor protein kinesin (Fig. 6.17.3). A number of technical and methodological developments, including in particular crystallographic studies at ultra-high resolution (Fig. 6.17.4), cryo-crystallography, experimental phasing using anomalous scattering, and time-resolved protein crystallography, made DORIS, despite its relatively high emittance, to one of the worldwide most productive facilities for biological structural research. At the same time, such developments provided the basis for many applications that have been carried out in the field of industrial pharmaceutical and agronomic research. An overview over the scientific applications on beamline BW6 at DORIS III is provided by a list of selected references (Blume et al., 2001; Bochtler et al., 2000; Burkhard et al., 2000; Einsle et al., 1999; Fritz et al., 2002; Gomis-Rüth et al., 1997; Groll et al., 1997; Groll et al., 2003; Hagemeier et al., 2003; Harms et al., 2001; Harms et al., 2003; Henrich et al., 2003; Kachalova, Popov & Bartunik, 1999; Kozielski et al., 1997; Macedo-Ribeiro et al., 1999; Sack et al., 1997; Scheufler et al., 2000; Schlünzen et al., 2000; Song et al., 2001; Than et al., 2002; Worbs et al., 2001).
The resolution that was reached in the analysis of supramolecular structures, however, was affected by the experimental limits of DORIS. Studying such structures of very high molec-

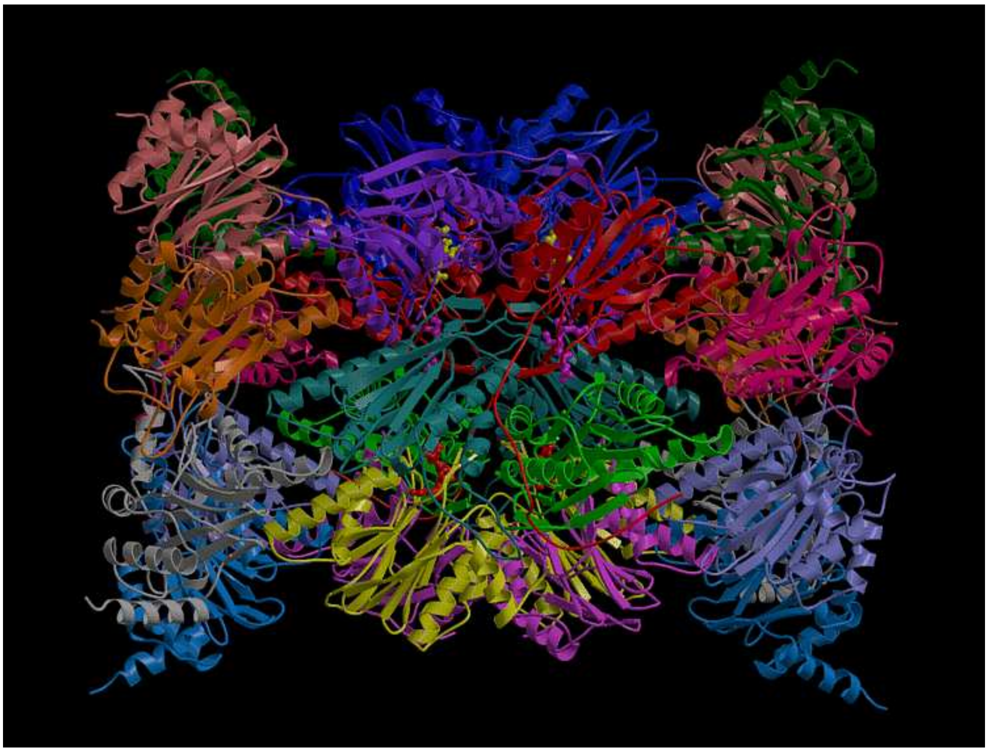

Figure 6.17.1: 26S proteasome from yeast (Groll et al., 1997).

ular weight per asymmetric unit using small crystal volumes in fact requires a source with low emittance and high brilliance. Similar demands exist for other applications including, e.g., investigations of short-lived structural states with time-resolved diffraction methods. The upgrade of PETRA fundamentally improves the conditions for such experiments. Its low emittance creates the potential for PETRA III to become the world's top performing synchrotron radiation source for biological structural research in the hard X-ray regime. In order to be able to efficiently use this potential, experimental stations have to be developed that fulfill the requirements defined by the known types of applications and offer the possibility to be adapted to new future applications. The present proposal aims to design and construct instrumentation for one sector of PETRA III. In addition, the automation of parts of the data acquisition that has already been realized at the beamline BW6/DORIS shall be extended to include all experimental aspects of crystal structure analysis and its control by an expert system. Furthermore, adequate infrastructure facilities for sample preparation and for immediate solution and interpretation of crystal structures shall be set up in the close vicinity of the beamlines.

An important aspect is the intended setup of a network of biological structural research that is embedded in related activities (structural genomics, proteomics, biomedical and pharmaceutical applications) in the Hamburg area and closely connected to research activities in other regions. The universities in Hamburg and its surrounding (Univ. Hamburg, Univ. Lübeck, TU Hamburg-Harburg) are going to widen their activities in the field of biological structural

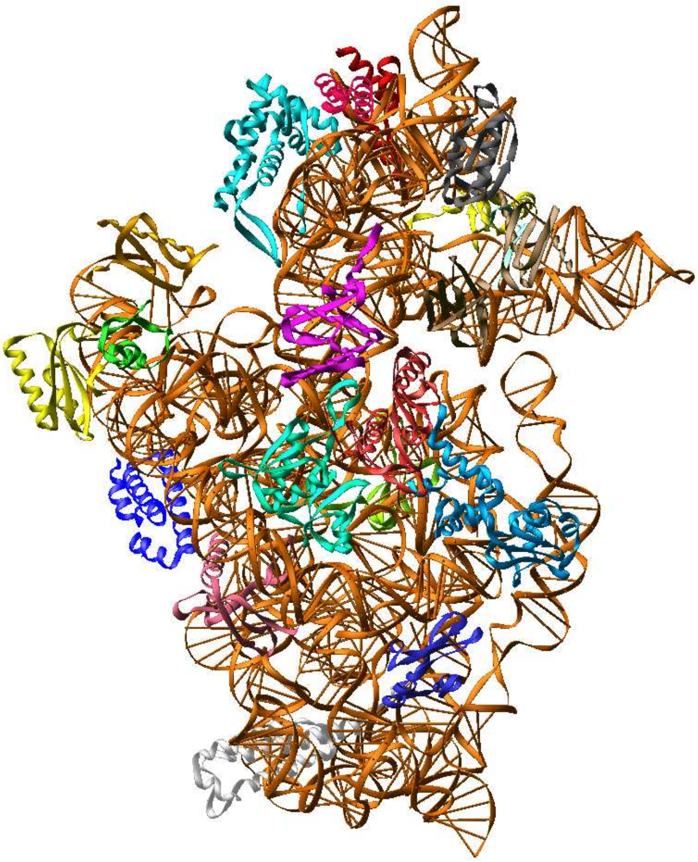

Figure 6.17.2: 30S ribosomal subunit (Schlünzen et al., 2000).

research using synchrotron radiation following the creation of new professorships. This offers outstanding possibilities for long-time cooperations in the development of technologies, in research, and in the professional training of students. At the same time, the experimental facilities and methods will continue to be accessible and available to structural biologists within the MPG and other German and foreign research institutions.

6.17.2 Basic concept of the beamlines

Fig. 6.17.5 shows a schematic view of the sector with two beamlines, which have common infrastructure but may be operated independently. By using as far as possible identical beamline components and diffraction equipment as well as a joint computer system for control, data acquisition and evaluation, both the investment costs and the technical personnel required for the construction and operation will be reduced to a minimum. This concept requires a joint scientific-technical direction of both beamlines.
The two beamlines each include a 2 m long undulator as source (Fig. 4.1.1). The present planning assumes the use of fixed-period undulators. Both beamlines shall be optimized for

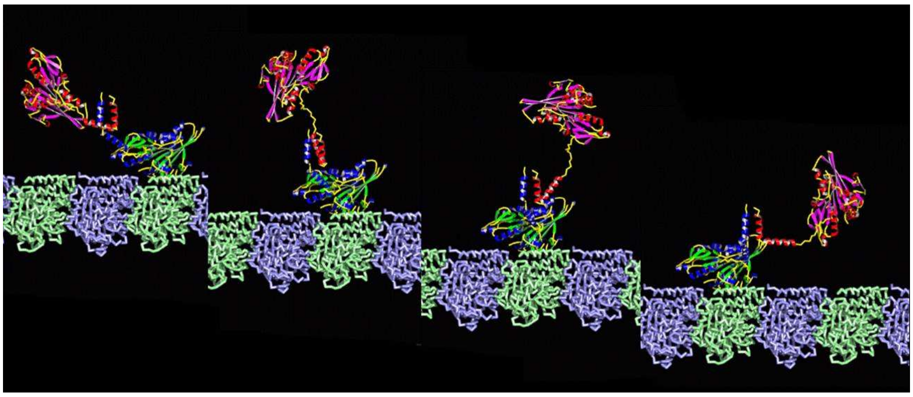

Figure 6.17.3: Kinesin dimer moving along the microtubule proto-filament (Song et al., 2001).

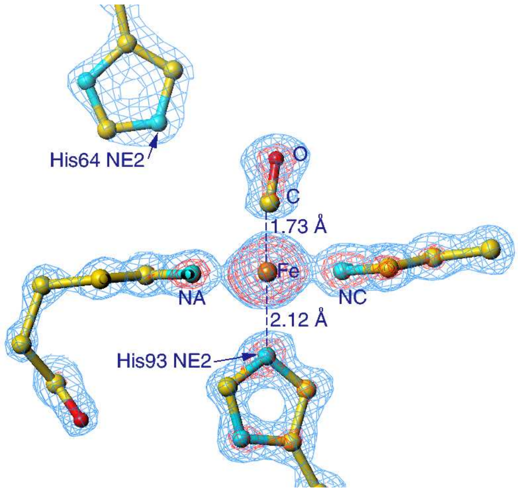

Figure 6.17.4: Fe-CO in myoglobin at ultra-high resolution (Kachalova, Popov & Bartunik, 1999).

MAD phasing applications in protein crystallography and at the same time offer small beam cross-sections (1–30 μm) and high flux at the sample position. The relevant parameters are listed in Tab. 6.17.1. The concept of the beamlines permits macromolecular crystal structure analysis as well as other applications. For example, experimental setups involving grazing-incidence beam conditions for investigating structures at surfaces, diffraction measurements from fibers with extremely narrow diameters, topographic techniques, and a combination of X-ray diffraction with X-ray fluorescence spectroscopy may be possible.

Beamline BL1 has priority in the planning. BL1 presently is designed for applications to supramolecular structures and very small crystal volumina. It will be tunable through the entire energy range from 3.5–35 keV. Both Si (111) and Si (311) monochromators will be available, including rapid switching from one to the other as function of the energy range and the desired energy resolution. The focusing may be adapted to particular requirements. This includes the option for micro-focusing (1–3 μm). PETRA III offers excellent conditions

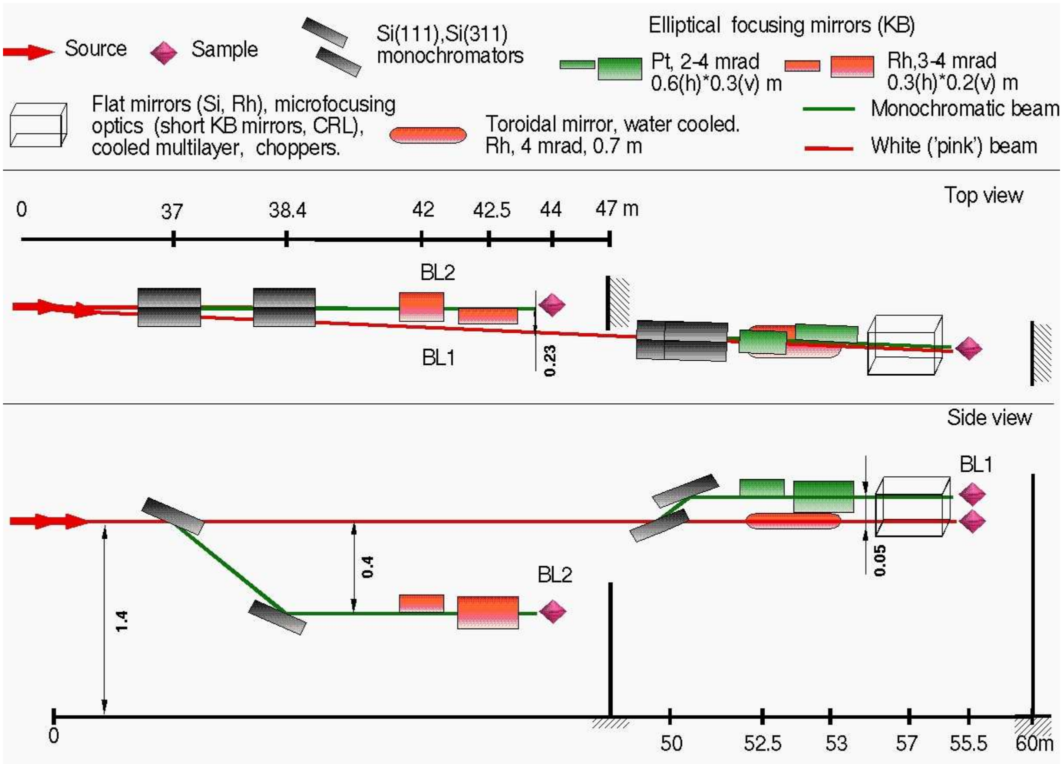

Figure 6.17.5: Scheme of the sector at PETRA III with two beamlines that may be operated independently. BL1 may be operated either with monochromatic beam or with "pink beam" (bandwidth 2–3 %). Under monochromatic conditions, the beam cross-section at the sample position may be adjusted to 1–30 μm (FWHM) and thus adapted to the experimental requirements. BL2 will be operated under monochromatic conditions. A vertical shift of the beam results in a work height of 1 m at the sample position.

for work using micro-focus conditions, due to its low emittance and high beam stability. As a further option, BL1 may be operated using a "pink beam" (bandwidth $\Delta E/E = 2\text{–}3\,\%$); this condition in particular is of interest for Laue diffraction measurements and diffuse scattering experiments. Thus, we plan to provide experimental facilities on PETRA III, which will also be of considerable importance for preparing time-resolved investigations at the X-ray laser (XFEL), in particular for the development and testing of external excitation conditions.

Beamline BL2 will be operated in monochromatic mode only. Using a Si (111) monochromator, the tuning range for high-flux applications will extend from the uranium M_5 edge to the bromium K edge. As an alternative option, a Si (311) monochromator may be used to provide high energy resolution, e.g. for determining an oxidation state, within the range between the K edges of molybdenum and iron. In order to create sufficient space for diffraction equipment at BL2, the monochromator setup is designed to change the beam height by 0.4 m (to a height of 1 m). BL2 will be optimized in particular for structural proteomic projects.

6.17.3 Auxiliary installations

Automatic beamline control: High beam stability at the sample position is of importance for most applications, in particular for work under micro-focus conditions. The components of the X-ray optics and diffraction equipment therefore will be designed to permit automatic control on the basis of automatic beam diagnostics and continuous re-alignment.

Automation of measurements: All experimental steps of protein crystal structure analysis extending from sample mounting to phasing will be automated as far as possible and controlled by an expert system. This includes the control of the sample environment (temperature, humidity, anaerobic conditions etc.), remote control of experiments, and compatibility with

A. Monochromatic conditions	BL1	BL2
Energy range, keV	3.5 – 35	3.5 – 14 Si (111)
		7 – 20 Si (311)
Energy resolution ΔE/E 10^{-4}	0.4 - 2.5	0.4 - 2.5
Focused beam at the sample, FWHM		
Min. size, HxV μm	30 x 15	15 x 10
Max. divergence, HxV μrad	400 x 200	600 x 300
Flux at the sample, ph/sec/100mA		
@ 12 keV	$3 \cdot 10^{13}$	$3 \cdot 10^{13}$
@ 35 keV	10^{12}	
Microfocus option		
Focus size, HxV μm	3 x 1	
Divergence, mrad	2.2 x 1.2	
Flux @12 keV	$> 10^{12}$	
B. Pink beam conditions		
Bandwidth < 9 keV	ca. 3 %	
> 9 keV	2 – 3 %	
Photon flux, photon/sec/100mA		
9 keV, 10%	$2 \cdot 10^{16}$	
12 keV, 3% (fixed-period undulator)	$1 \cdot 10^{15}$	
12 keV, 10% (variable-period undulator,	$\sim 2 \cdot 10^{16}$	
1^{st} harmonic shifted to 12 keV)		
Photons per bunch @100mA, 40 bunches (192 ns)		
9 keV, 10%	$4 \cdot 10^{10}$	
12 keV, 3% (fixed-period undulator)	$2 \cdot 10^{9}$	
12 keV, 10% (variable-period undulator,	$\sim 4 \cdot 10^{10}$	
1^{st} harmonic shifted to 12 keV)		
Min. focus size, HxV μm	80 x 20	
Chopper time window, ns / 1000rpm	25	
(rotating mirror chopper)		

Table 6.17.1: Parameters of the protein crystallography beamlines.

high-throughput (HTP) applications.
Sample preparation: Facilities for sample preparation and sample mounting will be available in the immediate vicinity and jointly used for both beamlines. These include in particular devices for ad-hoc derivatization (e.g. with xenon), possibilities for developing and testing cryo-solvents, and air-conditioned rooms or incubators for crystallization and preparation. Storage of samples at low temperatures and equipment for transferring samples to the beamlines are required for HTP applications. The coding and identification of samples shall be standardized within the framework of a European project (BIOXHIT).
Data evaluation and structure solution: Complete evaluation of the experimental data, including an assessment of the quality and interpretability of electron density maps, in general shall be feasible within short time immediately after completion of the data collection. This aim has already been reached in many cases on BW6. Furthermore, we aim to an interactive control of the experiment on the basis of the currently evaluated data. This requires high data transfer rates and computing performance. An Intel cluster shall be used for this purpose, and software that is part of the expert system will be parallelized as far as possible. Both beamlines will be equipped with the same front-end computers and bus systems and connected to a joint computing facility, in order to facilitate the system management and software development. Measuring strategy, interactive data acquisition, and evaluation methods will be standardized as far as possible within the framework of BIOXHIT.

6.17.4 Capital investment and personnel

The total investment costs for the proposed beamline endstations without optics, vacuum system and hutches is **4** M€.
For the operation of both lines 4–6 scientists and 2–4 engineers/technicians will be needed.

6.18 Experimental Techniques with no Dedicated Beamline Proposal

In this section two experimental techniques will be presented that certainly benefit from the beam properties of a 3^{rd} generation synchrotron radiation source, but for which no specialized beamline proposal has been made. The first technique, high pressure experiments using diamond anvil cells, is meanwhile almost a standard at many synchrotron radiation beamlines. The second one, which is topography, can easily be carried out at any beamline that provides a suitable beam such as high a resolution diffraction beamline.

6.18.1 High pressure diamond anvil cell laboratory

Current state of the scientific field Pressure is besides temperature one of the most important thermodynamical parameters. Its variation over a large range is crucial for many experiments. Diamond anvil cells (DAC) are a high-pressure technique, which combines several advantages. They are able to achieve the highest static pressures: several Mbars are currently possible (1 Mbar = 100 GPa). DACs are compact and can easily be transferred from one beamline to another. They are a versatile tool enabling to couple X-rays studies with other physical characterization methods (e.g. Raman scattering, electrical resistance, magnetic susceptibility, and fluorescence measurements) as well as experiments at low and high temperature. At moderate pressures they are easy to handle and can be used by experimentalists not specialized in this field. Meanwhile, DACs have become a 'standard' sample environment option at all major synchrotron facilities.

Most X-ray experiments using DACs are powder or single-crystal diffraction studies for the determination of the crystal structure or the equation of state. Single-crystal diffraction provides more precise data, however, measurements are only possible under (quasi-) hydrostatic conditions. In addition, this method requires DACs with large X-rays windows, thus limiting the maximum achievable pressures to $\sim$ 50 GPa. Powder diffraction is less demanding to the cell design and is used in the whole pressure range achievable with DACs. The method increasingly requires advanced methods for structure analysis, which in particular includes the application of area detectors for data recording in order to provide the possibility for texture analysis during data processing.

New 3^{rd} generation synchrotron sources open up new possibilities: (i) studying low-Z materials (e.g. H_2, Li), (ii) sampling data as function of the pressure gradients across the anvil working flat with high spatial resolution, (iii) studying protein crystals by single-crystal diffraction. They also enabled the application of new X-ray methods such as inelastic scattering, fluorescence measurements, and X-ray absorption spectroscopy, which became a standard method in high-pressure experiments.

In many studies a combination of pressure with for example low/high temperature, external magnetic fields etc. is applied. Laser heating in a DAC has become a special area of research often called 'Studies of matter under extreme conditions'. Currently, temperatures as high as $\sim$ 4000 K at pressures up to $\sim$200 GPa are achievable. However, the issues of absolute temperature and pressure determination at high temperatures, as well as the characterization of the sample exhibit an experimental challenge leading to a number of fundamental physical, chemical and metrology problems. The role of X-ray based methods is especially important since at high temperatures the applicability of the optical methods is limited due to the fact that the signal is obscured by thermal emission. The pressure and temperature gradients imply further constraints for the incident beam, which should be 3-10 μm in size. To obtain sufficient statistics for powder diffraction a micro-focused high-brilliance incident beam is needed, which can only be provided by a 3^{rd} generation synchrotron radiation source.

6.18.1.1 DAC facility

Since the parameters of all PETRA III beams (in divergence and size) are in fact suitable for the application of DACs no special beamline is dedicated to high-pressure experiments. Instead, the DAC sample environment is an integrated part of the whole facility. It consists of a number of systems and modules, which are transferable between beamlines such as powder diffraction, single crystal diffraction, micro fluorescence, structural biology, absorption spectroscopy, nuclear and inelastic scattering. The DAC environment aims to provide users with all basic experimental options: compression under quasi-hydrostatic conditions, pressure generation in the multi-Mbar range, measurements at low and high temperatures. Accordingly, the environment will include:

- a set of the cells with different geometry ,
- a sample preparation facility (gasket drilling, sample loading etc.),
- a mobile spectroscopic system for online pressure measurement by the ruby fluorescence method,
- an off line spectroscopic system for pressure measurement in the multi-Mbar range by optical methods,
- a gas loading system,
- and a laser heating system.

High pressures cells: The Mao-Bell type cells are proposed for powder diffraction. The design is most suitable for ultra-high pressure experiments (above 100 GPa). For single-crystal diffraction two types are suggested: the Merritt-Bassett and the IKAN designs. The X-ray windows of these cells cover different parts in reciprocal space, so both types are complimentary to each other. In addition to the DACs mentioned two more anvil-type cells can be used. In the Paris-Edinburgh cell tungsten-carbide anvils are used. The cell has a large working volume and it is suitable for high-temperature experiments with resistive heating. The Kurchatov-Institute cell is made of non-magnetic material. Sapphire anvils are used with a working volume intermediate between a DAC and the Paris-Edinburgh type. The cell is suitable for magnetic-scattering experiments.
Low temperature option: These cells are equipped with pneumatic drives to apply force to the anvils. The drives are used instead of the standard screw mechanisms; which are impractical at low temperatures because of difficulties to transfer mechanical motion into a cryostat.
DAC mounting and sample preparation facility: The facility will include a set of microscopes and tools for DAC handling. Basically the facility exists at HASYLAB/DESY. However

some more developments are required to provide conditions for ultra-high pressures.
A gas loading system: The system is necessary for both to provide possibility to study gaseous samples and to provide studies under quasi hydrostatic conditions.
A mobile spectrometer system for online pressure measurements: This system is the standard option for the measurement of pressure in the range up to $\sim$120 GPa.
An off line spectrometer system: This system is necessary to measure pressure in the multi-Mbar pressure range. It is based on a triple monochromator with subtractive dispersion. Two lasers Ar+ and Kr+ are included to excite the fluorescence and to initiate Raman scattering. High-quality optics elements are used to keep the background low and to provide effective spatial filtering of the signal in the imaging system. A CCD detector will be used to collect the signal.
Laser heating system: Basic elements of these systems include: (i) one laser for heating opaque samples (with a wavelength $\sim$1 μm – Nd:YAG or Nd:YLF), (ii) another laser for heating transparent samples (CO_2 laser with a wavelength of 10.64 μm), (iii) an imaging spectroradiometric system for temperature measurements, and (iv) a feedback system for temperature control. The exact configuration will be defined depending on the progress achieved in this field by the time when PETRA III becomes operational.
Laboratory space: Two rooms in the experimental hall will be required. One room will be used for sample preparation. Another room is used as an optical laboratory for the off line fluorescence/Raman measurements as well as for the development of the laser heating system. A separate place about 4 m^2 is needed for the gas loading system. For security reasons the compressor together with the high pressure vessel should be situated in a large hole (to allow gas expansion in case of an accident) and should be surrounded by a strong protective fence.

6.18.1.2 Capital investment and personnel

The proposed high pressure equipment amounts to about 400 k€, the laser heating system will cost another 550 k€. One scientist will be needed to run the high pressure laboratory with support of the engineer and technician allocated for the general sample environment facility.

6.18.2 X-ray topography

6.18.2.1 Introduction

X-Ray Topography (XRT) is a non-destructive technique, which can provide a map of the strain or defect distributions in crystals. This technique is based on the difference in reflecting power between perfect and distorted parts of a crystal. It is sensitive to strain fields extending over more than several micrometers and therefore XRT is mainly used for the study of strain, dislocations, planar defects, stacking faults, domain walls in ferroelectric and magnetic materials, growth defects, and large precipitates.
Localized imperfections may act as independent scattering centers e.g. small angle scattering by small precipitates or thermal diffuse scattering, but it is the *strains* they induce which

modify the diffraction of X-rays by a good quality crystal. These strains due to the dislocation perturb the crystal for several microns from the defect, and it is these regions far from the dislocation core itself, which give rise to the defect image, through a deviation from the ideal Bragg reflection observed in the more perfect crystalline regions. An example of the experimental arrangement for a white beam transmission (i.e. Laue mode) X-ray topographic experiment is shown in Fig. 6.18.1

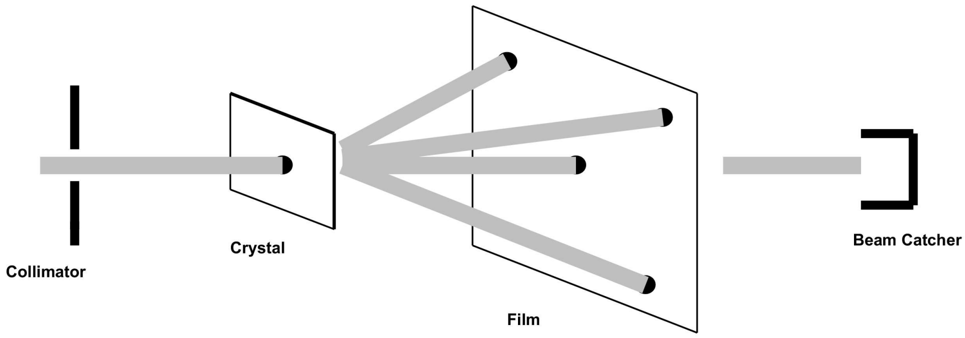

Figure 6.18.1: Schematic setup of Laue topography.

When a single crystal is immersed in a white X-ray beam a number of lattice planes (h k l) select out of the continuous spectrum the proper wavelengths to be reflected according to Bragg's Law:

$$2 \cdot d_{\mathrm{hkl}} \sin \Theta_{\mathrm{B}} = \lambda \tag{6.18.1}$$

where d_{hkl} is the inter-planar spacing of (hkl) lattice planes and Θ_{B} is the Bragg angle. A beam diffracted in a certain direction $2\theta_{\mathrm{B}}$ with respect to the incident beam has a spectrum of wavelengths λ, λ/2, λ/3, etc. corresponding to diffraction lattice planes (h k l), (2h 2k 2l), (3h 3k 3l) etc. The fundamental reflection h k l or its harmonics may, however, be structure factor forbidden.

Geometrical resolution is governed by the incident beam local divergence on the sample and, for typical experimental conditions, lies in the micron range at a 2^{nd} generation synchrotron radiation source.

6.18.2.2 Technical issues

From the viewpoint of X-ray topography the ultimate achievable resolution on the recording medium (film, CCD array, etc.) is limited by the apparent source sizes in the horizontal and vertical dimensions. This is illustrated by the diagram in Fig. 6.18.2. The situation is little different for back reflection (i.e. Bragg case) X-ray topography. From the above we find that

$$h = \frac{D}{L} H \tag{6.18.2}$$

In Tab. 6.18.1 the achievable resolution for different topography setups at DORIS III, ESRF and PETRA III are compared.

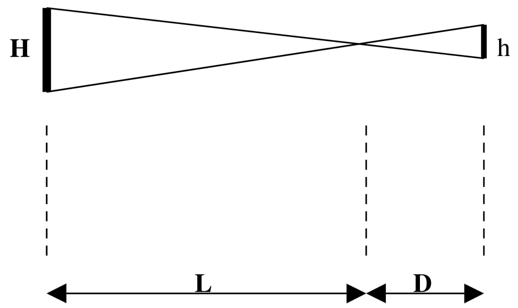

Figure 6.18.2: Achievable resolution in X-ray topography: The geometry shown is for the case of a Laue (transmission) X-ray topography, where L = distance from the synchrotron source to the sample, D = distance from the sample to the recording film, H = source size (in either the vertical or horizontal directions), h = best achievable resolution on the film due to the beam divergence and geometrical conditions (“hor” - horizontal direction, “vert” - vertical direction).

	DORIS III	ESRF ID19	PETRA III
L [m]	32	150	100
$h_{\mathrm{horiz.}}$	4700 nm	200 nm	180 nm
$h_{\mathrm{vert.}}$	470 nm	3 nm	3 nm

Table 6.18.1: Comparison of the theoretically achievable resolution (RMS-values) at DORIS III, PETRA III and the presently available best topography station (ID19 at ESRF). The comparison was carried out for D=50 mm (Eq. 6.18.2).

6.18.2.3 Conclusions

The upgrades of PETRA will ensure the competitiveness of HASYLAB/DESY for X-ray topography experiments. Longer source-to-sample distances (e.g. L > 100 m) will ensure spatial resolution capabilities superior to current 3^{rd} generation synchrotrons.
Monochromatic experiments should be possible at any beamline with a suitable monochromator, diffractometer to position the sample, and an exposure shutter that is fast enough. For white (or pink) beam topography the beamline needs to support the pink beam option in addition.

Chapter 7

Civil Engineering

7.1 Site Characterization

The outstanding property of PETRA III is the extremely small beam which will be supplied to the experiments. Using moderate focussing a beamsize of several μm^2 can be achieved. To make efficient use of this beam the positioning of all optical elements and the sample must be even more precise than that. In general a positional accuracy of 10 % of the beam size is stipulated. This requires a high level of thermal stability (air conditioning) and ground stability. In the following section we describe the efforts to characterize the local situation and compare the expected stability to the situation at similar installations world wide.

7.1.1 Description of the DESY site, geological overview

The ground at the DESY site was mainly formed during the last glacial period. The soil consists mostly of permeable sands with a few impervious layers of marl or loam of the Quaternary period. Concerning the area of PETRA the site investigations from 1975 show sands and glacial loam. The loam in itself is sandy and contains smaller sandy layers within. The density of the sand is at least middle (see Fig. 7.1.1). The point resistance of the penetrations tests shows low values for the loam but this does not necessarily mean also low bearing capacity. Of great advantage is the deep ground water table of more than 20 m below surface level. This results in low effects on the surface by changing ground water table.

7.1.2 Ground motion

Optimal use of the micrometer beam delivered by PETRA III requires a stability of the order of 10 % of the beam size. Of importance is the relative stability of the experimental setup with respect to the beam, i.e. the undulator source. Long wavelength motions or slow drifts pose only a minor problem. Given the size of the facility and a speed of sound in sand of 150 m/s, seismic waves with a frequency higher than roughly 0.5 Hz are potential sources of instabilities.
DESY has taken a large effort to compare different accelerator sites around the world concerning ground motions. Fig. 7.1.2 shows power spectral densities of the ground motion

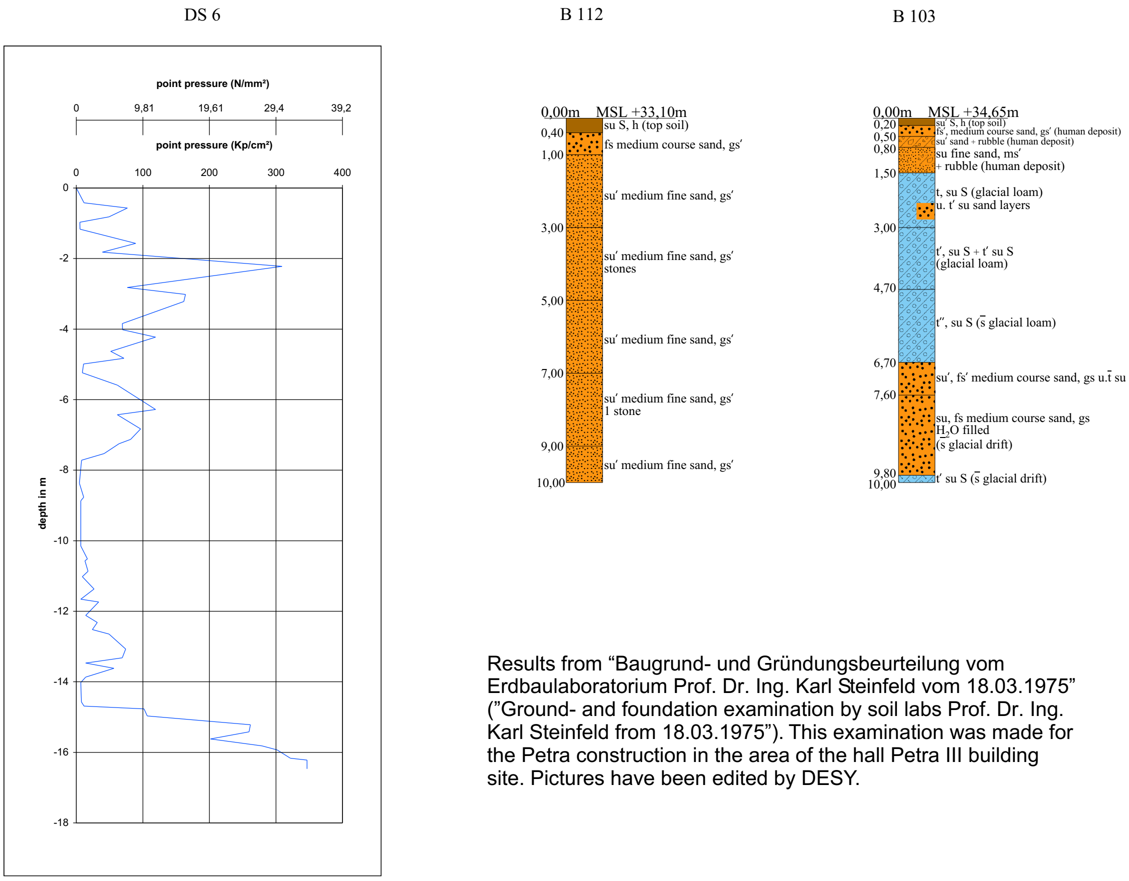

Figure 7.1.1: Point resistance of the penetrations tests (left) and layering of the ground below the experimental hall (right).

measured at ESRF, APS, CERN and DESY. All data were taken during the night and are averaged over 15 minutes. The overall shape of the spectral densities is determined by the normal f^{-4} decay (best seen in the CERN curve). In the range around 10 Hz ”cultural noise” leads to a significant increase of the vibrational amplitudes. This contribution is almost absent at the CERN location. In the range below 1 Hz the ”echo” of ocean waves dominates the spectrum. Comparing the selected curves the following can be stated:

- the DESY site has the most quiet ground in the range below 1 Hz. This is of particular interest, as usual measuring times are in the order of seconds

- between 1 Hz and 5 Hz the situation at DESY compares well to the one at ESRF

- above 5 Hz the ground is more stable than the ESRF site and almost identical to the conditions at APS.

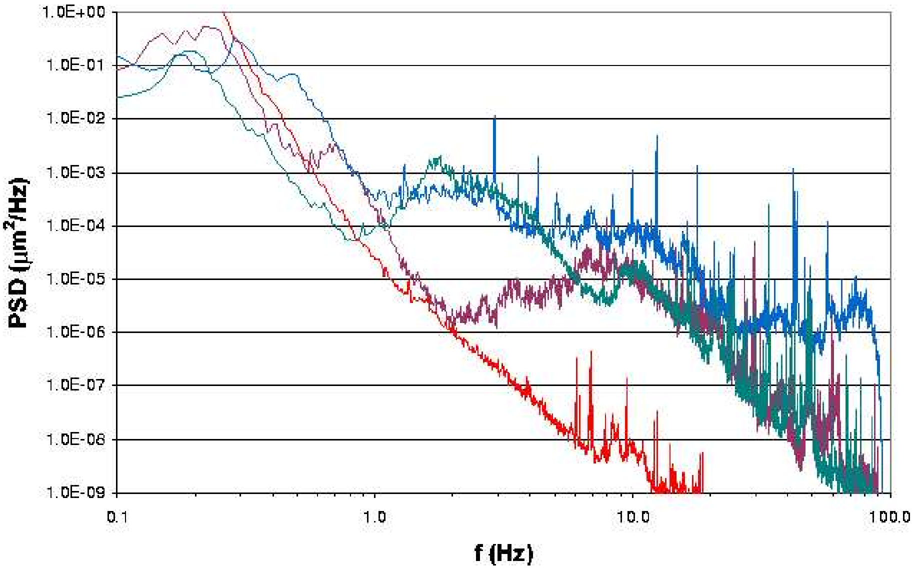

Figure 7.1.2: Power spectral densities of ground motions measured at different accelerator sites. Red: CERN; dark red: APS; blue: ESRF; dark green: DESY.

The spikes superimposed on the smooth decay are due to local resonances. Those may originate from the geometry of the concrete structure at the location of the measurement or local activities. Also the vibrational damping characteristics of the ground influences the curves in detail.

7.2 Experimental Hall

The design of the experimental hall was guided by several boundary conditions:

- The large radius of the machine and the optimal use of the low emittance requires mostly rather long beamlines (up to 100 m or more).
- The building has to be kept compact in order to minimize costs and to fit on the area available.
- Due to the radiation shielding concept offices and laboratory space have to be located on the outer perimeter of the hall.
- The design has to allow a building phase not exceeding eight month.

Thus a concept similar to the experimental hall of ESRF was chosen. However, as experience showed that offices and laboratory space should be located close to the beamlines, the outer perimeter of the hall will be used for offices and laboratories from the outset.

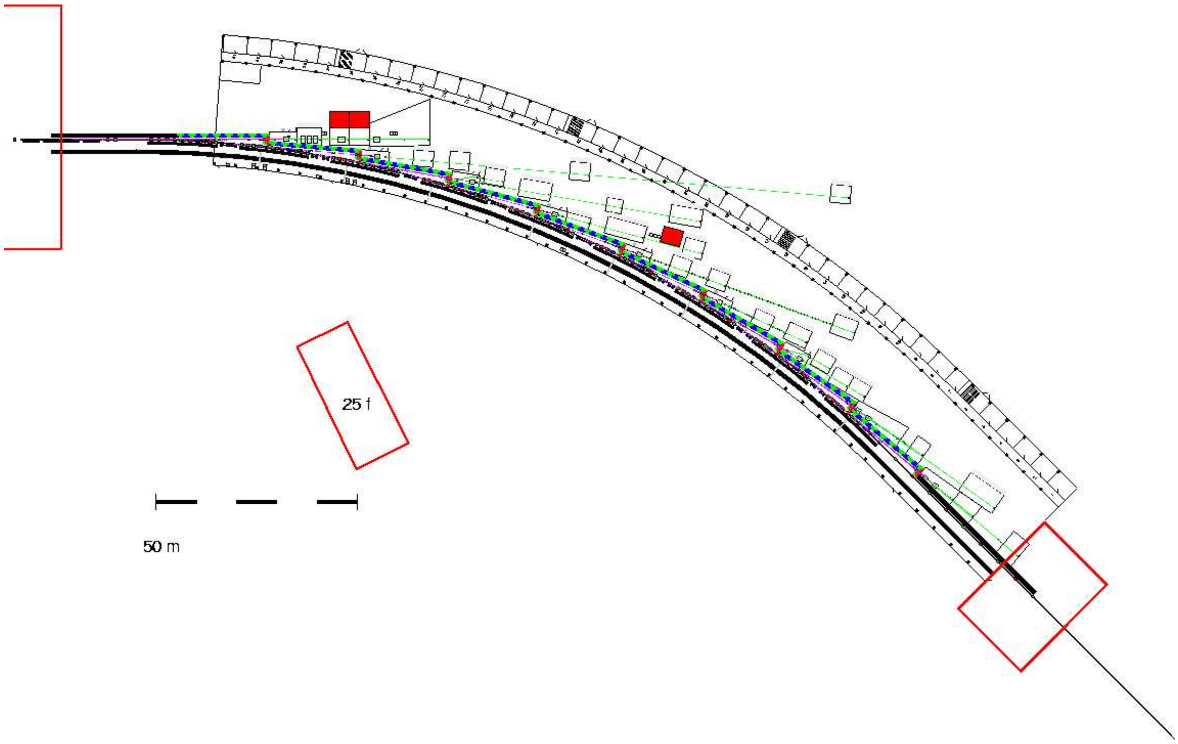

Figure 7.2.1: Schematic top view of the new PETRA III experimental hall.

7.2.1 Overview of the arrangement of the rooms, staircases, elevator, etc.

As seen in Fig. 7.2.1 the top view of the building describes mainly a segment of a circle with an inner radius of 260 m, the angle of the sector of the circle is 40°. In the southeast the segment is extended tangentially about 36.20 m to meet building 48 (a former PETRA experimental hall). Due to construction purposes the building walls will not exactly follow an arc but a polygon line, each straight lined over three posts. The hall is 32 m wide; thereof the innermost 2.5 m are used as service area mostly for power supplies of quadrupole magnets. The ring tunnel covers another 5 to 6 m. The actual experimental floor is 20 m wide. The remaining 6.5 m are covered by the outer bow of the building which accommodate laboratories, offices and plant rooms, especially for air conditioning.
The total space of the ground floor is 7514 m^2, whereof 86 % is experimental area. The hall will have four doors on each longitudinal side. The ones of the eastern side will have a clearance height of 2.5 m in order to let forklift trucks pass through. At each of the front sides the hall will have one larger entrance gate for lorry traffic. The main door will be the one at the northern side, where lorries must pass a lock in order to prevent a greater impact on the thermal conditions in the experimental area.
An overhead crane will span over the total experimental area. Its hook clearance will be 6.0 m, its load capacity 20 tons.
Above the experimental area the building will be one-storied with a height of 8 m underneath

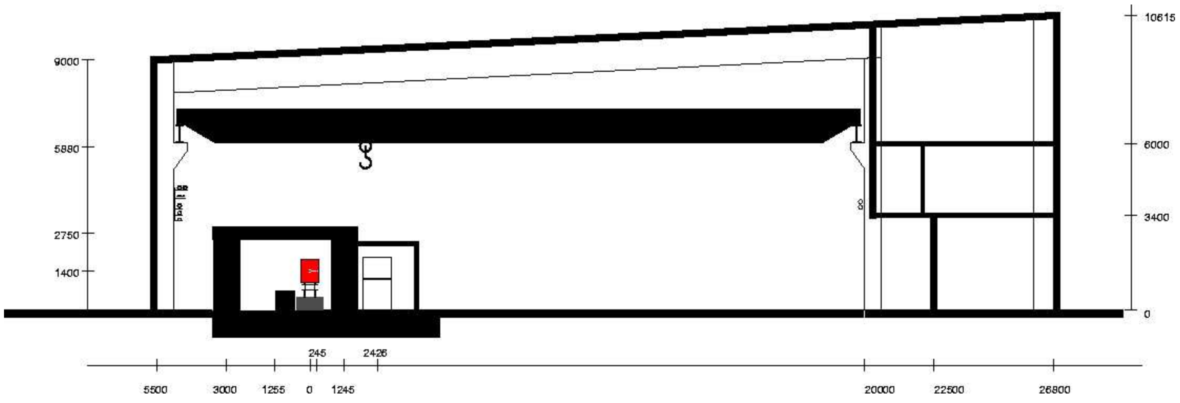

Figure 7.2.2: Schematic cross section of the new PETRA III experimental hall.

the trusses of the roof. The outer bow of the building will have 3 storeys. Therefore four staircases and an elevator will be provided.

Laboratories will be located on the ground floor with a height of 3.3 m and width of 6 m each. A schematic cross section of the experimental hall is shown in Fig. 7.2.2. The partitions should be built in a lightweight construction mode so that the length of the rooms is adjustable to their particular purposes. The laboratories will stretch over a total of 705 m^2. There will be a service corridor (”freeway”) between the laboratories and the experimental area with an aisle width of about 2 m. On the first floor there will be an office area and the usual rest rooms. The offices will occupy a total of about 886.5 m^2. Along side the offices will be a corridor which provides visual contact to the experimental area. The aisle width will be 1.50 m.

On the second floor will be space for technical equipment such as air conditioning devices and electrical power distribution. The total space will be some 1380 m^2. As stability is one of the major issues for a third generation source both temperature and mechanical stability of the floor will be addressed. Again the experience of third generation sources built in the last decade has proven that inside the ring tunnel a temperature stability of the order of 0.1 K is required. Similar values have to be achieved in some (most) of the experimental hutches. Thus also the temperature in the experimental hall has to be stabilized to within 1 K. A temperature change of 1 K changes the length of a steel bar by roughly 10^{-5}, i.e. a monitor sitting on a 1 m long bar changes its height by 10 μm. This is roughly half of the maximum beam height in PETRA III and three times the minimum beam height. Concerning the floor stability both APS and SLS have made good experience with a monolithic ring carrying both machine and experiments. A floor thickness between 30 cm (APS) and 40 cm (SLS) seems to be appropriate. Below the ring tunnel a foundation of 1 m concrete is planned to ensure ultimate stability. Currently two schemes to minimize the influence of local vibrations are discussed:

- to have one monolithic ring segment decoupled from the ”freeway” and the inner service area. Needless to say that the crane pillars have to be founded outside this segment.

- to separate the above mentioned segment with tangential cuts between adjacent beamlines to prevent vibrations to propagate from one experiment to the next.

In any case it seems to be important to have a rigid connection between beamline and machine (undulator). As beam stability will be one of the main issues at PETRA III and vibrations of the experimental floor disturb experiments using a μ-beam as well as movements of the particle beam a vibrational monitoring system will be installed on the experimental floor. This will allow to identify possible sources of ”home-made” vibrations.

7.2.2 Construction method

The building will have to be made of prefabricated elements as far as possible, because of the requirement to build the entire hall within 8 months.
The load-bearing structure will be made of pillars and trusses probably of pre-cast concrete. The distance between the posts on the outer perimeter of the hall will be 6 m. A steel or wooden framework is imaginable as well. This depends on demands coming from structural fire protection or later adaptation issues.
As there is a high requirement on temperature stability in the hall some special means have to be considered in the layout of the structure and panelling (in order to reduce impact of solar radiation and the consequential daily changes of temperature):

1. there should be no windows except in the area of the offices and laboratories (which are in north eastern direction).

2. the basic material of all structural and panelling elements should be of high volume density (to get a higher heat storage capacity). The panelling material will either be of gas concrete with relatively high density or of lime malm brickwork.

3. the entire hall will be thermally insulated.

4. there will be a curtain wall in front of the load bearing inner wall on the southwestern side. The space between will be about 30 cm where a free airflow is guaranteed.

5. the advantages of a roof with natural cover are being investigated.

6. instead of the above mentioned roof there is also the possibility of a double deck roof in which a free airflow under the upper deck is guaranteed as well.

As outlined above a high ground stability is required. The definite solution is still under investigation. The slab for the experimental area will be separated from the foundations of the hall by using vibration-insulating material. It is also considerated whether to dig a deep ditch around the building to reflect ground noise near the surface or to put the concrete slab on a pile foundation.
The floor of the experimental area must be covered with anti-static material. The flatness is specified to be 1 mm over a distance of 1 m.

7.2.3 General power supplies

The general power supply contains the 10 kV medium voltage and the 400 V low voltage equipment. It includes the electrical installation of the building (power sockets, lighting, etc.) and the cables to the consumer loads. The interfaces to the consumers are the power sockets or, with hard-wired consumers, the terminal blocks.
The requirement for electric power for the new experimental hall amounts to 2.500 kVA. This is divided into three fields of application:

- 1.100 kVA for the operation of the hall
- 600 kVA as a tranquilized net for the experimental hutches
- 800 kVA for the power supply units of the magnets

For each field its own 10/0.4 kV transformer is necessary. With some spare capacity one 1.250 kVA and two 800 kVA transformers are needed. The 1.250 kVA transformer (Trafo 1) supplies the electrical load of the hall, such as power sockets, lighting, offices, laboratories, and air conditioning. The second transformer (Trafo 2) powers the experimental hutches. A constant voltage, without influences or peaks from other customers will be reached with this own power-net for the experimental hutches.
The second 800 kVA transformer (Trafo 3) feeds in the power supply units.
Transformers 1 and 2 are set up in a laboratory-room on the ground floor. In order to achieve cable lengths as short as possible, this room should be in the center of the hall (halfway down, Fig. 7.2.3). Special dampers are mounted between the transformer and the mounting rail to prevent vibrations emitted by the transformers. These dampers absorb approx. 90% of the transformer-vibrations. Next to the transformer-room is the low-voltage room (Fig. 7.2.3). Here are the two 400 V main distribution boards (Niederspannungshauptverteilung NSHV). The first NSHV (NSHV 1) is supplied from Trafo1 and feeds six sub-distributions (Unterverteilung UV). Three of them (UV1 - UV3) are on the ground floor and three are on the second floor (UV4 - UV6). The sub-distributions on the ground floor supply the power sockets and the laboratories. Each laboratory is separately fused and has its own fuse-box for the power-sockets. The benefit is that, in a case of defects, the fuse in the fuse-box in the lab can be disconnected.
At each pillar in the hall one 400 V and one 230 V power-sockets, supplied from the sub-distributions on the ground-floor (UV1 - UV3), will be installed.
The three sub-distributions on the top floor (UV4 - UV6) supply the offices on the first floor. Again we will take care of short cable lengths getting the additional benefit of low fire load. The ventilation, the crane, the elevator, the lighting and the rolling gates are supplied directly from NSHV 1. The lighting control is also in the low-voltage room on the ground floor. The brightness in the hall is designed as a storage hall (100 lux) according to the workplace guideline (Arbeitsstättenrichtlinie 7/3). Therefore it is mandatory to have additional lights at the workplaces.
The second main distribution board (NSHV 2) feeds three sub-distributions (UV7 - UV9) which are also on the ground floor. From these sub-distributions the experimental hutches

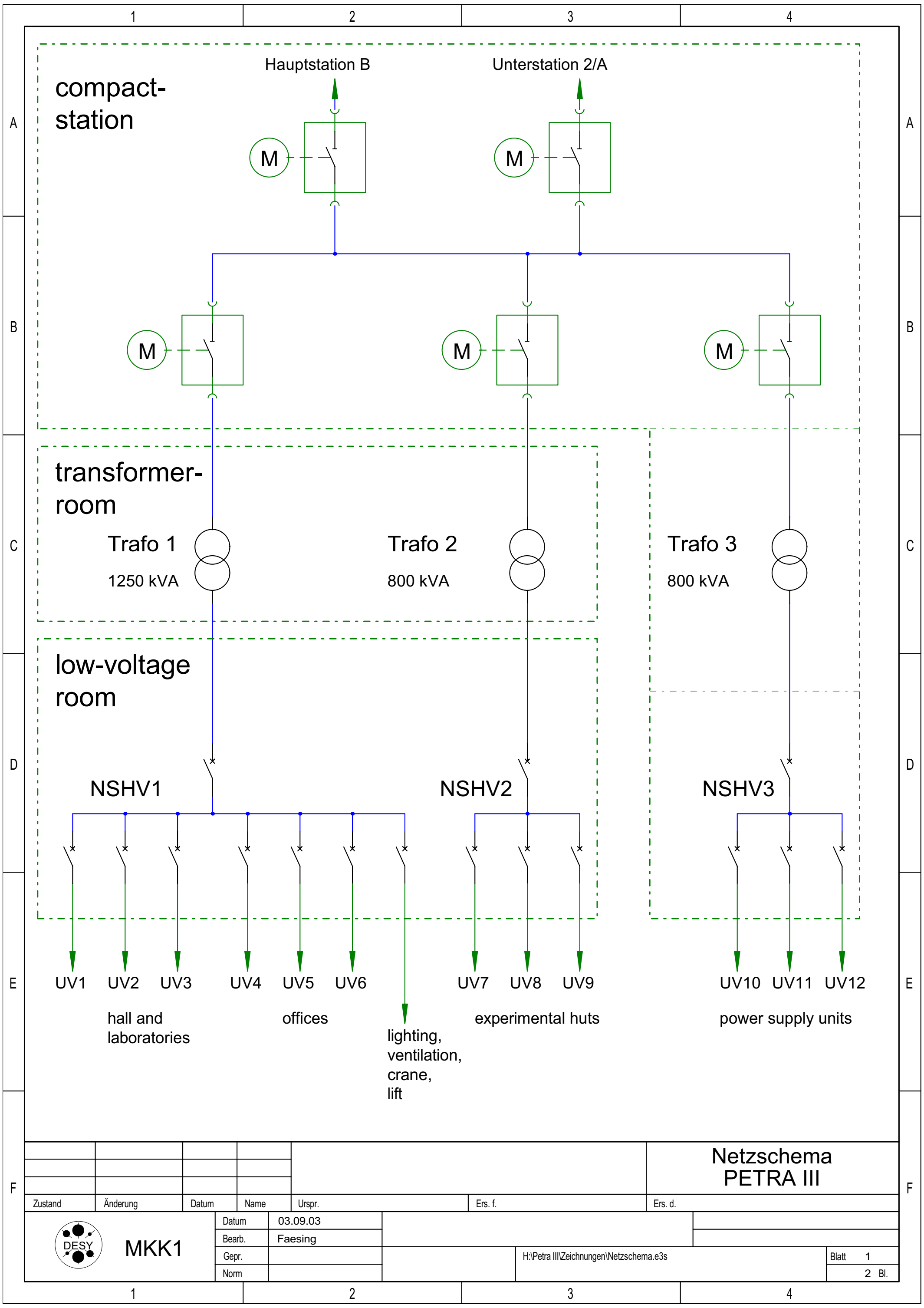

Figure 7.2.3: Schematic representation of the power supply in the PETRA III experimental hall.

are supplied. The hutches contain 'Elektranten' (Boxes with several 400 V and 230 V power-sockets) to supply the experimental equipment.
The sub-distributions on the ground-floor (UV1 - UV3 and UV7 - UV9) are also located in lab-rooms (Fig. 7.2.3). In the top the sub-distributions UV4 - UV6 are in similar positions like the UVs on the ground-floor.
The third transformer (Trafo 3) is in a separate building on the west side halfway down the hall (Fig. 7.2.3). The medium voltage switchgear and the main distribution boards (NSHV 3) are also in this building.
The medium voltage switchgear is a redundant system with two input cables. The main input is from the Hauptstation B, the second from the Unterstation 2/A. In the case of a breakdown of one of these inputs switching over to the other input is possible. The advantage is an higher reliability. The input cables run on the west side of the hall (Fig. 7.2.3) to the switchgear building. There will be another two cables from the switchgear to the transformers 1 and 2 on the other side of the hall. These cables run from the switchgear building on a cable tray in the hall, from there up under the roof, onto the other side of the hall and then down to the transformer room.
The NSHV 3 is fed from Trafo 3. This main distribution board supplies three sub-distributions (UV10 - UV12) which are located on the west side of the hall. These sub-distributions feed the power supply units. The cables between the sub-distributions (UV10 - UV12) and the power supply units are lying on cable trays, which are mounted on the pillars at a height of 5 m (Fig. 7.2.4). On the cable tray the cables are stranded with a twist length of 1 m. With this configuration it is possible to reduce the magnetic field, excited from the 400 V cables, lower than 0.1 μT in the area of the beam line.

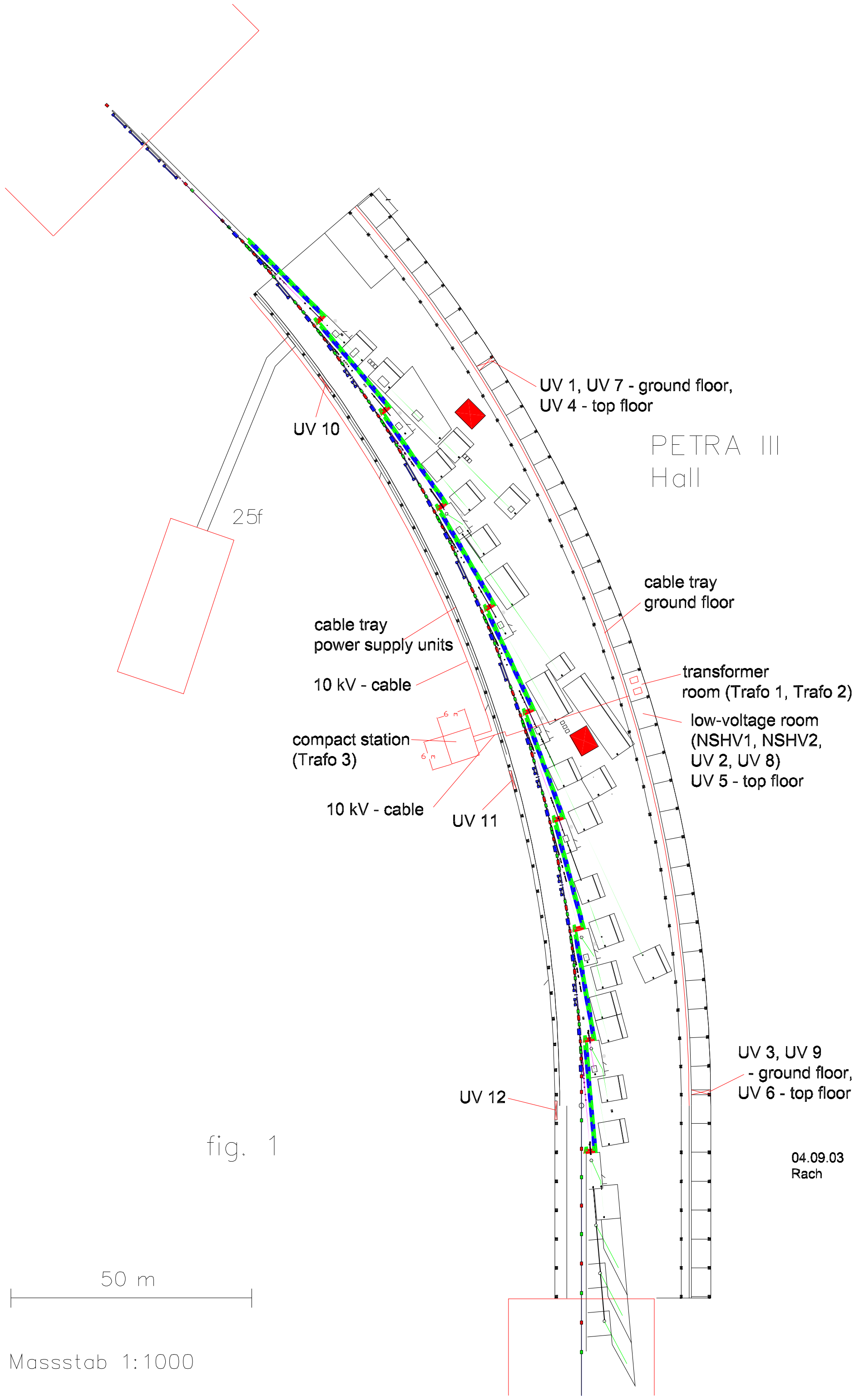

Figure 7.2.4: Bird eyes view of the main power supply installations in the PETRA III experimental hall.

7.2.4 Air conditioning

7.2.4.1 Chilled-water systems

The layout of the chilled-water system is shown in Fig. 7.2.5. For the air-conditioning of the experimental hall and the experimental hutches, chilled water with a temperature of 6°C is needed. This water is provided by three special coolers. They will be installed in a pumping station to be build near the PETRA-location *Northeast*.
For the air-conditioning of the experimental hall, a total cooling power of 840 kW is necessary. The experimental hutches require a cooling power of 250 kW.
The cooling circuit for the experiments and laboratories is connected to the chilled-water circuit by an extra heat exchanger. Consequently, this circuit needs extra pumps and a pressure regulation. The water temperature of 20°C is adjusted at the primary side of the heat exchanger. To avoid condensed water, all pipes for chilled water will be insulated with a closed-cell material.

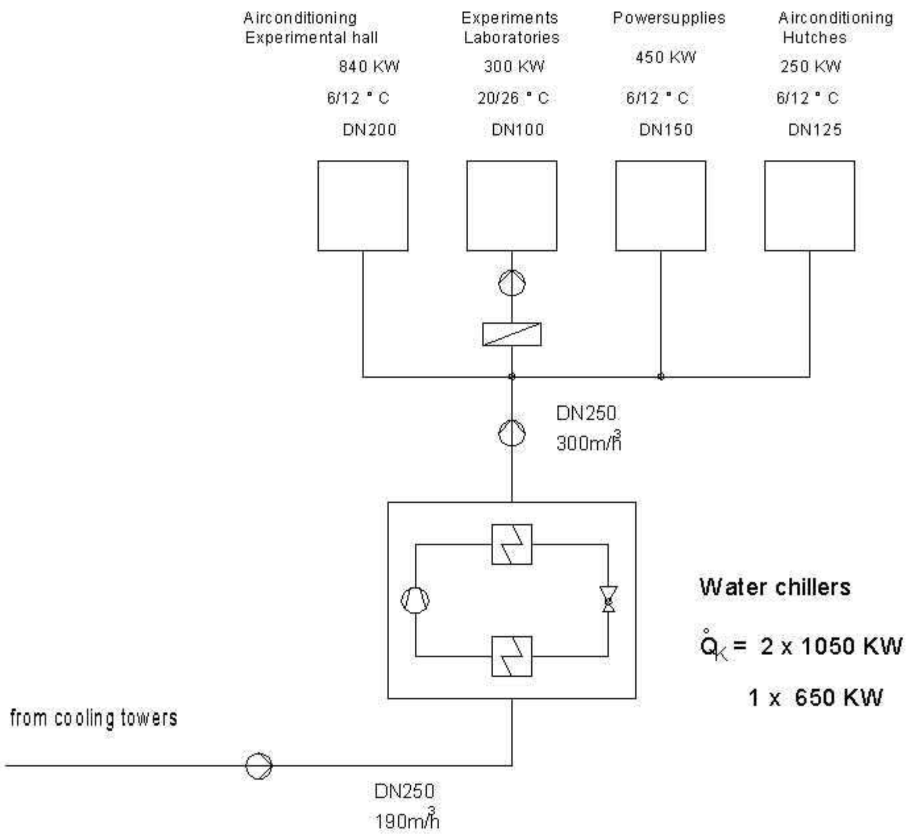

Figure 7.2.5: Scheme of chilled-water circuits

7.2.4.2 Air conditioning of the experimental hall

For the air conditioning of the experimental hall six climate-control devices working independently of each other are conceived. These devices are mounted in the top floor on the north-east side of the experimental hall.
Fresh air is drawn in from outside via a weather protection barrier at the mixing chamber of the device. In this device recirculated air can be mixed in upon demand. After filtering and temperature adjustment, this air is blown by a fan through galvanized steel canals and twist diffusers into the experimental hall. The direction of the air flow from the twist diffusors is adjusted depending on the temperature: during heating operation the air stream is directed vertically while in chilling mode the air stream is directed horizontally. The air that is extracted from the hall is guided through galvanized steel canals to the exhaust fan. The exhaust part of the air is blown out via a weather protection grid at the mixing chamber. The air conditioning system for the experimental hall is shown schematically in Fig. 7.2.6.
Continuous speed regulation of the ventilating fans is carried out with frequency converters. The climate-control devices are supplied with heating and cooling water through the water supply network of DESY. For the cooling water of a temperature of 8(12)°C and for the heating water of 50(30)°C will be used. The heating of the experimental hall in winter will occur through the air condition devices.

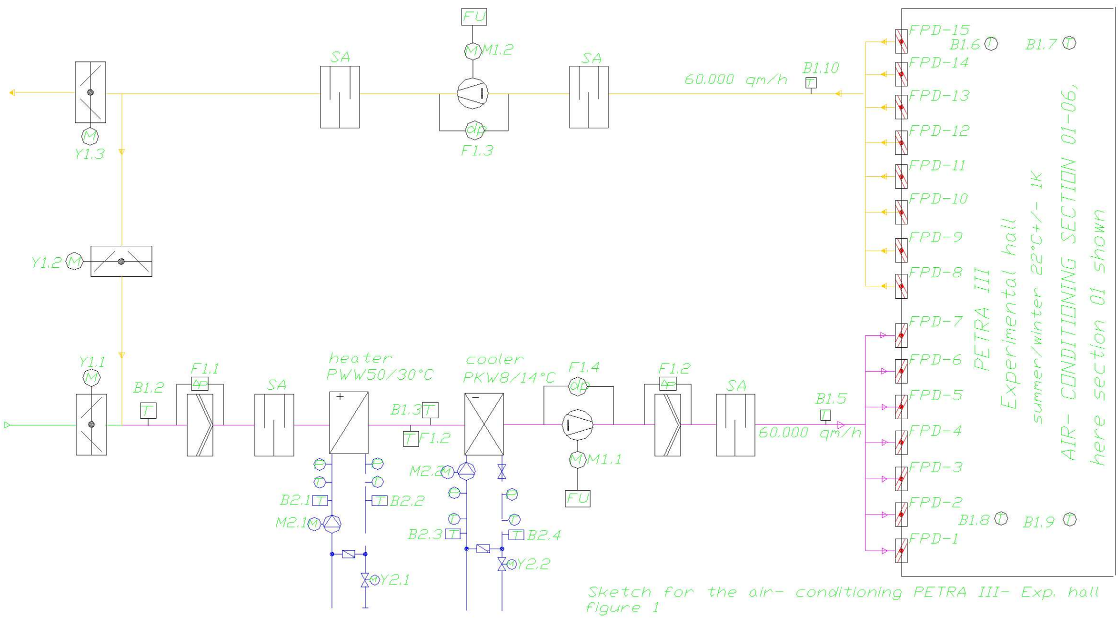

Figure 7.2.6: Scheme of the air conditioning for the experimental hall

- **Temperature control**
  For the feedback control of the air condition, each system will be equipped with an individual DDC regulation. The regulation of the temperate is realized as a cascade

control of the intake/interior air. The cascade consists of a guiding regulator and subsequent regulators. The guiding regulator shifts the set-point of the air supply proportional to the deviation of the temperature in the experimental hall. The measurement of the temperature proceeds via four sensors from which the average will be taken as the actual value. For the experimental hall no humidification or drying of the air is foreseen. Within this concept, hot air exhaust of the experimental hall up to temperatures of 70°C is possible.

- **Technical Data**

Incoming air volume stream	:	$6 \times 60.000\,m^3/h = 360.000\,m^3/h$
Used air volume stream	:	$6 \times 60.000\,m^3/h = 360.000\,m^3/h$
Ratio intake/exhaust air	:	0 – 100 % variable
Temperature in the experimental hall	:	22 °C ± 1 K

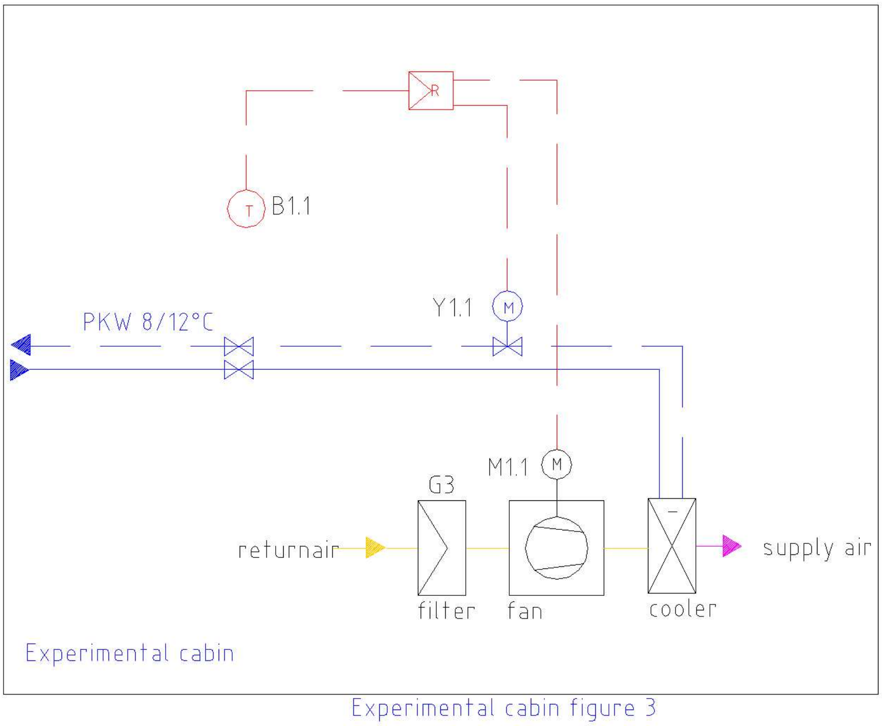

Figure 7.2.7: Scheme of the air conditioning for the experimental cabins

7.2.4.3 Air Conditioning of the experimental cabins

Every experimental cabin is equipped with an recirculating air condition device which is suitable for ceiling installation, stand installation and wall installation. The device is cooled with water of 8(12) °C. The air conditioning system for the experimental cabins is shown schematically in Fig. 7.2.7.

- **Temperature control**
  - DDC single-room regulation with communication
  - Three-stage ventilating fan control
  - Limitation of minimum incoming air temperature
  - Ambient temperature sensor
- **Technical Data**

Circulating air volume stream	:	1300 m^3/h
Cooling power	:	7.6 kW
Cabin temperature	:	22 °C ± 0.1 K

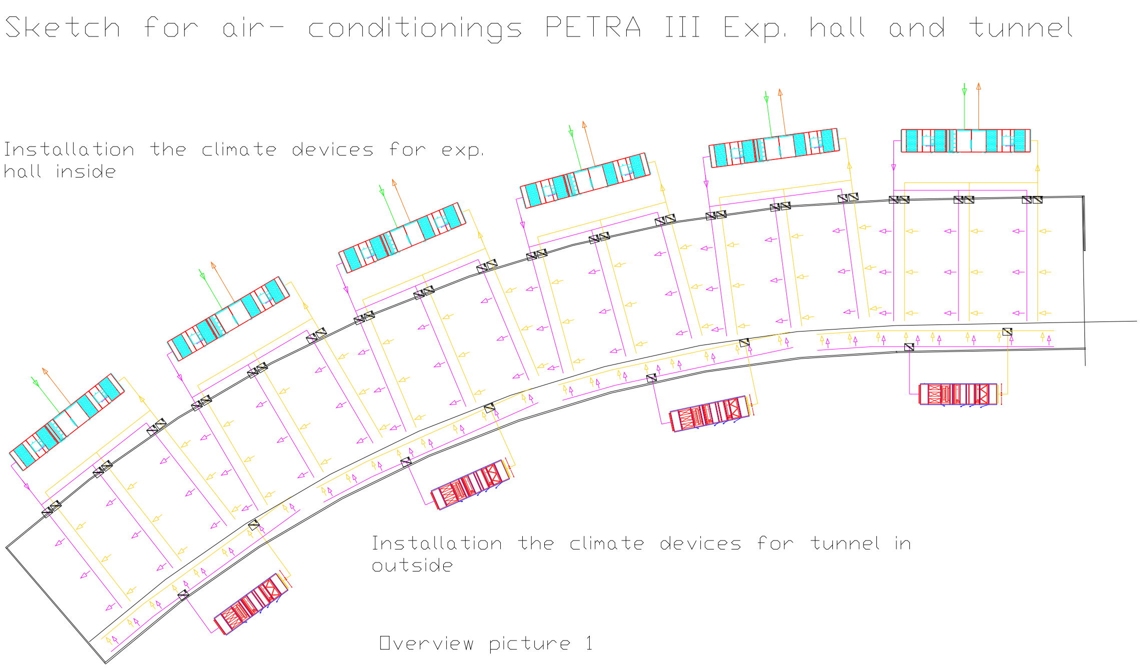

Figure 7.2.8: Scheme of the air conditioning system for PETRA III

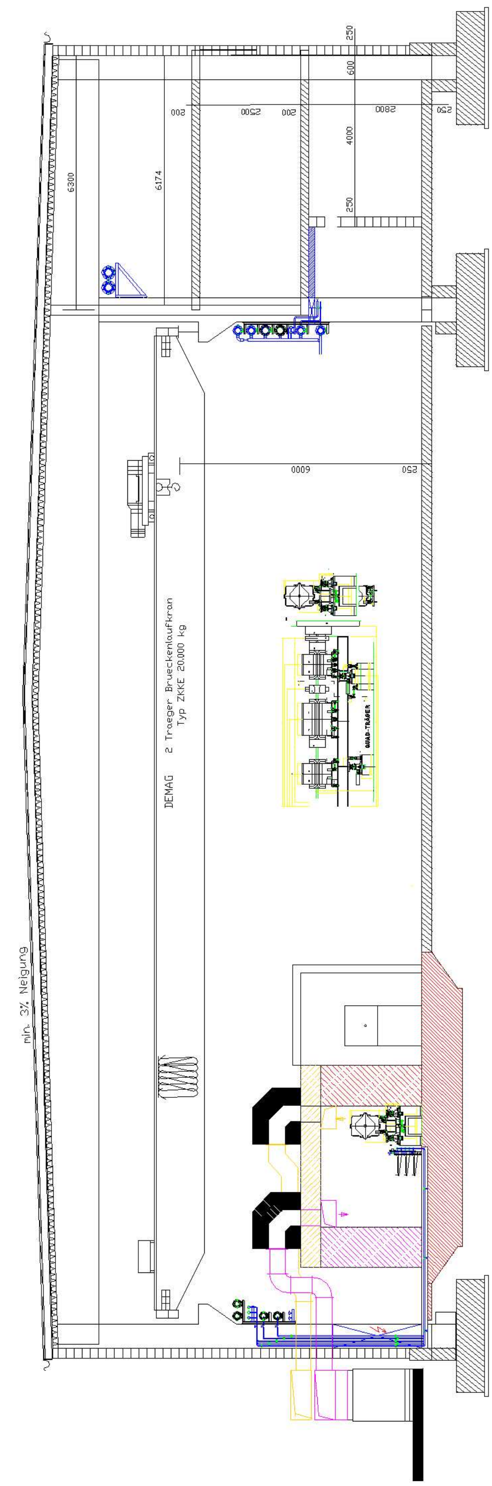

Figure 7.2.9: Cross section of the experimental hall with the main elements of the air conditioning systems

7.3 Computing Infrastructure, Experiment Control

The PETRA III computing model involves the IT infrastructure at the experimental stations, the beamline PCs and supporting IT services. Fig. 7.3.1 shows a schematic view of these components, which are discussed in the following sections. We start with some general statements:

- Standards will be employed wherever possible. In the hardware sector this minimizes the maintenance effort. Also in the software sector standards are important, since beam time can be used more efficiently, if visiting scientists find software interfaces that are well known to them.
- The computing power, which is needed in the experimental hall, will be provided by PCs, because they are very cost-effective. From our present experiences we know that PCs are well suited for instrument control purposes.
- There will be a clear cut between local and DESY-central IT services. Only those IT components that are indispensable for the operation of the experiments will be installed in the PETRA hall. The rest of the necessary IT infrastructure will be provided by the DESY-central IT group.

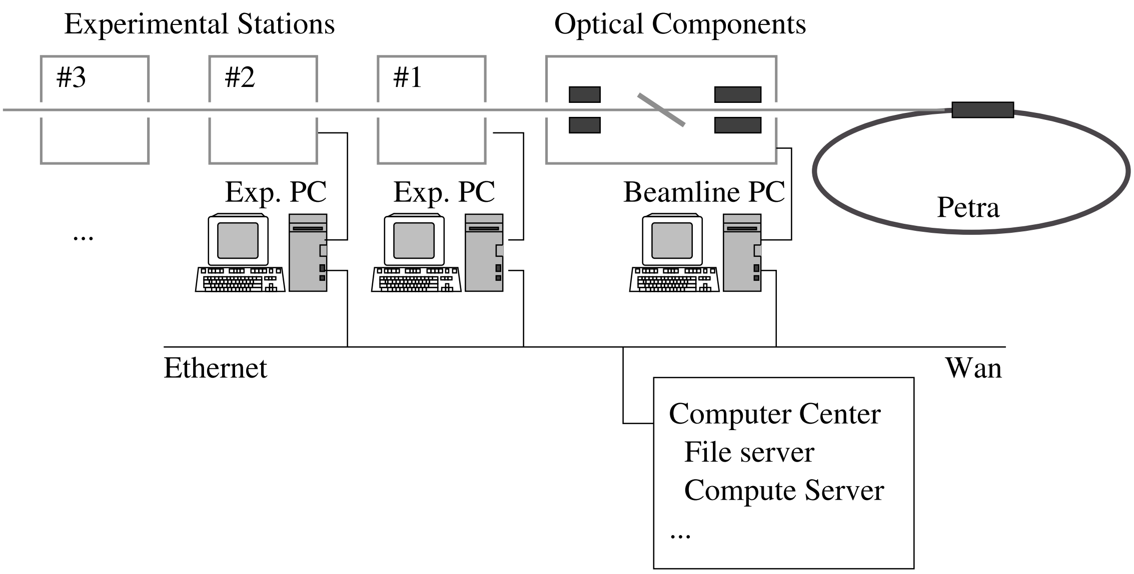

Figure 7.3.1: Computing at PETRA III

7.3.1 Computing at the experimental stations

It is planned to develop a standard online system which includes computers, electronic components, interfaces and online software.

Instrument control, data acquisition and monitoring will be done by Linux PCs with VME, GPIB and CanBus interfaces. This way network overhead caused by I/O operations to these busses is avoided. In addition, socket interfaces are expected to be of great importance and serial lines (RS232), provided by terminal servers, will still be needed.
The following table displays a list of those electronics which are going to be standardized. The interfaces are also given:

- **VME:** Stepping motor controller, ADC, MCA, timer, counter, I/O register, position encoder.
- **GPIB:** Multimeter, amplifier, temperature controller, position encoder.
- **CanBus:** I/O register, stepping motor control.
- **Socket:** Communication with the beamline PC, CCD cameras.
- **RS232:** Monochromator stabilizer.

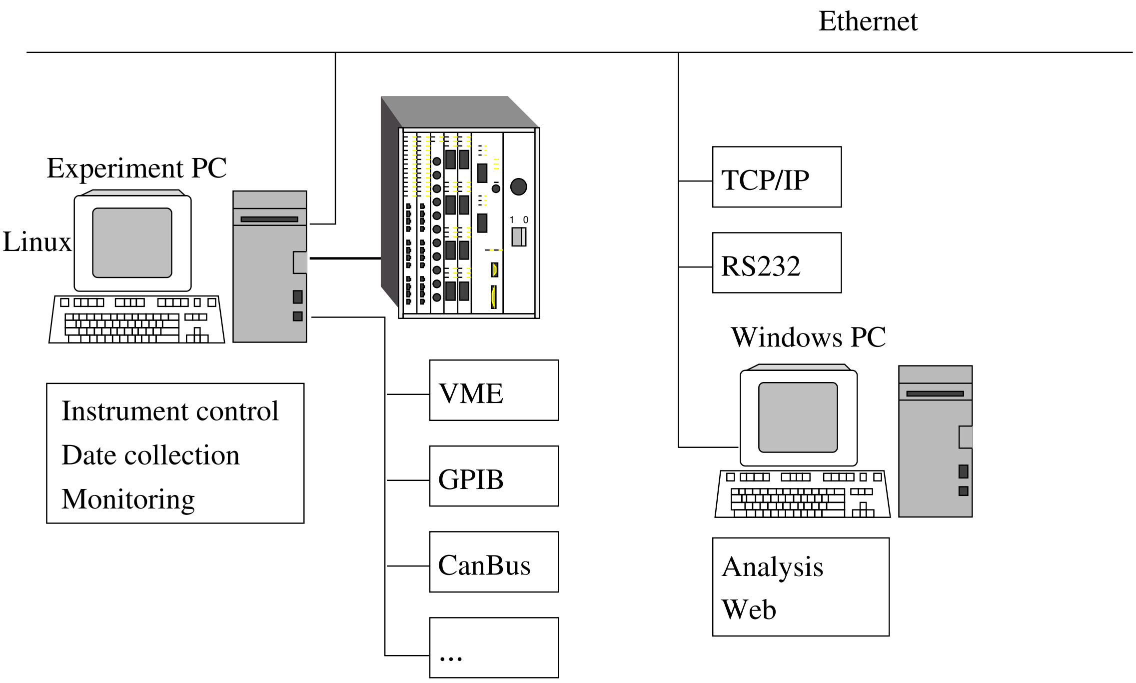

Figure 7.3.2: Instrument control and data acquisition

It is intended to hold spare parts for all standard components in store and make them available in case of hardware failures. This applies also for PCs. A backup-restore procedure will be implemented which allows an almost automatic recovery from disk crashes or other severe computer break-downs.
Spectra serves as an online program, using Perl as the scripting language and PerlTk for the graphical user interfaces. The program Spec (Certified Scientific Software, CSS), which

is known to many of our guests, will be available at the PETRA III beamlines on request. Spectra and Spec have interfaces to the same hardware and it is ensured that the stepping motor positions are maintained between two online sessions. Both programs have network interfaces which enable them to be used as servers or clients depending on the application.
The beamlines will also be equipped with Windows PCs. They can be used to for data analysis and internet access.
Some experimental stations will be operated by external groups. They are invited to adopt the standard system. Only this way they can benefit from support by DESY staff.

7.3.2 The beamline PC

The status of the insertion devices, mirrors and absorbers will be made available by a dedicated PC, the beamline PC. The data will be communicated using an ASCII protocol on a TCP/IP socket connection. In addition, the beamline PC is going to distribute information about the accelerator: the insertion device status, the beam current and the beam position.
The beamline PC will not be associated with a specific experiment. Read-access will be granted to all experimental stations, write-access to one at a time.

7.3.3 Data storage

Depending on the amount of incoming data, the disk space of the experiment PC may be sufficient to store the data before it is transfered to the home institutes. Other experiments that generate more data than can be hold on local disks need a network file system, the large file store (LFS). It is accessible from Linux and Windows, it has a short connection to compute servers and it is backuped regularly. The LFS is installed and operated by the DESY IT group.

7.3.4 Compute servers

In general, data processing will be carried out at the home institutes. There are exceptions to this rule:

- Data has to be analyzed at DESY, if the ongoing measurement critically depends on these results.
- It can be useful to perform the necessary calculations at DESY, if the data analysis is a part of the experimental method, especially if the analysis requires an amount of CPU power that is not available at all home institutes.
- Data reduction should be considered, if it leads to a considerably lower network load or disk usage.

Compute servers will be installed and operated by the central DESY IT group.

7.3.5 Data transfer

In general, data will be copied via the network to the home institutes. DESY is a member of the DFN. It is expected that the bandwidth grows with the need of our user community.
For those who do not have sufficient internet access, it will be possible to copy data to some medium and carry it back.

7.3.6 Summary

DESY develops a standard system for instrument control and data acquisition and invites external groups to use it. Beamline PCs will provide an interface to the optical components and accelerator data. File and compute servers will be supplied by DESY-central IT group.

Chapter 8

Project Costs, Personnel, and Management

8.1 Project Cost Estimate

The estimate of the total PETRA III project costs includes all costs related to

- the refurbishment of 7/8, and the conversion of 1/8 of the PETRA storage ring,
- the refurbishment of the pre-accelerators and accelerator infrastructure,
- all construction work necessary for the new experimental hall including radiation protection, offices and laboratories,
- the insertion devices, beamlines, and experimental stations to be built and operated by DESY,
- all R&D activities necessary for the storage ring, insertion devices, and beamline components from year 2005 on,
- and all costs for personnel.

Within the PETRA III upgrade about 13 beamlines at independent undulators will be provided. According to the present plan seven of these undulator beamlines will be constructed and operated by DESY. It is expected that some of the remaining beamlines will be built and/or financed by external institutions such as EMBL, GKSS, and the Max Planck Society (MPG). In these cases DESY will cover the costs for beamline front ends, vacuum systems, and radiation safety measures, which amounts to about 1 M€ for each beamline and is already included in the total capital investment presented here. The remaining costs of the externally built experimental stations are not included.
The PETRA III project amounts to about **192 M€** in year 2003 prices, where

- **71 M€** of capital investment are needed for the storage ring,
- **64 M€** of capital investment are required for the new experimental hall including the insertion devices and the DESY operated beamlines, and
- **57 M€** cover the total personnel costs.

The estimates concerning costs and personnel requirements for the work at the storage ring are based on the longtime experience of the DESY machine group in the construction and operation of accelerators and storage rings. The numbers were compiled in close collaboration with the leaders of the respective DESY groups.
The costs of the experimental hall were estimated by the civil construction group at DESY within an engineering study.
The beamlines costs for insertion devices, vacuum system, beamline optics, and experimental endstations are based on DESY's experience in operating DORIS III as a synchrotron radiation source and on expert knowledge from the most recently built synchrotron radiation sources like SLS, ESRF, and APS. On average about 4 M€ capital investment were assumed for the construction of each beamline not counting the investment for the undulator.

The cost estimate for personnel assumes about 77 k€/a/FTE[1]. This amount includes costs for the working environment and overhead (10%).

A graphical representation of the required cost profile is shown in Fig. 8.1.1. The schedule presented in Chapter 9 is based on this cost profile.

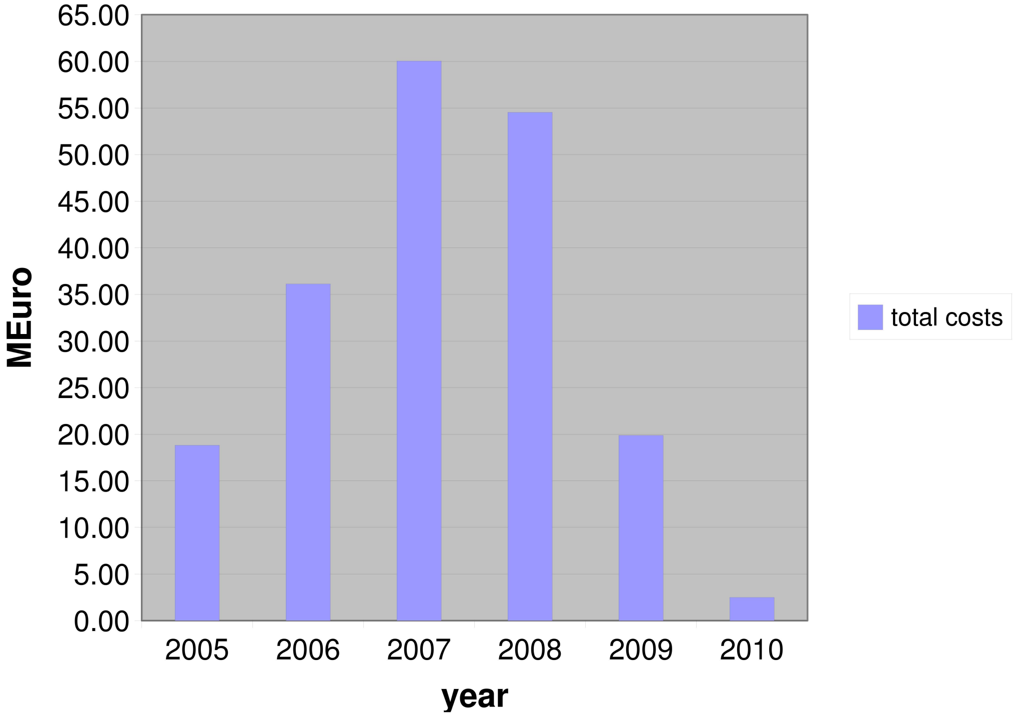

Figure 8.1.1: Cost profiles for PETRA III in M€ for start of construction work in mid 2007.

[1]Full time equivalent

Explanation of the proposed spending profile.

PETRA II will be used as a pre-accelerator for HERA until June 2007. In parallel it will be used for synchrotron radiation experiments and to develop and test components for PETRA III.
In order to keep the time for the transformation into PETRA III as short as possible, all R&D and design work and a significant amount of the production work will be carried out well in advance. This has the advantage that the production of components can be spread over several years which is more cost effective. This is particularly true for the production of the magnets, vacuum components, and the radiation protection walls.

8.2 Personnel Requirement

About 830 person years are estimated for the PETRA III project for the years 2005–2008. The required personnel and the personnel available at DESY for this project are shown in Fig. 8.2.1. The difference in personnel has to be employed for the duration of the project.

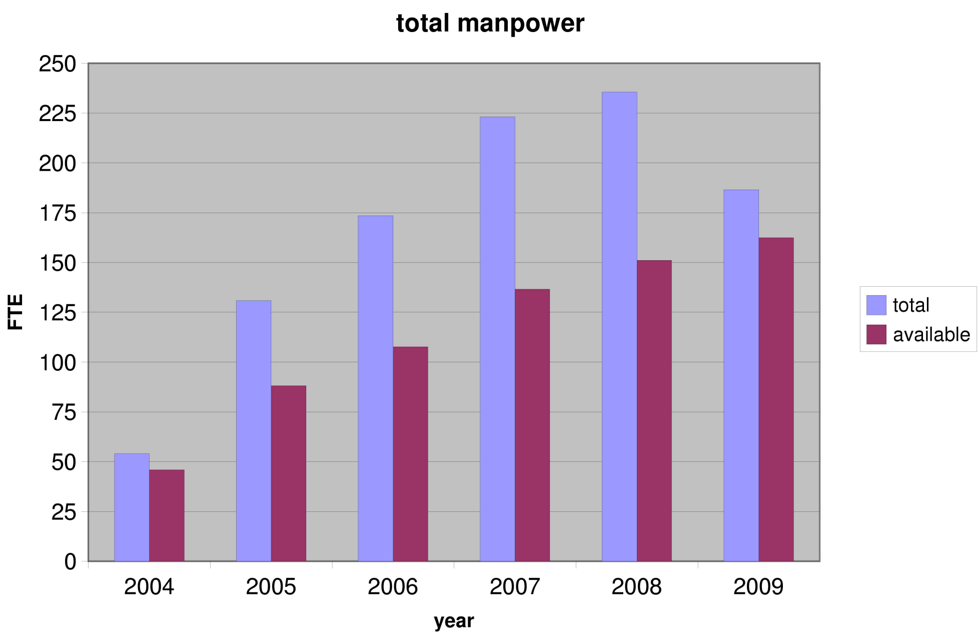

Figure 8.2.1: Total required personnel and personnel available at DESY for the PETRA III project.

8.3 Operating Costs

For the operation of the PETRA III storage ring, the pre-accelerators, and for general infrastructure about 100 FTEs will be needed. In addition the experimental hall including the experiments will be staffed with about 50 FTEs. This means, that each DESY beamline will be staffed with 4–5 FTEs and a number of FTEs will be available for technical infrastructure, experiment support group, safety, hall services, etc.. Therefore, the total personnel costs amount to **8.25 M€**/a.

For 5500 h/a operation of the storage ring and the pre-accelerators about 6.5 M€/a will be needed for energy, spares, replacement, etc.. In addition, about 4.5 M€/a will be needed for the operation, replacements, infrastructure costs and upgrades of the DESY operated beamlines.

Therefore, in total an operational budget for the PETRA III facility including personnel of **19.25 M€**/a based on year 2003 prices is estimated.

8.4 Management

8.4.1 Definition of the work packages

The entire PETRA III project is divided into a number of work packages (WP). A short description of these work packages will be given in the next sections.

8.4.1.1 Reconstruction of the storage ring

All work packages related to the refurbishment and construction of the PETRA III storage ring are listed in Tab. 8.4.1. For each work package a responsible person has been appointed.

name	description	name	description
WPM1	Magnets	WPM2	Magnet Supports and Girders
WPM3	Mains and Utilities	WPM4	Magnet Power Supplies
WPM5	RF Power Supplies	WPM6	Water Cooling System
WPM7	Vacuum System	WPM8	RF System
WPM9	LINAC / PIA	WPM10	Kicker and Septum Magnets
WPM11	DESY II	WPM12	Topping up Feature
WPM13	Multi Bunch Feedback System	WPM14	Damping Wigglers
WPM15	Control and Interlock System	WPM16	Diagnostics
WPM17	Beam Protection System	WPM18	Alignment
WPM19	Installation / Time Schedule	WPM20	Beam Optics / Beam Dynamics
WPM21	Beam Instabilities	WPM22	Orbit Movement and Correction

Table 8.4.1: Definition of the work packages for the storage ring related activities.

8.4.1.2 Experimental hall, beamlines and insertion devices

The tasks for each beamline/experimental station has been merged into one work package (WPE1 to WPE13, see Tab. 8.4.2). The exact objective of these WPs will be defined as soon as the final decision on the experiments to be built has taken place. For those beamlines not to be built by DESY the corresponding WP includes only the DESY portion of the respective beamline (front end, vacuum and safety system). In addition to the beamlines there will be two WPs for beamline R&D of critical components that will be common to all beamlines and one WP for insertion devices. The last WP will take care of general infrastructure and safety aspects.
The construction of the experimental hall will be within the responsibility of DESY and has been summarized in one work package (WPE24).

Name	description
WPE[1-13]	WPs for the 13 beamlines
WPE21	Critical beamline and optical components, design and prototyping
WPE22	Adaption of the generic vacuum and optics design to all other beamlines
WPE23	Design, prototyping, production, and installation of undulators
WPE24	Experimental hall, floor, offices, and laboratories
WPE25	Experimental hall general infrastructure, safety, media

Table 8.4.2: List of work packages related to the experimental hall and the beamlines.

Chapter 9

Timetable, Milestones

Tentative time tables for the PETRA III upgrade are given in the following sections. Most important milestones from the present point of view are the start of reconstruction in July 2007 and first light for user experiments in 2009. A simplified overview about the schedule of the entire project in which summaries of the following schedules have been merged is shown in Fig. 2.5.1.

9.1 Storage Ring

A first tentative schedule for the refurbishment of the 7/8 of the PETRA II storage ring and for the construction of the new 1/8 of the PETRA III is given in Figs. 9.1.1–9.1.4. This schedule includes also necessary work for R&D, tendering and the entire preparation phase.

9.2 Experimental Hall

The schedule for the construction of the experimental hall including all preparation work is given in Fig. 9.2.1.

9.3 Experiments and Radiation Sources

A schedule for all beamline related activities including the preparation and R&D activities is given in Figs. 9.3.1 and 9.3.2.

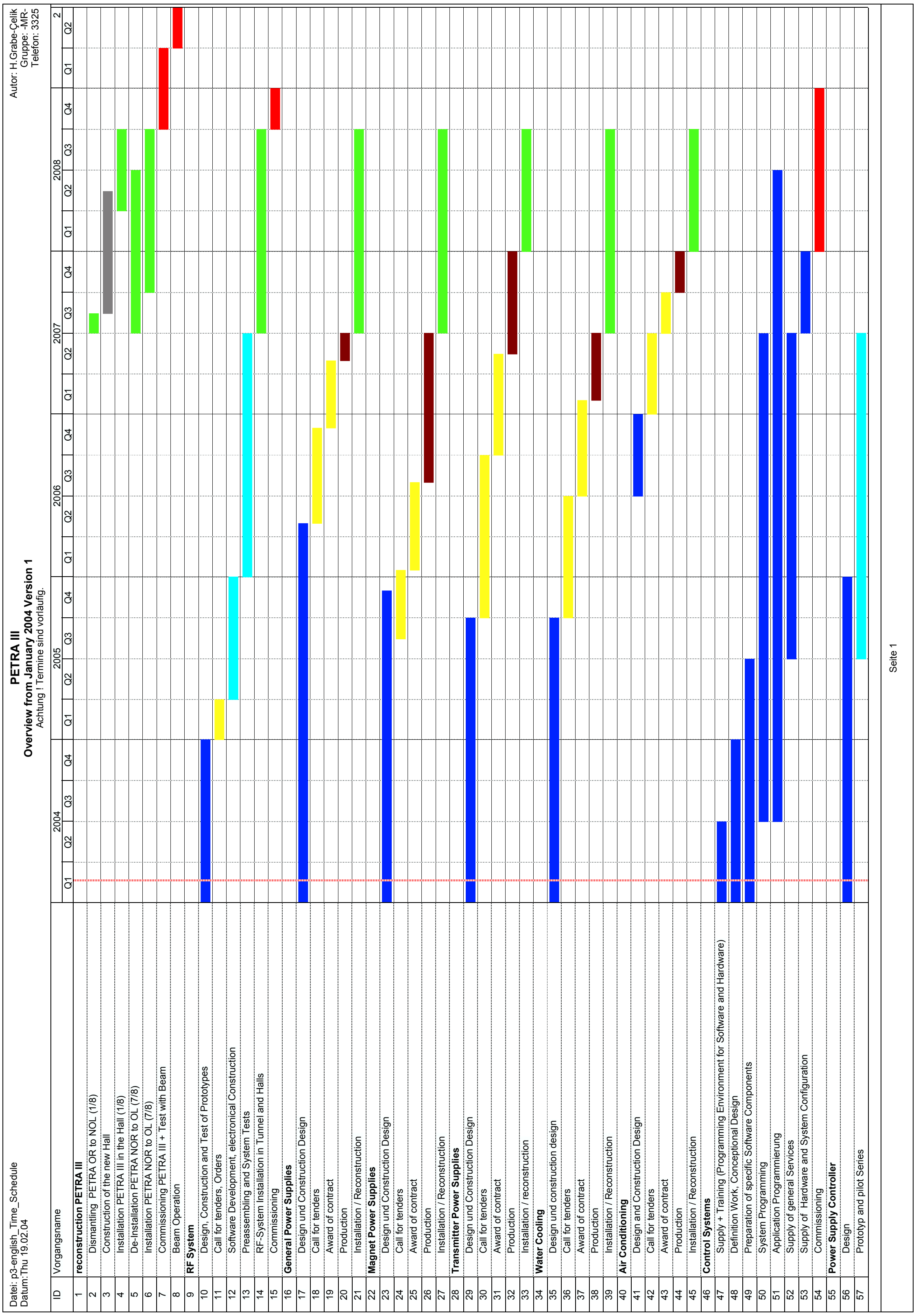

Figure 9.1.1: Time table (1/4) for the PETRA III storage ring reconstruction. (Please use your readers zoom function for details.)

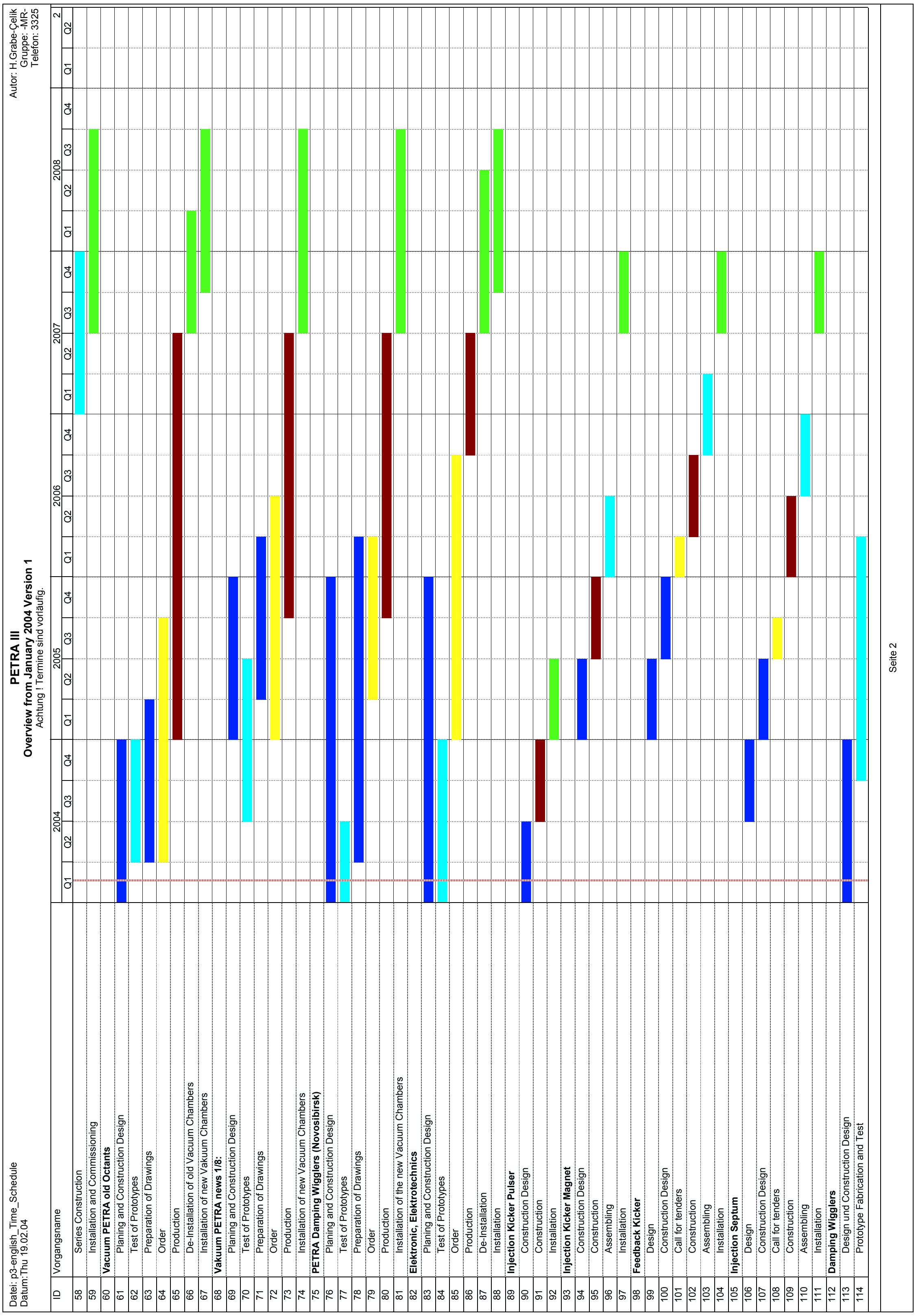

Figure 9.1.2: Time table (2/4) for the PETRA III storage ring reconstruction. (Please use your readers zoom function for details.)

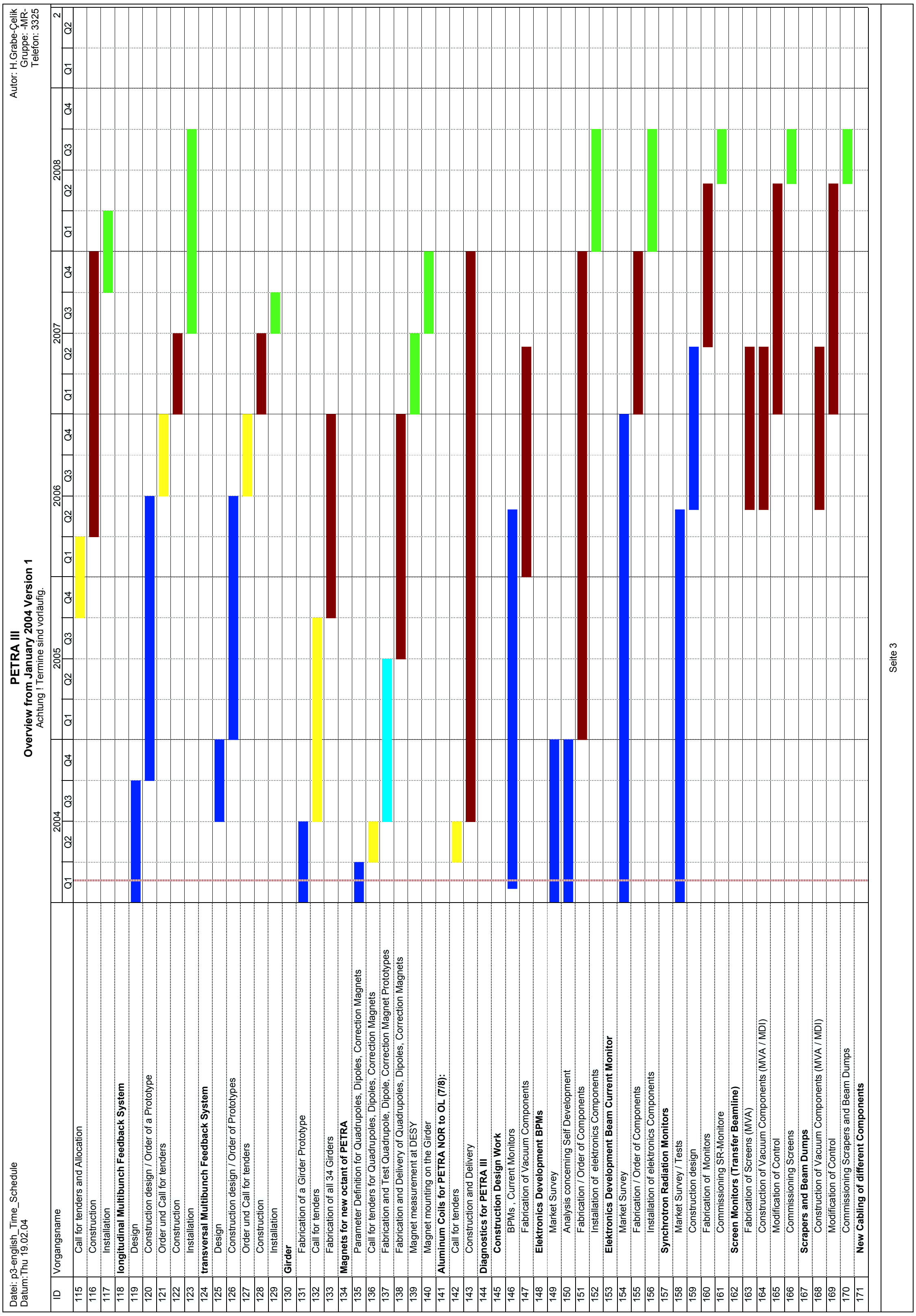

Figure 9.1.3: Time table (3/4) for the PETRA III storage ring reconstruction. (Please use your readers zoom function for details.)

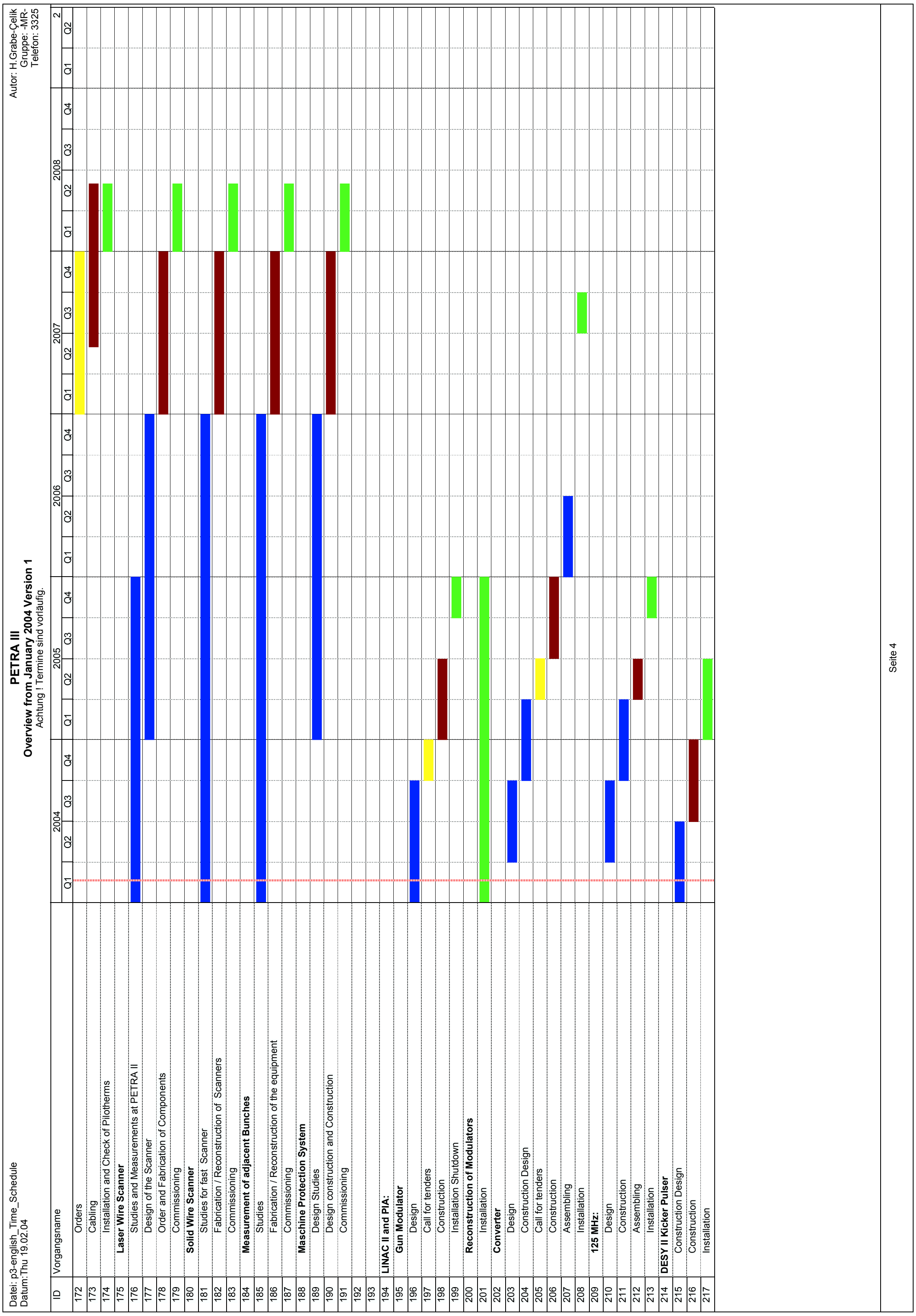

Figure 9.1.4: Time table (4/4) for the PETRA III storage ring reconstruction. (Please use your readers zoom function for details.)

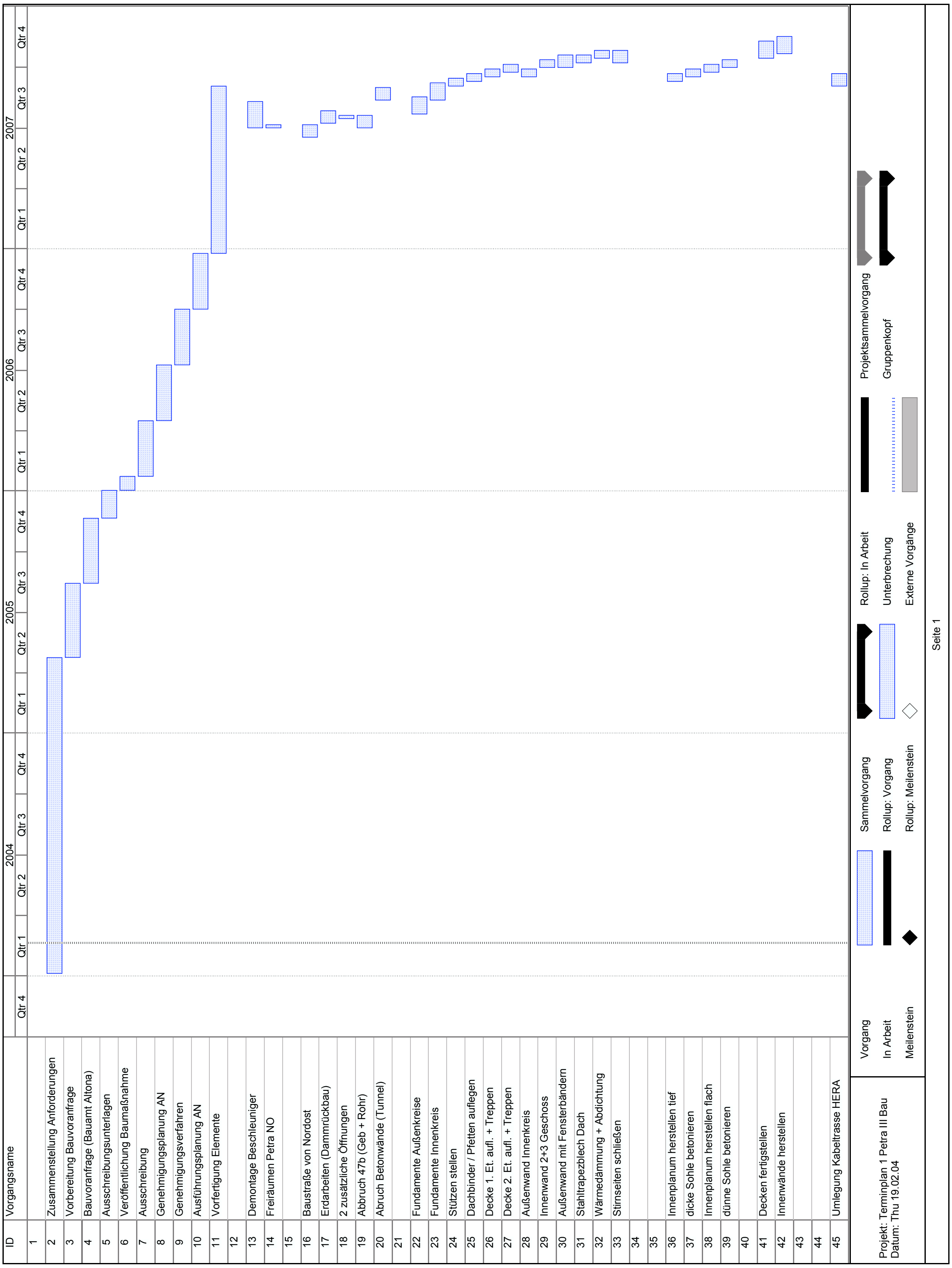

Figure 9.2.1: Preliminary time table for the PETRA III experimental hall construction. (Please use your readers zoom function for details.)

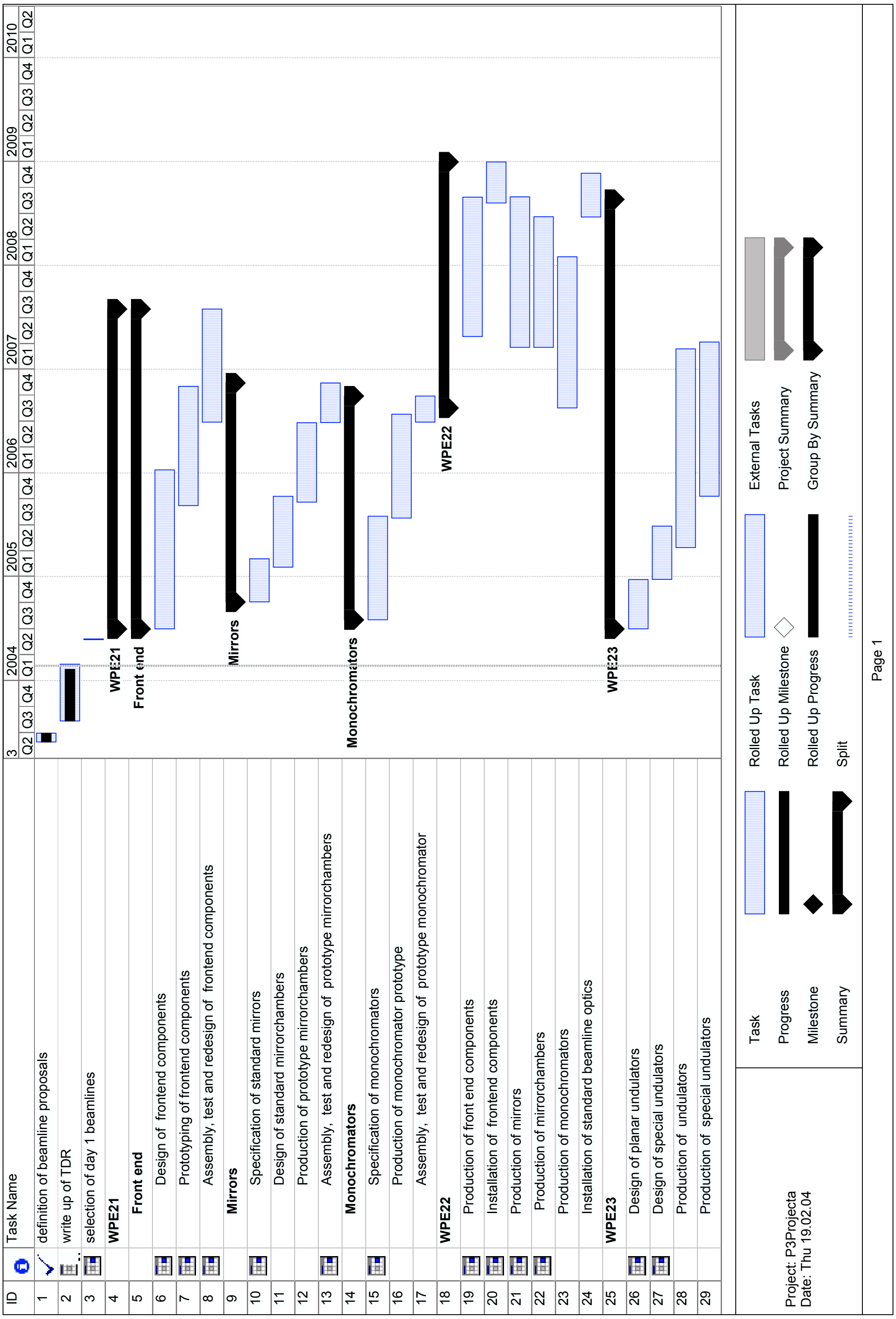

Figure 9.3.1: Preliminary time table (1/2) for the beamline, insertion device, optics, and experimental endstation design, prototyping, production, installation, and commissioning. (Please use your readers zoom function for details.)

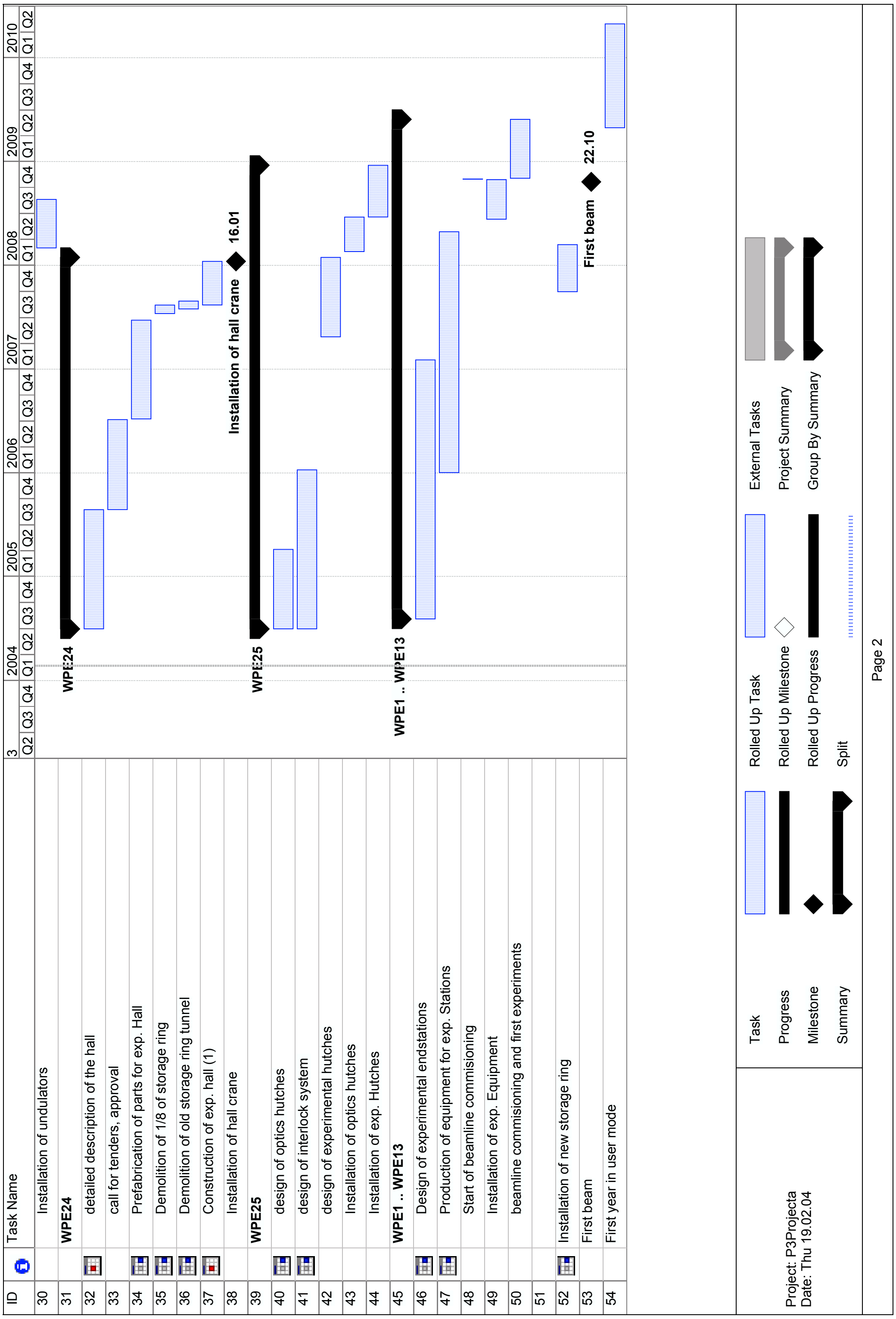

Figure 9.3.2: Preliminary time table (2/2) for the beamline, insertion device, optics, and experimental endstation design, prototyping, production, installation, and commissioning. (Please use your readers zoom function for details.)

Chapter 10

Further Upgrade Possibilities

10.1 Beamlines at Damping Wigglers

In order to reach the emittance of 1.0 nmrad damping wigglers will be installed in the long straight sections of PETRA (Sec. 3.4). In total a magnetic length of 80 m is required which will be distributed in the west and north. These wigglers produce a rather wide fan of hard X-rays. The power emitted amounts to 205 kW at a stored current of 100 mA in each straight section. This is more power than any existing insertion device produces to date. The critical energy E_c is 35.9 keV. Fig. 4.2.1 shows the spectral distribution emitted by the present wiggler design (3.4). The beam size at a distance of 70 m (the location of a potential experiment) amounts to 200 x 5 mm^2 FWHM.

Given the fixed budget of the upgrade project the radiation produced by these wigglers will be dumped in special absorbers inside the ring tunnel. A wide beam port will extract a decent fraction of the power emitted in forward direction and guide it to a dump, remote of the storage ring vacuum chamber. This dump can be replaced by a high power front end in an upgrade step. Furthermore, we will prepare the tunnel shielding to allow for a later use of these beams.

These beam may be used for different purposes:

- The wide fan can be split by a comb–like slit system to feed several consecutive or even parallel stations. Each beam would have a size of some mm^2. The calculated intensity is of the order of 10^{10} photons/(s mm^2) behind a Si(111) monochromator. So these beams would compare to a typical bending magnet station at a third generation source, however the spectrum extends to higher energies..

- The beam can be used in total to perform tomography experiments on large (scale of 10 cm) samples. This application would profit most from the hard spectrum of the wiggler radiation.

- Experiments depending on a white X-ray spectrum which can not be delivered by the undulator beamlines in the new experimental hall would find an almost ideal source. This could e.g. be white beam Laue techniques or fast EXAFS measurements over a wide energy range.

In addition, the long straight **east** can be used for a specialized ID, for example to provide a large hard X-ray beam for material science experiments. Between the quadrupole magnets Q6N and Q7N, a drift of $L = 7.2\,m$ offers space for one long device (see Fig 10.1.1). The beta functions at this position are suited even for an undulator ($\beta_x \approx 20\,m, \beta_y \approx 11\,m, \alpha_x < 0, \alpha_y > 0,$). The hall to accommodate the experiment would be located on a free area behind the buildings of the University of Hamburg. Most of the experimental area will be below surface, facilitating radiation shielding. The length of the beamline can be between 70 m and 170 m.

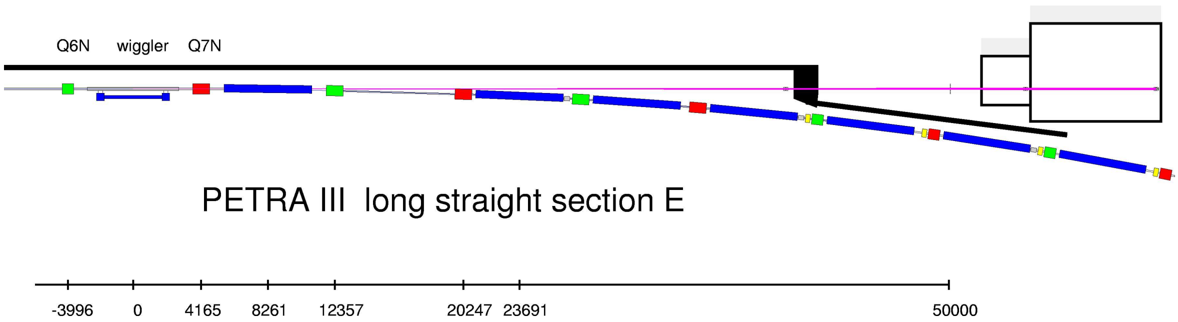

Figure 10.1.1: Sketch of the downstream part of the straight section east.

10.2 Additional 20 m IDs

The symmetry of PETRA offers two more straight sections equivalent to the short straight NE where the 20 m ID will be installed. Potentially another two long IDs could be placed in the ring at these locations in the SW and SE. The corresponding straight in the SE hosts the injection area, and moreover this part of the ring tunnel is below ground, making the construction of a beamline rather involved. In the SW and NW, however, additional experimental halls could be built (see Fig. 2.2.1). The properties of the radiation emitted by these devices are equal to the planned ID in the NE (Sec. 4.1.8) unless other optimization criteria should be used for the design of the ID. A very coarse estimate on the investment required for the installation of a beamline results in 6.5 million Euro including ID and infrastructure.

10.3 Bending Magnet Beamlines

The flux and brilliance of the PETRA III bending magnets has already been discussed in Sec. 4.3. Since the angle between neighboring insertion device beams at PETRA III will be only 5° it is hardly possible to use the radiation from bending magnets in a systematic way as it is the case at ESRF, for example.

In order to make more efficient use of the available straight sections the scheme of canted undulators (Sec.2.2.1, 6) has been proposed for PETRA III. In these cases two experimental stations will use photon beams with an angular difference of 5 mrad. In a similar way

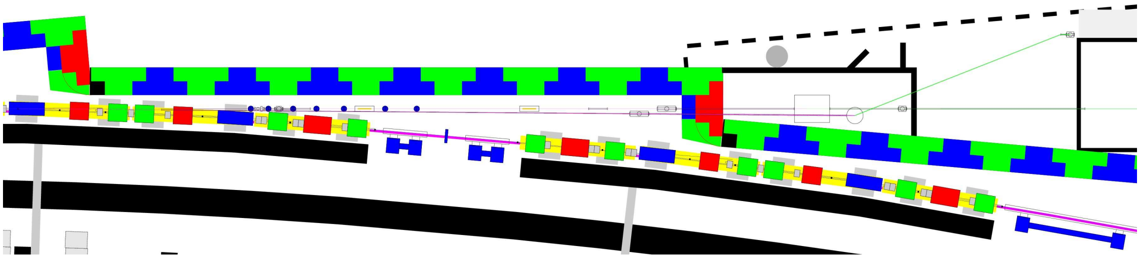

Figure 10.3.1: Scheme for the use of bending magnet radiation in horizontal direction. The center of the bending magnet beam is indicated in pink color below the undulator beam pipe. A monochromator vessel is indicated in the optics hutch. A diffracted beam is shown for 20 keV photon energy using a Si (1 1 3) monochromator crystal.

one could consider for a future upgrade to use the radiation of the bending magnet downstream of the undulator in those straight sections where only one insertion device is located. The angular separation of the two beams could be about 8 mrad which is sufficient to install separate safety systems and optics which is mandatory for an independent operation of the undulator and the bending magnet beamline. However, such a scheme will impose some space restrictions on each beamline which will be less severe if the undulator station needs a large source to sample distance and if it does not require bulky optics components in the vicinity of a possible bending magnet station.

In Figs. 10.3.1 and 10.3.2, a horizontal and a vertical scheme, respectively, are shown for the use of the bending magnet radiation. The vertical scheme has the advantage that the reflectivity of the monochromator is not affected by the polarization of the synchrotron radiation. The advantage of the horizontal scheme is that eventually larger separations from the beam pipe of the undulator can be achieved, thus providing sufficient space for larger endstation equipment at the bending magnet station. An angle of 8 mrad between the undulator and the center of a possible bending magnet beam results in 32 cm separation between both beams in 40 m distance (7 m behind the shielding wall) from the undulator source. If we assume, for example, that the translation of a Si (1 1 1) double crystal monochromator with 30 cm beam offset needs to be about 1 m long for an accessible energy range from 8–25 keV, then more than 40 cm space is available to the beam pipe of the neighboring station. This is sufficient

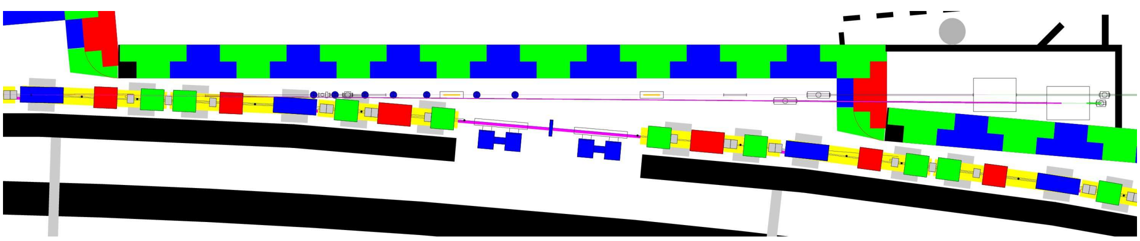

Figure 10.3.2: Scheme for the use of bending magnet radiation in the vertical direction. The center of the bending magnet beam is indicated in pink color below the undulator beam pipe.

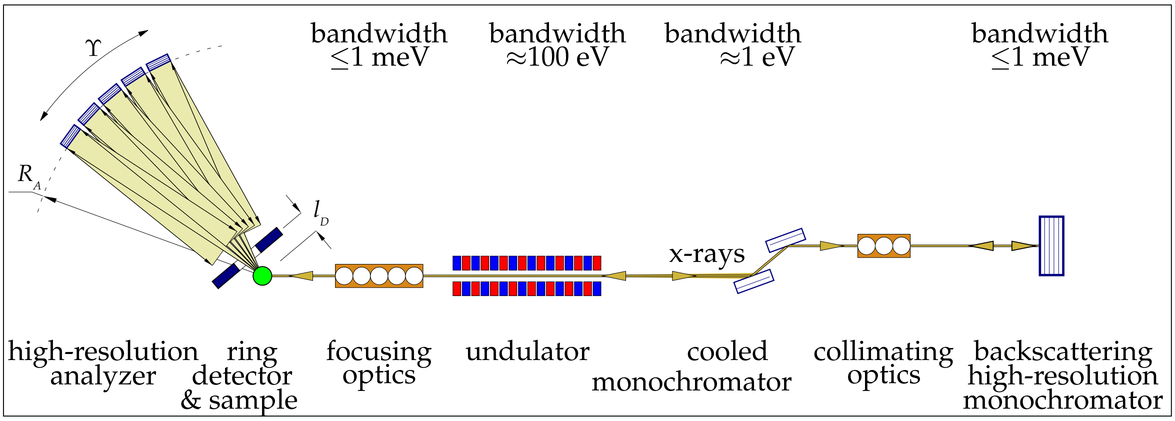

Figure 10.4.1: Layout of an exact backscattering beamline with the high-photon-energy inelastic x-ray scattering spectrometer. The main components are the high energy-resolution backscattering monochromator and the analyzer, a two-dimensional array of flat backscattering analyzer crystals mounted on a surface with spherical shape of a radius $R_{\mathrm{A}} \simeq 5 - 15$ m. The *exact backscattering* version of the analyzer in combination with the ring detector is shown. Parameters of the optical elements of the spectrometer optimized for the desired spectral resolution, such as Miller indices of Bragg back-reflections, photon energy, radius of the sphere R_{A}, size of the flat crystal elements, detector-sample distance l_{D}, etc., are given in Shvyd'ko, 2003.

for quite a number of experimental techniques that do not need large sample environments or surrounding equipment.

10.4 Exact Backscattering Beamline

Experiments requiring very high energy resolution suffer most from low count rates. A new ansatz to improve the performance of high energy-resolution beamlines like IXS or NRS has recently been installed at the APS, Argonne National Lab. The idea is to use exact backscattering from a monochromator crystal and reflect the beam back through the undulator. The experiment is then set up on the upstream side of the insertion device.

This set up can be ideally combined with the backscattering analyzer proposed by Shvyd'ko, 2003. The backscattering beamline could use either a 20 m long undulator in the short straight section or one of the first straight sections in the new arc. The experimental hutch would in the latter case be located between the new experimental hall and the existing hall 47. The big advantage of exact backscattering is that the energy resolution is decoupled from the beam divergence. This fact is extensively used in neutron spectrometers (for example IN10, IN13 and IN16 at ILL, Grenoble). This allows a much higher throughput of the optics. Moreover one reflection is sufficient to monochromatize the beam and the sample environment is not disturbed by a white beam transfer line as in a conventional backscattering set up.

Appendix A

Supplementary Material

A.1 Additional Material: EMBL Structural Biology Proposal

A.1.1 Beamline parameters for the structural biology stations

For the MX beamlines, the high beta section 2 m undulators were considered as a source of radiation. The following parameters were used for calculations: PETRA III U(2m): 6 GeV, ϵ = 1 nmrad, κ = 1%, β_x = 20 m, β_y = 2.38 m, K$_{max}$ = 2.2, 100 mA, 29 mm period.

Size x [mm]	Size y [mm]	Divergence x [μrad]	Divergence y [μrad]
0.1407	0.0052	8.97	5.93

Table A.1.1: Source beam parameters in RMS values (K = 0.66).

Detector type	Size	Readout time	Costs	Comments
Modular 3x3 CCD	315 x 315 mm^2 (ADSC)	a few sec	high	reliable
Flat panel	420 x 320 mm^2 (MAR)	1 sec	moderate	not yet proven
CsI scintillator and amorphous Si	410x 410 mm^2 (GeE Medical Systems)	25 msec	moderate	being tested
Pixel detector	400 x 400 mm^2	a few msec	high	not yet used

Table A.1.2: Overview of possible X-ray detectors to be installed on MX end-stations.

Optics, vacuum components and support equipment	2.2
X-ray detectors	1.9
End-stations and sample environment	1.0
Computer support and networking	0.6
Personnel	3.2
Infrastructure	0.6
Total	**9.5**

Table A.1.3: Estimated resource requirements (in M€) for the construction of three EMBL MX beamlines at the PETRA ring.

A.1.2 Ray-tracing parameters for the BioSAXS beamlines

Position, cm / y mode of z operation x	3700–3710, 0–2.0 0	3800–3837, 0–2.0 0	4000, 2 0	4320, 0, 0	4500, -1.1, 0	7300, -18.7, 17.6
Double crystal-monochromator $\Delta\lambda/\lambda$=10^{-4}	DCM ~5–29° Si 111 2×2 cm^2	-	VFM1 0.18° Si/Rh 4×35 cm^2 r=11.5 km	-	HFM 0.18° Si/Rh 4×50 cm^2 r=11.0 km	F
Multilayers $\Delta\lambda/\lambda$=1.5×10^{-2}	-	MLM 1.55° Mo/C 4×6 cm^2 d=2.97 nm 100 pairs	VFM1 0.18° Si(Si/Rh) 4×35 cm^2 r=11.5 km	-	HFM 0.18° Si(Si/Rh) 4×50 cm^2 r=11.0 km	F
Pink beam $\Delta\lambda/\lambda$=2.0×10^{-2}	-	-	-	VFM2 0.18° Si 4×35 cm^2 r=11.2 km	HFM 0.18° Si(Si/Rh) 4×50 cm^2 r=11.0 km	F

Table A.1.5: Materials, positions and orientations of optical elements of the BioSAXS beamline used for SHADOW simulations. Specifications for mirrors: type, grazing angle, material, size, radius of curvature. Monochromators: type, grazing angle, material, size, period (for ML only) and number of pairs (for ML only).

Bibliography

Abbamonte, P., Venema, L., Rusydi, A., Sawatzky, G. A., Logvenov, G. & Bozovic, I. (2002). *Science* **297**, 581.

Abola, E., Kuhn, P., Earnest, T. & Stevens, R. C. (2000). *Nat. Struct. Biol* **7**, 973–977.

Adachi, S., Park, S. Y., Tame, J., Shiro, Y. & Shibayama, N. (2003). *Proc. Natl. Acad. Sci. USA* **100**, 7039–7044.

Akimov, I. A., Sirenko, A. A., Clark, A. M., Hao, J.-H. & Xi, X. X. (2000). *Phys. Rev. Lett.* **84**, 4625.

Akiyama, S., Takahashi, S., Kimura, T., Ishimori, K., Morishima, I., Nishikawa, Y. & Fujisawa, T. (2002). *Proc. Natl. Acad. Sci. USA* **99**, 1329–1334.

Alexe, M., Gruverman, A., Harnagea, C., Zakharov, N. D., Pignolet, A. & Hesse, D. (1999). *Appl. Phys. Lett.* **75**, 1158.

Alferov, D. F., Bashmakov, Y. & Bessonov, E. G. (1974). *Sov. Phys. Tech. Phys.* **18**, 1336.

Allen, A., Andreani, C., Hutchings, M. T. & Windsor, C. G. (1981). *NDT Int.* **14**, 249–254.

Aloy, P., Ciccarelli, F., Leutwein, C., Gavin, A., Superti-Furga, G., Bork, P., Bottcher, B. & Russell, R. (2002). *EMBO Rep.* **3**, 628–635.

Andersen, E. K., Andersen, I. G. K., Norby, P. & Hanson, J. C. (1998). *J. Solid State Chem.* **141**, 235–240.

Anderson, A. J., Mayanovic, R. A. & Bajt, S. (1995). *Canad. Mineral.* **33**, 499–508.

Antonangeli, D. (2004). Dissertation, ESRF. in preparation.

Arnesano, F., Banci, L., Bertini, I., Mangani, S. & Thompsett, A. (2003). *Proc. Natl. Acad. Sci. USA* pages 3814 – 3819.

Asone, I., Meyer-Klaucke, W. & Murphy, L. (2003). *J. Synchrotron Rad.* **10**, 16–22.

Assmann, R., Raimondi, P., Roy, G. & Wenninger, J. (2000). Proceedings of the 7th European Particle Accelerator Conference (EPAC 2000), Vienna, Austria.

Asthalter, T., Sergueev, I., Franz, H., Rüffer, R., Petry, W., Messel, K., Härter, P. & Huwe, A. (2001). *Eur. Phys. J. B* **22**, 301–306.

Astuto, M. D., Mang, P. K., Giura, P., Shukla, A., Ghigna, P., Mirone, A., Braden, M., Greven, M., Krisch, M. & Sette, F. (2002). *Phys. Rev. Lett.* **88**, 167002.

Baehtz, C., Buhrmester, T., Bramnik, N. N., Nikolowski, K., Ehrenberg, H. & Fuess, H. (2004). submitted.

Bahrdt, J., Frentrup, W., Gaupp, A., Scheer, M., Gudat, W., Ingold, G. & Sasaki, S. (2001a). *Nucl. Instr. Methods Phys. Res. A* **467-468**, 21–29.

Bahrdt, J., Frentrup, W., Gaupp, A., Scheer, M., Gudat, W., Ingold, G. & Sasaki, S. (2001b). *Nucl. Instr. Methods Phys. Res. A* **467-468**, 130–133.

Bahrdt, J. & Wüstefeld, G. (1990). A new tracking routine for particles in undulator and wiggler fields. Technical report. BESSY Internal Report TB 90-158.

Bains, J. S. & Shaw, C. A. (1997). *Brain Res. Rev.* **25**, 335–358.

Bak, P. (1985). *Phys. Rev. B* **32**, 5764.

Balewski, K., Ehrlichmann, H., Kouptsidis, J. & Wittenburg, K. (1996). Proceedings of the 5th European Particle Accelerator Conference (EPAC 1996), Barcelona, Spain, p. 2667-2669.

Banci, L., Bertini, I., Conte, R. D., Mangani, S. & Meyer-Klaucke, W. (2003). *Biochemistry* **42**, 2467–2474.

Baraldi, A., Comelli, G., Lizzit, S., Kiskinova, M. & Paolucci, G. (2003). *Surf. Sci. Rep.* **49**, 169.

Barbi, V., Funari, S., Gehrke, R., Scharnagl, N. & Stribeck, N. (2003a). *Polymer* **44**, 4853.

Barbi, V., Funari, S., Gehrke, R., Scharnagl, N. & Stribeck, N. (2003b). *Macromolecules* **36**, 749.

Barla, A., Sanchez, J., Haga, Y., Lapertot, G., Doyle, B., Leupold, O., Rüffer, R., Abd-Elmeguid, M., Lengsdorf, R. & Flouquet, J. (2004). *Phys. Rev. Lett.* 92, 066401.

Barla, A., Sanchez, J., Ni, B., Boyle, B., Vulliet, P., Leupold, O., Rüffer, R., Kaczorowski, D., Plessel, J. & Abd-Elmeguid, M. (2002). *Phys. Rev. B* **66**, 094425.

Baron, A. Q. R., Chumakov, A. I., Grünsteudel, H. F., Grünsteudel, H., Niesen, L. & Rüffer, R. (1996). *Phys. Rev. Lett.* **77**, 4808.

Baron, A. Q. R., Franz, H., Meyer, A., Rüffer, R., Chumakov, A. I., Burkel, E. & Petry, W. (1997). *Phys. Rev. Lett.* **79**, 2823.

Baron, A. Q. R., Tanaka, Y., Miwa, D., Ishikawa, D., Miwa, D., Yabashi, M. & Ishikawa, T. (2001a). *J. Synchrotron Rad.* **8**, 1127.

Baron, A. Q. R., Tanaka, Y., Miwa, D., Ishikawa, D., Mochizuki, T., Takeshita, K., Goto, S., Matsushita, T., Kimura, H., Yamamoto, F. & Ishikawa, T. (2001b). *Nucl. Instrum. Methods Phys. Res. A* **467-468**, 627.

Barrett, C. J., Natansohn, A. L. & Rochon, P. L. (1996). *J. Phys. Chem.* 100, 8836.

Bassett, W., Anderson, A.J., Mayanovic, R. & Chou, I.-M. (2000). *Z. Kristall.* **215**, 711–717.

Batrakov, A., Jurba, V., Khrushchev, S., Kulipanov, G., Kuper, E., Kuzin, M., Medvedko, A., Mezentsev, N., Shkaruba, V., Zangrando, D., Diviacco, B. & Walker, R. P. (2002). *Proceedings of the 8th European Particle Accelerator Conference (EPAC 2002), Paris, France* page 2634.

Beach, G., Berkowitz, A., Parker, F. & Smith, D. (2001). *Appl. Phys. Lett.* **79**, 224.

Becker, U. & Shirley, D. A. (1996). *VUV and Soft X-ray Photoionization* Plenum Press (New York).

Beckmann, F., Bonse, U., Busch, F. & Günnewig, O. (1997). *J. Comput. Assist. Tomogr.* **21**, 539–553.

Beckmann, F., Heise, K., Kölsch, B., Bonse, U., Rajewsky, M. F., Bartscher, M. & Biermann, T. (1999). *Biophys. J.* **76**, 98–102.

Beckmann, F., Lippmann, T., Metge, J., Dose, T., Donath, T., Tischer, M., Liss, K.-D. & Schreyer, A. (2003). HARWI-II, The New High-Energy Beamline for Materials Science at HASYLAB / DESY. *Proceedings of the 8th International Conference on Synchrotron Radiation Instrumentation (SRI'03)*, San Francisco, USA.

Bengtzelius, U., Götze, W. & Sjölander, A. (1984). *J. Phys. C* **17**, 5915.

Bentley, J. & Stewart, R. F. (1974). *Acta Cryst.* **A30**, 60–67.

Berar, J., Blanquart, L., Boudet, N., Breugnon, P., Caillot, B., Clemens, J.-C., Delpierre, P., Koudobine, I., Mouget, C., Potheau, R. & Valin, I. (2002). *J. Appl. Cryst.* **35**, 471–476.

Berger, D., Weihreter, E., Mezentsev, N. & Shkaruba, V. (2002). *Proceedings of the 8th European Particle Accelerator Conference (EPAC 2002), Paris, France* page 2595.

Bergmann, U., Horne, C. R., Collins, T. J. & Cramer, S. P. (1999). *Chem. Phys. Lett.* **302**, 119–124.

Bergström, O., Gustafsson, T. & Thomas, J. O. (1998). *J. Appl. Cryst.* **31**, 103–105.

Berkvens, P. et al. (2002). Injection with front ends open at the ESRF. *2nd International Workshop on Radiation Safety at Synchrotron Radiation Sources*, Grenoble.

Bernstein, F., Koetzle, T., Williams, G., Meyer Jr., E., Brice, M., Rodgers, J., Kennard, O., Shimanouchi, T. & Tasumi, T. (1977). *J. Mol. Biol.* **112**, 535–542.

Bethe, H. A. & Salpeter, E. E. (1957). *Quantum Mechanics of One and Two Electron Atoms*. Springer, Berlin.

Bilderback, D. H., Freund, A. K., Knapp, G. S. & Mills, D. M. (2000). *J. Synchrotron Rad.* **7**, 53–60.

Billy, J. C., Bojon, J. P., Gröbner, O., Hilleret, N., Jimenez, M., Laugier, I. & Strubin, P. (2000). The lep vacuum system: A summary of 10 years of operation. *Proceedings of the 7th European Particle Accelerator Conference (EPAC 2000), Vienna, Austria*, pages 2286–2288.

Bilodeau, R., Ackerman, G., Aguilar, A., Bozek, J., Turri, G. & Berrah, N. (2003). *ICPEAC 2003 Stockholm*.

Bimberg, D., Grundmann, M. & Ledentsov, N. N. (1999). *Quantum dot heterostructures*. Chichester, New York: Wiley.

Binder, K. (1983). *in : Domb, C., Lebowitz, J. L. (Eds.), Phase Transitions and Critical Phenomena*. London: Academic Press.

Birgenau, R. J. & Kastner, M. A. (2000). *Science* **288**, 437.

Björneholm, O., Bässler, M., Ausmees, A., Hjelte, I., Feifel, R., Wang, H., Miron, C., Piancastelli, M., Svensson, S., Sorensen, S., Gel'mukhanov, F. & Agren, H. (2000). *Phys. Rev. Lett.* **84**, 2826.

Blair, G., Kamps, T., Poirier, F., Balewski, K., Honkavaara, K., Schlarb, H., Schmueser, P., Schreiber, S., Walker, N., Wendt, M., Wittenburg, K., Frisch, J., Ross, M., Ross, I. & Sertore, D. (2001a). Compton scattering techniques for the measurement of the transverse beam size of particle beams at future linear colliders. *Proc. of 21st ICFA Beam Dynamics Workshop on Laser-Beam Interactions*, Stony Brook USA.

Blair, G. A., Poirier, F., Kamps, T., Balewski, K., Sertore, D. & Wittenburg, K. (2001b). Simulation studies and background measurements for a laser based beam size monitor for the future linear collider. *Proc. of PAC2001*.

Blume, H., Bösecke, P., Bourenkov, G. P., Kosciesza, D. & Bartunik, H. D. (2001). *Nucl. Instr. Methods Phys. Res. A* **467–468**, 1358–1362.

Blume, M. (1985). *J. Appl. Phys.* **57**, 3615.

Bochtler, M., Hartmann, C., Song, H., Bourenkov, G. P., Bartunik, H. D. & Huber, R. (2000). *Nature (London)* **403**, 800–805.

Bohic, S., Simionovici, A., Ortega, R., Heymann, D., Schroer, C. & Snigirev, A. (2001). *Nucl. Instr. Methods Phys. Res. A* **181**, 728–733.

Bonse, U. & Busch, F. (1996). *Prog. Biophys. Molec. Biol.* **65**, 133–169.

Bonse, U., Busch, F., Günnewig, O., Beckmann, F., Pahl, R., Delling, G., Hahn, M. & Graeff, W. (1994). *Bone and Mineral* **25**, 25–38.

Borland, M. & Emery, L. (1999). Tracking studies of top-up safety for the Advanced Photon Source. *PAC 99*, volume 4 of *Particle Accelerator*, pages 2319–2321, New York.

Borowski, M., Bowron, D. T. & Panfilis de, S. (1999). *J. Synchrotron Rad.* **6**, 179.

Bota, A., Goerigk, G., Drucker, T., Haubold, H.-G. & Petro, J. (2002). *J. Catalysis* **205**, 354–357.

Bourgeois, D., Vallone, B., Schotte, F., Arcovito, A., Miele, A., Sciara, G., Wulff, M., Anfinrud, P. & Brunori, M. (2003). *Proc. Natl. Acad. Sci. USA* . **100**, 8704–8709.

Bourke, M. A. M., Dunand, D. C. & Ustundag, E. (2002). *Appl. Phys. A* **74**, S1707–S1709.

Braun, A., Shrout, S., Fowlks, A. C., Osaisai, B. A., Seifert, S., Granlund, E. & Cairns, E. J. (2003). *J. Synchrotron Rad.* **10**, 320–325.

Bravin, A. (2003). *J. Phys. D: Appl. Phys* **36**, A24–A29.

Brenker, F. E., Vincze, L., Vekemans, B., Nasdala, L., Stachel, T., Kersten, M., Drakopoulos, M., Vollmer, C., Adams, F., Joswig, W. & Harris, J. W. (2003). *Nature (London)* submitted.

Brinkmann, R. & Rossbach, J. (1994). *Nucl. Instrum. Methods Phys. Res. A* **350**, 8–12.

Brookes, N. B. (2003). private communication.

Brookes, N. B., Sinkovic, B., Tjeng, L., Goedkoop, J. B., Hesper, R., Pellegrin, E., Groot de, F. M. F., Altieri, S., Hulbert, S., Shekel, E. & Sawatzky, G. (1998). *J. Elect. Spec. Rel. Phen.* **92**, 11–18.

Brückel, T., Lippert, M., Bouchard, R., Schmidt, T., Schneider, J. R. & Jauch, W. (1993). *Acta Cryst. A* **49**, 679.

Buchanan, S. (2002). *Curr. Opin. Drug Discov. Devel.* **5**, 367–381.

Buffet, B. & Wenk, H. (2001). *Nature (London)* **413**, 60.

Bulfone, D. et al. (2002). The ELETTRA digital multi-bunch feedback systems. *Proceedings of the 8th European Particle Accelerator Conference (EPAC 2002)*, volume 2, pages 2061–2063, Paris.

Bunge, H. J., Wcislak, L., Klein, H., Garbe, U. & Schneider, J. R. (2003). *J. Appl. Cryst.* **36**, 1240.

Bunk, O., Nielsen, M. M., Sölling, T. I., Craats van de, A. M. & Stutzmann, N. (2003). *J. Am. Chem. Soc.* **125**, 2252–2258.

Burandt, B., Press, W. & Haussühl, S. (1993). *Phys. Rev. Lett.* **71**, 1188.

Burger, S., Carli, C., Priestnall, K. & Raich, U. (2003). The ps booster fast wire scanner. Technical report, CERN.

Burkel, E. (2000). *Rep. Prog. Phys.* **63**, 171.

Burkhard, P., Kammerer, R. A., Steinmetz, M. O., Bourenkov, G. P. & Aebi, U. (2000). *Structure* **8**, 223–230.

Burley, S. & Bonanno, J. (2002). *Curr. Opin. Struct. Biol* **12**, 383–391.

Bush, A. I. (2000). *Curr. Opin. Chem. Biol.* **4**, 184–191.

Caciuffo, R., Paolasini, L., Sollier, A., Ghigna, P., Pavarini, E., Brink van den, J. & Altarelli, M. (2002). *Phys. Rev. B* **65**, 174425.

Camas, J., Crockford, G., Ferioli, G., Fischer, C., Gras, J. J., Jung, R., Koopman, J. & Mann, J. (1993). Resolution measurements of lepton beam transverse distributions with the lep wire scanners. *Proceedings of the 1993 Particle Accelerator Conference (PAC 93)*, pages 2504–2506, Washington, DC. IEEE.

Campbell, C. T., Daube, K. A. & White, J. M. (1987). *Surf. Sci.* **182**, 458–476.

Carra, P., Thole, B. T., Altarelli, M. & Wang, X. (1993). *Phys. Rev. Lett.* **70**, 694.

Carrington, P., Chivers, P., Al-Mjeni, F., Sauer, R. & Maroney, M. (2003). *Nature Struct. Biol.* **10**, 126–130.

Carwardine, L. et al. (1997). Presented at IEEE Particle Accelerator Conference (PAC1997), Vancouver, Canada, 12-16 May 1997.

Casarin, K. et al. (2002). Injection and FEL Lasing with Front End Open at ELETTRA. priv. communication.

Cassarino, D. S. & Bennett, J. P. (1999). *Brain Res. Rev.* **29**, 1–25.

Castelnau, O., Drakopoulos, M., Schroer, C., Snigireva, I., Snigirev, A. & Ungar, T. (2001). *Nucl. Instr. Methods Phys. Res. A* **467**, 1245–1248.

Castleton, C. & Altarelli, M. (2000). *Phys. Rev. B* **62**, 1033.

Chakarian, V. et al. (1996). *Synchrotron Radiation Techniques in Industrial, Chemical and Material Science*. New York: Plenum Press.

Chavanne, J., Elleaume, P. & Vaerenbergh, P. V. (1998). A novel fast switching linear/helical undulator. *Proceedings of the 6th EPA*, pages 317–319, Stockholm, Sweden.

Chavanne, J., Elleaume, P. & Vaerenbergh van, P. (1998). *Proceedings of the 6th European Particle Accelerator Conference (EPAC 1998), Stockholm, Sweden* page 2213.

Chavanne, J., Elleaume, P. & Vaerenbergh van, P. (2000). *Proceedings of the 7th European Particle Accelerator Conference (EPAC 2000), Vienna, Austria* page 2346.

Chavanne, J., Plan, B., Penel, C. & Vaerenbergh van, P. (2002). *Proceedings of the 8th European Particle Accelerator Conference (EPAC 2002), Paris, France* page 2604.

Chen, C. T., Idzerda, Y. U., Lin, H.-J., Smith, N. V., Meigs, G., Chaban, E., Ho, G. H., Pellegrin, E. & Sette, F. (1995). *Phys. Rev. Lett.* **75**, 152.

Chen, C. T., Sette, F., Ma, Y. & Modesti, S. (1990). *Phys. Rev. B* **42**, 7262.

Chouhan, S., Rossmanith, R., Strohmer, S., Doelling, D., Geisler, A., Hobl, A. & Kubsky, S. (2003). *Proceedings of the PAC 2003, Portland, USA*.

Chubar, O. & Elleaume, P. (1998). And efficient computation of synchrotron radiation in the near field region. *Proceedings of the 6th European Particle Accelerator Conference (EPAC 1998)*, pages 1177–1179.

Chubar, O., Snigirev, A., Kuznetsov, S., Weitkamp, T. & Kohn, V. (2001). X-ray interference methods of electron beam diagnostics. *Proceedings of the 5th European Workshop on Diagnostics and Beam Instrumentation (DIPAC 2001)*, Grenoble. ESRF.

Chumakov, A. I., Metge, J., Baron, A. Q. R., Grünsteudel, H., Rüffer, R. & Ishikawa, T. (1996). *Nucl. Instrum. Methods Phys. Res. A* **383**, 642.

Chupas, P. J., Ciralo, M. F., Hanson, J. C. & Grey, C. P. (2001). *J. Am. Chem. Soc.* **123**, 1694–1702.

Cirlin, G. E., Talalaev, V. G., Zakharov, N. D., Egorov, V. A. & Werner, P. (2002). *phys. stat. sol (b)* **232**, R1–3.

Clausen, B., Grabaek, L., Steffensen, G., Hansen, P. & Topsøe, H. (1993). *Catal. Lett.* **20**, 23.

Clausen, B., Topsøe, H. & Frahm, R. (1998). *Adv. in Catal.* **42**, 315.

Cloetens, P., Barrett, R., Baruchel, J., Guigay, J.-P. & Schlenker, M. (1996). *J. Phys. D* **29**, 133–146.

Cloetens, P., Ludwig, W., Baruchel, J., Dyck, D. V., Landuyt, J. V., Guigay, J. P. & Schlenker, M. (1999). *Appl. Phys. Lett.* **75**, 2912–2914.

Coindreau, O., Vignoles, G. & Cloetens, P. (2003). *Nucl. Instr. and Methods Phys. Res. B* **200**, 308–314.

Cole, R. J., Macdonald, B. F. & Weightman, P. (2002). *J. Electron Spec. Rel. Phenom.* **125**, 147–152.

Coppens, P. (1997). *X–ray charge densities and chemical bonding*. Oxford Science Publications.

Corredoura, P. (1999). Architecture and performance of the PEP-II low-level RF system. *SLAC-PUB-8124, March 1999*.

Craats van de, A., Stutzmann, N., Bunk, O., Nielsen, M., Watson, M., Müllen, K., Chanzy, H., Sirringhaus, H. & Friend, R. (2003). *Adv. Mater.* **15**, 495–499.

Cras, F. L., Anne, M., Bloch, D. & Strobel, P. (1998). *Solid State Ionics* **106**, 1–10.

Creager, K. C. (1997). *Science* **278**, 1284.

Dallera, C. et al. (2003). *Appl. Phys. Lett.* submitted.

Danger, J., LeFevre, P., Magnan, H., Chandesris, D., Bourgeois, S., Jupille, J., Eickhoff, T. & Drube, W. (2002). *Phys. Rev. Lett.* **88**, 243001.

Danneau, R., Ayari, A., Rideau, D., Requardt, H., Lorenzo, J. E., Ortega, L., Monceau, P., Currat, R. & Grübel, G. (2002). *Phys. Rev. Lett.* **89**, 106404.

Das, R., Mills, T. T., Kwok, L. W., Maskel, G. S., Millett, I. S., Doniach, S., Finkelstein, K. D., Herschlag, D. & Pollack, L. (2003). *Phys Rev Lett.* **90**, 188103.

Dau, H. & Haumann, M. (2003). *J. Synchrotron Rad* **10**, 76–85.

Dau, H., Liebisch, P. & Haumann, M. (2003). *Anal. Bioanal. Chem.* **376**, 562–583.

Dauter, Z. & Dauter, M. (2001). *Structure* **7**, R21–R26.

Dauter, Z., Lamzin, V. & Wilson, K. (1997). *Curr. Opin. Struct. Biol* **7**, 681–688.

David, W. I. F. (2003). Structure determination from powders - crossing the 100-atom threshold. *Proccedings of European Crystallographic Meeting*, Durban, South Africa.

David, W. I. F., Shankland, K., McCusker, L. B. & Baerlocher, C. (2002). *Structure determination from powder diffraction data*. Number 13 in IUCr Monographs on Crystallography. Oxford University Press.

De Caro, L., Tapfer, L. & Giuffrida, A. (1996). *Phys. Rev. B* **54**, 10575.

Decking, W., Flottmann, K. & Rossbach, J. (1990). Proceedings of the 2nd European Particle Accelerator Conference (EPAC 1990), Nice, France.

Dehler, M. (2002). Kicker design for the ELETTRA/SLS longitudinal multi-bunch feedback. *Proceedings of the 8th European Particle Accelerator Conference (EPAC 2002)*, volume 2, pages 2070–2072, Paris.

Dehler, M. et al. (1999). *Proc. of the 1999 Particle Accelerator Conference*, pages 2087–2089, New York, USA.

Delling, G., Hahn, M., Bonse, U., Busch, F., Günnewig, O., Beckmann, F., Uebbing, H. & Graeff, W. (1995). *Pathologe* **16**, 342–347.

Denecke, R., Kinne, M., Whelan, C. & Steinrück, H.-P. (2002). *Surf. Rev. Lett.* **9**, 797.

Dennis, C. & Campbell, P. (2003). *Nature (London)* **421**, 396.

D'Haese, P., Behets, G., Bervoets, A., Oste, L., Broe, M. D., Verberckmoes, S., Janssens, K., Somogyi, A. & Drakopoulos, M. (2002). *ESRF Experimental Report* LS 2137.

D'Haese, P., Behets, G., Verberckmoes, S., Bervoets, A., Debroe, M., Janssens, K. & Salomé, M. (2001). *ESRF Experimental Report* LS1709.

D'Haese, P. C., Schrooten, I., Goodman, W. G., Cabrera, W. E., Lamberts, L. V., Elseviers, M. M., Couttenye, M. M. & Broe, M. E. D. (2000). *Kidney Int.* **57**, 1107–1114.

Diehl, H. W. (1986). *Phase transitions and critical phenomena, Vol.10*. London: Academic Press.

Dierker, S. B., Pindak, R., Fleming, R. M., Robinson, I. K., & Berman, L. (1995). *Phys. Rev. Lett.* **75**, 449.

Dietrich, S. & Wagner, H. (1983). *Phys. Rev. Lett.* **51**, 1469.

Diviacco, B., Bracco, R., Millo, D., Walker, R. P., Zalateu, M. & Zangrando, D. (2000). *Proceedings of the 7th European Particle Accelerator Conference (EPAC 2000), Vienna, Austria* page 2322.

Dorner, B., Burkel, E., Illini, T. & Peisl, J. (1987). *Z. Phys. B* **69**, 179.

Dorner, B., Burkel, E. & Peisl, J. (1986). *Nucl. Instrum. Methods Phys. Res. A* **246**, 450.

Dreele von, R. B. (2003). volume 368, chapter Protein crystal structure analysis from high-resolution X-ray powder-diffraction data Macromolecular, pages 254–267. New York: Academic Press.

Drube, W., Grehk, T. M., Treusch, R., Materlik, G., Hansen, J. E. & Åberg, T. (1999). *Phys. Rev. B* **60**, 15507–15510.

Drube, W., Treusch, R. & Materlik, G. (1995). *Phys. Rev. Lett.* **74**, 42.

Dürr, H., Dudzik, E., Dhesi, S. S., Goedkoop, J. B., Laan van der, G., Belakhovsky, M., Mocuta, C., Marty, A. & Samson, Y. (1999). *Science* **284**, 2166.

Dykes, D. M., McIntosh, P. A., Poole, M. W. & Suller, V. P. (2000). Superconducting RF systems for light sources ? *Proceedings of the 7th European Particle Accelerator Conference (EPAC 2000), Vienna, Austria*.

Ebert, M. (2000). Automatic phasing of the HERA RF systems. *Proceedings of the CW-RF Users Group Meeting*. Argonne National Laboratory, 1.-3. March 2000.

Ebert, M. et al. (1991). DESY Internal Report 91-036.

Edmonds, K. W., Binns, C., Baker, S. H., Thornton, S. C., Goedkoop, C. N. J. B., Finazzi, M. & Brookes, N. B. (1999). *Phys. Rev. B* **60**, 472.

Egelstaff, P. A. (1983). *Adv. Chem. Phys.* **53**, 1.

Ehrlichmann, H. & Bialowons, W. (2003). DESY Internal Report M-03-04.

Eickhoff, T., Medicherla, V. & Drube, W. (2004). *J. Electron Spec. Rel. Phenom.* in press.

Einsle, O., Messerschmidt, A., Stach, P., Bourenkov, G., Bartunik, H., Huber, R. & Kroneck, P. (1999). *Nature (London)* **400**, 476–480.

Eisebitt, S., Lörgen, M., Eberhardt, W., Lüning, J., Stöhr, J., Rettner, C., Helwig, O., Fullerton, E. & Denbeaux, G. (2003). *Phys. Rev. B* **68**, 104419.

Elleaume, P. (1994). *J. Synchrotron Rad.* **1**, 19–26.

Elleaume, P. (2002). *ESRF Highlights 2002*.

Elleaume, P., Chavanne, J. & Faatz, B. (2000). *Nucl. Instr. Methods Phys. Res. A* **455**, 503–523.

Ellis, P., Cohen, A. & Soltis, S. (2003). *J. Synchrotron Rad.,* **10**, 287–288.

Emery, L. & Borland, M. (1999a). Analytical Studies of Top-Up Safety for the Advanced Photon Source. *PAC 99*, volume 4 of *Particle Accelerator*, pages 2939–2941, New York.

Emery, L. & Borland, M. (1999b). Top-Up Operation Experience at the Advanced Photon Source, booktitle = PAC 99. volume 1 of *Particle Accelerator*, pages 200–202, New York.

Fienup, J. (1982). *Appl. Opt.* **21**, 2748.

Fiori, F., Girardin, E., Giuliani, A., Lorentzen, T., Pyzalla, A., Rustichelli, F. & Stanic, V. (2000). *Physica B* **276–278**, 923–924.

Fiquet, G., Badro, J., Guyot, F., Requardt, H. & Krisch, M. (2001). *Science* **291**, 468.

Fischer, G. E. (1984). Invited talk given at 1984 Summer School on High Energy Particle Accelerators, Batavia, IL, Aug 13-24, 1984.

Fischer, P., Denbeaux, G., Stoll, H., Puzic, A., Raabe, J., Nolting, F., Eimüller, T. & Schütz, G. (2003). *J. de Physique IV* **104**, 471.

Fischer, P., Zeller, R., Schütz, G., Goerigk, G., Haubold, H.-G., Pruegl, K. & Bayreuther, G. (1998). *J. Appl. Phys.* **83**, 7088–7090.

Flechsig, U., Patthey, L. & Quitmann, C. (2001). *Nucl. Instr. Methods Phys. Res. A* **467**, 479–481.

Flynn, G. J., Keller, L. P., Wirick, S., Jacobsen, C. & Sutton, S. R. (2003). *J. Physique* **104**, 367–372.

Follath, R., Senf, F. & Gudat, W. (1998). *J. Synchrotron Rad.* **5**, 769.

Foster, A., Brown, G. E., Tingle, T. N. & Parks, G. (1998). *Am. Mineral.* **83**, 553–568.

Frahm, R. (1988). *Nucl. Instrum. Methods Phys. Res. A* **270**, 578.

Frahm, R. (1989a). *Rev. Sci. Instr.* **60**, 2315.

Frahm, R. (1989b). *Rev. Sci. Instrum.* **60**, 2515.

Franz, H., Seebach, M., Ehnes, A. & Werner, M. (2003). Parasitic bunch measurement in e+/e storage rings. *Proc. of DIPAC 2003*, Mainz. GSI.

Fratzl, P. (2003). *J. Appl. Cryst.* **36**, 397–404.

Freeland, J. W., Chakarian, V., Bussmann, K., Idzerda, Y. U., Wende, H. & Kao, C.-C. (1998). *J. Appl. Phys.* **83**, 6290–6292.

Frenken, J. W. M. & Veen van der, J. F. (1985). *Phys. Rev. Lett.* **54**, 134.

Frischholz, H. (2000). 10 years of operational experience with the LEP/RF high power system. *Proceedings of the CW-RF Users Group Meeting*. Argonne National Laboratory, 1.-3. March 2000.

Fritz, G., Roth, A., Schiffer, A., Buchert, T., Bourenkov, G., Bartunik, H., Huber, H., Stetter, K., Kroneck, P. & Ermler, U. (2002). *Proc. Natl. Acad. Sci. USA* **99**, 1836–1841.

Fujisawa, T., Inoue, K., Oka, T., Iwamoto, H., Uruga, T., Kumasaka, T., Inoko, Y., Yagi, N., Yamamoto, M. & Ueki, T. (2000). *J. Appl. Cryst.* **33**, 797–800.

Fukuda, T., Mizuki, J., Ikeuchi, K., Fujita, M., Yamada, K., Baron, A. Q. R., Tsutsui, S., Tanaka, Y. & Endoh, Y. (2003). *arXiv: cond-mat* **0306190**, v1.

Fultz, B., Ahn, C. C., Alp, E. E., Sturhahn, W. & Toellner, T. S. (1997). *Phys. Rev. Lett.* **79**, 937.

Funari, S., Barcelo, F. & Escriba, P. V. (2003). *J. Lipid. Res.* **44**, 567.

Garbe, S., Poulsen, H. F. & Juul Jensen, D. (1996). *Texture of materials. Proc. of the 11^{th} int. conf. on textures of materials. ICOTOM-11, Xi'an (CN), 16-20 Sep 1996* 1, 100–105.

Gavin, A., Bosche, M., Krause, R., Grandi, P., Marzioch, M., A., B., Schultz, J., Rick, J., Michon, A., Cruciat, C., Remor, M., Hofert, C., Schelder, M., Brajenovic, M., Ruffner, H., Merino, A., Klein, K., Hudak, M., Dickson, D., Rudi, T., Gnau, V., Bauch, A., Bastuck, S., Huhse, B., Leutwein, C., Heurtier, M., Copley, R., Edelmann, A., Querfurth, E., Rybin, V., Drewes, G., Raida, M., Bouwmeester, T., Bork, P., Seraphin, B., Kuster, B., Neubauer, G. & Superti-Furga, G. (2002). *Nature (London)* **415**, 141–147.

Geck, J., Bruns, D., Hess, C., Klingeler, R., Reutler, P., Zimmermann v., M., Cheong, S. W. & Büchner, B. (2002). *Phys. Rev. B* **66**, 184407.

Geissler, J., Goering, E., Justen, M., Weigand, F., , Schütz, G., Langer, J., Schmitz, D., Maletta, H. & Mattheis, R. (2002). *Phys. Rev. B* **65**, 020405(R).

Gel'mukhanov, F., Plashkevych, O. & Ågren, H. (2001). *J. Phys. B* **34**, 869.

Genzel, C. (1994). *Phys. Status Solidi A* **146**, 629–637.

Gerdau, E., Rüffer, R., Winkler, H., Tolksdorf, W., Klages, C. & Hannon, J. (1985). *Phys. Rev. Lett.* **54**, 835.

Gerke, H., Scholz, H. P., Sommerfeld, M. & Zolfaghari, A. (1977). The PETRA cavity (in German). *DESY Internal Report PET 77/08, August 1977.*

Geue, T., Saphiannikova, M. G., Henneberg, O. & Pietsch, U. (2003). *J. Appl. Phys.* **93**, 3161.

Ghigo, A. et al. (1996). Kickers and power amplifiers for the dafne bunch-by- bunch longitudinal feedback system. *Proceedings of the 6th European Particle Accelerator Conference (EPAC 1996).*

Gibbs, D., Harshman, D., Isaacs, E., McWhan, D., Mills, D. & Vettier, C. (1988). *Phys. Rev. Lett.* **61**, 1241.

Giefers, H., Lübbers, R., Rupprecht, K., Wortmann, G., Alf, D. & Chumakov, A. I. (2002). *High Pressure Research* **22**, 501.

Gilfrich, J. V., Huang, T. C., Hubbard, C. R., James, H. R., Jenkins, R., Lachance, G. R. & Smith, D. K. (1993). *Advances in X-ray Analysis*. Dordrecht, The Netherlands: Kluwer Academic/Plenum Publishers.

Gluehmann, M., Zarivach, R., Bashan, A., Harms, J., Schluenzen, F., Bartels, H., Agmon, I., Rosenblum, G., Pioletti, M., Auerbach, T., Avila, H., Hansen, H., Franceschi, F. & Yonath, A. (2001). *Methods* **25**, 292–302.

Gluskin, E. (1998). *J. Synchrotron Rad.* **5**, 189–195.

Gnäupel-Herold, T., Haeffner, D., Prask, H. & Matejicek, J. (2000). *Proc. ICRS6, IOM Communications Ltd., London (UK)* pages 751–758.

Goerigk, G., Gorke, H., Hartmann, R., Strüder, L., Hamann, D. & Zwoll, K. (2002). *HASY-LAB Annual report*.

Goerigk, G., Haubold, H. G., Lyon, O. & Simon, J. P. (2003). *J. Appl. Cryst.* **36**, 425–429.

Goerigk, G., Schweins, R., Huber, K. & Ballauff, M. (2004). *Europhys. Lett.* accepted.

Goerigk, G. & Williamson, D. L. (1998). *Solid State Commun.* **108**, 419.

Goerigk, G. & Williamson, D. L. (2001a). *J. Appl. Phys.* **90**, 5808–5811.

Goerigk, G. & Williamson, D. L. (2001b). *J. Non-Cryst. Solids* **281**, 181.

Golosio, B., Simionovici, A., Somogyi, A., Camerani, C. & Steenari, B. M. (2003). *J. de Physique IV* **104**, 647–650.

Golovchenko, J. A., Kincaid, B. M., Levesque, R. A., Meixner, A. E. & Kaplan, D. R. (1986). *Phys. Rev. Lett.* **57**, 202.

Gomis-Rüth, F., Maskos, K., Betz, M., Bergner, A., Huber, R., Suzuki, K., Yoshida, N., K. Brew amd, H. N., Bourenkov, G., Bartunik, H. & Bode, W. (1997). *Nature (London)* **389**, 77–81.

Graafsma, H., Souhassou, M., Puig-Molina, A., Harkema, S., Lecomte, C. & Kvick, A. (1998). *Acta Cryst. B* **54**, 193–195.

Greegor, R., Pingitore Jr., N. & Lytle, F. (1997). *Science* **275**, 1452–1454.

Grenzer, J., Darowski, N., Pietsch, U., Daniel, A., Reithmaier, J. P., Rennon, S. & Forchel, A. (2000). *Appl. Phys. Lett.* **77**, 4277.

Grenzer, J., Grigorian, S. A., Feranchuk, S., Pietsch, U., Zeimer, U., Fricke, J., Kissel, H., Knauer, A. & Weyers, M. (2004). *Phys. Rev. B* submitted.

Groll, M., Brandstetter, M., Bartunik, H., Bourenkow, G. & Huber, R. (2003). *J. Mol. Biol.* **327**, 75–83.

Groll, M., Ditzel, L., Löwe, J., Stock, D., Bochtler, M., Bartunik, H. & Huber, R. (1997). *Nature (London)* **386**, 463–471.

Groot de, F. (2001). *Chem. Rev.* **101**, 1779–1808.

Groot de, F. M. F., Krisch, M. H. & Vogel, J. (2002). *Phys. Rev. B* **66**, 195112.

Grübel, G., Abernathy, D., Riese, D., Vos, W. & Wegdam, G. (2000). *J. Appl. Cryst.* **33**, 424.

Grunwaldt, J.-D.and Lützenkirchen-Hecht, D., Richwin, M., Grundmann, S., Clausen, B. S. & Frahm, R. (2001). *J. Phys. Chem. B* **105**, 5161.

Grunwaldt, J.-D., Caravati, M., Ramin, M. & Baiker, A. (2003). *Catal. Lett.* in press.

Grunwaldt, J.-D. & Clausen, B. (2002). *Topics Catal.* **18**, 37.

Grunwaldt, J.-D., Molenbroek, A., Topsøe, N.-Y., Topsøe, H. & Clausen, B. (2000). *J. Catal.* **194**, 452.

Grunwaldt, J.-D., Wandeler, R. & Baiker, A. (2003). *Catal. Rev. - Sci. Eng* **45**, 1.

Guilleaume, B., Ballauff, M., Goerigk, G., Wittemann, M. & Rehahn, M. (2001). *Colloid Polym. Sci.* **279**, 829–835.

Guilleaume, B., Blaul, J., Ballauff, M., Wittemann, M., Rehahn, M. & Goerigk, G. (2002). *Eur. Phys. J. E* **8**, 299–309.

Gundlach, C., Pantleon, W., Lauridsen, E. M., Margulies, L., Doherty, R. D. & Poulsen, H. F. (2004). *Scripta Materialia* **50**, 477–481.

Guo, J. H., Luo, Y., Augustsson, A., Kashtanov, S., Rubensson, J. E., Shuh, D. K., Agren, H. & Nordgren, J. (2003). *Phys. Rev. Lett.* **91**, 157401.

Guo, J. H., Luo, Y., Augustsson, A., Rubensson, J. E., Sathe, C., Agren, H., Siegbahn, H. & Nordgren, J. (2002). *Phys. Rev. Lett.* **89**, 137402.

Gutt, C., Ghaderi, T., Chamard, V., Madsen, A., Seydel, T., Tolan, M., Sprung, M., Grübel, G. & Sinha, S. K. (2003). *Phys. Rev. Lett.* **91**, 076104.

Hagemeier, C., Shima, S., Thauer, R., Bourenkov, G., Bartunik, H. & Ermler, U. (2003). *J. Mol. Biol.* **332**, 1047–1057.

Hahn, U. (2003). HASYLAB vacuum guidelines for beamlines and experiments, www-hasylab.desy.de/services/vacuum/guides.htm. Technical report, HASYLAB at DESY.

Hahn, U., Brefeld, W., Hesse, M., Schneider, J. R., Schulte-Schrepping, H., Seebach, M. & Werner, M. (1998). *J. Synchrotron Rad.* **5**, 627–629.

Hahn, U. & Schulte-Schrepping, H. (2003). Crystal monochromator based emittance measurements at the PETRA undulator beam line. *Proceedings of the 8th International Conference on Synchrotron Radiation Instrumentation (SRI'03)*, San Francisco, USA.

Hajdu, J., Neutze, R., Sjogren, T., Edman, K., Szoke, A., Wilmouth, R. & Wilmot, C. (2000). *Nat. Struct. Biol.* **7**, 1006–1012.

Halbach, K. (1981). *Nucl. Instrum. Methods Phys. Res. A* **187**, 109–177.

Hämäläinen, K., Siddons, D. P., Hastings, J. B. & Berman, L. E. (1991). *Phys. Rev. Lett.* **67**, 2850–2853.

Hanan, J. C., Swift, G. A., Üstündag, E., Beyerlein, I. J., Almer, J. D., Lienert, U. & Haeffner, D. R. (2002). *Metall. Mater. Trans. A* **33**, 3839–3845.

Hannon, J. P., Trammell, G. T., Blume, M. & Gibbs, D. (1988). *Phys. Rev. Lett.* **61**, 1245.

Hansel, C. M., Fendorf, S., Sutton, S. & Newville, M. (2001). *Environ. Sci. Technol.* **35**, 3863.

Hansel, C. M., Laforce, M. K., Fendorf, S. & Sutton, S. (2002). *Environ. Sci. Technol.* **36**, 1988–1994.

Hansen, K. & Tröger, L. (2000). *IEEE Transactions on Nucl. Science* **47**, 2748–2757.

Hara, T., Tanaka, T., Tanabe, T., Marchal, X.-M., Okada, S. & Kitamura, H. (1998). *J. Synchrotron Rad.* **5**, 403–405.

Harata, K. & Kanai, R. (2002). *Proteins* **48**, 53–62.

Harding, M. M. (1996). *J. Synchrotron Rad.* **3**, 250–259.

Harkay, K. (2002). Proceedings of the 8th European Particle Accelerator Conference (EPAC 2002), Paris 2002, p. 1505-1507.

Harms, J., Schlünzen, F., Zarivach, R., Bashan, A., Gat, S., Agmon, I., Bartels, H., Franceschi, F. & Yonath, A. (2001). *Cell* **107**, 679–688.

Harms, J. M., Bartels, H., Schlünzen, F. & Yonath, A. (2003). *J. Cell Sci.* **116**, 1391–1393.

Harris, H., Pickering, I. & George, G. (2003). *Science* **301**, 1203.

Harrison, S. (2003). *Cell* **112**, 737–740.

Hartman, Y., Tarazona, E., Elleaume, P., Snigireva, I. & Snigirev, A. (1995). *Rev. Sci. Instrum.* **66**, 1978.

Hartog, P. D., Gagliano, J., Goeppner, G., Noonan, J., Trakhtenberg, E. & Wiemerslage, G. (2001). Vacuum system of the APS: Operation experience and status report. *Proceedings of the 2001 Particle Accelerator Conference*, pages 607–609.

Hasan, M., Isaacs, E., Shen, Z.-X., Miller, L., Tsutsui, K., Tohoyama, T. & Meakawa, S. (2000). *Science* **288**, 1811.

Hashimoto, S. & Sasaki, S. (1995). *Nucl. Instr. Methods Phys. Res. A* **361**, 611–622.

Haskel, D., Srajer, G., Choi, Y., Lee, D. R., Lang, J. C., Meersschaut, J., Jiang, J. S. & Bader, S. D. (2003). *Phys. Rev. B* **67**, 180406.

Haskel, D., Srajer, G., Lang, J. C., Pollmann, J., Nelson, C. S., Jiang, J. S. & D., B. S. (2001). *Phys. Rev. Lett.* **87**, 207201.

Hasnain, S. S. & Strange, R. (2003). *J. Synchrotron Rad.* **10**, 9–15.

Haubold, H.-G., Vad, T., Waldöfner, N. & Bönnemann, H. (2003). *J. Appl. Cryst.* **36**, 617–620.

Hauk, V. (1997). *Structural and Residual Stress Analysis by Nondestructive Methods*. Amsterdam: Elsevier.

Häussler, P. (1992). *Phys. Rep.* **222**, 65.

He, H., Marchesini, S., Howells, M., Weierstall, U., Chapman, H., Hau-Riege, S., Noy, A. & Spence, J. (2003). *Phys. Rev. B* **67**, 174114.

Heinemann, U., Frevert, J., Hofmann, K., Illing, G., Maurer, C., Oschkinat, H. & Saenger, W. (2000). *Prog. Biophys. Mol. Biol .* **73**, 347–362.

Henrich, S., Cameron, A., Bourenkov, G. P., Kiefersauer, R., Huber, R., Lindberg, I., Bode, W. & Than, M. E. (2003). *Nat. Struct. Biol.* **10**, 520–526.

Hermsdorf, N., Sahre, K., Volodin, P., Stamm, M., Eichhorn, K. J., Gehrke, R., Panagiotou, P., Titz, T. & Müller-Buschbaum, P. (2003). *in preparation*.

Hesse, M. & Seebach, M. (1997). Photon beam position monitors at DORIS. *Proc. of 3RD European Workshop on Beam Diagostics and Instrumentation for Particle Accelerators*, INFN Frascati, Italy.

Hignette, O., Cloetens, P., Lee, W. K., Ludwig, W. & Rostaing, G. (2003). *J. de Physique IV* **104**, 231–234.

Hofmann, A. & Meot, F. (1982). *Nucl. Instr. Methods Phys. Res.* **203**, 483.

Hohlneicher, G., Pulm, H. & Freund, H.-J. (1985). *J. Electron Spec. Rel. Phenom.* **37**, 209–224.

Holldack, K., Erko, A., Noll, T. & Peatman, W. B. (1995). *Nucl. Instr. Methods Phys. Res. A* **365**, 40.

Holldack, K., J.Feikes & Peatman, W. B. (2001). Review of emittance and stability monitoring using synchrotron radiation monitors. *Proc. of the 5th European Workshop on Diagnostics and Beam Instrumentation (DIPAC 2001)*, Grenoble. ESRF.

Holldack, K., Ponwitz, D. & Peatman, W. B. (2001). *Nucl. Instr. Methods Phys. Res. A* **467–468**, 213–220.

Hoppe, U., Kranold, R., Barz, A., Stachel, D. & Neuefeind, J. (2000). *Solid State Commun.* **115**, 559.

Horan, D. (2002). Performance of the APS 350 MHz RF systems. *Proceedings of the CW-RF Users Group Meeting*. Argonne National Laboratory, 13.-15. March 2002.

Howells, M. R. (1999). ALS report LSBL-538. Technical report, LBNL, USA.

Huber, R. (1989). *EMBO J.* **8**, 2125–2147.

Hüfner, S. (1996). *Photoelectron Spectroscopy: Principles and Applications*. Springer, Berlin.

Ice, G., Chung, J., J.Z., T., Lunt, A. & Assoufid, L. (2000). *Rev. Sci. Instrum.* **71**, 2635–2639.

Ice, G. & Larson, B. (2000). *Adv. Eng. Mater.* **10**, 643–646.

Imada, M., Fujimori, A. & Tokura, Y. (1998). *Rev. Mod. Phys.* **70**, 1039.

Inami, T., Fukuda, T., , Mizuki, J., Ishihara, S., Kondo, H., Nakao, H., Matsumura, T., Hirota, K., Murakami, Y., Maekawa, S. & Endoh, Y. (2003). *Phys. Rev. B* **67**, 045108.

Ingold, G. (2000). Insertion devices: New concepts and performance. *Proceedings of the 7th European Particle Accelerator Conference (EPAC 2000)*, pages 222–226, Vienna, Austria.

Irizawa, A., Yamasaki, A., Okazaki, M., Kasai, S., Sekiyama, A., Imada, S., Suga, S., Kulatov, E., Ohta, H. & Nanba, T. (2002). *Solid State Commun.* **124**, 1–5.

Irving, T. C. (1998). *Nat. Struct. Biol.* **5**, Suppl. 648–650.

Ishikawa, T., Hirano, K., Kanzaki, K. & Kikuta, S. (1992). *Rev. Sci. Instrum.* **63**, 1098–1103.

Iwasaki, T., Suga, S., Imada, S., Sekiyama, A., Matsuda, K., Kotsugi, M., An, K., Muro, T., Ueda, S., Matsushita, T., Saitoh, Y., Nakatani, T., Ishii, H., Sakai, O., Takayama, R., Suzuki, T., Oguchi, T., Katoh, K. & Ochiai, A. (2000). *Phys. Rev. B* **61**, 4621–4628.

Jackson, G. J., Woodruff, D. P., Jones, R. G., Singh, N. K., Chan, A. S. Y., Cowie, B. C. C. & Vormoso, V. (2000). *Phys. Rev. Lett.* **84**, 119–122.

Jahnke, T., Weber, T., Landers, A. L., Knapp, A., Schössler, S., Nickles, J., Kammer, S., Jagutzki, O., Schmidt, L., Czasch, A., Osipov, T., Arenholz, E., Young, A. T., Muino, R. D., Rolles, D., Abajo de, F. J. G., Fadley, C. S., Hove, M. A. V., Semenov, S. K., Cherepkov, N. A., Rösch, J., Prior, M. H., Schmidt-Böcking, H., Cocke, C. L. & Dörner, R. (2002). *Phys. Rev. Lett.* **88**, 73002.

Janssens, K., Adams, F. & Rindby, A. (2000). *Microscopic X-ray Fluorescence Analysis*. Wiley, Chichester, UK.

Jaouen, N., Tonnerre, J. M., Raoux, D., Bontempi, E., Ortega, L., Müenzenberg, M., Felsch, W., Rogalev, A., Dürr, H. A., Dudzik, E., Laan van der, G., Maruyama, H. & Suzuki, M. (2002). *Phys. Rev. B* **66**, 134420.

Jelsch, C., Teeter, M., Lamzin, V., Pichon-Pesme, V., Blessing, R. & Lecomte, C. (2000). *Proc. Nat. Acad. Sci. USA* **97**, 3171–3176.

Jephcoat, A. & Refson, K. (2001). *Nature (London)* **413**, 27.

Jiang, X. L., Li, L., Kumar, J., Kim, D. Y., Shivshankar, V. & Tripathy, S. K. (1996). *Appl. Phys. Lett.* **68**, 2618.

Job, P. K. (2002). Experiences in Radiation Safety during the Top-Up Operation at the Advanced Photon Source. 2^{nd} *International Workshop on Radiation Safety at Synchrotron Radiation Sources*, Grenoble.

Johnson, E. D. & Oversluizen, T. (1989). *Rev. Sci. Instrum.* **60**, 1947.

Johnson, J. & Chiu, W. (2002). *Curr. Opin. Struct. Biol.* **10**, 229–235.

Juul Jensen, D. & Kjems, J. (1983). *Texture Microstruct.* **5**, 239–251.

Kachalova, G., Popov, A. & Bartunik, H. (1999). *Science* **284**, 473–476.

Kaldis, E. (2001). *Handbook of the Physics and Chemistry of the Rare Earths*, volume 31, Amsterdam. North-Holland.

Kamps, T., Blair, G. A., Poirier, F., Lewin, H., Schreiber, S., Walker, N. & Wittenburg, K. (2002). R&D towards a laser based beam size monitor for the future linear collider. *Proceedings of the 8th European Particle Accelerator Conference (EPAC 2002).*

Kao, C.-C., Calibe, W. A. L., Hastings, J. B. & Gillet, J.-M. (1996). *Phys. Rev. B* **54**, 16361.

Kao, C.-C., Chen, C. T., Johnson, E. D., Hastings, J. B., Lin, H. J., Ho, G. H., Meigs, G., Brot, J.-M., Hulbert, S. L., Idzerda, Y. U. & Vettier, C. (1994). *Phys. Rev. B* **50**, 9599.

Kao, C.-C., Hastings, J. B., Johnson, E. D., Siddons, D. P., Smith, G. C. & Prinz, G. A. (1990). *Phys. Rev. Lett.* **65**, 373.

Karl, A., Cunis, S., Gehrke, R., Krosigk, G. v., Lode, U., Luzinov, I., Minko, S., Pomper, T., Senkovsky, V., Voronov, A. & Wilke, W. (1999). *J. Macromol. Sci., Phys. B* **38**, 901.

Kelly, S. D., Newville, M. G., Cheng, L. L., Kemner, K. M., Sutton, S. R., Fenter, P., Sturchio, N. C. & Spotl, C. (2003). *Env. Sci. Technol.* **37**, 1284–1287.

Kelly IV, J. J., Barnes, B. M., Flack, F., Lagally, D. P., Savage, D. E., Friesen, M. & Lagally, M. G. (2002). *J. Appl. Phys.* **91**, 9978–9986.

Kempenaers, L., Janssens, K., Vincze, L., Vekemans, B., Somogyi, A., Drakopoulos, M., Simionovici, A. & Adams, F. (2002). *Anal. Chem.* **74**, 5017–5026.

Kevan, S. D. (1992). *Angle-Resolved Photoemission: Theory and Current Applications*. Elsevier, Amsterdam.

Khomskii, D. & Sawatzky, G. (1997). *Solid State Commun.* **102**, 87.

Kikutani, E. et al. (2002). Present status of the KEKB bunch feedback systems. *Proceedings of the 8th European Particle Accelerator Conference (EPAC 2002)*, volume 2, pages 2085–2087, Paris.

Kim, C. D., Pillet, S., Wu, G., Fullagar, W. K. & Coppens, P. (2002). *Acta Cryst.* **A58**, 133–137.

Kim, D. Y., Tripathy, S. K., Li, L. & Kumar, J. (1995). *Appl. Phys. Lett.* **66**, 1166.

Kim, K.-J. (1995). *Optical Engineering* **34**, 342–352.

King, Q. (1988). Analysis of the influence of fibre diameter on wirescanner beam profile measurements. Technical report, DESY.

Kinne, M., Fuhrmann, T., Whelan, C., Zhu, J., Pantförder, J., Probst, M., Held, G., Denecke, R. & Steinrück, H.-P. (2002). *J. Chem. Phys.* **117**, 10852.

Kinne, M., Fuhrmann, T., Zhu, J., Whelan, C. M., Denecke, R. & Steinrück, H.-P. (2004). *J. Chem. Phys.* in print.

Kirfel, A., Krane, H. G., Blaha, P., Schwarz, K. H. & Lippmann, T. (2001). *Acta Cryst. A* **57**, 663–677.

Kitamura, H., Bizen, T., Hara, T., Marchal, X., Seike, T. & Tanaka, T. (2001). *Nucl. Instr. Methods Phys. Res. A* **467-468**, 110–113.

Kivimäki, A., Maier, K., Hergenhahn, U., Piancastelli, M. N., Kempgens, B., Rüdel, A. & Bradshaw, A. M. (1998). *Phys. Rev. Lett* **81**, 301–304.

Klatt, R., Kohaupt, R. D. & Weiland, T. (1985). *IEEE Trans. Nucl. Sci.* **32**, 2356–2358.

Klatt, R. & Weiland, T. (1988). DESY Internal Report M-88-04, p53-55.

Kleibert, A. et al. (2003). *BESSY Jahresbericht 2002* page 89.

Kleifeld, O., Frenkel, A., Martin, J. & Sagi, I. (2003). *Nature Struct. Biol.* **10**, 98–103.

Klopf, F., Reithmayer, J. P. & Forchel, A. (2000). *Appl. Phys. Lett.* **77**, 1419.

Knapp, M., Baehtz, C., Ehrenberg, H. & Fuess, H. (2003). *J. Appl. Cryst.* submitted.

Knapp, M., Ehrenberg, H., Fuess, H., Hahn, U., Hesse, M., Schulte-Schrepping, H. & Wroblewski, T. (2001). *Nucl. Instr. Methods Phys. Res. A* **467-468**, 291–293.

Knapp, M., Joco, V., Baehtz, C., Brecht, H. H., Berghäuser, A., Ehrenberg, H., Seggern von, H. & Fuess, H. (2004). *Nucl. Instrum. Methods Phys. Res. A* in print.

Knowles, D., Foloppe, N., Matassova, N. & Murchie, A. (2002). *Curr. Opin. Pharmacol.* **2**, 501–506.

Kobayashi, K., Yabashi, M., Takata, Y., Tokushima, T., Shin, S., Tamasaku, K., Miwa, D., Ishikawa, T., Nohira, H., Hattori, T., Sugita, Y., Nakatsuka, O., Sakai, A. & Zaima, S. (2003). *Appl. Phys. Lett.* **83**, 1005–1007.

Kodre, A., Arčon, I., Padežnik Gomilšek, I., Prešeren, J. & Frahm, R. (2002). *J. Phys. B* **35**, 3497.

Kohn, V., Snigireva, I. & Snigirev, A. (2000). *Phys. Rev. Lett.* **85**, 2745.

Konarev, P., Volkov, V. V., Sokolova, A. V., Koch, M. H. J. & Svergun, D. I. (2003). *J. Appl. Cryst.* **36**, 1277–1282.

Konarev, P. V., Petoukhov, M. V. & Svergun, D. I. (2001). *J. Appl. Cryst.* **34**, 527–532.

Koritsánszky, T., Flaig, R., Zobel, D., Krane, H.-G., Morgenroth, W. & Luger, P. (1998). *Science* **279**, 356–358.

Kostorz, G. (1991). *J. Appl. Cryst.* **24**, 444–456.

Kotani, A. & Shin, S. (2001). *Rev. Mod. Phys.* **73**, 203.

Kouptsidis, J. et al. (1980). Technical report, DESY Jahresbericht.

Kövér, L., Drube, W., Berényi, Z., Cserny, I., Medicherla, V. R. R., Ishii, T., Ikeno, H. & Adachi, H. (2003). *Phys. Rev. B.* submitted.

Kozielski, F., Sack, S., Marx, A., Thormählen, M., Schönbrunn, E., Biou, V., Thompson, A., Mandelkow, E.-M. & Mandelkow, E. (1997). *Cell* **91**, 985–994.

Kraack, H., Deutsch, M., Ocko, B. M. & Pershan, P. S. (2002). *Science* **298**, 1404.

Kramer, M., Margulies, L., Goldmann, A. & Lee, P. (2002). *J. Alloys Comp.* **338**, 235–241.

Krimmel, S., Donner, W., Nickel, B., Dosch, H., Sutter, C. & Grübel, G. (1997). *Phys. Rev. Lett.* **78**, 3880.

Kroha, H. (2000). *Mat. Sci. Eng. A* **294-296**, 500.

Krumhansl, J. A. & Barsch, G. R. (1992). *Proc. Int. Conf. on Martensitic Transformations, Monterey Inst. of Advanced Studies* page 25.

Kubsky, S., Dölling, D., Geisler, A., Hobl, A., Klein, U., Krischel, D., Moser, H., Rossmanith, R. & Couhan, S. (2003). *Proceedings of the 8th conference on synchrotron radiation instrumentation (SRI'03), San Francisco, USA* in press.

Kuhn, P., Wilson, K., Patch, M. & Stevens, R. (2002). *Curr. Opin. Chem. Biol.* **6**, 704–710.

Laaziri, K., Robertson, J. L., Roorda, S., Chicoine, M., Kycia, S., Wang, J. & Moss, S. C. (1999). *J. Appl. Cryst.* **32**, 322.

Lai, B., Khounsary, A., Savoy, R., Moog, L. & Gluskin, E. (1993). Undulator A characteristics and specifications. Technical report, ANL/APS.

Laidler, H., Pape, I., Gregory, C. I., Hickey, B. J. & Tanner, B. K. (1996). *J. Magn. Magn. Mater.* **154**, 165–174.

Landau, D. P. & Binder, K. (1990). *Phys. Rev. B* **41**, 4786.

Landers, A., Weber, T., Ali, I., Cassimi, A., Hattass, M., Jagutzi, O., Nauert, A., Osipov, T., Staudte, A., Prior, M. H., Schmidt-Böcking, H. & R. Dörner und, C. L. C. (2001). *Phys. Rev. Lett.* **87**, 13002.

Lang, J. C., Srajer, G. & Dejus, R. J. (1996). *Rev. Sci. Instrum.* **67**, 62–67.

Langevin, D. (1992). *Light scattering by liquid surfaces and complementary techniques*. New York: Marcel Dekker.

Lankosz, M., Szczerbowska-Boruchowska, M., Ostachowicz, J., Adamek, D., Krygowska-Wajs, A., Tomik, B., Bohic, S. & Simionovici, A. (2002). *ESRF Highlights 2002* pages 87–88.

Larson, B., Yang, W., Ice, G., Budai, J. & Tischler, J. (2002). *Nature (London)* **415**, 887–890.

Larson, B., Yang, W., Tischler, J., Ice, G., Budai, J., Liu, W. & Weiland, H. (2003). *Int. J. Plasticity* in press.

Laskar, J. (1994). Workshop on Nonlinear Dynamics in Particle Accelerators: Theory and Experiments, Arcidosso, Italy, 4-9 Sep 1994.

Lau, J. T., Föhlisch, A., Nietubyc, R., Reif, M. & Wurth, W. (2002). *Phys. Rev. Lett* **89**, 057201.

Lauridsen, E., Juul Jensen, D., Poulsen, H. & Lienert, U. (2000). *Scripta Mater.* **43**, 561–566.

Lauridsen, E. M., Schmidt, S., Suter, R. M. & Poulsen, H. F. (2001). *J. Appl. Cryst.* **34**, 744.

LeBlanc, G. & Wallén, E. (2002). *Proceedings of the 8th European Particle Accelerator Conference (EPAC 2002), Paris, France* page 2622.

Lee, T. L. et al. (2003). *Sol. State Commun.* submitted.

Lee, Y., Kim, S. J., Schoonen, M. A. A. & Parise, J. B. (2000). *Chem. Mater.* **12**, 1597–1603.

Lemly, A. D. (2002). *Aquatic Toxicology* **57**, 39–49.

Lengeler, B., Schroer, C., Tümmler, J., Benner, B., Richwin, M., Snigirev, A., Snigireva, I. & Drakopoulos, M. (1999a). *J. Synchrotron Rad.* **6**, 1999.

Lengeler, B., Schroer, C. G., Kuhlmann, M., Benner, B., Günzler, T. F., Kurapova, O., Rau, C., Weitkamp, T., Simionovici, A., Snigirev, A. & Snigireva, I. (2003). *J. de Physique IV* **104**, 221.

Lengeler, B., Schroer, C. G., Richwin, M., Tümmler, J., Drakopoulos, M., Snigirev, A. A. & Snigireva, I. I. (1999b). *Appl. Phys. Lett.* **74**, 3924–3926.

Leuschner, A. (2002). Sicherheit gegenüber ionisierender Strahlung an der TESLA Test Facility, Phase 2 (TTF-II). Laborbericht DESY D3-118, DESY.

Leverenz, T., Eigenmann, B. & Macherauch, E. (1996). *Z. Metallkd.* **87**, 616–625.

Ley, L. & Cardona, M. (1979). *Photoemission in Solids II: Case Studies*. Springer, Heidelberg.

Li, Z. G., Harlow, R. L., Gao, F., Lin, P., Miao, R. & Liang, L. (2003). *J. Electrochem. Soc.* **150**, A1171–A1175.

Lichtenegger, H. C., Müller, M., Paris, O., Riekel, C. & Fratzl, P. (1999). *J. Appl. Cryst.* **32**, 1127.

Lidström, E., Mannix, D., Hiess, A., Rebizant, J., Wastin, F., Lander, G. H., Marri, I., Carra, P., Vettier, C. & Longfield, M. J. (2000). *Phys. Rev. B* **61**, 1375.

Lienert, U. & Keitel, S. (2001). *Nucl. Instrum. Methods Phys. Res. A* **467**, 659.

Lienert, U., Martins, R., Grigull, S., Pinkerton, M., Poulsen, H. F. & Kvick, Å. (2000). *Mat. Res. Soc. Symp. Proc.* **590**, 241–246.

Lienert, U., Poulsen, H. F., Honkimäki, V., Schulze, C. & Hignette, O. (1999). *J. Synchrotron Radiat.* **6**, 979–984.

Lienert, U., Poulsen, H. F. & Kvick, Å. (1999). *Proc. 40th Conf. of AIAA: Structures, structural dynamics and materials, St. Louis, USA* pages 206–214.

Lienert, U. & Schulze, C. (1998). *J. Synchrotron Rad.* **5**, 226.

Lienert, U., Schulze, C., Honkimäki, V., Tschentscher, T., Garbe, S., Hignette, O., Horsewell, A., Lingham, M., Poulsen, H. F., Thomsen, N. B. & Ziegler, E. (1998). *J. Synchrotron Rad.* **5**, 226–231.

Lind, O. C., Salbu, B., Janssens, K. & Simionovici, A. (2002). Radioactive particle characterization by means of synchrotron radiation-based x-ray micro beam techniques. *Proceedings of the 5th Int. Conference on Environmental Radioactivity in the Arctic & Antarctic*, edited by P. Strand, pages 260–263.

Lippmann, T., Blaha, P., Andersen, N. H., Poulsen, H. F., Wolf, T., Schneider, J. R. & Schwarz, K. H. (2003). *Acta Cryst. A* **59**, 437–451.

Lippmann, T. & Schneider, J. R. (2000a). *J. Appl. Cryst.* **33**, 156–167.

Lippmann, T. & Schneider, J. R. (2000b). *Acta Cryst. A* **56**, 575–584.

Liss, K.-D., Bartels, A., Schreyer, A. & Clemens, H. (2003). *Texture Microstruct.* in press.

Litvinenko, V. et al. (2001). IEEE Particle Accelerator Conference (PAC2001), Chicago, Illinois, 18-22 Jun.

Loa, I., Kunc, K., Syassen, K., Krisch, M., Mermet, A. & Hanfland, M. (2003). *High Pressure Research* **23**, 1.

Lorenz-Haas, C., Müller-Buschbaum, P., Ittner, T., Kraus, J., Mahltig, B., Cunis, S., Krosigk, G. v., Gehrke, R., Creton, C. & Stamm, M. (2003). *Phys. Chem. Chem. Phys* **5**, 1235.

Lübbers, R., Grünsteudel, H. F., Chumakov, A. I. & Wortmann, G. (2000). *Science* **287**, 1250.

Lübbers, R., Rupprecht, K. & Wortmann, G. (2000). *Hyperfine Interact.* **128**, 115.

Lübbers, R., Wortmann, G. & Grünsteudel, H. F. (1999). *Hyperfine Interact.* 123/124, 529.

Ludwig, W., Buffiere, J.-Y., Savelli, S. & Cloetens, P. (2003). *Acta Materialia* 51, 585–598.

Luedeke, A. & Munoz, M. (2002). Top-Up Operation Experience at the Swiss Light Source. *Proceedings of the 8th European Particle Accelerator Conference (EPAC 2002)*, pages 721–723, Paris.

Lurio, L. B., Lumma, D., Sandy, A. R., Borthwick, M. A., Falus, P., Mochrie, S. G. J., Pelletier, J. F., Sutton, M., Regan, L., Malik, A. & Stephenson, G. B. (2000). *Phys. Rev. Lett.* **84**, 785.

Lützenkirchen-Hecht, D. & Frahm, R. (2001). *Phys. Chem. B* **105**, 9988.

Lützenkirchen-Hecht, D., Grundmann, S. & Frahm, R. (2001). *J. Synchrotron Rad.* **8**, 6.

Lützenkirchen-Hecht, D., Grunwaldt, J.-D., Richwin, M., Griesebock, B., Baiker, A. & Frahm, R. (2003). *Phys. Scripta* in press.

Lützenkirchen-Hecht, D. & Strehblow, H.-H. (2003). *Synchrotron Methods in Corrosion Research*. Marcel-Dekker.

Macedo-Ribeiro, S., Bode, W., Huber, R., Quin-Allen, M. A., Kim, S. W., Ortel, T. L., Bourenkov, G. P., Bartunik, H. D., Stubbs, M. T., Kane, W. H. & Fuentes-Prior, P. (1999). *Nature (London)* **402**, 434–439.

MacKay, J. F., Teichert, C., Savage, D. E. & Lagally, M. G. (1996). *Phys. Rev. Lett.* **77**, 3925.

MacMahon, P. J., Peele, A. G., Paterson, D., Lin, J. J. A., Irving, T. H. K. & McNulty, I. (2003). *Opt. Commun.* **217**, 53–58.

Maddison, D., Swofford, D. & Maddison, W. (1997). *Syst. Biol.* **46**, 590–621.

Madsen, A., Als-Nielsen, J. & Grübel, G. (2003). *Phys. Rev. Lett.* **90**, 85701.

Magnussen, O. M., Ocko, B. M., Deutsch, M., Regan, M. J., Pershan, P. S., Berman, L. E., Abernathy, D., Legrand, J. F. & Grübel, G. (1996). *Nature (London)* **384**, 250.

Magnussen, O. M., Ocko, B. M., Regan, M. J., Penanen, K., Pershan, P. S. & Deutsch, M. (1995). *Phys. Rev. Lett.* **74**, 4444.

Maire, E., Fazekas, A., Salvo, L., Dendievel, R., Youssef, S., Cloetens, P. & Letang, J. M. (2003). *Composites Science and Technology* **63**, 2431–2443.

Malfois, M. & Svergun, D. I. (2000). *J. Appl. Cryst.* **34**, 812–816.

Manley, M. E., Lander, G. H., Sinn, H., Alatas, A., Hults, W. L., McQueeney, R. J., Smith, J. L. & Willit, J. (2003). *Phys. Rev. B* **67**, 052302.

Mao, H. K., Xu, J., Struzhkin, V. V., Shu, J., Hemley, R. J., Sturhahn, W., Hu, M. Y., Alp, E. E., Vocadlo, L., Alf, D., Price, G. D., Gilan, M. J., Schwoerer-Böhning, M., Häusermann, D., Eng, P., Shen, G., Giefers, H., Lübbers, R. & Wortmann, G. (2001). *Science* **292**, 914.

Marcellini, F. et al. (1996). Technical report, INFN-LNF, Frascati, Italy. DAΦNE Technical Note, Note: CD-6.

Margulies, L., Lorentzen, T., Poulsen, H. F. & Leffers, T. (2002). *Acta Mater.* **50**, 1771–1779.

Margulies, L., Winther, G. & Poulsen, H. F. (2001). *Science* **291**, 2392–2394.

Marion, P. & Zhang, L. (2003). New high power primary slit for the ESRF beamlines. *Proceedings of the International Conference on Synchrotron Radiation Instrumentation (SRI 2003)*, San Francisco, USA.

Martinetto, P., Anne, M., Dooryhee, E., Drakopoulos, M., Dubus, M., Salomon, J., Simionovici, A. & Walter, P. (2001). *Nucl. Instr. Methods Phys. Res. B* **181**, 744–748.

Martins, R. V. & Honkimäki, V. (2003). *Texture Microstruct.* **35**, 145–152.

Martins, R. V., Lienert, U., Margulies, L. & Pyzalla, A. (2002). *Mater. Science Forum* **404–407**, 115–120.

Maruyama, H., Suzuki, M., Kawamura, N., Ito, M., Arakawa, E., Kokubun, J., Hirano, K., Horie, K., Uemura, S., Hagiwara, K., Mizumaki, M., Goto, S., Kitamura, H., Namikawa, K. & Ishikawa, T. (1999). *J. Synchrotron Rad.* **6**, 1133–1137.

Masaki, M., Ohkuma, H., Sasaki, S., Shoji, M., Takano, S. & Tamura, K. (2001). Planned X-ray imaging of the electron beam at the spring-8 diagnostics beamline bl38b2. *Proc. of the 5th European Workshop on Diagnostics and Beam Instrumentation (DIPAC 2001)*, Grenoble. ESRF.

Masciovecchio, C., Bergmann, U., Krisch, M., Ruocco, G., Sette, F. & Verbeni, R. (1996). *Nucl. Instrum. Methods Phys. Res. B* **111**, 181.

Mathewson, A. G., Gröbner, O., Strubin, P., Martin, P. & Souchet, R. (1990). Comparison of synchrotron radiation induced gas desorption from Al, stainless steel and Cu chambers. Technical report, CERN.

Mattson, M. P., LaFerla, F. M., Chan, S. L., Leissring, M. A., Shepel, P. N. & Geiger, J. D. (2000). *Trends Neurosci.* **23**, 222–229.

Mavrogenes, J. A., Berry, A. J., Newville, M. & Sutton, S. R. (2002). *Am. Mineral.* **87**, 1360–1364.

May, F., Tischer, M., Arvanitis, D., Russo, M., Dunn, J. H., Henneken, H., Wende, H., Chauvistre, R., Martensson, N. & Baberschke, K. (1996). *Phys. Rev. B* **53**, 1076.

McCusker, L. B., Dreele von, R. B., Cox, D. E., Louer, D. & Scardi, P. (1999). *J. Appl. Cryst.* **32**, 36–50.

McMorrow, D. F., McEwen, K. A., Steigenberger, U., Rønnow, H. M. & Yakhou, F. (2001). *Phys. Rev. Lett.* **87**, 057201.

McNulty, I., Lai, B., Maser, J., Paterson, D. J., Evans, P., Heald, S. M., Ice, G. E., Isaacs, E. D., Rivers, M. L. & Sutton, S. R. (2003). *Synchrotron Radiation News* **16**, 34–42.

Ménez, B., Philippot, P., Bonnin-Mosbah, M., Simionovici, A. & Gibert, F. (2002). *Geochimica Cosmochimica Acta* **66**, 561–576.

Mercier, J. M. (2002). Operation of the RF at the ESRF. *Proceedings of the CW-RF Users Group Meeting*. Argonne National Laboratory, 13.-15. March 2002.

Meulenkamp, E. A. (1998). *J. Electrochem. Soc.* **145**, 2759–2762.

Miao, J., Charalambous, P., Kirz, J. & Sayre, D. (1999). *Nature (London)* **400**, 342.

Miao, J., Hodgson, K. & Sayre, D. (2001). *Proc. Nat. Acad. Sci. USA* **98**, 6641.

Micossi, E., Hunter, W. & Leonard, G. (2002). *Acta Cryst. D* **58**, 21–28.

Milchev, A., Müller, M., Binder, K. & Landau, D. P. (2003). *Phys. Rev. Lett.* **90**, 136101.

Minko, S., Karl, A., Senkovsky, V., Pomper, T., Cunis, S., Gehrke, R., Krosigk, G. v., Lode, U., Luzinov, I., Voronov, A. & Wilke, W. (1999). *J. Macromol. Sci., Phys. B* **38**, 913.

Minor, W., Tomchick, D. & Otwinowski, Z. (2000). *Structure* **8**, R105–R110.

Mishin, O. V., Lauridsen, E. M., Krieger-Lassen, N. C., Brückner, G., Tschentscher, T., Bay, B., Juul Jensen, D. & Poulsen, H. F. (2000). *J. Appl. Cryst.* **33**, 364–371.

Mitsuhashi, T. (1998). Beam profile and size measurements by SR interferometers. *Proc. Joint US-CERN-Japan-Russian School on Particle Accelerators*, edited by S. Kurokawa, S. Y. Lee, E. Perevedentsev & S. Turner, page 399. World Scientific, London.

Mittemeijer, E. J. & Scardi, P. (2004). *Diffraction analysis of the microstructure of materials*. Berlin, Heidelberg: Springer Verlag.

Mo, S. K., Denlinger, J. D., Kim, H. D., Park, J. H., Allen, J. W., Sekiyama, A., Yamasaki, A., Kadono, K., Suga, S., Saitoh, Y., Muro, T., Metcalf, P., Keller, G., Held, K., Eyert, V., Anisimov, V. I. & Vollhardt, D. (2003). *Phys. Rev. Lett.* **90**, 186403.

Mochrie, S., Mayes, M., Sandy, A., Sutton, M., Brauer, S., Stephenson, G., Abernathy, D. & Als-Nielsen, J. (1997). *Phys. Rev. Lett.* **78**, 1275.

Moffat, K. (2001). *Chem. Rev.* **101**, 1569–1581.

Momose, A. (1995). *Nucl. Instrum. Methods Phys. Res. A* **352**, 622–628.

Momose, A. (2002). *J. Synchrotron Rad.* **9**, 136–142.

Mook, H. A. & Dogan, F. (1999). *Nature (London)* **401**, 145.

Mooney, T. M., Toellner, T. S., Sturhahn, W., Alp, E. E. & Shastri, S. D. (1994). *Nucl. Instrum. Methods Phys. Res. A* **347**, 348.

Morcrette, M., Chabre, Y., Vaughan, G., Amatucci, G., Leriche, J.-B., Patoux, S., Masquelier, C. & Tarascon, J.-M. (2002a). *Electrochim. Acta* **47**, 3137–3149.

Morcrette, M., Chabre, Y., Vaughan, G., Amatucci, G., Leriche, J.-B., Patoux, S., Masquelier, C. & Tarascon, J.-M. (2002b). *Electrochimica Acta* **47**, 3137–3149.

Moss, C. E., Butler, M. F., Müller, M. & Cameron, R. E. (2002). *J. Appl. Polym. Sci.* **83**, 2799.

Mukerjee, S., Thurston, T. R., Jisrawi, N. M., Yang, X. Q., McBreen, J., Daroux, M. L. & Xing, X. K. (1998). *J. Electrochem. Soc.* **145**, 466–472.

Müller, A., Phaneuf, R. A., Aguilar, A., Gharaibeh, M. F., Schlachter, A. S., Alvarez, I., Cisneros, C., Hinojosa, G. & McLaughlin, B. M. (2003). *Nucl. Instrum. Methods Phys. Res. B* **205**, 301.

Müller, B., Beckmann, F., Huser, M., Maspero, F., Szekely, G., Ruffieux, K., Thurner, P. & Wintermantel, E. (2002). *Biomolecuar Engineering* **19**, 73–78.

Müller, M., Burghammer, M., Flot, D., Riekel, C., Morawe, C., Murphy, B. & Cedola, A. (2000a). *J. Appl. Cryst.* **33**, 1231.

Müller, M., Burghammer, M. & Riekel, C. (2001). *Nucl. Instrum. Methods Phys. Res. A* **467**, 958.

Müller, M., Czihak, C., Burghammer, M. & Riekel, C. (2000b). *J. Appl. Cryst.* **33**, 817.

Müller-Buschbaum, P. (2003). *Anal. Bioanal. Chem.* **376**, 3.

Müller-Buschbaum, P., Casagrande, M., Gutmann, J. S., Kuhlmann, T., Stamm, M., Krosigk, G. v., Lode, U. & Gehrke, R. (1998). *Europhys. Lett.* **42**, 517.

Müller-Buschbaum, P., Gutmann, J. S., Stamm, M., Cubitt, R., Krosigk, G. v., Gehrke, R. & Petry, W. (2000). *Physica B* **283**, 53.

Müller-Buschbaum, P., Hermsdorf, N., Roth, S. V., Wiedersich, J., Cunis, S. & Gehrke, R. (2003a). *submitted to Elsevier Science*.

Müller-Buschbaum, P., Roth, S. V., Burghammer, M., Diethert, A., Panagiotou, P. & Riekel, C. (2003b). *Europhys. Lett.* **61**, 639.

Murakami, Y., Hill, J. P., Gibbs, D., Blume, M., Koyama, I., Tanaka, M., Kawata, H., Arima, T., Tokura, Y., Hirota, K. & Endoh, Y. (1998a). *Phys. Rev. Lett.* **81**, 582–585.

Murakami, Y., Kawada, H., Kawata, H., Tanaka, M., Arima, T., Moritomo, Y. & Tokura, Y. (1998b). *Phys. Rev. Lett.* **80**, 1932–1935.

Nakao, H., Wakabayashi, Y., Kiyama, T., Murakami, Y., Zimmermann v., M., Hill, J. P., Gibbs, D., Ishihara, S., Taguchi, Y. & Tokura, Y. (2002). *Phys. Rev. B* **66**, 184419.

Narayanan, T., Diat, O. & Boesecke, P. (2001). *Nucl. Instr. Methods Phys. Res. A* **346**, 1005–1009.

Nasdala, L., Brenker, F. E., Glinnemann, J., Hofmeister, W., , Gasparik, T., Harris, J. W., Stachel, T. & Reese, I. (2003). *Eur. J. Mineral.* accepted.

Nelson, C. S., Srajer, G., Lang, J. C., Venkataraman, C. T., Sinha, S. K., Hashizume, H., Ishimatsu, N. & Hosoito, N. (1999). *Phys. Rev. B* **60**, 12234.

Neutze, R., Wouts, R., Spoel van der, D., Weckert, E. & Hajdu, J. (2000). *Nature (London)* **408**, 752–757.

Nielsen, S., Poulsen, H., Beckmann, F., Thorning, C. & Wert, J. (2003). *Acta Mater.* **51**, 2407–2415.

Nielsen, S. F., Wolf, A., Poulsen, H. F., Ohler, M., Lienert, U. & Owen, R. A. (2000). *J. Synchrotron Radiat.* **7**, 103–109.

Norby, P. (1997). *J. Am. Chem. Soc.* **119**, 5215–5221.

Occelli, F., Krisch, M., Loubeyre, P., Sette, F., Toullec, R. L., Masciovecchio, C. & Rueff, J.-P. (2001). *Phys. Rev. B* **63**, 224306.

Ogasawara, H., Kotani, A., LeFevre, P., Chandesris, D. & Magnan, H. (2000). *Phys. Rev. B* **62**, 7970.

Ogawa, N. & Miyano, K. (2002). *Appl. Phys. Lett.* **80**, 3225–3227.

Ohno, H., Kohara, S., Umesaki, N. & Suzuya, K. (2001). *J. Non-Cryst. Solids* **293-295**, 125.

Onuki, H. & Elleaume, P. (2003). *Undulators, wigglers and their applications*. New York: Taylor & Francis.

Orenstein, J. & Millis, A. (2000). *Science* **288**, 468.

Osgood III, R. M., Sinha, S. K., Freeland, J. W., Idzerda, Y. U. & Bader, S. D. (1999). *J. Appl. Phys.* **85**, 4619–4621.

P. Den Hartog, G. A. Decker, L. J. E. (2003). Dual canted undulators at the Advanced Photon Source. *Proceedings of the PAC03 Conference*, pages 833–835, Portland, Oregon, USA.

Pagot, E., Cloetens, P., Fiedler, S., Bravin, A., Coan, P., Baruchel, J. & Härtwig, J. (2003). *Appl. Phys. Lett.* **82**, 3421–3423.

Paolasini, L., Caciuffo, R., Sollier, A., Ghigna, P. & Altarelli, M. (2002). *Phys. Rev. Lett.* **88**, 106403.

Paolasini, L., Vettier, C., Bergevin de, F., Yakhou, F., Mannix, D., Stunault, A., Neubeck, W., Altarelli, M., Fabrizio, M., Metcalf, P. A. & Honig, J. M. (1999). *Phys. Rev. Lett.* **82**, 4719–4722.

Parak, F. & Achterhold, K. (1999). *Hyperfine Interact.* **123/124**, 825.

Paris, O., Loidl, D., Müller, M., Lichtenegger, H. C. & Peterlik, H. (2001). *J. Appl. Cryst* **34**, 473.

Parise, J. B., Cahill, C. L. & Lee, Y. (2000). *Can. Mineral.* **38**, 777–800.

Penner-Hahn, J. (2004). *in preparation*.

Peters, J., deVries, M., Miguel, J., Toulemonde, O. & Goedkoop, J. (2000). *ESRF Newsletter* **34**, 15.

Petkov, V., Billinge, S. J. L., Shastri, S. D. & Himmel, B. (2000). *Phys. Rev. Lett.* **85**, 3436.

Petkov, V., Qadir, D. & Shastri, S. D. (2004). *Solid State Commun.* **129**, 239.

Petoukhov, M., Eady, N. A., Brown, K. A. & Svergun, D. I. (2002). *Biophys J.* **83**, 3113–3125.

Petracic, O., Kleemann, W., Binek, C., Kakazei, G., Pogorelov, Y., Sousa, J., Cardoso, S. & Freitas, P. (2002). *Phase Transitions* **75**, 73.

Petrov, A. (2003). private communication.

Pettifer, R. & Hermes, C. (1985). *J. Appl. Cryst.* **18**, 404–412.

Pfeiffer, F., David, C., Burghammer, M., Riekel, C. & Salditt, T. (2002). *Science* **297**, 230–234.

Pflüger, J. & Tischer, M. (2000). A prototype phase shifter for the undulator systems at the TESLA X-ray FEL. Technical report, DESY.

Pinzani, M. C. C., Somogyi, A., Simionovici, A. S., Ansell, S., Steenari, B. M. & Lindqvist, O. (2002). *Env. Sci. Technol.* **36**, 3165–3169.

Pizzini, S., Bonfim, M., Baudelet, F., Tolentino, H., San Miguel, A., Mackay, K., Malgrange, C., Hagelstein, M. & Fontaine, A. (1998). *J. Synchrotron Rad.* **5**, 1298–1303.

Pleimling, M. (2002). *Phys. Rev. B.* **65**, 184406.

Plouviez, E., Koch, J. M. & Uberto, F. (1998). Proceedings of the 6th European Particle Accelerator Conference (EPAC 1998), Stockholm, Sweden.

Pohl, E., Haller, J. C., Mijovilovich, A., Meyer-Klaucke, W., Garman, E. & Vasil, M. L. (2003). *Molec. Microbiol.* **47**, 903–915.

Polizzi, S., Riello, P., Balerna, A. & Benedetti, A. (2001). *Phys. Chem. Chem. Phys.* **3**, 4614–4619.

Poulsen, H. F. & Fu, X. (2003). *J. Appl. Cryst.* **36**, 1062.

Poulsen, H. F., Neuefeind, J., Neumann, H. B., Schneider, J. R. & Zeidler, M. D. (1995). *J. Non-Cryst. Solids* **188**, 63.

Poulsen, H. F., Nielsen, S. F., Lauridsen, E. M., Schmidt, S., Suter, R. M., Lienert, U., Margulies, L., Lorentzen, T. & Juul Jensen, D. (2001). *J. Appl. Cryst.* **34**, 751.

Poulsen, H. F. & Schmidt, S. (2003). *J. Appl. Cryst.* **36**, 319.

Prado, L. A. S. A., Wittich, H., Schulte, K., Goerigk, G., Haramus, V., Willumeit, R., Ruffmann, B. & Nunes, S. P. (2003). *J. Polym. Sci. Polym. Phys.* **42**, 567–575.

Press, W., Flannery, B., Teukosky, S. & Vetterling, W. (1987). *Numerical Recipes*. Cambridge University Press.

Prestemon, S., Dietderich, D., Marks, S. & Schlueter, R. (2003). *Proceedings of the 8th conference on synchrotron radiation instrumentation (SRI'03), San Francisco, USA* in press.

Preuss, M., Withers, P. J., Maire, E. & Buffière, J.-Y. (2002). *Acta Mater.* **50**, 3175–3190.

Pufahl, R. A., Singer, C., Peariso, K. L., Lin, S. J., Schmidt, P. J., Fahmi, C. J., Cizewski Culotta, V., Penner-Hahn, J. E. & O'Halloran, T. V. (1997). *Science* **278**, 853–856.

Pyzalla, A., Jacques, A., Feiereisen, J. P., Buslaps, T., D'Almeida, T. & Liss, K. D. (2001a). *J. Neutron Research* **9**, 435–442.

Pyzalla, A., Wang, L., Wild, E. & Wroblewski, T. (2001b). *Wear* **251**, 901–907.

Rahmin, A., Tixier, S., Tiedje, T., Eisebitt, S., Lörgen, M., Scherer, R., Eberhardt, W., Lüning, J. & Scholl, A. (2002). *Phys. Rev. B* **65**, 235241.

Ralle, M., Lutsenko, S. & Blackburn, N. (2003). *J. Biol. Chem.* **278**, 2316–2317.

Ramagopal, U. A., Dauter, M. & Dauter, Z. (2003). *Acta Cryst. D* **59**, 1020–1027.

Rasmussen, F. B., Molenbroek, A. M., Clausen, B. S. & Feidenhansl'l, R. (2000). *J. Catalysis* **190**, 205–208.

Rau, C., Weitkamp, T., Snigirev, A., Schroer, C., Tümmler, J. & Lengeler, B. (2001). *Nucl. Instr. Methods Phys. Res. A* **467–468**, 929–931.

Raven, C., Snigirev, A., Snigireva, I., Spanne, P., Souvorov, A. & Kohn, V. (1996). *Appl. Phys. Lett.* **69**, 1826–1828.

Raymond, S., Rueff, J. P., Astuto, M. D., Braithwaite, D., Krisch, M. & Flouquet, J. (2002). *Phys. Rev. B* **66**, 220301.

Reichert, H., Bugaev, V. N., Shchyglo, O., Schöps, A., Sikula, Y. & Dosch, H. (2001). *Phys. Rev. Lett.* **87**, 236105.

Reichert, H., Honkimäki, V., Snigirev, A., Engemann, S. & Dosch, H. (2003a). *Physica B* **336**, 46.

Reichert, H., Klein, O., Bugaev, V., Shchyglo, O., Udyanskyy, A., Dosch, H. & Peters, K. F. (2003b). *Phys. Rev. Lett.* **90**, 185504.

Reichert, H., Klein, O., Dosch, H., Denk, M., Honkimäki, V., Lippmann, T. & Reiter, G. (2000). *Nature (London)* **408**, 839–841.

Reimers, W., Pyzalla, A., Broda, M., Brusch, G., Dantz, D., Liss, K.-D., Schmackers, T. & Tschentscher, T. (1999). *J. Mater. Sci. Lett.* **18**, 581–583.

Reisner, B. A., Lee, Y., Hanson, J. C., Jones, G. A., Parise, J. B., Corbin, D. R., Toby, B. H., Freitag, A., Larese, J. Z. & Kahlenberg, V. (2000). *Chem. Commun.* **22**, 2221–2222.

Renner, T. R., Padmore, H. A. & Keller, R. (1996). *Rev. Sci. Instrum.* **67**, 1.

Richard, M. N., Koetschau, I. & Dahn, J. R. (1997). *J. Electrochem. Soc.* **144**, 554–557.

Richardsen, H., Vierl, U., Cevc, G. & Fenzl, W. (1996). *Europhys. Lett.* **34**, 543–548.

Richwin, M., Zaeper, R., Lützenkirchen-Hecht, D. & Frahm, R. (2001). *J. Synchrotron Rad.* **8**, 354–356.

Richwin, M., Zaeper, R., Lützenkirchen-Hecht, D. & Frahm, R. (2002). *Rev. Sci. Instrum.* **73**, 1668–1670.

Riekel, C., Burghammer, M. & Müller, M. (2000). *J. Appl. Cryst.* **33**, 421.

Riekel, C., Müller, M. & Vollrath, F. (1999). *Macromolecules* **32**, 4464.

Rietveld, H. M. (1969). *J. Appl. Cryst.* **2**, 65–71.

Robberecht, W. J. (2000). *Neurol.* **247**, I/1 – I/6.

Roch, T., Holy, V., Hesse, A., Stangl, J., Fromherz, T., Bauerand, G., Metzger, T. H. & Ferrer, S. (2002). *Phys. Rev. B* **65**, 245324.

Rochon, P., Batalla, E. & Natansohn, A. (1995). *Appl. Phys. Lett.* **66**, 136.

Rodriguez, J. A., Hanson, J. C., Frenkel, A. I., Kim, J. Y. & Perez, M. (2002). *J. Am. Chem. Soc.* **124**, 346–354.

Röhlsberger, R. (2001). *J. Phys.: Condens. Matter* **13**, 7659–7677.

Röhlsberger, R., Bansmann, J., Senz, V., Jonas, K. L., Bettac, A., , Meiwes-Broer, K. H. & Leupold, O. (2003). *Phys. Rev. B* **67**, 245412.

Röhlsberger, R., Thomas, H., Schlage, K., Burkel, E., Leupold, O. & Rüffer, R. (2002). *Phys. Rev. Lett.* **89**, 237201.

Ropert, A., Filhol, J., Elleaume, P., Farvacque, L., Hardy, L., Jacob, J. & Weinrich, U. (2000). Towards the ultimate storage ring-based light source. *Proceedings of the 7th European Particle Accelerator Conference (EPAC 2000)*, pages 83–87.

Ross, M. (2003). Laser-based profile monitor for electron beams. *Proc. of Particle Accelerator Conference (PAC03)*, Portland, Oregon. SLAC.

Rossbach, J. (1987). DESY Internal Report HERA-87-06.

Rossbach, J. (1988). *Part. Accel.* **23**, 121.

Ruckert, T., Keune, W., Sturhahn, W., Hu, M. Y., Sutter, J. P., Toellner, T. S. & Alp, E. E. (2000). *Hyperfine Interact.* **126**, 363.

Rühle, M., Dosch, H., Mittemeijer, E. J. & Voorde van de, M. H. (2001). *European White Book on Fundamental Research in Materials Science*. Stuttgart: Max Planck Institute for Metals Science.

Ruocco, G. & Sette, F. (1999). *J. Phys.: Cond. Matt.* **11**, R259.

Ruocco, G., Sette, F., Bergmann, U., Krisch, M., Masciovecchio, C., Mazzacurati, V., Signorelli, G. & Verbeni, R. (1996). *Nature (London)* **379**, 521.

Ruppersberg, H., Detemple, I. & Krier, J. (1989). *Phys. Status Solidi A* **116**, 681–687.

Rupprecht, K., Friedmann, T., Giefers, H., Wortmann, G., Doyle, B. & Zukrowski, J. (2002). *High Pressure Research* **22**, 189.

Rupprecht, K., Ponkratz, U. & Wortmann, G. (2003). *ESRF Exp. Report HE-1490* submitted.

Russell, R., Millett, I. S., Tate, M. W., Kwok, L. W., Nakatani, B., Gruner, S. M., Mochrie, S. G., Pande, V., Doniach, S., Herschlag, D. & Pollack, L. (2002). *Proc. Natl. Acad. Sci. USA* **99**, 4266–4271.

Sack, S., Müller, J., Marx, A., Thormählen, M., Mandelkow, E.-M., Brady, S. & Mandelkow, E. (1997). *Biochemistry* **36**, 16155–16165.

Saenger, W., Jordan, P. & Krauss, N. (2002). *Curr. Opin. Struct. Biol.* **12**, 244–254.

Saitoh, Y., Kimura, H., Suzuki, Y., Nakatani, T., Matsushita, T., Muro, T., Miyahara, T., Fujisawa, M., Soda, K., Ueda, S., Harada, H., Kotsugi, M., Sekiyama, A. & Suga, S. (2000). *Rev. Sci. Instr.* **71**, 3254–3259.

Saitoh, Y., Nakatani, T. & Matsushita, T. (1998). *J. Synchrotron Rad.* **5**, 542–544.

Saitoh, Y., Nakatani, T., Matsushita, T., Miyahara, T., Fujisawa, M., Soda, K., Muro, T. ., Ueda, S., Harada, H., Sekiyama, A., Imada, S., Daimon, H. & Suga, S. (1998). *J. Synchrotron Rad.* **5**, 542–544.

Salbu, B., Janssens, K., Lind, O. C., Proost, K. & Danesi, P. R. (2003). *J. Env. Radioactivity* **64**, 167–173.

Salbu, B., Krekling, T., Lind, O. C., Oughton, D. H., Drakopoulos, M., Simionovici, A., Snigireva, I., Snigirev, A., Weitkamp, T., Adams, F., Janssens, K. & Kashparov, V. A. (2001). *Nucl. Instr. Methods Phys. Res. A* **467**, 1249–1252.

Salditt, T., Metzger, T. H. & Peisl, J. (1994). *Phys. Rev. Lett.* **73**, 2228.

Sali, A., Glaeser, R., Earnest, T. & Baumeister, W. (2003). *Nature (London)* **422**, 216–225.

Salvo, L., Cloetens, P., Maire, E., Zabler, S., Blandin, J. J., Buffiere, J. Y., Ludwig, W., Boller, E., Bellet, D. & Josserond, C. (2003). *Nucl. Instr. Methods Phys. Res. B* **200**, 273–286.

Sanosian, K. N. (2002). Radiation safety considerations for candle light source. *Proceedings of the 8th European Particle Accelerator Conference (EPAC 2002)*, volume 2, pages 2667–2669, Paris.

Sasaki, S. (1994). *Nucl. Instr. Methods Phys. Res. A* **347**, 83–86.

Sasaki, S. (1998). Technical report, Sincrotrone Trieste.

Sasaki, S., Diviacco, B. & Walker, R. P. (1998). *Proceedings of the 6th European Particle Accelerator Conference (EPAC 1998), Stockholm, Sweden* page 2237.

Sasaki, S., Kakuno, K., Takada, T., Shimada, T., Yanegida, K. & Miyahara, Y. (1993). *Nucl. Instr. Methods Phys. Res. A* **331**, 763–767.

Sasaki, S., Kobayashi, H., Takao, M., Miyahara, Y. & Hashimoto, S. (1995). *Rev. Sci. Instrum.* **66**, 1953.

Sawhney, K. J. S., Senf, F., Scheer, M., Schäfers, F., Bahrdt, J., Gaupp, A. & Gudat, W. (1997). *Nucl. Instr. Methods Phys. Res. A* **390**, 395–402.

Scheufler, C., Brinker, A., Bourenkov, G., Pegoraro, S., Moroder, L., Bartunik, H., Hartl, F. & Moarefi, I. (2000). *Cell* **101**, 199–210.

Schiller, C., Rasche, C., Wehmöller, M., Beckmann, F., Eufinger, H., Epple, M. & Weihe, S. (2004). *Biomaterials* **25**, 1239–1247.

Schippers, S., Müller, A., Ricz, S., Bannister, M. E., Dunn, G. H., Schlachter, A. S., Hinojosa, G., Cisneros, C., Aguilar, A., Covington, A. M., Gharaibeh, M. F. & Phaneuf, R. A. (2003). *Phys. Rev. A* **67**, 032702.

Schlott, V. (2002). Proceedings of the 8th European Particle Accelerator Conference (EPAC 2002), Paris, France.

Schlünzen, F., Tocilj, A., Zarivach, R., Harms, J., Glühmann, M., Janell, D., Bashan, A., Bartels, H., Agmon, I., Franceschi, F. & Yonath, A. (2000). *Cell* **102**, 615–623.

Schmahl, W. W., Khalil-Allafi, J., Hasse, B., Wagner, M., Heckmann, A. & Somsen, C. (2004). *Materials Science & Engineering* A, in print.

Schmidbauer, M., Wiebach, T., Raidt, H., Hanke, M., Wawra, H. & Köhler, R. (1998). *Phys. Rev. B* **58**, 10523.

Schmidt, A. & Lamzin, V. (2002). *Curr. Opin. Struct. Biol.* **12**, 698–703.

Schmidt, C. & Rickers, K. (2003). *Am. Mineral.* **88**, 288 – 292.

Schmidt, F. (1991). CERN-SL-91-52-AP.

Schmidt, F. (2000). Geneva, CERN, 2002.

Schmidt, S., Poulsen, H. F. & Vaughan, G. B. M. (2003). *Journal of Applied Crystallography* 36**2**, 326–332.

Schmidt, T. (2003). *private communication*.

Schmidt, T., Groh, U., Fink, R., Umbach, E., Schaff, O., Engel, W., Richter, B., Kuhlenbeck, H., Schlögl, R., Freund, H.-J., Bradshaw, A. M., Preikszas, D., Hartel, P., Spehr, R., Rose, H., Lilienkamp, G., Bauer, E. & Benner, G. (2003). *Surf. Rev. Lett.* **9**, 223.

Schmolzer, S., Grabner, D., Gradzielski, M. & Narayanan, T. (2002). *Phys. Rev. Lett.* **88**, 258301.

Schotte, F., Lim, M., Jackson, T., Smirnov, A., Soman, J., Olson, J., Phillips, G. J., Wulff, M. & Anfinrud, P. (2003). *Science* **300**, 1944–1947.

Schröder, W., Schroer, C., Lengeler, B., Tümmler, J., Günzler, F., Simionovici, A. & Snigirev, A. (1999). *ESRF Highlights 1999*.

Schröder, W. H. & Fain, G. L. (1984). *Nature (London)* **309**, 268–270.

Schroer, C. G., Kuhlmann, M., Günzler, T. F., Lengeler, B., Richwin, M., Griesebock, B., Lützenkirchen-Hecht, D., Frahm, R., Ziegler, E., Mashayekhi, A., Haeffner, D. R., Grunwaldt, J.-D. & Baiker, A. (2003a). *Appl. Phys. Lett.* **82**, 3360–3362.

Schroer, C. G., Kuhlmann, M., Hunger, U. T., Günzler, T. F., Kurapova, O., Feste, S., Frehse, F., Lengeler, B., Drakopoulos, M., Somogyi, A., Simionovici, A., Snigirev, A., Snigireva, I., Schug, C. & Schroder, W. H. (2003b). *Appl. Phys. Lett.* **82**, 1485–1487.

Schroer, C. G., Meyer, J., Kuhlmann, M., Benner, B., Günzler, T. F., Lengeler, B., Rau, C., Weitkamp, T., Snigirev, A. & I, I. S. (2003c). *J. de Physique IV* **104**, 271.

Schroer, C. G., Meyer, J., Kuhlmann, M., Benner, B., Günzler, T. F., Lengeler, B., Rau, C., Weitkamp, T., Snigirev, A. & Snigireva, I. (2002a). *Appl. Phys. Lett.* **81**, 1527–1529.

Schroer, C. G., Meyer, J., Kuhlmann, M., Brenner, B., Günzler, T. & Lengeler, B. (2002b). *Appl. Phys. Lett.* **81**, 1527–1529.

Schulte-Schrepping, H., Hahn, U., Tiedke, K., Brüggmann, U. & Jastrow, U. (2003). Beam position detection using ionized gases. Technical report, HASYLAB at DESY.

Schüßler-Langeheine, C., Weschke, E., Grigoriev, A. Y., Ott, H., Meier, R., Vyalikh, D. V., Mazumdar, C., Sutter, C., Abernathy, D., Grübel, G. & Kaindl, G. (2001). *Journ. Electron. Spectrosc. Relat. Phenom.* **114-116**, 953.

Schütz, G., Wagner, W., Wilhelm, W., Kienle, P., Zeller, R., Frahm, R. & Materlik, G. (1987). *Phys. Rev. Lett.* **58**, 737.

Scott, R. (2004). submitted.

Scott, R. A., Hahn, J. F., Doniach, S., Freeman, H. C. & Hodgson, K. O. (1982). *J. Am. Chem. Soc.* **104**, 5364–5369.

Seemann, J. T. (1999). Commissioning results of the KEKB and PEP-II B-factories. *PAC 1999*, New York.

Sekiyama, A., Fujiwara, H., Imada, S., Eisaki, H., Uchida, S. I., Takegahara, K., Harima, H., Saitoh, Y. & Suga, S. (2003a). *Phys. Rev. Lett.* submitted,cond-mat/0206471.

Sekiyama, A., Fujiwara, H., Imada, S., Suga, S., Eisaki, H., Uchida, S. I., Takegahara, K., Harima, H., Saitoh, Y., Nekrasov, I. A., Keller, G., Kondakov, D. E., Kozhevnikov, A. V., Pruschke, T., Held, K., Vollhardt, D. & Anisimov, V. I. (2003b). *Phys. Rev. Lett.* submitted,cond-mat/0312429.

Sekiyama, A., Iwasaki, T., Matsuda, K., Saitoh, Y., Onuki, Y. & Suga, S. (2000). *Nature (London)* **403**, 396 – 398.

Sepiol, B. & Vogl, G. (2003). *Diffusion in Condensed Matter - From the Elementary Step to Transport in Complex Systems*. Heidelberg: Springer.

Sepliarsky, M. & Phillpot, S. R. (2000). *Appl. Phys. Lett.* **76**, 3986.

Serda, P., Grochowski, J. & Duddeck, H. (2004). *J. Alloys Comp.* **362**, 224–230.

Sergueev, I., Bürck van, U., Chumakov, A. I., Asthalter, T., Smirnov, G. V., Franz, H., Rüffer, R. & Petry, W. (2003). *Phys. Rev. Lett.* submitted.

Sergueev, I., Franz, H., Asthalter, T., Petry, W., Bürck van, U. & Smirnov, G. (2002). *Phys. Rev. B* **66**, 184210.

Sette, F., Krisch, M. H., Masciovecchio, C., Ruocco, G. & Monaco, G. (1998). *Science* **280**, 1550.

Sette, F., Ruocco, G., Krisch, M., Masciovecchio, C. & Verbeni, R. (1996). *Physica Scripta* T**66**, 48.

Sève, L., Jaouen, N., Tonnerre, J. M., Raoux, D. & Bartolomé, F. (1999). *Phys. Rev. B* **60**, 9662.

Seydel, T., Madsen, A., Tolan, M., Grübel, G. & Press, W. (2001). *Phys. Rev. B* **63**, 73409.

Shapiro, S. M., Yang, B. X., Shirane, G., Noda, Y. & Tanner, L. E. (1989). *Phys. Rev. Lett.* **62**, 1298.

Shastri, S. D. (2004). *J. Synchrotron Rad.* **11**, 150–156.

Shastri, S. D., Fezzaa, K., Mashayekhi, A., Lee, W.-K., Fernandez, P. B. & Lee, P. L. (2002). *J. Synchrotron Rad.* **9**, 317–322.

Shastri, S. D., Maser, J. M., Lai, B. & Tys, J. (2001). *Opt. Commun.* **197**, 9.

Shen, Q., Kycia, S. W., Tentarelli, E. S., Schaff, W. J. & Eastman, L. F. (1996). *Phys. Rev. B* **54**, 16381.

Shenoy, G., Lewellen, J., Shu, D. & Vinokurov, N. (2003a). Variable-Period Undulators-A Potential Source for Storage Ring, ERL and FEL Applications. *Proceedings of the 8th International Conference on Synchrotron Radiation Instrumentation (SRI'03)*, San Francisco, USA.

Shenoy, G. K., Lewellen, J. W., Shu, D. & Vinokurov, N. A. (2003b). *J. Synchrotron Rad.* **10**, 205–213.

Shiltsev, V. D. (1996). Talk given at 5th European Particle Accelerator Conference (EPAC 96), Sitges, Spain, 10-14 Jun 1996.

Shu, D., Toellner, T. S. & Alp, E. E. (2001). *Nucl. Instrum. Methods Phys. Res. A* **467-468**, 771.

Shu, Q. & Rand, S. (1997). *Phys. Rev. B* **55**, 8776.

Shukla, A., Calandra, M., Astuto, M. D., Lazzeri, M., Mauri, F., Bellin, C., Krisch, M., Karpinski, J., Kazakov, S. M., Jun, J., Daghero, D. & Parlinski, K. (2003). *Phys. Rev. Lett.* **90**, 095506.

Shvyd'ko, Y. V. (2003). *X-ray optics. High Energy-Resolution Applications*. Optical Sciences. Berlin: Springer.

Shvyd'ko, Y. V. (2004). *X-ray Optics. High Energy-Resolution Applications*. Berlin: Springer Verlag.

Shvyd'ko, Y. V., Gerken, M., Franz, H., Lucht, M. & Gerdau, E. (2001). *Europhys. Lett.* **56**, 39.

Shvyd'ko, Y. V., Lerche, M., Jäschke, J., Lucht, M., Gerdau, E., Gerken, M., Rüter, H. D., Wille, H. C., Becker, P., Alp, E. E., Sturhahn, W., Sutter, J. & Toellner, T. S. (2000). *Phys. Rev. Lett.* **85**, 495.

Sikharulidze, I., Dolbnya, I., Fera, A., Madsen, A., Ostrovskii, B. & Jeu de, W. (2002). *Phys. Rev. Lett.* **88**, 115503.

Simon, J. P., Lyon, O. & Fontaine de, D. (1985). *J. Appl. Cryst.* **18**, 230–236.

Sinha, S. K., Sirota, E. B., Garoff, S. & Stanley, H. B. (1988). *Phys. Rev. B* **38**, 2297.

Sinn, H., Alp, E. E., Alatas, A., Barraza, J., Bortel, G., Burkel, E., Shu, D., Sturhahn, W., Sutter, J. P., Toellner, T. S. & Zhao, J. (2001). *Nucl. Instrum. Methods Phys. Res. A* **467-468**, 1545.

Sinn, H., Moldovan, N., Said, A. H. & Alp, E. E. (2002). *Proc. SPIE - Int. Soc. Opt. Eng.* **4783**, 123.

Sirringhaus, H., Brown, P., Friend, R., Nielsen, M., Bechgaard, K., Langeveld-Voss, B., Spiering, A., Janssen, R., Meijer, E., Herwig, P. & Leeuw de, D. (1999). *Nature (London)* **401**, 685.

Sitepu, H., Klönne, M., Schmahl, W. W., Predki, W. & Pirling, T. (2003). *J. de Physique IV* **112**, 811–814.

Sittner, P., Novak, V., Lukas, P., Lugovyy, D., Neov, D. & Tovar, M. (2002). *Mater. Sci. Forum* **404**, 829–834.

Sladecek, M., Sepiol, B., Kaisermayr, M., Korecki, J., Handke, B., Thiess, H., Leupold, O., Rüffer, R. & Vogl, G. (2001). *Surf. Sci.* **507–510C**, 124.

Sladecek, M., Sepiol, B., Korecki, J., Handke, B., Rüffer, R. & Vogl, G. (2003). *Surf. Sci.* to be published.

Sloutskin, E., Gang, O., Kraack, H., Ocko, B. M., Sirota, E. B. & Deutsch, M. (2002). *Phys. Rev. Lett.* **89**, 065501.

Smith, T. (2003). *Nature (London)* **423**, 799–800.

Snell, G., Drescher, M., Müller, N., Heinzmann, U., Hergenhahn, U., Viefhaus, J., Heiser, F., Becker, U. & Brookes, N. (1996). *Phys. Rev. Lett.* **76**, 3923.

Snigirev, A., Kohn, V., Snigireva, I. & Lengeler, B. (1996). *Nature (London)* **384**, 49–51.

Snigirev, A., Snigireva, I., Kohn, V., Kuznetsov, S. & Schelokov, I. (1995). *Rev. Sci. Instrum.* **66**, 5486–5492.

Sokolova, A. V., Volkov, V. V. & Svergun, D. I. (2003). *J. Appl. Cryst.* **36**, 865–868.

Somogyi, A., Drakopoulos, M., Vincze, L., Vekemans, B., Camerani, C., Janssens, K., Snigirev, A. & Adams, F. (2001). *X-ray Spectrometry* **30**, 242–252.

Song, Y.-H., Marx, A., Müller, J., Woehlke, G., Schliwa, M., Krebs, A., Hoenger, A. & Mandelkow, E. (2001). *EMBO J.* **20**, 6213–6225.

Spanne, P., Raven, C., Snigireva, I. & Snigirev, A. (1999). *Phys. Med. Biol.* **44**, 741–749.

Stampanoni, M., Borchert, G., Abela, R. & Rüegsegger, P. (2002). *J. Appl. Phys.* **92**, 7630–7635.

Steinle-Neumann, G., Stixrude, L., Cohen, R. E. & Gülseren, O. (2001). *Nature (London)* **413**, 57.

Stöhr, J. (1999). *J. Magn. Magn. Mater.* **200**, 470.

Strempfer, J., Rütt, U., Bayrakci, S. P., Brückel, T. & Jauch, W. (2004). *Phys. Rev. B* **69**, 014417.

Strempfer, J., Zegkinoglou, I., Nelson, C., Hill, J., Lang, J., Srajer, G. & Keimer, B. (2003). *to be published*.

Stribeck, N., Bayer, R., Krosigk, G. & Gehrke, R. (2002a). *Polymer* **43**, 3779.

Stribeck, N., Buzdugan, E., Ghioca, P., Serban, S. & Gehrke, R. (2002b). *Macromol. Chem. Phys.* **203**, 636.

Stribeck, N., Fakirov, S., Apostolov, A. A., Denchev, Z. & Gehrke, R. (2003). *Macromol. Chem. Phys.* **204**, 1000.

Struzhkin, V. V., Mao, H. K., Hu, J., Schwoerer-Böhning, M., Shu, J., Hemley, R. J., Sturhahn, W., Hu, M. Y., Alp, E. E., Eng, P. & Shen, G. (2001). *Phys. Rev. Lett.* **87**, 255501.

Stuart, A. D., McKee, T. A., Williams, P. A., Harley, C., Shen, S., Stuart, D. I., Brown, T. D. & Lea, S. M. (2002). *J. Virol* **76**, 7694–7704.

Stuhrmann, H. B. (1985). *Advances in Polymer Science* **67**, 123–163.

Suck, J. B., Rudin, H., Güntherodt, H. J. & Beck, H. (1983). *Phys. Rev. Lett.* **50**, 1983.

Suortti, P., Lienert, U. & Schulze, C. (1994). *Nucl. Instrum. Methods Phys. Res. A* **338**, 27.

Suortti, P. & Schulze, C. (1995). *J. Synchrotron Rad.* **2**, 6.

Susini, J., Salome, M., Fayard, B., Ortega, R. & Kaulich, B. (2002). *Surf. Rev. Lett.* **9**, 223–232.

Susini, J., Salome, M., Neuhaeusler, U., Dhez, O., Fayard, B., Somogyi, A., Bohic, S., Bleuet, P., Martinex-Criado, G., Tucoulou, R., Simionovici, A., Barrett, R., & Drakopoulos, M. (2003). *Synchrotron Radiation News* **16**, 35–43.

Sutton, M., Nagler, S., Mochrie, S., Greytak, T., Bermann, L., Held, G. & Stephenson, G. (1991). *Nature (London)* **352**, 608.

Sutton, S. R., Bertsch, P. M., Newville, M., Rivers, M., Lanzirotti, A. & Eng, P. (2002). *Rev. Mineral Geochem.* **49**, 429–483.

Suzuki, Y., Watanabe, N., Aoki, S. & Kagoshima, Y. (2003). *Synchrotron Radiation News* **16**, 44–48.

Svergun, D. I. (1999). *Biophys J.* **76**, 2879–2886.

Svergun, D. I. & Koch, M. H. J. (2002). *Curr. Opin. Struct. Biol.* **12**, 654–660.

Svergun, D. I., Konarev, P. V., Volkov, V. V., Koch, M. H. J., Sager, W. F. C., Smeets, J. & Blokhuis, E. M. (2000). *J. Chem. Phys.* **113**, 1651–1665.

Svergun, D. I., Petoukhov, M. V. & Koch, M. H. J. (2001). *Biophys J.* **80**, 2946–2953.

Swamy, V., Dubrovinsky, L. S., Dubrovinskaia, N. A., Simionovici, A. S., Drakopoulos, M., Dmitriev, V. & Weber, H. P. (2003). *Sol. State Comm.* **125**, 111–115.

Swartjes, F. H. M., Peters, G. W. M., Rastogi, S. & Meijer, H. E. H. (2003). *Int. Polym. Proc.* **18**, 53–66.

Szczerbowska-Boruchowska, M., Lankosz, M., Ostachowicz, J., Adamek, D., Krygowska-Wajs, A., Tomik, B., Szczudlik, A., Simionovici, A. & Bohic, S. (2003). *J. de Physique IV* **104**, 325–328.

Takahashi, S., Aoyagi, H., Mochizuki, T., Oura, M., Sakurai, Y., Watanabe, A. & Kitamura, H. (2001). *Nucl. Instrum. Methods Phys. Res. A* **467-468**, 758–761.

Takeda, T., Momose, A., Ueno, E. & Itai, Y. (1998). *J. Synchrotron Rad.* **5**, 1133–1135.

Tamura, S., Murai, K., Kamijo, N., Yoshida, K., Kihara, H. & Suzuki, Y. (2000). *Vacuum* **59**, 553–558.

Tanaka, T. & Kitamura, H. (1995). *Nucl. Instr. Methods Phys. Res. A* **364**, 368–373.

Tanaka, T. & Kitamura, H. (2000). *Nucl. Instr. Methods Phys. Res. A* **449**, 629–637.

Tanaka, T. & Kitamura, H. (2001). *J. Synchrotron Rad.* **8**, 1221.

Tanaka, T. & Kitamura, H. (2003). *Program: SPECTRA*. RIKEN, Institute of Physical and Chemical Research.

Tanida, H. & Ishii, M. (2001). *Nucl. Instrum. Methods Phys. Res. A* **467–468**, 1564–1567.

Tarazona, E. & Elleaume, P. (1995). *Rev. Sci. Instrum.* **66**, 1974.

Tarazona, E., Elleaume, P., Chavanne, J., Hartman, Y., Snigirev, A. & Snigireva, I. (1994). *Rev. Sci. Instrum.* **65**, 1959.

Templeton, A. S., Trainor, T. P., Spormann, A. M., Newville, M., Sutton, S. R., Dohnalkova, A., Gorby, Y. & Brown, G. E. (2003). *Env. Sci & Techn.* **37**, 300–307.

Terry, A. E., Hobbs, J. K., Organ, S. J. & J., B. P. (2003). *Polymer* **44**, 3001–3008.

Than, M., Henrich, S., Huber, R., Ries, A., Mann, K., Kuhn, K., Timpl, R., Bourenkov, G., Bartunik, H. & Bode, W. (2002). *Proc. Natl. Acad. Sci. USA* **99**, 6607–6612.

Thole, B. T., Carra, P., Sette, F. & Laan van der, G. (1992). *Phys. Rev. Lett.* **68**, 1943.

Thurn-Albrecht, T., Steffen, W., Patkowski, A., Meier, G., Fischer, E., Grübel, G. & Abernathy, D. (1996). *Phys. Rev. Lett.* **77**, 5437.

Thurn-Albrecht, T., Zontone, F., Grübel, G., Steffen, W., Müller-Buschbaum, P. & Patkowski, A. (2003). *Phys. Rev. E* **68**, 31407.

Toellner, T. S., Hu, M. Y., Sturhahn, W., Quast, K. & Alp, E. E. (1997). *Appl. Phys. Lett.* **71**, 2112.

Toellner, T. S. & Shu, D. (2001). private communication.

Toellner, T. S., Shu, D., Sturhahn, W., Alp, E. E. & Zhao, J. (2002). private communication.

Tokunaga, T. K., Wan, J. M., Hazen, T. C., Schwartz, E., Firestone, M. K., Sutton, S. R., M, M. N., Olson, K. R., Lanzirotti, A. & Rao, W. (2003). *J. Env. Qual.* **32**, 541–549.

Tokura, Y. & Nagaosa, N. (2000). *Science* **288**, 462.

Tolan, M. (1999). *X-Ray Scattering from Soft-Matter Thin Films: Materials Science and Basic Research*. Berlin: Springer Verlag.

Topsøe, H. J. (2003). *Catal.* **216**, 155.

Trakhtenberg, E. et al. (2003). New insertion device vacuum chambers at the Advanced Photon Source. *Proceedings of the 2003 Particle Accelerator Conference*.

Tranquada, J. M., Buttrey, D. J., Sachan, V. & Lorenzo, J. E. (1994). *Phys. Rev. Lett.* **73**, 1003.

Tranquada, J. M., Sternlieb, B. J., Axe, J. D., Nakamura, Y. & Uchida, S. (1995). *Nature (London)* **375**, 561.

Trautwein, A. X. & Winkler, H. (1999). *Hyperfine Interact.* **123/124**, 561.

Uson, I., Schmidt, B., Bulow von, R., Grimme, S., Figura von, K., Dauter, M., Rajashankar, K., Dauter, Z. & Sheldrick, G. (2003). *Acta Cryst. D* **59**, 57–66.

Vad, T., Haubold, H.-G., Waldöfner, N. & Bönnemann, H. (2002). *J. Appl. Cryst.* **35**, 459–470.

Van Acker, K., De Buyser, L., Celis, J. P., Van Houtte, P. & Aernoudt, E. (1993). *Proc. First Forum Young Researchers, July 18-23, 1993* pages 61–66.

Vanko, D. A., Bonnin-Mosbah, M., Philippot, P., Roedder, E. & Sutton, S. (2001). *Chemical Geology* **173**, 227–238.

Varga, L., Giles, C., Zheng, Y. L., Pizzini, S., Bergevin de, F., Fontaine, A. & Malgrange, C. (1999). *J. Synchrotron Rad.* **6**, 1125–1132.

Vasiliu-Doloc, L., Rosenkranz, S., Osborn, R., Sinha, S. K., Lynn, J. W., Mesot, J., Seeck, O. H., Preosti, G., Fedro, A. J. & Mitchell, J. F. (1999). *Phys. Rev. Lett.* **83**, 4393.

Vekemans, B., Vincze, L., Somogyi, A., Drakopoulos, M., Kempenaers, L., Simionovici, A. & Adams, F. (2003). *Nucl. Instr. Methods Phys. Res. B* **199**, 396–401.

Verbeni, R., Sette, F., Krisch, M. H., Bergmann, U., Gorges, B., Halcoussis, C., Martel, K., Masciovecchio, C., Ribois, J. F., Ruocco, G. & Sinn, H. (1996). *J. Synchrotron Rad.* **3**, 62.

Viefhaus, J., Cvejanović, S., Langer, B., Lischke, T., Prümper, G., Rolles, D., Golovin, A. V., Grum-Grzhimailo, A. N., Kabachnik, N. M. & Becker, U. (2004). *Phys. Rev. Lett.* **92**, 083001.

Vincze, L., Somogyi, A., Osan, J., Vekemans, B., Török, S., Janssens, K. & Adams, F. (2002a). *Analytical Chemistry* **74**, 1128–1135.

Vincze, L., Vekemans, B., Szalki, I., Janssens, K., VanGrieken, R., Feng, H., Jones, K. W. & Adams, F. (2002b). High-resolution x-ray fluorescence micro-tomography on single sediment particles. *Proceedings SPIE conference on "Developments in X-ray tomography"*, edited by U. Bonse, pages 240–245.

Virojanadara, C., Johansson, L. I., Glanz, P. A., Eickhoff, T. & Drube, W. (2001). *Appl. Surf. Sci.* **172**, 253–259.

Vogl, G. & Sepiol, B. (1999). *Hyperfine Interact.* **123/124**, 595–609.

Voigt, J., Kentzinger, E., Rücker, U., Wermeille, D., Hupfeld, D., Schweika, W., Schmidt, W. & Brückel, T. (2004). *Europhys. Lett.* **65**, 560–566.

Wagner, C. D. (1975). *Farad. Discuss. Chem. Soc.* **60**, 291.

Wakimoto, S., Birgeneau, R. J., Fujimaki, Y., Ichikawa, N., Kasuga, T., Kim, Y. J., Kojima, K. M., Lee, S.-H., Niko, H., Tranquada, J. M., Uchida, S. & Zimmermann v., M. (2003). *Phys. Rev. B* **67**, 184419.

Walker, R. P. (1993). *Nucl. Instr. Methods Phys. Res. A* **335**, 328–337.

Wang, J., Sood, A., Satyam, P., Feng, Y., Wu, X., Cai, Z., Yun, W. & Sinha, S. (1998a). *Phys. Rev. Lett.* **80**, 1110.

Wang, L., Pyzalla, A., Stadlbauer, W. & Werner, E. A. (2003a). *Mat. Sci. Eng. A* **359**, 31–43.

Wang, Y., Carlo, F. D., Mancini, D. C., McNulty, I., Tieman, B., Bresnahan, J., Foster, I., Insley, J., Lane, P., Laszewski von, G., Kesselman, C., Su, M.-H. & Thiebaux, M. (2001). *Rev. Sci. Instrum.* **72**, 2062–2068.

Wang, Y., DuBois, J. L., Hedman, B., Hodgson, K. O. & Stack, T. D. P. (1998b). *Science* **35**, 537–540.

Wang, Z. & Hahn, U. (1996a). Design analysis with XRAP for PETRA/HASYLAB beamline filters/windows. *Optics for High brightness synchrotron radiation beamlines*, volume 2856, pages 268–278.

Wang, Z. & Hahn, U. (1996b). Geometry and parameter optimization of PETRA undulator beamline slits. *Optics for High brightness synchrotron radiation beamlines*, volume 2855, pages 242–249.

Wang, Z., Hsiao, B. S., Stribeck, N. & Gehrke, R. (2003b). *Macromolecules* **35**, 2200.

Wanzenberg, R. (2003). DESY Internal Report M-03-02.

Warwick, T., Andresen, N., Comins, J., Franck, A., Gilles, M., Tonnessen, T. & Tyliszczak, Y. (2003). *AIP Conf. Proc.* to be published.

Watson, G. M., Gibbs, D., Lander, G. H., Gaulin, B. D., Berman, L. E., Matzke, H. & Ellis, W. (2000). *Phys. Rev. B* **61**, 8966.

Wcislak, L., Klein, H., Bunge, H. J., Garbe, U., Tschentscher, T. & Schneider, J. R. (2002). *J. Appl. Cryst.* **35**, 82–95.

Webster, P. J., Oosterkamp, L. D., Browne, P. A., Hugues, D. J., Kang, W. P., Withers, P. J. & Vaughan, G. B. M. (2001). *J. Strain Anal.* **36**, 61–70.

Weiland, T. (1981a). DESY Internal Report M-81/04.

Weiland, T. (1981b). DESY Internal Report M-81/23.

Weiss, P., Obadia, L., Magne, D., Bourges, X., Rau, C., Weitkamp, T., Khairoun, I., Bouler, J., Chappard, D., Gauthier, O. & Daculsi, G. (2003). *Biomaterials* **24**, 4591–4601.

Werner, M. & Wittenburg, K. (2001). A new wirescanner control unit. *Proc. of 5th European Workshop on Diagnostics and Beam Instrumentation*, Grenoble. ESRF.

Wess, T., Alberts, I., Hiller, J., Drakopoulos, M., Chamberlain, A. T. & Collins, M. (2002). *Calcif. Tissue Int.* **70**, 103–110.

Whittaker & Whittaker (1996). *Biochemistry* **35**, 6762–6770.

Wichtendahl, R., Fink, R., Kuhlenbeck, H., Preikszas, D., Rose, H., Spehr, R., Hartel, P., Engel, W., Schlögl, R., Freund, H.-J., Bradshaw, A. M., Lilienkamp, G., Schmidt, T., Bauer, E., Benner, G. & Umbach, E. (1998). *Surf. Rev. Lett.* **5**, 1249.

Wiedemann, H. (1993). *PARTICLE ACCELERATOR PHYSICS: Basic principles and linear beam dynamics*. Springer.

Wienands, U. (2001). Vacuum performance and beam lifetime in the PEP II storage rings. *Proceedings of the 2001 Particle Accelerator Conference*, pages 597–601.

Wierzbicka, M., Wysocka, I. A., Bulska, E. & Caruso, J. (2003). *Analyst* in press.

Wilkins, S. B., Hatton, P. D., Roper, M. D., Prabhakaran, D. & Boothroyd, A. T. (2003a). *Phys. Rev. Lett.* **90**, 187201.

Wilkins, S. B., Spencer, P. D., Hatton, P. D., Collins, S. P., Roper, M. D., Prabhakaran, D. & Boothroyd, A. T. (2003b). *Phys. Rev. Lett.* **91**, 167205.

Williams, G., Pfeifer, M., Vartanyants, I. & Robinson, I. (2003). *Phys. Rev. Lett.* **90**, 175501.

Withers, P. J., Preuss, M., Webster, P. J., Hughes, D. J. & Korsunsky, A. M. (2002). *Materials Science Forum* **404–407**, 1–12.

Wittenburg, K. (2000). Conventional wire scanners at tesla. Technical report, DESY.

Wlodawer, A. (2002). *Annu. Rev. Med.* **53**, 595–614.

Woicik, J. C., Nelson, E. J., Heskett, D., Warner, J., Berman, L. E., Karlin, B. A., Vartanyants, I. A., Hasan, M. Z., Kendelewicz, T., Shen, Z. X. & Pianetta, P. (2001). *Phys. Rev. B* **64**, 125115.

Woicik, J. C., Nelson, E. J., Kronik, L., Jain, M., Chelikowski, J. R., Heskett, D., Berman, L. E. & Herman, G. S. (2002). *Phys. Rev. Lett.* **89**, 077401.

Woicik, J. C., Nelson, E. J. & Pianetta, P. (2000). *Phys. Rev. Lett.* **84**, 773–776.

Wolff, S. (1978a). DESY - Internal Report PET-78-06, p. 23 and Internal Report B1-78-01, p. 23.

Wolff, S. (1978b). DESY - Internal Report B1-78-02, p. 51.

Wong, J., Krisch, M., Farber, D. L., Occelli, F., Schwartz, A. J., Chiang, T.-C., Wall, M., Boro, C. & Xu, R. (2003). *Science* **301**, 1078.

Worbs, M., Bourenkov, G. P., Bartunik, H. D., Huber, R. & Wahl, M. V. (2001). *Mol. Cell* **7**, 1177–1189.

Wroblewski, T. (1991). *Acta Cryst. A* **47**, 571–577.

Wroblewski, T. (2002). *Mater. Science Forum* **404–407**, 121–126.

Wroblewski, T., Clauss, O., Crostack, H.-A., Ertel, A., Fandrich, F., Genzel, C., Hradil, K. & Woldt, E. (1999). *Nucl. Instrum. Methods Phys. Res. A* **428**, 570–582.

Wu, R. & Freeman, A. J. (1994). *Phys. Rev. Lett.* **73**, 1994.

Xu, B., Ye, Y., Cross, L. E., Bernstein, J. J. & Miller, R. (1999). *Appl. Phys. Lett.* **74**, 3549.

Yabashi, M., Tamasaku, K. & Ishikawa, T. (2001). *Phys. Rev. Lett.* **87**, 140801.

Yabashi, M., Tamasaku, K., Kikuta, S. & Ishikawa, T. (2001). *Rev. Sci. Instrum.* **72**, 4080.

Yavari, A., Le Moulec, A., Inoue, A., Vaughan, G. & Kvick, Å. (2002). *Annales de Chimie Science des Matriaux* **27**, 107–112.

Yokoyama, T., Amemiya, K., Miyachi, M., Yonamoto, Y., Matsumura, D. & Ohta, T. (2000). *Phys. Rev. B* **62**, 14191.

Yonath, A. (2002). *Annu. Rev. Biophys. Biomol. Struct.* **31**, 257–73.

edited by R. A. Young (1993). *The Rietveld method.* Oxford University Press.

Yun, W., Lai, B., Krasnoperova, A. A., Fabrizio, E. D., Cai, Z., Cerrina, F., Chen, Z., Gentili, M. & Gluskin, E. (1999). *Rev. Sci. Instrum.* **70**, 3537.

Zaanen, J. & Gunnarsson, O. (1989). *Phys. Rev. B* **40**, 7391.

Zakharov, N. D., Talalaev, V. G., Werner, P., Tonkikh, A. A. & Cirlin, G. E. (2003). *Appl. Phys. Lett.* **83**, 3084–6.

Zegenhagen, J. (1993). *Surf. Sci. Rep.* **18**, 202–271.

Zhang, K., Rosenbaum, G. & Bunker, G. (1998). *J. Synchroton Rad.* **5**, 1227–1234.

Zhang, K., Rosenbaum, G. & Bunker, G. (1999). *J. Synchrotron Rad.* **6**, 220–221.

Zhang, L., Freund, A. K., Tschentscher, T. & Schulte-Schrepping, H. (2003). *Proceedings of the 8th International Conference on Synchrotron Radiation Instrumentation (SRI'03)*, San Francisco, USA.

Zhong, Z., Chapman, L. D., Bunker, B. A., Bunker, G., Fischetti, R. & Segre, C. U. (1999). *J. Synchroton. Rad.* **6**, 212–214.

Zhong, Z., Halilovich, A., Fromherz, T., Schäffler, F. & Bauer, G. (2003). *Appl. Phys. Lett.* **82**, 4779–4781.

Zhu, X. M., Feidenhans'l, R., Zabel, H., Als-Nielsen, J., Du, R., Flynn, C. P. & Grey, F. (1998). *Phys. Rev. B* **37**, 7157.

Zimmermann v., M., Schneider, J. R., Frello, T., Andersen, N. H., Madsen, J., Käll, M., Poulsen, H. F., Liang, R., Dosanjh, P. & Hardy, W. N. (2003). *Phys. Rev. B* **68**, 104515.

Zimmermann v., M., Vigliante, A., Niemöller, T., Ichikava, N., Frello, T., Madsen, J., Uchida, S., Andersen, N. H., Wochner, P., Tranquada, J. M., Gibbs, D. & Schneider, J. R. (1998). *Europhys. Lett.* **41**, 629–634.